

# Advances in Computational Fluid Dynamics and Its Applications

Guest Editors: Guan Heng Yeoh, Chaoqun Liu, Jiyuan Tu,  
and Victoria Timchenko





---

# **Advances in Computational Fluid Dynamics and Its Applications**

Modelling and Simulation in Engineering

---

## **Advances in Computational Fluid Dynamics and Its Applications**

Guest Editors: Guan Heng Yeoh, Chaoqun Liu, Jiyuan Tu,  
and Victoria Timchenko



---

Copyright © 2011 Hindawi Publishing Corporation. All rights reserved.

This is a special issue published in volume 2011 of “Modelling and Simulation in Engineering.” All articles are open access articles distributed under the Creative Commons Attribution License, which permits unrestricted use, distribution, and reproduction in any medium, provided the original work is properly cited.

## Editorial Board

K. Al-Begain, UK  
Adel M. Alimi, Tunisia  
Zeki Ayag, Turkey  
Andrzej Bargiela, UK  
Philippe Boisse, France  
Agostino Bruzzone, Italy  
Hing Kai Chan, UK  
Andrzej Dzielinski, Poland  
Xiaosheng Gao, USA  
F. Gao, UK  
Ricardo Goncalves, Portugal  
Ratan K. Guha, USA  
Chung-Souk Han, USA

Joanna Hartley, UK  
Jing-song Hong, China  
MuDer Jeng, Taiwan  
Iisakki Kosonen, Finland  
Laurent Mevel, France  
A. Mohamed, Malaysia  
Antonio Munjiza, UK  
Petr Musilek, Canada  
Tomoharu Nakashima, Japan  
Gaby Neumann, Germany  
Alessandra Orsoni, UK  
Javier Otamendi, Spain  
Evtim Peytchev, UK

Luis Carlos Rabelo, USA  
Ahmed Rachid, France  
Sellakkutti Rajendran, Singapore  
Waleed Smari, USA  
Boris Sokolov, Russia  
Rajan Srinivasan, India  
S. Taib, Malaysia  
Andreas Tolk, USA  
Bauke Vries, The Netherlands  
Farouk Yalaoui, France  
Ivan Zelinka, Czech Republic  
Qing-An Zeng, USA

# Contents

**Advances in Computational Fluid Dynamics and Its Applications**, Guan Heng Yeoh, Chaoqun Liu, Jiyuan Tu, and Victoria Timchenko  
Volume 2011, Article ID 304983, 3 pages

**New Findings by High-Order DNS for Late Flow Transition in a Boundary Layer**, Chaoqun Liu, Lin Chen, and Ping Lu  
Volume 2011, Article ID 721487, 16 pages

**Implicit LES for Supersonic Microramp Vortex Generator: New Discoveries and New Mechanisms**, Qin Li and Chaoqun Liu  
Volume 2011, Article ID 934982, 15 pages

**An Initial Investigation of Adjoint-Based Unstructured Grid Adaptation for Vortical Flow Simulations**, Li Li  
Volume 2011, Article ID 217326, 9 pages

**Assessment of Turbulence Models for Flow Simulation around a Wind Turbine Airfoil**, Fernando Villalpando, Marcelo Reggio, and Adrian Ilinca  
Volume 2011, Article ID 714146, 8 pages

**Computation of Ice Shedding Trajectories Using Cartesian Grids, Penalization, and Level Sets**, Héloïse Beaugendre, François Morency, Federico Gallizio, and Sophie Laurens  
Volume 2011, Article ID 274947, 15 pages

**Aerodynamic Optimization of an Over-the-Wing-Nacelle-Mount Configuration**, Daisuke Sasaki and Kazuhiro Nakahashi  
Volume 2011, Article ID 293078, 13 pages

**New Evaluation Technique for WTG Design Wind Speed Using a CFD-Model-Based Unsteady Flow Simulation with Wind Direction Changes**, Takanori Uchida, Takashi Maruyama, and Yuji Ohya  
Volume 2011, Article ID 941870, 6 pages

**Comparisons between the Wake of a Wind Turbine Generator Operated at Optimal Tip Speed Ratio and the Wake of a Stationary Disk**, Takanori Uchida, Yuji Ohya, and Kenichiro Sugitani  
Volume 2011, Article ID 749421, 7 pages

**Experimental and Numerical Simulations Predictions Comparison of Power and Efficiency in Hydraulic Turbine**, Laura Castro, Gustavo Urquiza, Adam Adamkowski, and Marcelo Reggio  
Volume 2011, Article ID 146054, 8 pages

**Simulating Smoke Filling in Big Halls by Computational Fluid Dynamics**, W. K. Chow, C. L. Chow, and S. S. Li  
Volume 2011, Article ID 781252, 16 pages

**Numerical Simulations for a Typical Train Fire in China**, W. K. Chow, K. C. Lam, N. K. Fong, S. S. Li, and Y. Gao  
Volume 2011, Article ID 369470, 7 pages

**Simulation of Pharyngeal Airway Interaction with Air Flow Using Low-Re Turbulence Model**, M. R. Rasani, K. Inthavong, and J. Y. Tu  
Volume 2011, Article ID 510472, 9 pages



---

**CFD-Guided Development of Test Rigs for Studying Erosion and Large-Particle Damage of Thermal Barrier Coatings**, Maria A. Kuczmarski, Robert A. Miller, and Dongming Zhu

Volume 2011, Article ID 837921, 13 pages

**Investigation of Swirling Flows in Mixing Chambers**, Jyh Jian Chen and Chun Huei Chen

Volume 2011, Article ID 259401, 15 pages

**Numerical Computation and Investigation of the Characteristics of Microscale Synthetic Jets**,

Ann Lee, Guan H. Yeoh, Victoria Timchenko, and John Reizes

Volume 2011, Article ID 358940, 8 pages

**Recent Efforts for Credible CFD Simulations in China**, Li Li, Bai Wen, and Liang Yihua

Volume 2011, Article ID 861272, 8 pages

## Editorial

# Advances in Computational Fluid Dynamics and Its Applications

**Guan Heng Yeoh,<sup>1,2</sup> Chaoqun Liu,<sup>3</sup> Jiyuan Tu,<sup>4</sup> and Victoria Timchenko<sup>2</sup>**

<sup>1</sup> Australian Nuclear Science Technology Organisation (ANSTO), Locked Bag 2001, Kirrawee, Sydney, NSW 2233, Australia

<sup>2</sup> School of Mechanical and Manufacturing Engineering, The University of New South Wales, Sydney, NSW 2052, Australia

<sup>3</sup> Center for Numerical Simulation and Modeling, Department of Mathematics, The University of Texas at Arlington, Arlington, TX 76019-0408, USA

<sup>4</sup> School of Aerospace, Mechanical and Manufacturing Engineering, RMIT University, P.O. Box 71, Bundoora, Melbourne, VIC 3083, Australia

Correspondence should be addressed to Guan Heng Yeoh, [guan.yeoh@ansto.gov.au](mailto:guan.yeoh@ansto.gov.au)

Received 14 October 2011; Accepted 17 October 2011

Copyright © 2011 Guan Heng Yeoh et al. This is an open access article distributed under the Creative Commons Attribution License, which permits unrestricted use, distribution, and reproduction in any medium, provided the original work is properly cited.

Computational fluid dynamics, better known by CFD, is certainly very prevalent in many fields of engineering research and application. There is no doubt that we are certainly witnessing a renaissance of computer simulation technology where the ever-changing landscape is as a result of the rapid evolution of CFD techniques and models and the decreasing computer hardware costs accompanied by faster computing times. In spite of the many significant achievements, there remains much concerted development and advancement of CFD to meet the increasing demands bolstered from various emerging industries such as biomedical and bioengineering, uncharted areas in process, chemical, civil, and environmental engineering as well as traditionally renowned high-technology engineering areas in aeronautics and astronautics and automotive. In this special issue, we believe that significant coverage on the advances and applications of CFD has been achieved via the selected topics and papers which incidentally represent a good panel addressing the many different aspects of CFD in this special issue. Of course, we realise that these selected topics and papers are not an exhaustive representation. Nevertheless, they still represent the rich and many-faceted knowledge that we have the great pleasure of sharing with the readers. We certainly would like to thank the numerous authors for their excellent contributions and patience in assisting us. More importantly, the tiresome work of all referees on reviewing these papers is very warmly acknowledged.

This special issue contains sixteen papers. The advances and wide applications of CFD in each of the papers are detailed in the following.

In the first paper, “*New findings by high-order DNS for late flow transition in a boundary layer*,” C. Liu et al. present a summary of new discoveries by direct numerical simulation (DNS) for late stages of flow transition in a boundary layer. Based on the new findings, ring-like vortex is found to be the only form existing inside the flow field and the result of the interaction between two pairs of counter-rotating primary and secondary streamwise vortices. Following first Helmholtz vortex conservation law, the primary vortex tube rolls up and is stretched due to the velocity gradient. In order to maintain vorticity conservation, a bridge must be formed to link two  $\Lambda$ -vortex legs. The bridge finally develops as a new ring. This process proceeds to form a multiple ring structure. U-shaped vortices are not new but existing coherent vortex structure. U-shaped vortex, which is a third level vortex, serves as a second neck to supply vorticity to the multiple rings. The small vortices can be found on the bottom of the boundary layer near the wall surface. It is believed that the small vortices, and thus turbulence, are generated by the interaction of positive spikes and other higher level vortices with the solid wall.

In the second paper, “*Implicit LES for supersonic micro-ramp vortex generator: new discoveries and new mechanisms*,” Q. Li and C. Liu present the application of an implicitly large eddy simulation (ILES) via fifth-order WENO scheme to study the flow around the microramp vortex generator (MVG) at Mach 2.5 and  $Re_\theta = 1440$ . A number of new discoveries on the flow around supersonic MVG have been made including spiral points, surface separation topology, source of the momentum deficit, inflection surface,

Kelvin-Helmholtz instability, vortex ring generation, ring-shock interaction, 3D recompression shock structure, and influence of MVG decline angles. A new 5-pair-vortex-tube model near the MVG is given based on the ILES observation. The vortex ring-shock interaction is found as the new mechanism of the reduction of the separation zone induced by the shock-boundary layer interaction.

In the third paper, “*An initial investigation of adjoint-based unstructured grid adaptation for vortical flow simulations*,” L. Li presents a CFD method utilizing unstructured grid technology to compute vortical flow around a  $65^\circ$  delta wing with sharp leading edge, specially known as the geometry of the second international vortex flow experiment (VFE-2). The emphasis of this paper is to investigate the effectiveness of an adjoint-base grid adaptation method for unstructured grid in capturing concentrated vortices generated at sharp edges or flow separation lines of lifting surfaces flying at high angles of attack. Earlier vortical flow simulations indicated that the vortex behaviour has been found to be highly dependent on the local grid resolution both on body surface and space. The basic idea of the adjoint-based adaptation method has been to construct a new adaptive sensor in a grid adaptation process with the intent to allocate where the elements should be smaller or larger through the introduction of an adjoint formulation to relate the estimated functional error to local residual errors of both the primal and adjoint solutions.

In the fourth paper, “*Assessment of turbulence models for flow simulation around a wind turbine airfoil*,” F. Villalpando et al. present the investigation of flows over a NACA 63–415 airfoil at various angles of attack. With the aim of selecting the most suitable turbulence model to simulate flow around ice-accreted airfoils, this work concentrates on assessing the prediction capabilities of various turbulence models on clean airfoils at the large angles of attack that cause highly separated flows to occur. CFD simulations have been performed employing the one-equation Spalart-Allmaras model, the two-equation RNG  $k-\epsilon$  and SST  $k-\omega$  models, and Reynolds stress model.

In the fifth paper, “*Computation of ice shedding trajectories using cartesian grids, penalization, and level sets*,” H. Beaugendre et al. present the modelling of ice shedding trajectories by an innovative paradigm based on Cartesian grids, penalization, and level sets. The use of Cartesian grids bypasses the meshing issue, and penalization is an efficient alternative to explicitly impose boundary conditions so that the body-fitted meshes can be avoided, making multifluid/multiphysics flows easy to set up and simulate. Level sets describe the geometry in a nonparametric way so that geometrical and topological changes due to physics and in particular shed ice pieces are straightforward to follow. The capabilities of the proposed CFD model are demonstrated on ice trajectories calculations for flow around iced cylinder and airfoil.

In the sixth paper, “*Aerodynamic optimization of an over-the-wing-nacelle-mount configuration*,” D. Sasaki and K. Nakahashi present the CFD investigation of an over-the-wing-nacelle-mount airplane configuration which is known to prevent the noise propagation from jet engines toward

ground. Aerodynamic design optimization is conducted to improve aerodynamic efficiency in order to be equivalent to conventional under-the-wing-nacelle-mount configuration. The nacelle and wing geometry are modified to achieve high lift-to-drag ratio, and the optimal geometry is compared with a conventional configuration. Pylon shape is also modified to reduce aerodynamic interference effect. The final wing-fuselage-nacelle model is compared with the DLR F6 model to discuss the potential of over-the-wing-nacelle-mount geometry for an environmental-friendly future aircraft.

In the seventh paper, “*New evaluation technique for WTG design wind speed using a CFD-model-based unsteady flow simulation with wind direction changes*,” T. Uchida et al. present the development of a CFD model called RIAM-COMPACT, based on large eddy simulation (LES), that can predict airflow and gas diffusion over complex terrain with high accuracy and simulates a continuous wind direction change over 360 degrees. The present paper proposes a technique for evaluating the deployment location of wind turbine generators (WTGs) since a significant portion of the topography in Japan is characterized by steep, complex terrain thereby resulting in a complex spatial distribution of wind speed, in which great care is necessary for selecting a site for the construction of WTG.

In the eighth paper, “*Comparisons between the wake of a wind turbine generator operated at optimal tip speed ratio and the wake of a stationary disk*,” T. Uchinda et al. present the investigation that the wake of a wind turbine generator (WTG) operated at the optimal tip speed ratio is compared to the wake with its rotor replaced by a stationary disk. Numerical simulations are conducted with a large eddy simulation (LES) model. The characteristics of the wake of the stationary disk are significantly different from those of the WTG. The velocity deficit at a downstream distance of  $10D$  ( $D$  being the rotor diameter) behind the WTG is approximately 30 to 40% of the inflow velocity. In contrast, flow separation is observed immediately behind the stationary disk ( $\leq 2D$ ), and the velocity deficit in the far wake ( $10D$ ) of the stationary disk is smaller than that of the WTG.

In the ninth paper, “*Experimental and numerical simulations predictions comparison of power and efficiency in hydraulic turbine*,” L. Castro et al. present the CFD simulations performed to principal components of a hydraulic turbine: runner and draft tube. On-site power and mass flow rate measurements have been conducted in a hydroelectric power plant (Mexico). Mass flow rate has been obtained using Gibson’s water hammer-based method. Inlet boundary conditions for the runner have been obtained from a previous simulation conducted in the spiral case. Computed results at the runner’s outlet are used to conduct the subsequent draft tube simulation. Numerical results from the runner’s flow simulation provide data to compute the torque and the turbine’s power. Power-versus-efficiency curves are built.

In the tenth paper, “*Simulating smoke filling in big halls by computational fluid dynamics*,” W. K. Chow et al. present the use of CFD in addressing the key hazard due to smoke filling within the enclosure in the event of a fire. This aspect

primarily concerns the many tall halls of big space volume that have been and to be built in many construction projects in the Far East, particularly Mainland China, Hong Kong, and Taiwan. On the basis of the CFD simulations, it can be anticipated that better understanding of the smoke filling phenomenon and design of appropriate smoke exhaust systems can be realised.

In the eleventh paper, “*Numerical simulations for a typical train fire in china*,” W. K. Chow et al. present the use of CFD in addressing the fire safety in passenger trains due to big arson and accidental fires since railway is the key transport means in China including the Mainland, Taiwan, and Hong Kong. The predicted results such as the air flow, temperature distribution, smoke layer height, and smoke spread patterns inside a train compartment are useful for working out appropriate fire safety measures for train vehicles and determining the design fire for subway stations and railway tunnels.

In the twelfth paper, “*Simulation of pharyngeal airway interaction with air flow using low-Re turbulence model*,” M. R. Rasani et al. present the CFD simulation of the interaction between a simplified tongue replica with expiratory turbulent air flow. A three-dimensional model with a low-Re SST turbulence model is adopted. An Arbitrary Eulerian-Lagrangian description for the fluid governing equation is coupled with the Lagrangian structural solver via a partitioned approach, allowing deformation of the fluid domain to be captured. Numerical simulations confirm expected predisposition of apneic patients with narrower airway opening to flow obstruction and suggest much severe tongue collapsibility if the pharyngeal flow regime is turbulent compared to laminar.

In the thirteenth paper, “*CFD-guided development of test rigs for studying erosion and large-particle damage of thermal barrier coatings*,” M. A. Kuczmariski et al. present the use of CFD to accelerate the successful development and continuous improvement of combustion burner rigs for meaningful materials testing. Rig development is typically an iterative process of making incremental modifications to improve the rig performance for testing requirements. Application of CFD allows many of these iterations to be done computationally before hardware is built or modified, reducing overall testing costs and time, and it can provide an improved understanding of how these rigs operate. This paper focuses on the study of erosion and large-particle damage of thermal barrier coatings (TBCs) used to protect turbine blades from high heat fluxes in combustion engines. The steps used in this study—determining the questions that need to be answered regarding the test rig performance, developing and validating the model, and using it to predict rig performance—can be applied to the efficient development of other test rigs.

In the fourteenth paper, “*Investigation of swirling flows in mixing chambers*,” J. J. Chen and C. H. Chen present the CFD investigation of the three-dimensional momentum and mass transfer characteristics arising from multiple inlets and a single outlet in micromixing chamber. The chamber consists of a right square prism, an octagonal prism, or a cylinder. Numerical results have indicated that the swirling

flows inside the chamber dominate the mixing index. Particle trajectories demonstrate the rotational and extensional local flows which produce steady stirring, and the configuration of coloured particles at the outlet section expressed at different Reynolds numbers ( $Re$ ) represented the mixing performance qualitatively. Effects of various geometric parameters and  $Re$  on the mixing characteristics have been investigated. An optimal design of the cylindrical chamber with 4 inlets is found. At  $Re > 15$ , more inertia causes more powerful swirling flows in the chamber, and the damping effect on diffusion is diminished, which subsequently increases the mixing performance.

In the fifteenth paper, “*Numerical computation and investigation of the characteristics of microscale synthetic jets*,” A. Lee et al. present the CFD investigation of a synthetic jet generated as a result of the periodic oscillations of a membrane in a cavity. A novel moving mesh algorithm to simulate the formation of jet is presented. The governing equations are transformed into the curvilinear coordinate system in which the grid velocities evaluated are then fed into the computation of the flow in the cavity domain thus allowing the conservation equations of mass and momentum to be solved within the stationary computational domain. Numerical solution generated using this moving mesh approach is compared with experimental measurement. Comparisons between numerical results and experimental measurement on the streamwise component of velocity profiles at the orifice exit and along the centerline of the pulsating jet in microchannel as well as the location of vortex core indicate that there is good agreement, thereby demonstrating that the moving mesh algorithm developed is valid.

In the sixteenth paper, “*Recent efforts for credible CFD simulations in china*,” L. Li et al. present the initiation of a series of workshops on credible CFD simulations similar to activities in the West such as ECARP and AIAA Drag Prediction Workshops. Another major effort in China is the ongoing project to establish a software platform for studying the credibility of CFD solvers and performing credible CFD simulations. The platform, named WiseCFD, has been designed to implement a seamless CFD process and to circumvent tedious repeating manual operations. A concerted focus is also given on a powerful job manager for CFD with capabilities to support plug and play (PnP) solver integration as well as distributed or parallel computations. Some future work on WiseCFD is proposed and also envisioned on how WiseCFD and the European QNET-CFD Knowledge Base can benefit mutually.

Guan Heng Yeoh  
Chaoqun Liu  
Jiyuan Tu  
Victoria Timchenko

## Research Article

# New Findings by High-Order DNS for Late Flow Transition in a Boundary Layer

Chaoqun Liu,<sup>1</sup> Lin Chen,<sup>1,2</sup> and Ping Lu<sup>1</sup>

<sup>1</sup>Mathematics Department, University of TX at Arlington, Arlington, TX 76019, USA

<sup>2</sup>Aerodynamics Department, Nanjing University of Aeronautics and Astronautics, Nanjing 210016, China

Correspondence should be addressed to Chaoqun Liu, cliu@omega.uta.edu

Received 6 October 2010; Accepted 24 November 2010

Academic Editor: Guan Yeoh

Copyright © 2011 Chaoqun Liu et al. This is an open access article distributed under the Creative Commons Attribution License, which permits unrestricted use, distribution, and reproduction in any medium, provided the original work is properly cited.

This paper serves as a summary of new discoveries by DNS for late stages of flow transition in a boundary layer. The widely spread concept “vortex breakdown” is found theoretically impossible and never happened in practice. The ring-like vortex is found the only form existing inside the flow field. The ring-like vortex formation is the result of the interaction between two pairs of counter-rotating primary and secondary streamwise vortices. Following the first Helmholtz vortex conservation law, the primary vortex tube rolls up and is stretched due to the velocity gradient. In order to maintain vorticity conservation, a bridge must be formed to link two  $\Lambda$ -vortex legs. The bridge finally develops as a new ring. This process keeps going on to form a multiple ring structure. The U-shaped vortices are not new but existing coherent vortex structure. Actually, the U-shaped vortex, which is a third level vortex, serves as a second neck to supply vorticity to the multiple rings. The small vortices can be found on the bottom of the boundary layer near the wall surface. It is believed that the small vortices, and thus turbulence, are generated by the interaction of positive spikes and other higher level vortices with the solid wall. The mechanism of formation of secondary vortex, second sweep, positive spike, high shear distribution, downdraft and updraft motion, and multiple ring-circle overlapping is also investigated.

## 1. Introduction

The transition process from laminar to turbulent flow in boundary layers is a basic scientific problem in modern fluid mechanics and has been the subject of study for over a century. Many different concepts for the explanation of the mechanisms involved have been developed based on numerous experimental, theoretical, and numerical investigations. After over a century study on the turbulence, the linear and early weakly nonlinear stages of flow transition are pretty well understood. However, for late non-linear transition stages, there are still many questions remaining for research [1–5].

Ring-like vortices play a key role in the flow transition. They generate rapid downward jets (second sweep) which induce the positive spike and bring the high energy to the boundary layer and work together with the upward jets (ejection) to mix the boundary layer. In other words, the ring-like vortex formation and development are a key topic for late flow transition in boundary layer. It appears that

there is no turbulence without ring-like vortices. It is natural to give comprehensive study on the ring formation and development.

*1.1. Ring-Like Vortex Formation.* Hama and Nutant [6] described the process of formation of “ $\Omega$ -shaped vortex” in the vicinity of the  $\Lambda$ -vortex tip. They found that “...a simplified numerical analysis indicates that the hyperbolic vortex filament deforms by its own induction into a milk-bottle shape (the “ $\Omega$ -vortex”) and lifts up its tip...”. Later, Moin et al. [7] used numerical method with the Biot-Savart law and concluded that the ring is formed through a mechanism of self-induction and the multiple ring formation is a result of first ring “pinching off.” They believe that the solution of Navier-Stokes equation does not change the mechanism but may delay the ring “pinching off.” However, they may be somewhat right, but what they discussed is not relevant to the boundary layer transition since the ring-like vortex is formed in a boundary layer and viscosity and full 3D time-dependent

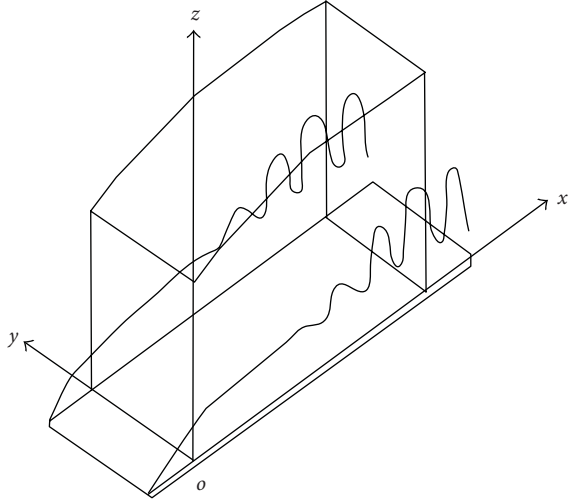


FIGURE 1: Computation domain.

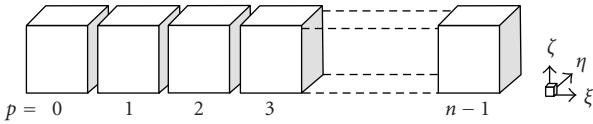


FIGURE 2: The domain decomposition along streamwise direction in the computational space.

Navier-Stokes equations must be considered. In addition, our new DNS results show, the ring is a perfect circle not a deformed shape, the ring stands perpendicularly with 90 degree not 45 degree, and, more important, “ring pinch off.” is never found. The ring-like vortex has its own coherent structure as we show below, which is quite different from what Moin et al. have shown [7].

**1.2. Multiple Ring Formation.** Crow theory [8] has been considered as the mechanism of multiple ring formation [2]. They pointed out that “the formation of a set of vortex rings from two counter-rotating vortices is usually called “Crow instability.” This instability could be involved at the stage of formation of the ring-like vortices due to interaction of the  $\Lambda$ -vortex legs.” However, there is no evidence to prove such a mechanism. We cannot find any links between Crow theory and multiple ring formation. Apparently, Crow theory is not related to multiple ring formation in a boundary layer.

**1.3. Vortex Breakdown.** “Vortex Breakdown” has been widely spread in many research papers and textbooks [5, 9–11]. However, our analysis found that “Vortex Breakdown” is theoretically impossible. In practice, “Vortex Breakdown” can never happen. It is found that “Vortex Breakdown” described by exiting publications [5, 9, 10] is either misinterpreted by 2D visualization or by using the pressure center as the vortex center.

**1.4. U-Shaped Vortex.** U-shaped vortex [9] or barrel-shaped wave [5] is still a mystery and thought as a newly formed

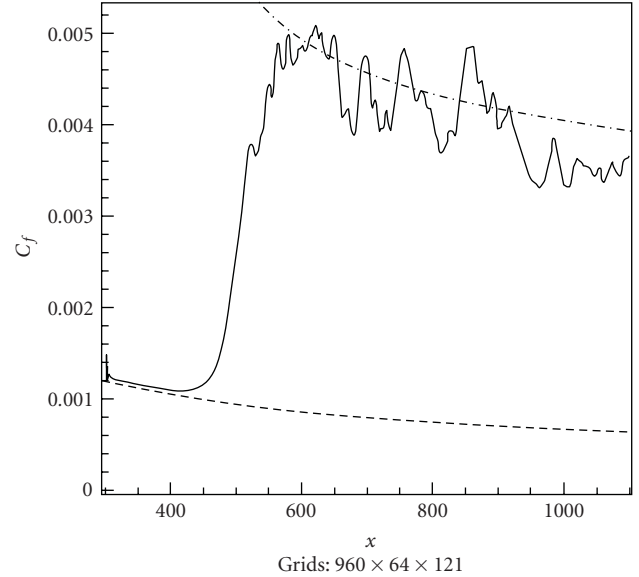


FIGURE 3: Streamwise evolution of the time- and spanwise-averaged skin-friction coefficient.

secondary vortex or waves. However, it is found by our new DNS that the U-shaped vortex was an original coherent structure and it is a tertiary (not secondary) vortex with same vorticity sign as the ring legs. The U-shaped vortices serve as a second neck to supply vorticity to the rings and keep the leading ring alive.

**1.5. High Shear Distribution.** The high shear (HS) distribution can be found in the paper by Bake et al. [3], but it is questionable why the HS disappears near the neck where the flow is very active. However, our new DNS found that there is no normal direction velocity component and then no sweeps and ejections in that area.

Anyway, there are many questions, which are related to late flow transition, that have not been answered or misinterpreted. In order to get deep understanding on the late flow transition in a boundary layer, we recently conducted a large grid high-order DNS with  $1920 \times 241 \times 128$  grid points and about 600,000 time steps to study the mechanism of the late stages of flow transition in a boundary layer. Many new findings are made, and new mechanisms are revealed. Here, we use the  $\lambda_2$  criterion [12] for visualization.

The paper is organized in the following way: Section 2 presents the governing Navier-Stokes equations and numerical approaches; Section 3 shows the code verification and validation to make sure that the DNS code is correct; Section 4 provides the new DNS results and summarizes the new discoveries and new mechanism of formation and further development of ring-like vortices. A number of conclusions are made in Section 5.

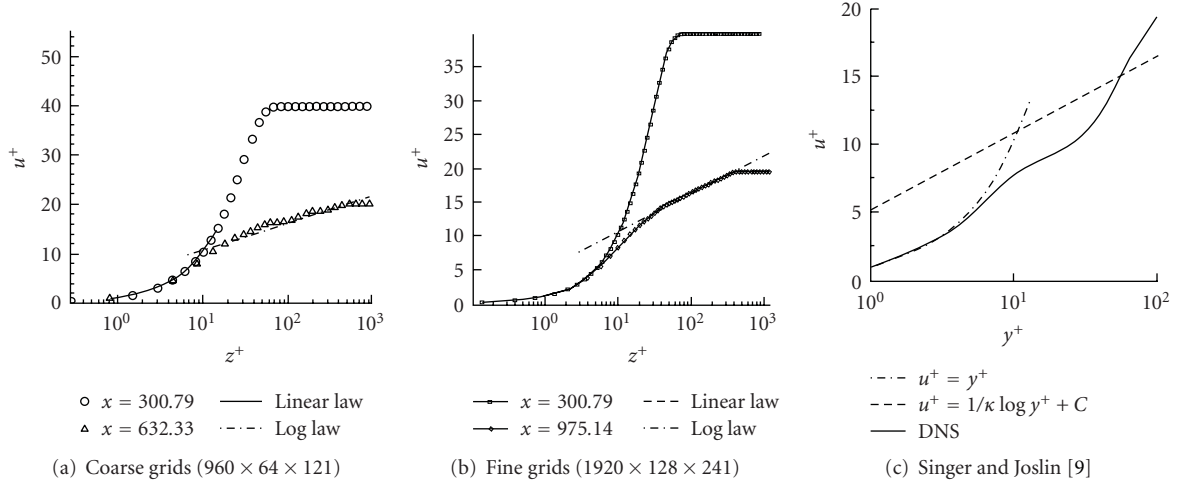


FIGURE 4: Log-linear plots of the time- and spanwise-averaged velocity profile in wall unit.

TABLE 1: Flow parameters.

$M_\infty$	Re	$x_{in}$	$Lx$	$Ly$	$Lz_{in}$	$T_w$	$T_\infty$
0.5	1000	$300.79\delta_{in}$	$798.03\delta_{in}$	$22\delta_{in}$	$40\delta_{in}$	273.15 K	273.15 K

## 2. Governing Equations and Numerical Methods

The governing equations we used are the three-dimensional compressible Navier-Stokes equations in generalized curvilinear coordinates and in a conservative form:

$$\frac{1}{J} \frac{\partial Q}{\partial t} + \frac{\partial(E - E_v)}{\partial \xi} + \frac{\partial(F - F_v)}{\partial \eta} + \frac{\partial(H - H_v)}{\partial \zeta} = 0. \quad (1)$$

The vector of conserved quantities  $Q$ , inviscid flux vector ( $E, F, G$ ), and viscous flux vector ( $E_v, F_v, G_v$ ) are defined as

$$Q = \begin{pmatrix} \rho \\ \rho u \\ \rho v \\ \rho w \\ e \end{pmatrix}, \quad E = \frac{1}{J} \begin{pmatrix} \rho U \\ \rho u U + p \xi_x \\ \rho v U + p \xi_y \\ \rho w U + p \xi_z \\ U(e + p) \end{pmatrix},$$

$$F = \frac{1}{J} \begin{pmatrix} \rho V \\ \rho u V + p \eta_x \\ \rho v V + p \eta_y \\ \rho w V + p \eta_z \\ V(e + p) \end{pmatrix}, \quad H = \frac{1}{J} \begin{pmatrix} \rho W \\ \rho u W + p \zeta_x \\ \rho v W + p \zeta_y \\ \rho w W + p \zeta_z \\ W(e + p) \end{pmatrix},$$

$$E_v = \frac{1}{J} \begin{pmatrix} 0 \\ \tau_{xx} \xi_x + \tau_{yx} \xi_y + \tau_{zx} \xi_z \\ \tau_{xy} \xi_x + \tau_{yy} \xi_y + \tau_{zy} \xi_z \\ \tau_{xz} \xi_x + \tau_{yz} \xi_y + \tau_{zz} \xi_z \\ q_x \xi_x + q_y \xi_y + q_z \xi_z \end{pmatrix},$$

$$F_v = \frac{1}{J} \begin{pmatrix} 0 \\ \tau_{xx} \eta_x + \tau_{yx} \eta_y + \tau_{zx} \eta_z \\ \tau_{xy} \eta_x + \tau_{yy} \eta_y + \tau_{zy} \eta_z \\ \tau_{xz} \eta_x + \tau_{yz} \eta_y + \tau_{zz} \eta_z \\ q_x \eta_x + q_y \eta_y + q_z \eta_z \end{pmatrix},$$

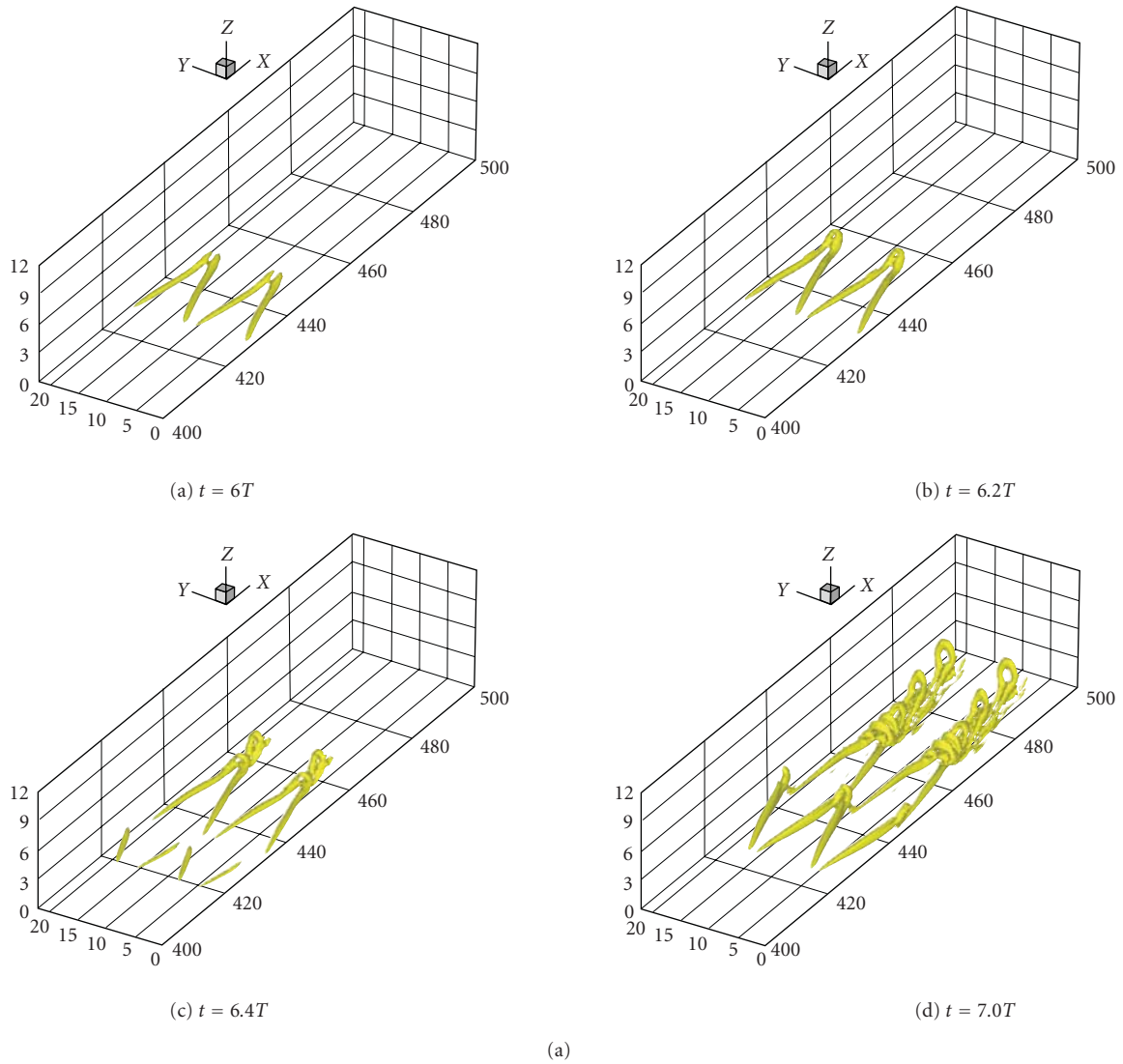
$$H_v = \frac{1}{J} \begin{pmatrix} 0 \\ \tau_{xx} \zeta_x + \tau_{yx} \zeta_y + \tau_{zx} \zeta_z \\ \tau_{xy} \zeta_x + \tau_{yy} \zeta_y + \tau_{zy} \zeta_z \\ \tau_{xz} \zeta_x + \tau_{yz} \zeta_y + \tau_{zz} \zeta_z \\ q_x \zeta_x + q_y \zeta_y + q_z \zeta_z \end{pmatrix}, \quad (2)$$

where  $J$  is the Jacobian of the coordinate transformation between the curvilinear  $(\xi, \eta, \zeta)$  and Cartesian  $(x, y, z)$  frames and  $\xi_x, \xi_y, \xi_z, \eta_x, \eta_y, \eta_z, \zeta_x, \zeta_y, \zeta_z$  are coordinate transformation metrics. The contravariant velocity components  $U, V, W$  are defined as  $U = u\xi_x + v\xi_y + w\xi_z$ ,  $V = u\eta_x + v\eta_y + w\eta_z$ ,  $W = u\zeta_x + v\zeta_y + w\zeta_z$ ;  $e$  is the total energy. The components of viscous stress and heat flux are denoted by  $\tau_{xx}, \tau_{yy}, \tau_{zz}, \tau_{xy}, \tau_{xz}, \tau_{yz}$ , and  $q_x, q_y, q_z$ , respectively.

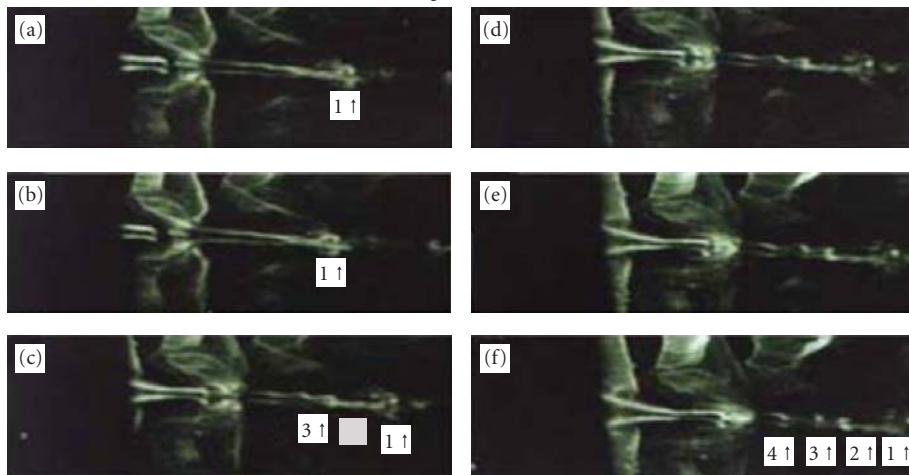
In the dimensionless form of (1), the reference values for length, density, velocities, temperature, and pressure are  $\delta_{in}, \rho_\infty, U_\infty, T_\infty$ , and  $\rho_\infty U_\infty^2$ , respectively. The Mach number and Reynolds number are expressed as

$$M_\infty = \frac{U_\infty}{\sqrt{\gamma RT_\infty}}, \quad Re = \frac{\rho_\infty U_\infty \delta_{in}}{\mu_\infty}, \quad (3)$$

where  $R$  is the ideal gas constant,  $\gamma$  the ratio of specific heats,  $\delta_{in}$  the inflow displacement thickness, and  $\mu_\infty$  the viscosity.



Where  $T$  is period of T-S wave



(b)

FIGURE 5: (A) The evolution of vortex structures at the late stage of transition (where  $T$  is period of T-S wave). (B) Evolution of type ring-like vortices chain by experiment [13].

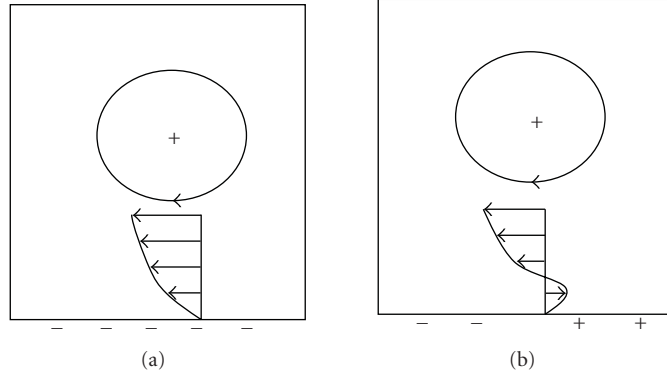


FIGURE 6: Sketch of secondary vortex and third level vorticity formation.

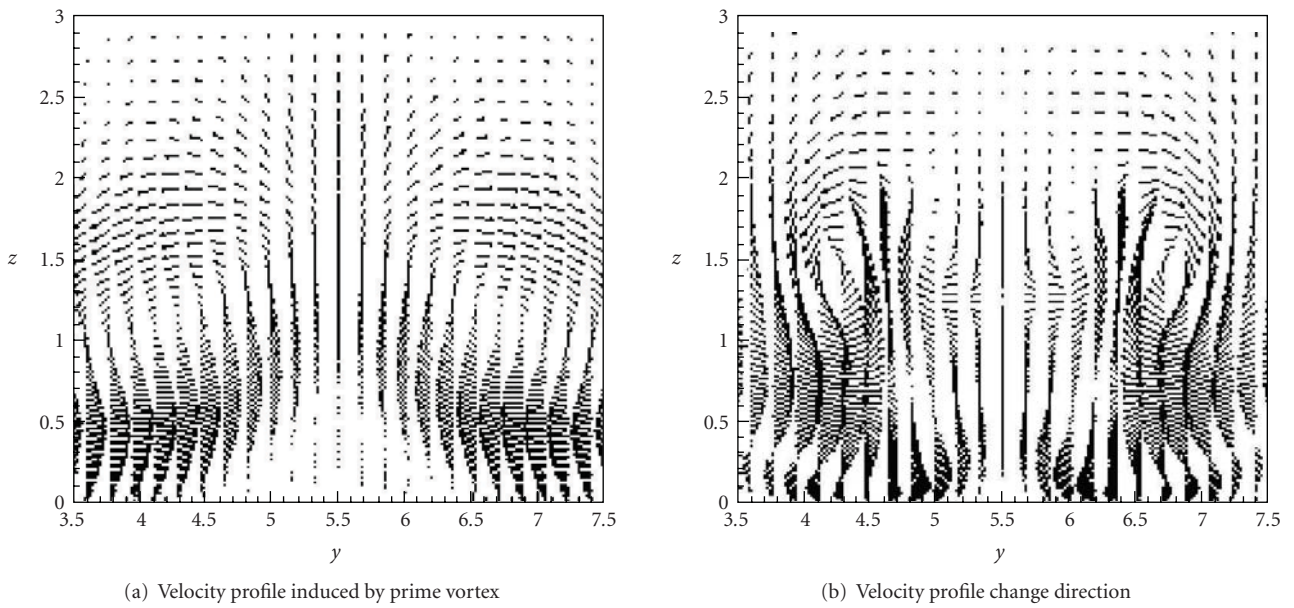


FIGURE 7: DNS results of secondary vortex and third level vorticity formation.

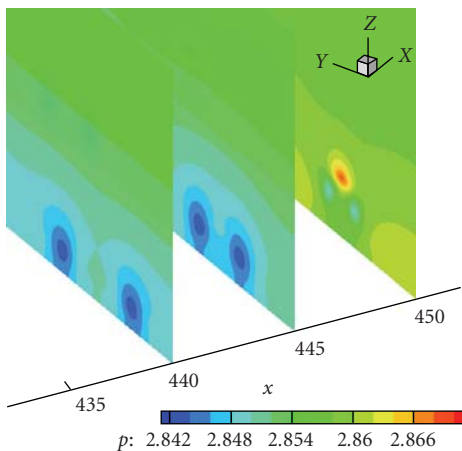


FIGURE 8: Pressure distributions in the evolution of vortex structure ( $t = 6.2T$ )

A sixth-order compact scheme [14] is used for the spatial discretization in the streamwise and wall normal directions. For internal points  $j = 3, \dots, N - 2$ , the sixth-order compact scheme is as follows:

$$\begin{aligned} & \frac{1}{3} f'_{j-1} + f'_j + \frac{1}{3} f'_{j+1} \\ & = \frac{1}{h} \left( -\frac{1}{36} f_{j-2} - \frac{7}{9} f_{j-1} + \frac{7}{9} f_{j+1} + \frac{1}{36} f_{j+2} \right), \end{aligned} \quad (4)$$

where  $f'_j$  is the derivative at point  $j$ . The fourth order compact scheme is used at points  $j = 2, N - 1$ , and the third order one-sided compact scheme is used at the boundary points  $j = 1, N$ .

In the spanwise direction where periodical conditions are applied, the pseudospectral method is used. In order to eliminate the spurious numerical oscillations caused by central difference schemes, a high-order spatial scheme is

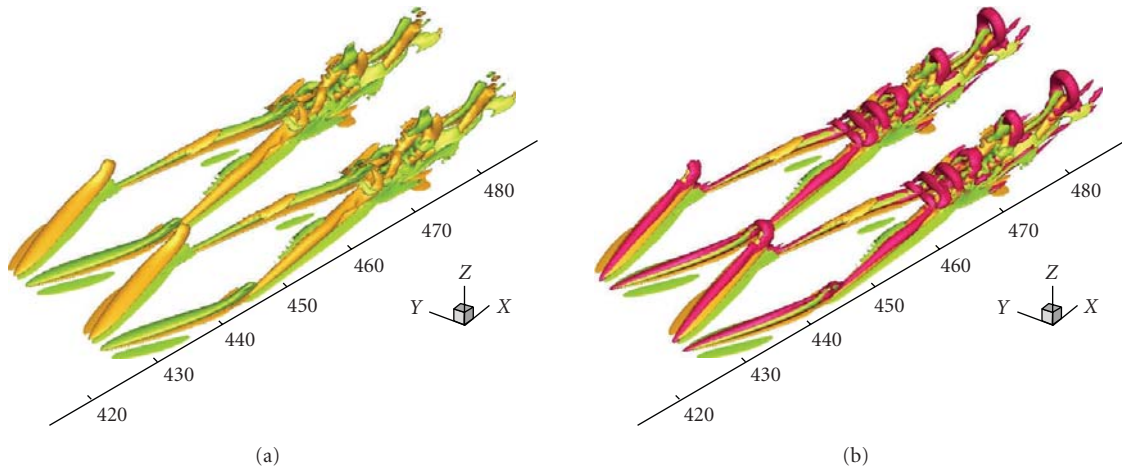


FIGURE 9: Sketch of the relationship of ring-like vortices and streamwise vortices.

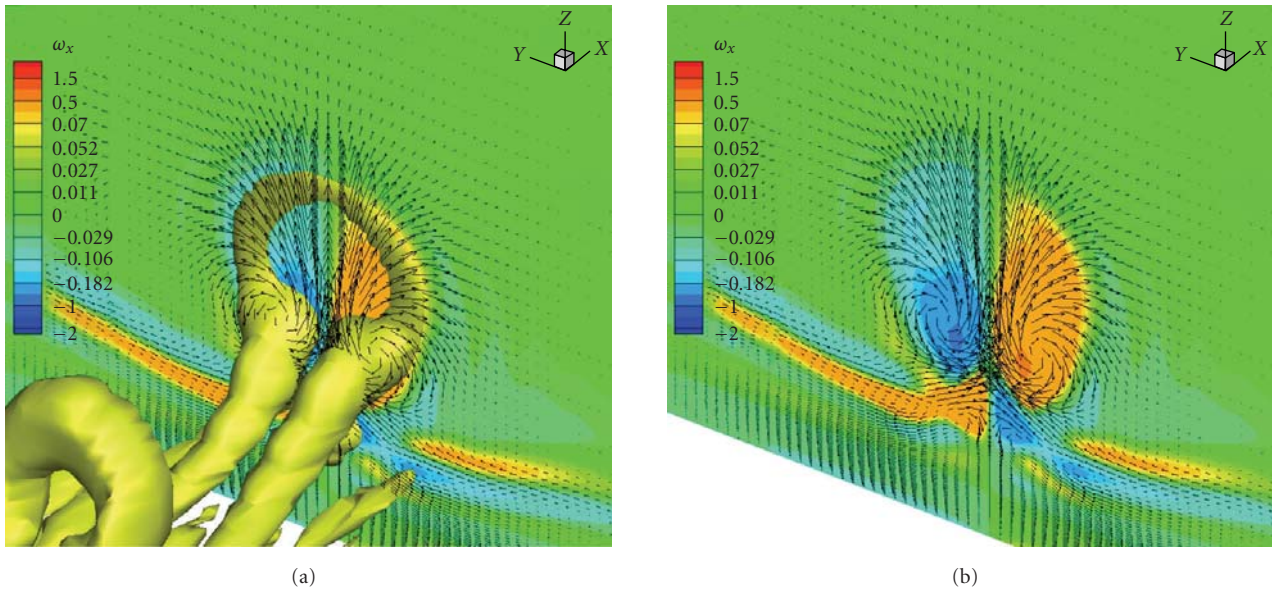


FIGURE 10: Formation process of ring-like vortices.

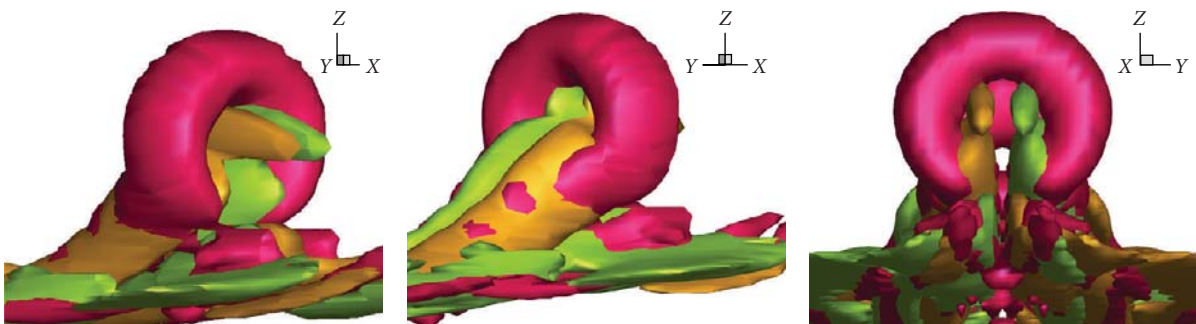


FIGURE 11: Four-vortex tube and ring-like vortices from three different view angles. Ring like vortex given by our DNS.

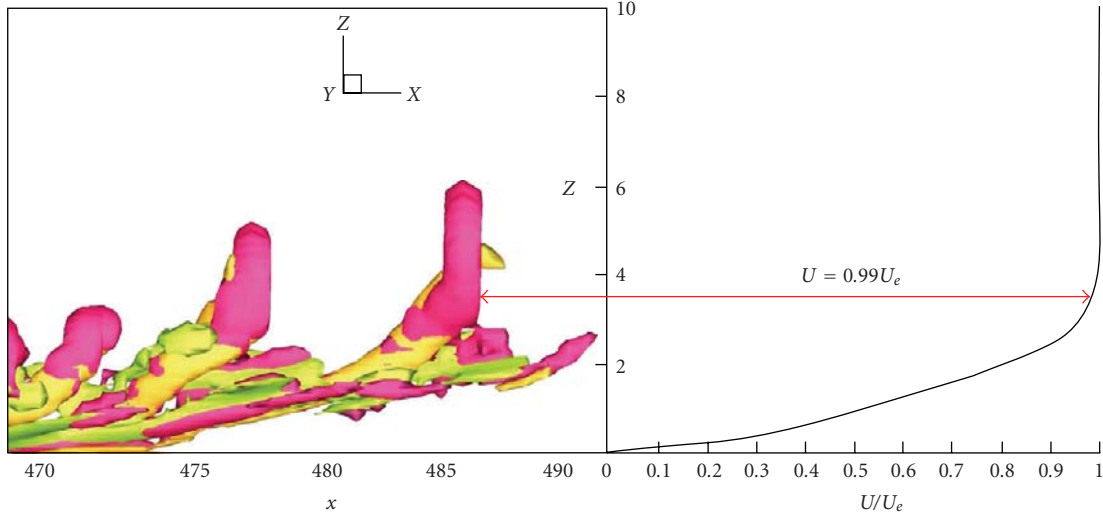


FIGURE 12: The position of ring-like vortices in boundary layer ( $z = 3.56$ ,  $U = 0.99U_e$ )

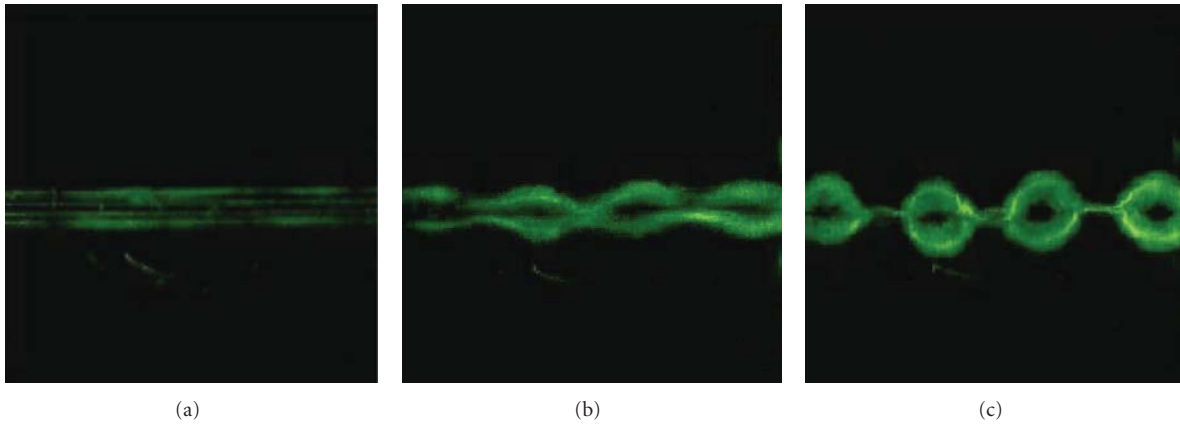


FIGURE 13: Crow theory about vortex ring chain formation (provided by Dr. Kachanov at FTT09 Short Course).

used instead of artificial dissipation. An implicit sixth-order compact scheme for space filtering is applied to the primitive variables  $u, v, w, \rho, p$  after a specified number of time steps.

The governing equations are solved explicitly by a 3rd-order TVD Runge-Kutta scheme [15]:

$$\begin{aligned} Q^{(0)} &= Q^n, \\ Q^{(1)} &= Q^{(0)} + \Delta t R^{(0)}, \\ Q^{(2)} &= \frac{3}{4}Q^{(0)} + \frac{1}{4}Q^{(1)} + \frac{1}{4}\Delta t R^{(1)}, \\ Q^{n+1} &= \frac{1}{3}Q^{(0)} + \frac{2}{3}Q^{(2)} + \frac{2}{3}\Delta t R^{(2)}, \end{aligned} \quad (5)$$

$CFL \leq 1$  is required to ensure the stability.

The adiabatic and the nonslipping conditions are enforced at the wall boundary on the flat plate. On the far field and the outflow boundaries, the nonreflecting boundary conditions [16] are applied.

The inflow is given in the form of

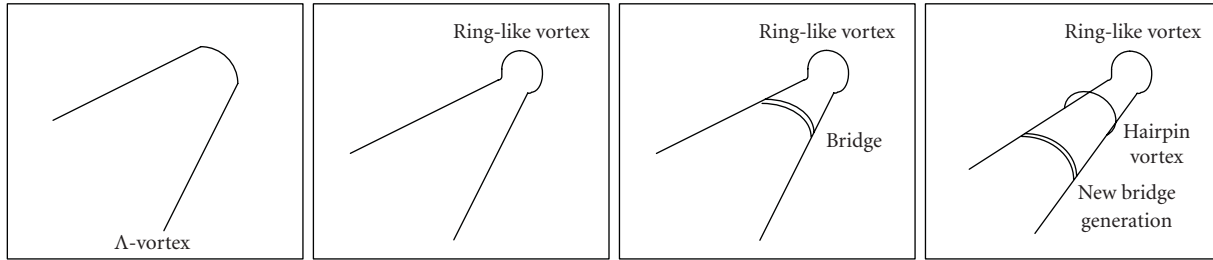
$$q = q_{\text{lam}} + A_{2d}q'_{2d}e^{i(\alpha_{2d}x - \omega t)} + A_{3d}q'_{3d}e^{i(\alpha_{3d}x \pm \beta y - \omega t)}, \quad (6)$$

where  $q$  represents  $u, v, w, p$ , and  $T$ , while  $q_{\text{lam}}$  is the Blasius solution for a two-dimensional laminar flat plate boundary layer. The streamwise wavenumber, spanwise wavenumber, frequency, and amplitude are

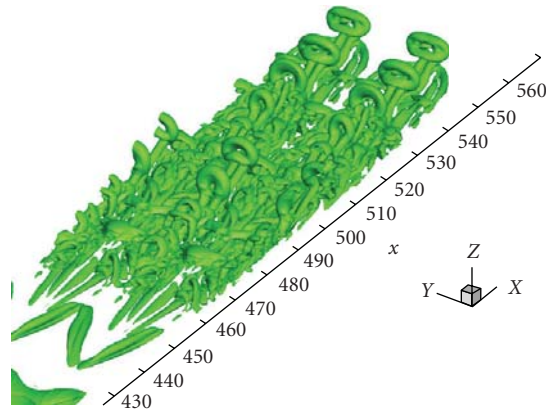
$$\begin{aligned} \alpha_{2d} &= 0.29919 - i5.09586 \times 10^{-3}, & \beta &= \pm 0.5712, \\ \omega &= 0.114027, & A_{2d} &= 0.03, & A_{3d} &= 0.01, \end{aligned} \quad (7)$$

respectively. The T-S wave parameters are obtained by solving the compressible boundary layer stability equations [17].

The computational domain is displayed in Figure 1. The grid level is  $1920 \times 128 \times 241$ , representing the number of grids in streamwise ( $x$ ), spanwise ( $y$ ), and wall normal ( $z$ ) directions. The grid is stretched in the normal direction and uniform in the streamwise and spanwise directions. The length of the first grid interval in the normal direction at the entrance is found to be 0.43 in wall unit ( $Y^+ = 0.43$ ).



(a)



(b)

FIGURE 14: (a) Sketch for mechanism of multi-ring generation. (b) Multiple ring formation.

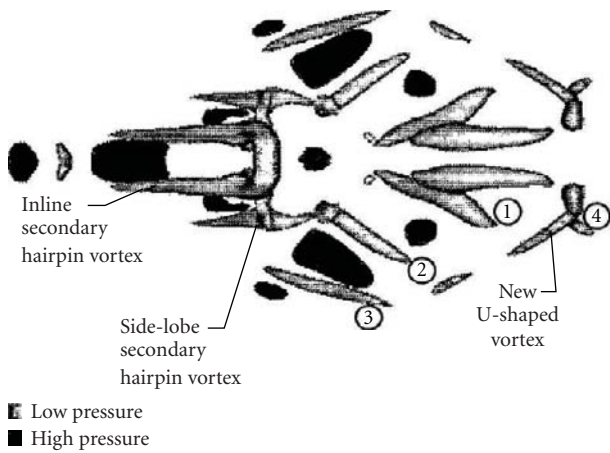


FIGURE 15: U-shaped vortex [9].

The parallel computation is accomplished through the Message Passing Interface (MPI) together with domain decomposition in the streamwise direction. The computational domain is partitioned into  $N$  equally sized subdomains along the streamwise direction (Figures 1 and 2).  $N$  is the number of processors used in the parallel computation. The flow parameters, including Mach number, Reynolds number are listed in Table 1.

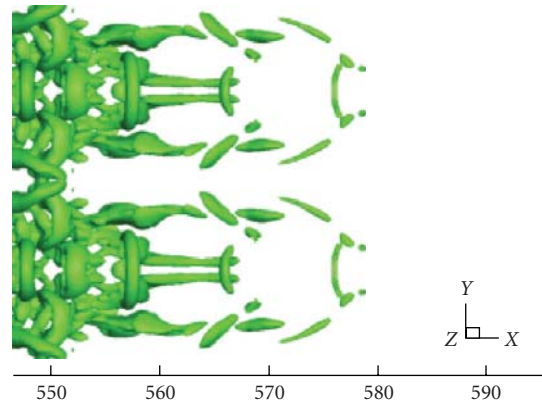


FIGURE 16: Our new DNS with a different  $\lambda$ -value.

### 3. Verification and Validation

The skin friction coefficient calculated for the time- and spanwise-averaged profile is displayed in Figure 3. The spatial evolution of skin friction coefficients of laminar flow is also plotted out for comparison. It is observed from these figures that the sharp growth of the skin-friction coefficient occurs after  $x \approx 450\delta_{in}$ , which is defined as the “onset point”. The skin friction coefficient after transition is in good agreement with the flat-plate theory of turbulent boundary layer by Cousteix in 1989 [18].

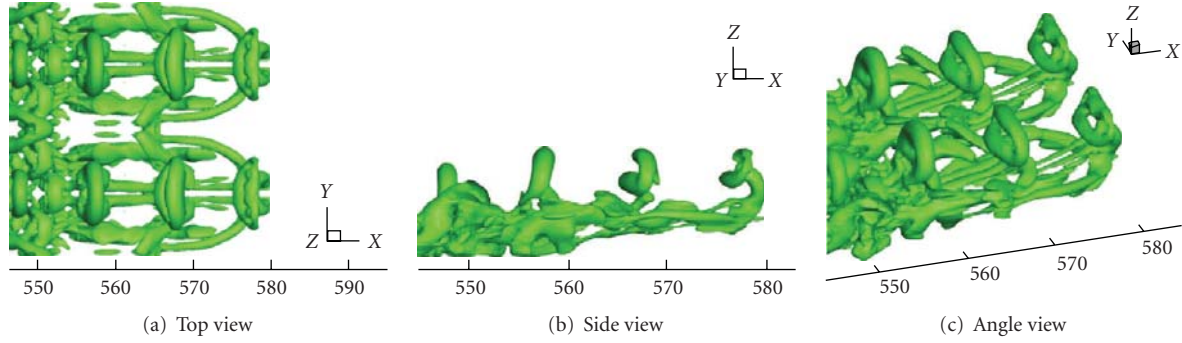


FIGURE 17: View of young turbulence spot head from different directions ( $t = 8.8T$ ).

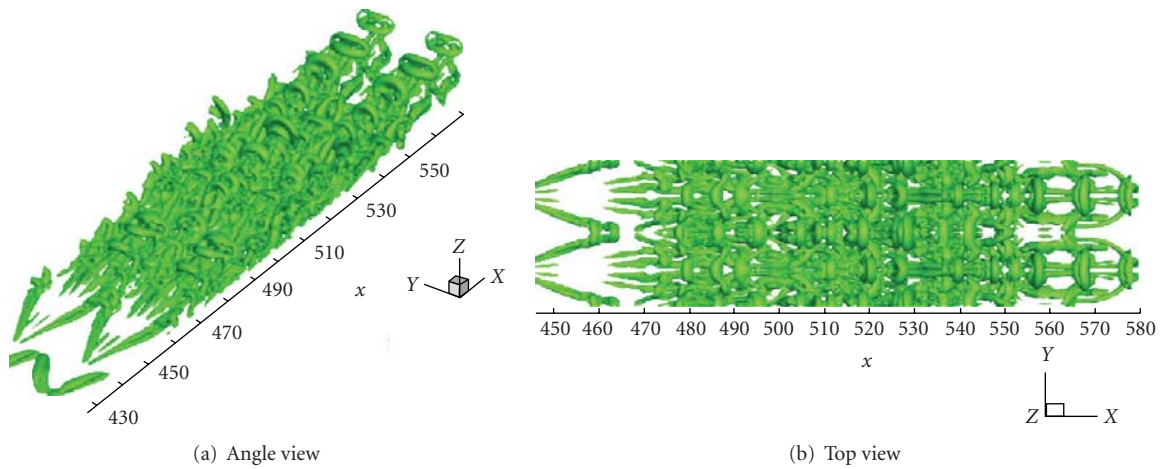


FIGURE 18: 3D angle view and 2D top view of the young turbulence spot ( $t = 8.8T$ ).

Time- and spanwise- averaged streamwise velocity profiles for various streamwise locations in two different grid levels are shown in Figure 4. The inflow velocity profiles at  $x = 300.79\delta_{in}$  is a typical laminar flow velocity profile. At  $x = 632.33\delta_{in}$ , the mean velocity profile approaches a turbulent flow velocity profile (Log law). Note that there are quite few publications (e.g., Figure 4(c)) which have large discrepancy in velocity profile with Log law.

A vortex identification method introduced by Jeong and Hussain [12] is applied to visualize the vortex structures by using an iso-surface of a  $\lambda_2$ -eigenvalue. The vortex cores are found by the location of the inflection points of the pressure in a plane perpendicular to the vortex tube axis. The pressure inflection points surround the pressure minimum that occurs in the vicinity of the vortex core. By this visualization method, the vortex structures shaped by the nonlinear evolution of T-S waves in the transition process are shown in Figure 5(A). The evolution details are studied in our previous papers [19–23], and the formation of ring-like vortices chains is consistent with the experimental work (see [13], Figure 5(B)) and previous numerical simulation by Bake et al. [3].

## 4. New Discoveries and Mechanisms Revealed by Our DNS

### 4.1. Mechanism on Secondary Streamwise Vortex Formation.

As shown in Figure 6(a), the primary vortex induces a backward velocity which generates negative vorticity by the wall surface due to the zero velocity on the wall surface. However, negative vorticity generation does not mean formation of the secondary vortex tube. The secondary vortex tube must be generated by the flow separation. This means that the flow direction near the wall must change the sign from backward to forward (Figure 6(b)). This process is directly shown by the DNS results in Figures 7(a) and 7(b). The separation can only be done by pressure gradients. The question is where the pressure gradients come from. From Figure 8, we can clearly find that the streamwise vortex center is the low pressure center and the pressure outside the primary vortex tube is much higher than the center of the primary vortex center. Also from Figure 8, it is shown that the prime vortex changes the streamwise pressure gradient. These pressure gradients change the flow direction from backward to forward, and the secondary vortex tube forms, separates from the wall surface, and rises up.

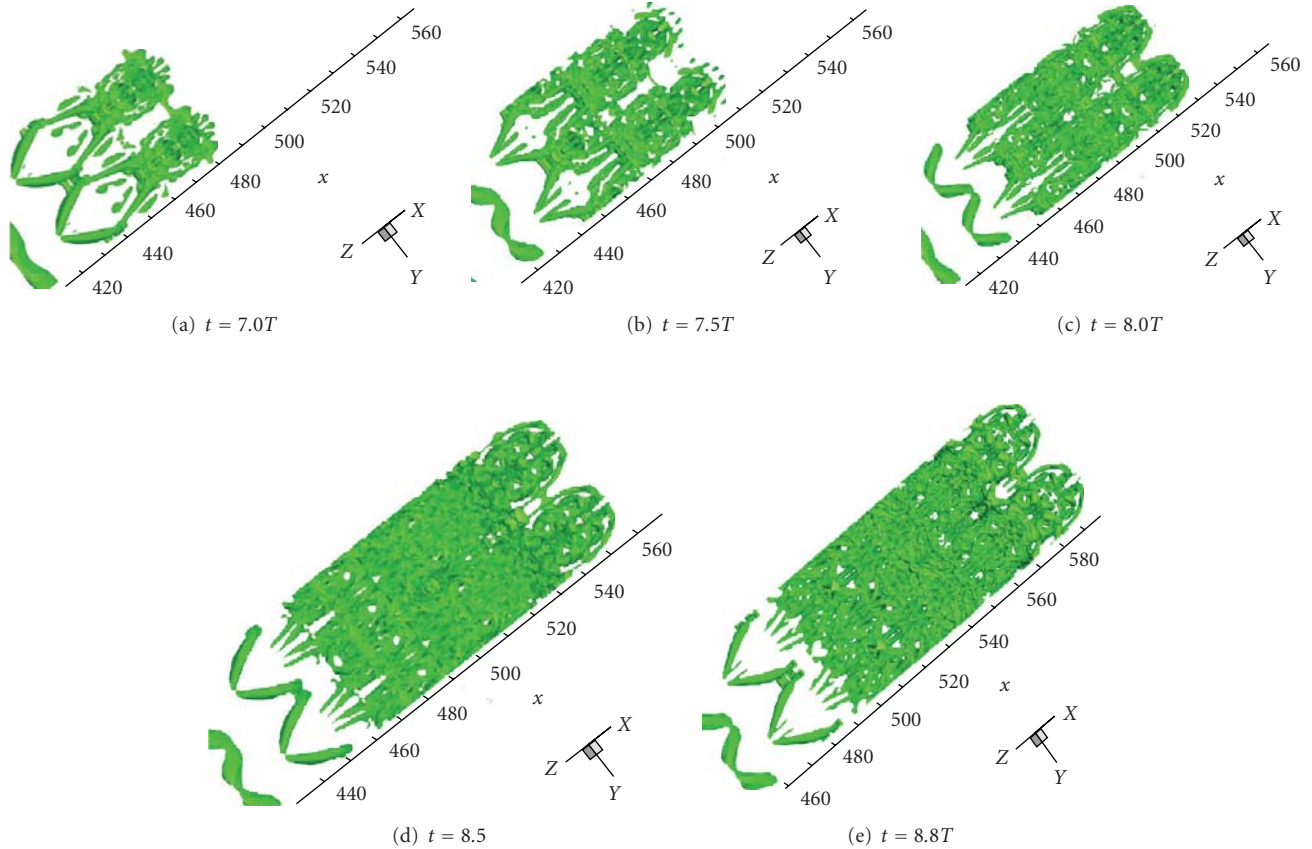


FIGURE 19: Small length scale vortex generation at different time steps (view up from bottom): small length scale vortices are generated by the solid wall near the ring necks from the beginning to the end.

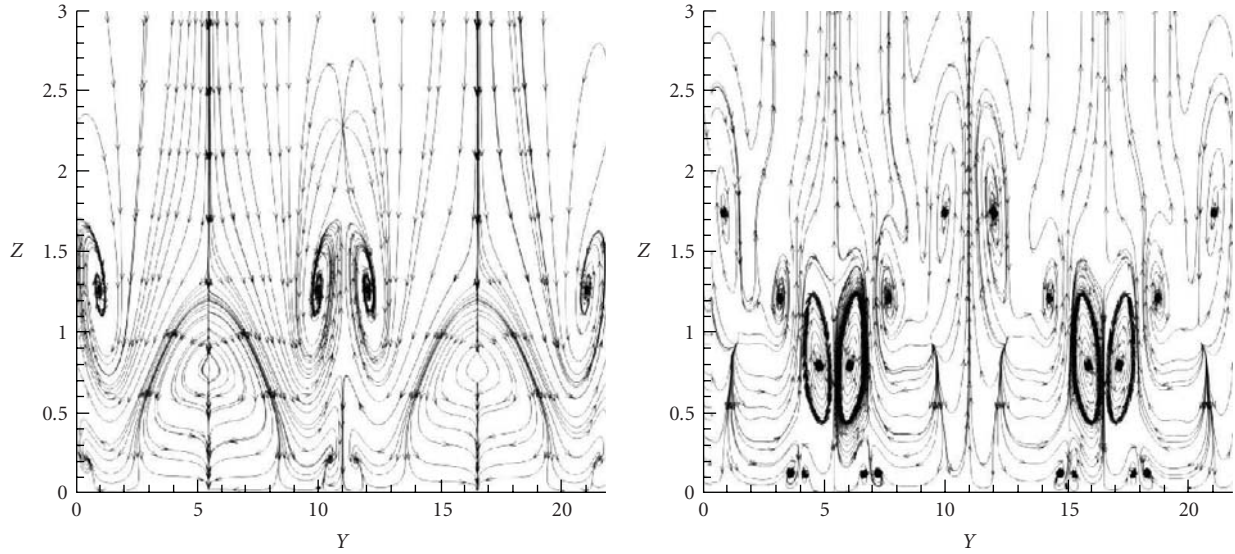
**4.2. Mechanism of First Ring Formation.** Ring-like vortices play a vital role in the transition process of wall boundary layer flow. Based on our numerical simulation, the generation of ring-like vortices is the product of the interaction between the prime streamwise vortices and secondary streamwise vortices. A ring is the consequence when the interaction between prime and secondary streamwise vortex becomes strong enough. The formation details are shown in Figure 9. The prime streamwise vortices are inside the ring, while the secondary streamwise vortices are outside the ring. According to the velocity vector trace, the prime streamwise vortices push flow outward, and the secondary streamwise vortices pull flow in from underneath (Figure 10). These movements bend and stretch the hairpin vortices and then generate a narrow neck. Finally a ring is formed at the tip of the  $\Lambda$ -vortices. For comparison, the ring-like vortex shape given by Moin et al. [7] is taken as a reference. The detail structure of four vortex tubes and ring-like vortices is depicted in Figure 11 from three different view angles. They are quite different.

Apparently, our new DNS results show that the ring is a perfect circle (Figure 11(b)) not a deformed shape as shown by Moin et al. [7], the ring stands perpendicularly with 90 degrees not 45 degrees as shown by Moin et al. [7], and, more

important, “ring pinch off” given by Moin et al. [7] is never found. The ring-like vortex has its own coherent structure as we show in Figure 11.

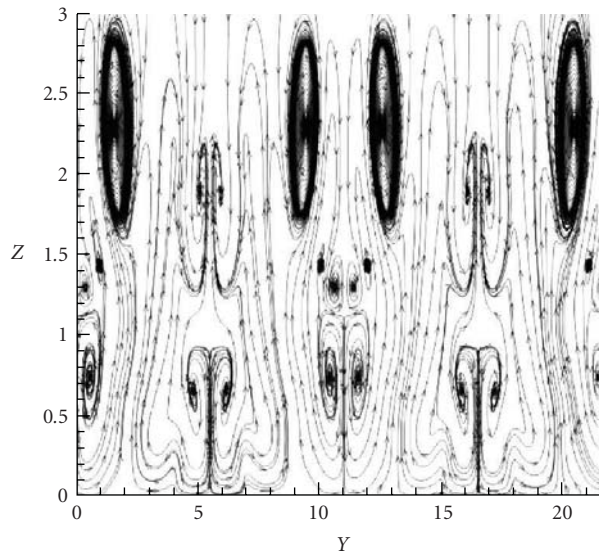
The profile in Figure 12 is a spanwise and time average streamwise velocity profile at location  $x = 486$  (the location of first ring-like vortices). As shown in Figure 12, the ring-like vortices are located outside the boundary layer or in other words located in the inviscid zone ( $z = 3.56$ ,  $U = 0.99U_e$ ). Because the leading rings are in the inviscid zone where the flow is almost uniform and isotropic, the shape of the ring is almost perfectly circular. It is believed that the velocity in normal direction is almost zero in the inviscid zone and the ring stands almost perpendicularly.

**4.3. Mechanism of Multiple Ring Formation.** Crow theory [8] has been considered as the mechanism of multiple ring formation [2]. Figure 13 shows a typical vortex chain formation by Crow theory. However, there is no evidence to prove such a mechanism for flow transition. According to our DNS, Figure 14(a) gives a schematic about the process of a single ring and multiple ring formation. Following the first Helmholtz vorticity conservation law, when the vortex tube is stretched and rolls up, the tube is narrowed, and an additional bridge is developed across the two legs of the



(a)  $t = 7.0T$  and  $x = 442\delta_{in}$ . Primary  $z = 1.3\delta_{in}$ , Secondary  $z = 0.8\delta_{in}$ , Third  $z = 0.2\delta_{in}$

(b)  $t = 7.8T$  and  $x = 475\delta_{in}$ . Induced small vortex at  $z = 0.2\delta_{in}$



(c)  $t = 8.2T$  and  $x = 515\delta_{in}$ . More small vortices are generated

FIGURE 20: Small vortices are generated by the wall surface at different time steps and streamwise locations by interaction with secondary vortices and positive spikes.

prime vortex tube to maintain the vorticity conservation. Consequently, the second, third, and so forth, rings are formed. Figure 14(b) shows that the multiple rings (over 8 rings) are formed and the first heading ring (right) is skewed and sloped (not perpendicular any more). From our new DNS, the so-called “spike” is nothing but formation of multi-ring (bridge) vortex structure which is quite stable. The multiple rings were generated one by one but not simultaneously like Crow theory, and the rings are perpendicular to the wall not parallel to the wall like Crow theory. Apparently, we cannot find any links between the Crow theory and the multiple ring formation.

**4.4. U-Shaped Vortex Development.** A description of the development of the U-shaped vortex can be found in the paper by Singer and Joslin [9]. Figure 15 has a 2D top view and uses low pressure contour to represent the vortex tube, which could lead to a misinterpretation that the secondary vortex is broken in to smaller pieces. Figure 16 is a 2D top view given by our new DNS with a different  $\lambda_2$ -value which gives a similar structure to Figure 15. However, there is no evidence that the secondary vortex breaks down. Let us look at the head of the so-called “turbulence spot” from different directions of view (Figure 17). The large vortex structure of the leading head of the turbulence spot is stable and is

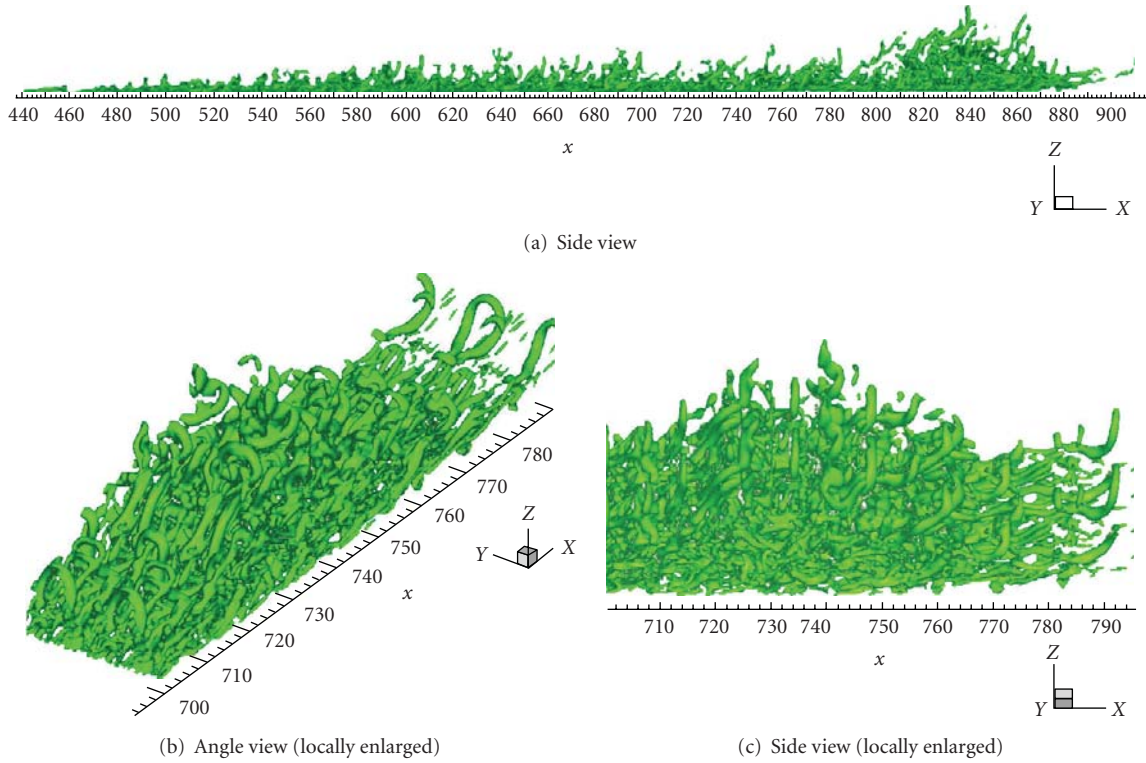


FIGURE 21: Vortex cycle overlapping and boundary layer thickening.

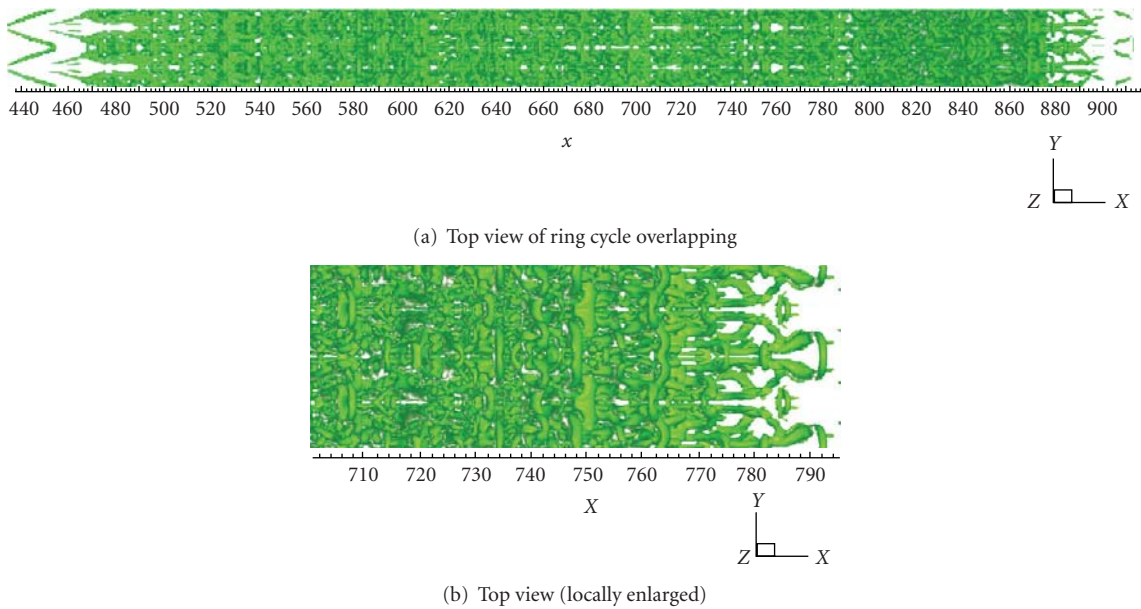


FIGURE 22: Ring cycle overlapping, but never mixing.

still there. It travels for a long distance and never breaks down. We found that the head shape looks U-shaped, but the basic vortex structure really does not change and the heading hairpin vortex never breaks down. The real situation is that the heading primary ring is still there but skewed and sloped, which leads to a disappearance of the second sweep.

The consequences are that no more energy is transported down to the boundary sublayer by the second sweep which is weakened in the area near the head of the spot. The small length-scale-structures located near the laminar bottom damped, and the originally existing U-shaped vortex is rising and becomes clearly. It was thought [9] that the U-shaped

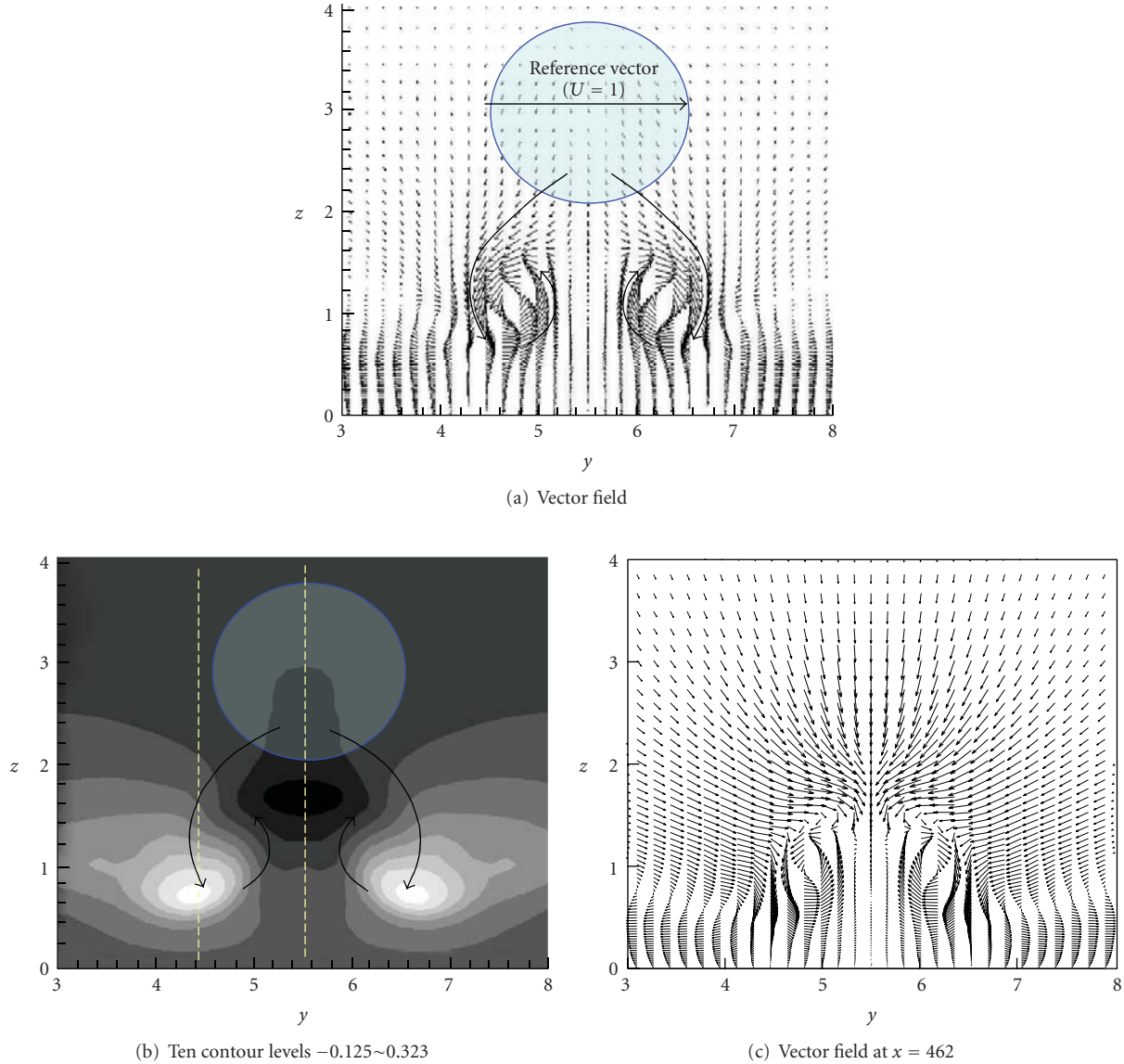


FIGURE 23: Vector field of  $(v, w)$ -velocity disturbance (a) and contours of streamwise velocity disturbance  $u$  (b) in the  $(y, z)$ -plane at  $t = 6.6T$ ,  $x = 464$ , (c)  $t = 6.6T$  and  $x = 462$ . Thick arrows display downward and upward motions associated with sweep 2 and ejection 2 events, respectively.

vortex is a newly formed secondary vortex. However it really exists for some time. The reason that the U-shaped vortex is not clearly visible at previous times is that the U-shaped vortex is surrounded by many small length scale structures. When the heading primary ring is perpendicular, it will generate a strong second sweep which brings a lot of energy from the inviscid area to the bottom of the boundary layer and makes that area very active. However, when the heading primary ring is no longer perpendicular, skewed and sloped, the second sweep disappears. The small length scale structures rapidly damp and the originally existing U-shaped vortex becomes clear since they are part of the large scale structure. Different from Singer and Joslin [9], the U-shaped vortex is found not a secondary, but tertiary vortex with same sign of vorticity of the corresponding ring leg. Actually, the

U-shaped vortex is a second neck to supply vorticity to the ring (Figures 17(b) and 17(c)).

Due to the increase of the ring (bridge) number and vorticity conservation, the leading rings will become weaker and weaker until they cannot be detected, but they never break down (see Figure 17). The multiring structure is pretty stable and the rings can travel for long distances (Figure 18) because they are located in an inviscid area and the U-shaped neck provides more vorticity.

**4.5. Mechanism of Small Length Scale Generation.** It is natural that one question will be raised. The question is where the small vortex length scales come from? We believe that these small length scale vortices are generated by the interaction of secondary and third level vortices with the wall surface.

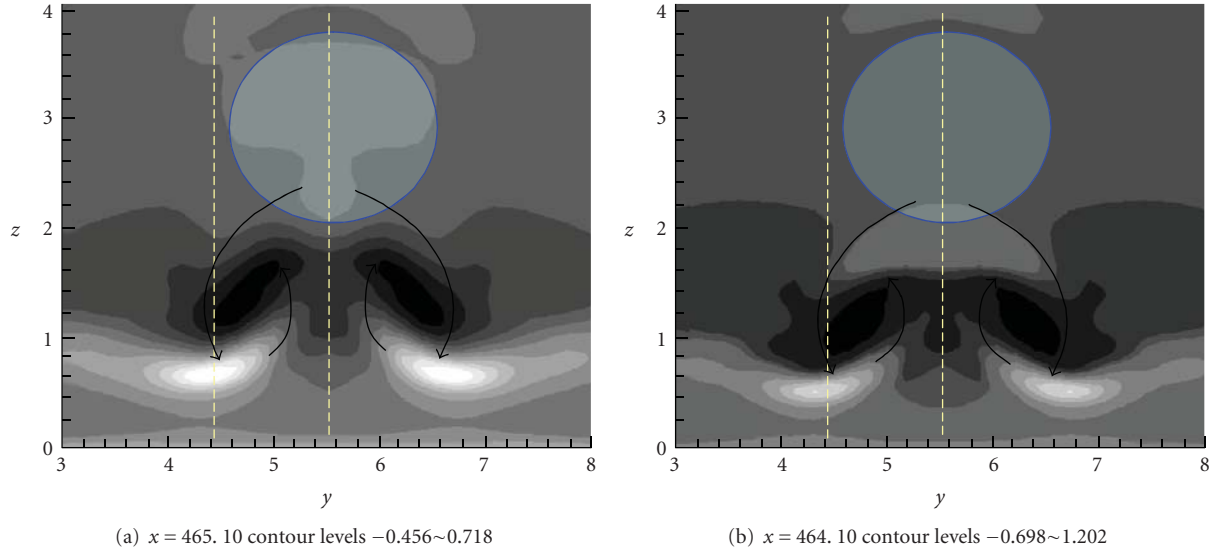


FIGURE 24: Contours of spanwise component of the vorticity disturbance in the  $(y, z)$ -plane at  $t = 6.6T$ . Light shades of gray correspond to high values.

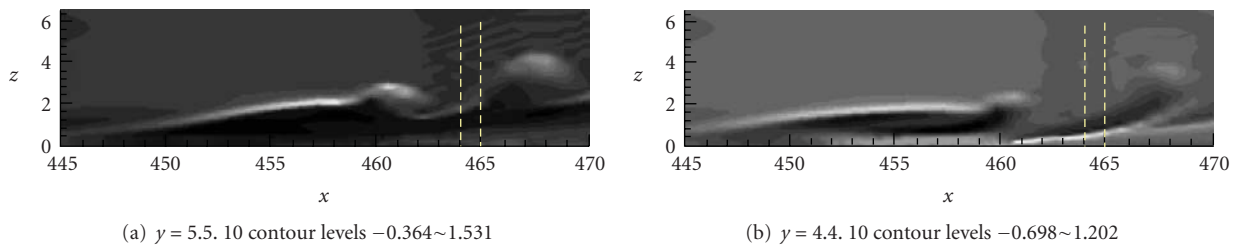


FIGURE 25: Contours of spanwise component of the vorticity disturbance in the  $(x, z)$ -plane at  $t = 6.6T$ . Light shades of gray correspond to high values.

As we know, the vorticity can only be given or generated in boundaries, but it cannot be generated inside the flow field. Actually, the wall surface is the sole source of the vorticity generation for boundary layer. Our new DNS gives the preliminary answer that the small length scale vortices are generated by the wall surface and near the wall surface as they are generated by second sweep instead of hairpin vortex breakdown. Actually, vortex breakdown is theoretically impossible and practically never found. The animations of our DNS results give details of flow transition at every stage and new mechanisms of small length scale vortex generation. We provide some snap shots here (Figure 19). Since we believe that the small vortices are generated by the wall surface and near wall region, we take snap shots in the direction of view from the bottom to top. It is easily found that the small length scale structures first appear on the wall near the ring neck area in the streamwise direction.

All evidences provided by our new DNS confirm that the small length scale vortices are generated near the bottom (Figures 19 and 20) by secondary vortices or third level vortices, especially by the positive spike caused by strong second sweeps which bring high streamwise velocity from inviscid area to sublayer.

**4.6. Vortex Cycle Overlapping.** As we discussed before, the ring head is located in the inviscid area and has much higher moving speed than the ring legs which are located near the bottom of the boundary layer. It is the reason that the hairpin vortex is stretched and multiple rings are generated. This will lead to an overlapping of second ring cycle upside of the first ring cycle. However, no mixing of two cycles is observed by our new DNS (Figures 21 and 22). The second ring is separated from first ring cycle by a secondary group of rings which are generated by the wall surface, separated from wall, and convected to downstream. This is the reason why the transitional boundary layer becomes thicker and thicker.

**4.7. High Shear Distribution.** The  $(v, w)$ -velocity disturbance vectors and the  $u$ -velocity contours are presented in Figure 23 in the  $(y, z)$ -plane. The projection of the approximate location of the first vortex ring onto this  $(y, z)$ -plane is indicated in Figure 23 with semitransparent circles. It is seen that there are two *strong downdraft jets* produced by the first vortex ring behind it at two sides of the structure centerline. The existence of these jets was called “*sweep 2*” events [5, 24].

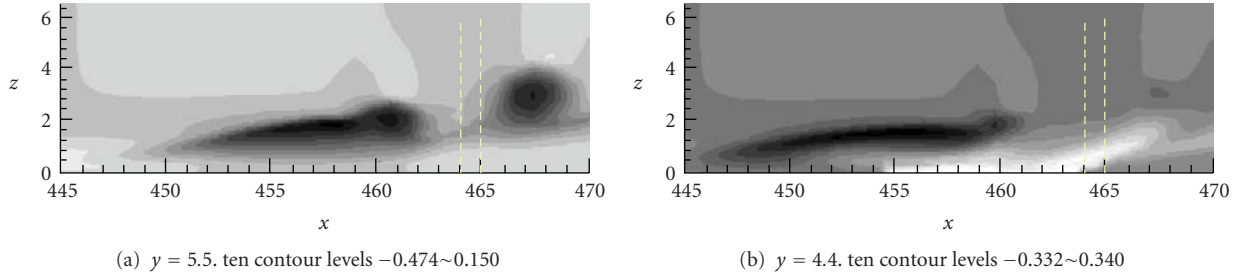


FIGURE 26: Contours of streamwise velocity disturbance  $u$  in the  $(x, z)$ -plane at  $t = 6.6T$ . Light shades of gray correspond to high values.

Formation of a low speed region between the  $\Lambda$ -vortex legs and appearance of an HS-layer slightly above and inside of the  $\Lambda$ -vortex can be found in Figures 24, 25, and 26. It is found (based on comparison of instantaneous fields calculated for various time instants) that the low-speed streaks and high-shear layers associated with the ejection 2 events seem to become weaker when the ring-like vortex propagates downstream and finally disappears. This result is consistent with observations by Bake et al. [3]. They believe that low-speed streaks and high-shear layers become weak and finally disappear because the “tail vortices” connecting the ring-like vortices move towards the wall. Based on our new DNS results, it shows that the main reason for the above phenomena is that in the middle between the two positive spikes near the ring neck, there is an area where the normal velocity component is almost zero (see Figures 23(a) and 23(c)).

## 5. Conclusions

Based on our new DNS study, the following conclusions can be made.

- (1) Vorticity is generated by the wall. The secondary vortex can be developed only through flow separation which is caused by the adverse pressure gradient.
- (2) A vortex tube inside the flow field cannot have ends, and thus vortex ring is the only form existing inside the flow field because the ring has no ends, head, or tail.
- (3) There are four streamwise vorticity lines around the  $\Lambda$ -shaped vortex, two primary inside and two secondary outside. The inside two primary streamwise vorticity lines pull out the  $\Lambda$ -shaped vortex to form the ring, but the outside two secondary vorticity lines push the  $\Lambda$ -shaped vortex to form the neck. Therefore, the formation of a ring-like vortex is the interaction between the primary and secondary streamwise vorticity lines.
- (4) The leading ring-vortices are almost perfectly circular and stand almost perpendicularly. The so-called “ring pinch off” is not found.
- (5) The stretched vortex tube will be narrowed with stronger vorticity along with faster rotation as a result

of narrowing. According to the first Helmholtz vorticity conservation law, this will lead to development of a bridge and further become a second ring, and so on.

- (6) U-shaped vortex is a coherent structure and serves as second neck to supply the rings.
- (7) Since the head of the hairpin vortex, that is, rings, is located in the inviscid area and the U-shaped vortex supplies vorticity to the ring, the consequent multiple ring-like vortex structure can travel for long distance in the flow field. The hairpin vortex will become weak until being nondetectable, but never breaks down.
- (8) The small length scales are generated by the wall surface and near the wall region, but not by the hairpin vortex breakdown.
- (9) The ring head speed is faster than the ring legs, which leads to ring cycle overlapping. Multiple ring cycle overlapping will lead to thickening of the transitional boundary layer. The multiple rings overlap, but never mix. They are separated by secondary rings which are generated by the wall surface, separated from the wall, and convected to downstream.
- (10) The updraft motion leads to the  $\Lambda$ -shaped high-speed streaks and an HS-layer near the wall outside the  $\Lambda$ -vortex legs. However, the HS-layer disappears near the ring neck because the normal velocity in the near neck area is almost zero.

## Nomenclature

- $M_\infty$ : Mach number  
 $Re$ : Reynolds number  
 $\delta_{in}$ : Inflow displacement thickness  
 $T_w$ : Wall temperature  
 $T_\infty$ : Free stream temperature  
 $Lz_{in}$ : Height at inflow boundary  
 $Lx$ : Length of computational domain along  $x$  direction  
 $Ly$ : Length of computational domain along  $y$  direction  
 $x_{in}$ : Distance between leading edge of flat plate and upstream boundary of computational domain  
 $A_{2d}$ : Amplitude of 2D inlet disturbance

$A_{3d}$ : Amplitude of 3D inlet disturbance  
 $\omega$ : Frequency of inlet disturbance  
 $\alpha_{2d}$ : Streamwise wave number of inlet disturbance  
 $\beta$ : Spanwise wave number of inlet disturbance  
 $R$ : Ideal gas constant  
 $\gamma$ : Ratio of specific heats  
 $\mu_\infty$ : Viscosity  
 $\omega_x$ : Streamwise vorticity  
 $\lambda_2$ : Const representing vortex tube surface.

## Acknowledgments

This work was supported by AFOSR grant FA9550-08-1-0201 supervised by Dr. John Schmisser. The authors are grateful to Texas Advanced Computing Center (TACC) for providing computation hours. This work is accomplished by using Code DNSUTA which was released by Dr. Chaoqun Liu at University of Texas at Arlington in 2009.

## References

- [1] L. Kleiser and T. A. Zang, "Numerical simulation of transition in wall-bounded shear flows," *Annual Review of Fluid Mechanics*, vol. 23, no. 1, pp. 495–537, 1991.
- [2] V. I. Borodulin, V. R. Gaponenko, Y. S. Kachanov et al., "Late-stage transitional boundary-layer structures. Direct numerical simulation and experiment," *Theoretical and Computational Fluid Dynamics*, vol. 15, no. 5, pp. 317–337, 2002.
- [3] S. Bake, D. G. W. Meyer, and U. Rist, "Turbulence mechanism in Klebanoff transition: a quantitative comparison of experiment and direct numerical simulation," *Journal of Fluid Mechanics*, vol. 459, pp. 217–243, 2002.
- [4] Y. S. Kachanov, "On a universal mechanism of turbulence production in wall shear flows," in *Notes on Numerical Fluid Mechanics and Multidisciplinary Design*, vol. 86 of *Recent Results in Laminar-Turbulent Transition*, pp. 1–12, Springer, Berlin, Germany, 2003.
- [5] H. Guo, J. J. Wang, Q. X. Lian et al., "Spatial reconstruction of vortical structures in transitional boundary layer based on synchronous hydrogen-bubble visualization," in *Proceedings of the 12th International Conference on Methods of Aerophysical Research Part 1*, pp. 118–124, Institute of Theoretical and Applied Mechanics, Novosibirsk, Russia, 2004.
- [6] F. R. Hama and J. Nutant, "Detailed flow-field observations in the transition process in a thick boundary layer," in *Proceedings of the Heat Transfer and Fluid Mechanics Institute*, pp. 77–93, Stanford University Press, Palo Alto, Calif, USA, 1963.
- [7] P. Moin, A. Leonard, and J. Kim, "Evolution of a curved vortex filament into a vortex ring," *Physics of Fluids*, vol. 29, no. 4, pp. 955–963, 1986.
- [8] S. C. Crow, "Stability theory for a pair of trailing vortices," *AIAA Journal*, vol. 8, no. 12, pp. 2173–2179, 1970.
- [9] B. A. Singer and R. D. Joslin, "Metamorphosis of a hairpin vortex into a young turbulent spot," *Physics of Fluids*, vol. 6, no. 11, pp. 3724–3736, 1994.
- [10] C. B. Lee and J. Z. Wu, "Transition in wall-bounded flows," *Applied Mechanics Reviews*, vol. 61, no. 1–6, pp. 030802–03080219, 2008.
- [11] H. Schlichting and K. Gersten, *Boundary Layer Theory*, Springer, Berlin, Germany, 8th edition, 2000.
- [12] J. Jinhee Jeong and F. Hussain, "On the identification of a vortex," *Journal of Fluid Mechanics*, vol. 285, pp. 69–94, 1995.
- [13] C. Lee and R. Li, "Dominant structure for turbulent production in a transitional boundary layer," *Journal of Turbulence*, vol. 8, no. 5, pp. 1–34, 2007.
- [14] S. K. Lele, "Compact finite difference schemes with spectral-like resolution," *Journal of Computational Physics*, vol. 103, no. 1, pp. 16–42, 1992.
- [15] C. W. Shu and S. Osher, "Efficient implementation of essentially non-oscillatory shock-capturing schemes," *Journal of Computational Physics*, vol. 77, no. 2, pp. 439–471, 1988.
- [16] L. Jiang, H. Shan, and C. Liu, "Non-reflecting boundary conditions for DNS in curvilinear coordinates," in *Proceedings of the 2nd AFOSR International Conference on DNS/LES, Recent Advances in DNS and LES*, Rutgers-The State University of New Jersey, New Brunswick, NJ, USA, June 1999.
- [17] M. R. Malik, "Numerical methods for hypersonic boundary layer stability," *Journal of Computational Physics*, vol. 86, no. 2, pp. 376–413, 1990.
- [18] F. Ducros, P. Comte, and M. Lesieur, "Large-eddy simulation of transition to turbulence in a boundary layer developing spatially over a flat plate," *Journal of Fluid Mechanics*, vol. 326, pp. 1–36, 1996.
- [19] L. Chen, D. B. Tang, X. B. Liu, M. Oliveira, and C. Q. Liu, "Evolution of the ring-like vortices and spike structure in transitional boundary layers," *Science China: Physics, Mechanics and Astronomy*, vol. 53, no. 3, pp. 514–520, 2010.
- [20] L. Chen, X. Liu, M. Oliveira, and C. Liu, "DNS for ring-like vortices formation and roles in positive spikes formation," Tech. Rep. 2010-1471, AIAA, 2010.
- [21] C. Liu and L. Chen, "DNS for late stage structure of flow transition on a flat-plate boundary layer," Tech. Rep. 2010-1470, AIAA, 2010.
- [22] X.-B. Liu, Z.-Q. Chen, and C.-Q. Liu, "Late-stage vortical structures and eddy motions in a transitional boundary layer," *Chinese Physics Letters*, vol. 27, no. 2, Article ID 024706, 2010.
- [23] X. Liu, L. Chen, and C. Liu, "Study of mechanism of ring-like vortex formation in late flow transition," Tech. Rep. 2010-1456, AIAA, 2010.
- [24] H. Guo, Q. X. Lian, C. Pan et al., "Sweep and ejection events in transitional boundary layer. Synchronous visualization and spatial reconstruction," in *Proceedings of the 13th International Conference on Methods of Aerophysical Research Part 4*, pp. 192–197, Publishing House "Parallel", Novosibirsk, Russia, 2007.

## Research Article

# Implicit LES for Supersonic Microramp Vortex Generator: New Discoveries and New Mechanisms

**Qin Li and Chaoqun Liu**

*Math Department, University of Texas at Arlington, 411 S. Nedderman Drive, Arlington, TX 76019-0408, USA*

Correspondence should be addressed to Chaoqun Liu, cliu@exchange.uta.edu

Received 6 October 2010; Accepted 12 January 2011

Academic Editor: Guan Yeoh

Copyright © 2011 Q. Li and C. Liu. This is an open access article distributed under the Creative Commons Attribution License, which permits unrestricted use, distribution, and reproduction in any medium, provided the original work is properly cited.

This paper serves as a summary of our recent work on LES for supersonic MVG. An implicitly implemented large eddy simulation (ILES) by using the fifth-order *WENO* scheme is applied to study the flow around the microramp vortex generator (MVG) at Mach 2.5 and  $Re_\theta = 1440$ . A number of new discoveries on the flow around supersonic MVG have been made including spiral points, surface separation topology, source of the momentum deficit, inflection surface, Kelvin-Helmholtz instability, vortex ring generation, ring-shock interaction, 3D recompression shock structure, and influence of MVG decline angles. Most of the new discoveries, which were made in 2009, were confirmed by experiment conducted by the UTA experimental team in 2010. A new 5-pair-vortex-tube model near the MVG is given based on the ILES observation. The vortex ring-shock interaction is found as the new mechanism of the reduction of the separation zone induced by the shock-boundary layer interaction.

## 1. Introduction

It is well known that for the supersonic ramp jet flow, shock boundary layer interaction (SBLI) can significantly degrade the quality of the flow field by triggering large-scale separation, causing total pressure loss, making the flow unsteady and distorted, and can even make an engine unable to start. In order to improve the “health” of the boundary layer, a series of new devices named as micro vortex generator is designed for flow control, which is with a height approximately 20–40% (more or less) of the boundary layer thickness. Because of the robust structure, the specific microramp vortex generator (MVG) becomes more attractive to the inlet designer. Intensive computational and experimental studies have been made on the MVG recently.

Lin indicated [1] that the device like MVG could alleviate the flow distortion in compact ducts to some extent and control boundary layer separation due to the adverse pressure gradients. Similar comments were made in the review by Ashill et al. [2]. The formal and systematic studies about the micro VGs including micro ramp VG can be found in

the paper by Anderson et al. [3]. Babinsky et al. [4–7] made a series of experiments on different kinds of micro VGs and investigated their control effects in details. The mechanism of MVG flow control from his work was described as that a pair of counter-rotating primary streamwise vortices is generated by MVG, which is mainly located within the boundary layer and travel downstream for a considerable distance. Secondary vortices are located underneath the primary ones and even more streamwise vortices could be generated under suitable conditions. Streamwise vortices inside the boundary layer will bring low-momentum fluids up from the bottom and high-momentum fluids down to the boundary layer. A striking circular momentum deficit region is observed in the wake behind the MVG. The vortices will keep lifting up slowly, which is thought to be the consequence of the upwash effect of the vortices.

Numerical simulations have been made on MVG for comparative study and further design purposes. Ghosh et al. [8] made detailed computations under the experimental conditions given by Babinsky by using RANS, hybrid RANS/LES, and immersed boundary (IB) techniques. Lee et al. [9, 10] also made computations on the micro VGs problems

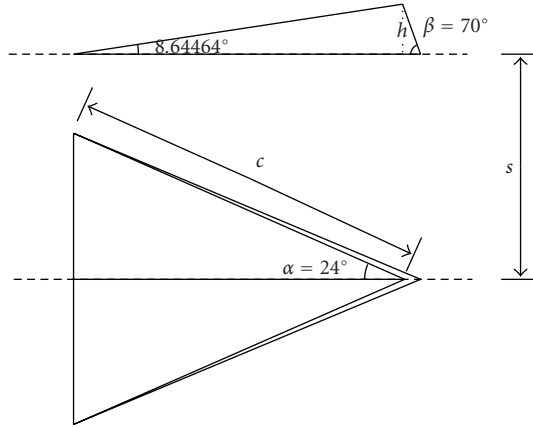


FIGURE 1: The geometry of MVG.

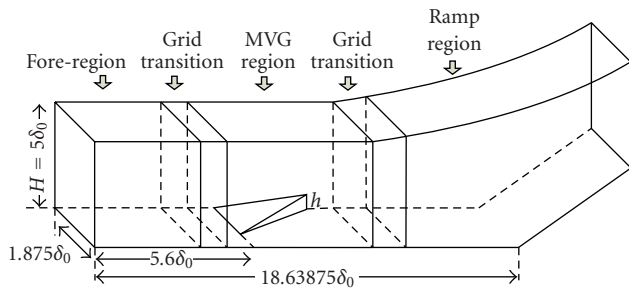
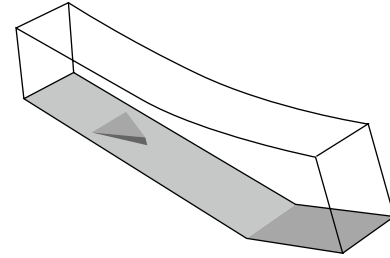


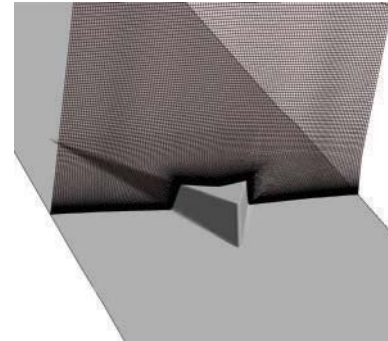
FIGURE 2: The schematic of the half-grid system of case (1).

by using Monotone Integrated Large Eddy Simulations (MILES). Basic flow structures like momentum deficit and streamwise vortices were reproduced in the computation. Further studies were also conducted on the improvement of the control effect.

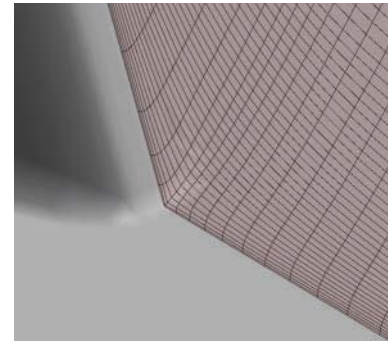
Finding physics of MVG for design engineers is definitely needed. RANS, DES, RANS/DES, RANS/LES, and so forth are good engineering tools, but may not be able to reveal the mechanism and get deep understanding of MVG. We need high-order DNS/LES. A powerful tool is the integration of high-order LES and experiment. Recently, an implicit LES for MVG to control the shock-boundary layer interaction around a 24 degree ramp at Mach number of 2.5 and Reynolds number of 1440 has been carried out in 2009 [12]. In this work, several new discoveries have been made and the mechanism of MVG is found quite different from those reported by previous experimental and numerical work in the literature. The new findings include (1) spiral points and flow topology around MVG, (2) new theory of five pairs of vortices near MVG, (3) origin of momentum deficit, (4) inflection points (surface for 3D) and Kelvin-Helmholtz- (K-H-) type instability, (5) vortex ring generation, (6) ring-shock interaction and separation reduction, (7) 3D re-compressed shock structure, and (8) effects of trailing-edge decline angles.



(a) Computational domain



(b) The grid section intersecting the middle of MVG



(c) The grids at the corner of MVG

FIGURE 3: Body-fitted grid system.



FIGURE 4: The digital schlieren at central plane.

Most of the new discoveries were made by October 2009 and were later confirmed by the UTA experimental work in April 2010 [13]. Based on our observation, the mechanism of MVG to reduce the flow separation is really caused by interaction of shock and vortex rings generated by MVG.

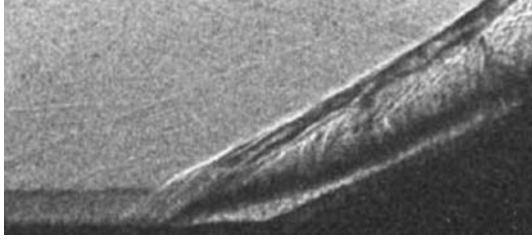


FIGURE 5: The experimental schlieren by Loginov et al. [11].

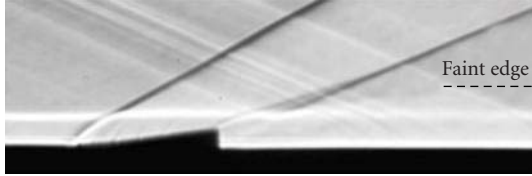


FIGURE 6: The experimental schlieren by Babinsky et al. [7].

The paper is arranged as following. The numerical methods are discussed in Section 2. In Section 3, all new discoveries are summarized and analyzed and the new mechanism is described. Finally, conclusions are made in Section 4.

## 2. Numerical Methods

*2.1. Governing Equations.* The governing equations are the nondimensional Navier-Stokes equations in conservative form as follows:

$$\frac{\partial Q}{\partial t} + \frac{\partial E}{\partial x} + \frac{\partial F}{\partial y} + \frac{\partial G}{\partial z} = \frac{\partial E_v}{\partial x} + \frac{\partial F_v}{\partial y} + \frac{\partial G_v}{\partial z}, \quad (1)$$

where

$$Q = \begin{bmatrix} \rho \\ \rho u \\ \rho v \\ \rho w \\ e \end{bmatrix}, \quad E = \begin{bmatrix} \rho u \\ \rho u^2 + p \\ \rho uv \\ \rho uw \\ (e+p)u \end{bmatrix}, \quad F = \begin{bmatrix} \rho v \\ \rho vu \\ \rho v^2 + p \\ \rho vw \\ (e+p)v \end{bmatrix}, \quad G = \begin{bmatrix} \rho w \\ \rho wu \\ \rho wv \\ \rho w^2 + p \\ (e+p)w \end{bmatrix},$$

$$E_v = \frac{1}{\text{Re}} \begin{bmatrix} 0 \\ \tau_{xx} \\ \tau_{xy} \\ \tau_{xz} \\ u\tau_{xx} + v\tau_{xy} + w\tau_{xz} + q_x \end{bmatrix}, \quad F_v = \frac{1}{\text{Re}} \begin{bmatrix} 0 \\ \tau_{yx} \\ \tau_{yy} \\ \tau_{yz} \\ u\tau_{yx} + v\tau_{yy} + w\tau_{yz} + q_y \end{bmatrix}, \quad G_v = \frac{1}{\text{Re}} \begin{bmatrix} 0 \\ \tau_{zx} \\ \tau_{zy} \\ \tau_{zz} \\ u\tau_{zx} + v\tau_{zy} + w\tau_{zz} + q_z \end{bmatrix},$$

$$e = \frac{p}{\gamma - 1} + \frac{1}{2}\rho(u^2 + v^2 + w^2), \quad q_x = \frac{\mu}{(\gamma - 1)M_\infty^2 \text{Pr}} \frac{\partial T}{\partial x}, \quad q_y = \frac{\mu}{(\gamma - 1)M_\infty^2 \text{Pr}} \frac{\partial T}{\partial y},$$

$$q_z = \frac{\mu}{(\gamma - 1)M_\infty^2 \text{Pr}} \frac{\partial T}{\partial z}, \quad p = \frac{1}{\gamma M_\infty^2} \rho T, \quad \text{Pr} = 0.72,$$

$$\tau = \mu \begin{bmatrix} \frac{4}{3} \frac{\partial u}{\partial x} - \frac{2}{3} \left( \frac{\partial v}{\partial y} + \frac{\partial w}{\partial z} \right) & \frac{\partial u}{\partial y} + \frac{\partial v}{\partial x} & \frac{\partial u}{\partial z} + \frac{\partial w}{\partial x} \\ \frac{\partial u}{\partial y} + \frac{\partial v}{\partial x} & \frac{4}{3} \frac{\partial v}{\partial y} - \frac{2}{3} \left( \frac{\partial w}{\partial z} + \frac{\partial u}{\partial x} \right) & \frac{\partial v}{\partial z} + \frac{\partial w}{\partial y} \\ \frac{\partial u}{\partial z} + \frac{\partial w}{\partial x} & \frac{\partial v}{\partial z} + \frac{\partial w}{\partial y} & \frac{4}{3} \frac{\partial w}{\partial z} - \frac{2}{3} \left( \frac{\partial u}{\partial x} + \frac{\partial v}{\partial y} \right) \end{bmatrix}. \quad (2)$$

The viscous coefficient is given by Sutherland's equation:

$$\mu = T^{3/2} \frac{1+C}{T+C}, \quad C = \frac{110.4}{T_\infty}. \quad (3)$$

The nondimensional variables are defined as follows:

$$x = \frac{\tilde{x}}{L}, \quad y = \frac{\tilde{y}}{L}, \quad z = \frac{\tilde{z}}{L},$$

$$u = \frac{\tilde{u}}{U_\infty}, \quad v = \frac{\tilde{v}}{U_\infty}, \quad w = \frac{\tilde{w}}{U_\infty},$$

$$T = \frac{\tilde{T}}{T_\infty}, \quad \mu = \frac{\tilde{\mu}}{\mu_\infty}, \quad k = \frac{\tilde{k}}{k_\infty},$$

$$\rho = \frac{\tilde{\rho}}{\rho_\infty}, \quad p = \frac{\tilde{p}}{\rho_\infty U_\infty^2}, \quad e = \frac{\tilde{e}}{\rho_\infty U_\infty^2}, \quad (4)$$

where the variables with “~” are the dimensional counterparts.

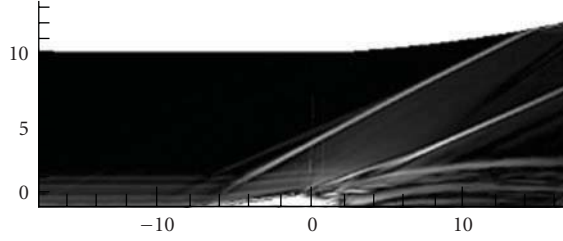


FIGURE 7: The numerical schlieren at central plane.

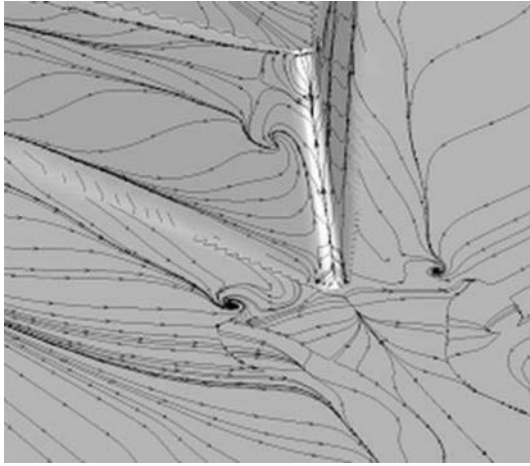


FIGURE 8: Spiral point pairs by ILES in 2009.

Considering the following grid transformation,

$$\begin{aligned}\xi &= \xi(x, y, z), \\ \eta &= \eta(x, y, z), \\ \zeta &= \zeta(x, y, z),\end{aligned}\quad (5)$$

the Navier-Stokes equations can be transformed to the system using generalized coordinates:

$$\frac{\partial \hat{Q}}{\partial \tau} + \frac{\partial \hat{E}}{\partial \xi} + \frac{\partial \hat{F}}{\partial \eta} + \frac{\partial \hat{G}}{\partial \zeta} = \frac{\partial \hat{E}_v}{\partial \xi} + \frac{\partial \hat{F}_v}{\partial \eta} + \frac{\partial \hat{G}_v}{\partial \zeta}, \quad (6)$$

where  $\hat{Q} = J^{-1}Q$  and

$$\begin{aligned}\hat{E} &= J^{-1}(\xi_x E + \xi_y F + \xi_z G), \\ \hat{F} &= J^{-1}(\eta_x E + \eta_y F + \eta_z G), \\ \hat{G} &= J^{-1}(\zeta_x E + \zeta_y F + \zeta_z G), \\ \hat{E}_v &= J^{-1}(\xi_x E_v + \xi_y F_v + \xi_z G_v), \\ \hat{F}_v &= J^{-1}(\eta_x E_v + \eta_y F_v + \eta_z G_v), \\ \hat{G}_v &= J^{-1}(\zeta_x E_v + \zeta_y F_v + \zeta_z G_v),\end{aligned}\quad (7)$$

$J^{-1}$ ,  $\xi_x$ , and so forth, are grid metrics, and  $J^{-1} = \det(\partial(x, y, z)/\partial(\xi, \eta, \zeta))$ ,  $\xi_x = J(y_\eta z_\zeta - z_\eta y_\zeta)$ , and so forth.

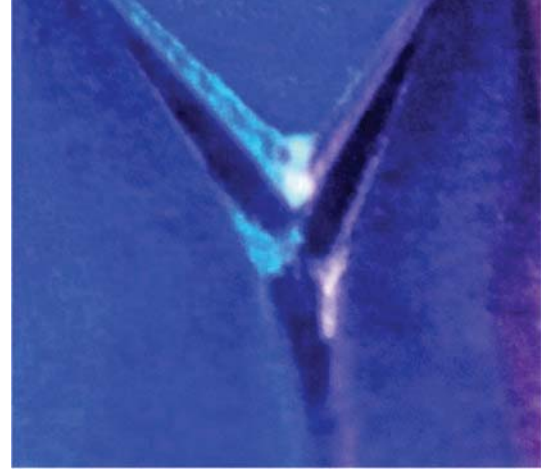
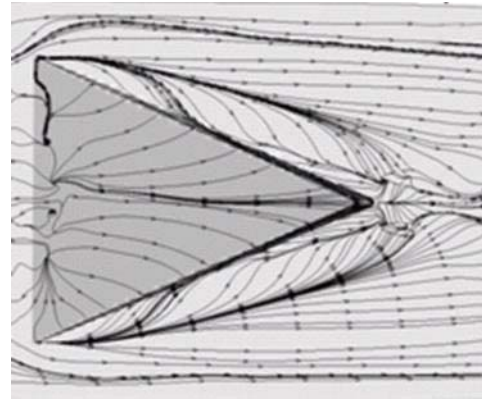
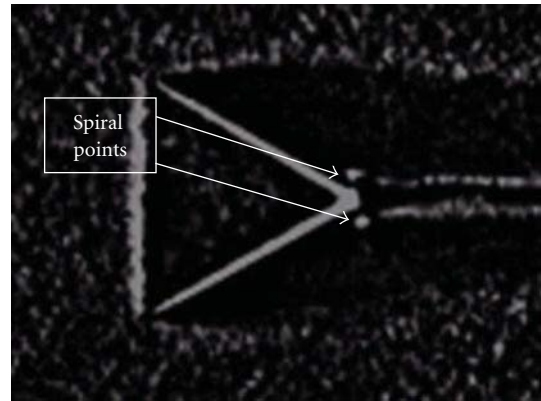


FIGURE 9: Oil accumulation blocks by UTA experiment in 2010.



(a)



(b)

FIGURE 10: Comparison of ILES with UTA experiment.

## 2.2. Finite Difference Schemes and Boundary Conditions

1. *The Fifth-Order WENO Scheme for the Convective Terms [14]*. In order to decrease the dissipation of the scheme, the less dissipative Steger-Warming flux splitting method is used in the computation, but not the commonly used dissipative Lax-Friedrich splitting method.

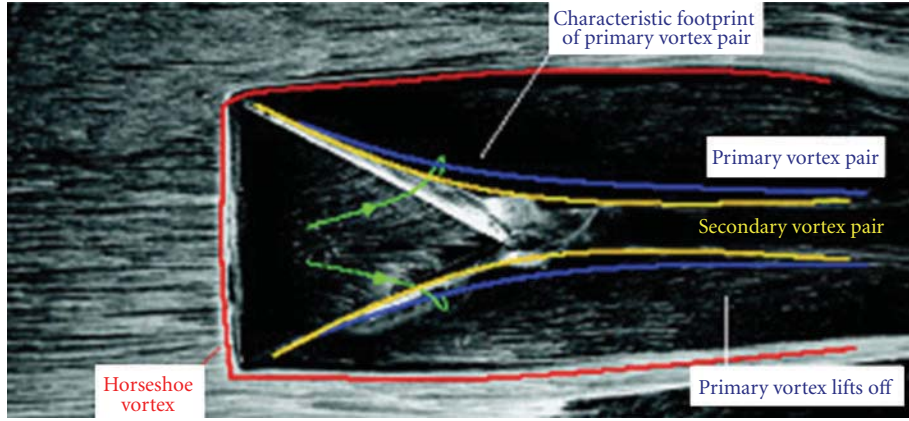


FIGURE 11: Traditional vortex structure around MVG.

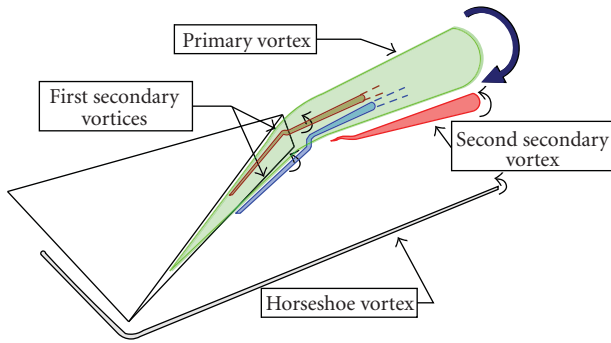


FIGURE 12: New 5-pair-vortex-tube model near MVG.

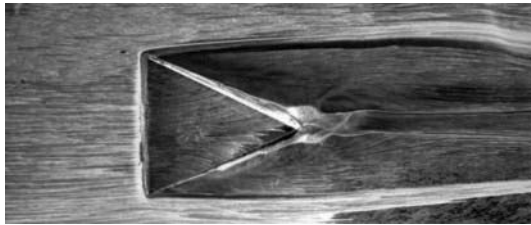


FIGURE 13: The surface oil flow by Babinsky7.

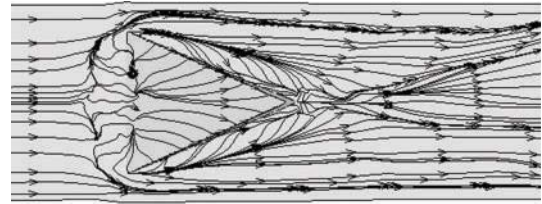


FIGURE 14: The surface limiting streamlines by computation.

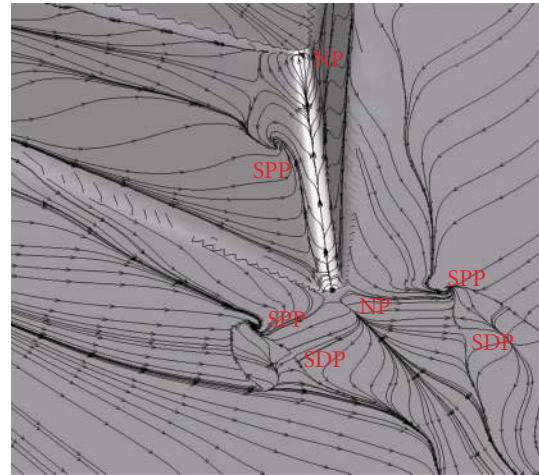


FIGURE 15: The separation pattern near the end of MVG.

2. *The Difference Scheme for the Viscous Terms.* Considering the conservative form of the governing equations, the traditional fourth-order central scheme is used twice to compute the second-order derivatives for viscous terms.

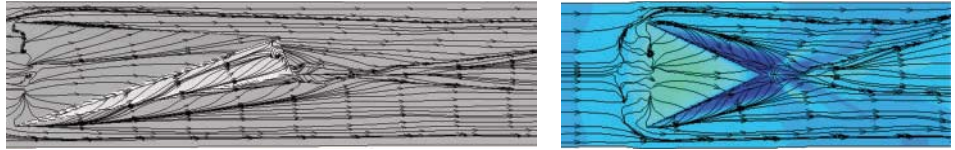
3. *The Time Schemes.* The basic methodology for the temporal terms in the Navier-Stokes equations adopts the explicit third-order TVD-type Runge-Kutta scheme:

$$\begin{aligned}
 u^{(1)} &= u^n + \Delta t L(u^n), \\
 u^{(2)} &= \frac{3}{4}u^n + \frac{1}{4}u^{(1)} + \frac{1}{4}\Delta t L(u^{(1)}), \\
 u^{n+1} &= \frac{1}{3}u^n + \frac{2}{3}u^{(2)} + \frac{2}{3}\Delta t L(u^{(2)}).
 \end{aligned}
 \tag{8}$$

4. *Boundary Conditions.* The adiabatic, zero-gradient of pressure and nonslipping conditions are used for the wall as

$$\frac{\partial T}{\partial n} = 0, \quad \frac{\partial p}{\partial n} = 0, \quad \vec{U} = 0. \tag{9}$$

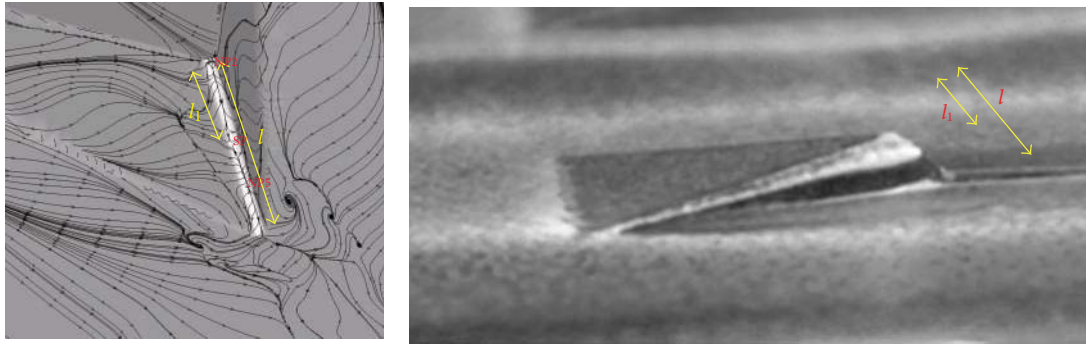
To enforce the free stream condition, fixed-value boundary condition with the free parameters is used on the upper boundary. The boundary conditions at the front and back boundary surface in the spanwise direction are given as the mirror-symmetry condition. The outflow boundary conditions are specified as a kind of characteristic-based condition, which can handle the outgoing flow without



(a) SSP on the side of MVG

(b) SSP backgrounded using the pressure contour

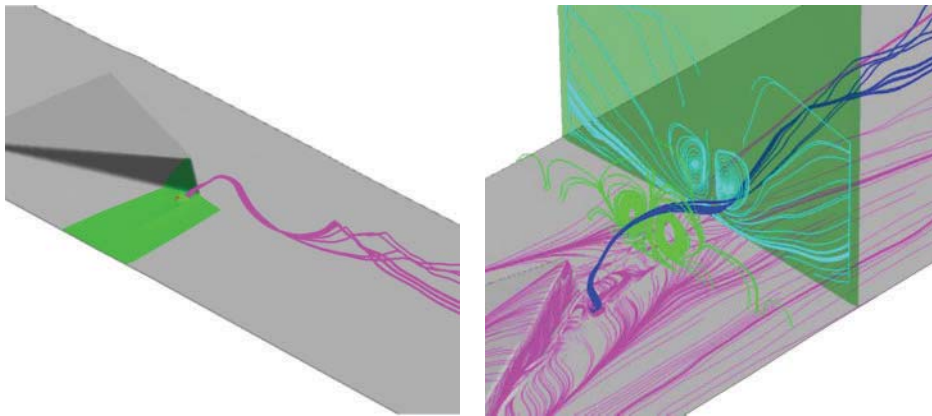
FIGURE 16: The various views of surface separation pattern (SSP).



(a) Computation:  $l_1/l = 0.57$

(b) Experiment:  $l_1/l = 0.545$

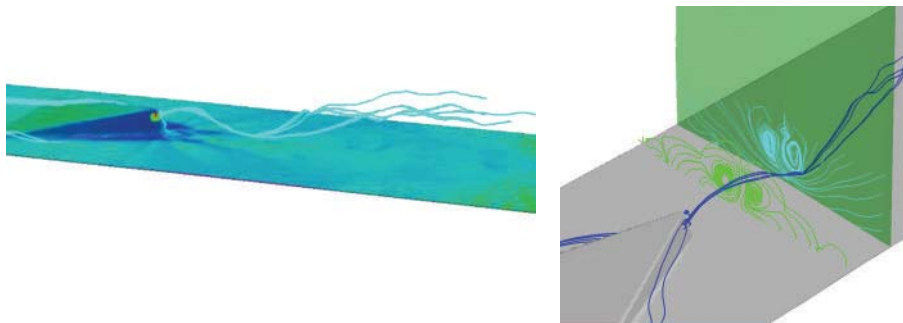
FIGURE 17: Comparison of ILES and experiment in surface flow topology.



(a) Secondary vortex lifts up

(b) Moving downstream around the primary

FIGURE 18: Secondary vortex tubes lift up from the bottom plate.



(a) Secondary vortex lifts up

(b) Moving downstream around the primary

FIGURE 19: Secondary vortex tubes lift up from MVG sides.

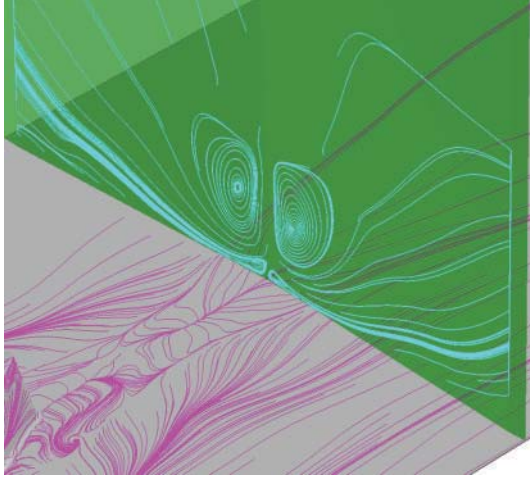


FIGURE 20: New secondary vortex tubes induced by the primary.

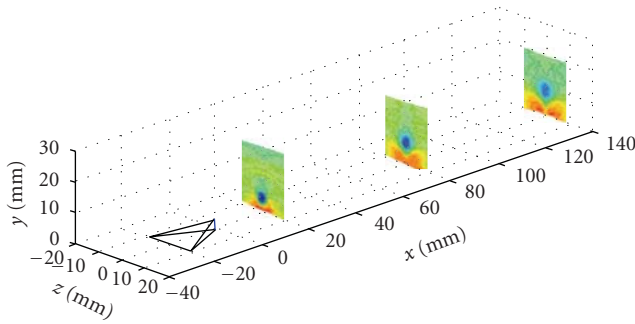


FIGURE 21: Momentum deficit shown in different streamwise directions.

reflection. The inflow conditions are generated using the following steps.

- A turbulent mean profile is obtained from DNS by Liu and Chen [15] for the streamwise velocity ( $w$ -velocity) and the distribution is scaled using the local displacement thickness and free stream velocity.
- Random fluctuations are added on the primitive variables, that is,  $u$ ,  $v$ ,  $w$ ,  $p$ ,  $\rho$ . The disturbance has the form:  $\varepsilon_{\text{distb}} e^{-(y-y_w)^2/\Delta y_{\text{distb}}} \times (\text{random} - 0.5)/2$ , where the subscript “distb” means the disturbance, “random” is the random function with the value between 0~1,  $\varepsilon_{\text{distb}}$  equals to 0.1, and  $\Delta y_{\text{distb}}$  equals to  $2/3\delta_0$ .

Such inflow conditions are, of course, not the fully developed turbulent flow, but we can consider it as a weakly disturbed inflow while propagating downstream.

**5. Body-Fitted Grid Generation.** The geometry of MVG is shown in Figure 1. In order to alleviate the difficulty to grid generation caused by original vertical trailing-edge, a modification is made by declining the edge to  $70^\circ$ . The other geometric parameters in the figure are the same as those given by Holden and Babinsky [5], that is,  $c = 7.2h$ ,  $\alpha = 24^\circ$ ,

and  $s = 7.5h$ , where  $h$  is the height of MVG and  $s$  is the distance between the center lines of two adjacent MVGs. So the distance from the center line to the spanwise boundary of the computation domain is  $3.75h$ . According to experiments by Holden and Babinsky [5], the ratio  $h/\delta_0$  of the models has the range from 0.3~1. The appropriate distance from the trailing-edge to the control area is around  $19\sim 56h$  or  $8\sim 19\delta_0$ . So in this study, the height of MVG  $h$  is assumed to be  $\delta_0/2$  and the horizontal distance from the apex of MVG to the ramp corner is set to be  $19.5h$  or  $9.75\delta_0$ . The distance from the end of the ramp to the apex is  $32.2896h$ . The distance from the starting point of the domain to the apex of MVG is  $17.7775h$ . The height of the domain is from  $10h$  to  $15h$  and the width of the half domain is  $3.75h$ . The geometric relation of the half of the domain can be seen in Figure 2, where the symmetric plane is the centre plane. The grid number for the whole system is  $n_{\text{spanwise}} \times n_{\text{normal}} \times n_{\text{streamwise}} = 128 \times 192 \times 1600$ . We try to make the grids smooth and orthogonal as much as possible (Figure 3).

### 2.3. Code Validation

**1. Supersonic Ramp.** Figure 4 gives the instantaneous numerical schlieren image of the central plane, which uses the value of  $|\nabla\rho|$ . For qualitative comparison, an experimental picture of ramp flow at  $M = 2.9$  with large Reynolds number is given in Figure 5 obtained from the experiment by Loginov et al. [11]. From both pictures, we can observe that the separation shock wave has a declining angle which is a little larger but nearly same to the ramp angle and is almost aligned with the reflection shock (which is more obvious in the picture of the experiment); complex compressive waves are generated underneath the shock by vortices in the boundary layer.

**2. Supersonic MVG.** Based on the schlieren picture of the experiment, Babinsky et al. [7] presented the structure of the wave system, that is, the first reflection shock, the expansion wave system, and the recompression shock, as shown in Figure 6. The first shock will bend within the incoming boundary layer due to “the change in Mach number”, and “a second shock wave then turns the flow back to horizontal”. A subtle oblique “ $\lambda$ ” structure is observed at the foot of the recompression shock from the picture. The numerical schlieren picture of the time-averaged flow field at the central plane is presented in Figure 7. From the figure, the two shock waves are well described by the computation. The bending of the main shock to the wall can be distinguished; the oblique “ $\lambda$ ” structure can be found on the foot of the second shock as well. Table 1 gives a comparison between numerical and experimental results. The measured shock angles from Babinsky’s experiment are  $26.869^\circ$  for the first shock and  $21.93^\circ$  for the recompression shock. In contrast, the computational values are  $26.988^\circ$  for the first shock, and  $24.656^\circ$  for the recompression shock. Considering the declining angle of the trailing-edge is  $70^\circ$ , not the  $90^\circ$  as in the experiment, the computational results show a reasonable agreement with experiment and of a high degree of resolution.

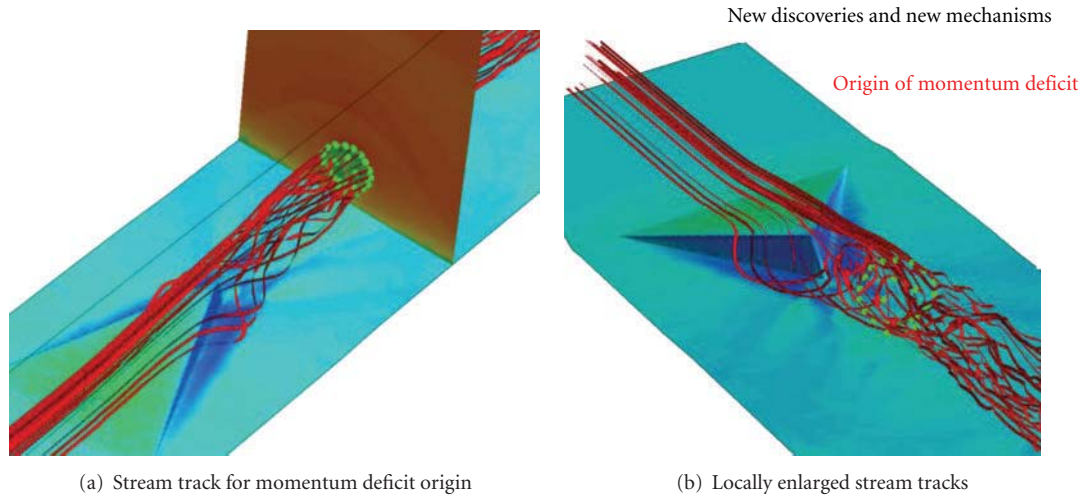


FIGURE 22: Origin of the momentum deficit comes from the upper surface flow of MVG entrained by the primary vortex tubes.

TABLE 1: Comparison between ILES and experiment in shock angles.

	1st shock	2nd shock
Experiment	26.869°	21.93°
Computation	26.988°	24.656°

### 3. New Discoveries

**3.1. Discovery I: Spiral Points and Vortex Structure around MVG.** A pair of spiral points on the bottom plate and another pair on the sides of MVG (Figure 8) have been found by ILES. These spiral points indicate the rising from the wall surface of the secondary vortex pairs. These new findings have been confirmed by UTA oil flow experiment (Figure 9), which shows accumulation blocks of paint. A further comparison is given in Figure 10.

**3.2. Discovery II: New Model of Five Pairs of Vortices near MVG.** The traditional vortex structure around MVG is depicted in Figure 11 by Babinsky et al. [7], that is, a pair of counter-rotating primary streamwise vortices is generated by MVG, which is mainly located within the boundary layer and travel downstream for a considerable distance. Secondary vortices are located underneath the primary ones and even more streamwise vortices could be generated under suitable conditions. However, a new model of 5 pairs of vortex tubes near MVG is given by us in Figure 12. The main difference between the two models is about the secondary vortex structures. There are two pairs of rising secondary vortex tubes corresponding to two pairs of spiral points. After the two pairs of secondary vortex tubes rising, a new pair of the secondary tubes is induced by the primary vortex tubes. Of course, there is additional one pair of horseshoe vortices. Recently, in April 2010, the experimentalists in the University of Texas at Arlington (UT Arlington) took a video from the top view to record the process of the MVG oil flow. A distinct pair of oil accumulating points was found in the video (see the experimental snapshot in Figures 9 and 10).

**3.3. Discovery III: Surface Separation Topology.** For comparison, the pictures of the surface oil flow from experiment and limiting streamlines from the computation are given in Figures 13 and 14. The topology of the two figures is essentially the same. The separation lines of the horseshoe vortex, the secondary separation lines beside the MVG, and the ones after the MVG are clearly described by computation (Figures 15 and 16). Such lines are the most obvious traces found in experiment due to the deposit of the oil. Figure 17 provides a comparison of computation and experiment in surface topology. The black area in experiment shows no oil flow from MVG top surface, which is corresponding to flow separation in computation. The agreement between computation and experiment is well obtained.

The original secondary vortex tubes induced by the primary vortex tubes on the bottom plate and MVG sides were lifted up from the spiral points and further move downstream around the primary (Figures 18 and 19). After that, a pair of new secondary vortex tubes is induced by the primary vortex tubes (Figure 20).

**3.4. Discovery IV: Origin of Momentum Deficit.** The momentum deficit is a unique phenomenon which was first observed in the experiment by Ford and Babinsky [6], and later confirmed by the computation of Ghosh et al. [8] and Lee et al. [10], as shown in Figure 21, using the averaged streamwise velocity at different sections. About the mechanism of the deficit, Babinsky thought it is the wake of MVG, and Lee only mentioned “the two vortical tubes merge together to create a larger tube with two counter-rotating vortices inside”. What is the relation of the deficit to the flow structure? What does the low-speed flow come from? The existing explanations did not provide a clear mechanism about the formation of the deficit.

In order to investigate the origins of the deficit, a heuristic analysis is made by investigating specific streamlines that are defined by certain cross-section of the momentum deficit. First, a cross-section after the MVG is selected as a reference

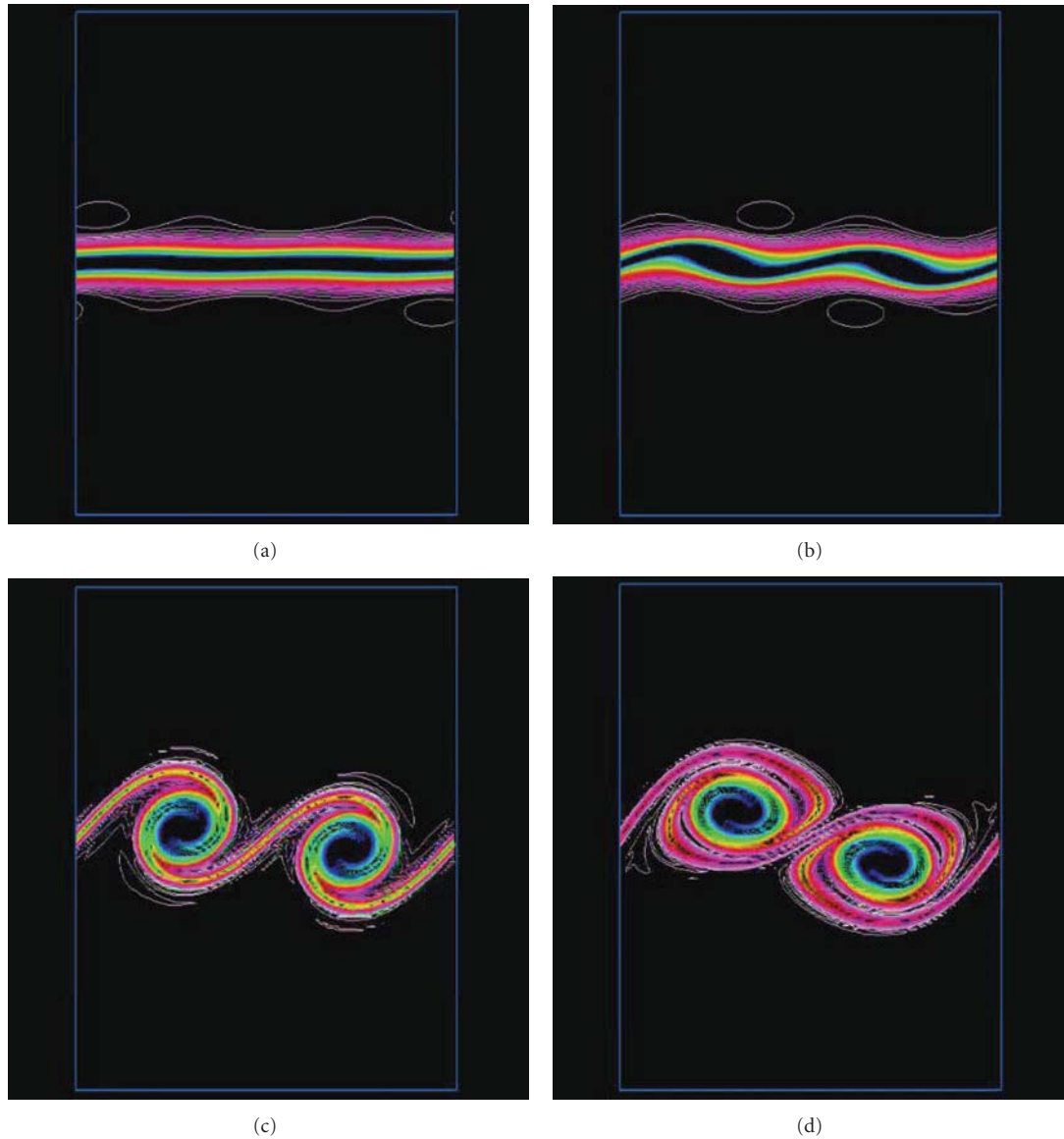


FIGURE 23: 2D Kelvin-Helmholtz instability and vortex ring formation.

plane as shown in Figure 22, and the momentum deficit on the plane is shown by using the contour of the instantaneous streamwise velocity, which appears in a green circular region. Next, we put some seeds around the boundary of the deficit and within the deficit area. Then we draw the 3D streamlines starting from the seeds in both backward and forward directions. Because the seeds surround or locate within the deficit, the distribution of the backward streamlines qualitatively reflects the origins of the deficit. It can be seen from Figure 22 that (a) all backward streamlines rotate around the primary streamwise vortex, which indicates that the formation of the deficit is caused by primary vortices; (b) all backwards streamlines come from the upper surface of the MVG, which indicates that the main source of the deficit is the shedding of the upstream low-speed boundary layer, but is not the boundary layer flow around the MVG or after the MVG.

### 3.5. Discovery V: Inflection Surface, K-H Instability, and Vortex Ring Generation by MVG

**3.5.1. 2D Kelvin-Helmholtz Instability.** 2D instability caused by shear layer with inflow disturbances and formation of pairing vortex rings was obtained by our previous calculation (Figure 23). It is usually called Kelvin-Helmholtz instability which is described as inviscid instability.

**3.5.2. Inflection Surface in 3D Flow behind MVG.** In order to explore the mechanism of the vortex ring generation, the distributions of averaged streamwise velocity are given in Figure 24 along the normal grid lines at the center plane. The streamwise positions of the lines are  $L_{\text{from apex}}/h \approx 3.3, 6.7, 10, \text{ and } 11$ , where  $L_{\text{from apex}}$  is the streamwise distance measured from the apex of MVG. The dip of the lines

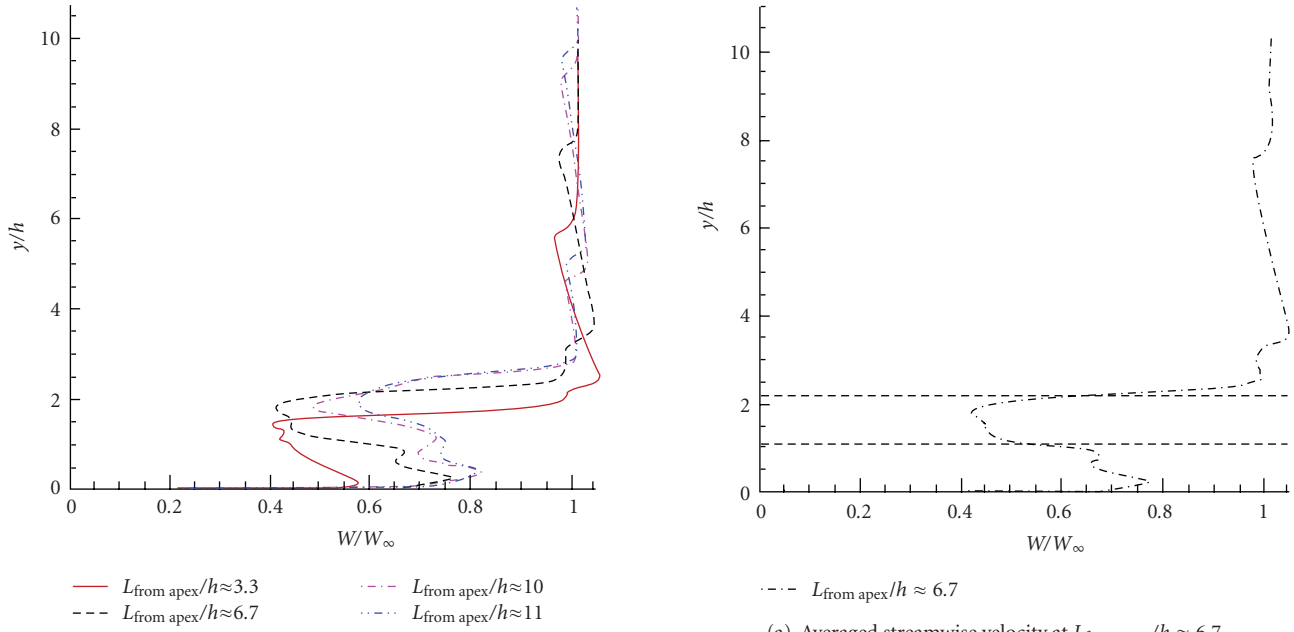


FIGURE 24: Averaged streamwise velocity at different sections.

corresponds to the momentum deficit. From the results, it can be clearly seen that there are at least two high-shear layers in the central plane: one is located at the upper edge of the dip and the other is located at the lower edge. Within the shear layer, there is at least one inflection point. In order to demonstrate the existence of the inflection points, the second-order derivative  $\partial^2 w / \partial y^2$  ( $w$  is the streamwise velocity and  $y$  is the normal direction) is calculated along the lines, and the result of the line at  $L_{\text{from apex}}/h \approx 6.7$  is plotted in Figure 25 as an example. The existence and correspondence of the inflection points at the upper and lower shear layers is illustrated by two dashed lines intersecting the distribution of the streamwise velocity and its second-order derivative.

**3.5.3. Vortex Ring Generation.** Based on the above analyses, it can be concluded that the existence of the inflection points (surface in 3D) in the shear layer causes the flow instability and generates vortex rollers by K-H instability in a cylindrical coordinate system. Therefore, the mechanism of the vortex ring generation should be K-H instability. The loss of the stability of the shear layer will result in the roll-up of the vortex, which appears in ringlike structure in a 3D view (Figure 26). In the Figure 26(b),  $\lambda_2$  is a certain eigenvalue of the stress tensor, and its iso-surface is usually used to describe the vortex surface. The intensity of the upper shear layer appears to be stronger than that of the lower shear layer (Figure 26).

In Figure 27, another qualitative checking about the shear layer and K-H instability is made by using the instantaneous flow field. In the figure, the background at the central plane and the spanwise plane is colored by the value of the streamwise velocity, so that the green regions in two planes represent the momentum deficit. In the central plane,

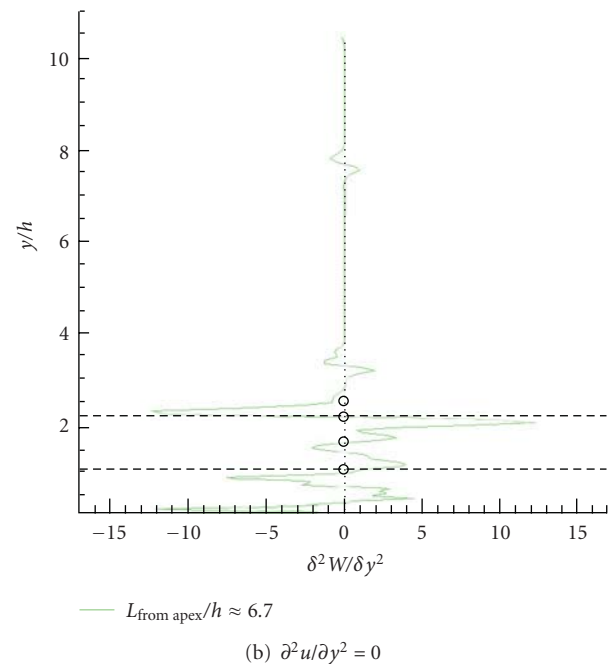


FIGURE 25: Inflection points (surface for 3D).

the pressure contours are superimposed on the background cloud-map. The figure shows that the blue circle structures, which indicate the core of the ringlike vortices cut by the plane, are located on the boundary of the deficit circle. Such positions are exactly the same place where the high-shear layer exists.

In Figure 28, we give the instantaneous numerical schlieren picture at the central plane. From the figure, we can see many vortex rings appear in the circular shapes; after being told the prediction of the vortex rings, the same experimentalists in UT Arlington tried some techniques

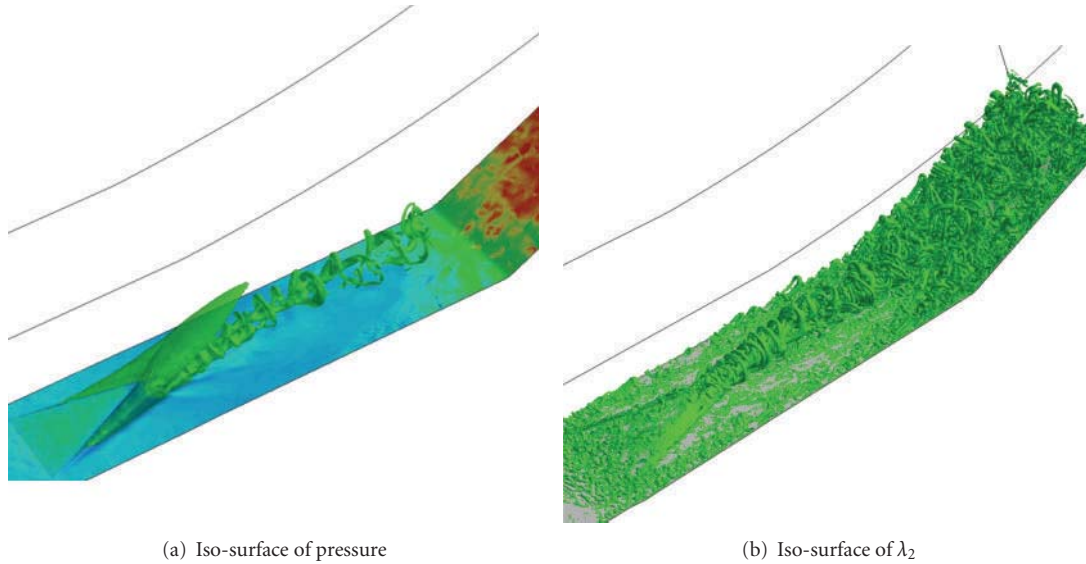


FIGURE 26: Vortex ring generation by MVG due to K-H instability.

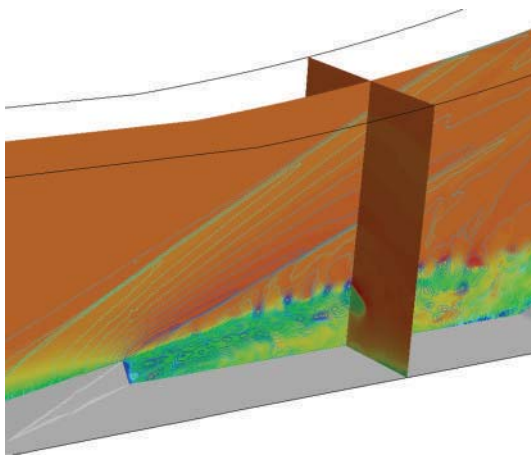


FIGURE 27: The instantaneous pressure and streamwise velocity contour on different cross-sections.

to validate the discovery. They used techniques of the particle image velocimetry (PIV) and the acetone vapor screen visualization to track the movement of the flow, and specifically the flash of a laser sheet is used to provide the light exposure at the time level of micro seconds. In Figure 29, a typical image at the center plane is presented taken by using PIV and the acetone vapor [13]. It is clearly demonstrated that a chain of vortex rings exist in the flow field after the MVG! And these structures qualitatively resemble those in Figures 27 and 28.

### 3.6. Discovery VI: Reduction of Separation Zone by Ring-Shock Interaction

3.6.1. New Mechanism of Separation Zone Reduction by MVG. Traditional concept for MVG is that the MVG produces



FIGURE 28: The numerical schlieren at the center plane.

streamwise vortices inside the boundary layer, which will bring low-momentum fluid up from the bottom and high-momentum fluid down to the boundary layer and then the flow separation induced by shock will be reduced due to the higher shear. However, our LES just gives a quite different mechanism which can be described as MVG generates vortex rings and vortex rings destroy the shocks and reduce the boundary layer separation bubble size, which was induced by the separation bubble and reflection shocks.

Figure 30 shows a graphic about the shock structure around a supersonic ramp, which includes a separation bubble shock and a reflection shock. The boundary layer separation is caused by the strong adverse pressure gradients induced by the shock. Many vortex rings are generated by MVG and convect downstream toward the ramp. The ring first destroys the separation bubble shock and the separation bubble looks broken (Figure 31). The vortex rings are very stable and continue to move downstream to destroy the reflection shock as shown in Figure 32. After many rings continuously move toward the reflection shock, the shock tail

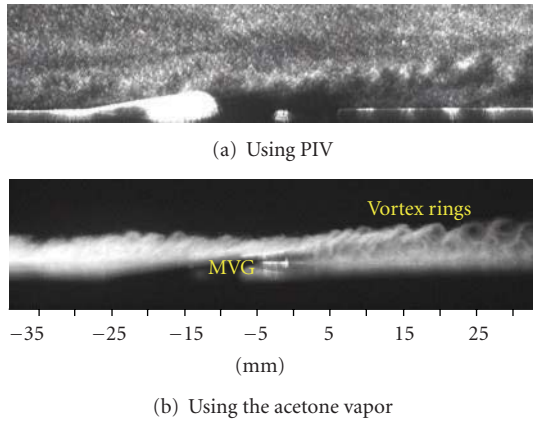


FIGURE 29: The laser-sheet flash image at the center plane.

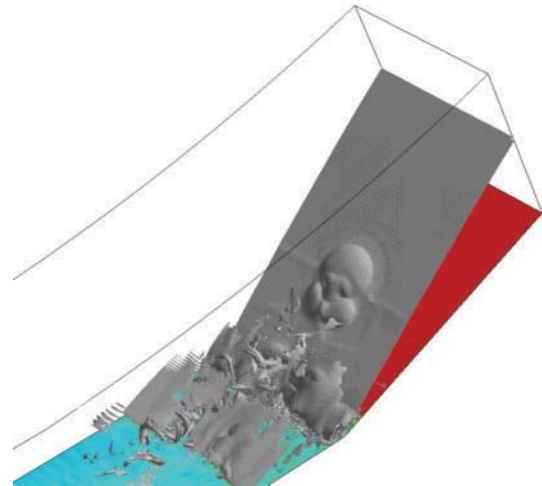


FIGURE 32: Ring-reflection shock interaction.

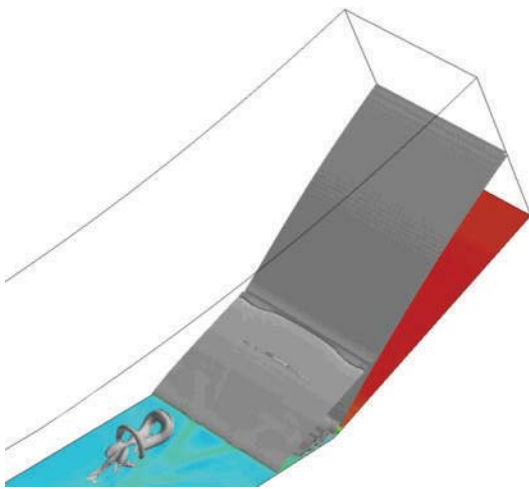


FIGURE 30: Shock structure around ramp.

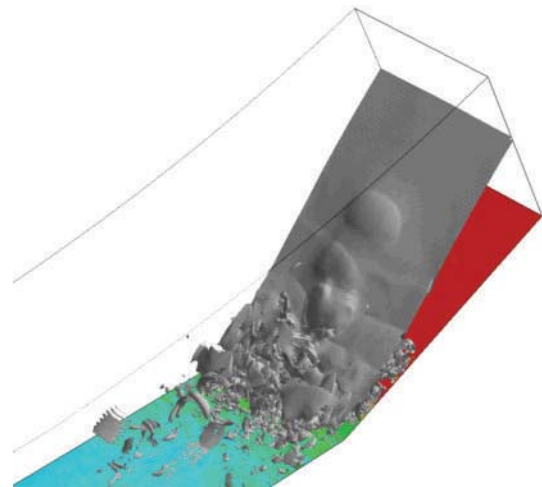


FIGURE 33: Separation reduction by vortex rings.

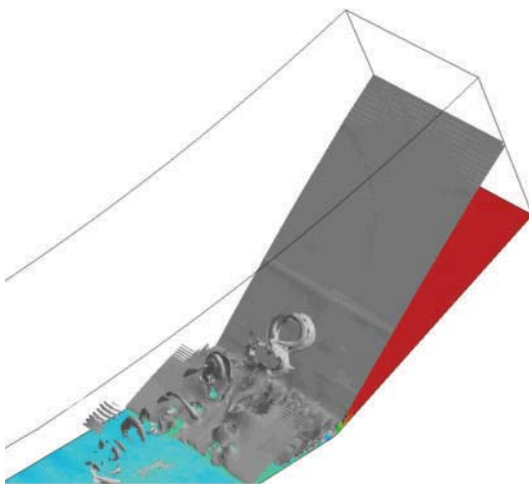


FIGURE 31: Ring-separation bubble shock interaction.

disappeared and the separation area is substantially reduced (Figure 33).

**3.6.2. Shock-Vortex Ring Interaction.** The mechanism why the vortex ring can destroy the shock is believed as that the vortex ring has a low pressure line inside the ring which could destroy the shock. On the other hand, the ring has a high-pressure area outside the ring and near the center of ring, which will change the shock location. The fast rotation of the ring could make the shock surface deformed like a bump.

**3.6.3. Stable Structure of the Vortex Ring.** The shock is pretty strong and the pressure gradients are pretty large. We use both digital schlieren (Figure 34) and  $\lambda_2$  techniques (Figure 35) for 3D visualization and 2D visualization on a central plane in the spanwise direction. The vortex rings are found very stable and keep their forms unchanged after

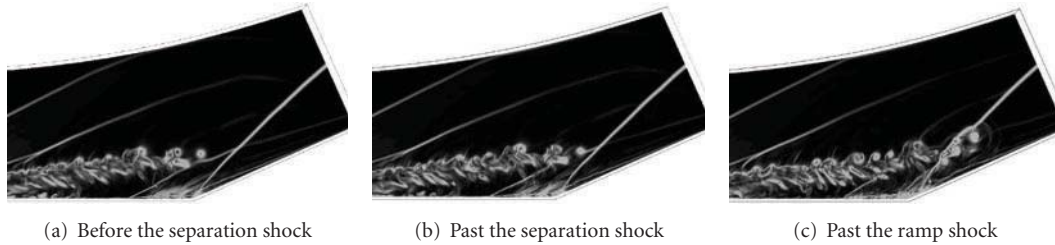


FIGURE 34: Vortex ring-shock interaction at the central plane (numerical schlieren).

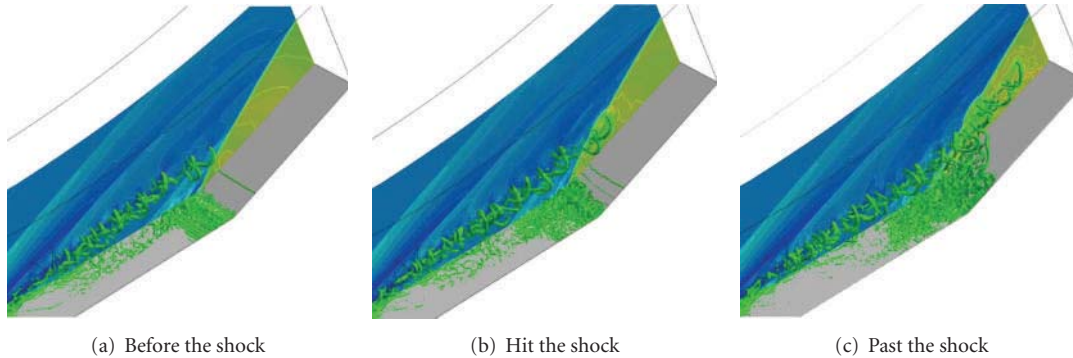


FIGURE 35: Vortex ring-shock interaction at the central plane ( $\lambda_2$  techniques).

passing the weak separation bubble shock and strong ramp shock.

**3.7. Discovery VII: Three-Dimensional Recompressed Shock Structure.** In Figure 36, the spatial structures of the wave system are given by instantaneous cross-section pressure contours. From the first section in Figure 36(a), the wave system is found to be the main reflection shock above the MVG and the expansion wave emanating from the edge of the MVG. The remaining sections show an arc-like structure of the recompression shock wave, which is located behind the first reflection shock. The size of the arc keeps growing while moving downstream. The curve shape of the recompression shocks implies that the function of the recompression shock wave is to make the expansion flow satisfy the “virtual” boundary condition created by the streamwise vortices, at least at the initial stage of the formation of the shock wave. Detailed investigations show that the head and feet of the arc-like shock are separated from each other in the initial stage (see Figure 36(b)). They begin to connect and form a complete arc curve at a certain downstream location, as shown in Figure 36(c).

**3.8. Discovery VIII: Effects of Trailing-Edge Decline Angles.** Comparative studies are made on the MVG flow at  $M = 2.5$  and  $Re_\theta = 1440$  while the MVGs are of different declining angle, that is,  $\beta = 70^\circ$  and  $\beta = 45^\circ$ . The numerical study finds (see Figure 37) the following

- (1) The basic structures are similar in two cases, like the wave system, separation pattern, momentum deficit, and the vortex rings. The effect of declining angle

does not bring about the structural difference, while differences exist in the details of the flow.

- (2) The smaller declining angle at  $\beta = 45^\circ$  makes the vortices closer to the wall, which include the initial streamwise vortices and the layer vortex rings. This should be more favorable to flow control. Nevertheless, the quantitative analyses on the time-averaged data at a downstream do not exhibit a significant improvement about the quality of the boundary layer.

## 4. Conclusions

The following new discoveries and new mechanisms have been made by implicit LES since 2009. Most of these new findings were confirmed later by UTA experiment in 2010.

- (1) Detailed flow structures (topology) around MVG and spiral points are found. Then the new five pairs of vortex tubes model around MVG are given.
- (2) Origin of the momentum deficit is found, not only caused by stream wise vortices through mushroom, but also, mainly, viscosity of MVG and wall surface.
- (3) Inflection points (surface in 3D) inside the deficit area are found.
- (4) Kelvin-Helmholtz-type instability is caused by the momentum deficit.
- (5) Vortex rings are generated by K-H-type instability after MVG.
- (6) Shock-ring interaction is found.

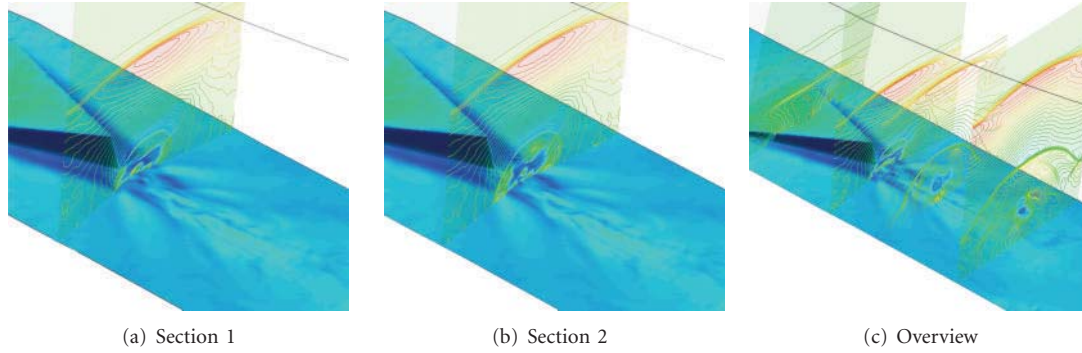


FIGURE 36: The 3D structure of the recompression shock.

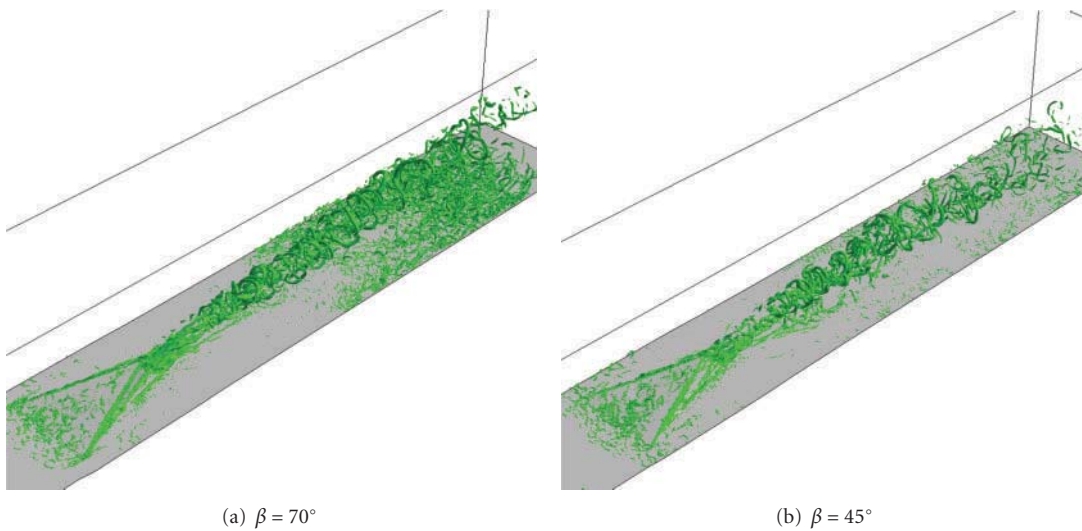


FIGURE 37: Comparison of the vortex structure with different decline angles of MVG trailing edge.

- (7) Mechanism of MVG for separation reduction is due to the ring shock interaction, not only mixing as traditional explanation on VG or MVG.
- (8) Ring is the only form of vortex inside the fluid field and never breaks down.
- (9) Structure of recompressed shock is found.
- (10) Influence of the MVG trailing edge decline angles is studied.

All these new findings may be very important to regular VG, subsonic flow, flow control, flow transition, and turbulence studies.

## Nomenclature

$M$ : Mach number  
 $Re_\theta$ : Reynolds number based on momentum thickness  
 $c$ : Micro ramp vortex generator side length  
 $h$ : MVG height

$\alpha$ : MVG half angle  
 $\beta$ : MVG declining angle of the trailing edge  
 $\delta$ : Incompressible boundary-layer nominal thickness  
 $\delta^*$ : Incompressible boundary-layer displacement thickness  
 $\theta$ : Incompressible boundary-layer momentum thickness  
 $H_i$ : Incompressible boundary-layer shape factor  $\delta^*/\theta$   
 $x, y, z$ : Spanwise, normal, and streamwise coordinate axes  
 $u, v, w$ : Spanwise, normal, and streamwise velocities  
 $p_0$ : Pitot pressure  
 $C_{P_{tot,rc}}$ : Pitot pressure recovery coefficient  
 $Pr$ : Prandtl number  
 RANS: Reynolds-averaged Navier-Stokes  
 LES: Large eddy simulation  
 DNS: Direct numerical simulation  
 WENO: Weighted essentially nonoscillatory scheme  
 TVB: Total variation bounded

SBLI: Shock wave boundary layer interaction  
 VG: Vortex generator  
 MVG: Microramp VG.

### Subscript

$w$ : Wall  
 $\infty$ : Free stream  
 0: Representing the location at the inlet if  
 without special explanation.

## Acknowledgments

This work is supported by AFOSR Grant FA9550-08-1-0201 supervised by Dr. John Schmisser. The authors are grateful to Texas Advantage Computing Center (TACC) for providing computation hours. The authors thank Dr. Frank Lu for providing some experimental snapshots.

## References

- [1] J. C. Lin, "Review of research on low-profile vortex generators to control boundary-layer separation," *Progress in Aerospace Sciences*, vol. 38, no. 4-5, pp. 389–420, 2002.
- [2] P. R. Ashill, J. L. Fulker, and K. C. Hackett, "A review of recent developments in flow control," *Aeronautical Journal*, vol. 109, no. 1095, pp. 205–232, 2005.
- [3] B. H. Anderson, J. Tinapple, and L. Surber, "Optimal control of shock wave turbulent boundary layer interactions using micro-array actuation," in *Proceedings of the 3rd AIAA Flow Control Conference*, pp. 880–893, San Francisco, Calif, USA, June 2006, AIAA paper 2006-3197.
- [4] H. A. Holden and H. Babinsky, "Vortex generators near shock/boundary layer interactions," in *Proceedings of the 42nd AIAA Aerospace Sciences Meeting and Exhibit*, pp. 9975–9983, Reno, Nev, USA, January 2004, AIAA paper 2004-1242.
- [5] H. Holden and H. Babinsky, "Effect of microvortex generators on separated normal shock/boundary layer interactions," *Journal of Aircraft*, vol. 44, no. 1, pp. 170–174, 2007.
- [6] C. W. P. Ford and H. Babinsky, "Micro-ramp control for oblique shock wave / boundary layer interactions," in *Proceedings of the 37th AIAA Fluid Dynamics Conference*, pp. 972–985, Reno, Nev, USA, June 2007, AIAA paper 2007-4115.
- [7] H. Babinsky, Y. Li, and C. W. P. Ford, "Microramp control of supersonic oblique shock-wave/boundary-layer interactions," *AIAA Journal*, vol. 47, no. 3, pp. 668–675, 2009.
- [8] S. Ghosh, J. I. Choi, and J. R. Edwards, "Numerical simulations of effects of micro vortex generators using immersed-boundary methods," *AIAA Journal*, vol. 48, no. 1, pp. 92–103, 2010.
- [9] S. Lee and E. Loth, "Supersonic boundary-layer interactions with various micro-vortex generator geometries," in *Proceedings of the 39th AIAA Fluid Dynamics Conference*, June 2009, AIAA paper 2009-3712.
- [10] S. Lee, M. K. Goettke, E. Loth, J. Tinapple, and J. Benek, "Microramps upstream of an oblique-shock/boundary-layer interaction," *AIAA Journal*, vol. 48, no. 1, pp. 104–118, 2010.
- [11] M. S. Loginov, N. A. Adams, and A. A. Zheltovodov, "Large-eddy simulation of shock-wave/turbulent-boundary-layer interaction," *Journal of Fluid Mechanics*, vol. 565, pp. 135–169, 2006.
- [12] Q. Li and C. Liu, "Numerical investigations on the effects of the declining angle of the trailing-edge of MVG," in *Proceedings of the 48th AIAA Aerospace Sciences Meeting*, Orlando, Fla, USA, 2010, AIAA 2010-714.
- [13] F. Lu, A. Pierce, and Y. Shih, "Experimental study of near wake of micro vortex generators in supersonic flow," AIAA paper 2010-4623.
- [14] G. S. Jiang and C. W. Shu, "Efficient implementation of weighted ENO schemes," *Journal of Computational Physics*, vol. 126, no. 1, pp. 202–228, 1996.
- [15] C. Liu and L. Chen, "Study of mechanism of ring-like vortex formation in late flow transition," AIAA Paper 2010-1456.

## Research Article

# An Initial Investigation of Adjoint-Based Unstructured Grid Adaptation for Vortical Flow Simulations

Li Li

*Aeronautics Computing Technique Research Institute (ACTRI), P.O. Box 90, Xi'an 710068, China*

Correspondence should be addressed to Li Li, westlili@163.com

Received 6 October 2010; Accepted 19 January 2011

Academic Editor: Guan Yeoh

Copyright © 2011 Li Li. This is an open access article distributed under the Creative Commons Attribution License, which permits unrestricted use, distribution, and reproduction in any medium, provided the original work is properly cited.

A computational fluid dynamics (CFDs) method utilizing unstructured grid technology has been employed to compute vortical flow around a  $65^\circ$  delta wing with sharp leading edge, which is specially known as the geometry of the second international vortex flow experiment (VFE-2). In VFE-2,  $65^\circ$  delta wings with different leading edges had been broadly investigated by experiments, which resulted in a special database for CFDs codes validation. The emphasis of this paper is to investigate the effectiveness of an adjoint-base grid adaptation method for unstructured grid in capturing concentrated vortices generated at sharp edges or flow separation lines of lifting surfaces flying at high angles of attack. Earlier experiences in vortical flow simulations had indicated that the vortex behavior is highly dependent on the local grid resolution both on body surface and space. The adjoint-based adaptation method used here is hoped to save grid points with a reasonable grid resolution for vortical flow simulations. The basic idea is to construct a new adaptive sensor in a grid adaptation process with the intent to tell where the elements should be smaller or larger by introducing an adjoint formulation to relate the estimated functional error to local residual errors of both the primal and adjoint solutions.

## 1. Introduction

In recent years, computational fluid dynamics (CFDs) has matured as a routine tool to predict complex genuine flows at designed condition. However, it is still difficult to deal with complex flows at off-design conditions where flow separations and vortices are dominated. For these flows, inappropriate grid resolution has been recognized as one of the dominant reasons for inaccurate predictions of flow features and aerodynamic forces. Actually, in general, the computational grid may become rapidly coarser as it becomes far away from the body surface. In this case, the vortices would be highly diffused due to the numerical discretization error. A possible way to minimize the numerical dissipation of the vortices is to use a highly dense grid. But flow computations around three-dimensional complex bodies with large-scale separations and vortices are difficult within the realistic number of grid points. In order to obtain numerical results for such flows with a given level of accuracy by a limited capacity of the computer, the method for grid adaptation is very useful for practical computations,

which offers the possibilities to avoid the use of overly refined grids to guarantee accuracy. The basic premise is to locally enrich the computational grids in regions which most adversely affect the accuracy of the final solution. Its emphasis is to define a proper adaptive criterion (also known as the adaptive sensor) combined with distinct methods to automatically generate an adaptive mesh.

Currently, many sensors for unstructured grid adaptation are available, for example, the wake sensor based on difference in velocity, the shock sensor based on ratio of total pressure, the vortex sensor based on creation of entropy, and the vortex sensor based on eigenvalue analysis of the velocity-gradient tensor, and so forth [1]. These adaptation methods are often referred to as feature-based adaptation, which mainly focus on resolving discontinuities or strong gradients in the flow field. The assumption herein is that regions of larger gradients are associated with regions of larger error. The use of unstructured grid technology for CFDs simulations allows more freedom in adapting the discretization of the meshes to improve the fidelity of the simulation. Unfortunately, continuous local refinement of

the dominant features of the flow does not necessarily guarantee that the global error will simultaneously be reduced. In some cases, this may even lead to incorrect results [2]. The reason is that the adaptive sensor has failed to correctly indicate the location where the elements should be larger or smaller due to errors elsewhere in the flow field. Also, since the feature-based adaptation methods are nearly without regard to an output quality (e.g., lift coefficient, drag coefficient, moment coefficient, and so on), they may distort to resolve the flow in regions with large local error that may have a minimal effect on the output.

In this paper, an adjoint-based adaptation with isotropic h-refinement for unstructured grid is introduced to catch the vortex-dominant flow. These kinds of methods are firstly proposed in finite element communities [3] and were then extended to finite volume computations, for example, [4–10]. The basic idea of the adjoint-based adaptation method is to construct an adaptive sensor from a more robust and accurate error estimation by introducing the adjoint formulation to relate the estimated functional error to local residual errors of both the primal and adjoint solutions. The adjoint solutions provide a very powerful approach to compute output error estimation as well as to systematically adapt grids to reduce spacial discretization errors. It has also been observed that the adjoint-based adaptation can greatly reduce unnecessary grid point compared with the feature-based adaptation both for 2D and 3D flows [11]. The application of the adjoint-based adaptation here is hoped to economize the grid points with a reasonable grid resolution for vortical flow simulations. The test case is a 65° swept delta wing with sharp-leading edge from the second interactional vortex experiment (VFE-2) whose experimental data have been authorized to use by German Aerospace Center (DLR), Göttingen, Germany. This test case is also from NASA Langley national transonic facility (NTF) that has been used to illustrate effectiveness of the vortex sensors developed by us [1]. Besides, inviscid transonic flows over RAE2822 airfoil and ONERA M6 wing are given to validate the adjoint-based adaptation method used here.

## 2. Methodology

**2.1. Flow Solver.** The flow solver used in this paper is WoF90, which is developed by ACTRI. It is a solver employing hybrid unstructured grid both for Euler and Reynolds-averaged Navier-Stokes (RANS) equations. The solver can deal with arbitrary types of unstructured elements including tetrahedrons, hexahedrons, prisms, and pyramids. It is based on an edge-based formulation and uses a node-centered finite volume technique to solve the governing equations. The control volumes are nonoverlapping and are formed by a dual grid, which is computed from the control surfaces for each edge of the primary input mesh. The equations are integrated explicitly towards steady state with Runge-Kutta time integration. The spatial discretization is either central with artificial dissipation or upwind; both approaches are second order accurate. The solver also adopts an agglomeration multigrid algorithm and an implicit residual smoothing algorithm to accelerate the convergence of a simulation.

In this current study, Euler equation is solved by WoF90 for conserved variables  $\mathbf{Q} = (\rho, \rho u, \rho v, \rho w, E)^T$ , where  $\rho$  is density,  $u, v, w$  is velocity components,  $E$  is total energy per unit volume. The semidiscretization of Euler equation in space using finite volume technique leads to the following ordinary differential equation (ODE):

$$V_k \frac{d\mathbf{Q}}{dt} + \mathbf{R}(\mathbf{Q}) = 0, \quad (1)$$

where  $\mathbf{R}$  is the flow equation residual to steady-state solution and  $V_k$  is volume of a control volume.

**2.2. Adjoint Solver.** Let  $f$  is the objective output function we are interested in. Often we can choose lift coefficient, drag coefficient, moment coefficient, or their combinations, and so on, as the objective output quality. The adjoint variable  $\lambda$  is defined as the linearized effect of a flow residual source term on the output function [10, 11]:

$$\lambda = \frac{\partial f}{\partial \mathbf{R}}. \quad (2)$$

It can be found by solving a set of linear equations, which is derived with application of the chain rule for differential

$$\left(\frac{\partial \mathbf{R}}{\partial \mathbf{Q}}\right)^T \lambda = \left(\frac{\partial f}{\partial \mathbf{Q}}\right)^T. \quad (3)$$

After the flow solution is known, this set of linear equations can be solved much like the flow solver by adding a pseudotime item in order to result in a more robust adjoint solver [7, 12]

$$\frac{\partial \lambda}{\partial t} + \mathbf{R}_\lambda(\lambda) = 0, \quad (4)$$

where  $\mathbf{R}_\lambda(\lambda)$  is the adjoint equation residual

$$\mathbf{R}_\lambda(\lambda) = \left(\frac{\partial \mathbf{R}}{\partial \mathbf{Q}}\right)^T \lambda - \left(\frac{\partial f}{\partial \mathbf{Q}}\right)^T. \quad (5)$$

This equation has a form similar to the flow equation so that it can be integrated toward steady solution with the same Runge-Kutta time integration as the solver. An inviscid adjoint solver has been implemented in WoF90.

**2.3. Adaptive Sensor Based on Error Estimation with Adjoint Solution.** The adjoint solutions can provide an efficient way to estimate error of the objective output function  $f$ . Following the derivation in [7–9], we give a brief derivation here. Firstly, let us assume  $\mathbf{Q}^0$  is a solution on the initial coarser mesh, which can be defined as a perturbation to a solution on a much finer mesh  $\mathbf{Q}^*$  as

$$\mathbf{Q}^0 = \mathbf{Q}^* + \delta \mathbf{Q}, \quad (6)$$

where the fine-mesh solution  $\mathbf{Q}^*$  and the error  $\delta \mathbf{Q}$  are not known in practice. The resulting errors in the output function and the flow equation residual are, respectively,

$$\begin{aligned} \delta f &= f(\mathbf{Q}^0) - f(\mathbf{Q}^*), \\ \delta \mathbf{R} &= \mathbf{R}(\mathbf{Q}^0) - \mathbf{R}(\mathbf{Q}^*) = \mathbf{R}(\mathbf{Q}^0). \end{aligned} \quad (7)$$

Here, the residual on the much finer mesh is assumed to be zero, that is,  $\mathbf{R}(\mathbf{Q}^*) = 0$ . Linearizing about the fine-mesh solution yields,

$$\delta f \cong \frac{\partial f}{\partial \mathbf{Q}^*} \delta \mathbf{Q}, \quad (8)$$

$$\delta \mathbf{R} \cong \frac{\partial \mathbf{R}}{\partial \mathbf{Q}^*} \delta \mathbf{Q}. \quad (9)$$

From (8) and by introducing the adjoint variable from (3), we can give an alternative formula for the error in the output function as

$$\delta f \cong (\lambda^*)^T \frac{\partial \mathbf{R}}{\partial \mathbf{Q}^*} \delta \mathbf{Q} = (\lambda^*)^T \delta \mathbf{R} = (\lambda^*)^T \mathbf{R}(\mathbf{Q}^0), \quad (10)$$

where  $\lambda^*$  is the adjoint solution on the much finer mesh, which is often undesirable. Instead, it is assumed an approximate adjoint solution  $\lambda^0$  is available as a substitute. In a notation of the error of adjoint solution  $\delta \lambda = \lambda^0 - \lambda^*$ , equation (10) can now be rewritten as

$$\begin{aligned} \delta f &\cong (\lambda^0)^T \mathbf{R}(\mathbf{Q}^0) + (\lambda^* - \lambda^0)^T \mathbf{R}(\mathbf{Q}^0) \\ &= (\lambda^0)^T \mathbf{R}(\mathbf{Q}^0) - (\delta \lambda)^T \delta \mathbf{R} \\ &= (\lambda^0)^T \mathbf{R}(\mathbf{Q}^0) - (\delta \lambda)^T \frac{\partial \mathbf{R}}{\partial \mathbf{Q}^*} \delta \mathbf{Q} \\ &= (\lambda^0)^T \mathbf{R}(\mathbf{Q}^0) + \left( \mathbf{R}_\lambda^*(\lambda^0) \right)^T (\mathbf{Q}^* - \mathbf{Q}^0), \end{aligned} \quad (11)$$

where  $\mathbf{R}_\lambda^*(\lambda)$  is the adjoint equation residual on the much finer mesh, and  $\mathbf{R}_\lambda^*(\lambda^*) = 0$  is assumed.

As shown in (11), the error in the output function can be classified two classes: a computable correction  $(\lambda^0)^T \mathbf{R}(\mathbf{Q}^0)$  that can be evaluated with the solution on current coarse mesh and a remaining error that generally cannot be evaluated without solving for qualities on the much finer mesh, that is,

$$\begin{aligned} \varepsilon &\cong (\lambda^* - \lambda^0)^T \mathbf{R}(\mathbf{Q}^0) \\ &\cong \left( \mathbf{R}_\lambda^*(\lambda^0) \right)^T (\mathbf{Q}^* - \mathbf{Q}^0). \end{aligned} \quad (12)$$

The average of the absolute values of the two remaining errors is defined as the adjoint-based adaptive sensor

$$\varepsilon = \frac{\left| (\lambda^* - \lambda^0)^T \mathbf{R}(\mathbf{Q}^0) \right| + \left| \left( \mathbf{R}_\lambda^*(\lambda^0) \right)^T (\mathbf{Q}^* - \mathbf{Q}^0) \right|}{2}, \quad (13)$$

where, in practice, both the adjoint solution error  $\lambda^* - \lambda^0$  and the flow solution error  $\mathbf{Q}^* - \mathbf{Q}^0$  would be replaced by interpolation errors

$$\lambda^* - \lambda^0 = \lambda^h - \lambda^0, \quad \mathbf{Q}^* - \mathbf{Q}^0 = \mathbf{Q}^h - \mathbf{Q}^0, \quad (14)$$

and  $\lambda^h, \mathbf{Q}^h$  are obtained by interpolating  $\lambda^0, \mathbf{Q}^0$  into a globally refined mesh.

*2.4. Grid Adaptation and Smoothing.* A general introduction to the flow chart of grid adaptation can be found in [1, 13]. In the current study, the local h-refinement technique is used due to its robustness and efficiency, which divides existing elements in the mesh according to initial solution (also see examples in [14, 15]). For an inviscid calculation, the unstructured grid only has elements of the tetrahedrons in three dimension (3D) or of the triangles in two dimension (2D). These elements are refined isotropically employing the binary division according to marked edges. It should be pointed out that since the binary division will bring the so-called ‘‘hanging node’’ and unavoidable elements differ from tetrahedrons and triangles, the method to eliminate these nodes or elements is also used here [16]. Besides, after adaptation the mesh may have a worse quality (e.g., the aspect ratio) for some of elements, while they may significantly impact the accuracy and convergence of a solution. We recommend to import the adapted mesh into a general grid generator (e.g., ICEM-CFDs, etc.) for smoothing the mesh in order to improve the global mesh quality.

To use the adjoint-based adaptive sensor defined in (13) and (14) to indicate where to be refined, a globally h-refinement mesh is firstly created by Octree division, in which a new node is inserted at the midpoint of each existing edge, and then both solutions of the flow equation  $\mathbf{Q}^h$  and the adjoint solution  $\lambda^h$  on the much finer mesh are evaluate by piecewise linear interpolation. The local adjoint-based adaptive sensor now can be evaluated from (13) by exploring all nodes  $l(k)$  of the much finer mesh within each element

$$\begin{aligned} \varepsilon_k &= \frac{1}{2} \sum_{l(k)} \left\{ \left| (\lambda^h - \lambda^0)^T \mathbf{R}(\mathbf{Q}^0) \right| + \left| \left( \mathbf{R}_\lambda^*(\lambda^0) \right)^T (\mathbf{Q}^h - \mathbf{Q}^0) \right| \right\}. \end{aligned} \quad (15)$$

The criterion for refinement is given as follows: given a user-specified desired error  $\varepsilon$ , let  $\eta_k = N \cdot \varepsilon_k / \varepsilon$ , where  $N$  is the total number of elements in current mesh, and judge if  $\eta_k > 1$  is satisfied. In this paper, a desired error  $\varepsilon = 0.1$  is used for all cases.

### 3. Results

*3.1. Validation for 2D Case.* Inviscid transonic flow over RAE2822 airfoil is chosen to validate the rationality of adjoint-based adaptive method for two-dimensional test cases. This test case is a classical validation case, which has been used worldwide, especially in EUROVAL project and by AGARD. The simulation is performed at the flow condition as  $M_\infty = 0.734$  and  $\alpha = 2.79^\circ$ , which is a corrected condition from case 9 in EUROVAL project.

The initial mesh has a total of 15,852 nodes and 31,388 triangles, which is shown in Figure 1. For flow solution, the central scheme is employed for spatial discretization, and 3 multigrid levels with W-cycle are used for acceleration. The result of Mach contours employing the initial mesh is given in Figure 2. The primary flow feature is evident.

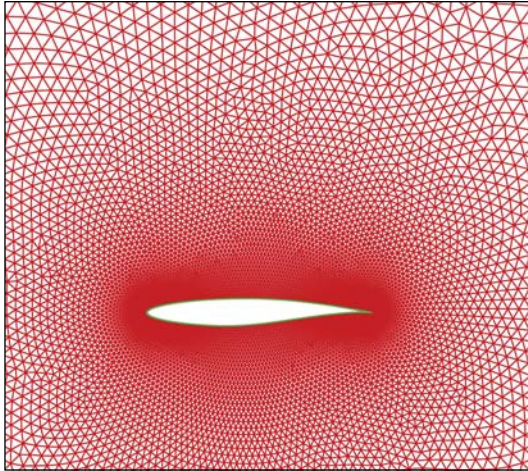


FIGURE 1: Initial (unadapted) RAE2822 airfoil mesh.

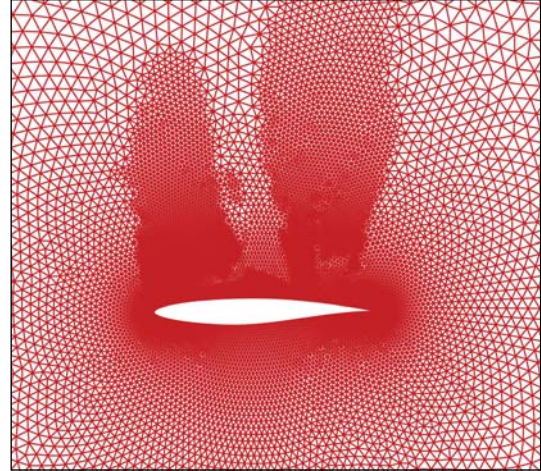


FIGURE 3: Adapted RAE2822 airfoil mesh.

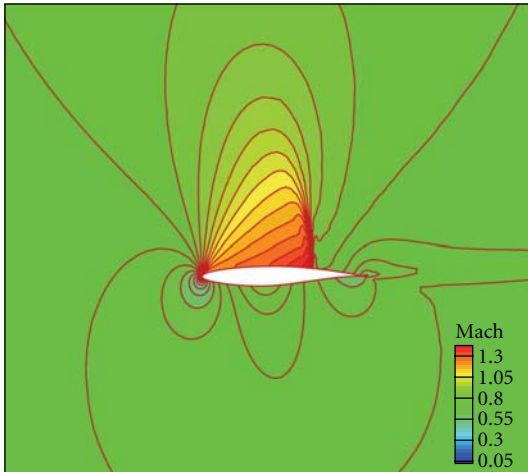
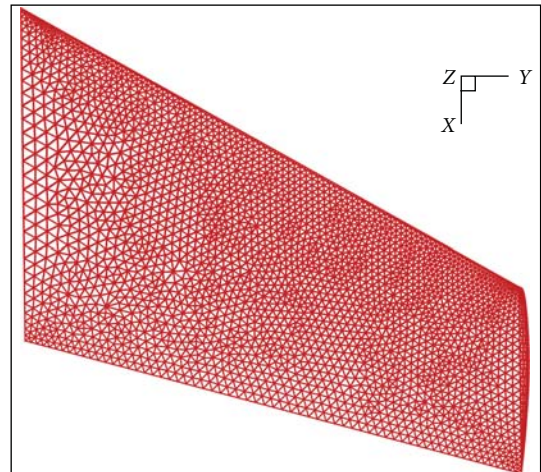
FIGURE 2: Initial Mach contours for RAE2822 airfoil at  $M_\infty = 0.734$  and  $\alpha = 2.79^\circ$ .

FIGURE 4: Initial (unadapted) surface mesh of ONERA M6 wing.

To apply adjoint-based adaptation method, we choose the lift coefficient as the objective output function for adjoint solutions. The final adapted mesh using adjoint-based sensor and isotropic adaptation with h-refinement is shown in Figure 3, which contains a total of 20,763 nodes and 41,141 triangles after mesh adaptation. It is clearly shown that a large portion of new nodes have been appended to leading edge, upper surface and shock regions. This finding also fits the primary feature of the flow very well. The initial mesh has been sufficiently refined in high-difference regions in flow velocity.

**3.2. Validation for 3D Case.** Inviscid transonic flow over ONERA M6 wing is chosen to validate the rationality of adjoint-based adaptive method for three-dimensional test cases. This configuration is simulated at the flow condition at  $M_\infty = 0.8395$  and  $\alpha = 3.06^\circ$ . The initial mesh contains a total of 52,144 nodes and 296,517 tetrahedrons, where there

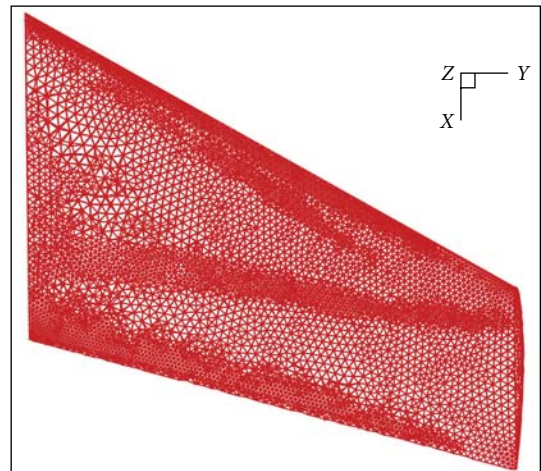


FIGURE 5: Adapted surface mesh of ONERA M6 wing.

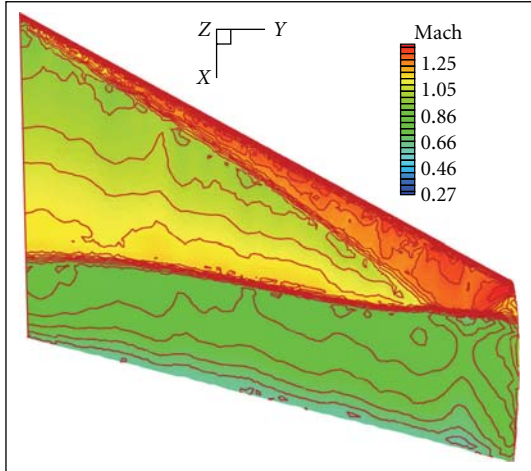


FIGURE 6: Mach contours on adapted surface of ONERA M6 wing at  $M_\infty = 0.8395$  and  $\alpha = 3.06^\circ$ .

are 5,459 boundary nodes on the wing surface. The initial wing surface mesh is shown in Figure 4, which has a coarse spacing, especially at the trailing edge. It is designed with the intention to resolve the surface curvature of the leading edge and the wingtip, but it has no particular considerations of flow features. For the flow solution, the central scheme is used for spatial discretization, and 3 multigrid levels with W-cycle are used for acceleration.

Again, we choose the lift coefficient as the objective output function for adjoint solutions. After grid adaptation using adjoint-based sensor and isotropic adaptation with h-refinement, the adapted mesh contains a total of 128,386 nodes and 740,366 tetrahedrons, where there are 8,041 boundary nodes on the wing surface. The adapted wing surface mesh is shown in Figure 5. A dense region with distinct lambda structure is found in the mesh after adaptation, which just indicates the shock region of M6 wing under current circumstance. It is also found that sufficient nodes have been enriched both at the leading edge and the trailing edge.

The Mach contours on the adapted upper wing surface are shown in Figure 6. A lambda shock structure is clearly visible in these Mach contours, which also indicates the flow physics of M6 wing under the current flow condition. Figure 7 further gives the comparisons of the surface pressure coefficient (noted by  $C_p$ ) at different typical location along the spanwise direction. The experimental data are compared with the original results and the adapted results for both upper and lower surface of the wing. It is evident that the surface pressure distribution has been successfully improved by the grid refinements with current adjoint-based adaptation method.

### 3.3. Application to Complex Vortical Flows of Delta Wing.

As mentioned above, the test case of  $65^\circ$  delta wing with sharp leading edge is from VFE-2 as well as from NASA NTF. The emphasis of this test is to validate the vortex-capturing capability of the adjoint-based adaptation

method. It is worth mentioning that while it is hard to accurately predict this kind of complex vortex flows by Euler calculation, the knowledge of vortex location obtained with grid adaptation from the inviscid solution may greatly help viscous simulations [17].

The detailed description of the model can be found in [18]. The experiment was conducted both in the NASA NTF [18] and in the transonic wind tunnel at Göttingen (TWG) of German Dutch wind tunnels (DNW) [19]. In the current study, all computations were performed on a semispan model at the flow condition at  $M_\infty = 0.4$  and  $\alpha = 20.3^\circ$ . For the flow equation solution, the central scheme is used for spatial discretization and 3 multigrid levels with W-cycle is used for acceleration.

The initial mesh contains a total of 64,835 nodes and 365,681 tetrahedrons, where there are 9,464 boundary nodes on the wing surface. No attempt has been made to cluster extra grid points in the field at the vortex location. The initial surface mesh on the upper surface is shown in the upper portion of Figure 8. A fine grid resolution has been prescribed at the edges of the wing, whereas the mesh on the flat portion of the wing is nearly uniform. The corresponding flow solution on this mesh is displayed in the lower portion of Figure 8, where the distribution of pressure coefficient is represented by variation of colors. The footprint of a leading-edge vortex on the surface is clearly found from the low-pressure region.

To apply the adjoint-based adaptation, we also choose the lift coefficient as the output function. After the application of grid adaptation, the adapted mesh contains a total of 139,682 nodes and 766,948 tetrahedrons, where there are 13,333 nodes boundary nodes on the wing surface. The adapted upper surface mesh and the corresponding Euler solution on the adapted mesh are shown in Figure 9. It is evident that a large portion of new nodes have been enriched on the leading edge, the trailing edge, and the concentrated primary vortex regions such that the footprint of a leading-edge vortex on the surface becomes clearer. Furthermore, the primary vortex appears to be shifted slightly towards the wing root as compared with unadapted solution. In Figure 10, two typical sections at  $x/c = 0.4$  and  $x/c = 0.6$  were chosen for grid resolution comparison before and after mesh adaptation. Obviously, the mesh has been refined in the vortex region above the upper wing surface, while remaining unchanged under the lower wing surface. It can be also noticed that the grid density of refined regions varies with movement of the vortex core. However, it is also been found that, unlike using the adaption based on some elaborated vortex sensors [1], the spatially refined elements from adjoint-based adaptation were not over concentrated along the vortex core.

In Figure 11, the spanwise surface pressure coefficient distributions at different chordwise positions ( $x/c = 0.2, 0.4, 0.6,$  and  $0.8,$  resp.) were compared between before and after mesh adaptation. In these figures, experimental data both from NASA and DLR are depicted. The improvement for prediction of the vortex flows is obvious by using the adjoint-based adaptation and h-refinement. The unadapted Euler simulation has produced a poor solution with underpredicted vortex in the upstream stations due to

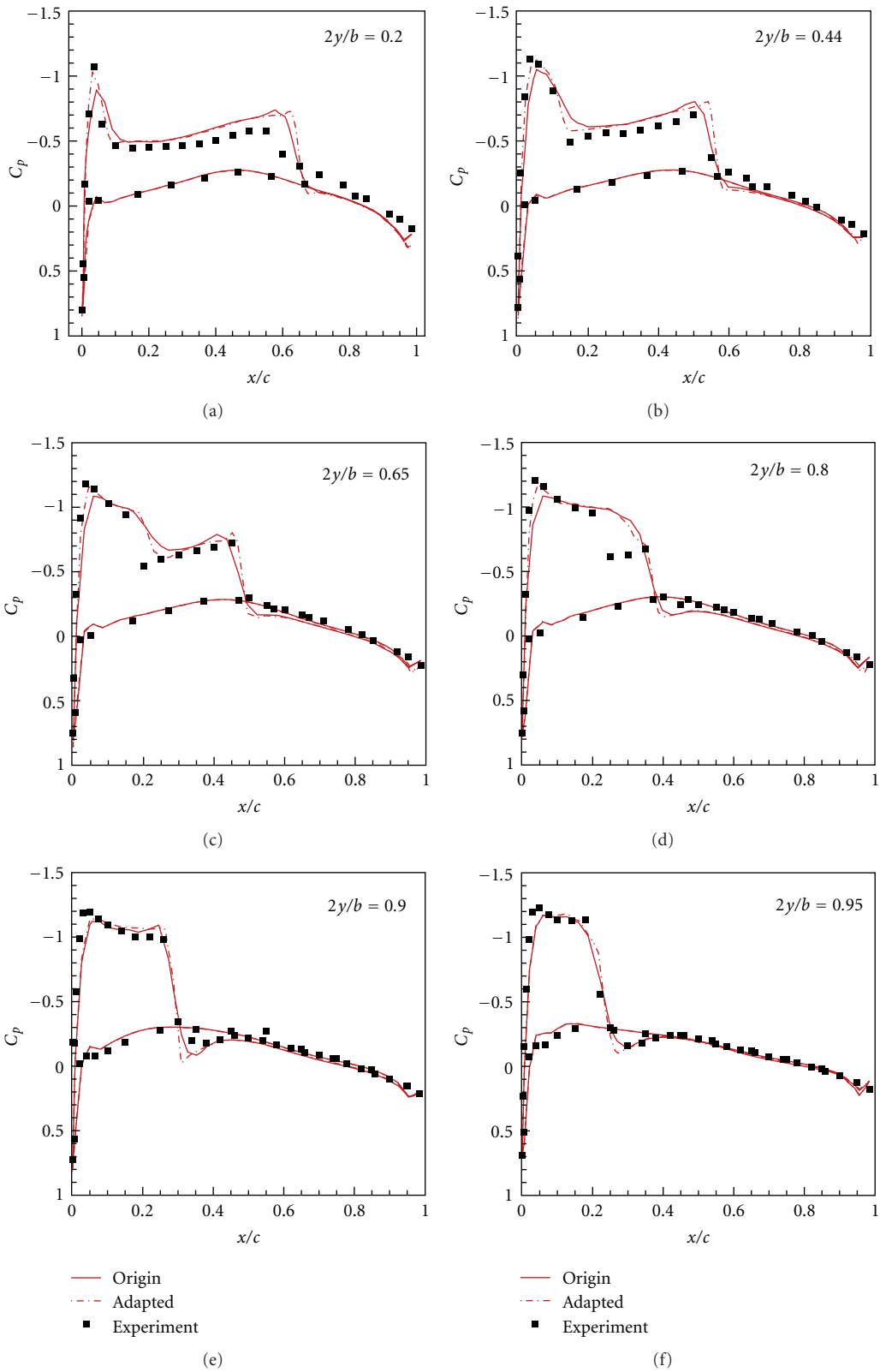


FIGURE 7: Comparisons of spanwise pressure coefficient distributions for ONERA M6 wing between before and after adaptation.

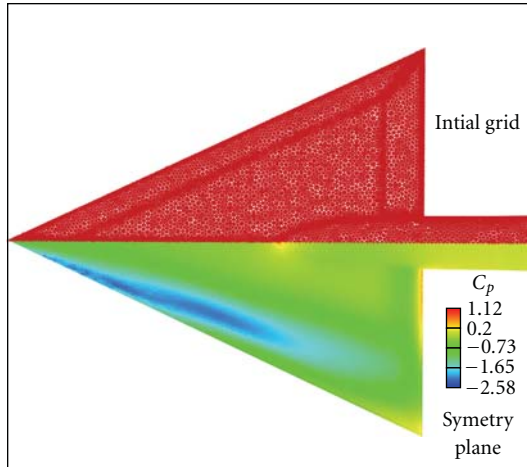


FIGURE 8: Initial (unadapted) upper surface mesh and Euler inviscid solution on the sharp leading-edge delta wing at  $M_\infty = 0.4, \alpha = 20.3^\circ$ .

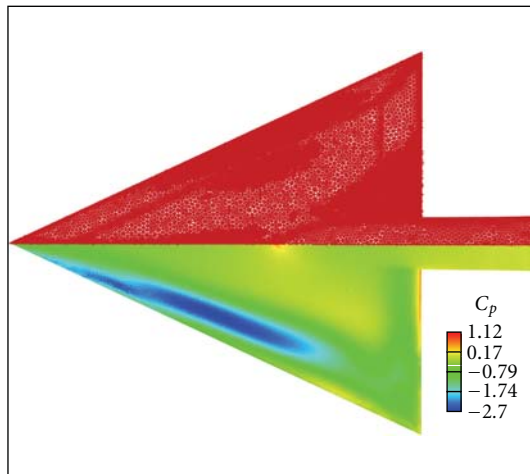
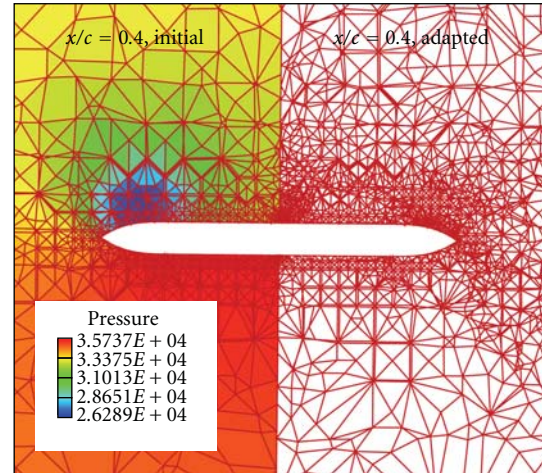


FIGURE 9: Adapted upper surface mesh and Euler inviscid solution on the sharp leading-edge delta wing at  $M_\infty = 0.4, \alpha = 20.3^\circ$ .

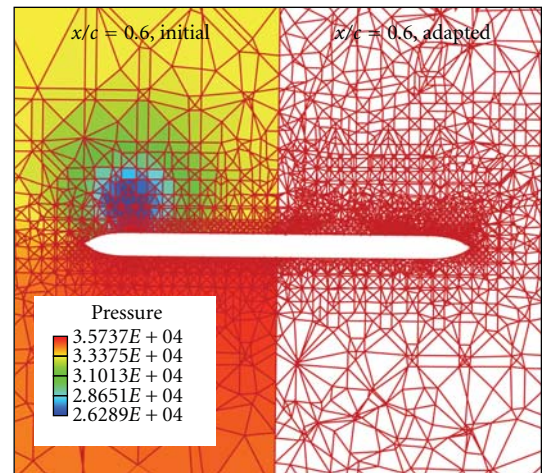
uniform grid spacing, especially, it has caused a severe shift of the peak value of  $C_p$  on the upper surface to the wing tip. After adaptation, things have been changed greatly. At all chordwise positions except  $x/c = 0.2$ , it appears to give a more reasonable result. At  $x/c = 0.2$  position, similarly poor results are obtained with initial and adapted meshes. It may be said that the two meshes have the same insufficient grid resolution around this section (compare Figure 8 and Figure 9). This deficiency may be ameliorated by adapting the new mesh or by altering the desired error level used in the adjoint-based adaptation.

#### 4. Conclusions

An adjoint-based adaptation on unstructured grid has been implemented and is applied to simulate the complex vortex flow of a  $65^\circ$  delta wing with sharp leading edge at high angle of attack. Firstly, an adaptive sensor for grid adaptation



(a)



(b)

FIGURE 10: Comparisons of the grid resolution in space from two typical sections at  $x/c = 0.4$  and  $x/c = 0.6$  for the sharp leading-edge delta wing.

is constructed from an accurate error estimation to output function with adjoint solution, which combines residuals of the flow equation and the adjoint equation. Then, the rationality and capability of the adjoint-based adaptation is validated by choosing the transonic flow over RAE2822 airfoil as 2D case and the transonic flow over ONERA M6 wing as 3D case. Reasonable results have been obtained. After that, results from initial numerical investigation of  $65^\circ$  delta wing are given. We can conclude that although the spatial refinements from adjoint-based adaptation were not over concentrated along the vortex core of the flow, the results were greatly improved. The greatest advantage of an adjoint-based adaptation is that it easily reaches an improved and convergent grid resolution and saves unnecessary nodes which have a minimal effect on the desired output function.

It should be pointing out that although all simulations in this study are limited to inviscid Euler computations, the adjoint-based adaptive method itself can be extended to

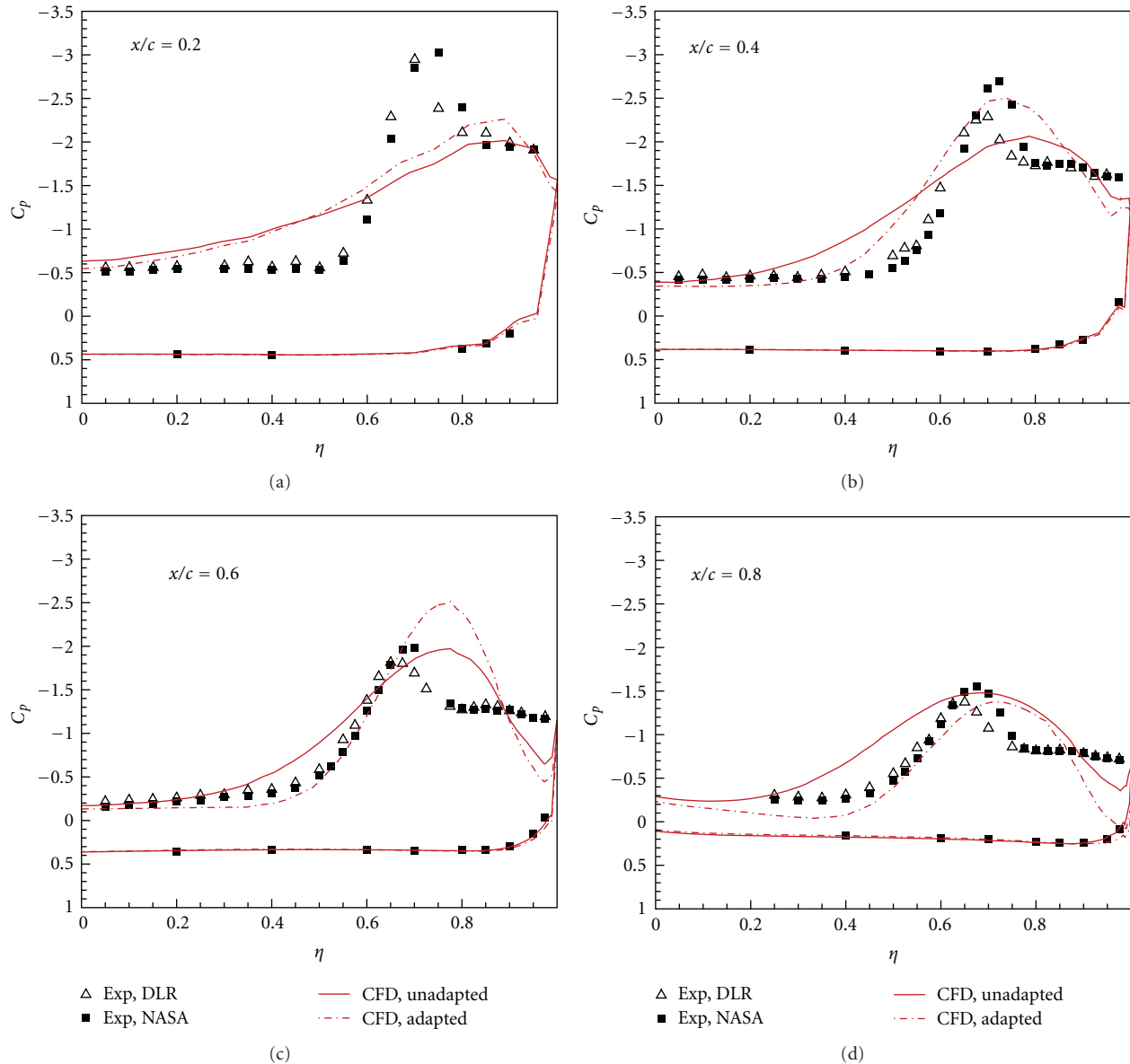


FIGURE 11: Comparisons of spanwise pressure coefficient distributions for delta wing with sharp leading edge between before and after mesh adaptation.

viscous calculations by developing a viscous adjoint solver and using anisotropic refinement for grid within boundary layers [9]. These work is currently under way at ACTRI.

## Acknowledgments

This work is supported by the State Key Development Program of Basic Research of China (973) under Grant no. 2009CB723804. The authors would like to thank the German Aerospace center (DLR) for proving and authorizing to use the experimental data of delta wing in VFE-2 project. Mr. YANG Zhenhu, one of our colleagues at ACTRI, is also appreciated due to his part of work on adjoint-based mesh adaptive method.

## References

- [1] B. Wen, Q. Zheng, and L. Li, "Recent efforts to establish adaptive hybrid grid computing capability at ACTRI," *Journal of Computational Fluid Dynamics*, vol. 7, no. 4, pp. 438–449, 2007.
- [2] G. P. Warren, J. T. Anderson, J. T. Thomas, and S. L. Krist, "Grid convergence for adaptive methods," AIAA Paper 1991-1592, 1991.
- [3] P. Monk and E. Süli, "The adaptive computation of far-field patterns by a posteriori error estimation of linear functionals," *SIAM Journal on Numerical Analysis*, vol. 8, pp. 251–274, 1998.
- [4] D. A. Venditti and D. L. Darmofal, "Adjoint error estimation and grid adaptation for functional outputs: application to quasi-one-dimensional flow," *Journal of Computational Physics*, vol. 164, no. 1, pp. 204–227, 2000.

- [5] J. D. Müller and M. B. Giles, "Solution adaptive mesh refinement using adjoint error analysis," AIAA Paper 2001-2550, 2001.
- [6] D. A. Venditti and D. L. Darmofal, "Grid adaptation for functional outputs: application to two-dimensional inviscid flows," *Journal of Computational Physics*, vol. 176, no. 1, pp. 40–69, 2002.
- [7] D. A. Venditti, *Grid adaptation for functional outputs of compressible flow simulations*, Ph.D. thesis, Massachusetts Institute of Technology, Cambridge, Mass, USA, 2002.
- [8] M. A. Park, "Adjoint-based, three-dimensional error prediction and grid adaptation," AIAA Paper 2002-3286, 2002.
- [9] M. A. Park, "Three-dimensional turbulent RANS adjoint-based error correction," AIAA Paper 2003-3849, 2003.
- [10] E. M. Lee-Rausch, M. A. Park, W. T. Jones, D. P. Hammond, and E. J. Nielsen, "Application of parallel adjoint-based error estimation and anisotropic grid adaptation for three-dimensional aerospace configurations," in *Proceedings of the 23rd AIAA Applied Aerodynamics Conference*, vol. 1, pp. 511–533, Toronto, Canada, June 2005.
- [11] E. J. Nielsen, "Adjoint-based algorithms for adaptation and design optimization on unstructured grids," in *Proceedings of the 3rd East-West High-Speed Flow-field Conference*, Beijing, China, October 2005.
- [12] E. J. Nielsen, J. Lu, M. A. Park, and D. L. Darmofal, "An exact dual discrete adjoint solution method for turbulent flows on unstructured grids," AIAA Paper 2003-0273, 2003.
- [13] S. Z. Pirzadeh, "An adaptive unstructured grid method by grid subdivision, local remeshing, and grid movement," Tech. Rep. AIAA-99-3255, 1999.
- [14] Y. L. Moigne, "Adaptive mesh refinement sensors for Vortex flow simulations," in *Proceedings of the European Congress on Computational Methods in Applied Sciences and Engineering (ECCOMAS '04)*, July 2004.
- [15] R. Löher and J. D. Baum, "Adaptive h-refinement on 3D unstructured grids for transient problems," *International Journal for Numerical Methods in Fluids*, vol. 14, no. 12, pp. 1407–1419, 1992.
- [16] D. Sharov and K. Fujii, "Three-dimensional adaptive bisection of unstructured grids for transient compressible flow computations," AIAA Paper 95-1708, 1995.
- [17] S. Z. Pirzadeh, "Vortical flow prediction using an adaptive unstructured grid method," in *Proceedings of the RTO AVT Symposium on Advanced Flow Management: Part A—Vortex Flows and High Angle of Attack for Military Vehicles*, Loen, Norway, May 2001.
- [18] J. Chu and J. M. Luckring, "Experimental surface pressure data obtained on 65° delta wing across reynolds number and mach number ranges," NASA Technical Memorandum 4645, 1996.
- [19] R. Konrath, A. Schröder, and J. Kompenhans, "Analysis of PIV results obtained for the VFE-2 65° delta wing configuration at sub- and transonic speeds," in *Proceedings of the 24th Applied Aerodynamics Conference*, vol. 2, pp. 746–760, San Francisco, Calif, USA, June 2006.

## Research Article

# Assessment of Turbulence Models for Flow Simulation around a Wind Turbine Airfoil

Fernando Villalpando,<sup>1</sup> Marcelo Reggio,<sup>1</sup> and Adrian Ilinca<sup>2</sup>

<sup>1</sup>École Polytechnique de Montréal, Campus de l'Université de Montréal, 2500 Chemin du Polytechnique, Montréal, QC, Canada H3T 1J4

<sup>2</sup>Laboratoire de Recherche en énergie éolienne, Université du Québec à Rimouski, 300 Allée des Ursulines, Rimouski, QC, Canada G5L 3A1

Correspondence should be addressed to Marcelo Reggio, marcelo.reggio@polymtl.ca

Received 23 September 2010; Revised 10 February 2011; Accepted 15 February 2011

Academic Editor: Guan Yeoh

Copyright © 2011 Fernando Villalpando et al. This is an open access article distributed under the Creative Commons Attribution License, which permits unrestricted use, distribution, and reproduction in any medium, provided the original work is properly cited.

This investigation focuses on the application of the computational fluid dynamics tool FLUENT to the study of flows over the NACA 63–415 airfoil at various angles of attack. With the aim of selecting the most suitable turbulence model to simulate flow around ice-accreted airfoils, this work concentrates on assessing the prediction capabilities of various turbulence models on clean airfoils at the large angles of attack that cause highly separated flows to occur. The study was undertaken by conducting simulations with the one-equation Spalart-Allmaras (SA) model, the two-equation RNG  $k-\epsilon$  and SST  $k-\omega$  models, and the Reynolds stress model (RSM). Domain discretization was carried out using general quadrilateral grids generated with GAMBIT, the FLUENT preprocessing tool. Comparisons were made with available experimental data.

## 1. Introduction

Today, the worldwide concern for the environment can be expressed as a huge need for low entropy production during energy transformation processes. This essentially means low-polluting, low-wastage, and low energy-degradation methods and technologies. At the forefront of these is wind technology, and wind power plants constitute the world's fastest growing energy source [1]. Testament to this is the proliferation of wind farms that has occurred in recent years, and the planned installation of many others all around the world. However, in certain regions, wind energy extraction faces specific challenges imposed by climatic conditions.

In cold climates, the formation of ice on the wind turbine blades is one of the main concerns, as ice-induced roughness on the blades reduces lift and increases drag. This results in production losses that should be quantified, in order to obtain a picture of how much there is to be gained from the development of technologies designed to prevent ice accretion in cold regions.

The phenomenon of ice accretion and performance losses on wind turbine blades is a subject which is of particular interest to the wind turbine research community (see, e.g., [2–4]). The problem is that ice accretion on the blades will develop in a severe performance penalty, because large separated flow regions will develop at low angles of incidence (as they do on clean airfoils at high angles of incidence), followed by a significant lift reduction and an increase in drag. Few studies have analysed airfoils with large separated flows at Reynolds numbers characteristic of wind turbines [5, 6]. In fact, simulating the flow phenomenon around wind turbine blades is a challenging task, because that flow is three dimensional, unsteady, and turbulent. In wider spectra, it is useful to assess the ability of turbulence models to lead to an accurate prediction of lift and drag when separated flows occur.

In this investigation, only geometries contained in a two-dimensional space are addressed, and the flow is considered to be incompressible. This study concentrates on the aerodynamics of airfoils at low and high angles of attack.

To conduct the current computations, FLUENT [7], a finite-volume flow solver was applied, while the meshing process was achieved using the accompanying preprocessor, GAMBIT [8]. An initial grid with approximately 85 000 cells was generated. This mesh was then refined near the airfoil by applying FLUENT, which resulted in a typical grid of about 140 000 cells.

The 2D steady-state results on the NACA 63-415 airfoil are compared to data provided by the RISO National Laboratory [9]. This recognized research center carries out wind tunnel testing and also performs CFD calculations by applying their own code, EllipSys2D, to study and improve the efficiency of wind turbine blades.

## 2. Numerical Model

The numerical counterpart of the RISO experimental test is carried out on a 0.60 m chord, NACA 63–415 airfoil at  $Re = 1.6 \times 10^6$ . The flow parameters at the inlet are a velocity  $V = 40$  m/s and a turbulence intensity of 1%.

The meshed domain used for the calculations is shown in Figure 1. The top, bottom, and left boundaries were placed at a distance of 12 chords from the airfoil, while the right boundary was placed at 20 chords.

Focusing on the flow simulation over iced airfoils, for which the characteristics and the calculation of the flow near the airfoil are even more crucial than for clean airfoils, as in the case of ice accretion prediction, we chose to address the viscous sublayer. Thus, a grid with a dimensionless distance  $y^+$  close to 1 was generated.

The airfoil pressure and suction sides were meshed with 312 uniformly distributed nodes, and 100 nodes with a growth ratio of 1.06 were placed between the airfoil and the far-field boundaries. Then, the mesh was refined near the airfoil to obtain the established wall distance, leading to a final mesh with approximately 140 000 cells. An idea is given in Figure 2 of a typical resulting mesh (detail showing the grid after being adapted in FLUENT).

A grid independence study was performed to verify that the solution will not change subsequent additional refinements. The study was based on simulations performed at an angle of incidence of  $8^\circ$ , with the lift and drag coefficients taken as the control parameters. Figures 3(a) and 3(b) show the computed values of the lift and drag parameters according to the various turbulence models. At the second grid level (80 000 cells), the aerodynamic parameters calculated after the RNG  $k-\epsilon$  and SA models were applied showed no further variation, while slight differences remained following the application of SST  $k-\omega$ . The results obtained with the RSM continued to change up to the third grid level (140 000 cells). These calculations led us to conclude that it is reasonable to consider that the grid with 140 000 cells guarantees results on all four turbulence models, independently of grid size.

## 3. Turbulence Models

Before going into the details of the flow simulation around the NACA 63–415 airfoil, let us recall the basic notions

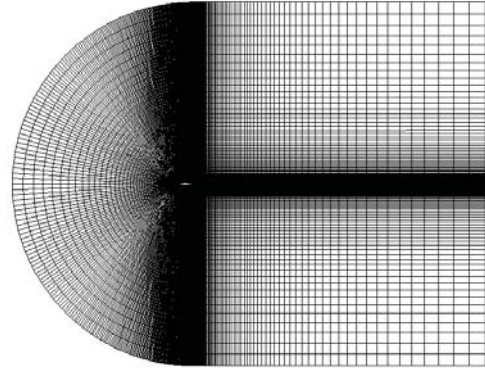


FIGURE 1: A global view of the mesh.

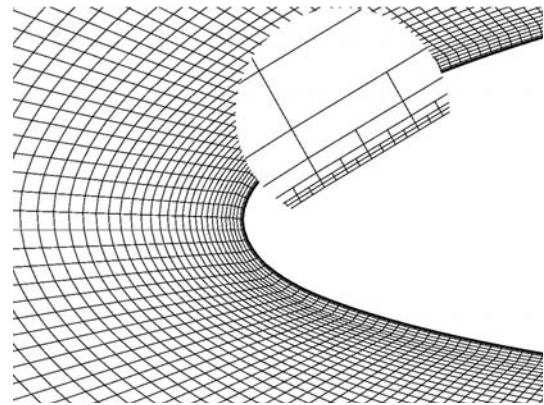


FIGURE 2: Near-wall view of the mesh.

underlying the turbulence models used in this investigation, namely, the RNG (renormalization group) variation of the  $k-\epsilon$  model, the SST  $k-\omega$  (Shear-Stress-Transport  $k-\omega$ ) model, the SA (Spalart-Allmaras) model, and the RSM (Reynolds stress model).

**3.1. RNG  $k-\epsilon$ .** The RNG model incorporates modifications over the standard  $k-\epsilon$  [10] model, which improve its performance. These modifications were derived using the mathematical technique derived from what is called “renormalization group” theory [11]. The transport equations for the turbulent kinetic energy  $k$  and the dissipation rate of the turbulent kinetic energy  $\epsilon$  are defined as follows:

$$\begin{aligned} \frac{\partial}{\partial t}(\rho k) + \frac{\partial}{\partial x_i}(\rho k U_i) &= \frac{\partial}{\partial x_j} \left( \alpha_k \mu_{\text{eff}} \frac{\partial k}{\partial x_j} \right) + G_k - \rho \epsilon + S_k, \\ \frac{\partial}{\partial t}(\rho \epsilon) + \frac{\partial}{\partial x_i}(\rho \epsilon U_i) &= \frac{\partial}{\partial x_j} \left( \alpha_\epsilon \mu_{\text{eff}} \frac{\partial \epsilon}{\partial x_j} \right) + C_{1\epsilon} \frac{\epsilon}{k} G_k \\ &\quad - \left( C_{2\epsilon} + \frac{C_\mu (S(k/\epsilon))^3 (1 - (S(k/\epsilon)/\eta_0))}{1 + \beta (S(k/\epsilon))^3} \right) \rho \frac{\epsilon^2}{k} + S_\epsilon. \end{aligned} \quad (1)$$

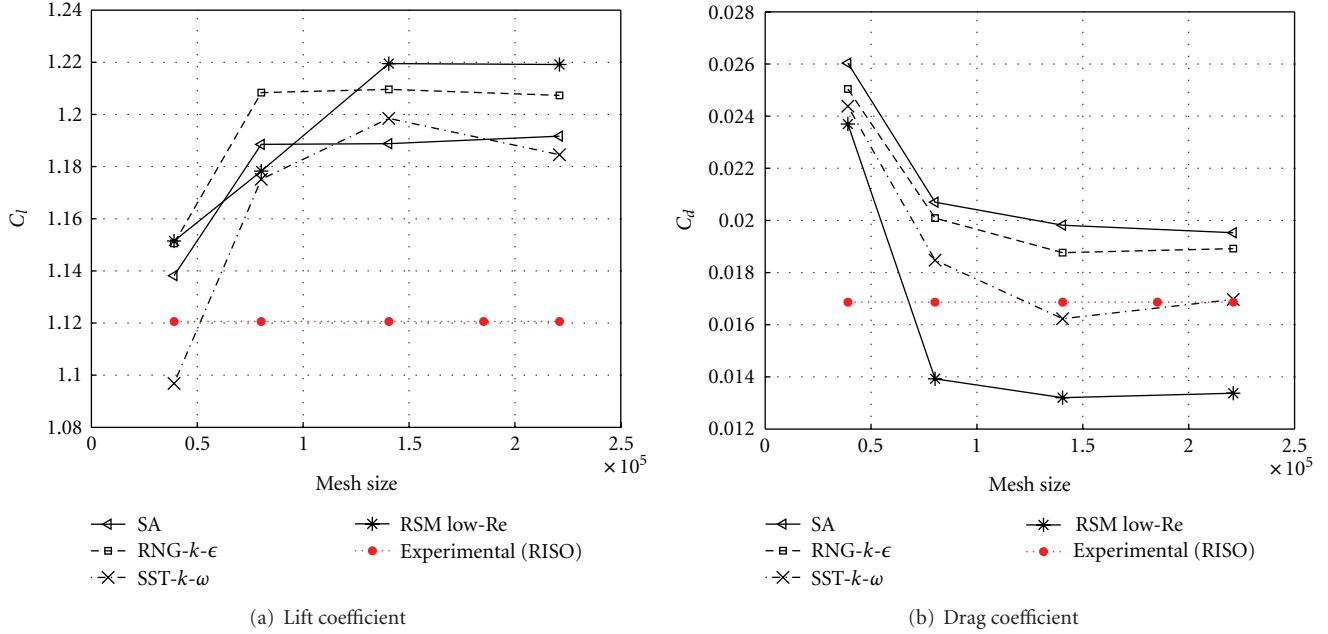


FIGURE 3: Grid convergence.

The turbulent kinetic energy production term is defined as follows:

$$G_k = -\rho \overline{u'_i u'_j} \frac{\partial U_j}{\partial x_i}. \quad (3)$$

The main modification is the addition of a second coefficient in the third term on the right side of (2). This coefficient becomes negative in regions of large strain rate ( $S$ ), reducing the destruction of epsilon, and, as a consequence,  $k$  is also reduced, yielding lower turbulent viscosity values.

Other modifications are a differential equation to calculate the turbulent viscosity and the equation to calculate the inverse effective Prandtl numbers ( $\alpha_k$ ,  $\alpha_\epsilon$ ). The constant values for this model are  $\eta_0 = 4.38$ ,  $\beta = 0.012$ ,  $C_\mu = 0.0845$ ,  $C_{1\epsilon} = 1.42$ , and  $C_{2\epsilon} = 1.68$ .

The RNG  $k$ - $\epsilon$  model is only suited for zones far from the wall and cannot address the viscous sublayer directly. In order to be able to do this, the *Enhanced Wall Treatment (EWT)* option was devised. Based on the turbulent Reynolds number, the EWT model specifies a near-wall zone, where the eddy viscosity is calculated using the one-equation model of (Wolfstein [12]). Outside this zone, the eddy viscosity is calculated, as usual, by the RNG  $k$ - $\epsilon$  model. Then, a blending equation for the eddy viscosity is used to couple the two zones.

**3.2. SA.** The SA [13, 14] is a one-equation model that solves an empirical transport equation for the eddy viscosity  $\tilde{\nu}$ . This equation models the production, transport, diffusion, and destruction of the modified turbulent kinematic viscosity. One of its advantages is the simplicity with which the free

stream and wall boundary conditions can be imposed. The transport equation for  $\tilde{\nu}$  is

$$\begin{aligned} & \frac{\partial}{\partial t}(\rho\tilde{\nu}) + \frac{\partial}{\partial x_i}(\rho\tilde{\nu}U_i) \\ &= G_\nu + \frac{1}{\sigma_{\tilde{\nu}}} \left[ \frac{\partial}{\partial x_j} \left\{ (\mu + \rho\tilde{\nu}) \frac{\partial \tilde{\nu}}{\partial x_j} \right\} + C_{b2}\rho \left( \frac{\partial \tilde{\nu}}{\partial x_j} \right)^2 \right] - Y_\nu + S_{\tilde{\nu}}. \end{aligned} \quad (4)$$

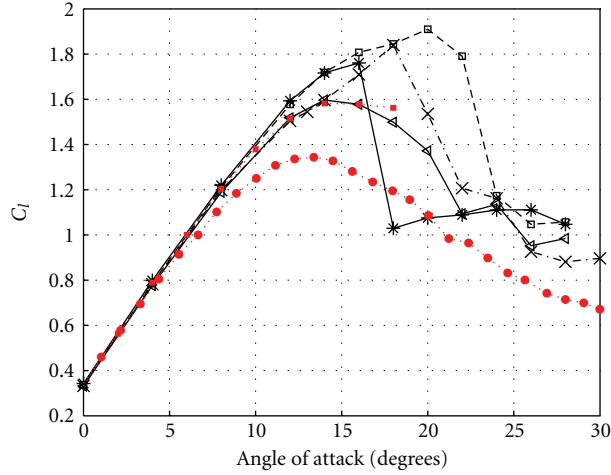
The production and destruction terms,  $G_\nu$  and  $Y_\nu$ , respectively, are defined as follows:

$$\begin{aligned} G_\nu &= C_{b1}\rho \left( S + \frac{\tilde{\nu}}{\kappa^2 y^2} f_{v2} \right) \tilde{\nu}, \\ Y_\nu &= C_{w1}\rho f_w \left( \frac{\tilde{\nu}}{y} \right)^2, \end{aligned} \quad (5)$$

where  $S$  is the mean strain rate,  $y$  is the wall distance, and  $f_{v2}$  and  $f_w$  are damping functions. The constant values are  $C_{b1} = 0.1355$ ,  $C_{b2} = 0.622$ , and  $\tilde{\nu} = 2/3$ .

The SA model is able to resolve the viscous sublayer when the mesh is fine enough near the walls.

**3.3. SST  $k$ - $\omega$ .** The original  $k$ - $\omega$  [15] model is reputed to be more accurate than  $k$ - $\epsilon$  in the near-wall layers. It has been successful for flows with moderate adverse pressure gradients, but it has a  $\omega$  equation which is very sensitive to the values of  $\omega$  in the free stream. The SST [16] corrects this problem by solving the standard  $k$ - $\epsilon$  in the far field and the standard  $k$ - $\omega$  near the walls. To improve its performance for adverse pressure flows, the SST considers the effects of the transport of the turbulent shear stress in the calculations of



(a) Lift coefficient

(b) Drag coefficient

FIGURE 4: Lift and drag coefficients.

the turbulent viscosity  $\mu_t$  and the turbulent Prandtl numbers  $\sigma_k$  and  $\sigma_\omega$ . The transport equation for  $k$  and the specific dissipation rate  $\omega$  are the following:

$$\begin{aligned} \frac{\partial}{\partial t}(\rho k) + \frac{\partial}{\partial x_i}(\rho k U_i) &= \frac{\partial}{\partial x_j} \left( \left( \mu + \frac{\mu_t}{\sigma_k} \right) \frac{\partial k}{\partial x_j} \right) \\ &\quad + \tilde{G}_k - Y_k + S_k, \\ \frac{\partial}{\partial t}(\rho \omega) + \frac{\partial}{\partial x_i}(\rho \omega U_i) &= \frac{\partial}{\partial x_j} \left( \left( \mu + \frac{\mu_t}{\sigma_\omega} \right) \frac{\partial \omega}{\partial x_j} \right) \\ &\quad + G_\omega - Y_\omega + D_\omega + S_\omega. \end{aligned} \quad (6)$$

The production terms of  $k$  and  $\omega$  are defined, respectively, as follows:

$$\tilde{G}_k = \min(G_k, 10\rho\beta^*k\omega), \quad (7)$$

$G_k$  being calculated with (3),

$$G_\omega = \frac{\alpha_\omega}{\gamma_t} \tilde{G}_k, \quad (8)$$

and the dissipation terms are given by

$$Y_k = \rho\beta^*k\omega, \quad (9)$$

$$Y_\omega = \rho\beta\omega^2.$$

The cross diffusion term that blends the two models is defined as follows:

$$D_\omega = 2(1 - F_1)\rho\sigma_{w,2} \frac{1}{\omega} \frac{\partial k}{\partial x_j} \frac{\partial \omega}{\partial x_j}, \quad (10)$$

$\beta^*$ ,  $\beta$ ,  $\alpha_\omega$ , and  $F_1$  are damping functions, and the constant value is  $\sigma_{w,2} = 1.168$ .

**3.4. RSM.** The RSM [17–19] solves a transport equation for each term of the Reynolds stress tensor and an equation for the dissipation rate. In 2D, five transport equations are solved, in addition to the continuity and momentum equations. The model takes into account effects that one- and two-equation models are not able to consider, for example, the anisotropy of the turbulence. However, the Reynolds stress transport equations require the modeling of complex terms, which may compromise the model's accuracy

$$\begin{aligned} &\frac{\partial}{\partial t}(\rho \overline{u'_i u'_j}) + \frac{\partial}{\partial x_k}(\rho U_k \overline{u'_i u'_j}) \\ &= -\frac{\partial}{\partial x_k} \left[ \overline{\rho u'_i u'_j u'_k} + p(\delta_{kj} u'_i + \delta_{ik} u'_j) \right] \\ &\quad + \frac{\partial}{\partial x_k} \left[ \mu \frac{\partial}{\partial x_k} (\overline{u'_i u'_j}) \right] - \rho \left( \overline{u'_i u'_k} \frac{\partial U_j}{\partial x_k} + \overline{u'_j u'_k} \frac{\partial U_i}{\partial x_k} \right) \\ &\quad + p \left( \frac{\partial u'_i}{\partial x_j} + \frac{\partial u'_j}{\partial x_i} \right) - 2\mu \frac{\partial u'_i}{\partial x_k} \frac{\partial u'_j}{\partial x_k} + S_{\text{RMS}}. \end{aligned} \quad (11)$$

To resolve the viscous sublayer with the RSM, the *Low-Re Stress-Omega* was selected. This option models the pressure strain term (fourth term on the right) of the Reynolds stress equations using the LRR approach (Launder-Reece-Rodi) [19] and solves the  $\omega$  equation [20]. This option gives the RSM model characteristics similar to those of the  $k$ - $\omega$  model.

The setup of the RSM model requires more attention than the others. With the default options and second-order discretization for the momentum and for the turbulence equations, the model showed early convergence problems at low angles of attack, and, in certain cases, the viscosity ratio reached unrealistic values (beyond  $10^5$ ). After several tests, we empirically determined the setup to be used for the

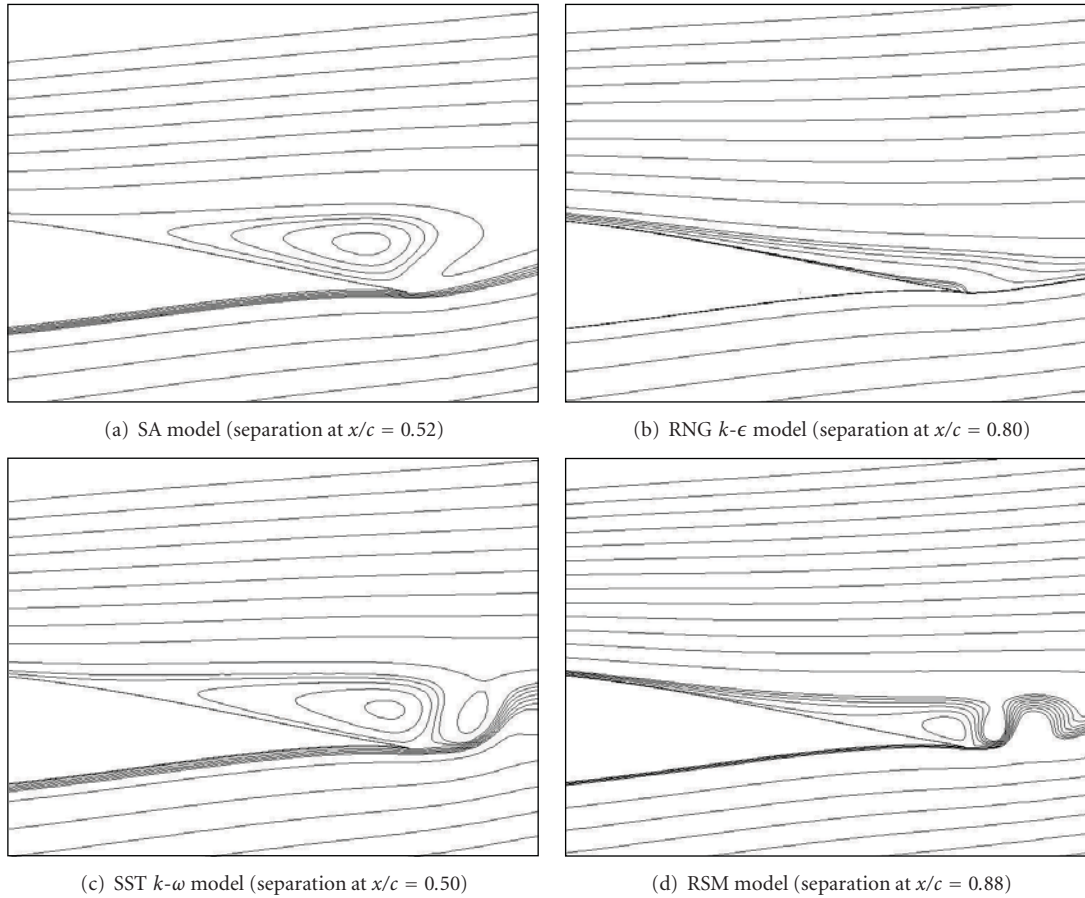


FIGURE 5: Streamlines after the application of various turbulence models at  $16^\circ$ .

simulations; at low ( $8^\circ$  or less) and high ( $26^\circ$  or more) angles of attack, the simulations were performed with the default setup. For the rest of the calculations ( $10^\circ$ – $24^\circ$ ), we disabled the *Shear Flow Corrections* option. All the simulations were performed with a second-order discretization for the momentum and a first-order discretization for the Reynolds stresses.

The *Shear Flow Corrections* option enables a function that modifies the values of the dissipation term in the  $\omega$  equation, the first pressure strain term, and the dissipation rate of the Reynolds stresses. Studying the influence of the turbulent kinetic energy  $k$  revealed that the main effect of this function is to reduce  $k$  ( $k$  is calculated with the diagonal of the Reynolds stresses).

#### 4. Numerical Simulations

An initial set of computations was carried out using the steady-state formulation with the SA, SST  $k$ - $\omega$ , RNG  $k$ - $\epsilon$ , and RSM models for the  $0^\circ$ – $28^\circ$  angle of attack range.

Figures 4(a) and 4(b) show the computed results using averaging to estimate the aerodynamic coefficients when oscillations occurred. In these figures, RISO Laboratory data are also shown, consisting of wind tunnel records, as well as numerical data calculated with the EllipSys2D program using the SST  $k$ - $\omega$  model.

At a low angle of attack (up to  $8^\circ$ ), the four models show good agreement with the experimental data. In the  $8^\circ$  to  $16^\circ$  range, lift and drag coefficients begin to show weak oscillations and numerical results that differ from the experimental results. At high angles ( $24^\circ$  and over), the four models give similar results, but overpredicted. In this range, the SST  $k$ - $\omega$  model gives the smoothest curve.

The SA model gives the best prediction of the maximal lift angle; however, the lift value is overpredicted. Also, this model gives the smoothest curves for the coefficients, except at high angles of attack.

The RNG  $k$ - $\epsilon$  model predicts the highest values of both coefficients and a maximal lift angle that is far from the experimental value. Between  $22^\circ$  and  $24^\circ$ , both coefficients change abruptly.

The SST  $k$ - $\omega$  model shows similar values to the SA model, except in the model's prediction of maximal lift. At high angles of attack, this model gives the smoothest curve.

The RSM model does not provide better results than the alternatives. It shows a drastic change in the coefficient behavior at  $18^\circ$ , which means that the model faces problems with handling large recirculation zones. Moreover, the simulations take much more time, since more equations are solved.

Figure 5 shows the computed streamlines at the trailing edge at an angle of attack of  $16^\circ$  for each turbulence

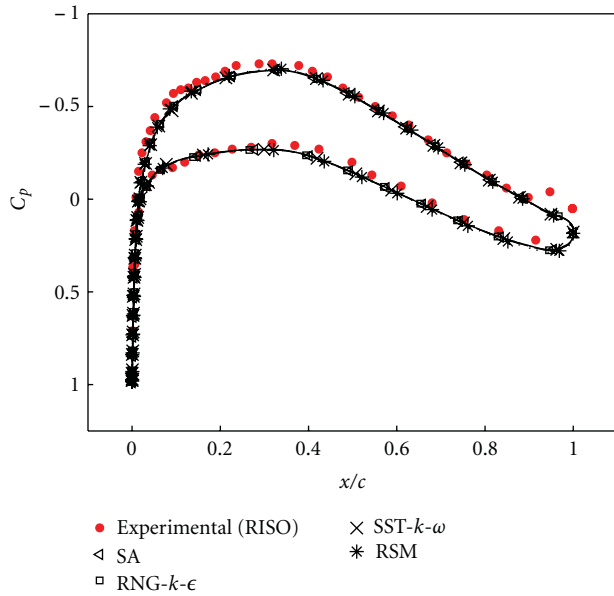


FIGURE 6: Pressure coefficient at  $0^\circ$  following application of various turbulence models.

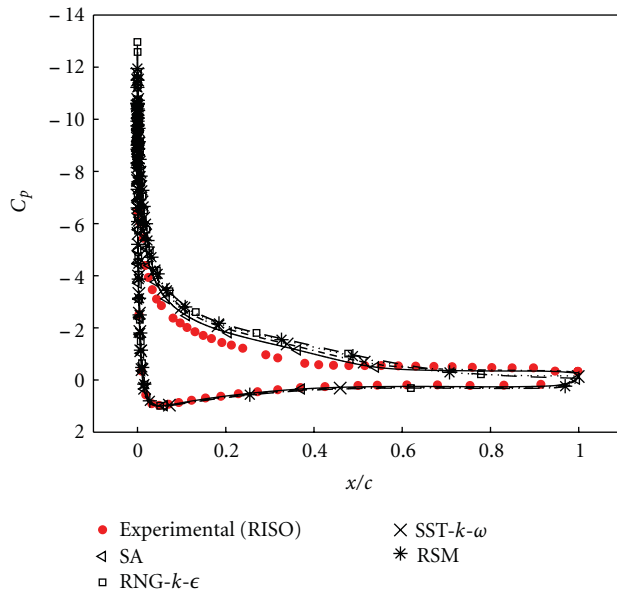


FIGURE 7: Pressure coefficient at  $16^\circ$  following application of various turbulence models.

model. The RNG  $k-\epsilon$  and RSM models predict the smallest zones that coincide with the highest  $C_l$  and the lowest  $C_d$  predicted at this angle. In the case of the RNG  $k-\epsilon$  model, the separation point is almost at the same place as the RSM, but the streamlines are barely perturbed, which may be because the  $k-\epsilon$  models overpredict the turbulence kinetic energy production, and momentum exchange allows the flow to remain close to the walls (Figures 4(a) and 4(b)). The SA and SST  $k-\omega$  models predict the largest zones that are of similar size. However, the SST  $k-\omega$  and RSM models predict unstable regions with vortex separation, which may explain

the difficulty the models have in reaching convergence at this angle. The similarity between the SA-SST  $k-\omega$  and RSM-RNG  $k-\epsilon$  models at the trailing edge is also present in the  $C_p$  curves shown in Figure 7.

Regarding the pressure coefficient, all the models give curves with similar shapes and values close to the experimental data. Figure 6 shows the pressure coefficient distribution at  $0^\circ$ . At this angle, the four models fully agree with the values given by RISO, except near the leading edge and at the stagnation point, where  $C_p$  is higher than the experimental value. Concerning the lift and drag, the four models give a good approximation of lift, and only the RSM gives a good estimate of drag, while the rest of models overpredict it.

Figure 7 shows the results for an angle of  $16^\circ$ . In this case, the pressure side agrees very well with the experimental values. On the suction side, however, the minimum  $C_p$  is underpredicted, which means that a higher suction acts on the upper side of the airfoil. There is an obvious relation between the peak found at this point and the overprediction of  $C_l$ . From Figures 4 and 7, we see that the RNG  $k-\epsilon$  model leads to the highest peak, which corresponds to the highest value of  $C_l$ , while the SA leads to the lowest peak and the lowest value of  $C_l$ . At the trailing edge, it can be seen that  $C_p$  depends on the size of the circulation zone. The smallest zone (RNG  $k-\epsilon$ ) has  $C_p$  values close to zero and the largest zone (SST  $k-\omega$ ) has the highest  $C_p$  values.

In order to understand the situation from a different perspective, a relative mass imbalance, defined as the mass imbalance on each cell divided by the mass of the cell, was introduced. Since this index can be positive or negative (mass source or mass sink), its absolute value was used to calculate the mean value over the whole domain.

For a flow having an angle of incidence of  $24^\circ$  and using the SST  $k-\omega$  model, the mean value was monitored during 10 000 iteration steps. Figures 8(a) and 8(b) show the cells having a relative mass imbalance of more than  $\pm 0.5\%$  at the iteration where the mean is at its highest and at its lowest value. This representation shows regions surrounding the airfoil in which a steady-state solution was not reached, suggesting that transient calculations need to be considered.

The reasonable approximation of the  $C_l$  and  $C_d$  values obtained by all the models may be explained by the fact that the relative mass imbalance remains low. It also indicates that steady-state solutions are a reasonable starting point for the transient calculations.

## 5. Conclusions

This paper has presented a study of the prediction of two-dimensional flows over a wind turbine airfoils. The methodology was based on the application of the commercial program FLUENT.

The intention was to provide wind turbine researchers with an assessment of turbulence modeling for the calculation of the fundamental lift and drag parameters for flows over wind turbine blade sections operating under icing conditions. Four turbulence models, the one-equation Spalart-Allmaras (SA) model, the two-equation RNG  $k-\epsilon$  and SST  $k-\omega$  models, and the Reynolds stress model (RSM),

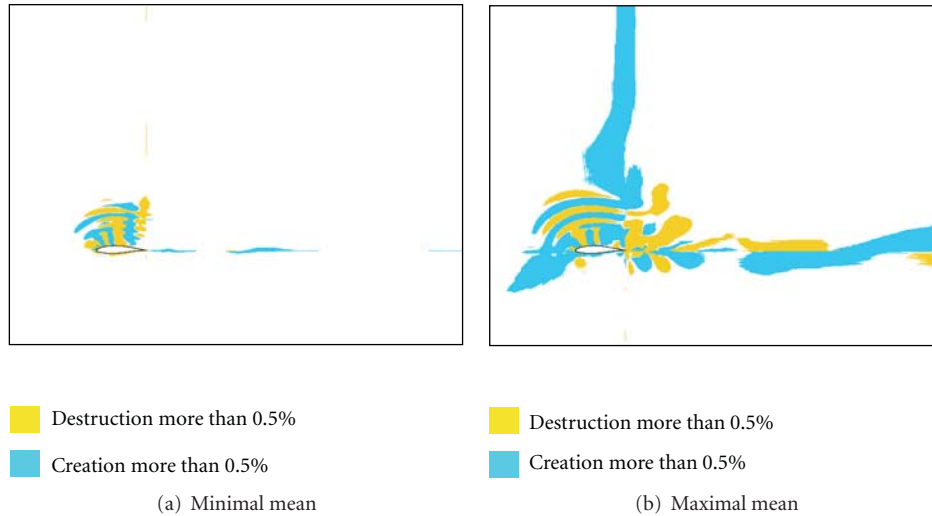


FIGURE 8: Relative mass imbalance contours.

were applied to predict flows over a clean NACA 63-415 airfoil at angles of attack ranging from  $0^\circ$  to  $28^\circ$ .

From these results, we estimate that the RSM is the least appropriate for solving this type of flow problem. It has shown to be much more sensitive in the presence of moderate to large recirculation zones, and it predicts high viscosity ratio values, requiring the readjustment of the setup options each time to prevent this problem from occurring. The calculations conducted with this model require more computational time with no noticeable improvement, when compared with the three alternatives for handling turbulence.

The RNG  $k-\epsilon$  model gives the highest prediction of lift and maximal lift angle. At  $16^\circ$ , the model also predicts the smallest recirculation zone and the separation point that is closest to the trailing edge.

The results obtained with the SA and the SST  $k-\omega$  models are very similar over the  $0^\circ$  to  $16^\circ$  range. In this work, these models always provided lower and less oscillatory aerodynamic coefficients and did so for the entire range of angles of attack tested. This behavior is not related to a faster or slower convergence rate.

The SA and SST  $k-\omega$  models were also found to be the most adequate for simulating the current flows. As seen in Figures 4(a) and 4(b), they are shown to have a better agreement with the solution shape given by the experimental data. Nevertheless, in this study, we noted that the SA model has a tendency to predict stable recirculation zones. Also, in this model, turbulence decay is only based on wall distance and velocity gradients and cannot handle turbulence dissipation, as the SST  $k-\omega$  model does. This implies that turbulence intensity remains constant in the wake. Although the other models are prone to showing similar nonphysical recirculation zones, this is the most unfavorable case.

Recirculation zones are present in both clean and iced wind turbine airfoils. In the case of ice accretion simulation, this zone impacts the water impingement calculation over

the suction side. Thus, a good approximation of flow in this zones is important in numerical studies of wind turbine flow.

Therefore, despite the fact that the SA gives better predictions near maximal lift, we conclude that the SST  $k-\omega$  model is the best suited to simulating flow around both clean and iced wind turbine airfoils.

## Acknowledgments

The authors gratefully acknowledge the financial support of the NSERC, through a strategic grant, and of FQRNT, through a team project grant.

## References

- [1] *World Wind Energy Report 2009*, World Wind Energy Association, Germany, 2009.
- [2] M. B. Bragg, A. P. Broeren, and L. A. Blumenthal, "Iced-airfoil aerodynamics," *Progress in Aerospace Sciences*, vol. 41, no. 5, pp. 323–362, 2005.
- [3] H. Seifert and F. Richert, "Aerodynamics of iced airfoils and their influence on loads and power production," in *Proceedings of the European Wind Energy Conference*, Dublin Ireland, October 1997.
- [4] C. Mayer, A. Ilinca, G. Fortin, and J. Perron, "Wind tunnel study of electrothermal de-icing of wind turbine blades," *The International Journal Society of Offshore and Polar Engineers*, vol. 17, pp. 182–188, 2007.
- [5] S. L. Yang, Y. L. Chang, and O. Arici, "Navier-Stokes computations of the NREL airfoil using a  $k-\omega$  turbulent model at high angles of attack," *Journal of Solar Energy Engineering, Transactions of the ASME*, vol. 117, no. 4, pp. 304–310, 1995.
- [6] Y. Chen, Y. Zhiqian, L. Deyuan, and H. Fupeng, "Numerical simulation of large angle-of-attack separated flows over airfoils of HAWT rotors," *Wind Engineering*, vol. 30, no. 1, pp. 35–42, 2006.
- [7] Fluent Inc., *Fluent 6.3.26 User's Guide*, Fluent Inc., 2005.
- [8] Fluent Inc., *Gambit 2.2.30 User's Guide*, Fluent Inc., 2004.

- [9] C. Bak, P. Fuglsang, J. Johansen, and I. Antoniou, "Wind tunnel tests of the NACA 63-415 and a modified NACA 63-415 airfoil," Tech. Rep. Risø-R-1193, Risø National Laboratory, Roskilde, Denmark, 2000.
- [10] W. P. Jones and B. E. Launder, "The prediction of laminarization with a two-equation model of turbulence," *International Journal of Heat and Mass Transfer*, vol. 15, no. 2, pp. 301–314, 1972.
- [11] V. Yakhot and S. A. Orszag, "Renormalization group analysis of turbulence. I. Basic theory," *Journal of Scientific Computing*, vol. 1, no. 1, pp. 3–51, 1986.
- [12] M. Wolfstein, "The velocity and temperature distribution of one-dimensional flow with turbulence augmentation and pressure gradient," *International Journal of Heat and Mass Transfer*, vol. 12, pp. 301–318, 1969.
- [13] P. Spalart and S. Allmaras, "A one-equation turbulence model for aerodynamic flows," *AIAA Paper*, no. 92-0439, 1992.
- [14] P. R. Spalart and S. R. Allmaras, "One-equation turbulence model for aerodynamic flows," *Recherche Aerospaciale*, no. 1, pp. 5–21, 1994.
- [15] D. C. Wilcox, "Reassessment of the scale-determining equation for advanced turbulence models," *AIAA Journal*, vol. 26, no. 11, pp. 1299–1310, 1988.
- [16] F. R. Menter, "Two-equation eddy-viscosity turbulence models for engineering applications," *AIAA Journal*, vol. 32, no. 8, pp. 1598–1605, 1994.
- [17] M. M. Gibson and B. E. Launder, "Ground effects on pressure fluctuations in the atmospheric boundary layer," *Journal of Fluid Mechanics*, vol. 86, no. 3, pp. 491–511, 1978.
- [18] B. E. Launder, "Second-moment closure: present ... and future?" *International Journal of Heat and Fluid Flow*, vol. 10, no. 4, pp. 282–300, 1989.
- [19] B. E. Launder, G. J. Reece, and W. Rodi, "Progress in the development of a reynolds-stress turbulence closure," *Journal of Fluid Mechanics*, vol. 68, no. 3, pp. 537–566, 1975.
- [20] D. Wilcox, "Turbulence modeling: an overview," *AIAA Paper*, no. 2001-0724, 2001.

## Research Article

# Computation of Ice Shedding Trajectories Using Cartesian Grids, Penalization, and Level Sets

Héloïse Beaugendre,<sup>1</sup> François Morency,<sup>2</sup> Federico Gallizio,<sup>3</sup> and Sophie Laurens<sup>4</sup>

<sup>1</sup>IPB, Université de Bordeaux, INRIA Bordeaux Sud-Ouest, Equipe-Projet MC2, IMB UMR 5251, 351 Cours de la Libération, 33405 Talence, France

<sup>2</sup>Département de Génie Mécanique, École de Technologie Supérieure, 1100 Rue Notre-Dame Ouest, Montréal, QC, Canada H3C 1K3

<sup>3</sup>Optimad Engineering s.r.l., Via Giacinto Collegno, 18, 10143 Turin, Italy

<sup>4</sup>Université de Bordeaux, INRIA Bordeaux Sud-Ouest, Equipe-Projet MC2, IMB UMR 5251, 351 Cours de la Libération, 33405 Talence, France

Correspondence should be addressed to François Morency, francois.morency@etsmtl.ca

Received 16 November 2010; Accepted 25 January 2011

Academic Editor: Guan Yeoh

Copyright © 2011 Héloïse Beaugendre et al. This is an open access article distributed under the Creative Commons Attribution License, which permits unrestricted use, distribution, and reproduction in any medium, provided the original work is properly cited.

We propose to model ice shedding trajectories by an innovative paradigm that is based on cartesian grids, penalization and level sets. The use of cartesian grids bypasses the meshing issue, and penalization is an efficient alternative to explicitly impose boundary conditions so that the body-fitted meshes can be avoided, making multifluid/multiphysics flows easy to set up and simulate. Level sets describe the geometry in a nonparametric way so that geometrical and topological changes due to physics and in particular shed ice pieces are straight forward to follow. The model results are verified against the case of a free falling sphere. The capabilities of the proposed model are demonstrated on ice trajectories calculations for flow around iced cylinder and airfoil.

## 1. Introduction

Ice accretion on aerodynamic bodies is a serious and not yet totally mastered meteorological hazard due to supercooled water droplets (liquid water droplets at a temperature below the dew point) that impact on surfaces. Ice accretion is a multiphysics phenomenon [1] including fluid mechanics, heat transfer, and solid mechanics. Ice accretions have several negative effects, especially performance degradations for both aircraft and wind turbine. For aircraft, sudden performance degradations due to ice accretion cause several incidents and accidents each year [2]. Performance degradations include substantial reduction of engine performance and stability, reduction in aircraft maximum lift and stall angle, and increase of drag. For wind turbine, ice accretion on blades is a major concern in northern climate. When adverse meteorological conditions occur, ice accretes at the outer part of the blade with an approximately linear increase with time [3]. With growing ice accretion, the blade drag

increases, diminishing the power output of the turbine and eventually causing a complete loss of production [4]. Other negative consequences include overloading due to delayed stall [5], increasing fatigue of components due to imbalance in the ice load, and damaging or harm caused by uncontrolled shedding of large ice chunks [6, 7].

In practice, ice accretion can be minimized by deicing systems [8] or prevented by anti-icing systems. By reducing the adhesive shear strength between ice and surface, deicing systems remove ice formed on the protected surfaces following a periodic cycle. This cycle is defined such that intercycle ice shapes remain acceptable from a performance point of view. Because they are activated periodically, deicing systems require less energy than anti-icing systems. Still, because of the enormous amounts of thermal or mechanical energy that would be required, complete removal of ice formation on large structure is not economically feasible. Only areas sensible to ice accretion, such as wing or blade leading edge, benefit from ice protection systems.

Actual concerns about greenhouse gases will lead to changes in the design of ice protection systems, thus renewing interest in de-icing simulation tools. To save fuel burn, aircraft manufacturers are investigating “new” ice protection systems such as electrothermal or electromechanical de-icing systems to replace anti-icing systems. One of the drawbacks of de-icing device is the ice pieces shed into the flow. The knowledge of ice shedding trajectories could allow assessing the risk of impact/ingestion on/in aircraft components located downstream [9]. When they leave the aircraft surface, ice pieces become projectiles that can hit and cause severe damage to aircraft surface or other components, as aircraft horizontal and vertical tails, or aircraft engine [10]. Aircraft certification authorities, such as FAA, have specific requirements for large ice fragment ingestion during engine certification. Control surfaces or wing flaps are also sensitive to ice shedding because they can be blocked by ice fragments. Aircraft manufacturers rely mainly on flight tests to evaluate the potential negative effects of ice shedding because of the lack of appropriate numerical tools [11]. The random shape and size taken by ice shed particles together with their rotation as they move make it difficult for classical CFD tools to predict trajectories.

For the wind turbine industry, new environmental pre-occupations mean building more wind turbines in less favorable sites, especially in northern countries like Canada. Wind turbines are going to be built in sites prone to atmospheric icing, and the use of de-icing systems may reduce production losses. Even if no ice protection systems are installed, vibration and aerodynamic forces can cause ice shedding. Ice shed trajectory computations are then needed to reduce damage risk.

Ice shedding phenomena is an emerging topic for researchers working in numerical simulation of ice accretion. Until recently, only a few research works have paid attention to it. In one of the first numerical works published on de-icing system, De Witt et al. [12] studied the three-dimensional transient heat transfer in a multilayered body that is ice covered. This work focuses mainly on modeling the phase change in the ice layer with the movement of the solid-liquid interface as the latent heat of fusion is absorbed or released. In an article by Henry [13], criteria based on water film thickness is used to predict ice break-up. Once the piece of ice break up, it simply leaves the computational domain, and no calculation of its trajectory is done. Stresses in accreted ice caused by aerodynamic forces have been studied by Scavuzzo et al. [14], and an ice failure criterion [15] based on both normal and shear interface stresses has been used in a finite elements code to simulate the electroimpulse deicing process of aircraft wings.

Kohlman and Winn [16] proposed a trajectory simulation method to compute the trajectories of ice particles, represented by square plates of uniform thickness, into a uniform velocity field. The lift and drag were obtained from empirical correlations, and initial displacement and rotation were imposed to initiate trajectory calculations. Santos et al. [17] used a similar method but, this time, the trajectories were calculated into a nonuniform flow field around a wing. The ice fragment, a square flat plate, was released from

a point in front of the leading edge of a wing. Initial position and velocities were varied, and the probabilities of ice impact at a location two chords downstream of the leading edge were obtained. Another method, based on a modified water droplet trajectory code, was used by Chandrasekharan and Hinson [18] to track trajectories of an ice disk and two ice slabs. The drag of the disk was assumed to be that of a sphere and the drag of the slabs to be that of a flat plate normal to the flow. Recently, Papadakis et al. [9] presented a statistical approach to perform trajectory computations for ice fragments shed from the wing and fuselage surfaces of a business jet. They carry an experimental study of aerodynamic loads around a potential ice fragment and derived empirical correlations. Those correlations have been used into a methodology based on trajectory calculation and probabilistic approach to identify areas where ice fragments most likely strike the aircraft.

On one side, some numerical codes predict ice break-up, and on the other side different numerical codes compute ice shedding trajectory. The numerical simulation of a full unsteady viscous flow, with a set of moving bodies immersed within, shows several difficulties for grid-based methods. Drawbacks income from the meshing procedure for complex geometries and the regriding procedure in tracing the body motion. A new approach capable of solving the complete de-icing problem is proposed in this paper. The approach is based on cartesian grids, penalization, and level sets.

The objective of the present paper is to demonstrate the approach capability to predict ice shedding trajectory, starting just after the ice break-up. First, a vortex method [19] is proposed to simulate the interaction of an incompressible flow with rigid bodies. For our method, we followed the innovative approach proposed by Coquerelle et al. [20, 21]. They propose an efficient and accurate technique to simulate unsteady incompressible viscous flows using hybrid vortex methods [22]. Hybrid vortex methods are based on the combination of Lagrangian mesh-free schemes and Eulerian grid-based schemes [22]. The Navier-Stokes equations are formulated in terms of the vorticity formulation, and the vorticity field is numerically determined by a particle discretization. The two schemes solve different terms of the equation, for example, the Lagrangian scheme is used to solve the nonlinear advective part of the equation while the Eulerian scheme is used to solve on the grid the diffusive part of the equation and the velocity term. A penalization method [23] is used to enforce the no-slip boundary condition inside the solid wall boundaries. The bodies around which the flow is computed are defined using the so-called penalization method or Brinckman-Navier-Stokes equations in which the bodies are considered as porous media with a very small intrinsic permeability. Level set functions are used to capture interfaces and compute rigid motions of the solid bodies [24].

After presenting the model equations, the numerical procedure is exposed. Then, numerical trajectories results are presented for sedimentation of a 2D cylinder on a flat plate, flow around an iced cylinder and an iced airfoil.

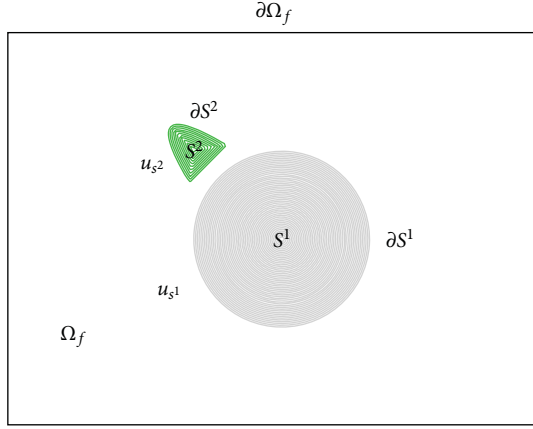


FIGURE 1: Schematic representation of a computational domain  $\Omega = \Omega_f \cup S^1 \cup S^2$ .  $\Omega_f$ : fluid domain,  $S^i$ : solid domains.

## 2. Fluid-Solid Flow Model

**2.1. Physical Model.** Given a computational domain  $\Omega$ , we consider incompressible flow in  $\Omega_f$  around rigid solids  $S^i$ . A schematic representation of a computational domain composed of two solids is sketched in Figure 1.

We assume that the density is constant in the fluid and in the solids. The fluid-solid interaction problem can be modeled by the incompressible Navier-Stokes equations

$$\begin{aligned} \frac{\partial \mathbf{u}}{\partial t} + (\mathbf{u} \cdot \nabla) \mathbf{u} - \nu \nabla^2 \mathbf{u} + \frac{1}{\rho} \nabla p - \mathbf{g} &= 0 \quad \text{in } \Omega_f, \\ \nabla \cdot \mathbf{u} &= 0 \quad \text{in } \Omega_f, \\ \mathbf{u} &= \mathbf{u}_{s^i} \quad \text{on } \partial S^i, \\ \mathbf{u} &= \mathbf{u}_f \quad \text{on } \partial \Omega_f. \end{aligned} \quad (1)$$

In the above system  $\mathbf{u}$  is the velocity,  $\nu$  is the kinematic viscosity,  $\rho$  is the density,  $\mathbf{g}$  is the gravity vector, and  $p$  is the pressure. Depending on the location in the computational domain, the velocity is either the fluid velocity  $\mathbf{u}_f$  or the solid velocity  $\mathbf{u}_{s^i}$ . The idea is to extend the velocity field inside the solid body and to solve the flow equations with a penalization term to enforce rigid motion inside the solid [21].

Given a penalization parameter  $\lambda \gg 1$  and denoting by  $\chi_{s^i}$  the characteristic function of the solid  $S^i$ , the model equation is the following:

$$\begin{aligned} \frac{\partial \mathbf{u}}{\partial t} + (\mathbf{u} \cdot \nabla) \mathbf{u} - \nu \nabla^2 \mathbf{u} + \frac{1}{\rho} \nabla p - \mathbf{g} \\ = \sum_{i=1}^{N_s} \lambda \chi_{s^i} (\mathbf{u}_{s^i} - \mathbf{u}) \quad \text{for } \mathbf{x} \in \Omega, t > 0, \end{aligned} \quad (2)$$

coupled with the incompressible mass conservation equation

$$\nabla \cdot \mathbf{u} = 0 \quad \text{for } \mathbf{x} \in \Omega. \quad (3)$$

The velocity of the moving rigid motion  $\mathbf{u}_{s^i}$  is obtained by averaging translation and angular velocities over the solid, with the following equation:

$$\begin{aligned} \mathbf{u}_{s^i} &= \frac{1}{|S^i|} \int_{\Omega} \chi_{s^i} \mathbf{u} d\mathbf{x} \\ &+ \left( J^{-1} \int_{\Omega} \chi_{s^i} \mathbf{u} \times (\mathbf{x} - \mathbf{x}_G) d\mathbf{x} \right) \times (\mathbf{x} - \mathbf{x}_G), \end{aligned} \quad (4)$$

where  $\mathbf{x}_G$  is  $S^i$  center of gravity,  $J$ , its inertia matrix, and  $\mathbf{x}$  is the coordinate at calculation point inside the domain. The rigid body  $S^i$  follows the trajectories of the flow with the advection velocity  $\mathbf{u}_{s^i}$ . Therefore,  $S^i$  characteristic function can be obtained by solving the advection equation

$$\frac{\partial \chi_{s^i}}{\partial t} + (\mathbf{u}_{s^i} \cdot \nabla) \chi_{s^i} = 0 \quad \text{for } \mathbf{x} \in \Omega. \quad (5)$$

In this paper  $\chi_{s^i}$  is computed from a level set function  $\Phi_{s^i}$  satisfying the same advection equation

$$\frac{\partial \Phi_{s^i}}{\partial t} + (\mathbf{u}_{s^i} \cdot \nabla) \Phi_{s^i} = 0 \quad \text{for } \mathbf{x} \in \Omega. \quad (6)$$

We initialize  $\Phi_{s^i}$  as the signed distance function to the boundary of  $S^i$ , because  $\phi_{s^i}$  is negative outside  $S^i$  and positive inside the solid:

$$\chi_{s^i} = H(\Phi_{s^i}), \quad (7)$$

where  $H$  is the Heaviside function.

It is important to notice here that, because  $u_{s^i}$  is a rigid body motion, one can guarantee that  $\Phi_{s^i}$  remains a signed distance for all time. To summarize, each body-fluid interface is captured by a level set function. These level set functions are moved in rigid motion by advection.

**2.2. Ice Shedding Law.** Ice accreted remains attached to surface until the adhesive bond between ice and substrate fails or until a fracture occurs in the ice. The ice adhesive shear strength may depend on substance, surface roughnesses, and coating on the surface side. The ice adhesive shear strength depends also on atmospheric conditions present during the accretion process: temperature, liquid water content, air velocity, and so forth [25]. Generally, the adhesive shear strength for rime ice is lower than for glaze ice.

Usually, the aerodynamic forces alone are not sufficient to detach accreted ice from airfoil. To deice airfoil, either the adhesive shear strength of the ice is reduced almost to zero by heating and melting the accreted ice, or mechanical forces break the ice and give an impulsion sufficient to detach ice from surface. In the two cases, shear stress inside the ice and, to a lesser extent, normal stress play a critical role in shedding.

The choice of an ice shedding law dictates the initial conditions for the ice trajectory calculation. At the end of the break-up process, an ice piece will have a definite shape, a translational velocity, and a rotational velocity that becomes input for the trajectory calculations, see [9, 14]. Although some researchers have proposed models [26], these models

are not commonly accepted and used to predict ice break up by the aircraft icing community.

In this paper we concentrate on ice trajectory calculation, and a method similar to the one proposed in [16, 17] is used to initiate trajectory calculations. In these papers, a statistical approach is used, and ice fragments are launched from several location points near an aircraft body. From the several trajectories, the probability of having an ice fragment in a given area near the aircraft is devised. In the present paper, an initial displacement, together with an initial velocity and initial rotation velocity equal to zero, is imposed on the ice piece to make it leave the body surface.

**2.3. Numerical Method.** In this paper, the penalized Navier-Stokes equation is defined in terms of a vorticity formulation, and the vorticity field is numerically determined by a particle discretization [19]. Let us consider the penalized Navier-Stokes equation in the vorticity formulation by applying the *curl* operator to (2)

$$\begin{aligned} \frac{\partial \boldsymbol{\omega}}{\partial t} + (\mathbf{u} \cdot \nabla) \boldsymbol{\omega} &= (\boldsymbol{\omega} \cdot \nabla) \mathbf{u} + \nu \nabla^2 \boldsymbol{\omega} - \nabla p \\ &\times \nabla \left( \frac{1}{\rho} \right) + \lambda \nabla \times \left[ \sum_{i=1}^{N_s} H(\Phi_{s^i}) (\mathbf{u}_{s^i} - \mathbf{u}) \right] \end{aligned} \quad (8)$$

with

$$\begin{aligned} \nabla \cdot \mathbf{u} &= 0 \quad \text{in } \Omega, \\ \nabla \times \mathbf{u} &= \boldsymbol{\omega} \quad \text{in } \Omega. \end{aligned} \quad (9)$$

The density  $\rho$  is computed from the fluid and solid densities, respectively,  $\rho_F$  and  $\rho_{s^i}$ , using the following equation:

$$\rho = \rho_F \left( 1 - \sum_{i=1}^{N_s} \chi_{s^i} \right) + \sum_{i=1}^{N_s} \rho_{s^i} \chi_{s^i}. \quad (10)$$

Equation (8) is required to compute the variation of the pressure. Usually, in vorticity formulation, this is not necessary. Indeed if the density is constant the term  $\nabla p \times \nabla(1/\rho)$  vanishes. To avoid an explicit computation of the pressure, (8) can be reformulated using (1), in the following way:

$$\begin{aligned} \frac{\partial \boldsymbol{\omega}}{\partial t} + (\mathbf{u} \cdot \nabla) \boldsymbol{\omega} &= (\boldsymbol{\omega} \cdot \nabla) \mathbf{u} + \nu \nabla^2 \boldsymbol{\omega} - \frac{\nabla \rho}{\rho} \\ &\times \left( \frac{\partial \mathbf{u}}{\partial t} + \mathbf{u} \cdot \nabla \mathbf{u} - \nu \nabla^2 \mathbf{u} - \mathbf{g} \right) \\ &+ \lambda \nabla \times \left[ \sum_{i=1}^{N_s} H(\Phi_{s^i}) (\mathbf{u}_{s^i} - \mathbf{u}) \right]. \end{aligned} \quad (11)$$

Following Cottet and Koumoutsakos [22], the hybrid vortex methods are based on the combination of Lagrangian mesh-free schemes and Eulerian grid-based schemes on the same flow region. The Vortex-In-Cell (VIC) scheme is an example of hybrid vortex method: the non linear advection is computed by tracking the trajectories of the Lagrangian

particles through a set of ODEs, whereas an Eulerian grid is adopted to solve efficiently the velocity field, the diffusive term, and the penalization term. Given  $D/Dt(\cdot)$ , the material derivative, by expanding the penalization term, (11) becomes

$$\begin{aligned} \frac{D\boldsymbol{\omega}}{Dt} &= (\boldsymbol{\omega} \cdot \nabla) \mathbf{u} + \nu \nabla^2 \boldsymbol{\omega} - \frac{\nabla \rho}{\rho} \\ &\times \left( \frac{\partial \mathbf{u}}{\partial t} + \mathbf{u} \cdot \nabla \mathbf{u} - \nu \nabla^2 \mathbf{u} + \mathbf{g} \right) \\ &+ \lambda \sum_{i=1}^{N_s} H(\Phi_{s^i}) (\boldsymbol{\omega}_{s^i} - \boldsymbol{\omega}) \\ &+ \lambda \sum_{i=1}^{N_s} \delta(\Phi_{s^i}) [\nabla(\Phi_{s^i}) \times (\mathbf{u}_{s^i} - \mathbf{u})], \end{aligned} \quad (12)$$

where  $\delta(\Phi_{s^i})$  is the 1D Dirac delta function and  $\boldsymbol{\omega}_{s^i} = \nabla \times \mathbf{u}_{s^i}$ . We recall that with level-set functions,  $\nabla \Phi_{s^i}$  is the unit normal to the interface  $\partial S^i$  oriented towards the solid. The last two terms on the right of (12) play a significant physical role in the model. The first term clears the vorticity difference within the bodies, whereas the second member represents a vorticity generation term that is localized on the solid boundaries and allows the no-slip condition to be imposed. The penalized vorticity equation means that the rate of change of the vorticity, advected by the fluid in a Lagrangian frame of reference, is governed by the diffusive effects, the stretching effects, the production of bound vorticity, and the vorticity cancellation within the solid bodies.

Let us introduce the level-set Vortex-In-Cell (VIC) algorithm. The domain  $\Omega$  is meshed using a uniform fixed cartesian grid. We denote by  $\Delta t$  the time step such as  $t^n = n\Delta t$  and  $\Phi_{s^i}^n$ ,  $\mathbf{u}^n$ ,  $\boldsymbol{\omega}^n$  are grid values of the level set functions, velocity and vorticity, respectively. In vortex methods, the rate of change of vorticity is modeled by means of discrete vortex particles, such that the solution of (12) is localized only in the rotational regions of the flow field. This is the most important advantage of the vortex methods, that is, the computational efforts are naturally addressed only to specific flow field zones. The vorticity field  $\boldsymbol{\omega}$  is represented by a set of particles

$$\boldsymbol{\omega}(\mathbf{x}) = \sum_{p=1}^N v_p \boldsymbol{\omega}_p \zeta(\mathbf{x} - \mathbf{x}_p), \quad (13)$$

where  $N$  is the number of particles,  $\mathbf{x}_p$  the particle location, and  $v_p$ ,  $\boldsymbol{\omega}_p$  are, respectively, the volume (constant due to the incompressibility) and the strength of a general particle  $p$ .  $\zeta$  is a smooth distribution function such that  $\int \zeta(x) dx = 1$  which acts on the vortex support. The interpolating-remeshing scheme is a fundamental tool for the accuracy of the whole method.

We propose a splitting algorithm to solve (8). Each time step  $\Delta t$  is solved using four substeps.

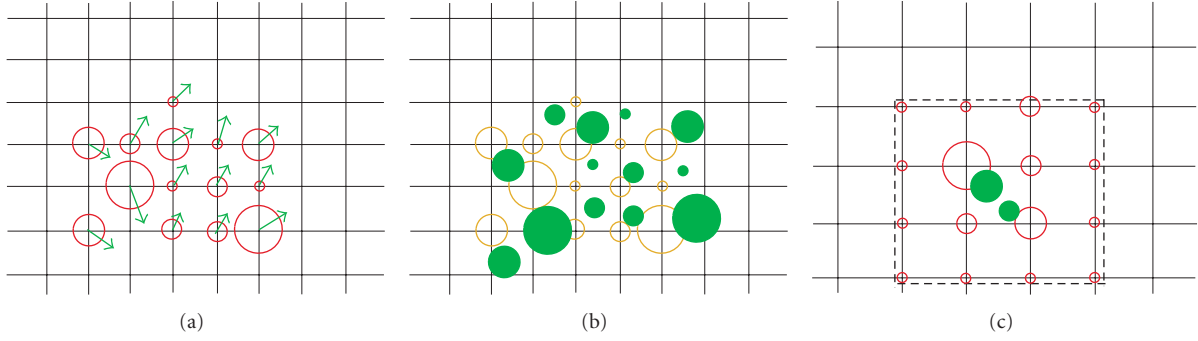


FIGURE 2: Particles interpolation scheme. The circle's size denotes the strength of the particle, and the solid circles represent the advected particles. (a) Vortex particles and velocity field; (b) advection step; (c) remesh-diffusion step.

*Substep 1* (advection). During the first substep, the vortex elements are advected by the local flow velocity

$$\frac{D\boldsymbol{\omega}}{Dt} = \frac{\partial\boldsymbol{\omega}}{\partial t} + (\mathbf{u} \cdot \nabla)\boldsymbol{\omega} = 0. \quad (14)$$

Grid vorticity above a certain cut-off is used to create particle at grid point locations [27], as shown in Figure 2(a). Using (14), particles are displaced with a fourth-order Runge-Kutta time-stepping scheme (Figure 2(b)). From the new vortex particles's locations, the vorticity field is remeshed on the grid by means of an interpolation procedure (Figure 2(c)).

The interpolation order is directly linked to the number of moments preserved by the new particles' distribution by comparison with the former one. In this paper, we used the following third-order interpolation kernel introduced by Monaghan [28]:

$$M'_4(x) = \begin{cases} 0 & \text{if } |x| > 2, \\ \frac{(2 - |x|)^2(1 + |x|)}{2} & \text{if } 1 \leq |x| \leq 2, \\ 1 - \frac{5x^2}{2} + \frac{3|x|^3}{2} & \text{if } |x| \leq 1, \end{cases} \quad (15)$$

where  $x$  is the distance from the point to interpolate. In this 1D example, the influenced stencil consists of four surrounding grid points. In the 2D case, the  $M'_4$  scheme takes into account the sixteen closest grid points around the particle to interpolate/remesh. In Figure 2(c) the particle interpolating/remeshing scheme is illustrated.

*Substep 2* (diffusion). Once Substep 1 is done, the remaining parts of the governing equation (11) can be solved. The equation to solve for the viscous contribution is then

$$\frac{\partial\boldsymbol{\omega}}{\partial t} = (\boldsymbol{\omega} \cdot \nabla)\mathbf{u} + \nu\nabla^2\boldsymbol{\omega}. \quad (16)$$

Equation (16) is approximated onto the grid by means of an Euler explicit scheme, while the Laplacian is evaluated, with a second-order accurate standard centered finite differences five points stencil.

*Substep 3* (pressure gradient contribution). The equation to solve for the pressure gradient contribution is

$$\frac{\partial\boldsymbol{\omega}}{\partial t} = -\frac{\nabla\rho}{\rho} \left( \frac{\partial\mathbf{u}}{\partial t} + \mathbf{u} \cdot \nabla\mathbf{u} - \nu\nabla^2\mathbf{u} - \mathbf{g} \right). \quad (17)$$

To solve (17), density values are obtained from (10). Grid values of  $\mathbf{u}^n$  and  $\mathbf{u}^{n-1}$  are used to compute  $\partial\mathbf{u}/\partial t$  and centered finite differences at  $t^n$  are used to compute  $\mathbf{u} \cdot \nabla\mathbf{u} - \nu\nabla^2\mathbf{u}$ .

*Substep 4* (penalization). Finally, the penalization term is evaluated using

$$\frac{\partial\boldsymbol{\omega}}{\partial t} = \lambda\nabla \times \left( \sum_{i=1}^{N_s} H(\Phi_{s^i})(\mathbf{u}_{s^i} - \mathbf{u}) \right). \quad (18)$$

The discretization and the integration of the penalization term affect the choice of the penalization parameter  $\lambda$  (the larger the parameter  $\lambda$ , the better the quality of the penalization in practice in our simulations  $\lambda$  is fixed to  $10^8$ ). An Euler explicit time discretization of (18) does not allow to use  $\lambda > 1/\Delta t$ . An implicit Euler time discretization is therefore used for the penalization term in the Navier-Stokes equation:

$$\mathbf{u}^{n+1} = \frac{\mathbf{u}^* + \lambda\Delta t \sum_{i=1}^{N_s} H(\Phi_{s^i})\mathbf{u}_{s^i}^n}{1 + \Delta t \sum_{i=1}^{N_s} H(\Phi_{s^i})}. \quad (19)$$

The vorticity field at  $t^{n+1}$  is evaluated on the grid by taking the *curl* of the velocity

$$\boldsymbol{\omega}^{n+1} = \nabla \times \mathbf{u}^{n+1} \quad (20)$$

and computing the derivative through the second-order centered finite differences approximation, while  $\mathbf{u}_{s^i}$  is evaluated using (4). This method is unconditionally stable.

Because the equations are not written in primitive variables, special treatments are needed to recover the velocity field and to impose the boundary conditions. Since the incompressible velocity field is divergence-free, from the vector field theory, we can define a vector potential  $\boldsymbol{\psi}$  such that

$$\mathbf{u} = \nabla \times \boldsymbol{\psi}. \quad (21)$$

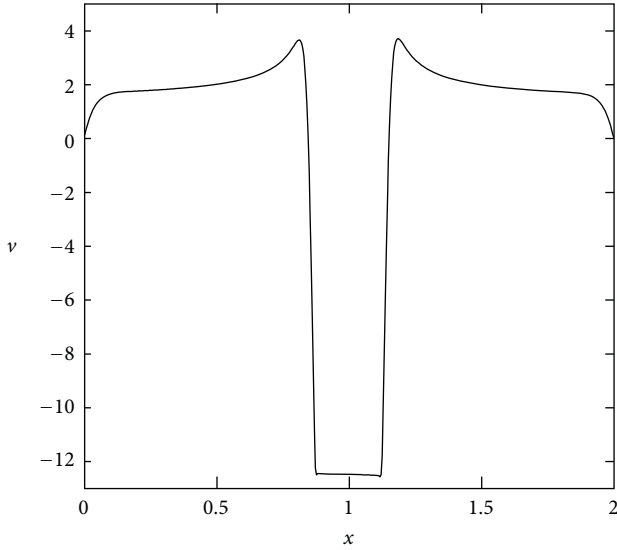


FIGURE 3: 2D cut of  $v$  component of velocity at time  $t = 0.3$ .

The vector potential  $\psi$  is a 3D extension of the so-called stream function  $\psi$ . This potential vector is imposed to be solenoidal  $\nabla \cdot \psi = 0$  and given  $\omega^{n+1}$  the updated vorticity field, the stream function field is computed by solving the linear Poisson equation,

$$\nabla^2 \psi = -\omega, \quad (22)$$

on the cartesian grid with boundary conditions on  $\partial\Omega$ .

In (19),  $\mathbf{u}^*$  is computed using (21) and (22) with  $\omega^*$  the vorticity resulting from Substep 3.

In vortex methods, boundary conditions are explicitly used only to solve the Poisson equation and are enforced on the nonprimitive variable  $\psi$ . In the present method, on the upstream and downstream boundaries (right and left boundaries on Figure 1), a Neumann condition,  $\partial\psi/\partial n = 0$ , is enforced. On the lower and upper boundaries, a Dirichlet condition sets the flow mass rate through the domain.

In our simulations, a Fast Poisson Solver is adopted (Fishpack90 library [29]).

For the present method, following [30], the forces can be evaluated without any information on the pressure field but only through the knowledge of the velocity and vorticity fields.

### 3. Numerical Simulations

The proposed approach results are validated against available literature results for the sedimentation of a 2D cylinder on a flat plate. Then, ice trajectory prediction capabilities are verified for two test cases at low Reynolds number. The first one, an iced cylinder, is representative of an unsteady flow around a bluff body. The second one, an iced airfoil, is more representative of the flow around an aerodynamic body, although with the attached ice shape, it behaves initially like a bluff body. For sake of aerodynamic force computations verification, the fluid and solid densities are assumed to be

the same in the ice trajectory calculations. Inertia and gravity effects are thus negligible.

**3.1. Sedimentation of a 2D Cylinder on a Flat Plane.** We consider the case of a 2D cylinder in a square cavity, falling under gravity on a flat plane. This test is used to verify the method by a comparison with Glowinski [31] and Coquerelle et al. [20]. The dimension of the cavity is  $[0, 2] \times [0, 6]$ . The viscosity is 0.01. The density inside and outside the cylinder is, respectively, 1.5 and 1. The cylinder has a radius of 0.125, no roughness, and is initially located at the point (1, 4). It accelerates under gravity, set to  $g = -980$ , then settles to a steady velocity, due to the friction forces, and eventually hit the bottom of the cavity and stops.

In Figure 3, the evolution of  $V$  velocity component along a line,  $y = 0.9$ , cutting the middle of the cylinder is drawn at time 0.3. The cylinder has almost reached its final velocity. Between  $x = 0.875$  and  $x = 1.125$  the velocity is the one inside the solid cylinder. Fluid is accelerated around the cylinder due to mass conservation principle. On the side of the cavity, fluid sticks to the wall, and thus the velocity is 0. To impose this boundary condition on the cavity walls a penalization technique has also been used.

In Figure 4, the barycenter computed position and the evolution of its vertical velocity as a function of time are plotted. The solution is in agreement with Coquerelle et al. [20] and Glowinski [31] solutions. Contrary to literature results, our cylinder simply stops when it hits the wall instead of bouncing. This is to be expected because no collision model is used in our simulation. Nevertheless, result comparisons indicate that inertia, gravity, and drag forces are correctly implemented in our code.

**3.2. Iced Cylinder.** We consider first an incompressible flow around two static rigid solids, the cylinder  $S^1$  and the ice piece  $S^2$ , in  $\Omega_f$ . A schematic representation of the computational domain  $\Omega$  composed of these two solids is sketched in Figure 1. The domain is a rectangular box  $[-3, 15] \times [-6, 6]$ . The diameter  $d$  of the circular cylinder is one unit, the free stream velocity  $u_\infty$  is one velocity unit, and the Reynolds number is defined by  $Re = u_\infty d/\nu$ . The whole computational domain is meshed by an equispaced Cartesian orthogonal grid  $1801 \times 1201$ . The choice of this mesh spacing is justified by a grid sensitivity study presented further in this section.

The ice piece, solid  $S^2$ , is defined by the area between the curve of (23) and the line of equation  $y = 0.3$  followed by a rotation of 45 degrees around cylinder center:

$$y = 0.9 - \frac{4}{0.3}x^2 \quad \text{for } x \in [-0.15; 0.15]. \quad (23)$$

For the subsequent simulations, the flow field is computed by solving the Poisson problem  $\nabla^2 \psi = -\omega$  with a homogeneous Neumann condition,  $\partial\psi/\partial n = 0$ , at downstream and upstream boundaries, while a Dirichlet condition of the stream function,  $\psi$ , is imposed on top and bottom boundaries. In particular the potential flow around

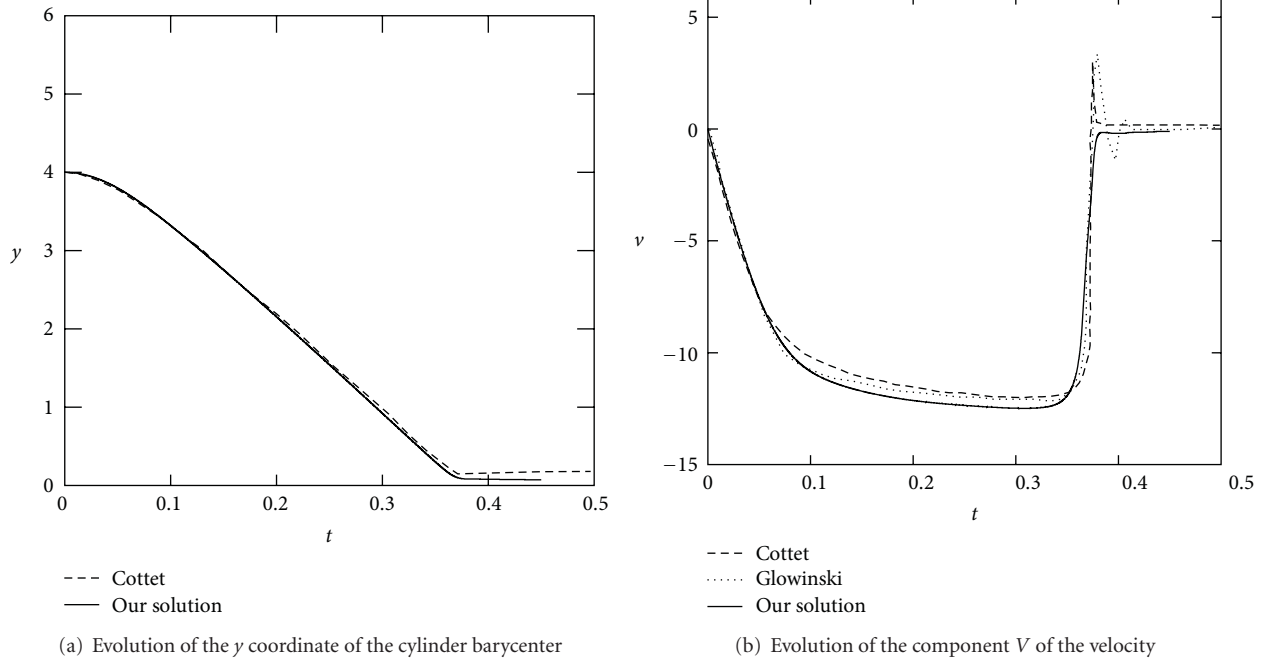


FIGURE 4: Sedimentation of a 2D cylinder on a flat plate.

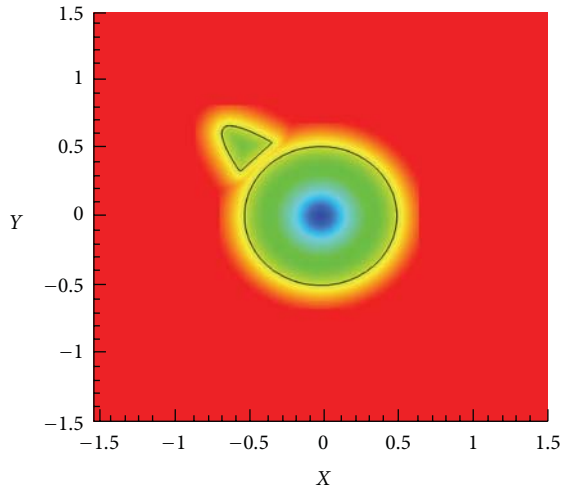


FIGURE 5: Cylinder distance level set function (negative inside the bodies positive outside) used in the penalization: iso-line 0 in black (color map from  $-0.5$  in blue to  $0.25$  in red).

the cylinder is considered, and the value of the associated stream function is enforced, that is,

$$\psi = u_{\infty} y \left( 1 - \frac{(d/2)^2}{x^2 + y^2} \right). \quad (24)$$

This is equivalent to imposing a symmetry condition on top and bottom.

The undisturbed stream  $u_{\infty}$  passing through the cylinder is used as initialization. The Reynolds number of the flow is  $Re = 550$ . Following [32], the time step for calculations is evaluated with the aim of solving with accuracy the diffusive

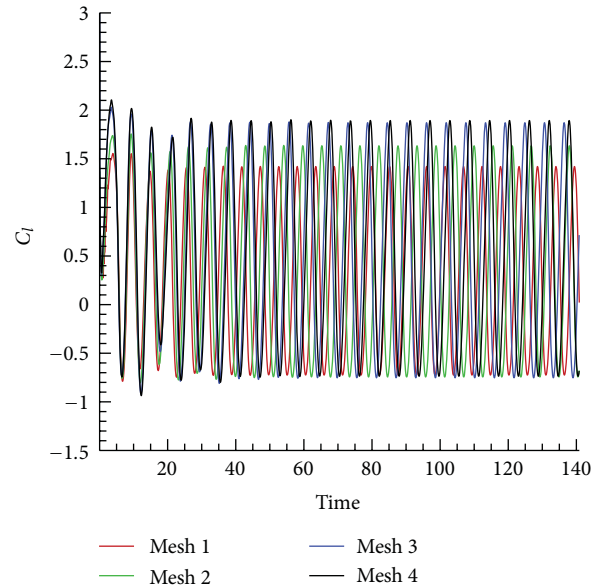


FIGURE 6: Grid sensitivity on lift coefficient around the iced cylinder.

phenomena. Since for detecting the principal diffusive scales with efficiency and accuracy the Von Neumann number (VNN)  $\nu \Delta t / \Delta x^2$  has to be in the order of unit, the nondimensional time step  $\Delta t$  is given by

$$\Delta t = VNN \Delta x^2 Re. \quad (25)$$

In present computations  $VNN = 0.25$ , then  $\Delta t = 0.01375$ .

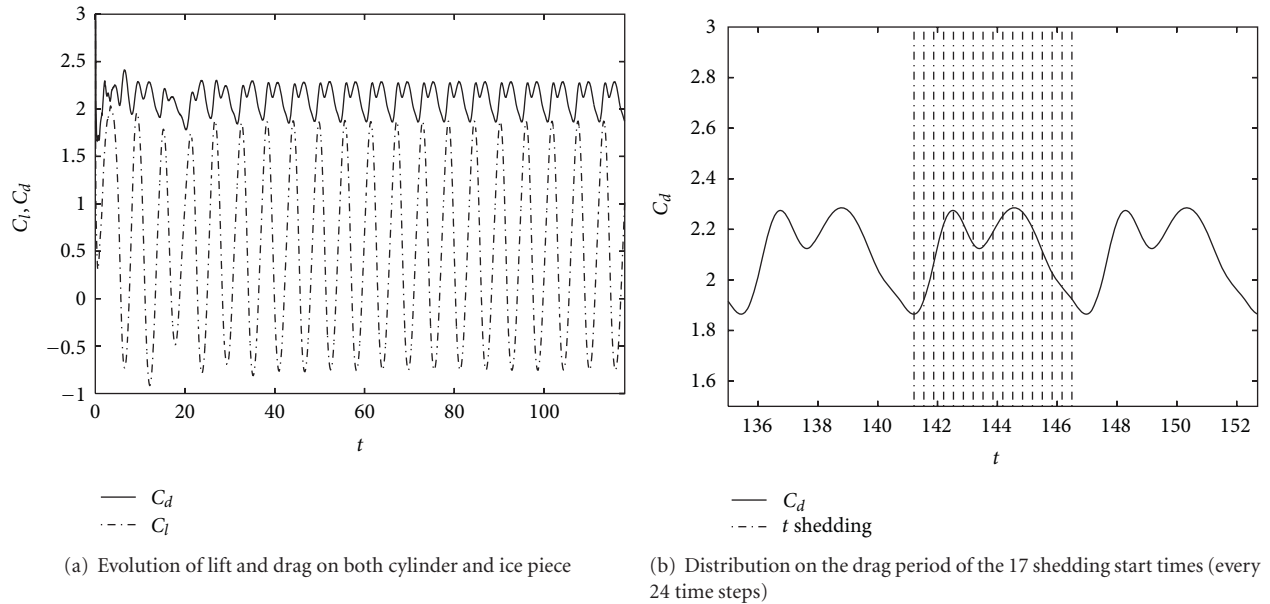


FIGURE 7: Lift and drag coefficients around the iced cylinder.

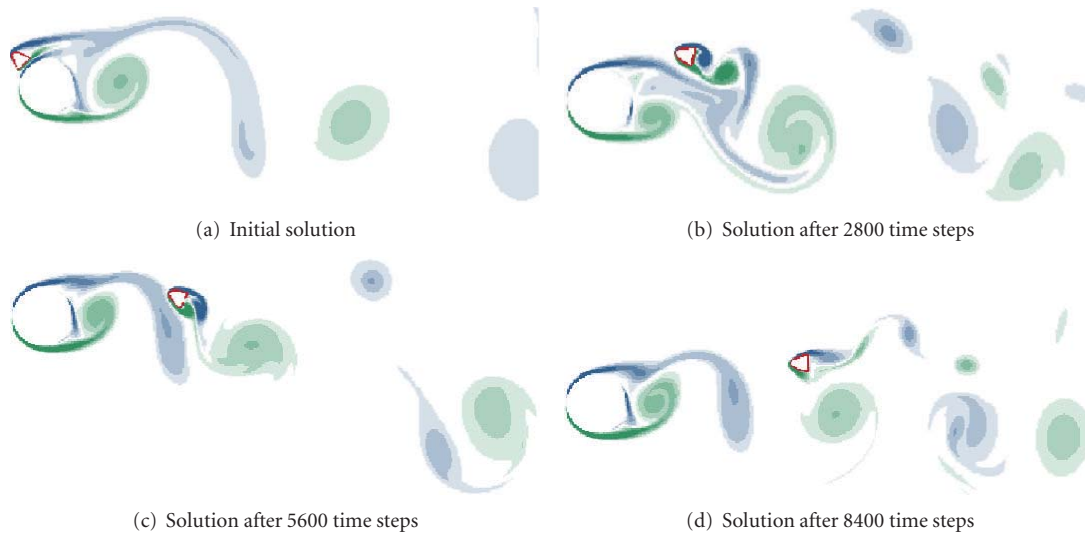
FIGURE 8: Cylinder at  $Re = 550$ . Vorticity contours corresponding to shed 13: green positive vorticity and blue negative vorticity.

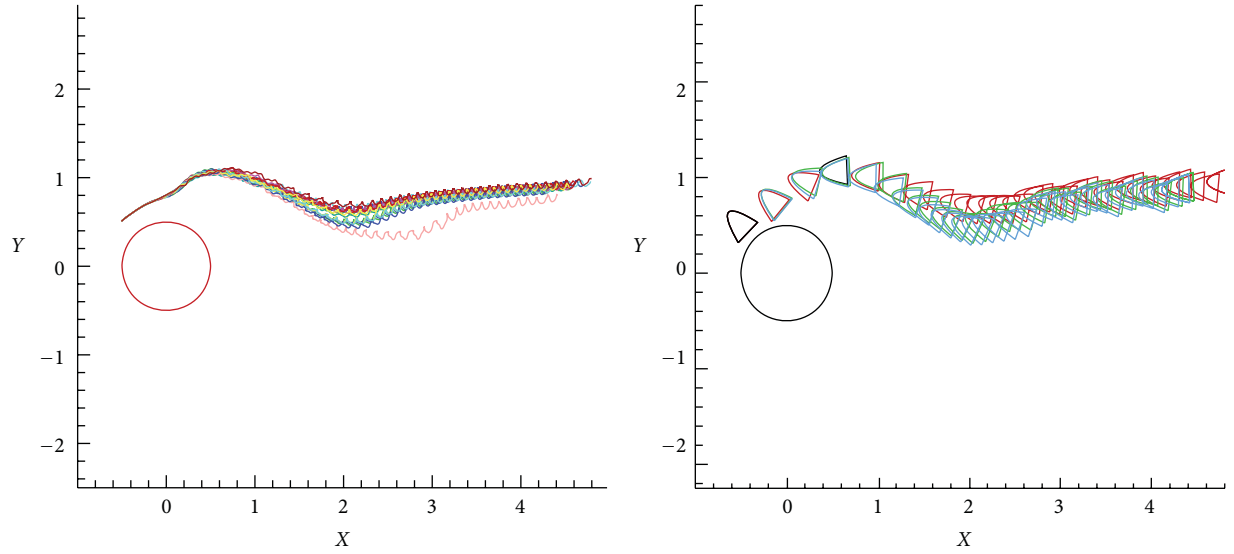
Figure 5 shows the distance level set function used for the penalization. The black line corresponds to the isoline 0, that is, it represents the fluid solid interfaces.

A grid sensitivity analysis using Mesh 1:  $901 \times 601$ , Mesh 2:  $1126 \times 751$ , Mesh 3:  $1801 \times 1201$ , and Mesh 4:  $2251 \times 1501$  has been performed to select the appropriate grid. Figure 6 shows the evolution in time of the lift coefficient,  $C_l = l/0.5\rho u_\infty d$ , around both the cylinder and the ice chunk for the four different meshes. Numerical solutions obtained with Mesh 3 and Mesh 4 are in very good agreement for the lift coefficient amplitude. A slight frequency difference is still visible, causing a shift in the maxima and the minima position between Mesh 3 and Mesh 4, visible for time greater

than 80. For the following study, Mesh 3 has been selected to perform ice shedding trajectory calculations.

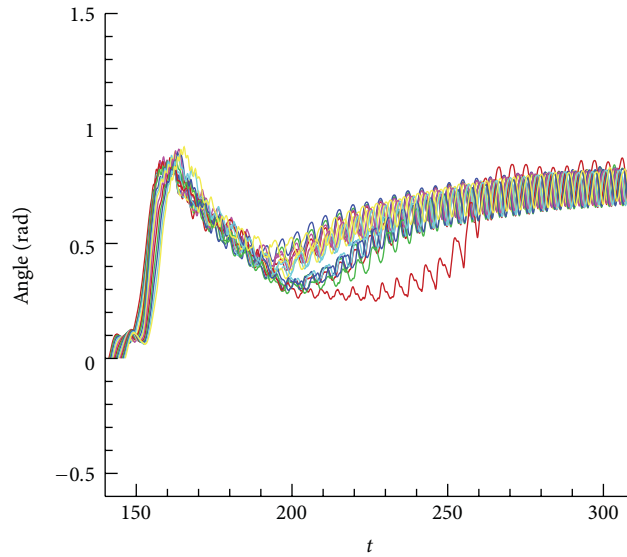
Using Mesh 3, the evolution of the lift coefficient,  $C_l$ , and drag coefficient,  $C_d = d/0.5\rho u_\infty d$ , around cylinder and ice piece is presented in Figure 7(a). The flow is well established around the two static solids at about nondimensional time  $t = 40$ . On the drag coefficient curve, there is two maximum values, indicating two distinct vortex shedding time. This is different from the usual drag coefficient curve obtained for a single cylinder in a flow.

Once the flow is established, the ice piece is released in the flow. Because of the vortex shedding induced by both the cylinder and the ice piece, several times of shedding start-up



(a) Ice piece barycenter trajectory for the 17 sheddings

(b) Typical ice shedding trajectories: in red shed 3; in green shed 10; in blue shed 13



(c) Evolution of the angle of rotation for the 17 sheddings

FIGURE 9: Ice piece trajectories.

are investigated. More precisely seventeen starting times are equally distributed (every 24 time steps) along an established  $C_d$  period (Figure 7(b)) to observe the effects of the vortex shedding on the ice trajectory. For the present paper, the 17 numerical simulations of ice shedding will be termed as shed 1, shed 2, ..., and shed 17, each one corresponding to the starting time 1, 2, ..., and 17 of Figure 7(b).

Once ice shedding starts, the ice piece  $S^2$  freely evolves in the incompressible flow contained in  $\Omega_f$ , whereas the cylinder  $S^1$  remains static, modeling a simplified situation of ice shedding. For the static body  $S^1$ ,  $\mathbf{u}_{s^1} = \mathbf{0}$  is fixed at any time. The ice piece velocity,  $\mathbf{u}_{s^2}$ , and angle of rotation are computed according to (4) and injected in the penalization term. Recall that the ice piece is assumed to be a rigid

solid body without any deformation. Figure 8 shows the vorticity contours of the flow corresponding to shed 13. In this figure, green contours correspond to positive vorticity whereas blue contours correspond to negative vorticity. Notice that once ice shedding starts, the time step does not remain constant and depends on the ice moving velocity  $\mathbf{u}_{s^2}$ .

As it is usually the case for flow around bluff bodies, the ice body creates its own vortex shedding. The ice initially moves downstream, for the first 2800 time steps. Then it gets trapped by the flow in one of the vortices behind the cylinder and start moving downward until around 5600 time steps, then upward around 8400 time steps, almost stopping its downstream motion.

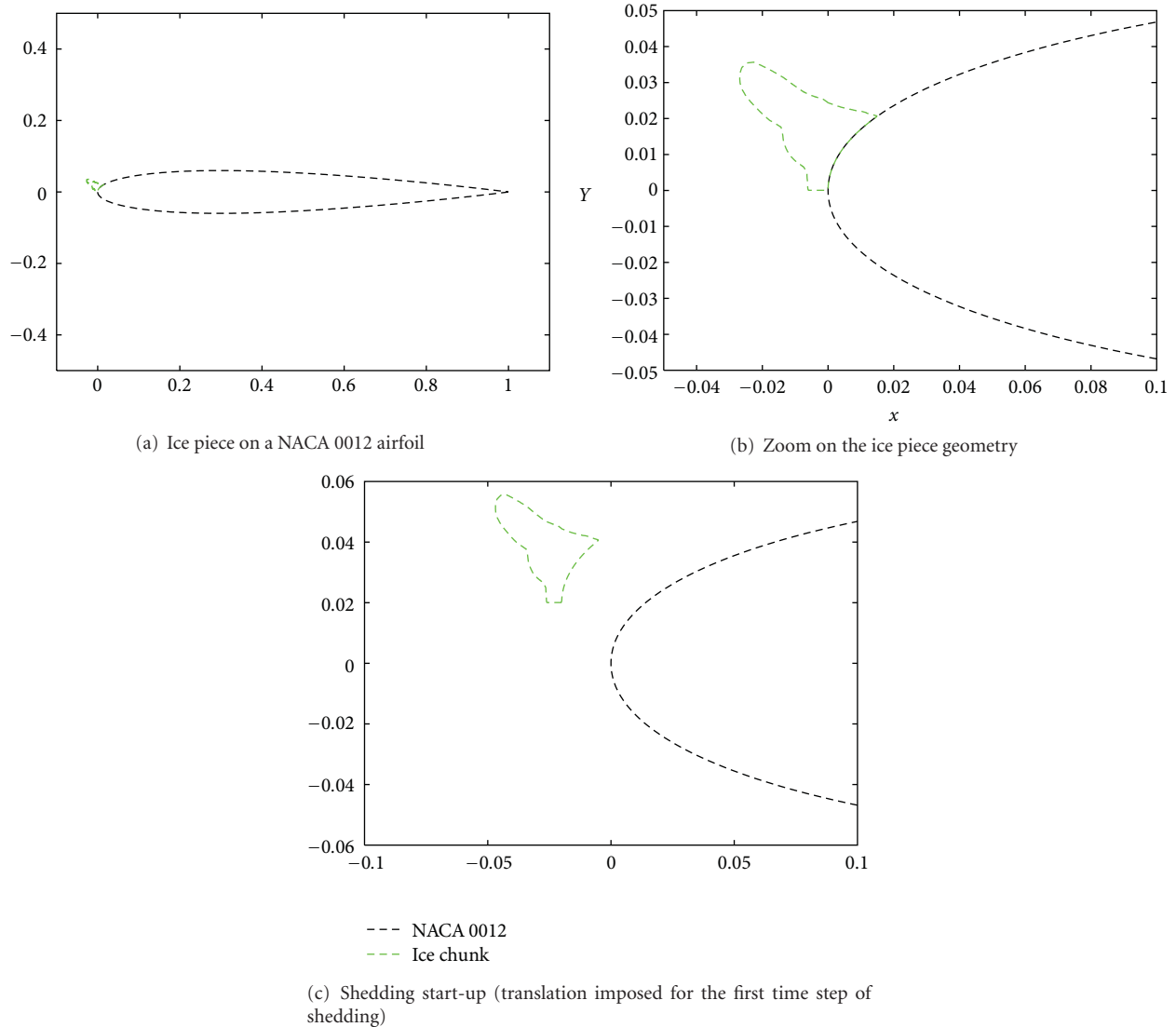


FIGURE 10: Iced NACA 0012.

In Figure 9, we investigate the effects of the vortex shedding on the ice trajectories. For the 17 simulations, the ice piece barycenter trajectories are drawn in Figure 9(a). As expected, the ice trajectory is quite different from one solution to another, especially behind the cylinder, around  $x = 2.5$ . This random aspect of the trajectories calculations is also observed by Papadakis et al. [9], and they use a statistical approach to take into account the randomness of the shedding process around an aircraft. Farther downstream, after  $x = 4$ , trajectories tend to get closer. In all the cases, no ice trajectory goes below  $y = 0$ . Details on the top trajectory (shed 3) in red, the bottom trajectory (shed 13) in blue and a middle trajectory (shed 10) in green are drawn in Figure 9(b).

Vortex shedding has also a significant influence on the ice angle of rotation. Due to the low ice density used in this verification, inertia forces are negligible, and ice piece align quickly with the flow. The ice piece rotates and tends to

keep its round side upstream, in a low drag orientation. The present method enables us to plot the rotation together with the displacement on Figure 9(c).

**3.3. Iced NACA 0012.** The computational domain shown in Figure 1 can be adopted for the ice shedding test over an infinite wing, by replacing the circular cylinder with an iced NACA 0012 airfoil. For this numerical test, the ice piece geometry (see Figures 10(a) and 10(b)) is numerized from Papadakis et al. [9] and scaled to be placed on a NACA 0012 airfoil of chord unity. The ice piece geometry with its horn shape is representative of a large glaze ice accretion. This kind of ice shape is more susceptible to break up due to aerodynamic forces. Such a large ice shape tends to have high pressure forces on the upstream side and low pressure forces on the downstream side, creating a strong bending moment at airfoil surface. In Figure 10(c), the initial displacement of the ice shape, just after breakup, is shown. This kind of initial

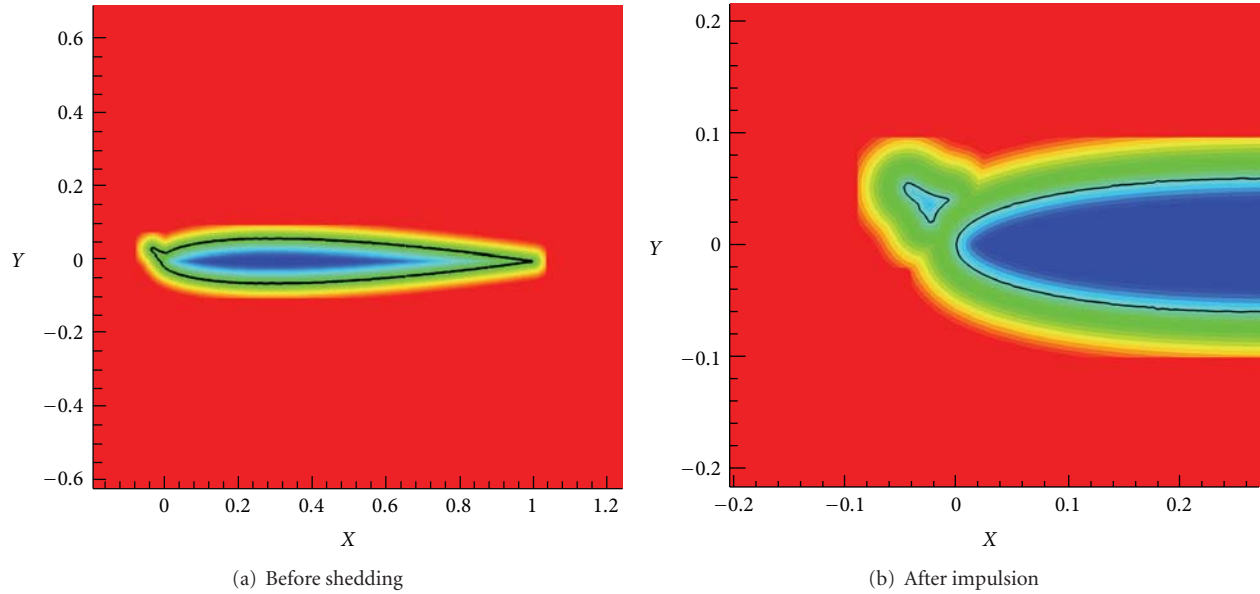


FIGURE 11: Iced NACA 0012 distance level set function used in the penalization iso-line 0 in black (color map from blue: negative distance to red: positive distance).

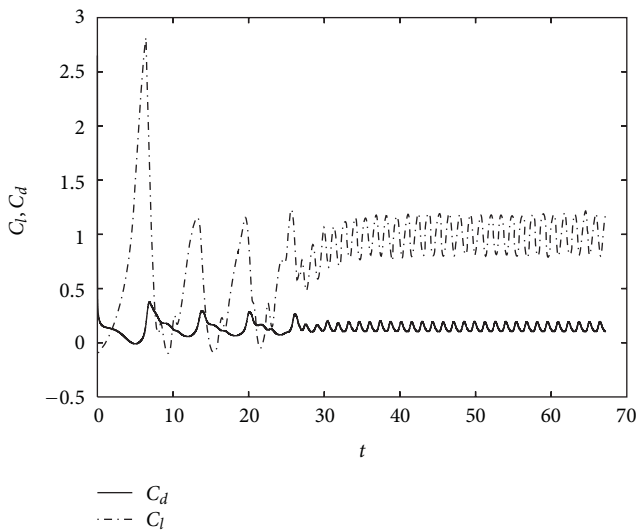


FIGURE 12: Iced NACA 0012 solution at  $Re = 1000$ , evolution of the lift and drag coefficient.



FIGURE 13: Established iced NACA 0012 solution at  $Re = 1000$ . Vorticity contours: green positive vorticity and blue negative vorticity.

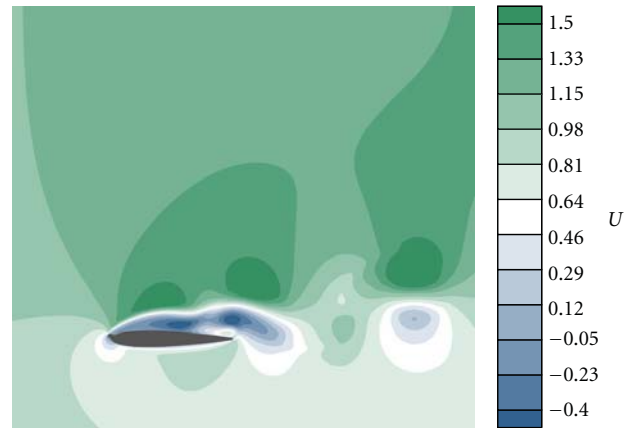


FIGURE 14: Established iced NACA 0012 solution at  $Re = 1000$ — $U$  velocity component.

displacement may be generated by mechanical devices, such as inflatable boot.

In such case the boundary conditions for the Poisson problem are modified as follows.

- (i) Dirichlet condition  $\psi = \mathbf{u}_\infty y$  in order to enforce the mass flow at upstream (left boundary).
- (ii) Neumann condition  $\partial\psi/\partial x = 0$  at downstream (right boundary).
- (iii) On the bottom and top boundaries Dirichlet boundaries conditions are prescribed ( $\psi = 0$  and  $\psi = q_\infty (y_{\text{top}} - y_{\text{bottom}})$ , resp.) in order to enforce a far-field undisturbed flow condition.

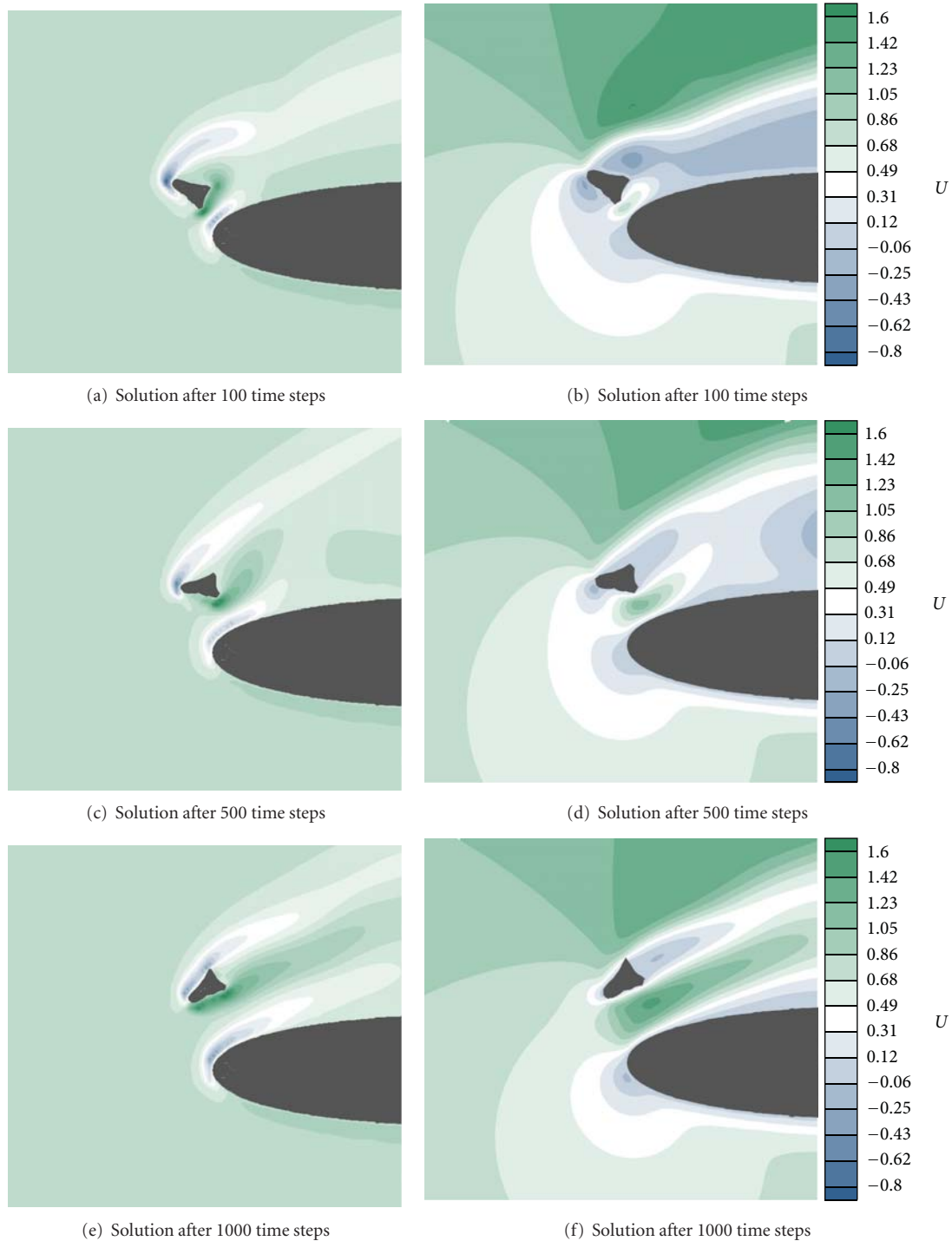


FIGURE 15: Ice shedding around NACA 0012 at  $Re = 1000$ . On the left: vorticity contours (green positive, blue negative). On the right:  $U$  velocity component.

First the flow is computed around the static iced NACA 0012 airfoil. The domain is a rectangular box of size  $[-3, 8] \times [-3, 3]$  and the size of the cartesian grid used is  $2751 \times 1501$ . The Reynolds number of the flow, based on airfoil chord  $c$ ,  $Re = u_\infty c / \nu$ , is 1000, and the dimensionless time step is  $\Delta t = 0.001$ . For this case, the distance level set function used for

the penalization is plotted in Figure 11(a) for initial flow and in Figure 11(b) for the start of trajectory calculation.

The periodic flow is well established at about  $t = 50$ , see Figure 12. Because of the ice shape, the drag is higher than on a clean airfoil, and a positive lift coefficient is generated, even if the airfoil's angle of attack is 0.

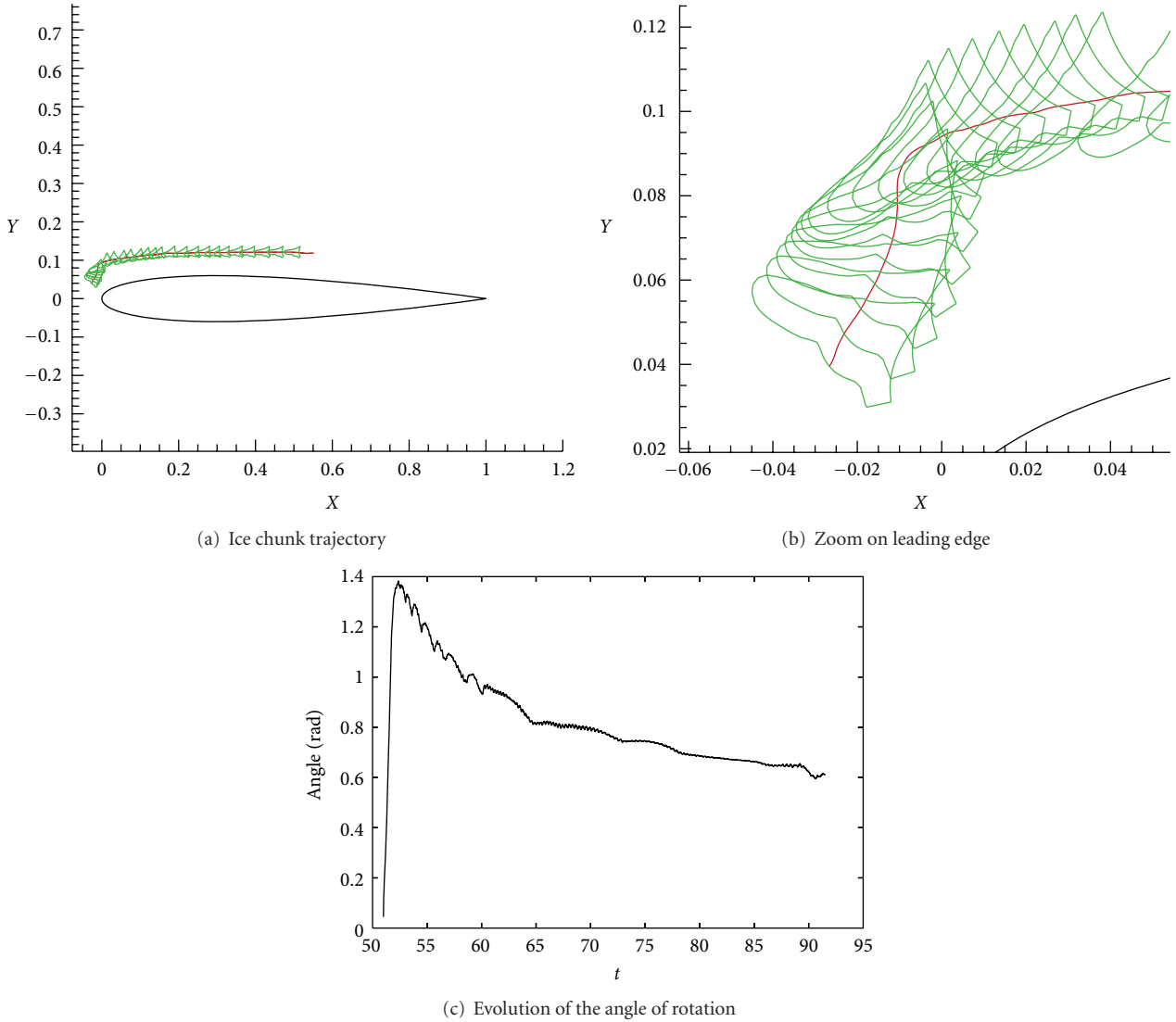


FIGURE 16: NACA 0012 airfoil: Ice piece trajectory details.

Figures 13 and 14 show, respectively, the vorticity and the  $u$  velocity for this established solution. In blue, the vorticity is negative, and in green, the vorticity is positive. The ice shape creates massive flow separation on the upper side of the airfoil, and large vortices of opposite vorticity sign are shed. As expected in the case of massive separation, there is a wake of vortices behind the airfoil. The velocity is accelerated outside of the separation area on the upper side of the airfoil. The separation area is indicated by the negative  $U$  velocity component area behind the ice shape. This negative area extend all over the airfoil upper side.

Then ice shedding is initiated. To model ice shedding and be sure that the ice piece will not collide with airfoil, we simply give an impulsion to the ice chunk, as if a deicing boot device has been used. The presented method can handle collisions between bodies, but it would involve defining an additional physical model. For sake of trajectory verification, the problem is kept as simple as possible. The impulsion is given

by the vector  $(5\Delta x, 5\Delta y)$ , see Figure 10(c). The distance level set function, after shedding, is presented in Figure 11(b), and the level set changes with the ice piece motion.

Details of the first moments after ice shedding are shown in Figure 15. On the left, vorticity contours are plotted and, on the right,  $U$  velocity components. The ice shape starts to move in the normal direction from the airfoil, then, it starts to rotate to align itself with the flow field around airfoil. Obviously, the vorticity field and the velocity field change drastically between initial time (Figures 15(a) and 15(b)) and final time (Figures 15(e) and 15(f)). The vorticity pattern, for example, in Figure 15(c), shows that the ice piece is slower than airflow because a secondary wake is created around the shape.

Finally, a sample trajectory is studied in more detail in Figure 16. Because the flow field around the clean airfoil is simpler than around a cylinder, the ice shape simply flows downstream in Figure 16(a). The details of the initial

movement of the shape gravity center are plotted as a red line. The shape slowly rotates and moves downstream, as Figure 16(c) shows. After a quick rotation between time 50 and 60, because of the low inertia of the ice piece, the angle of rotation becomes almost constant. The ice shape is outside of the boundary layer, even if this one is thick due to the low Reynolds number of the flow.

#### 4. Conclusions

The proposed approach based on cartesian grids, penalization, and level sets is promising. The originality of the numerical tools used enables to take easily into account the topology changes. The fluid-solid flow model has been described in detail together with the numerical method used to solve the problem. The trajectory calculation capabilities have been verified against other numerical results for the sedimentation of a cylinder on a flat plate. The approach enable us to calculate ice shedding trajectory around aerodynamic shape and bluff body. Verification of the results for bluff body calculation shows that trajectories depends strongly on flow condition at the shedding time for unsteady problem. Ice piece trajectories distribute themselves almost randomly around an area. For the rotation angle however, the ice chunks tend to orient themselves with the flow such as to reduce the drag. Further verifications of the approach for trajectory calculations around an iced airfoil show first that large separation occurs on the upper side of the airfoil, making the flow unsteady at the low Reynolds number studied. Secondly, ice trajectories are much simpler due to the fact that once ice separates from the airfoil, large vortex disappears from the flow.

The next step is to add high Reynolds number capabilities to the flow solver, more representative of wind turbine or aircraft physics. Model developments are also needed to study ice break-up and predict the correct initial conditions for trajectory calculations.

#### References

- [1] H. Beaugendre, F. Morency, and W. G. Habashi, "FENSAP-ICE: roughness effects on ice shape prediction," *Journal of Aircraft*, vol. 40, pp. 239–247, 2003.
- [2] K. R. Petty and C. D. J. Floyd, "A statistical review of aviation airframe icing accidents in the US," in *Proceedings of the 11th Conference on Aviation, Range, and Aerospace Hyannis*, 2004.
- [3] T. Laakso and E. Peltola, "Needs and requirements for ice detection in wind energy," in *Proceedings of the European Wind Energy Conference*, 2003.
- [4] A. Lacroix and J. F. Manwell, "Wind energy: cold weather issues," University of Massachusetts at Amherst, Renewable Energy Research Laboratory, 2000.
- [5] M. Selig, W. Jasinski, S. C. Noe, and M. Bragg, "Wind turbine performance under icing conditions," in *Proceedings of the 35th AIAA Aerospace Sciences Meeting & Exhibit*, January 1997, AIAA Paper 97-0977.
- [6] E. Bossanyi, C. Morgan, and H. Seifert, "Assessment of safety risks arising from wind turbine icing," in *Boreas IV Hetta*, 1998.
- [7] H. Seifert, "Technical requirements for rotor blades operating in cold climate," in *Proceedings of the 6th BOREAS Conference*, April 2003.
- [8] S. K. Thomas, R. P. Cassoni, and C. D. MacArthur, "Aircraft anti-icing and de-icing techniques and modeling," *Journal of Aircraft*, vol. 33, no. 5, pp. 841–854, 1996.
- [9] M. Papadakis, H. W. Yeong, and I. G. Soares, "Simulation of ice shedding from a business jet aircraft," in *Proceedings of the 45th AIAA Aerospace Sciences Meeting & Exhibit*, Reno, Nev, USA, 2007, AIAA Paper 2007-506.
- [10] J. Jacob, *Experimental and computational aerodynamic analysis of ice fragments shed from aircraft surface*, M.S. thesis, Wichita State University, December 2005.
- [11] I. G. Soares, *Ice particle trajectory simulation*, M.S. thesis, Wichita State University, December 2005.
- [12] K. J. De Witt, A. D. Yaslik, and T. G. Keith, "Three-dimensional simulation of electrothermal deicing systems," *Journal of Aircraft*, vol. 29, no. 6, pp. 1035–1042, 1992.
- [13] R. Henry, "Development of an electrothermal de-icing/anti-icing model," in *Proceedings of the 30th AIAA Aerospace Sciences Meeting & Exhibit*, Reno, Nev, USA, 1992, AIAA Paper 92-0526.
- [14] R. J. Scavuzzo, M. L. Chu, and V. Ananthaswamy, "Influence of aerodynamic forces in ice shedding," *Journal of Aircraft*, vol. 31, no. 3, pp. 526–530, 1994.
- [15] G. N. Labeas, I. D. Diamantakos, and M. M. Sunaric, "Simulation of the electroimpulse de-icing process of aircraft wings," *Journal of Aircraft*, vol. 43, no. 6, pp. 1876–1885, 2006.
- [16] D. L. Kohlman and R. C. Winn, "Analytical prediction of trajectories of ice pieces after release in an airstream," in *Proceedings of the 39th AIAA Aerospace Sciences Meeting & Exhibit*, January 2001.
- [17] L. C. C. Santos, R. Papa, and M. A. S. Ferrari, "A simulation model for ice impact risk evaluation," in *Proceedings of the 41th AIAA Aerospace Sciences Meeting & Exhibit*, January 2003, AIAA Paper 2003-0030.
- [18] R. Chandrasekharan and M. Hinson, "Trajectory simulation of ice shed from a business jet," in *Proceedings of the SAE World Aviation Congress and Exposition*, September 2003.
- [19] F. Gallizio, *Analytical and numerical vortex methods to model separated flows*, Ph.D. thesis, Politecnico di Torino, INRIA Université de Bordeaux 1, 2009.
- [20] M. Coquerelle, J. Allard, G. H. Cottet, and M. P. Cani, "A vortex method for bi-phasic fluids interacting with rigid bodies," <http://arxiv.org/abs/math/0607597>.
- [21] M. Coquerelle and G. H. Cottet, "A vortex level set method for the two-way coupling of an incompressible fluid with colliding rigid bodies," *Journal of Computational Physics*, vol. 227, no. 21, pp. 9121–9137, 2008.
- [22] G. H. Cottet and P. D. Koumoutsakos, *Vortex Methods: Theory Andpractice*, Cambridge University Press, Cambridge, UK, 2000.
- [23] P. Angot, C. H. Bruneau, and P. Fabrie, "A penalization method to take into account obstacles in incompressible viscous flows," *Numerische Mathematik*, vol. 81, no. 4, pp. 497–520, 1999.
- [24] J. A. Sethian, *Level Set Methods and Fast Marching Methods: Evolving Interfaces in Computational Geometry*, Cambridge University Press, Cambridge, UK, 1996.
- [25] M. C. Chu and R. J. Scavuzzo, "Adhesive shear strength of impact ice," *AIAA Journal*, vol. 29, no. 11, pp. 1921–1926, 1991.

- [26] I. D. Diamantakos, G. N. Labeas, and M. M. Sunaric, "Simulation of the electroimpulse de-icing process of aircraft wings," *Journal of Aircraft*, vol. 43, no. 6, pp. 1876–1885, 2006.
- [27] G. H. Cottet, B. Michaux, S. Ossia, and G. VanderLinden, "A comparison of spectral and vortex methods in three-dimensional incompressible flows," *Journal of Computational Physics*, vol. 175, no. 2, pp. 702–712, 2002.
- [28] J. J. Monaghan, "Extrapolating B splines for interpolation," *Journal of Computational Physics*, vol. 60, no. 2, pp. 253–262, 1985.
- [29] J. Adams, P. Swarztrauber, and R. Sweet, "FISHPACK: efficient FORTRAN subprograms for the solution of separable elliptic partial differential equations," 1999, <http://www.cisl.ucar.edu/css/software/fishpack/>.
- [30] F. Noca, D. Shiels, and D. Jeon, "A comparison of methods for evaluating time-dependent fluid dynamic forces on bodies, using only velocity fields and their derivatives," *Journal of Fluids and Structures*, vol. 13, no. 5, pp. 551–578, 1999.
- [31] R. Glowinski, T. W. Pan, T. I. Hesla, D. D. Joseph, and J. Périaux, "A fictitious domain approach to the direct numerical simulation of incompressible viscous flow past moving rigid bodies: application to particulate flow," *Journal of Computational Physics*, vol. 169, no. 2, pp. 363–426, 2001.
- [32] P. Ploumhans and G. S. Winckelmans, "Vortex methods for high-resolution simulations of viscous flow past bluff bodies of general geometry," *Journal of Computational Physics*, vol. 165, no. 2, pp. 354–406, 2000.

## Research Article

# Aerodynamic Optimization of an Over-the-Wing-Nacelle-Mount Configuration

**Daisuke Sasaki and Kazuhiro Nakahashi**

*Department of Aerospace Engineering, Tohoku University, Aoba 6-6-01, Sendai 980-8579, Japan*

Correspondence should be addressed to Daisuke Sasaki, [sasaki@ad.mech.tohoku.ac.jp](mailto:sasaki@ad.mech.tohoku.ac.jp)

Received 14 November 2010; Revised 21 February 2011; Accepted 21 February 2011

Academic Editor: Guan Yeoh

Copyright © 2011 D. Sasaki and K. Nakahashi. This is an open access article distributed under the Creative Commons Attribution License, which permits unrestricted use, distribution, and reproduction in any medium, provided the original work is properly cited.

An over-the-wing-nacelle-mount airplane configuration is known to prevent the noise propagation from jet engines toward ground. However, the configuration is assumed to have low aerodynamic efficiency due to the aerodynamic interference effect between a wing and a nacelle. In this paper, aerodynamic design optimization is conducted to improve aerodynamic efficiency to be equivalent to conventional under-the-wing-nacelle-mount configuration. The nacelle and wing geometry are modified to achieve high lift-to-drag ratio, and the optimal geometry is compared with a conventional configuration. Pylon shape is also modified to reduce aerodynamic interference effect. The final wing-fuselage-nacelle model is compared with the DLR F6 model to discuss the potential of Over-the-Wing-Nacelle-Mount geometry for an environmental-friendly future aircraft.

## 1. Introduction

With the growth in aircraft traffic, there is a strong demand to reduce the airport noise. The major sources of the airport noise are jet and fan noises caused by the engine. All over the world, regulations on airport noise have been tightened, thus it is a significant problem to reduce airframe and engine noises.

To reduce the airport noise, several aircraft configurations have been proposed lately. One is to install engine nacelles over the aft fuselage, and another is to install engine nacelles over the wing. In the latter case, successful experiences are only a few cases including the recent Honda Business jet [1]. The Over-the-Wing-Nacelle (OWN) configuration has a potential to reduce the noise drastically because the wing can block the propagation of fan and jet noises toward ground [2]. However, when the engine nacelles are installed over the wing, the aerodynamic performance tends to drop significantly due to the interference effect. If the interference effect between a nacelle and a wing is weakened and large increase in aerodynamic performance is achieved, OWN configuration will be a potential candidate to be a near-future quiet aircraft configuration.

Therefore, the purpose of this study is to investigate the aerodynamic feasibility of OWN configuration by making use of computational fluid dynamics (CFD) and optimization methods. The cruise Mach number is set to 0.70 to focus on mid-sized, short-range aircraft for the Japanese domestic or European use. In this study, aerodynamic interference effect between a nacelle and a wing is optimized through the modification of nacelle, wing, and pylon shapes. The Kriging model is adopted to build an approximation model of the objective functions to reduce the large computational burden demanded by a stochastic optimization method coupled with 3D high-fidelity CFD computation around a full aircraft geometry.

## 2. Optimization Method

In aerodynamic shape optimizations, nonlinearity of the objective functions must be taken into consideration. Therefore, stochastic optimization methods are required to obtain global optimal solutions. Genetic algorithms (GA) is one of the popular stochastic methods often used for aerodynamic optimizations [3, 4]. GA is a population-based optimization method simulating the evolutionary process of creatures,

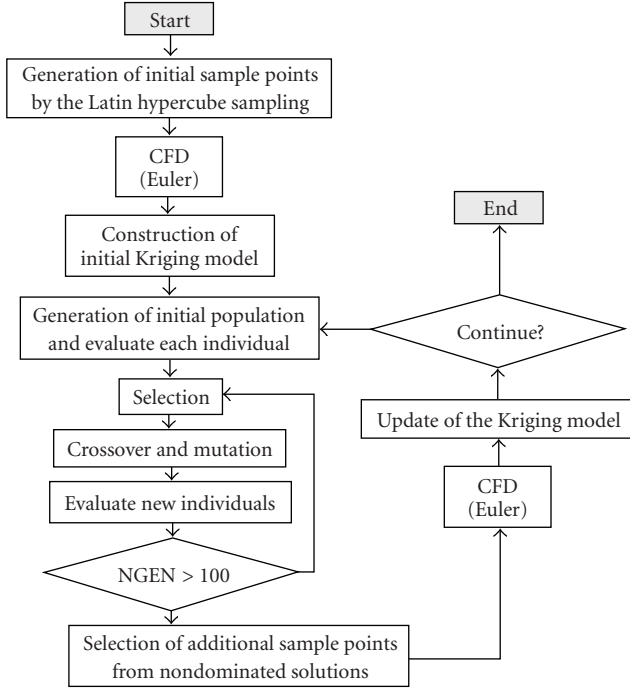


FIGURE 1: Flowchart of aerodynamic design system.

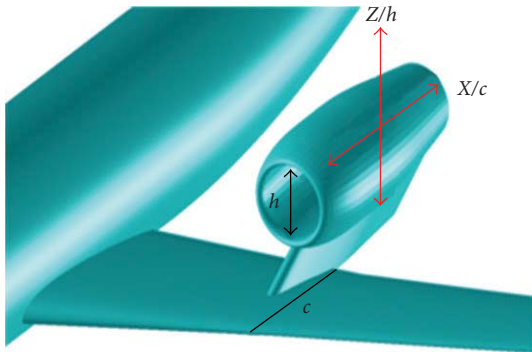
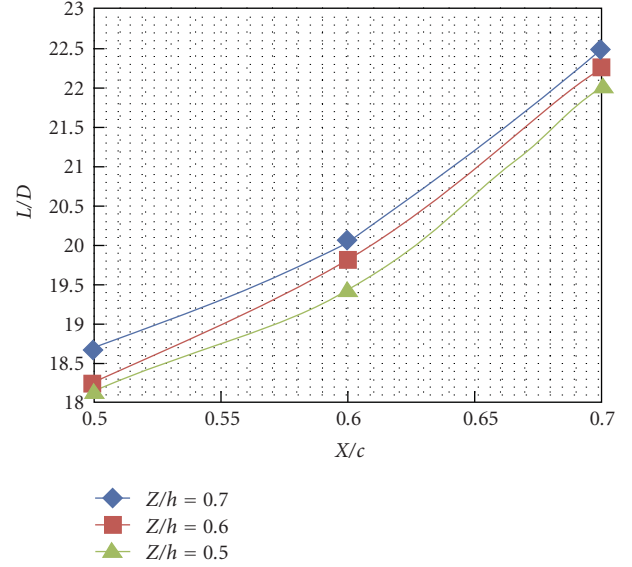


FIGURE 2: Definition of nacelle position.

in which the population evolves over generations to minimize/maximize the objective functions with the operations of selection, crossover, and mutation. In this research, an in-house solver of real-coded GA is adopted [3]. However, it is well-known that GA requires large computational cost due to population-based search, particularly coupled with expensive CFD solvers.

Therefore, surrogate model is used to approximate objective function values, which enables to prevent large number of expensive CFD evaluations and accelerate optimization procedure. Many surrogate models are proposed, but the Kriging model [5, 6] is adopted as it can predict nonlinear objective functions accurately. The Kriging model expresses the unknown function as sum of constant global model and local deviation from the global model. The surrogate model is built from the sampling points, where  $i$ th sampling point's

FIGURE 3:  $L/D$  with different nacelle position.

objective function value is  $y^i$  with the design variable vector of  $\mathbf{x}^i$ . Here, the number of sampling points is set to  $n$ , and the design vector size is set to  $k$ .

In the Kriging model, the predictor  $\hat{y}$  is represented to satisfy the following relation of correlation between real function value  $y$  of sampling points and the predictor  $\hat{y}$ :

$$\text{cor}(y(\mathbf{x}^i), \hat{y}(\mathbf{x})) = \psi^i = \exp\left(-\sum_{j=1}^k \theta_j |x_j^i - x_j|^2\right), \quad (1)$$

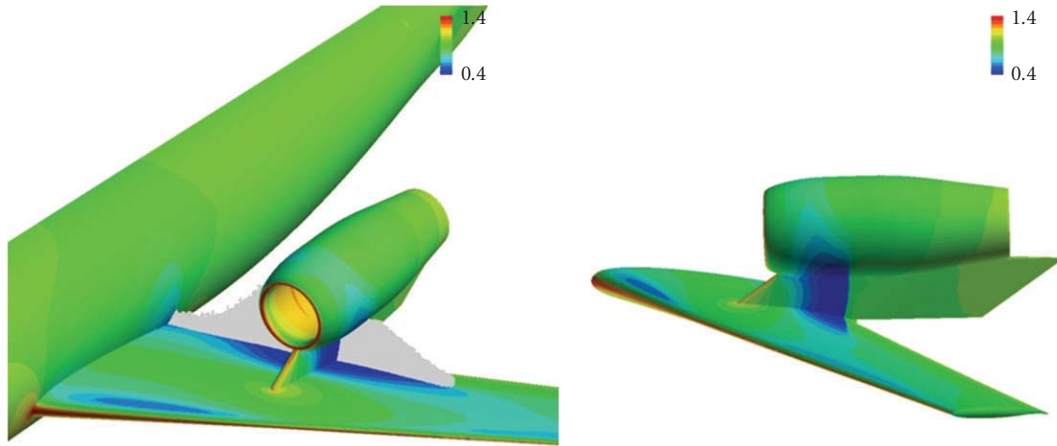
where  $\mathbf{x}$  is design variable vector of unknown objective function,  $x_j^i$  is  $j$ th design variable of  $i$ th sampling point, and  $x_j$  is  $j$ th design variable for the prediction. The correlation vector parameter  $\theta_j$  in (1) is the key of the Kriging model, and the best parameter needs to be obtained. The Kriging predictor is defined as

$$\hat{y}(\mathbf{x}) = \hat{\mu} + {}^t \boldsymbol{\psi} \boldsymbol{\Psi}^{-1} (\mathbf{y} - \mathbf{1} \hat{\mu}), \quad (2)$$

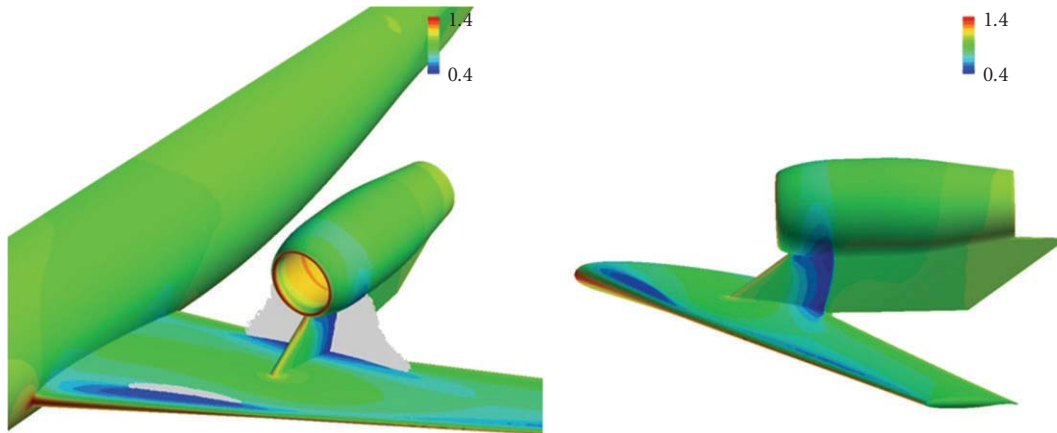
where  $\hat{\mu}$  is the estimated value of  $\mu$ ,  $\boldsymbol{\Psi}$  denotes  $n \times n$  correlation matrix whose  $(i, j)$  entry is correlation between the sampling points  $x^i$  and  $x^j$ , and  $\mathbf{1}$  is  $n$ -dimensional unit vector;

$$\hat{\mu} = \frac{{}^t \mathbf{1} \boldsymbol{\Psi}^{-1} \mathbf{y}}{{}^t \mathbf{1} \boldsymbol{\Psi}^{-1} \mathbf{1}}, \quad (3)$$

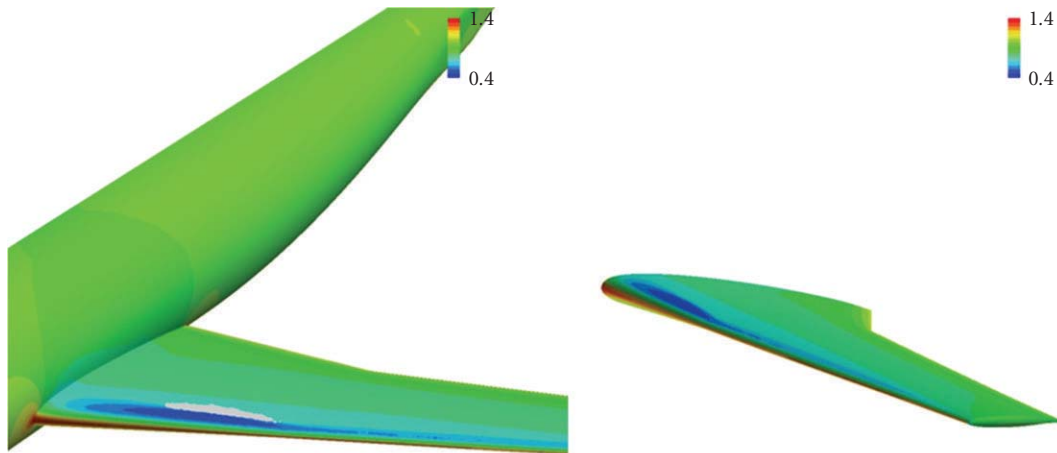
$$\sigma^2 = \frac{{}^t (\mathbf{y} - \mathbf{1} \hat{\mu}) \boldsymbol{\Psi}^{-1} (\mathbf{y} - \mathbf{1} \hat{\mu})}{n},$$



(a) Wing body with nacelle shape I ( $X/c = 0.50, Z/h = 0.5, L/D = 18.2$ )



(b) Wing body with nacelle shape II ( $X/c = 0.70, Z/h = 0.7, L/D = 22.5$ )



(c) Wing body without nacelle ( $L/D = 33.8$ )

FIGURE 4: Three wing body configurations with/without nacelle.

$\hat{\mu}$  and  $\sigma^2$  are used to specify the unknown parameter  $\theta$  by maximizing the following likelihood function:

$$\ln L \approx -\frac{n}{2} \ln \hat{\sigma}^2 - \frac{1}{2} \ln |\Psi|. \quad (4)$$

Here, GA is used to maximize the function to find the best parameter of  $\theta$  as it is  $k$ -dimensional unconstrained nonlinear problem. The Kriging model is then established, and the objective function is estimated using (2).

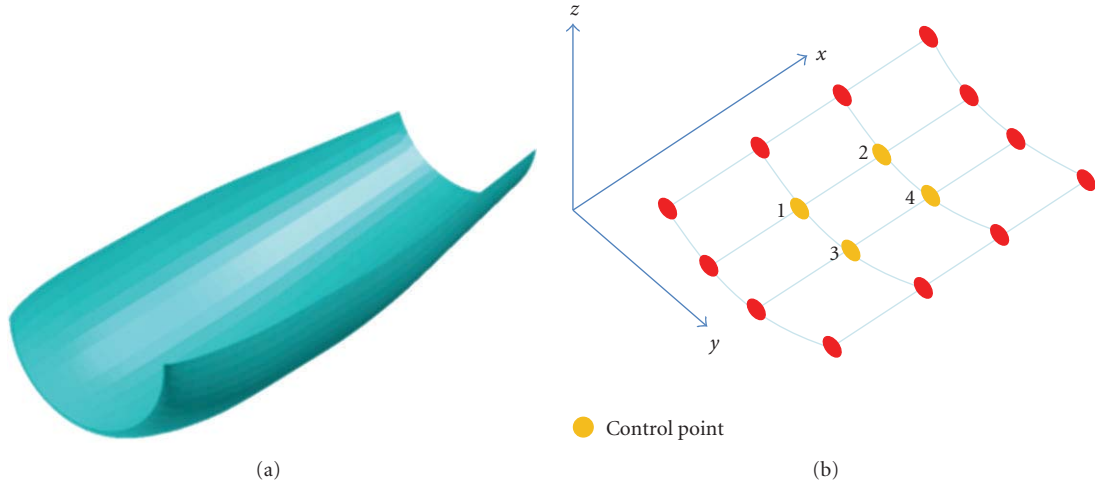


FIGURE 5: Nacelle lower shape definition.

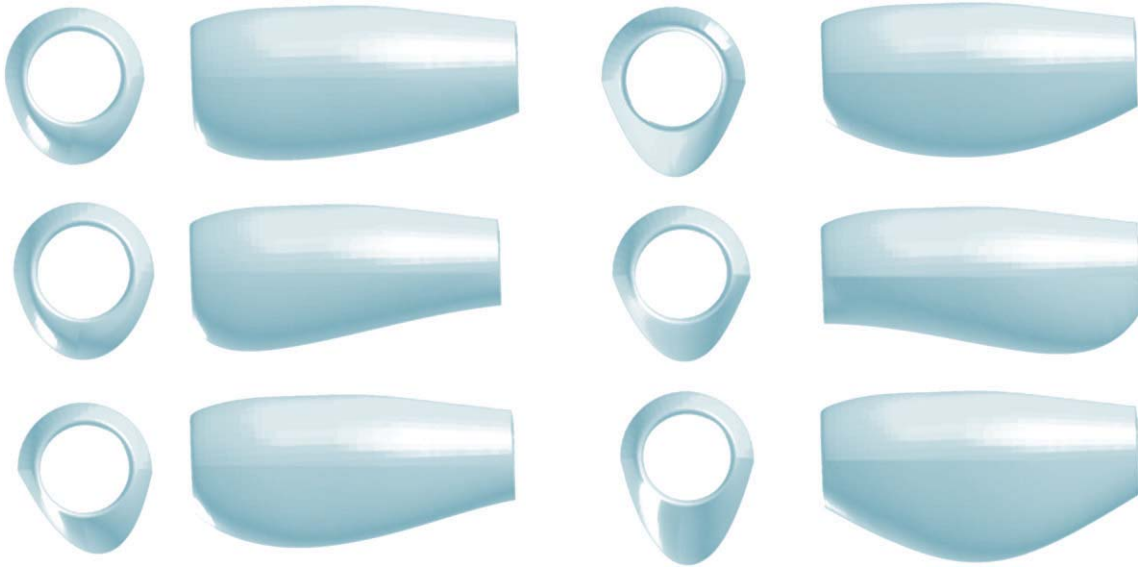


FIGURE 6: Examples of nacelle shape.

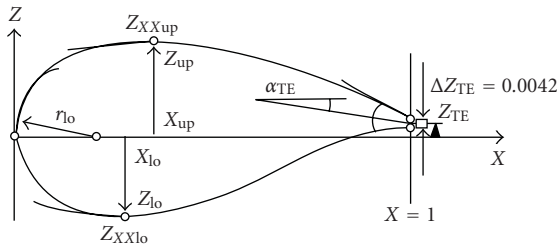


FIGURE 7: PARSEC airfoil definition.

One of advantages of the Kriging model is the capability to estimate the uncertainty of the estimated value. The mean square error  $s^2(\mathbf{x})$  at the point  $\mathbf{x}$  is expressed as

$$s^2(\mathbf{x}) = \hat{\sigma}^2 \left( 1 - \frac{\mathbf{t} \boldsymbol{\Psi} \boldsymbol{\Psi}^{-1} \boldsymbol{\psi}}{\mathbf{t} \mathbf{1} \boldsymbol{\Psi}^{-1} \mathbf{1}} + \frac{1 - \mathbf{t} \mathbf{1} \boldsymbol{\Psi}^{-1} \boldsymbol{\psi}}{\mathbf{t} \mathbf{1} \boldsymbol{\Psi}^{-1} \mathbf{1}} \right). \quad (5)$$

By integrating this with probability density function, the following so-called expected improvement (EI) value is obtained when minimization problem is considered:

$$EI(\mathbf{x}) = \int_{-\infty}^{y_{\text{opt}}} Y \frac{1}{s(\mathbf{x})\sqrt{2\pi}} \exp\left(-\frac{\{Y - \hat{y}(\mathbf{x})\}^2}{2s(\mathbf{x})^2}\right) dY, \quad (6)$$

where  $y_{\text{opt}}$  is the present optimal objective function value. The EI value represents the possible improvement at point  $\mathbf{x}$ . By using EI values, we can find design space where it is not explored yet but the objective function may be improved due to the high uncertainty.

In the present aerodynamic optimization, the above-mentioned Kriging approximate model is used to compute objective function values instead of CFD calculations. Here, the present Kriging model-based optimization procedure is described in Figure 1.

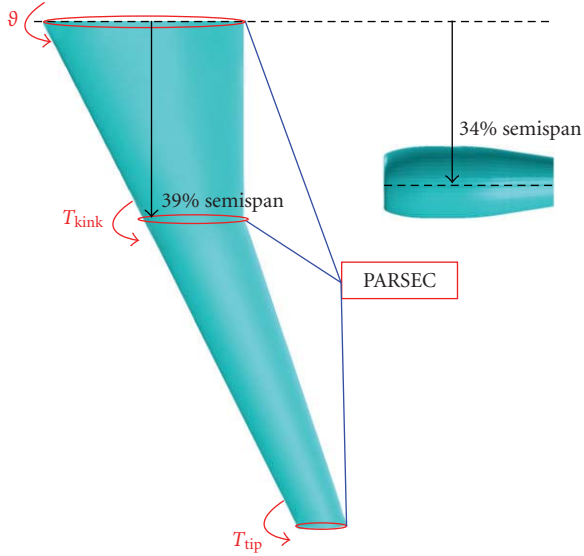


FIGURE 8: Planform shape, kink position, and nacelle location.

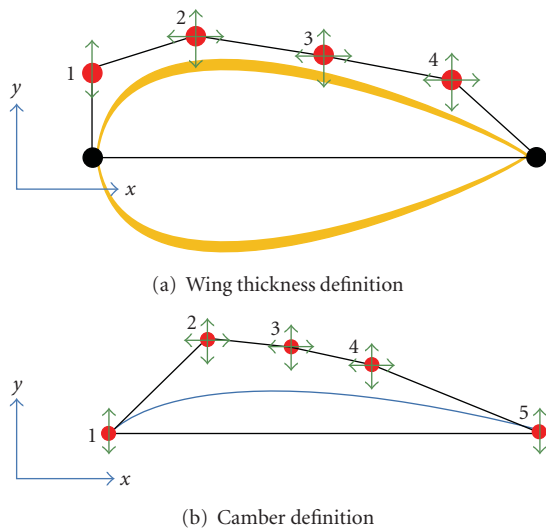


FIGURE 9: Pylon shape definition.

- (1) Select initial sampling points using the Latin hypercube sampling;
- (2) compute objective function value of sampling points;
- (3) build Kriging model for an objective function;
- (4a) minimize objective function on Kriging model using GA;
- (4b) maximize EI value using GA;
- (5) add optimal points with regard to objective (4a) or EI (4b) as additional sampling;
- (6) iterate item (2)–(5) until termination condition is met.

To build the reliable Kriging model, well-distributed sampling points are needed. The Latin hypercube sampling

(LHS) method [7], one of design of experiments, is used to distribute the points in equidistance space. It is computationally expensive to spread initial sampling points all over the domain densely to build the accurate Kriging model. Therefore, the adaptive Kriging model approach is employed, where the Kriging model is updated through the optimization process. After the optimization of GA coupled with the Kriging model, new sampling points are selected from optimal solutions to compute the updated Kriging model. This enables to improve the accuracy of the approximation to find global optimal solutions. In this study, EI values are also used for the optimization to obtain new sample points for the purpose of the robust search of global optimal solutions.

### 3. Preliminary Analysis

In this section, preliminary analyses are conducted to investigate the aerodynamic interference due to the existence of a nacelle above a wing at cruise conditions. The configuration is based on the DLR-F6 used in the Third AIAA Drag Prediction Workshop [8]. The DLR-F6 is a conventional under-the-wing-nacelle (UWN) configuration composed of fuselage, wing, nacelle, and pylon. The original design Mach number of the DLR-F6 configuration is 0.75. In this research, the flow condition is set to the Mach number of 0.70 to focus on mid-sized, short-range aircraft. The lift coefficient  $C_L$  was kept to 0.57 by adjusting the angle of attack. The numerical flow analysis is performed on wing-fuselage configuration with/without disjoint nacelles. Here, the flow-through nacelle is used because the validity of flow-through nacelle simulation was proved in [1].

The flow around nine different configurations was simulated by Euler solver for comparison. The nacelle height from the upper wing surface ( $Z/h$ ) and the distance from the leading edge ( $X/c$ ) in Figure 2 are changed, where  $h$  is nacelle inlet diameter and  $c$  is chord length at the pylon used for the normalization. The  $L/D$  values of nine different configurations are summarized in Figure 3. The graph represents that the aerodynamic performance is highly affected by the nacelle position. In addition, the existence of nacelle interrogates the performance badly since  $L/D$  of wing-fuselage without nacelle is 33.8. The pressure distributions of the two configurations with the nacelle and a configuration without the nacelle are shown in Figure 4. In the figures, the following shock function is used for the detection of the shock region:

$$f_{\text{shock}} = \frac{(\mathbf{u} \cdot \nabla P)}{(a|\nabla P|)}, \quad (7)$$

where  $\mathbf{u}$  is velocity vector,  $P$  is static pressure, and  $a$  is speed of sound. The gray region in the figure is the shock region. As shown in Figures 4(a) and 4(b) for the two OWN cases, generated shock waves between a wing and a nacelle are clearly observed. On the other hand, the shock region of the configuration without the nacelle is very small. These shock waves increase the drag and reduce the  $L/D$ . It concludes that OWN configuration tends to produce shock

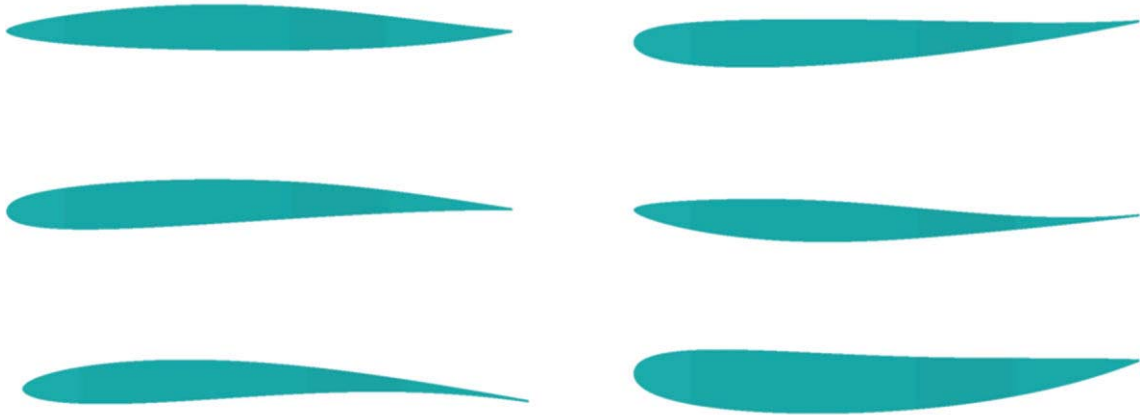


FIGURE 10: Examples of pylon shapes.

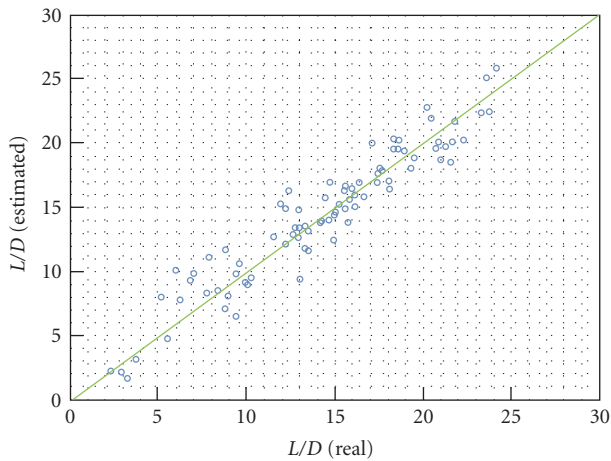


FIGURE 11: Cross-validation result of Kriging model built by first sampling points.

wave; however, the strength of shock waves strongly related to the position of engine nacelle installed. Therefore, by conducting the optimization of the nacelle position and the nacelle shape, aerodynamically feasible OWN configuration can be obtained.

#### 4. Problem Definition

In this paper, the objective is to improve aerodynamic performance of OWN configuration by modifying wing, nacelle, and pylon shapes. The first optimization is conducted to modify wing airfoil and nacelle shapes to reduce the aerodynamic interference effect between a wing and a nacelle. The optimal design is then further improved to optimize the pylon shape. Here, the optimization problem for the two cases is defined.

**4.1. Objective and Constraint.** The aim is to investigate the feasibility of aerodynamically efficient OWN configuration. When only the aerodynamic efficiency is considered, the

TABLE 1: Nacelle position range.

	Min	Max
$X/c$	0.47	0.85
$Z/h$	0.42	0.76

nacelle position tends to be away from the wing (higher and rearward). This causes the problem in maintainability and structure. Therefore, the consideration of structural and maintenance necessities is included in the optimization, geometric parameters of nacelle location as shown in Figure 2 are chosen to be optimized (lower and forward) as an incentive to more realistic design. The objectives and a constraint are summarized below.

Objectives:

- (1) maximize cruise  $L/D$ ,
- (2) minimize nacelle height ( $Z/h$ ),
- (3) minimize nacelle rearward location ( $X/c$ ).

Constraints:

- (1) constant  $C_L = 0.57$ .

The design is conducted under the cruise condition of Mach 0.70 with  $C_L$  of 0.57. This optimization problem is solved by GA coupled with Kriging approximation as described in Section 2.

**4.2. Nacelle Definition.** The nacelle position is defined by two design variables ( $X/c$ ,  $Z/h$ ) representing the front-rear and vertical movement as shown in Figure 3. The ranges of the variables are defined in Table 1.

The lower surface of nacelle is defined by Bezier surface of four by four control points shown in Figure 5. Bezier surface is controlled by the  $x$ ,  $y$ ,  $z$  coordinates of intermediate four control points, which correspond to 12 design variables ( $4 \times 3 = 12$  variables). The upper surface of nacelle is frozen to original DLR-F6 type [8]. Therefore, the designed lower

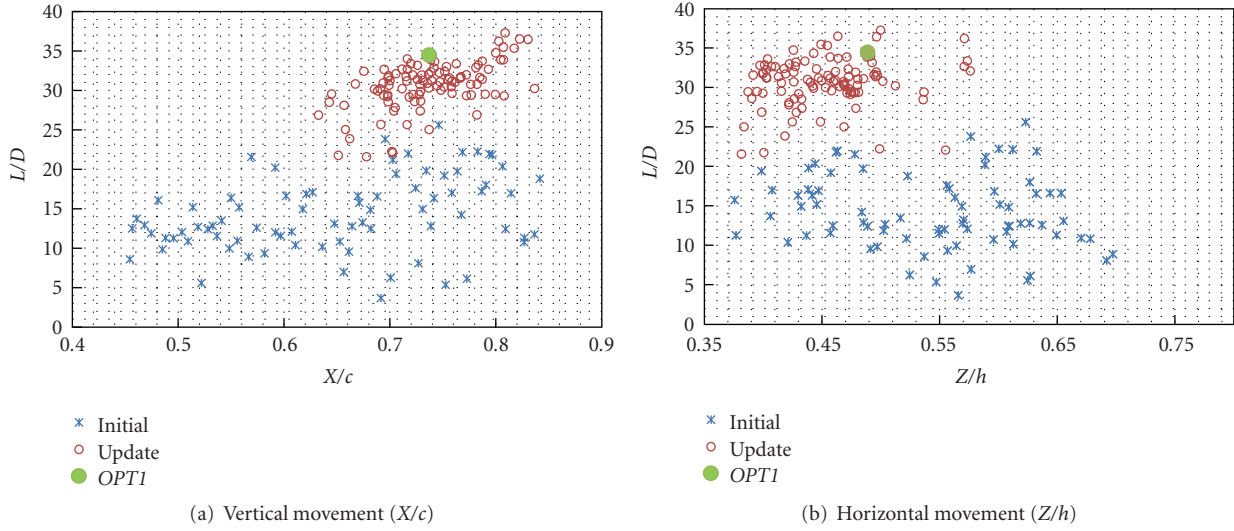


FIGURE 12:  $L/D$  distribution against nacelle position (blue: initial samples, red: update points).

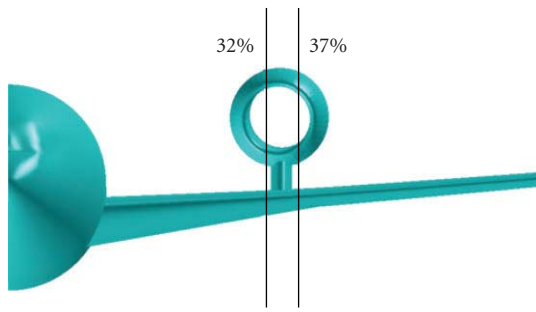


FIGURE 13: Cut planes at inner and outer nacelle.

nacelle surface is combined with the upper surface of DLR-F6's nacelle to define the whole nacelle. The examples of possible nacelle shape are represented in Figure 6.

**4.3. Wing Definition.** The 3-D wing shape is defined by the following 30 design variables to control the airfoil shapes while the planform of the wing is frozen to original DLR-F6 type. The root, tip, and kink sectional airfoils are defined by nine design variables each according to the PARSEC definition [4, 9] as shown in Figure 7. The remaining sectional airfoils are linearly interpolated. In such parameterization, the complex shape of each airfoil can be represented by a relatively small number of meaningful engineering parameters such as the crest of the upper surface's  $Z$  coordinate ( $Z_{up}$ ), the crest of the lower surface's  $Z$  coordinate ( $Z_{lo}$ ) and the leading edge radius ( $r_{LE}$ ). This engineering parameterization is useful for designers to analyze optimized data directly. In addition, the wash-out is defined by two design variables at tip and kink position ( $T_{kink}$ ,  $T_{tip}$ ). Furthermore, the incidence angle ( $\theta$ ) is defined at root position. The planform with the design (kink) section is shown in Figure 8, and the ranges of design parameters are summarized in Table 2.

TABLE 2: Range of design parameters for PARSEC airfoil and twist Angles.

Parameter	Min	Max
$r_{le}$	0.005	0.06
$Z_{Te}$	-0.015	0.015
$\alpha_{Te}$	-8 deg.	-3 deg.
$X_{up}$	0.35	0.50
$Z_{up}$	0.06	0.13
$Z_{xxup}$	-1.0	-0.2
$X_{lo}$	0.35	0.5
$Z_{lo}$	-0.13	-0.06
$Z_{xxlo}$	0.1	1.0
Washout at tip	-4 deg.	4 deg.
Washout at kink	-4 deg.	4 deg.
Incidence angle (root)	0 deg.	8 deg.

**4.4. Pylon Definition.** The wing thickness of the pylon is defined by Bezier curve of four control points shown in Figure 9(a). There are seven design variables to control the wing thickness of the pylon. By using this geometrical definition, symmetrical airfoil of the pylon is represented. In addition, the camber is defined by Bezier curve of five control points shown in Figure 9(b). The camber is controlled by the  $x$ ,  $y$  coordinates of four control points, which correspond to eight design variables. Finally, a new pylon shape is generated by combining the wing thickness of the pylon with the camber. Therefore, 15 design variables are used in total. The possible pylon shapes are shown in Figure 10.

**4.5. Flow Analysis.** Once a new wing-fuselage-nacelle shape is defined, new surface mesh is firstly generated based on the advancing front method [10]. The tetrahedral volume mesh is then generated using Delaunay approach [11].

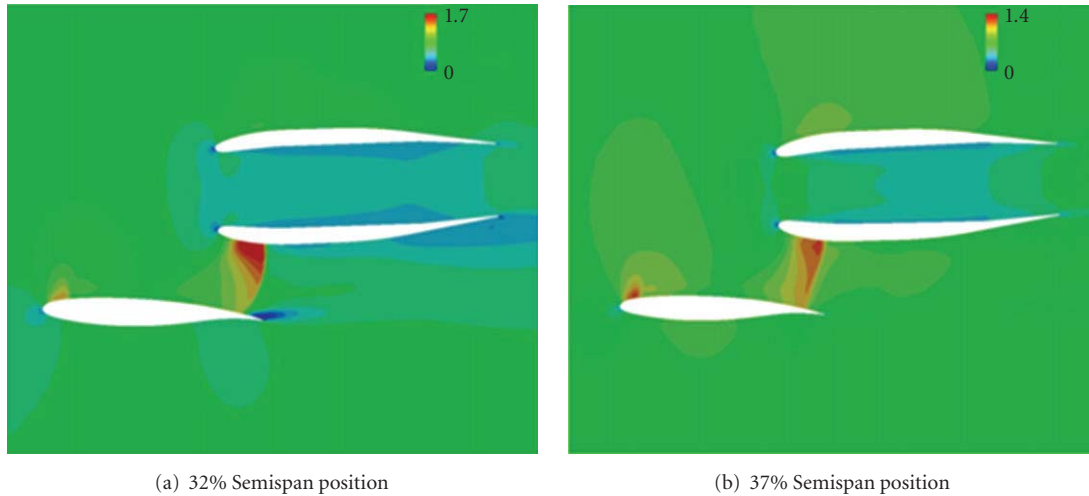
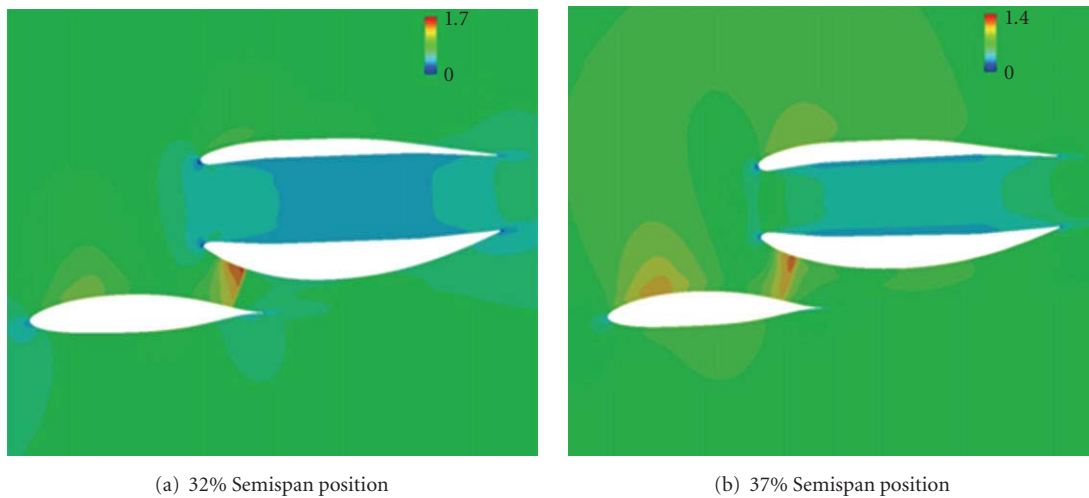
FIGURE 14: Cp distribution of *original* Geometry.

FIGURE 15: Cp distribution of OPT1 geometry.

Qualitative volume mesh for a new wing-fuselage-pylon-nacelle configuration is always generated with the number of nodes around 1.3 million.

In this research, a wing-fuselage configuration with a nacelle and a pylon is analyzed using three-dimensional unstructured mesh CFD solver, TAS (Tohoku University Aerodynamic Simulation) code [12]. The compressible Euler equations are solved by a finite-volume cell-vertex scheme. The numerical flux normal to the control volume boundary is computed using an approximate Riemann solver of Harten-Lax-van Leer-Einfeldt-Wada (HLLEW) [13]. The second-order spatial accuracy is realized by a linear reconstruction of the primitive gas dynamic variables inside the control volume with Venkatakrishnan's limiter [14]. The LU-SGS implicit method for unstructured meshes [15] is used for the time integration. The accuracy of the TAS-code has been validated for various flow problems [4, 12].

## 5. Optimization Results

**5.1. Wing and Nacelle Optimization.** In the first optimization, the nacelle position and shape in Section 4.2 and wing shape in Section 4.3 are modified to improve aerodynamic performance. The configuration is defined by 44 design variables. The pylon shape is fixed to NASA SC(2)-0008 airfoil. Horizontal and vertical tails are not modelled as they do not affect the whole aerodynamic performance.

The first Kriging model was constructed using 79 initial sampling points of the Latin hypercube sampling. The cross-validation of this model is shown in Figure 11, and it indicates that a reasonable approximation model was constructed. The final Kriging model was constructed with 169 sample points in total after 12 updates. Several non-dominated solutions on the approximate model were chosen at each update to increase accuracy of the approximation toward optimal solutions.

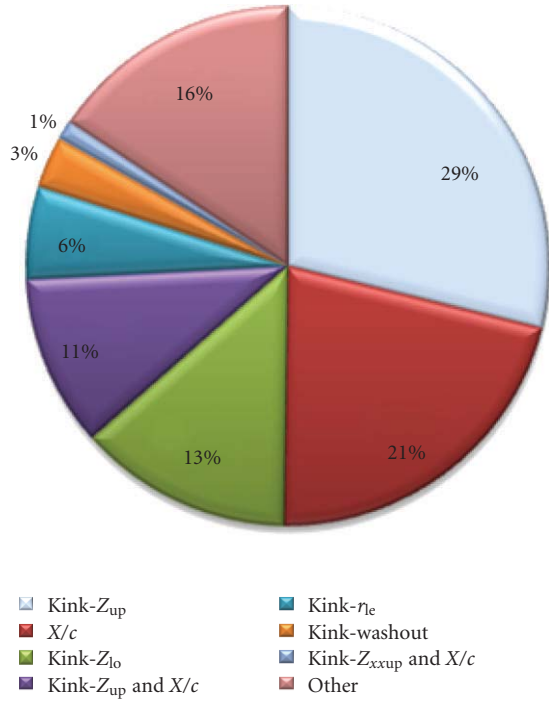


FIGURE 16: ANOVA result.

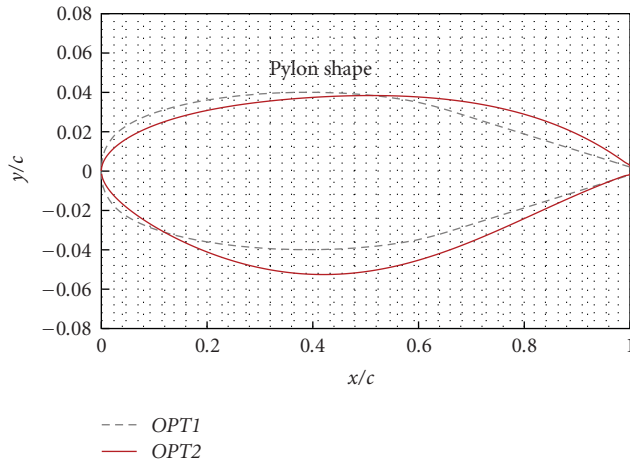


FIGURE 17: Comparison of pylon shape (blue: SC(2)-0008, red: OPT2).

Figure 12 shows objective-function space, which means the relation between  $L/D$  and nacelle position parameters. Due to the introduction of subobjectives ( $X/c$  and  $Z/h$ ), optimizer found higher  $L/D$  configurations at the nacelle position forward (low  $X/c$ ) and lower height (low  $Z/h$ ). One configuration having low  $X/c$  and  $Z/h$  parameters is chosen from non-dominated solutions ( $OPT1$ ), whose nacelle position parameters are  $X/c$  of 0.73 and  $Z/h$  of 0.48. This configuration achieved  $L/D$  of 34.5 at adjusted angle of attack of 5.71 degrees.

Mach number distributions of *ORIGINAL* ( $L/D$  of 25.0) and  $OPT1$  geometries at 32% and 37% semispan locations (viewed in Figure 13) are shown in Figures 14 and 15,

 TABLE 3: Pylon thickness and  $L/D$  for two optimal solutions ( $OPT1$  and  $OPT2$ ).

	$OPT1$	$OPT2$
Pylon thickness	8.0%	9.0%
$L/D$	34.5	35.5

respectively. From these figures, the shock wave of the  $OPT1$  is much weaker than that of the *ORIGINAL* because the flow channel between a wing and a nacelle is optimized to reduce interference effect. This is mainly due to the modification of lower nacelle shape.

To investigate the influence of each design variable to the objective function of  $L/D$ , ANOVA (functional analysis of variance) is conducted to the results. The result is shown in Figure 16, where the important design variables are shown in the figure. Many design variables related to the airfoil shape at the kink position are listed. Because the nacelle position is close to the kink position, the modification of the airfoil at the kink highly affects the flow between a nacelle and a wing.  $Z_{up}$ ,  $Z_{lo}$ ,  $r_e$  are the influenced factors and these three parameters are directly related to leading edge shape, which change the flow acceleration toward the nacelle.

**5.2. Pylon Optimization.** In the first optimization, wing and nacelle shapes are modified to improve aerodynamic efficiency. Here, further reduction of interference effect between a wing and a nacelle is intended by optimizing a pylon shape. In this section, the nacelle position and shape, and wing shape are frozen to the previous optimal geometry ( $OPT1$  configuration), and only the pylon is designed to be improved. The number of design variables is reduced to 15 in this case.

The first Kriging model was constructed using 41 sampling points of the Latin hypercube sampling, and the final Kriging model was constructed with 79 sample points in total after five updates.

The optimal design  $OPT2$  was obtained after the optimization and  $L/D$  of 35.4 was achieved at the angle of attack of 5.85 degrees. The results of  $OPT1$  and  $OPT2$  geometries are described in Table 3. The difference of  $L/D$  is tiny but  $OPT2$  actually achieved 5 counts drag reduction compared to  $OPT1$ . The modified pylon shapes are plotted in Figure 17. While the original SC (2)-0008 is symmetry, the designed pylon has camber and different leading edge radius, where positive  $y/c$  is inboard wing side and negative  $y/c$  is outboard wing side. In Figure 18, Mach contours of  $OPT1$  and  $OPT2$  are shown. According to the result, the  $OPT2$  reduces inboard shock waves due to the sharp leading edge and camber which enables to avoid flow acceleration between a wing and a nacelle. Pressure coefficient distributions at 32% and 37% semispan location are also plotted in Figure 19. This also indicates that inboard shock wave is weakened due to the pylon shape modification.

The pressure drag of the  $OPT1$  and the  $OPT2$  is shown in Figure 20. It indicates that optimization of the pylon shape is contributed to reduce the drag of inboard wing. On the other hand, the thrust of pylon is slightly weaker because the shock

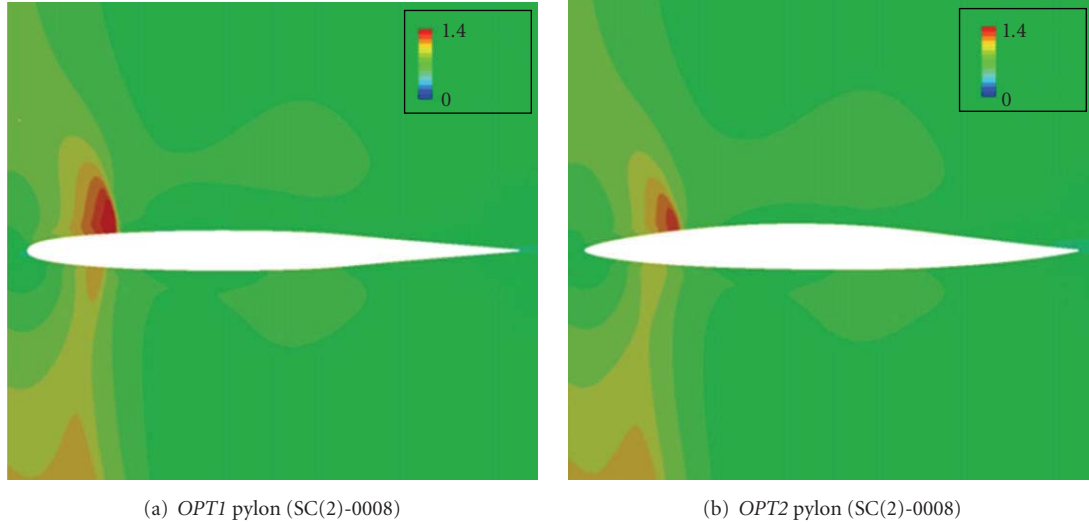
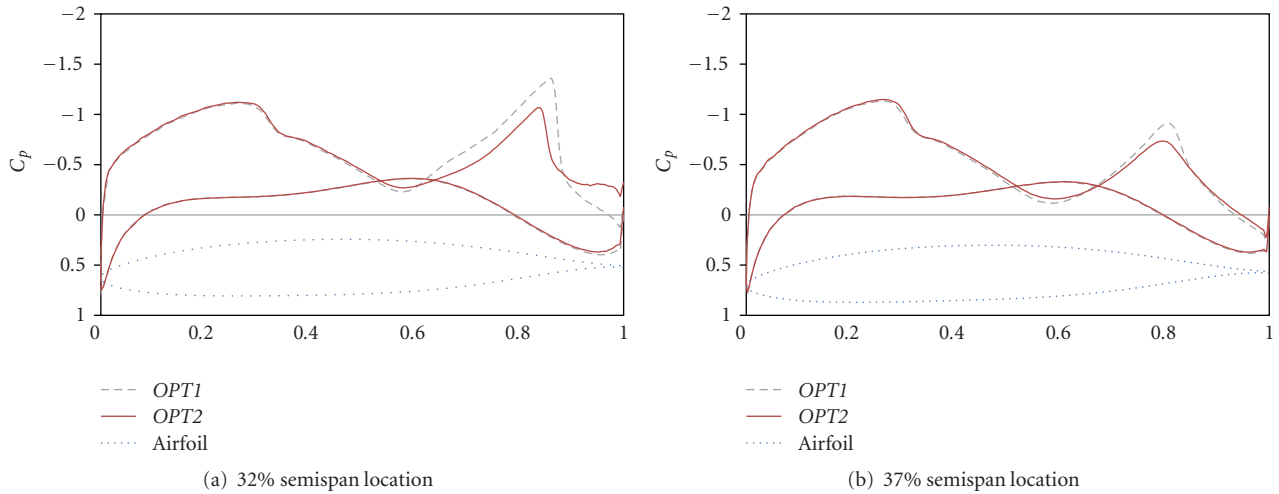


FIGURE 18: Comparison of Mach contours.

FIGURE 19: Comparison of  $C_p$  distribution (black line: *OPT1*, red line: *OPT2*).

wave near the leading edge of pylon is reduced by the pylon shape optimization.

**5.3. Performance of OWN Configuration.** The feasibility of OWN configuration is discussed herein through the comparison with DLR-F6 configuration that is conventional UWN configuration. The original design Mach number of DLR-F6 is 0.75. However, the Mach number in this research is set to 0.70 to focus on a mid-sized, short-range aircraft. Though they are not fully fair comparisons, the cruise performances of DLR-F6 and optimized OWN based on the *OPT2* at Mach number of 0.70 are compared in this section to investigate the aerodynamic feasibility of OWN configuration.

Surface pressure coefficient contours of both DLR-F6 and OWN configurations are shown in Figure 21. The aerodynamic performances are summarized in Table 4, and pressure drag components are plotted in Figure 22. From

TABLE 4: Cruise performance of DLR-F6 and OWN (*OPT2*) Configurations.

	DLR-F6	OWN ( <i>OPT2</i> )
$L/D$	31.7	35.5

this result, it demonstrates that optimized OWN configuration is able to achieve higher  $L/D$  than that of DLR-F6 configuration. This proves that OWN configuration has a potential to achieve high  $L/D$  comparable to conventional UWN by applying optimization techniques. When OWN configuration is realized, it is expected that the length of a landing gear can be much shortened compared to that of UWN configuration. This enables to reduce the total weight of the aircraft, which also leads to the increase of aerodynamic performance. In addition, as mentioned above, OWN configuration has an advantage of a shielding

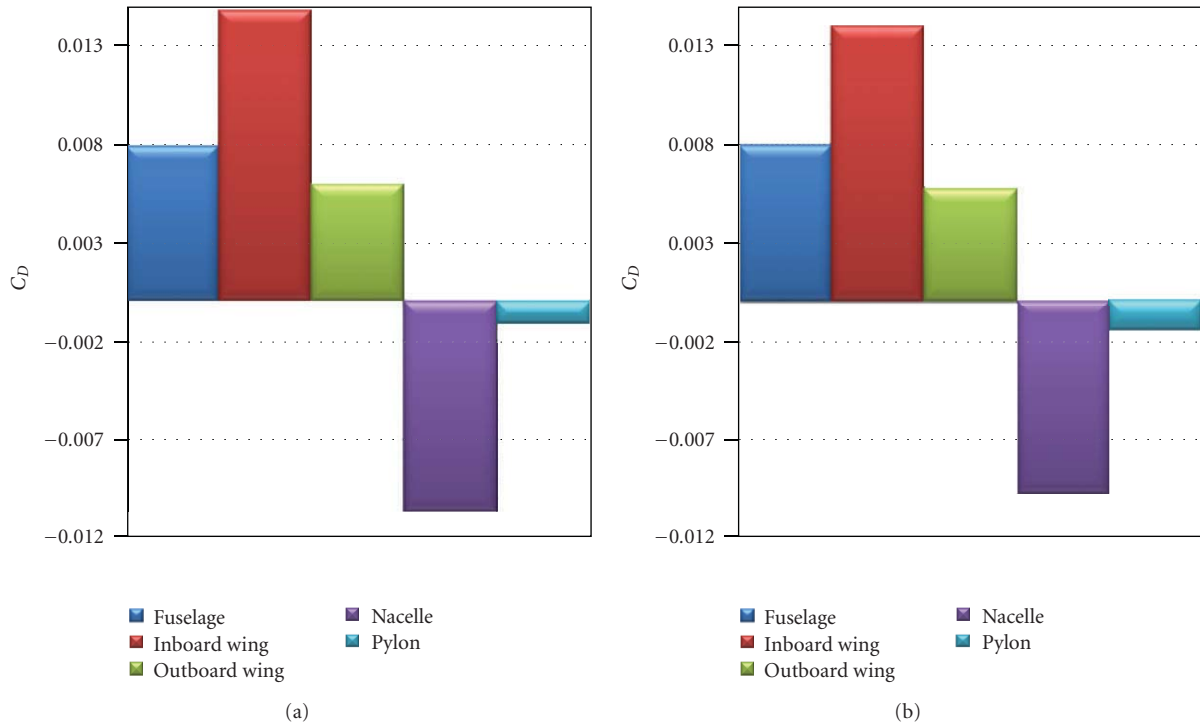


FIGURE 20: Proportion of pressure drag coefficient ((a) *OPT1*, (b) *OPT2*).

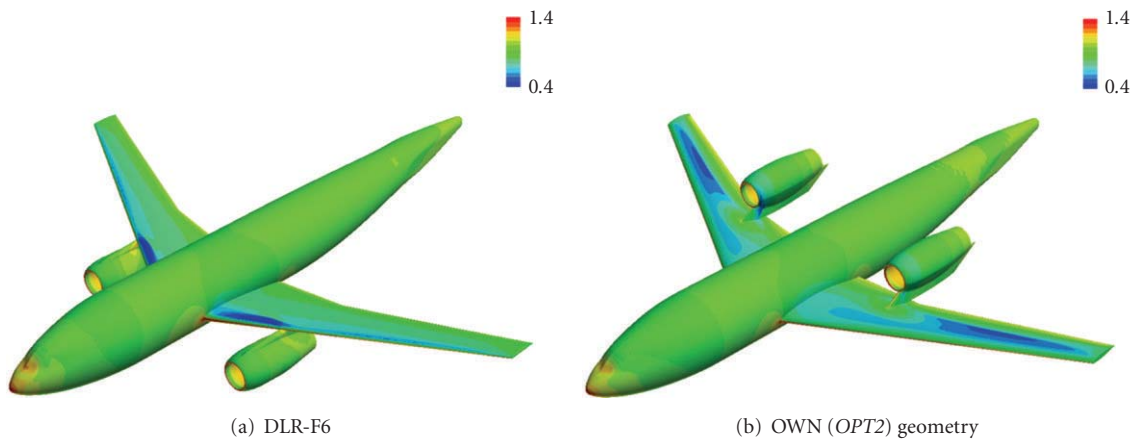


FIGURE 21: Comparison of surface pressure coefficient contours.

effect of the noise propagation toward the ground caused by fan and jet noises. By conducting further optimization integrating all the components at various flight conditions, OVN configuration will be able to prove that it is a potential candidate to be a near-future aircraft.

### 6. Conclusion

Aerodynamic optimizations of OVN configuration were conducted by modifying nacelle position, nacelle shape, wing shape, and pylon shape to investigate the usefulness of an OVN configuration. Firstly, the nacelle position and its shape as well as wing shape were optimized to maximize

$L/D$  and to achieve preferable nacelle position for a realistic aircraft design in terms of structural and maintenance points of view. As a result of the optimization, optimal configuration (*OPT1*) achieved  $L/D$  of 34.5. It reveals that the nacelle position is highly related to aerodynamic performance of OVN configuration; however, reasonable  $L/D$  can be obtained by the modification of nacelle and wing shape even when the nacelle is close to a wing.

Secondly, the pylon shape of the above optimal configuration was further optimized to reduce the interference effect between a wing and a nacelle. As a result of the optimization, the buffet near the trailing edge was weakened compared with original pylon shape. This enabled to

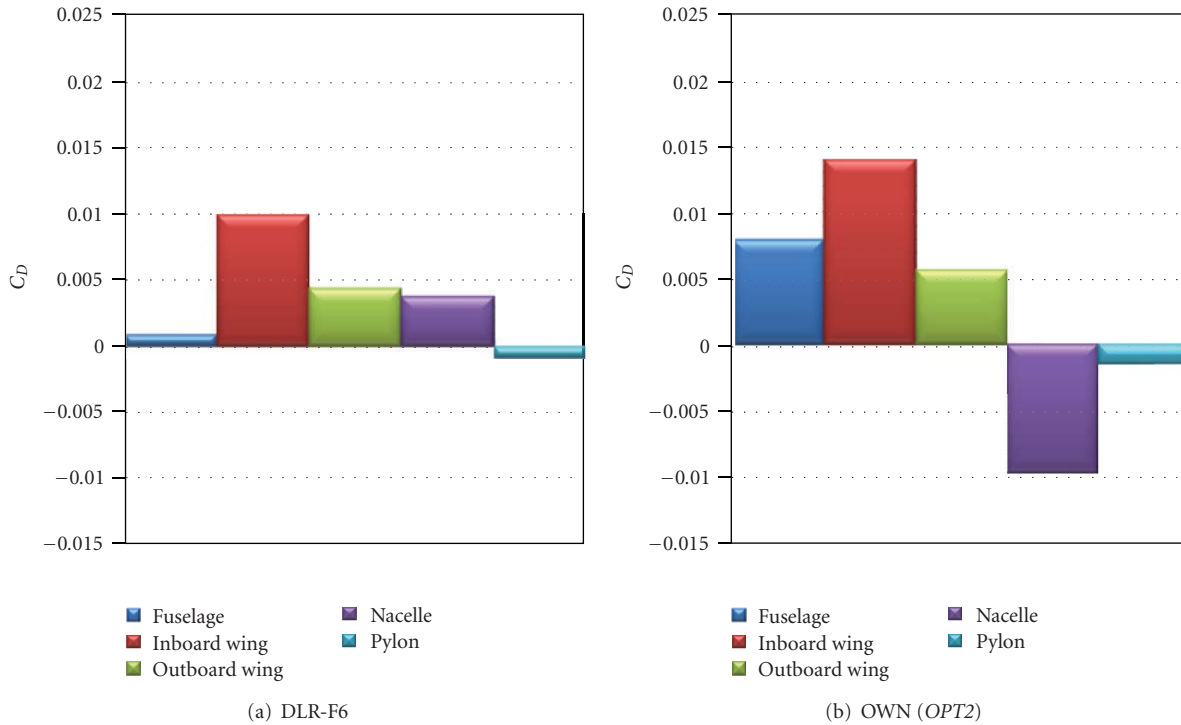


FIGURE 22: Proportion of pressure drag coefficient.

achieve higher  $L/D$  of 35.5 corresponding to 5 drag counts reduction from the first optimization. The optimal geometry (OPT2) is compared with DLR-F6 as a representative of conventional UWN. It proves that cruise performance of OWN can be comparable to that of UWN. Through the present aerodynamic optimizations of OWN configuration, it is concluded that an aerodynamically efficient OWN configuration comparable to conventional UWN will be realized feasible with further optimization under the various flight conditions and further integrated optimization of nacelle, wing, pylon and fuselage configuration.

## Acknowledgment

The present computation was executed by using NEC Vector Supercomputer of SX-9 in Cyberscience Center of Tohoku University.

## References

- [1] M. Fujino and Y. Kawamura, "Wave-drag characteristics of an over-the-wing nacelle business-jet configuration," *Journal of Aircraft*, vol. 40, no. 6, pp. 1177–1184, 2003.
- [2] J. Ricouard, R. Davy, P. Loheac, A. Moore, and O. Piccin, "ROSAS wind tunnel test campaign dedicated to unconventional aircraft concepts study," in *Proceedings of the 10th AIAA/CEAS Aeroacoustics Conference*, pp. 783–792, Manchester, UK, May 2004.
- [3] D. Sasaki and S. Obayashi, "Efficient search for trade-offs by adaptive range multi-objective genetic algorithms," *Journal of Aerospace Computing, Information and Communication*, vol. 2, no. 1, pp. 44–64, 2005.
- [4] M. Sunago, D. Sasaki, K. Takenaka, and K. Nakahashi, "Multipoint optimization of a short-range quiet passenger aircraft," *Journal of Aircraft*, vol. 46, no. 3, pp. 1070–1074, 2009.
- [5] S. Jeong, Y. Minemura, and S. Obayashi, "Optimization of combustion chamber for diesel engine using kriging model," *Journal of Fluid Science and Technology*, vol. 1, pp. 138–146, 2006.
- [6] S. Jeong, M. Murayama, and K. Yamamoto, "Efficient optimization design method using kriging model," *Journal of Aircraft*, vol. 42, no. 2, pp. 413–420, 2005.
- [7] M. D. McKay, R. J. Beckman, and W. J. Conover, "A comparison of three methods for selecting values of input variables in the analysis of output from a computer code," *Technometrics*, vol. 21, no. 2, pp. 239–245, 1979.
- [8] November 2010, <http://aaac.larc.nasa.gov/tsab/cfdlarc/aiaa-dpw/Workshop3/DPW3-geom.html>.
- [9] H. Sobieczky, "Parametric airfoils and wings," in *Notes on Numerical Fluid Mechanics*, pp. 71–88, 1998.
- [10] Y. Ito and K. Nakahashi, "Surface triangulation for polygonal models based on CAD data," *International Journal for Numerical Methods in Fluids*, vol. 39, no. 1, pp. 75–96, 2002.
- [11] D. Sharov and K. Nakahashi, "Hybrid prismatic/tetrahedral grid generation for viscous flow applications," *AIAA Journal*, vol. 36, no. 2, pp. 157–162, 1998.
- [12] K. Nakahashi, Y. Ito, and F. Togashi, "Some challenges of realistic flow simulations by unstructured grid CFD," *International Journal for Numerical Methods in Fluids*, vol. 43, no. 6-7, pp. 769–783, 2003.

- [13] S. Obayashi and G. P. Guruswamy, "Convergence acceleration of a Navier-Stokes solver for efficient static aeroelastic computations," *AIAA journal*, vol. 33, no. 6, pp. 1134–1141, 1995.
- [14] V. Venkatakrishnan, "On the accuracy of limiters and convergence to steady-state solutions," AIAA Paper 93-0880, 1992.
- [15] D. Sharov and K. Nakahashi, "Reordering of hybrid unstructured grids for lower-upper symmetric Gauss-Seidel computations," *AIAA Journal*, vol. 36, no. 3, pp. 484–486, 1998.

## Research Article

# New Evaluation Technique for WTG Design Wind Speed Using a CFD-Model-Based Unsteady Flow Simulation with Wind Direction Changes

Takanori Uchida,<sup>1</sup> Takashi Maruyama,<sup>2</sup> and Yuji Ohya<sup>1</sup>

<sup>1</sup>Research Institute for Applied Mechanics (RIAM), Kyushu University, 6-1 Kasuga-kouen, Kasuga, Fukuoka 816-8580, Japan

<sup>2</sup>Disaster Prevention Research Institute (DPRI), Kyoto University, Gokashyo, Uji, Kyoto 611-0011, Japan

Correspondence should be addressed to Takanori Uchida, takanori@riam.kyushu-u.ac.jp

Received 11 November 2010; Accepted 22 February 2011

Academic Editor: Guan Yeoh

Copyright © 2011 Takanori Uchida et al. This is an open access article distributed under the Creative Commons Attribution License, which permits unrestricted use, distribution, and reproduction in any medium, provided the original work is properly cited.

Because a significant portion of the topography in Japan is characterized by steep, complex terrain, which results in a complex spatial distribution of wind speed, great care is necessary for selecting a site for the construction of wind turbine generators (WTG). We have developed a CFD model for unsteady flow called RIAM-COMPACT (Research Institute for Applied Mechanics, Kyushu University, computational prediction of airflow over complex terrain). The RIAM-COMPACT CFD model is based on large eddy simulation (LES). The computational domain of RIAM-COMPACT can extend from several meters to several kilometers, and RIAM-COMPACT can predict airflow and gas diffusion over complex terrain with high accuracy. The present paper proposes a technique for evaluating the deployment location of a WTG. The proposed technique employs the RIAM-COMPACT CFD model and simulates a continuous wind direction change over 360 degrees.

## 1. Introduction

With the implementation of the revised Building Standard Law of Japan in June 2007, all structures which exceed a height of 60 m are now subject to a performance assessment by a designated institution and the approval of the Minister of Land, Infrastructure, Transport, and Tourism. These requirements are in addition to the application for the approval of the structure as stipulated by the prerevised law. In the case of wind turbine generators, these revisions to the law call for calculations of the reference wind speed at the wind turbine hubheight, which is relevant for the wind resistant design of turbines. Accordingly, the ratio of the wind speed at the hubheight subject to topographical effects to the wind speed at the hubheight free of topographical effects (fractional increase of hubheight wind speed), hereafter, needs to be evaluated by taking topographical factors into consideration. Given this background, the “Guidelines for the Design of Wind Turbine Support Structures/Commentary” [1] were published by the Japan

Society of Civil Engineers in 2007. The published Guidelines are based on the “Building Standard Law of Japan” [2] and the “Architectural Institute of Japan Recommendations for Loads on Buildings/Commentary” [3]. The Guidelines recommend the use of a numerical model for each of the 16 wind directions to evaluate the design wind speed for wind turbines.

In the meantime, we have proposed a technique to calculate the reference wind speed for use in the wind-resistant design of turbines [4]. This technique ensures operational safety of the wind turbines and is able to take into account high-wind-speed conditions which are similar to those observed in reality. Specifically, typhoons which have hit the site of interest in the past with high wind speed are simulated with a mesoscale meteorological model, and the directions from which high wind speeds are anticipated are identified. Subsequently, an analysis is performed for the identified wind directions using the RIAM-COMPACT computational fluid dynamics (CFD) model [5]. For that analysis, the influence of a continuous wind direction change

on the occurrence of high wind speed is evaluated from the analysis with the mesoscale meteorological model. However, in mesoscale meteorological models, numerous meteorological phenomena such as cumulus convection and rainfall are frequently modeled with a spatial resolution of a few hundred meters to a few kilometers (known as “parameterization” in the field of meteorology). Therefore, the spatial resolutions of mesoscale meteorological models are usually not high enough to be able to take into account the influence of the surrounding topography on the wind turbines, which is required for the wind-resistant design of the wind turbines. Furthermore, when coarse computational grids are used in a mesoscale meteorological model, wind velocity fluctuations cannot be simulated sufficiently. Even when high-resolution computational grids are used, as long as wind-direction-dependent simulations are performed, fine-scale variations of wind direction and speed due to the influence of the surrounding topography cannot easily be simulated with an accuracy larger than the angular resolution of the input wind directions (e.g.,  $22.5^\circ$  for a 16 wind direction simulation).

In this paper, a technique is proposed which resolves the above-mentioned drawbacks of the use of a mesoscale meteorological model. This technique utilizes the strengths of a CFD model, which is able to simulate unsteady turbulence fields, and the wind speed for the wind-resistant design of wind turbines is evaluated for all wind directions using a calculation in which the wind direction is varied continuously in time.

## 2. Numerical Computation Method

**2.1. CFD Model.** In this study, the RIAM-COMPACT natural terrain version model [5] is used in order to avoid numerical instability and to predict the airflow over complex terrain with high accuracy. The RIAM-COMPACT natural terrain version model uses collocated grids in a general curvilinear coordinate system. The velocity components and pressure are defined at the cell centers, and variables which result from the covariant velocity components multiplied by the Jacobian are defined at the cell faces. As for the computational technique, the finite-difference method (FDM) is adopted, and an LES model is used for the turbulence model. In LES, a spatial filter is applied on the flow field to separate eddies of various scales into grid-scale (GS) components, which are larger than the computational grids, and subgrid-scale (SGS) components, which are smaller than the computational grids. Large-scale eddies, that is, the GS components of turbulence eddies, are numerically simulated directly without relying on the use of a physically simplified model. The main effect of small-scale eddies, that is, the SGS components, is to dissipate energy, and this dissipation is modeled based on the physical considerations of the SGS stress. For the governing equations of the flow, a spatially filtered continuity equation for incompressible fluid and a spatially-filtered Navier-Stokes equation are used. Because the present study is on airflow prediction in high-wind conditions, the effect of the temperature stratification which is generally present in the atmosphere is neglected.

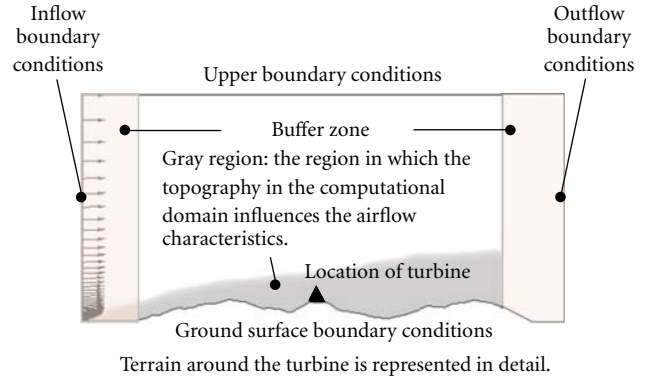


FIGURE 1: Computational domain and boundary conditions.

The computational algorithm and the time-marching method are based on a fractional step (FS) method and the Euler explicit method, respectively. The Poisson’s equation for pressure is solved by the successive overrelaxation (SOR) method. For discretization of all the spatial terms except for the convective term, a second-order central difference scheme is applied. For the convective term, a third-order upwind difference scheme is applied. An interpolation technique based on 4-point differencing and 4-point interpolation by Kajishima [6] is used for the fourth-order central differencing that appears in the discretized form of the convective term. In the weighting of the numerical dispersion term of the third-order upwind differencing,  $\alpha = 3.0$  is commonly applied in the Kawamura-Kuwahara Scheme [7]. However,  $\alpha$  is set to 0.5 in the present study to minimize the influence of numerical dispersion. For LES subgrid-scale modeling, the commonly used Smagorinsky model [8] is adopted. A wall-damping function is used with a model coefficient of 0.1. We have developed an LES-based model for analyzing neutral flow over variable orography and applied it to the problem of proper site selection. Model performance was evaluated using data from wind tunnel tests over simple geometries and from a real site [5].

**2.2. Computational Conditions.** The topography in the computational domain is reconstructed using mainly the 50-m-elevation data of the Geography Survey Institute of Japan. Fine grid spacing is adopted near the wind turbines in order to reconstruct the topographical features in detail. The computational domain is set up in such a way that airflow characteristics at the turbine location are subject to topographical influences (upwind zone) and that eddies flow out of the computational domain smoothly, and airflow at the turbine location is free from the influence of the outflow boundary (leeward zone) (Figure 1). For analyses of airflow over steep topography, a buffer zone is established which surrounds the computational domain. The terrain in the buffer zone is flat with an elevation close to zero meters and connects smoothly to the terrain in the computational domain.

As for the boundary conditions, slip conditions are applied to both the upper boundary and the side boundaries. For the upper boundary, the vertical gradient of the

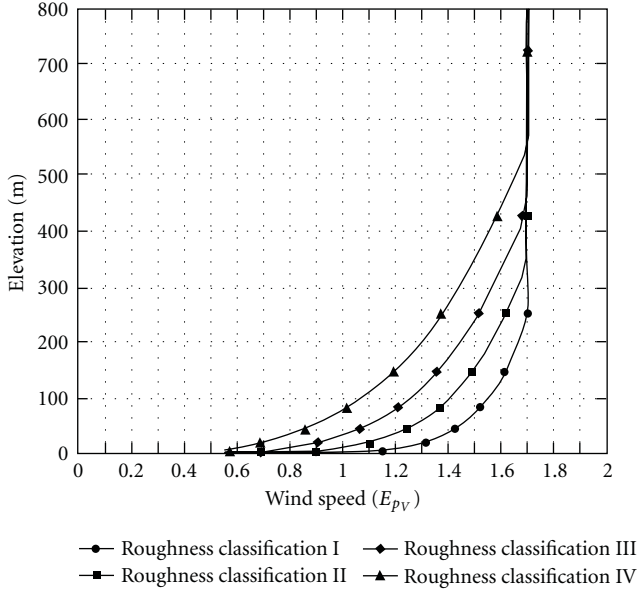


FIGURE 2: Vertical profiles of horizontal wind speed calculated from equations given in Bulletin no. 1454 of the Ministry of Construction, 2000.

TABLE 1: Coefficients for the vertical profiles of the mean horizontal wind speed which appear in Figure 2 (height correction coefficients for the mean horizontal wind speed  $E_{pv}$ .)

Roughness classification	$Z_b$ (m)	$Z_G$ (m)	$\alpha$
I	5	250	0.10
II	5	350	0.15
III	5	450	0.20
IV	10	550	0.27

For height  $H$  smaller than  $Z_b$ :  $E_{pv} = 1.7(Z_b/Z_G)^\alpha$

For height  $H$  larger than  $Z_b$ :  $E_{pv} = 1.7(H/Z_G)^\alpha$

The values of  $Z_b$  and  $Z_G$  in the table are used in the formula.

horizontal wind speed components ( $\bar{u}$ ,  $\bar{v}$ ) and the vertical wind velocity component ( $\bar{w}$ ) are all set to zero. For the side boundaries, the lateral gradient of the streamwise wind velocity component ( $\bar{u}$ ), that of the vertical wind velocity component ( $\bar{w}$ ), and that of the spanwise wind velocity component ( $\bar{v}$ ) are all set to zero. For the inflow boundary condition, a vertical profile of the mean horizontal wind speed which is based on Bulletin no. 1454 of the Ministry of Construction, is applied according to the roughness classification (Figure 2 and Table 1). Furthermore, a convective outflow condition and the no-slip condition are imposed for the outflow boundary and ground surface, respectively. Changes in the wind direction are taken into account in the calculations of the technique proposed in the present study. Therefore, inflow boundary conditions are used when the flow is directed into the computational domain through the side boundary, and outflow boundary conditions are used when the flow is directed out of the computational domain through the side boundary.

TABLE 2: Details of computational domain.

- (i) Computational domain: 8,500 m square wind farm with the observation pole located at the center. The vertical height of the computational domain is approximately 2,900 m
- (ii) Maximum elevation: 537 m
- (iii) Minimum elevation: 0 m
- (iv) Number of computational grids:  $101 \times 101 \times 51$
- (v) Number of computational grids including those in the buffer zone:  $121 \times 121 \times 51$
- (vi) Grid widths: 32 m ~ 769 m (horizontal direction); 1.7 m ~ 347 m (vertical direction)
- (vii) Reynolds number:  $Re = 10^4$  (based on the difference between the minimum and maximum elevations and the wind speed at the maximum elevation.)

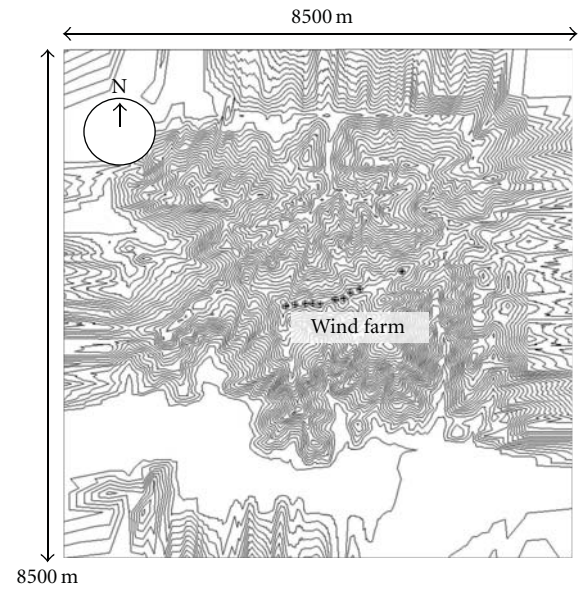


FIGURE 3: Wind turbine locations and computational domain.

### 3. An Example of Design Wind Speed Evaluation

**3.1. Summary of Wind Farm.** In this section, the proposed technique is applied to evaluate the appropriate wind speed for wind-resistant design of turbines for a wind farm in Japan. The evaluation is made for a wind farm which consists of ten wind turbines with rotor diameters of 62 m (Figure 3). The hubheight and the power output of each of the turbines are 60 m and 1.3 MW, respectively. Figure 3 shows the details of the computational domain (see Table 2).

**3.2. Wind Direction Change.** For the inflow profile, a vertical profile of the horizontal mean wind speed for roughness classification III is selected according to the previous literature [1]. This selection is based on the surface roughness around the wind turbine. Using the same vertical profile of wind speed, a simulation is performed in which the wind profile is rotated continuously over 360 degrees (Figure 4). In order to ensure that the wind direction change has little influence

on the statistical values calculated over approximately 10-minute intervals, the number of time steps required for the rotation of the wind profile over 360 degrees is set to an appropriate value. This value is selected according to the results of an investigation on the influence of the rate of wind direction change on the simulation results. In this investigation, which is conducted prior to the main simulation, the results of a simulation with a fixed vertical profile of wind speed rotated over 360 degrees are compared to the results of simulations with two different settings: (1) the number of time steps for the wind profile rotation is increased to 10 times that of the original; (2) the wind profile does not rotate, that is, wind flow comes from a fixed direction. In this study, 400,000 time steps are used to rotate the wind direction over 360 deg ( $9 \times 10^{-4}$  degs/step) with a dimensionless time interval of 0.002 (approximately 0.1 seconds in actual time). For the simulation, parallel computation was performed using a single computer with an Intel Core 2 Extreme 6850 (3 GHz, 4 core), 2 GB of memory, Intel Fortran v.10.1.025, and Windows XP SP3. The entire simulation required 70,790 s (approximately 20 hours) for the wind direction change of 360 degrees (400,000 time steps).

In the simulation, some fluctuations are observed immediately after the initiation of the simulation. This phenomenon implies that it takes some finite time for the velocity field to stabilize and for the pressure field to converge. Avoiding this phenomenon is generally not feasible for numerical wind synopsis simulations of unsteady wind flow. In order to avoid the influence of this phenomenon and to accurately evaluate the wind speed, the initial wind direction change over 360 degrees (400,000 time steps) is treated as the spin-up calculation. The computational results from the subsequent wind direction change of 360 degrees are used for the evaluation of the design wind speed discussed below.

**3.3. Computational Results.** Figure 5 shows the vertical profiles of wind velocity vectors (instantaneous values) at each of the turbine locations. These profiles were obtained after the wind direction was rotated over 360 degrees. This figure suggests that wind speed increases locally near the hubheight of each wind turbine due to topographical effects. Figure 6 shows that both the wind speed and turbulence intensity near the hubheight vary significantly according to the wind direction. In this figure, the wind speed at the hub height of a given turbine is illustrated in terms of the fractional increase of hubheight wind speed, that is, the ratio of the 10-minute-moving average value of the hubheight horizontal wind speed (scalar value) to the hubheight inflow horizontal wind speed which is free of topographical influence (the height correction coefficient  $E_{pV}$  in Table 1),

$$U_{EL} = \sqrt{\bar{u}^2 + \bar{v}^2}. \quad (1)$$

**3.4. Evaluation of Design Wind Speed.** In this subsection, the design wind speed is evaluated by calculating the fractional

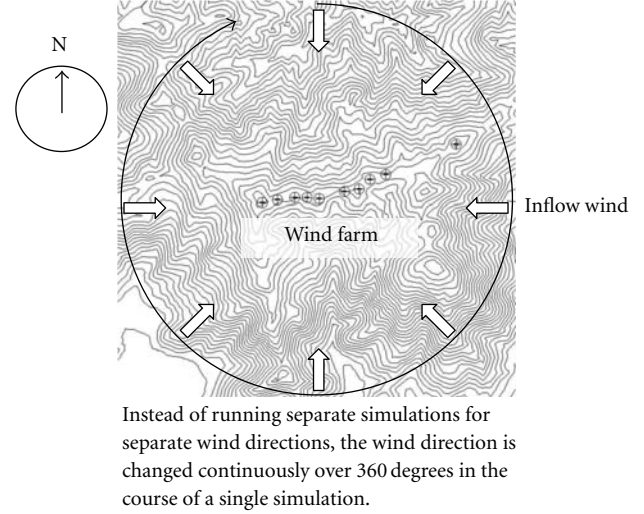


FIGURE 4: Continuous change of wind direction.

increase of hubheight wind speed from the simulation results. The design wind speed at the hubheight, denoted as  $U_h$ , can be estimated according to (3.1) in the literature [1] as:

$$U_h = E_{tV} E_{pV} V_0, \quad (2)$$

where  $E_{tV}$  is the fractional increase of hubheight wind speed,  $E_{pV}$  is the height correction coefficient given in Figure 2 and Table 1 in Section 2.2, and  $V_0$  is the design standard wind speed given in Article 87 of the Order for Enforcement of the Building Standards Act (for the target area of the current simulation,  $V_0 = 34$  m/s). Here, the maximum value of the fractional increase of hubheight wind speed in Figure 6(a) is used for  $E_{tV}$ , where  $E_{tV}$  is defined as (the horizontal wind speed at the turbine hubheight)/(the wind speed at the hubheight) in Figure 2, Table 1. The value of  $E_{tV}$  is 1.70 from Figure 6(a). For  $E_{pV}$ , the following value is used:

$$E_{pV} = 1.7(60/450)^{0.2} = 1.14, \quad (3)$$

where the estimate is made for a 60 m hubheight using the relevant values for roughness classification III.

The design wind speed  $U_h$  for the hubheight in the present study can be calculated as:

$$U_h = E_{tV} E_{pV} V_0 = 1.70 \times 1.14 \times 34 = 65.89 \text{ (m/s)}. \quad (4)$$

However, the designer needs to take into account a safety factor in order to finalize the value of the design wind speed for the hubheight.

## 4. Summary

In the present study, the design wind speed of a wind turbine generator was evaluated for the hubheight. The evaluation was made using the fluid dynamics model RIAM-COMPACT, which allows analyses of unsteady turbulence fields. The wind speed and direction change subject to the



FIGURE 5: Vertical profile of wind velocity vectors at the location of each turbine. Northerly wind case. Instantaneous values.

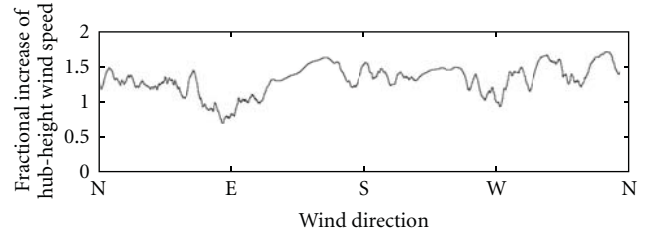
influence of the surrounding topography is simulated precisely, and the simulation result is used for evaluating the design wind speed in the proposed technique as outlined below:

#### Procedure for the Proposed Evaluation Technique:

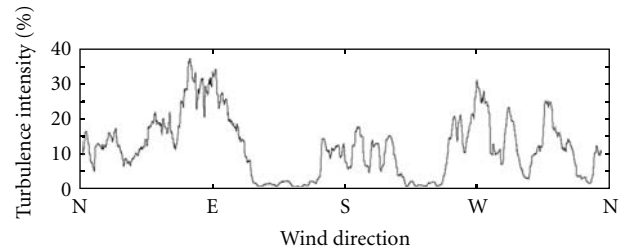
- (1) Complex terrain information is constructed using data such as the 50-m-elevation data of the Geographical Survey Institute of Japan. Fine grid spacing is adopted near the turbines in order to reproduce the terrain features in detail. When complex terrain is included in the computational domain, a buffer zone with flat, almost zero elevation is set up around the computational domain, and the ground surface in the buffer zone is adjusted to connect smoothly to the complex terrain in the computational domain.
- (2) Using previous literature [1], the vertical profile of the inflow wind speed is determined according to the surface roughness in the area surrounding the analysis domain.
- (3) A simulation is performed during which the vertical profile of the wind speed determined in Step 2 is rotated continuously through 360 degrees.
- (4) The fractional increase of hubheight wind speed is evaluated according to the literature [1], and the design wind speed is evaluated.

The proposed technique for the design wind speed evaluation was applied to a wind farm within Japan. A specific procedure for the design wind speed evaluation was laid out, and the design wind speed was evaluated for the turbine hubheight. The characteristics of the proposed technique include the following.

- (i) Fine-scale wind speed and direction change that are subject to the influence of the surrounding topography on the wind field can be simulated more accurately than feasible with the technique in which simulations are performed for a specific number of wind directions, for example, 8 or 16 directions.
- (ii) The proposed technique does not require the generation of new computational grids or spin-up calculations for wind field stabilization separately for each



(a) Fractional increase of hubheight wind speed = (horizontal wind speed at turbine hubheight)/(horizontal wind speed at hubheight) from Figure 2 and Table 1



(b) Turbulence intensity (%)

FIGURE 6: (a) 10-minute moving average values of the fractional increase of hubheight wind speed, and (b) corresponding turbulence intensity. Here, the results from Turbine no. 1 are given as an example.

of the predetermined wind directions. As a result, the simulation time can be reduced considerably.

Furthermore, possible applications of the present numerical wind synopsis prediction technique for unsteady wind flow which incorporates continuous wind direction change include:

- (i) numerical site calibration (NSC) [9],
- (ii) prediction of turbulence intensity over complex terrain,
- (iii) coupling with the numerical results from a mesoscale meteorological model.

## Acknowledgments

The present study was partially funded by (1) a Grants-in-Aid for Scientific Research for Young Researchers (A) for the fiscal year 2010~2011, "Development of a Local Wind Synopsis Prediction Technique for Improvement of the Atmospheric Environment in Mega-Cities in Asia and for the Effective Use of Wind Energy" (Principle Investigator: Takanori Uchida), (2) a 21st term research grant from the Research Foundation for Electrotechnology of Chubu: fiscal year 2010, "Development of a High-Accuracy Wind Turbine Micro-Siting Technique for the Dissemination of Wind Power Generation" (Principle Investigator: Takanori Uchida), and (3) a Research Grant from the Hatayama Cultural Foundation: fiscal year 2010, "Development of a Wind Turbine Micro-Siting Technique Contributing to the Appropriate Deployment of Wind Power Generation Facilities" (Principle Investigator: Takanori Uchida). Various

datasets used in the present study were provided by Graham Li of Eurus Energy Japan Corporation. The authors wish to express our gratitude to the above-mentioned funding agencies and individuals.

## References

- [1] *Guidelines for the Design of Wind Turbine Support Structures/ Commentary*, Japan Society of Civil Engineers, 2007.
- [2] Building Standard Law of Japan, 2000.
- [3] *Architectural Institute of Japan—Recommendations for Loads on Buildings / Commentary*, 2004.
- [4] T. Uchida, T. Maruyama, T. Takemi, Y. Oku, Y. Ohya, and Graham Li, “Proposal of designed wind speed evaluation technique in WTG installation point by using the meteorological model and CFD model,” *Journal of Wind Engineering and Industrial Aerodynamics*, vol. 34, pp. 118–124, 2010 (Japanese).
- [5] T. Uchida and Y. Ohya, “Micro-siting technique for wind turbine generators by using large-eddy simulation,” *Journal of Wind Engineering and Industrial Aerodynamics*, vol. 96, no. 10–11, pp. 2121–2138, 2008.
- [6] T. Kajishima, “Finite-difference method for convective terms using non-uniform grid,” *Transactions of the Japan Society of Mechanical Engineers, Part B*, vol. 65, no. 633, pp. 1607–1612, 1999.
- [7] T. Kawamura, H. Takami, and K. Kuwahara, “Computation of high Reynolds number flow around a circular cylinder with surface roughness,” *Fluid Dynamics Research*, vol. 1, no. 2, pp. 145–162, 1986.
- [8] J. Smagorinsky, “General circulation experiments with the primitive equations, part 1, basic experiments,” *Monthly Weather Review*, vol. 91, pp. 99–164, 1963.
- [9] T. Sanada, M. Fujino, D. Matsushita et al., “Numerical site calibration on a complex terrain and its application for wind turbine performance measurements,” in *Proceedings of the European Wind Energy Conference (EWEC)*, pp. 156–160, 2006.

## Research Article

# Comparisons between the Wake of a Wind Turbine Generator Operated at Optimal Tip Speed Ratio and the Wake of a Stationary Disk

Takanori Uchida, Yuji Ohya, and Kenichiro Sugitani

Research Institute for Applied Mechanics, Kyushu University, 6-1 Kasugakoen, Kasuga, Fukuoka 816-8580, Japan

Correspondence should be addressed to Takanori Uchida, takanori1211@gmail.com

Received 11 November 2010; Accepted 22 February 2011

Academic Editor: Guan Yeoh

Copyright © 2011 Takanori Uchida et al. This is an open access article distributed under the Creative Commons Attribution License, which permits unrestricted use, distribution, and reproduction in any medium, provided the original work is properly cited.

The wake of a wind turbine generator (WTG) operated at the optimal tip speed ratio is compared to the wake of a WTG with its rotor replaced by a stationary disk. Numerical simulations are conducted with a large eddy simulation (LES) model using a nonuniform staggered Cartesian grid. The results from the numerical simulations are compared to those from wind-tunnel experiments. The characteristics of the wake of the stationary disk are significantly different from those of the WTG. The velocity deficit at a downstream distance of  $10D$  ( $D$ : rotor diameter) behind the WTG is approximately 30 to 40% of the inflow velocity. In contrast, flow separation is observed immediately behind the stationary disk ( $\leq 2D$ ), and the velocity deficit in the far wake ( $10D$ ) of the stationary disk is smaller than that of the WTG.

## 1. Introduction

As a countermeasure against global warming, a substantial reduction in CO<sub>2</sub> emissions has become an urgent issue. Accordingly, the effective use of wind power energy is attracting attention as a clean and environmentally friendly solution. In Japan, the number of wind power generation facilities has been rapidly increasing to achieve the goal of 300 million kW of wind-generated energy in 2010. These wind power generation facilities range from those with a few wind turbine generators (WTG) to large wind farms (WF) with dozens of WTGs.

Given this background, we have developed RIAM-COMPACT (Research Institute for Applied Mechanics, Kyushu University, Computational Prediction of Airflow over Complex Terrain), a nonstationary, nonlinear wind synopsis simulator that is capable of predicting the optimum sites for wind turbine construction to the pin-point level within a target area of a few km or less [1]. RIAM-COMPACT can also estimate the annual energy generation and the utilized capacity of a proposed WTG with observational data. To model the wind field, RIAM-COMPACT has adopted a large-eddy simulation (LES) technique.

To achieve improved accuracy of the simulation result, a continuous effort has been made in the research and development of RIAM-COMPACT. As a part of this effort, a wake model of high accuracy is currently under development to evaluate the influence of the mutual interference between WTGs. The wake model will be able to determine an appropriate separation distance between WTGs to avoid the reduction of energy generation at a wind farm as a whole due to the mutual interference between WTGs at the farm. Development of such a wake model is necessary for the effective planning of wind farms, especially in countries with limited flat areas, including Japan, in which large WTGs are constructed in high concentrations.

When multiple WTGs are installed at a site, the following empirical values are generally considered appropriate for the separation distance between two WTGs: approximately ten-times the WTG rotor diameter in the streamwise direction and three times the WTG rotor diameter in the spanwise direction. A few wind-tunnel and field experiments have been conducted to study the wake flows of WTGs [2, 3]. However, the characteristics of the wake flow have not been sufficiently investigated.

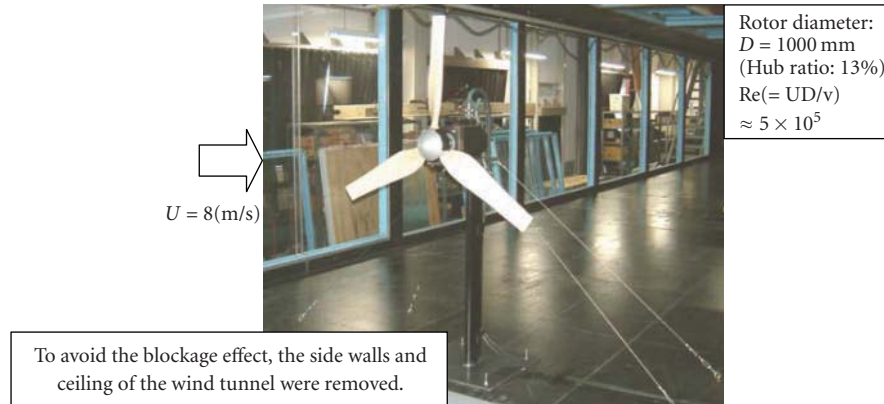


FIGURE 1: View of the small-scale WTG in the wind tunnel.

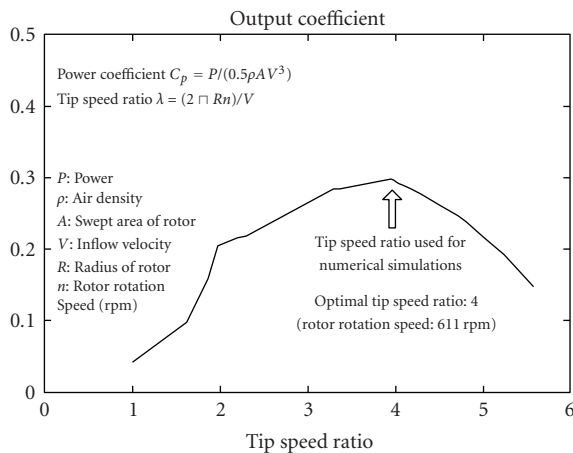


FIGURE 2: Relationship between the tip speed ratio and the power coefficient of the wind turbine generator (WTG) tested in the wind-tunnel experiments.

The present study examines the following two characteristics of the wake flow which will enable the construction of an accurate wake model. First, the mean wind velocity deficit is evaluated at the above-mentioned downstream distance of ten-times the rotor diameter of a single WTG. Second, the characteristics of the wake flow of a single WTG are compared to those of a stationary disk, which has been used as the basis of existing wake models. In both cases, the wake flow of the WTG operated at the optimal tip speed ratio (tip speed ratio at the maximum power output) is considered. The investigations are conducted with an LES model that uses a nonuniform staggered Cartesian grid system. The results from the numerical simulations are compared to those from wind-tunnel experiments.

## 2. Numerical Simulation Technique and Results

**2.1. Numerical Simulation Technique.** LES simulations are conducted using a staggered Cartesian grid with variable grid spacing. The finite difference method (FDM) is adopted for the computational technique. For the subgrid scale (SGS)

model, the mixed-time scale model [4] is utilized. The mixed-time scale model is characterized by a high degree of computational stability and does not require a near-wall damping function. For explicit filtering, Simpson's rule is applied. For the pressure-velocity coupling algorithm, the fractional-step (FS) method based on the first-order explicit Euler method [5] is used. The Poisson's equation for pressure is solved by the successive overrelaxation (SOR) method. For discretization of all the spatial terms except for the convective term, a second-order central difference scheme is applied. The convective term is discretized by a third-order upwind differencing scheme, which consists of a fourth-order central differencing term based on the interpolation technique of Kajishima [6] and a numerical dispersion term in the form of the fourth derivative. A weighting value of 3.0 is normally applied as the coefficient of the numerical dispersion term in the third-order upwind differencing scheme proposed by Kawamura and Kuwahara (the Kawamura-Kuwahara Scheme) [7]. However, the coefficient is set to 0.5 in the present study to minimize the influence of numerical dispersion.

**2.2. Modeling of the WTG.** Figure 1 shows the small-scale WTG investigated in the wind-tunnel experiments. The blades of the WTG model are MEL airfoils [8] with increased thickness. The performance curve of the WTG determined from the wind-tunnel experiments shows that the optimal tip speed ratio of the present WTG is 4 (see arrow in Figure 2). To recreate the conditions of the wind-tunnel experiments in the numerical simulations, the configurations of the spinner, nacelle, and tower were reconstructed with a rectangular grid approximation (Figure 4). To model the rotation of the WTG rotor, an actuator-disc approach based on blade element theory [9, 10] is applied. In the actuator-disc approach, the tangential and thrust forces generated by the rotating blade are added to the Navier-Stokes equations as external terms. These external terms represent the reaction forces exerted on the fluid in the direction of the streamwise flow and the rotation. Thus, no wall boundary condition exists for the rotor as an object. In the present study, because a nonuniform staggered Cartesian grid system has been adopted,

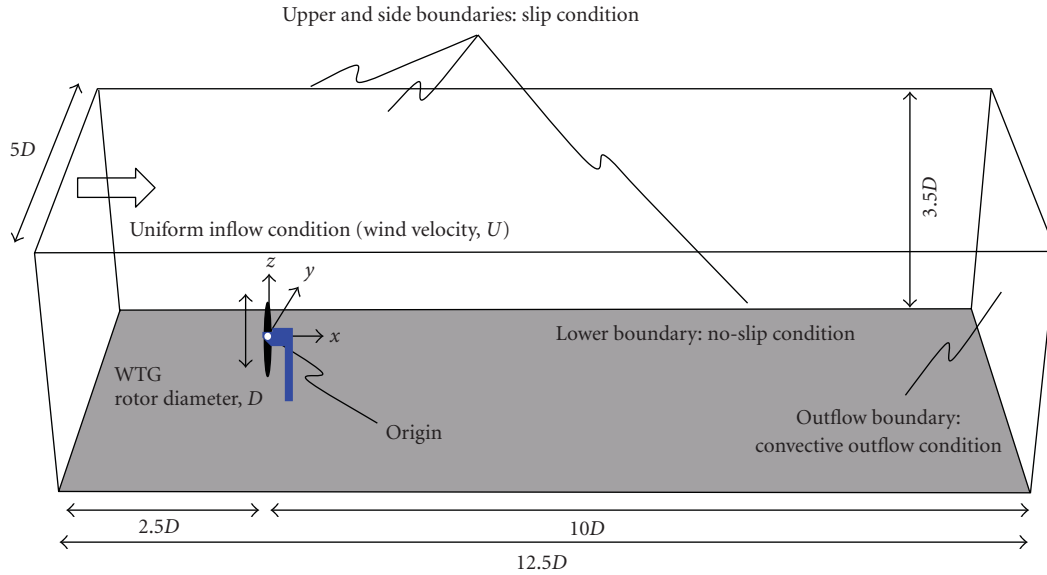


FIGURE 3: Computational domain and boundary conditions.

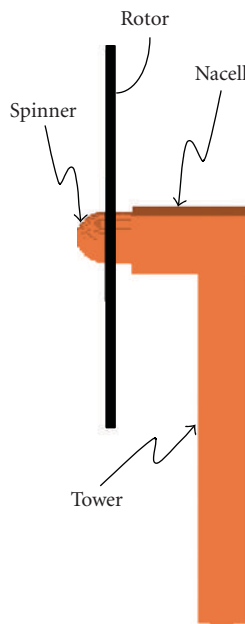


FIGURE 4: Enlarged view of WTG.

the component of the force in the direction of rotation is decomposed into the spanwise and vertical directions. In addition to the investigation of the decelerating effect of the WTG simply as a drag-inducing body, the adopted modeling approach allows the investigation of the effect of the blade rotation on the airflow, which is considered a major benefit of the adopted modeling approach. Furthermore, the model is designed so that it allows the user to simulate wake flows of various WTGs by inputting only the data of the blade chord length, the lift coefficient, the drag coefficient, and the angle of attack as a function of the distance from the center of the rotor. With the developed model, airflow past the entire

WTG, including the tower, is simulated for a tip speed ratio of 4, the optimal tip speed ratio.

**2.3. Computational Domain and Conditions.** Numerical simulations are conducted for (1) airflow past the WTG operated at the optimal tip speed ratio and (2) airflow past a WTG for which the rotor has been replaced by a stationary disk with a diameter identical to that of the rotor. The WTG with a stationary disk will be referred to simply as the stationary disk hereafter. The computational domain and boundary conditions applied in the simulations are summarized in Figure 3. The dimensions of the computational domain are  $12.5D \times 5D \times 3.5D$  (streamwise ( $x$ )  $\times$  spanwise ( $y$ )  $\times$  vertical ( $z$ )), where  $D$  is the rotor diameter. The computational domain consists of  $181 \times 171 \times 161$  grid points (approximately 5 million grid points) in the  $x$ ,  $y$ , and  $z$  directions, respectively. Sufficiently high grid resolution is provided around the WTG to analyze the flow field past the entire WTG, including the spinner, nacelle, and tower ( $\Delta x_{\min} = \Delta y_{\min} = \Delta z_{\min} = 0.005D$ ). The same set of boundary conditions is applied for the two simulations except for those of the wind velocity at the rotor; for the case with the stationary disk, the wind velocity is set to zero at all grid points on the surface and in the interior of the disk. In both cases, the wind velocity is set to zero at all grid points on the surface and in the interior of the spinner, nacelle, and tower. As for the boundary conditions for pressure, Neumann boundary conditions are applied at all surfaces. The Reynolds number of the flow based on the uniform inflow wind speed,  $U$ , and the rotor diameter,  $D$ , that is,  $Re (= UD/\nu)$ , is  $2 \times 10^4$  in the present study. For simulations, a time step of  $\Delta t = 2 \times 10^{-3} (D/U)$  is used.

**2.4. Computational Results and Discussion.** Figures 5 and 6 are contour plots of the streamwise ( $x$ ) wind velocity,  $u$ , in the vicinity of the WTG operated at the optimal tip speed

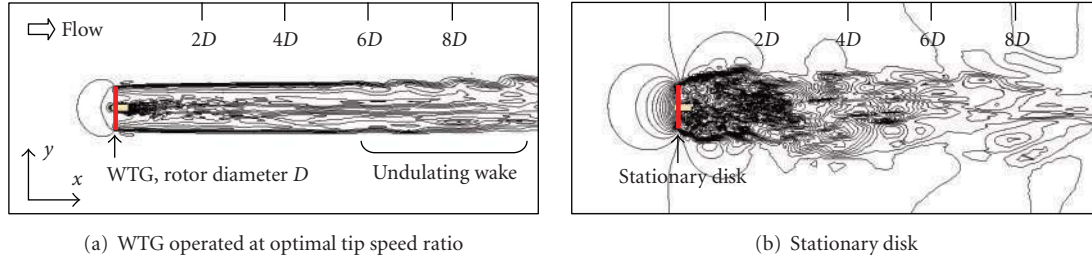


FIGURE 5: Contour plots of the streamwise ( $x$ ) velocity component,  $u$ , with 30 equally spaced contour intervals between  $u/U = -0.7$  and  $u/U = 1.4$ , instantaneous field, top view of entire domain at  $z = 0$ .

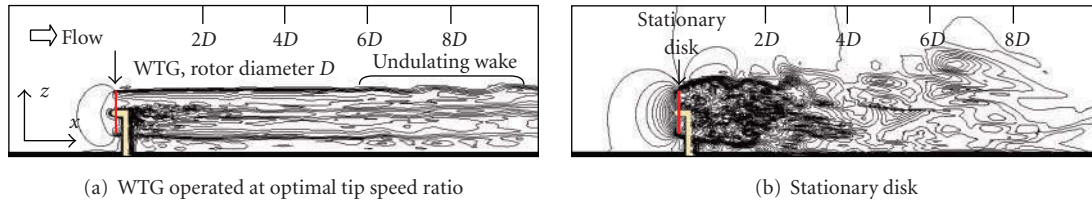


FIGURE 6: Contour plots of the streamwise ( $x$ ) velocity component,  $u$ , with 30 equally spaced contour intervals between  $u/U = -0.7$  and  $u/U = 1.4$ , instantaneous field, side view of entire domain at  $y = 0$ .

ratio and in the vicinity of the stationary disk, respectively. The former figure shows a cross-section of the streamwise ( $x$ ) wind velocity field viewed from top at  $z = 0$ , while the latter figure shows the same wind field viewed from the side at  $y = 0$ . In these figures, thirty equally spaced contour intervals are shown between  $u/U = -0.7$  and  $u/U = 1.4$ , and the entire computational domain is shown. The two figures suggest that the characteristics of the wake flow differ significantly between the WTG and the stationary disk. In the case of the WTG, the wake width is approximately the same as the rotor diameter, and undulating motions are observed in the wake at downstream distances larger than approximately  $6D$  as indicated in Figures 5 and 6. Furthermore, formation of strong tip vortices is evident at the blade tips of the WTG. It can be speculated that these vortices suppress the momentum exchange between the wake and its surrounding flow, and as a result, the wake width near the WTG is reduced approximately to the rotor diameter. However, at a downstream distance of approximately  $6D$ , the effect of the tip vortices becomes sufficiently weak for shear instability to cause undulations in the wake flow. In other words, the influence of the tip vortices generated at the optimal tip speed ratio extends to a downstream distance of at least  $6D$ .

In contrast, the characteristics of the wake flow behind the stationary disk are complex. A large area of reverse flow is formed immediately behind the stationary disk. As a result of the flow curling around the edge of the disk, the magnitude of the spanwise component of the flow behind the stationary disk is significantly larger than that behind the WTG (not shown). From the area of reverse flow, large vortices are shed periodically. The Strouhal number of the vortex shedding and the structure of the shed vortices behind the stationary disk are topics of high interest in fluid dynamics and will be investigated in future research. Figures 7 and 8 are enlarged

views of the flow near the WTG and disk in Figures 5 and 6, respectively, and also include the dynamic pressure field on the spinner, nacelle, and tower. The enlarged views provide confirmation of the above-mentioned differences between the wake flow around the WTG and that around the stationary disk. The same figures show vortex shedding from the individual components of the WTG, that is, spinner, nacelle, and tower, and the resulting formation of flow separation behind these components. Although not shown due to space limitations, a Karman vortex street was observed downstream of the WTG. These results suggest that analyses of the airflows simulated around an entire WTG rather than those around the individual components of a WTG are necessary in future discussions of vibrations of a WTG and the ability of a WTG to withstand high winds. To address these issues, the computational technique used in the present study may serve as an effective tool because it is user friendly and computationally inexpensive.

Figure 9 illustrates the streamlines of virtual fluid particles in the wake flows of the WTG operated at the optimal tip speed ratio and the stationary disk. In the case of the WTG (Figure 9(a)), a spiral flow forms as a result of the blade rotation. In contrast, in the case of the stationary disk (Figure 9(b)), complex three-dimensional streamlines are observed. These results confirm the presence of complex turbulent flow behind the stationary disk as shown in Figures 5–8.

A significant difference between the wake flow of the WTG and that of the stationary disk is also evident in the time-averaged fields of the streamwise ( $x$ ) component of the flow velocity (Figures 10 and 11). The time duration for obtaining the time-averaged streamwise velocity is  $t = 100(D/U)$ . These figures show the presence of a large region of reverse flow immediately behind the stationary

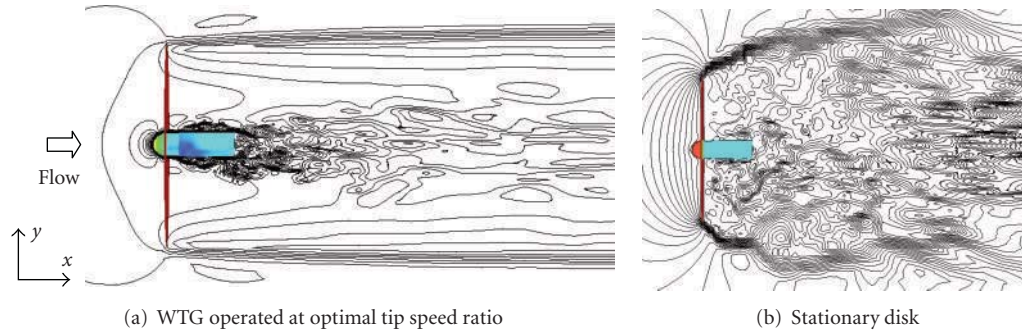


FIGURE 7: Enlarged view of Figure 5. The colors on the spinner and nacelle represent the dynamic surface pressure. Blue and red indicate the minimum (negative) and maximum values.

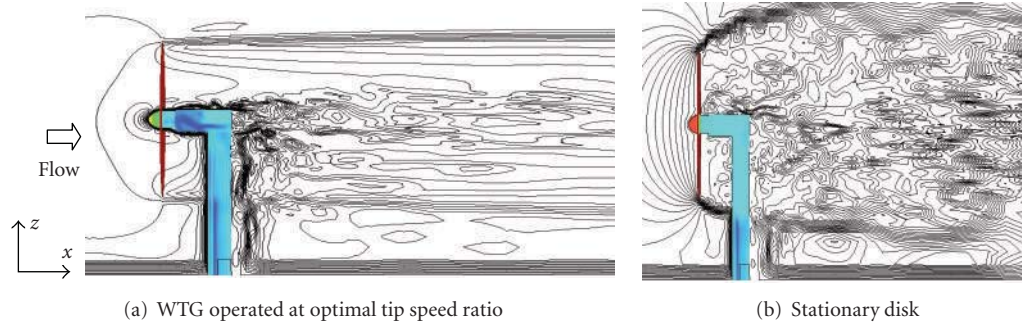


FIGURE 8: Enlarged view of Figure 6. The colors on the spinner, nacelle, and tower represent the dynamic surface pressure. Blue and red indicate the minimum (negative) and maximum values.

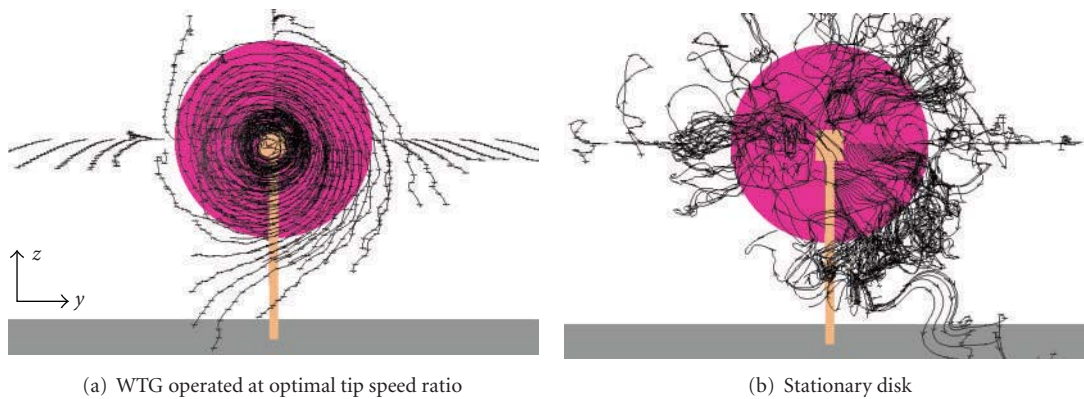


FIGURE 9: Flow visualization of the vortex structure of the wake flow. Rear view showing streamlines for the instantaneous field.

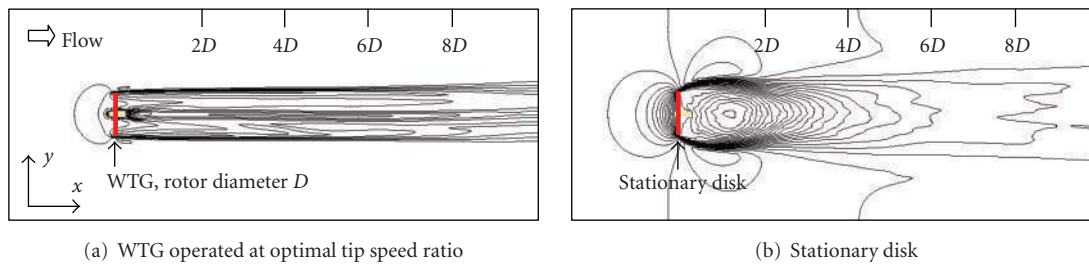


FIGURE 10: Contour plots of the streamwise ( $x$ ) velocity component,  $u$ , with 30 equally spaced contour intervals between  $u/U = -0.7$  and  $u/U = 1.4$ , time-averaged field, top view of the entire domain at  $z = 0$ .

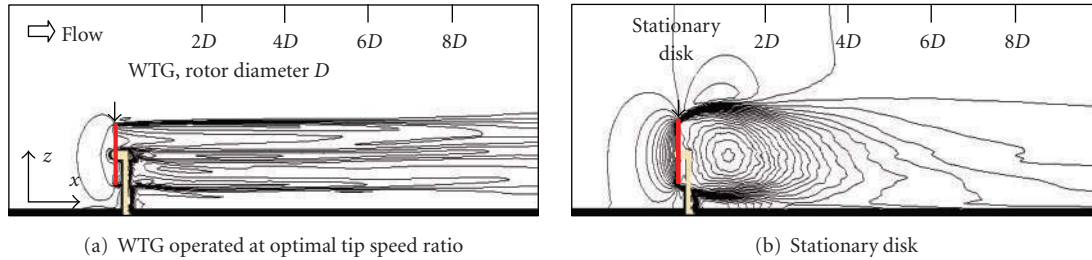


FIGURE 11: Same as Figure 10 except for side view of the entire domain at  $y = 0$ .

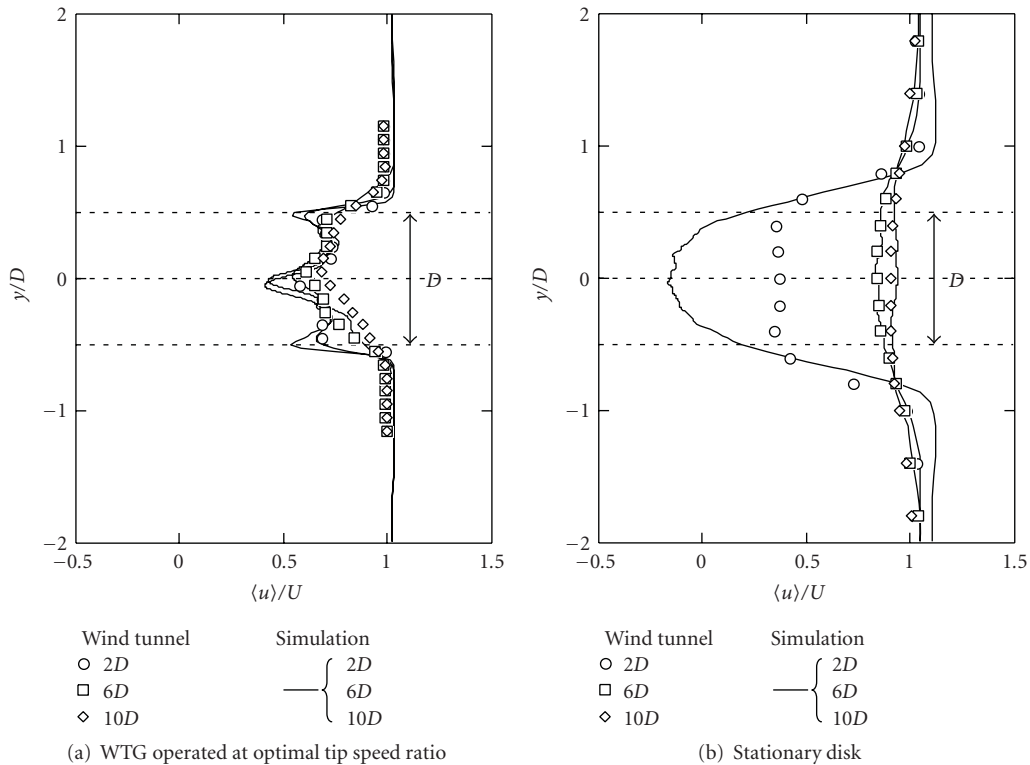


FIGURE 12: Spanwise profiles of the time-averaged streamwise ( $x$ ) velocity at  $z = 0$  ( $(x, y, z) = (0, 0, 0)$  indicates the center of the rotor; see Figure 3). The profiles are observed at  $x = 2D$  ( $\circ$ ),  $6D$  ( $\square$ ) and  $10D$  ( $\diamond$ ), where  $D$  is the rotor diameter. The streamwise velocity and the spanwise position on the  $y$ -axis are normalized by the uniform inflow velocity,  $U$ , and  $D$ , respectively. The  $y$ -coordinate of the rotor is shown with arrows.

disk; however, at a downstream distance of  $10D$ , the streamwise velocity deficit in the wake behind the disk is smaller than that behind the WTG.

To investigate this finding quantitatively, spanwise and vertical profiles of the time-averaged streamwise velocity are calculated (Figures 12 and 13). The profiles from the wind-tunnel experiments in these figures were obtained with an I-type hot wire probe. As for the spanwise profiles, the simulation (solid lines) and the experimental results (symbols) agree well for both the WTG and the stationary disk except for the profile at  $x = 2D$  in the wake of the stationary disk. The deviation of the spanwise profile in this case is attributable to the use of an I-type probe for the airflow measurement. The streamwise velocity deficits at a downstream distance of  $10D$  behind the center of the rotor are approximately 30–40% of the inflow velocity for the

WTG. These quantitative results confirm that the streamwise velocity deficit at a downstream distance of  $10D$  in the wake behind the disk is smaller than that behind the WTG. The large value of the velocity deficit behind the WTG is likely due to the tip vortices, the effect of which extends to a downstream distance of  $10D$ .

### 3. Conclusion

The present study investigated the characteristics of the wake flow behind a single wind turbine generator (WTG) operated at the optimal tip speed ratio. Even at a downstream distance of as large as ten-times the rotor diameter of a single WTG, the wind velocity behind the center of the rotor was approximately 30–40% of the inflow wind velocity. This large

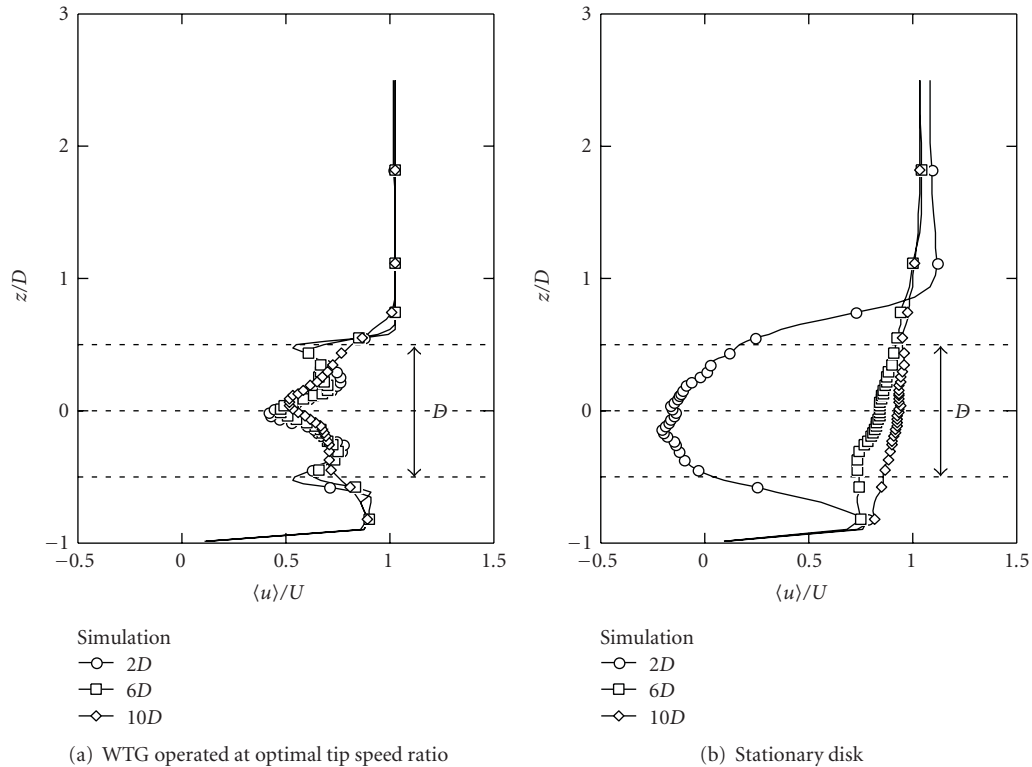


FIGURE 13: Same as Figure 12 except for the vertical profiles of time-averaged streamwise ( $x$ ) velocity at  $y = 0$ . The  $z$ -coordinate of the rotor is shown with arrows.

value of the wind velocity deficit was likely attributable to the tip vortices formed at the blade tips, which suppressed the momentum exchange between the wake flow of the WTG and the surrounding flow.

The wake of the WTG was also compared to that of a WTG with the rotor replaced by a stationary disk because existing wake models are based on the wake of a stationary disk. The diameter of the stationary disk was set equal to that of the rotor of the WTG. The wake flow of the WTG and that of the stationary disk were significantly different from each other. The wake flow of the stationary disk was characterized by a large area of reverse flow immediately behind the disk. However, at a downstream distance of  $10D$ , the streamwise velocity deficit in the wake behind the disk was smaller than that behind the WTG.

Our future research topics include investigations of the effects of the inflow turbulence on a WTG and turbulence distributions in the wake of a WTG. Numerical simulations of wake flows behind multiple WTGs are also planned as a future project.

## References

- [1] T. Uchida and Y. Ohya, "Micro-siting technique for wind turbine generators by using large-eddy simulation," *Journal of Wind Engineering and Industrial Aerodynamics*, vol. 96, no. 10–11, pp. 2121–2138, 2008.
- [2] L. P. Chamorro and F. Porté-Agel, "Effects of thermal stability and incoming boundary-layer flow characteristics on wind-turbine wakes: a wind-tunnel study," *Boundary-Layer Meteorology*, vol. 136, no. 3, pp. 515–533, 2010.
- [3] Y. Käsler, S. Rahm, R. Simmet, and M. Kühn, "Wake measurements of a multi-MW wind turbine with coherent long-range pulsed doppler wind lidar," *Journal of Atmospheric and Oceanic Technology*, vol. 27, no. 9, pp. 1529–1532, 2010.
- [4] M. Inagaki, T. Kondoh, and Y. Nagano, "A mixed-time-scale SGS model with fixed model-parameters for practical LES," *Journal of Fluids Engineering, Transactions of the ASME*, vol. 127, no. 1, pp. 1–13, 2005.
- [5] J. Kim and P. Moin, "Application of a fractional-step method to incompressible Navier-Stokes equations," *Journal of Computational Physics*, vol. 59, no. 2, pp. 308–323, 1985.
- [6] T. Kajishima, "Finite-difference method for convective terms using non-uniform grid," *Transactions of the Japan Society of Mechanical Engineers, Part B*, vol. 65, no. 633, pp. 1607–1612, 1999.
- [7] T. Kawamura, H. Takami, and K. Kuwahara, "Computation of high Reynolds number flow around a circular cylinder with surface roughness," *Fluid Dynamics Research*, vol. 1, no. 2, pp. 145–162, 1986.
- [8] <http://riodb.ibase.aist.go.jp/db060/index.html>.
- [9] J. N. Sørensen and A. Myken, "Unsteady actuator disc model for horizontal axis wind turbines," *Journal of Wind Engineering and Industrial Aerodynamics*, vol. 39, no. 1–3, pp. 139–149, 1992.
- [10] H. Snel, "Review of the present status of rotor aerodynamics," *Wind Energy*, vol. 1, pp. 46–69, 1998.

## Research Article

# Experimental and Numerical Simulations Predictions Comparison of Power and Efficiency in Hydraulic Turbine

Laura Castro,<sup>1</sup> Gustavo Urquiza,<sup>1</sup> Adam Adamkowski,<sup>2</sup> and Marcelo Reggio<sup>3</sup>

<sup>1</sup> Centro de Investigación en Ingeniería y Ciencias Aplicadas, Universidad Autónoma del Estado de Morelos, Avenida Universidad 1001, Col. Chamilpa, Cuernavaca, Morelos, CP 62209, Mexico

<sup>2</sup> The Szewalski Institute of Fluid-Flow Machinery, Polish Academy of Sciences, 80952 Gdansk, Poland

<sup>3</sup> Département de Génie Mécanique, Ecole Polytechnique de Montréal, 2500 Chemin de Polytechnique, Montréal, QC, Canada H3T 1J4

Correspondence should be addressed to Gustavo Urquiza, gurquiza@uaem.mx

Received 1 November 2010; Accepted 24 February 2011

Academic Editor: Guan Yeoh

Copyright © 2011 Laura Castro et al. This is an open access article distributed under the Creative Commons Attribution License, which permits unrestricted use, distribution, and reproduction in any medium, provided the original work is properly cited.

On-site power and mass flow rate measurements were conducted in a hydroelectric power plant (Mexico). Mass flow rate was obtained using Gibson's water hammer-based method. A numerical counterpart was carried out by using the commercial CFD software, and flow simulations were performed to principal components of a hydraulic turbine: runner and draft tube. Inlet boundary conditions for the runner were obtained from a previous simulation conducted in the spiral case. The computed results at the runner's outlet were used to conduct the subsequent draft tube simulation. The numerical results from the runner's flow simulation provided data to compute the torque and the turbine's power. Power-versus-efficiency curves were built, and very good agreement was found between experimental and numerical data.

## 1. Introduction

Nowadays, there is a clear need for low-degrading and low-polluting energy transformation processes. In this respect, wind and hydraulic turbines have taken an important role due to the intrinsic absence of combustion in the electricity production. Along this line of thinking, this work illustrates an effort taking place in Mexico which addresses the performance of hydropower stations and, in particular, the enhancement of the efficiency of the turbine components.

In Mexico, the energy generation through hydroelectric power plants corresponds to 22.14% of the total (11,094.90 MW) [1]. Most of these plants use turbines from the 1950s, and their current operating conditions are somehow different from those specified by the original design. It is, thus, necessary to assess the present conditions to look for possible modifications including optimization and corresponding refurbishing. In order to do this, it is essential to measure the water discharge. This task is not easy to perform in field conditions and is particularly complex in water power

plants with no access to the penstock from outside and with no suitable measurement installations prepared during construction. To solve this problem, the technique known as Gibson's method, by means of which the flow rate is obtained by integration in time of the pressure difference variation between two cross sections of the penstock, can be used.

Although Gibson's method has been recently improved [2], the handling of practical aspects still requires the installation of experimental apparatus (pressure transducer, gauges, holes, etc.) and, obviously, to operate the turbine in test rather than in production mode for a period of time. Considering this type of constraint, it is useful to apply computational fluid dynamics as an attempt to lower the cost of gathering experimental data.

In this work, both aspects have been considered. First, on-site measurements of flow rate and power were conducted at the hydropower plant in the state of Oaxaca in Mexico, then, simulations were performed using the commercial software ANSYS CFX to reproduce aspects of the real-life situation.

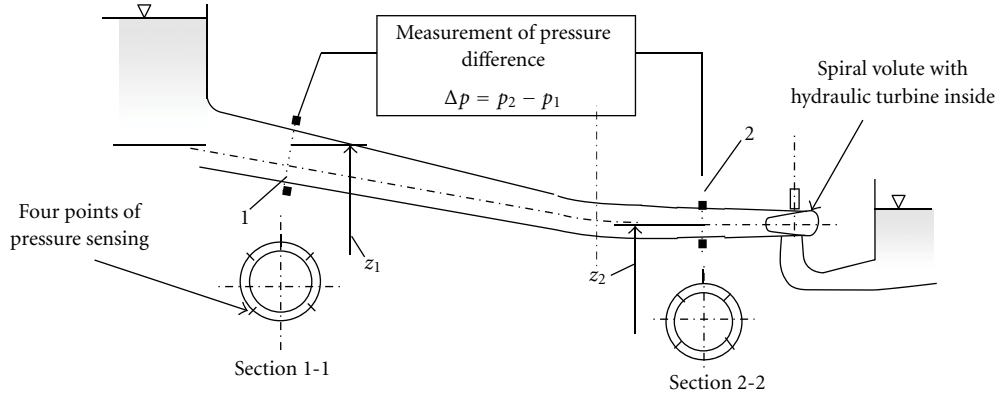


FIGURE 1: Penstock and measuring sections in Gibson's method.

## 2. Gibson's Method for Flow Measurements

This method, devised to measure the rate flow in a hydraulic turbine, is based on the water hammer phenomenon taking place in a closed pipe. It was introduced by Gibson [3], who benefitted from the work conducted by Jukowsky in 1898 concerning the water-hammer theory. Gibson's method measures a static pressure difference between two cross-sections of the penstock as a result of momentum variation caused by a quick closing of the wicket gates of the turbine. The flow rate is then obtained by integration, within a proper time interval ( $\sim 10$  s) [4–6]. Figure 1 illustrates the scheme of measuring in the penstock.

In order to derive a relationship for computing the flow rate  $Q$ , the following hypothesis are considered:

- (i) a closed pipe with a flow section area  $A$  that may change along its length,
- (ii) initial constant velocity and pressure fields between two given sections along of the penstock,
- (iii) that the water flow be completely stopped when the water hammer occurs,
- (iv) constants density and constant flow section during the water hammer.

Based in these assumptions, the relation between the parameters of the one-dimension unsteady flow between two selected sections of the pipe can be described using the energy balance equation

$$\frac{\rho v_1^2}{2} + p_1 + \rho g z_1 = \frac{\rho v_2^2}{2} + p_2 + \rho g z_2 + \Delta p_f + \rho \int_0^L \frac{\partial v}{\partial t} dx. \quad (1)$$

Considering  $Q = vA$ , the above equation becomes [6]:

$$\begin{aligned} \frac{\rho Q^2}{2A_1^2} + p_1 + \rho g z_1 &= \frac{\rho Q^2}{2A_2^2} + p_2 + \rho g z_2 + \Delta p_f \\ &+ \rho \int_0^L \left( \frac{dQ}{dt} \right) \frac{dx}{A(x)}. \end{aligned} \quad (2)$$

Integrating this equation between time interval  $(t_0, t_k)$ , and grouping terms yields:

$$Q_0 = \frac{1}{\rho C} \int_{t_0}^{t_k} [\Delta p(t) + \Delta p_d(t) + \Delta p_f(t)] dt + Q_k, \quad (3)$$

where  $Q_0 = v_0 A$  represents the flow rate at steady state before closing the wicket gates,  $\Delta p = p_2 + \rho g z_2 - p_1 - \rho g z_1$  indicates pressure difference between sections 1 and 2,  $\Delta p_d = \rho Q^2 / 2A_2^2 - \rho Q^2 / 2A_1^2$  Denotes dynamic pressure difference between sections 1 and 2,  $Q_k$ : Flow rate measured in the leaking test (ideally should be 0), and  $C =$  specifies the geometrical modulus of the penstock segment of a length  $L$  given by

$$C = \int_0^L \frac{dx}{A(x)}. \quad (4)$$

For a penstock with constant diameter  $C = L/A$ .

The leakage flow  $Q_k$  is determined by the empirical equation

$$Q_k = \mu A_s \sqrt{\frac{2\Delta p_k}{\rho}}. \quad (5)$$

## 3. Measurement Instrumentation

To carry out the measurements, two separate systems of signal acquisition were used [4]; the first consisted of a laptop computer and a 16 bits signal acquisition conditioning module card. The second consisted of a National Instrument PXI1010 system with signal acquisition module SCXI 16-bit card. The two pressure transducers used for testing were PS-2p (Vist, Gdańsk, Poland): range 0–700 kPa (relative) with accuracy of 0.1% and temperature compensated output current of 4–20 mA calibrated by the manufacturer and on site. In the case of the transducers of section 2-2, they were checked for calibration before the test. Figure 2 shows the scheme of the sensing points on penstock, and Figure 3, the waterproof manifold installed, with the pressure transducer, for measurements.

The signal acquisition system, in addition to capturing the behavior of the pressure, also recorded the opening of the

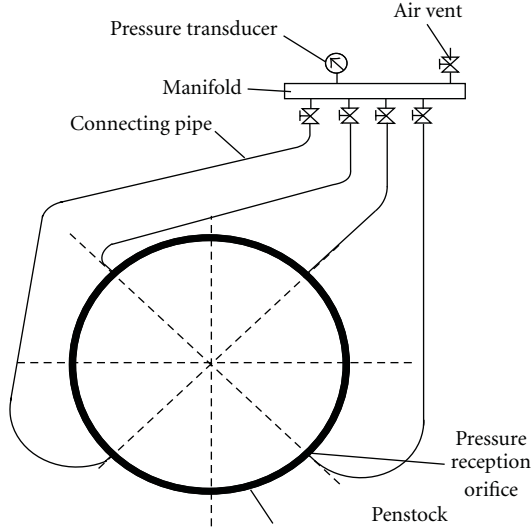


FIGURE 2: Scheme of sensing points.

wicked gates, the active power, and the level of tailwater. The level in the tailwater was measured manually and compared with indications from the pressure measured in Section 2-2; these measurements were necessary to calculate the efficiency of the turbine.

The data recording was made with the sampling frequency of 500 Hz, and the files are prepared in ASCII format with 100 Hz frequency. The flow rate was calculated with the program GIB-ADAM developed in the Szewalski Institute of Fluid-Flow Machinery in Poland [2, 6]. Each measurement required a quick closing of the distributor and the generator being connected to the network and in stable condition.

#### 4. Measurements Results

The flow rate was determined from the recorded pressure time histories using a GIB-ADAM [4] program. Figure 4 shows a sample of record of the time history of turbine guide vane closure and the differential pressure between the measuring sections of the penstock.

Once made, the 8 rejects of charge and recorded all the data. Flow measurements were conducted in five loading conditions: 25%, 50%, 75%, 85%, and 100% of load. A summary of measurements is show on Table 1.

#### 5. Governing Equations for Flow Simulation

For simulations a three-dimensional incompressible flow was considered, with constant properties and isothermal at 25°C.  $k$ - $\epsilon$  turbulence model standard. The flow inside the suction tube is described by the Navier-Stokes-Reynolds averaging for the  $k$ - $\epsilon$ .

*Continuity:*

$$\frac{\partial \rho}{\partial t} + \nabla \cdot (\rho \mathbf{U}) = 0, \quad (6)$$

where

$$\nabla = \left[ \frac{\partial}{\partial x}, \frac{\partial}{\partial y}, \frac{\partial}{\partial z} \right], \quad (7)$$

$$\mathbf{U} = \bar{\mathbf{U}} + \mathbf{u},$$

where  $\bar{\mathbf{U}} = (1/\Delta t) \int_t^{t+\Delta t} \mathbf{U} dt$ .

*Momentum:*

$$\begin{aligned} \frac{\partial \rho \mathbf{U}}{\partial t} + \nabla \cdot (\rho \mathbf{U} \otimes \mathbf{U}) - \nabla \cdot (\mu_{\text{eff}} \nabla \mathbf{U}) \\ = \nabla p' + \nabla \cdot (\mu_{\text{eff}} \nabla \mathbf{U})^T + \mathbf{B}, \end{aligned} \quad (8)$$

where  $\mathbf{B}$  is the sum of efforts,  $\mu_{\text{eff}}$  is the effective viscosity for turbulence, and  $p'$  is the modified pressure gives by

$$p' = p + \frac{2}{3} \rho k, \quad (9)$$

$$\mu_{\text{eff}} = \mu + \mu_t,$$

$k$ - $\epsilon$  model assumes that the turbulent viscosity is related to the turbulent kinetic energy and dissipation via the relation

$$\mu_t = C_{\mu} \rho \frac{k^2}{\epsilon}. \quad (10)$$

The values of  $k$  and  $\epsilon$  come directly from the transport equations for turbulent kinetic energy and dissipation range of turbulence

$$\begin{aligned} \frac{\partial (\rho k)}{\partial t} + \nabla \cdot (\rho \mathbf{U} k) = \nabla \cdot \left[ \left( \mu + \frac{\mu_t}{\sigma_k} \right) \nabla k \right] + P_k - \rho \epsilon, \\ \frac{\partial (\rho \epsilon)}{\partial t} + \nabla \cdot (\rho \mathbf{U} \epsilon) \end{aligned} \quad (11)$$

$$= \nabla \cdot \left[ \left( \mu + \frac{\mu_t}{\sigma_{\epsilon}} \right) \nabla \epsilon \right] + \frac{\epsilon}{k} (C_{\epsilon 1} P_k - C_{\epsilon 2} \rho \epsilon),$$

where  $C_{\epsilon 1}$ ,  $C_{\epsilon 2}$ ,  $\sigma_k$ , and  $\sigma_{\epsilon}$  are constants and  $P_k$  is the production of turbulence due to the forces of viscosity which is modeled as follows:

$$\begin{aligned} P_k = \mu_t \nabla \mathbf{U} \cdot (\nabla \mathbf{U} + \nabla \mathbf{U}^T) \\ - \frac{2}{3} \nabla \cdot \mathbf{U} (3\mu_t \nabla \cdot \mathbf{U} + \rho k) + P_{kb}. \end{aligned} \quad (12)$$

To incompressible flow,  $\nabla \cdot \mathbf{U}$  is small, and the second term at the right from equation does not contribute significantly in production.

*5.1. Numerical Analysis.* The commercial software used employs the finite volume numerical method for solving the RANS equations and  $k$ - $\epsilon$  standard model. To perform the numerical simulations, we used an unstructured mesh of 1,759,261 elements for the runner and a structured mesh of 1,024,956 elements for draft tube. Simulations were run on

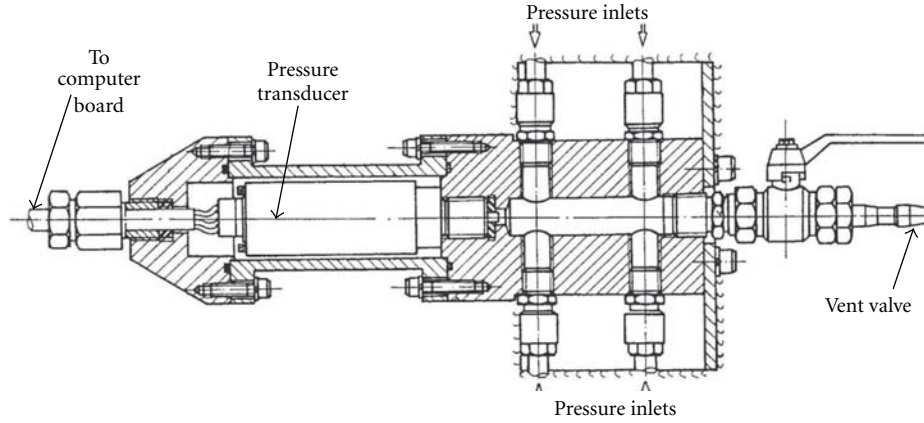


FIGURE 3: A waterproof manifold with details of the absolute pressure transducer location.

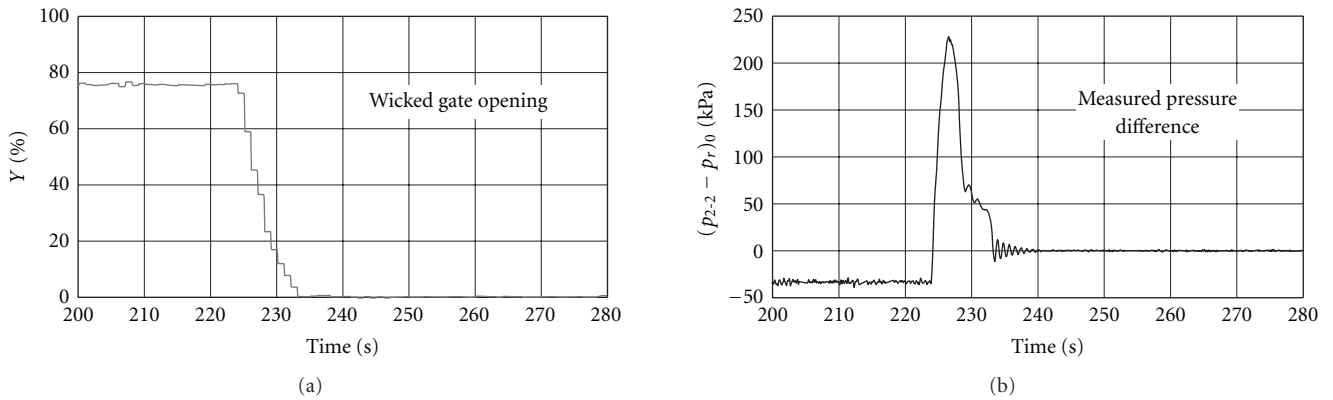


FIGURE 4: Guide vane closure percentage and change in pressure between section 2-2 depending on time  $t$ .

an HP Pavilion PC with two Intel 1.66 GHz each, with 2 GB of RAM.

To perform the numerical simulations, measurement results in Tests 1, 3, 5, 6, and 8 showed in Table 1 were used.

The selected convergence criteria of the numerical simulations was RMS (root mean square) normalized values of the equation residuals with a value of E-006.

5.2. *Boundary Conditions.* In the runner, the boundary conditions were stipulated as follows:

- (i) inlet: defined as Mass flow inlet,
- (ii) turbulence intensity:  $k$ -  $\varepsilon$  from spiral case,
- (iii) outlet: defined as Static Pressure (measured at the inlet of draft tube),
- (iv) turbulence intensity: zero gradient,
- (v) blade, shroud and hub: were defined as wall with no movement and as a smooth surface.

## 6. Results of Simulation

Before obtaining the final results of the numerical simulation, we carried out a mesh independence analysis called

grid convergence index (GCI for its acronym) to estimate the percentage of error in the solution. According to the work done by Roache [7], this is calculated by the following equation:

$$GCI = \frac{3|\varepsilon|}{r^p - 1}, \quad (13)$$

where

$$r = \frac{h_2}{h_1}, \quad (14)$$

$$\varepsilon = \frac{f_2 - f_1}{f_1},$$

where  $\varepsilon$  is the relative difference between the results of torque (a parameter selected, in this case, the most important to calculate the power of the runner) for the finest  $f_1$  and  $f_2$  for the coarsest,  $r$  is the ratio between the size of the element of finest mesh ( $h_1$ ) and coarsest ( $h_2$ ), and  $p$  is the order of the method used for the reference solutions; in this case, it was used second order. Table 2 shows the results of the analysis.

Considering the processing time and storage volume of the files generated by numerical simulation results, to

TABLE 1: Summary of measurements.

Test number	Opening of the wicket gate $Y$ [%]	Mechanical power $P_{\text{mech}}$ [MW]	Flow rate $Q_0$ [ $\text{m}^3/\text{s}$ ]	Leakage flow $Q_k$ [ $\text{m}^3/\text{s}$ ]	Total flow $Q_{\text{turbine}}$ [ $\text{m}^3/\text{s}$ ]	Net head $H_n$ [m]	Efficiency $\eta_t$ [%]
1	98.8	31.65	88.97	0.7	89.67	42.40	85.10
2	86.7	30.71	81.30	0.7	82.00	42.64	89.80
3	78.4	29.03	75.44	0.7	76.14	42.75	91.16
4	69.5	26.05	68.03	0.7	68.73	43.09	89.91
5	61.4	22.63	60.29	0.7	60.99	43.18	87.84
6	52.9	19.02	52.20	0.7	52.90	43.27	84.92
7	45.5	15.72	45.41	0.7	46.11	43.52	80.08
8	36.7	10.14	34.98	0.7	35.68	44.10	65.89

TABLE 2: Analysis GCI.

Mesh number	No. of elements	Average size of element [mm]	Torque [J]	$\epsilon$	$r$	GCI	GCI [%]
1	795,618	200	1,583,510				
2	965,632	150	1,613,960	-0.0189	1.33	0.0728	7.2771
3	1,759,261	75	1,634,405	-0.0125	2.00	0.0125	1.2509
4	3,284,658	50	1,638,950	-0.0028	1.50	0.0067	0.6655

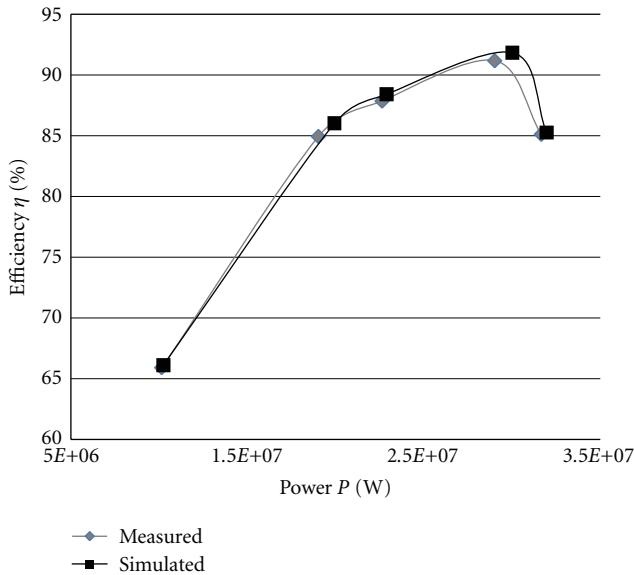


FIGURE 5: Efficiency curves.

obtain the final results mesh no. 3 was selected, which has a convergence index that is reasonable (according to references, it is ideal when it is less than 1.5)

**6.1. Runner.** From the simulations on the runner, torque was obtained, with which it proceeds to the calculation of mechanical power and compare it with the measurements. The results are presented in Table 3 and Figure 5.

At the point of 91.16% efficiency, special attention was taken on the results of simulations, which should be analyzed

carefully, as these results represent the maximum efficiency. One of the most important issues is the cavitation; in Figure 6, pressure contours do not show low pressure points over the blade that could produce it.

Figure 7 shows the blade loading, and it can be seen that there are no sudden changes in pressure around the blade, as well as negative pressure, which provides evidence that there is no possibility that air bubbles could form and cause cavitation.

In Figure 8, the velocity vectors show that the flow does not produce eddies when passing through the runner.

**6.2. Draft Tube.** From the results of simulations on the runner, the boundary condition at the draft tube inlet for different measured flow rates was obtained; thereby, the behavior in this component was discovered, which is significant because it is very difficult to make direct measurements.

Figures 9 and 10 show streamlines and pressure contours in the draft tube at different flow rates. The behavior of the flow in this component is expected as observed in the literature [1, 8–10]. The draft tube has the function of discharging water from a turbine, in addition to acting as a device for energy recovery, helping to improve the overall performance of the unit. It can also allow the water level downstream to be lower or higher than the equatorial plane of the turbine, according to the installation needs. The draft tube, because of its divergent shape, produces a slowdown velocity of the water leaving the turbine, converting fluid kinetic energy into pressure energy (Figure 10).

In Figure 9, it can be observed that as the flow moves into the tube, their behavior is changing and the speed at the elbow down to about half the initial velocity. Besides, because of the pier on the draft tube, there is a separation of the flow,

TABLE 3: Comparison between numerical and experimental data.

$Q_{\text{Turbine}}$ [ $\text{m}^3/\text{s}$ ]	Power measured [MW]	Power simulated [MW]	Efficiency measured [%]	Efficiency simulated [%]
89.67	31.65	31.95	85.10	85.25
76.14	29.03	30.02	91.16	91.82
60.99	22.63	22.88	87.84	88.39
52.90	19.02	19.93	84.92	86.00
35.68	10.14	10.23	65.89	66.09

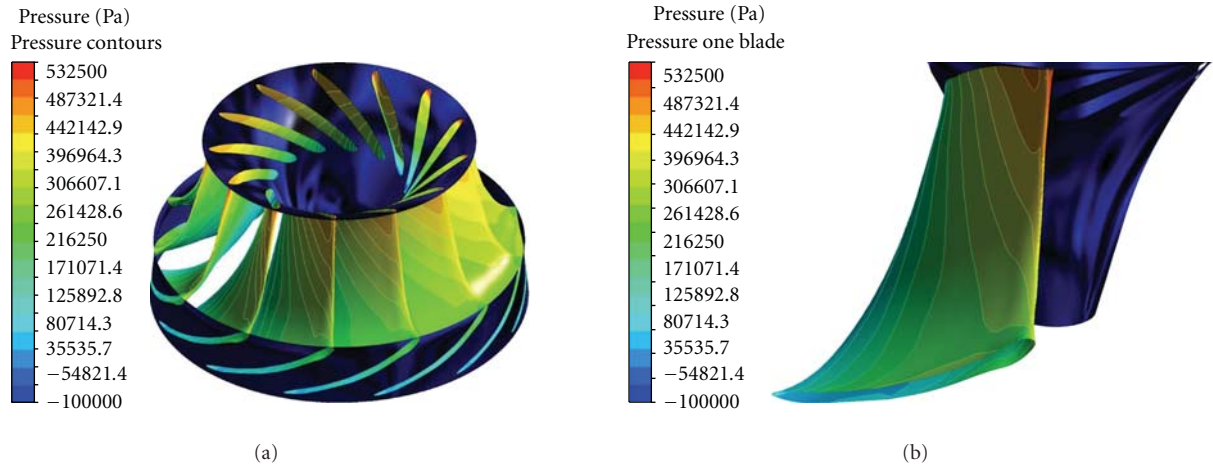


FIGURE 6: (a) Pressure contours at  $76.14 \text{ m}^3/\text{s}$ , (b) Pressure contours at one blade.

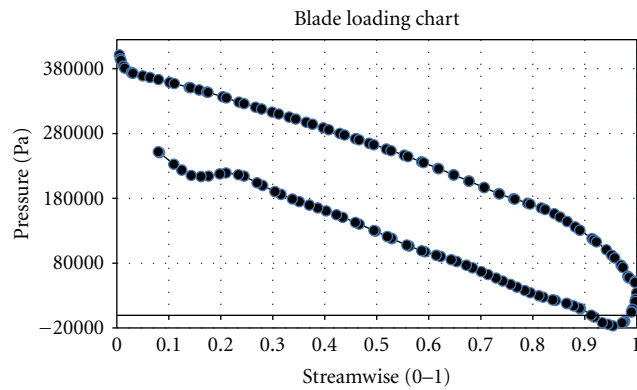


FIGURE 7: Blade loading in midspan, at  $76.14 \text{ m}^3/\text{s}$ .

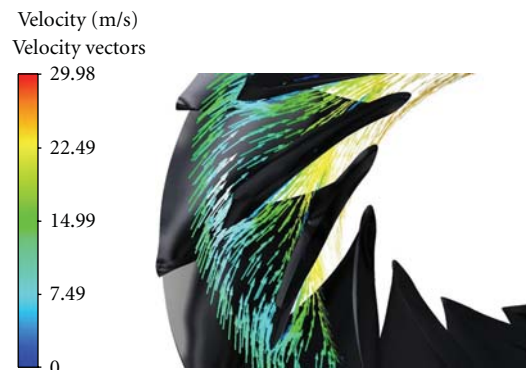


FIGURE 8: Velocity vectors at midspan.

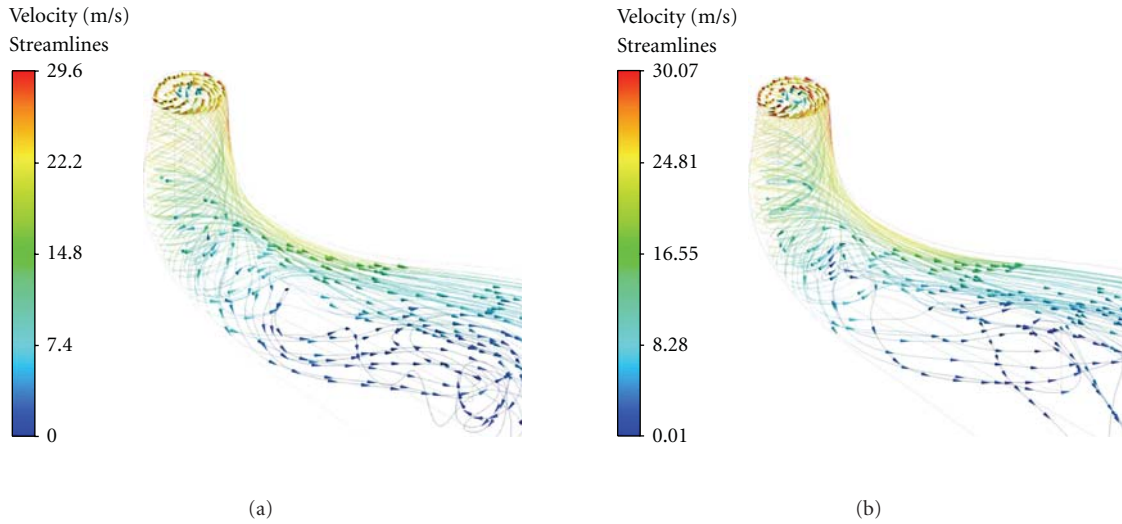


FIGURE 9: Streamlines at different flow rates (a)  $76.14 \text{ m}^3/\text{s}$  and (b)  $89 \text{ m}^3/\text{s}$ .

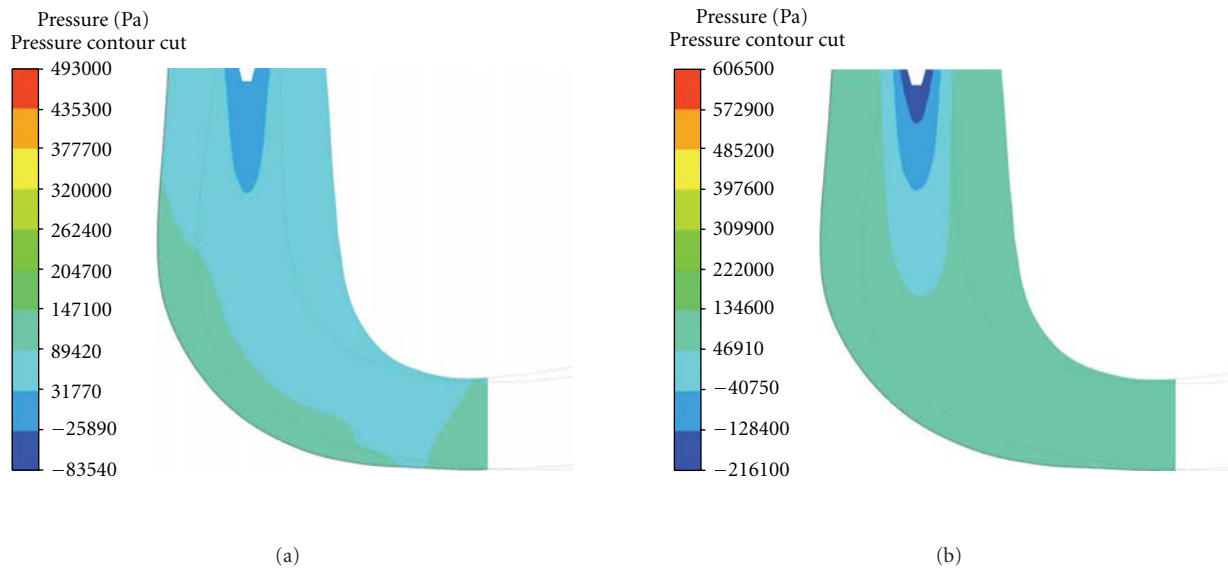


FIGURE 10: Pressure contours in cross-section at different flow rates (a)  $76.14 \text{ m}^3/\text{s}$  and (b)  $89 \text{ m}^3/\text{s}$ .

and the velocity decreases further in the side where the vortex produced by the runner is directed.

With these results, we will propose amendments to this component geometry to increase efficiency.

### 7. Conclusions

The mechanical power and efficiency obtained from the simulations have good agreement with those obtained on-site measurements.

From the results at the maximum efficiency, adverse conditions in the flow will not appear, so the turbine can work properly at this head, and thereby improve the performance of flow in the unit of study.

Therefore, these results can be considered reliable enough for the speeds at the exit of the runner and could be used in the boundary condition at the entrance of the draft tube.

The results show that the flow in draft tube is sufficiently approximate to the actual flow, according to revised bibliography.

## Notation

$\rho$ :	Density
$z_{1,2}$ :	Hydrometric levels
$\Delta p_f$ :	Pressure drop caused by friction losses
$Q_0$ :	Flow before the closing of the wicked gates
$Q_k$ :	Leakage flow
$C$ :	Geometrical modulus of the penstock segment
$L$ :	Length of the segment of the penstock
$A$ :	Transversal area of the penstock
$\mu$ :	Ratio of slack flow (0.65–0.7)
$A_s$ :	Clear area of the wicked gate
$\Delta p_k$ :	pressure difference between inlet and outlet of the distributor
$\eta_x$ :	Recovery ratio
$G$ :	Acceleration of gravity
$Re$ :	Reynolds Number
$D$ :	Diameter
$\nu$ :	Kinematic viscosity
$\dot{m}$ :	Mass flow
$\mu$ :	Dynamic viscosity
$C_\mu$ :	Empirical constant
$K$ :	Kinetic turbulent energy
$\varepsilon$ :	Turbulence dissipation rate
$U$ :	Axial velocity
$V$ :	Radial velocity
$W$ :	Tangential velocity
$P$ :	Static pressure
$\mu_{\text{eff}}$ :	Effective viscosity
$\mu_T$ :	Turbulent viscosity
$C_{\varepsilon 1}$ :	Turbulence constant
$C_{\varepsilon 2}$ :	Turbulence constant
$\sigma_k$ :	Turbulence constant
$\sigma_\varepsilon$ :	Turbulence constant
$P_k$ :	Turbulence production by viscosity forces
$\tau_\omega$ :	Shear stress
$\kappa$ :	Von Karman constant
GCI:	Grid Convergence Index
$\varepsilon$ :	Relative error
$R$ :	Element size ratio
$C_p$ :	Pressure coefficient
$\bar{p}$ :	Average static pressure
$V$ :	Volume
$\omega$ :	Turbulence frequency
$\eta_t$ :	Efficiency
$Q_t$ :	Flow
$P_m$ :	Mechanical power.

## Acknowledgments

The authors are grateful to the Federal Electricity Commission (CFE) for the facilities provided for the present study and to the National Council of Science and Technology (CONACYT) for the scholarship granted to the Ph.D. student.

## References

- [1] L. Castro, *Análisis del flujo turbulento en un tubo de aspiración de turbina hidráulica*, Tesis de maestría, UAEM-CIICAP, Cuernavaca, México, May 2008.
- [2] J. Kubiak, G. Urquiza, A. Adamkowski, F. Sierra, W. Janicki, and R. Rangel, "Special instrumentation and hydraulic turbine flow measurements using a pressure-time method," in *Proceedings of the ASME Fluids Engineering Division Summer Conference*, vol. 2, pp. 433–439, Houston, Tex, USA, June 2005.
- [3] N. R. Gibson, "The Gibson method and apparatus for measuring the flow of water in closed conduits," *ASME Power Division*, pp. 343–392, 1923.
- [4] G. Urquiza, J. Kubiak, A. Adamkoswki, and W. Janicki, "Resultados de medición de flujo y cálculo de eficiencia de la unidad no. 4 en la C. H. Temascal," Tech. Rep. 77P/DM/CIICAP.
- [5] IEC 41, International Standard: Field acceptance tests to determine the hydraulic performance of hydraulic turbines, storage pumps and pump-turbines, 1991.
- [6] A. Adamkowski, W. Janicki, J. Kubiak, G. Urquiza, E. F. Sierra, and R. Rangel, "Water turbine efficiency measurements using the gibson method based on special instrumentation installed inside pipelines," in *Proceedings of the 6th International Conference on Innovation in Hydraulic Efficiency Measurements*, Portland, Ore, USA, July-August 2006.
- [7] P. J. Roache, *Fundamentals of Computational Fluid Dynamics*, Hermosa Publishers, Albuquerque, NM, USA, 1998.
- [8] S. Mauri, *Numerical simulation and flow analysis of an elbow diffuser*, Ph.D. thesis, Ecole Polytechnique Fédérale de Lausanne, Lausanne, Switzerland, 2002, Tesis Doctoral no. 2527.
- [9] T. C. Vu and W. Shyy, "Navier-Stokes flow analysis for hydraulic turbine draft tubes," *Journal of Fluids Engineering, Transactions of the ASME*, vol. 112, no. 2, pp. 199–204, 1990.
- [10] M. Agouzoul, M. Reggio, and R. Camarero, "Calculation of turbulent flows in a hydraulic turbine draft tube," *Journal of Fluids Engineering, Transactions of the ASME*, vol. 112, no. 3, pp. 257–263, 1990.

## Research Article

# Simulating Smoke Filling in Big Halls by Computational Fluid Dynamics

W. K. Chow, C. L. Chow, and S. S. Li

*Research Centre for Fire Engineering, Department of Building Services Engineering, Area of Strength: Fire Safety Engineering, The Hong Kong Polytechnic University, Kowloon, Hong Kong*

Correspondence should be addressed to W. K. Chow, beelize@polyu.edu.hk

Received 15 November 2010; Accepted 18 January 2011

Academic Editor: Guan Yeoh

Copyright © 2011 W. K. Chow et al. This is an open access article distributed under the Creative Commons Attribution License, which permits unrestricted use, distribution, and reproduction in any medium, provided the original work is properly cited.

Many tall halls of big space volume were built and, to be built in many construction projects in the Far East, particularly Mainland China, Hong Kong, and Taiwan. Smoke is identified to be the key hazard to handle. Consequently, smoke exhaust systems are specified in the fire code in those areas. An update on applying Computational Fluid Dynamics (CFD) in smoke exhaust design will be presented in this paper. Key points to note in CFD simulations on smoke filling due to a fire in a big hall will be discussed. Mathematical aspects concerning discretization of partial differential equations and algorithms for solving the velocity-pressure linked equations are briefly outlined. Results predicted by CFD with different free boundary conditions are compared with those on room fire tests. Standards on grid size, relaxation factors, convergence criteria, and false diffusion should be set up for numerical experiments with CFD.

## 1. Introduction

Many fire models have been developed for studying pre-flashover fire and reported in the literature [1–3]. Computational Fluid Dynamics (CFD) or known as field models [4, 5], originally developed for fire simulations, are widely applied in smoke management system design. Development of fire field models started 30 years ago [6–10] at leading institutes all over the world. These are the Building Research Institute [11] and Tokyo University of Science in Japan; Notre Dame University [12] and the Fire Research Centre, National Bureau of Standards [13] in the USA; and the Fire Research Station [14] in the UK. Later, it was known as application of CFD [15] in mid 1990s. This was much widely applied when some of the research CFD softwares became commercial packages. Progress in CFD research for building fire applications was very slow in the past 10 years as explained in above. Most of the efforts were on applying CFD in performance-based design (PBD) on fire safety provisions. Fire Dynamics Simulator (FDS) [9, 10] is now commonly used.

Applications are now restricted to only smoke exhaust systems including both static smoke extract system or natural

venting, and dynamic smoke extract system with mechanical fans. Building fire is a low-speed chemically reacting flow [16] dominated by buoyancy [17]. Three key fluid flow phenomena [4, 5, 16, 17] on scalar transport are dominated by buoyancy-induced turbulence; heat transfer with thermal radiation at the burning object and the associated combustion chemistry involving hundreds of intermediate chemical reactions [18, 19] should be considered at the same time. It is difficult to develop a simple CFD model to include all these three parts realistically without using any simpler models with empirical parameters.

However, there are always difficulties in finding resources for in-depth research as pointed out [20, 21]. On the other hand, many engineers with some CFD training were recruited as fire engineers for handling PBD [22, 23] on building fire safety. Most of research efforts were therefore spent on applying CFD in building applications and generating beautiful graphics presentation, rather than working or getting more advanced CFD fires.

Therefore, CFD model was only used for designing smoke movement and design of air handling system such as smoke exhaust systems [24] or tunnel ventilation system.

Although the computing time required is still long, CFD has been improved with efficient numerical schemes. Faster personal computers with larger memory capacity are now available. Fluid flow problems up to 10 millions of computing cells can be accommodated with true 64-bit operating system. However, the computing time still takes several days. Efforts were even made on developing standards on using fire models [25, 26], but how?

It was believed [3, 15, 27] in 1990s that CFD field model has the greatest potential to simulate building fires as discussed in several classical publications [6–8]. A fire was taken as a heat source generating convective flow by buoyancy. A system of coupled, nonlinear, partial differential equations was set up on conservation of momentum, heat, and mass of smoke induced by fire. Temperature and velocity fields induced by the fire source were predicted. This approach is physical and incorporates basic principles supposed to predict more detailed information with minimum experimental data input. CFD model is good for predicting the thermal environment in big enclosures such as an atrium or a tunnel, though it is less suitable for regions near to a fire. The model should be developed by studying further on thermal radiation, combustion chemistry for common building materials, and turbulent mixing with air. Further, very few experimental verification and validation [28] were reported [28–31]. Most of the experimental data used for justifying CFD results are originally for studying fire zone models [32]. In fact, very limited systematic full-scale experimental works, except some by Ingasson and Olsson [33] on sprinkler fires and natural vents, were specially designed for justifying CFD models. The data reported by Steckler et al. [34] was performed originally for studying the doorway flow, but always used for verifying field models because of having many data at different positions. However, such limited studies did not give any promising results on CFD predictions as indicated by the VVT-FDS [35] study. Validation works were started as a longer-term project by the US Nuclear Regulatory Commission [36]. Therefore, CFD are limited on studying smoke movement in regions far away from the fire, to avoid simulating combustion and thermal radiation effects. Even so, there are always challenges on accepting design based on CFD predictions. Consequently, field tests are required to evaluate whether the system will perform as the design. Atrium hot smoke test [37–41] is then required in many places of the Far East. There are also problems in training sufficient number of government officers, engineers and facilities managers to understand CFD. An updated review on applying CFD in designing smoke exhaust system is presented in the paper.

## 2. Smoke Filling

Fire is taken [6–8, 10] as a physiochemical system of momentum, heat and mass transfer. A set of nonlinear and coupled partial-differential equations governing the conservation of momentum, heat, and mass are set up to describe the fire system. Whenever a fire occurs, natural convective flow fields would be generated, with the general

form of the conservation law for a time-averaged fluid property. The thermal power from a fire in an enclosure is of the order of megawatt, such as that produced by burning a polyurethane foam sofa. The resultant flow is turbulent and appropriate for the use of turbulence models.

There are three main parts [4, 5] in a CFD field model: turbulence in simulating the buoyancy induced motion, discretization of the set of partial differential equations, and algorithms in solving the velocity-pressure linked equations.

CFD predictions are mainly applied for designing smoke exhaust system in big space, particularly in atrium and tunnel. Static smoke extraction system is not so welcome by the Authority. Any change in the surrounding air pressure distribution due to wind or any other thermal perturbations will give very different system performance. Therefore, it is only suitable for small buildings with very low occupant loading, such as air cargo terminals. Performance of static smoke extraction system in crowded spaces such as shopping malls and public transport interchanges, particularly those located in deep underground, should be justified seriously by fire science and engineering. The scenario of pushing smoke down from air above must be demonstrated by full-scale burning tests that it would not happen. The design should not be accepted without such justification.

Other parameters including numerical parameters for stability and convergence such as relaxation factors, convergence criteria, residuals, and time steps, and parameters concerned in free boundaries, orifice coefficient of the openings, and how long the computing domain has to be extended to outside from an opening must be justified. Values of all these parameters should be selected very carefully with experiment. Different problems should be simulated by “trial and error” numerical experiments first.

## 3. Turbulence Model

Two common approaches [6, 10] were used to simulate turbulent flow. These are the Reynolds Averaging of Navier-Stokes Equation (RANS) method and Large Eddy Simulation (LES).

The time-averaged values of the air flow variables including the momentum, density, pressure, enthalpy, and smoke concentration are solved using RANS. Any instantaneous value for these variables  $\phi_t$  is expressed as its time-averaged value  $\phi$  plus the fluctuation  $\phi'$ . The set of equations describing conservation laws on  $\phi_t$  can be transformed in terms of  $\phi$  with the product of the fluctuation terms  $\phi'$  for different flow variables separated out. Different turbulent models (e.g., [6]) have been proposed to close the set of equations to make it look similar to those for  $\phi_t$ , but the diffusion coefficient concerned becomes an effective value which is much greater than the laminar one. The  $k$ - $\epsilon$  model family of turbulent model is commonly used in simulating fire-induced flow fields. Time averages of the velocity vector components  $u, v, w$  (in a Cartesian coordinate system), the enthalpy  $h$  and the turbulence parameters  $k$  and  $\epsilon$  are then taken as  $\phi$ . There are many CFD packages based on RANS available in the literature in the 1990s. Commercial software was used to

have a preprocessor menu for putting in building geometry. Because of the hardware limitation, CFD model based on RANS had been applied for designing smoke management systems in big halls and tunnels. However, there are criticisms on the accuracy due to grid size and boundary condition. The model cannot simulate combustion realistically and hence to predict carbon monoxide and soot concentrations in a fire.

In LES, turbulent motion is decomposed as large- and small-scale motions by filtering. The large-scale flow structures are calculated numerically by solving the differential equations concerned. Small-scale motions are modeled by subgrid-scale Reynolds stresses (e.g., [10]). The first step of LES is filtering. A flow variable  $\phi(\vec{x}, t)$  at position  $\vec{x}$  and time  $t$  is decomposed into a large-scale component  $\bar{\phi}(\vec{x}, t)$  and a small-scale (subgrid-scale) component  $\phi'(\vec{x}, t)$ . The large-scale component  $\bar{\phi}(\vec{x}, t)$  is a spatial average through a function  $G(\vec{x} - \vec{x}', \Delta)$  in the domain of interest  $\Omega$  through a filter width  $\Delta$  as

$$\bar{\phi}(\vec{x}, t) = \int_{\Omega} G(\vec{x}, \vec{x}', \Delta) \phi(\vec{x}', t) d\vec{x}'. \quad (1)$$

The choice of the filter function is important. LES approach would require much more computing cells than the RANS. There were discussions before that RANS with similar number of computing cells would give similar predictions by LES. LES is now commonly used in fire simulations. However, treatment of fire boundary should be watched.

There are many physical empirical parameters in both approaches. Values of empirical parameters  $C_1$ ,  $C_2$ ,  $C_3$ ,  $C_{\mu}$  and  $C_D$  used in RANS  $k-\epsilon$  model [6] had already led to argument. These parameters are suggested to be tuned for different flow problems. But doing this would take CFD as a curve-fitting exercise [42]. The parameter  $C_s$  in the subgrid-scale model in using LES [43] is important.

#### 4. Finite Volume Method

The set of partial differential equations describing the flow variable  $\phi$  is commonly solved by the Spalding-Patankar control volume method [6, 7]. This is a finite difference method with the equations discretized by integration over a control volume. Special attention is paid to the convective part which depends on the flow direction. All these have been discussed clearly in the literature and will not be repeated in detail here.

Different schemes are available in discretizing the equations with the finite volume (or control volume) method. Common differencing schemes in fire simulations [6, 20, 44] are the upwind scheme, the hybrid scheme, the power law scheme, and the second-order Quadratic Upstream Interpolation for Convective Kinematics (QUICK) scheme [44]. The central differencing scheme was tested to have difficulties in getting converged results in fire simulations [15, 45].

The upwind differencing scheme is equivalent to the zeroth-order interpolation with the choice of interfacial values depending on the sign of velocity. It is first-order accurate in terms of the Taylor series truncation error. Solution of the discretized equations based on this scheme is comparatively stable, seldom diverge or oscillate. Therefore, numerical schemes based on stable first-order upwinding are

popular in studying convective transport. However, the first-order accuracy makes it prone to numerical diffusion errors. False diffusion is a multidimensional phenomenon explained by taking the three-dimensional flow on each cell boundary as a one-dimensional flow. It occurs when the flow is oblique to the grid lines and when there is a nonzero gradient of the dependent variable in the direction normal to the flow. Such errors appear when the difference scheme fails to account for the true direction of the flow. Both the upwind and central difference schemes are not able to satisfy this requirement.

The false diffusion errors can be minimized by employing higher-order discretization. Scheme with second-order accuracy would involve a third-derivative truncation error. This becomes a source of unphysical oscillations under high convection conditions. Many schemes having higher order accuracy have been proposed to handle false diffusion. Those schemes involve discretization improvements in the simple upwind representation of the convection term. The QUICK scheme (e.g., [44]) is a popular one which uses a three-point upstream-weighted quadratic interpolation for each interface. The resulting finite difference equation is third-order accurate based on Taylor series analysis. This is a third-order accurate upwind difference scheme with additional control volume cells involved in the interpolation which will reduce diffusion errors to a certain extent by bringing in a wider influence. The scheme possesses the stability of first-order upwinding but is free of its second-order numerical diffusion.

#### 5. Velocity-Pressure-Linked Equations

There is no explicit equation to calculate air pressure distribution in a CFD model. However, pressure gradients appear in the momentum conservation equation. Staggered grid system with the pressure (and other scalar quantities) nodes coincided with the cell faces of the control volume for velocity component is used for solving the equations. In this way, the pressure gradient can be represented properly for flows with oscillating pressure. Further, the velocity components are calculated at the exact locations for computing other scalar quantities.

The velocity components  $u$ ,  $v$ , and  $w$  can be computed once the pressure field is known. But these computed velocity components might not satisfy the continuity equation. The Semi-Implicit Method for Pressure-Linked Equations (SIMPLE) algorithm was proposed for solving this problem [6, 44]. This is an important step in developing CFD. Since there is no explicit equation for calculating the pressure field, pressure distribution pattern has to be guessed at the beginning. Therefore, SIMPLE required long computing time if the guessed pressure distribution is different from the reality. Modifications of the scheme were proposed for fire simulations. Three common algorithms [46, 47] including the SIMPLE-Revised (SIMPLER), the noniterative Pressure Implicit with Splitting of Operators (PISOs); and the iterative PISOs were tested before on fire simulation for solving the velocity-pressure linked equations of the above problem [45].

The standard  $k-\epsilon$  turbulent model was employed for describing the turbulent effect. Numerical experiments were performed in simulating the fire-induced flow and temperature in the large test room reported by Ingason and Olsson [33]. The predicted results using the three algorithms were compared with the experimental data. The results show that iterative-type solution method is good for fire field modeling. Solutions predicted from the original noniterative PISO algorithm might not satisfy the continuity equation; but give preliminary estimation for fire engineering application as computation time required is very much reduced. The treatment of free boundary conditions for the cases studied is important in achieving a reasonably steady-state solution.

For reducing computing time and memory demand, the solution domains were usually confined in the fire compartment. The boundary condition for pressure  $P$  along  $x$ -direction was set to

$$\left(\frac{\partial P}{\partial x}\right) = 0. \quad (2)$$

However, reasonably steady-state results could not be obtained in this way. The flow field predicted used to be strong. In fact, the predicted mass drawn in and flow out from the compartment seems to be increasing indefinitely. One explanation for this phenomenon is that the fire source is located very close to the door opening where the free boundary conditions cannot be assumed. In order to overcome this problem, the solution domain must be extended to include the free space near the left door to a sufficient distance that the error due to the inaccuracy of boundary conditions was kept to minimum. In that study, the free boundary was extended to the outside air of the compartment. In this way, the neutral plane height can be predicted. But the computing time and memory requirement would be much longer and larger.

The noniterative PISO scheme, though much less computation time is required for the simulation, is not reliable enough where accurate results are desirable. The iterative PISO method is commonly applied for fire simulations though SIMPLER [7] also gives good results.

## 6. The Fire Dynamics Simulator

After releasing version 3.01 [9, 10] by the Building and Fire Research Laboratory, National Institute of Standards and Technology (NIST), USA in late 2002 [48, 49] after almost 30 years of research, FDS is then actively upgraded. It is now a popular fire engineering tool. Compressible fire-induced air flow can be simulated with hot smoke taken as a thermally expandable gas. A set of governing equations suitable for simulating fluid flow induced by buoyancy with a low Mach number have been derived. The Boussinesq approximation is no longer necessary and constraints on inviscid fluid have been removed. The FDS model allows larger variations of both density and temperature. An important assumption is that the pressure variation is small, so that the ideal gas law can be approximated by decomposing the pressure into a "background" component, a hydrostatic component, and a flow-induced perturbation.

This assumption is reasonable for flows with low Mach number because the temperature is inversely proportional to density. The pressure in the state and energy equation is replaced by the background pressure to filter out sound waves of speed much faster than the typical flow speeds expected in a compartment fire. The momentum equations were rearranged based on the assumption that vorticity generation due to buoyancy prevails over its generation due to the baroclinic effect. Short turbulence length scale will be simulated by LES with the Smagorinsky subgrid models.

Turbulence, intermediate combustion chemistry and thermal radiation have to be included instantaneously to study the heat released from combustion. Combustion chemistry should be incorporated properly in FDS. There have been studies on intermediate chemistry for polymethyl methacrylate (PMMA), polyvinyl chloride (PVC), polyurethane foam (PUF), and wood. Possible reaction kinetics from the predicted mixing with oxygen and temperature were studied. The chemical reactions of combustion for PMMA are very complex with intermediate reactions classified under the seven groups on thermal decomposition; thermal oxidative decomposition; decomposition of monomer MMA; methane combustion; methanol combustion; formaldehyde oxidation and acetylene combustion. For the group of methane combustion [19], 77 intermediate reactions were identified. This reaction identification process had been reported for the other six groups. Such reactions will be reviewed carefully for identifying the important ones such as those generating heat. Only those key reactions are considered to be put into FDS.

The Smagorinsky constant  $C_s$  in the subgrid-scale model used in FDS has to be evaluated [43]. The boundary layer is not so important for this scale. The coefficient  $C_s$  is varying from 0.1 to 0.25. Values of the Smagorinsky constant  $C_s$  would affect the results related to the grid refinement predicting indoor airflow. For coarser grids, a larger value of  $C_s$  would give better results. For fire simulations,  $C_s$  was selected as 0.2. Another important coefficient, the subgrid-scale turbulent Prandtl number  $P_{rt}$ , is varying from 0.2 to 0.9 as reported [50, 51]. Results for fire simulations are not very sensitive to changes in  $P_{rt}$ , taken as 0.5 [51] for simulating the indoor airflow.

The mixture fraction model [48, 49] is used in FDS to describe the fire burning process, and the model is based on the assumption that combustion is mixing-controlled. Each chemical specie of interest is described by a mixture fraction, which is a conserved quantity representing the fraction of its specie at a given position originating from the fuel. The mass fraction of each species is related to the mixture fraction by "state relations" from where necessary information can be extracted. For example, the state relation for the oxygen mass fraction would be used to calculate the local oxygen mass consumption rate. The local heat release rate can then be computed from the local oxygen consumption rate by assuming that it is directly proportional to the oxygen consumption rate and independent of the fuel involved. This procedure will be reviewed for its suitability in dealing with combustion chemistry.

## 7. Verification and Validation

CFD predicted results are always queried. A detailed analysis on quantifying the modeling and numerical uncertainties in those fire simulations is therefore required [28]. Within the last decade, the quality or credibility of CFD fire simulations has drawn increasing attention from the society of fire engineering. The procedures for assessing the credibility of fire simulation codes are not agreed [52].

The term verification and validation (V&V) was used in operations research with definitions of V&V reviewed [28]. Implementation of V&V for credibility quantification in CFD field model is studied in the preliminary stage. Some available CFD fire codes do not go through cautious tests of V&V, their work can only be regarded as just a demonstration that some special fire scenarios are probably simulated. This situation persists in the arena of CFD fire modeling, especially for the sector of CFD commercial codes [53]. One of the possible reasons is that there is no commonly accepted V&V methodology available, though at least three different standards on the credibility of CFD have been published [28, 51].

In contrast to zone models which have been well validated by experiments [15], to the best knowledge of the author, experimental validations of field models have not been carried out to the same extent as for zone models. In fact, very limited experimental work, except some by Ingason and Olsson [33] on sprinkler fires and natural vents, have been performed for verifying field models. Experimental data reported by Steckler et al. [34] originally for studying doorway flow have been used many times for verifying field models [29].

There are validation documents on FDS and on other models released by the US Nuclear Regulatory Commission. Seven volumes of the draft report have just been made available [36]. A series of 25 fire tests were conducted with primary purpose to provide data to validate computer models for nuclear power plant. The experiments were conducted in an enclosure of size 18 m by 12 m with height 6 m. The fires consisted of a simple gas burner, heptane or methanol liquid pools, or a PMMA solid fire. Four of the tests were conducted with a full-scale control room mockup in place. Parameters including the fire intensity, enclosure ventilation rate, and fire location were varied during the experiments.

Full-scale burning facilities should be developed for verifying and validating CFD results. Some on FDS had been reported [54]. An exhaust hood fitted with a fan-duct system is necessary to measure the heat release rate of burning combustibles by the oxygen consumption method. Different scenarios should be set up by burning combustibles of different sizes at different locations and ventilation conditions. Air temperature and velocity of the induced fire flow should be measured together with the heat release rate of the fire.

## 8. Functional Analysis

Functional analysis [55] was proposed to justify the CFD predicted results better. This is better than just saying

the agreement between predictions and measured values is “good” or “bad.” This method was proposed as a quantitative, statistical and analytical approach to evaluating fire zone models [32, 56] first, and applied to verify CFD models [57]. The transient measured  $(t_i, m_i)$  and predicted  $(t_i, p_i)$  curves are denoted by two vectors  $\vec{m}$  and  $\vec{p}$  by summing up all the  $n$  data points  $m_i$  and  $p_i$  at different time intervals  $t_i, i = 1, \dots, n$  vectorally. The vector  $\vec{m} - \vec{p}$  will give the deviation. Two parameters were defined to give a quantitative measure on the similarity of the curve shape.

- (i) The “norm” is the normalized relative distance between the vectors  $\vec{m}$  and  $\vec{p}$ . As recommended by Peacock et al. [55], the Euclidean “norm” for  $n$  data is calculated by  $m_i$  and the corresponding  $p_i$  at  $t_i$  with  $s$  data points used to smoothen the fluctuating curves to provide better estimates inside as

$$\text{norm} = \frac{|\vec{m} - \vec{p}|}{|\vec{m}|} = \frac{\sqrt{\sum_{i=1}^n (m_i - p_i)^2}}{\sqrt{\sum_{i=1}^n (m_i)^2}}. \quad (3)$$

- (ii) The parameter “cosine” (or “inner product”) is defined as the angular difference between the resultant vectors as

$$\begin{aligned} \text{cosine} &= \frac{\langle \vec{m}, \vec{p} \rangle}{|\vec{m}| \cdot |\vec{p}|} \\ &= \frac{\sum_{i=2}^n (m_i - m_{i-s})(p_i - p_{i-s})/s^2 \mathcal{A}}{\sqrt{\sum_{i=2}^n (m_i - m_{i-s})^2/s^2 \mathcal{A}} \sqrt{\sum_{i=2}^n (p_i - p_{i-s})^2/s^2 \mathcal{A}}}, \end{aligned} \quad (4)$$

where  $\mathcal{A}$  denotes  $(t_i - t_{i-1})$ .

The “norm” approaches zero and the “cosine” approaches 1 when the two curves are very close to each other.

## 9. An Example Case Study

Quality experiments on smoke filling were reported by Hägglund et al. [58], Li and Chow [59]. A single-storey building of floor area 11 m by 39 m and height 8 m as shown in Figure 1 was considered. The wall and ceiling were constructed by mineral wool, and the floor was concrete. There were three vents labeled D1, D2, and D3, each of area 2.2 m by 0.6 m on the top of the front wall. The upper edge of the openings was positioned 0.2 m below the ceiling level. Two air inlets A1 and A2 of area 1 m by 2 m were at the lower edge of the left wall and front wall as shown in Figure 1.

The fires were positioned in the center of one half of the building. Methanol was used as the fuel and was burnt in square steel pans of sizes 0.56 m<sup>2</sup> and 2.0 m<sup>2</sup>. The heat release rate per unit horizontal area of the fuel was 440 kWm<sup>-2</sup>. Hot air movement was observed by discharging smoke. The gas temperature was measured by thermocouples distributed over four vertical lines with 50 cm spacing as shown in

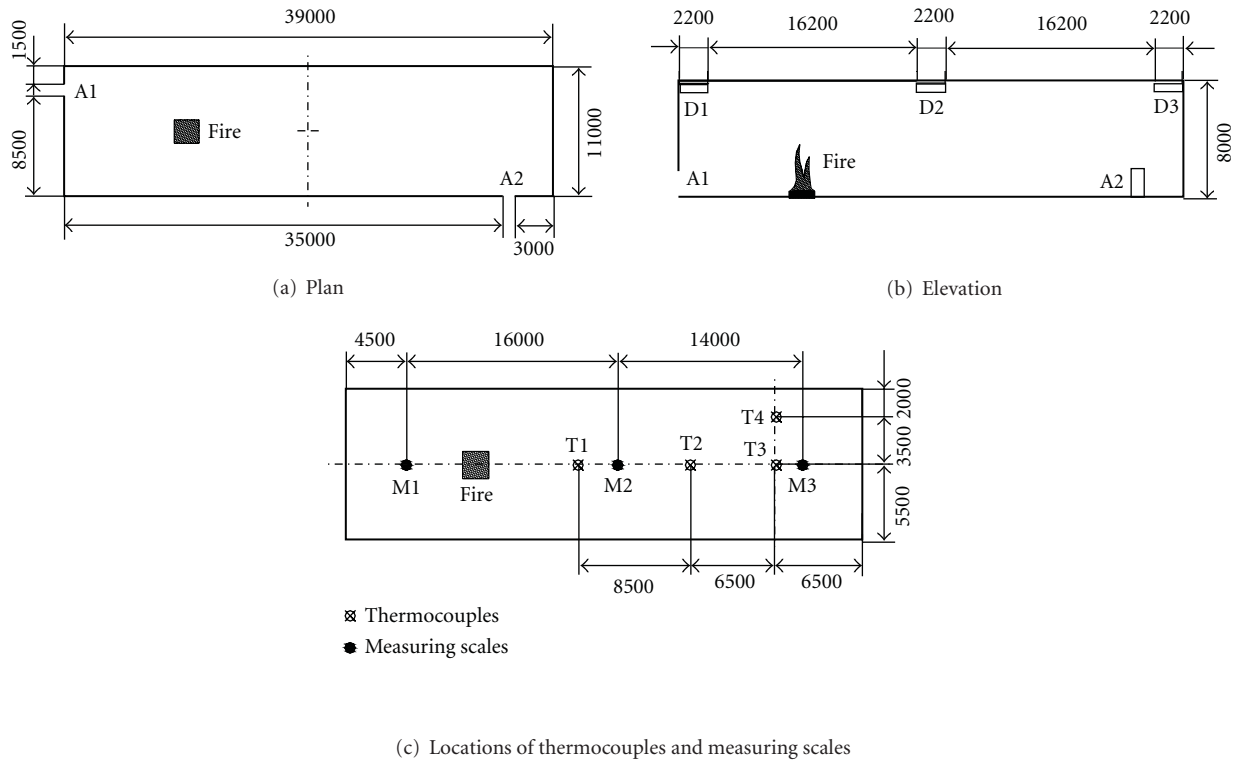


FIGURE 1: The test room.

Figure 1(c). Two video cameras were used to record the descending of smoke layer.

Two tests on smoke filling were selected to be simulated by CFD model FDS4. Smoke filling of two large room fire tests with and without wind outside the test room were studied. The numerical experiments are labeled as Cases 1 and 2 as follows.

*Case 1.* Fire size: 2.0 m<sup>2</sup>

Internal air temperature: 15°C

External air temperature: 8°C

External wind: 0 ms<sup>-1</sup>

Cubic grid of size: 0.2 m × 0.2 m × 0.2 m

Total number of grids: 429,000.

*Case 2.* Fire size: 0.56 m<sup>2</sup>

Internal air temperature: 13°C

External air temperature: 3°C

External wind: 6 ms<sup>-1</sup>

Cubic grid of size: 0.2 m × 0.2 m × 0.2 m

Total number of grids: 975,000.

The heat release rate per unit area of the fuel was 440 kWm<sup>-2</sup>. The growth period of the mass burning rate was set to 60 s. The input heat release rate curves are shown in Figure 2. The maximum heat release rates were 880 kW and 246.4 kW for Cases 1 and 2, respectively.

Four thermocouple trees labeled T1 to T4 were set as shown in Figure 4(a). Three predicted curves were all kept steady at about 3 m above floor and fluctuated in a small scale. The smoke layer height measured in experiment was

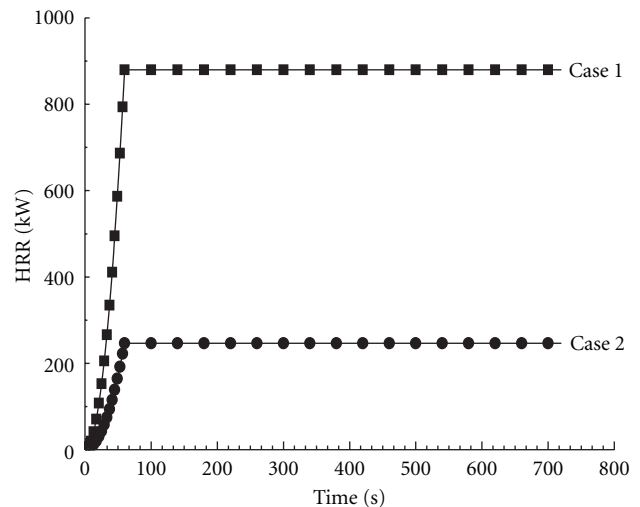
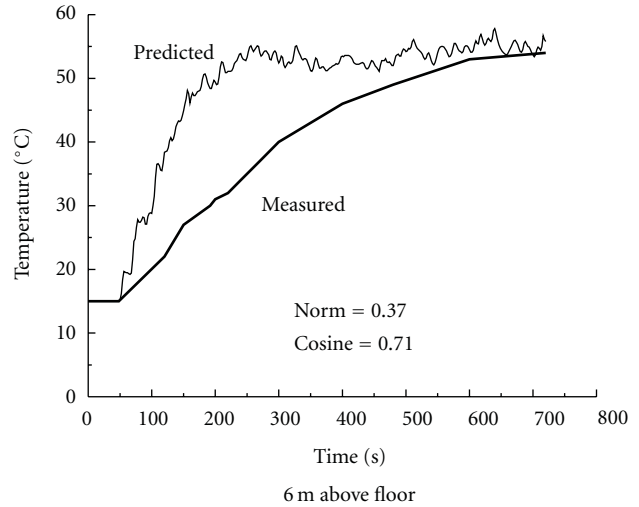
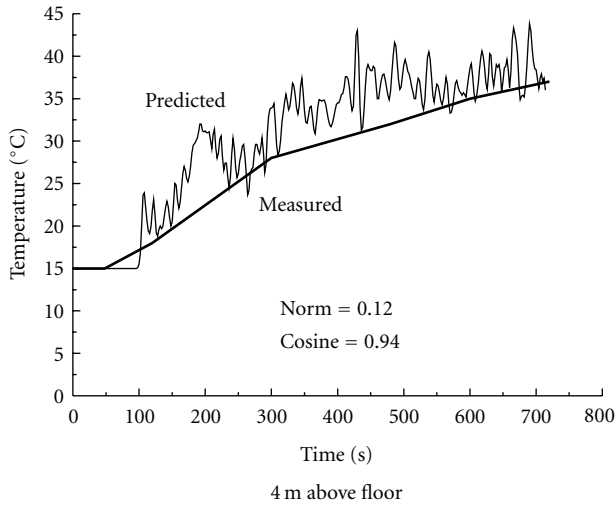


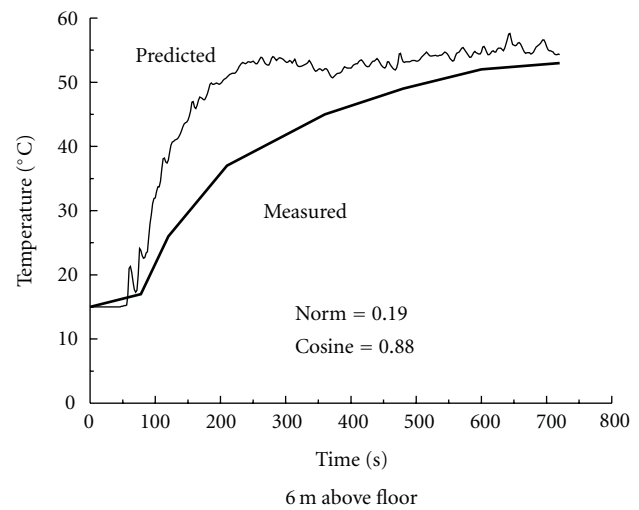
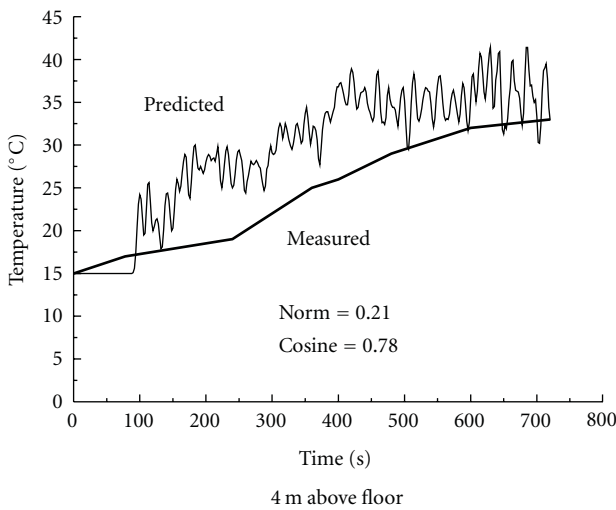
FIGURE 2: Input heat release rates.

It can be seen that the two curves matched better with each other at height 4 m above floor, but not so good for 6 m above floor in the four thermocouple trees. At 6 m above floor, the predicted temperature increased more rapidly than experiment.

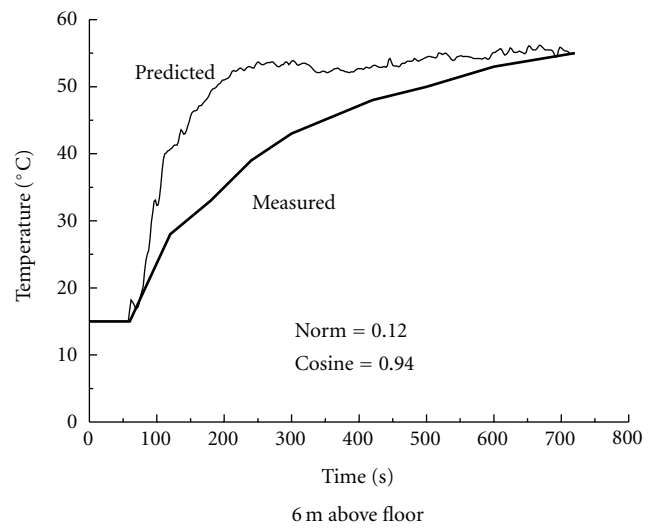
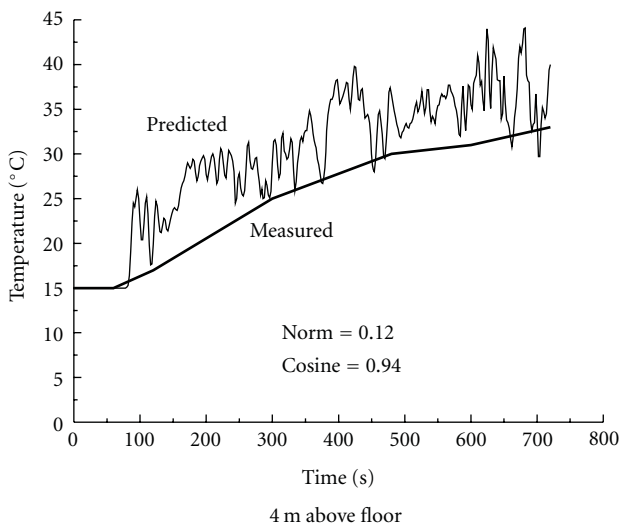
Hot smoke layer height results at M1, M2, and M3 are shown in Figure 4(a). Three predicted curves were all kept steady at about 3 m above floor and fluctuated in a small scale. The smoke layer height measured in experiment was



(a) T1

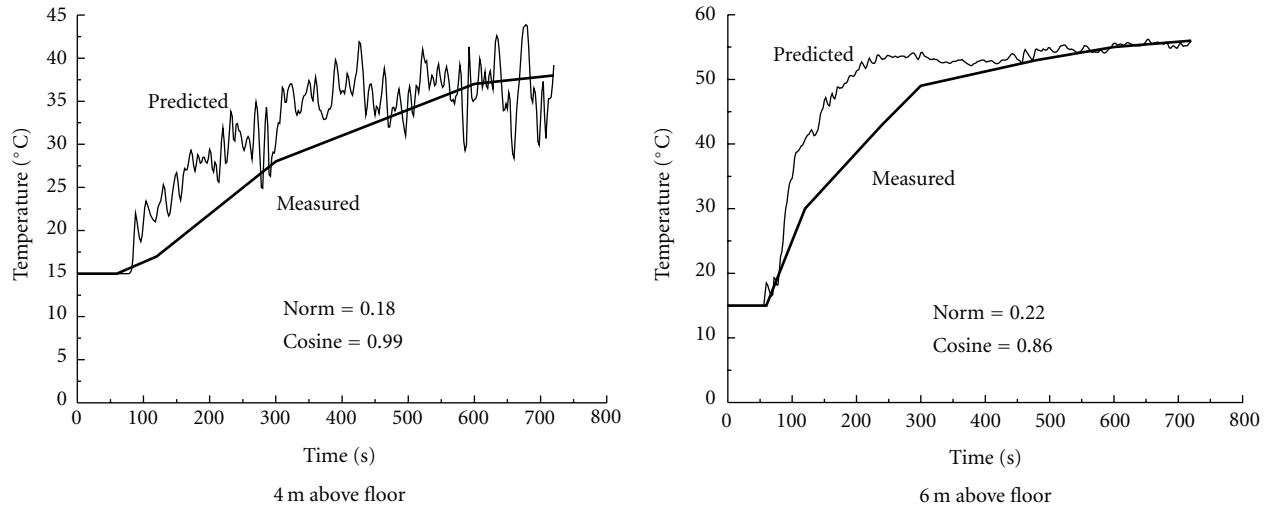


(b) T2



(c) T3

FIGURE 3: Continued.



(d) T4

FIGURE 3: Air temperature of Case 1.

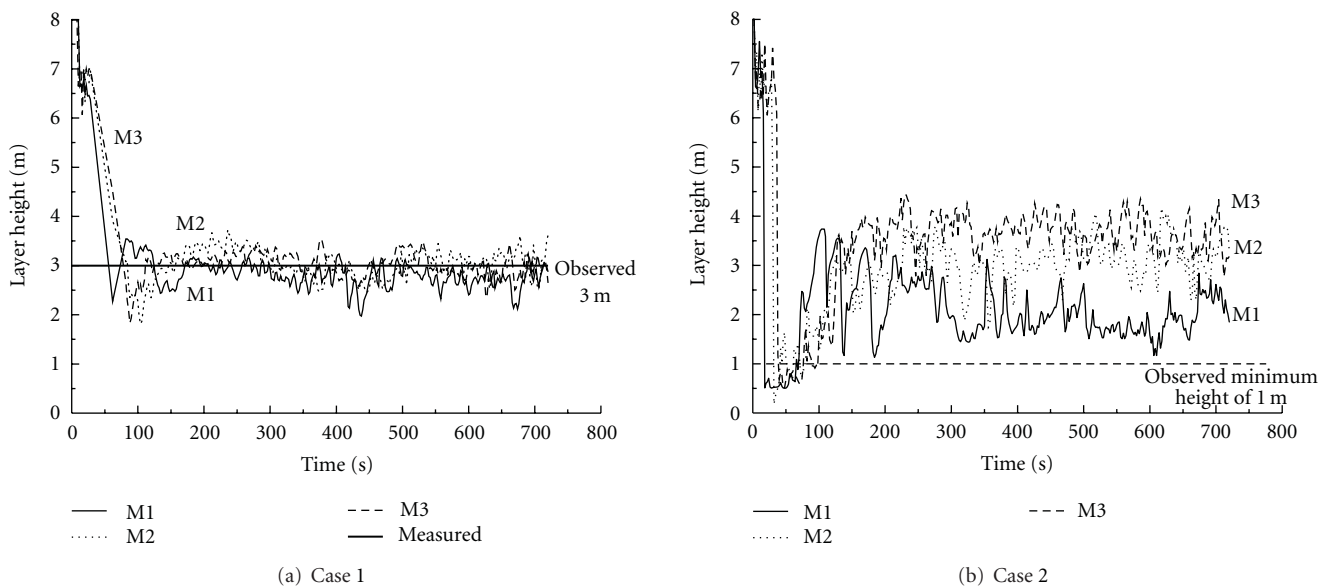


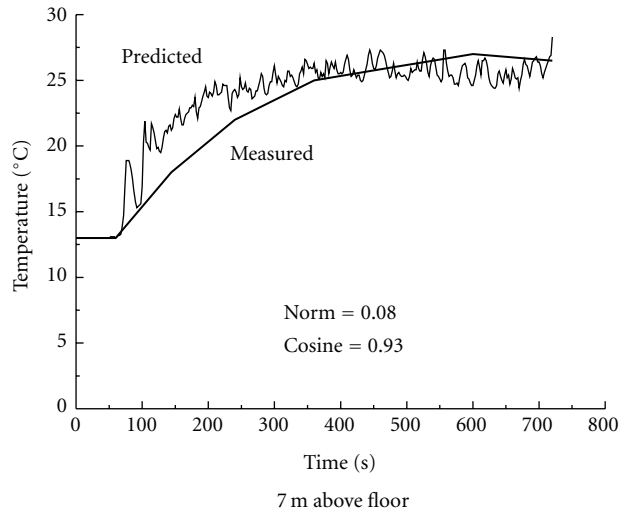
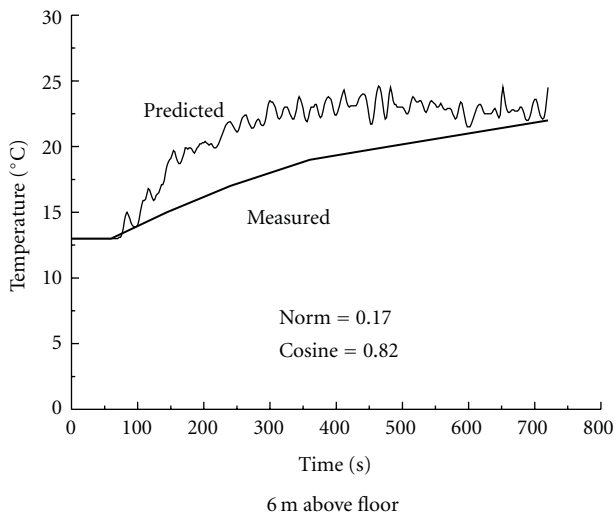
FIGURE 4: Smoke layer height.

just 3 m above floor. It appears that the predicted smoke layer height is reasonably good.

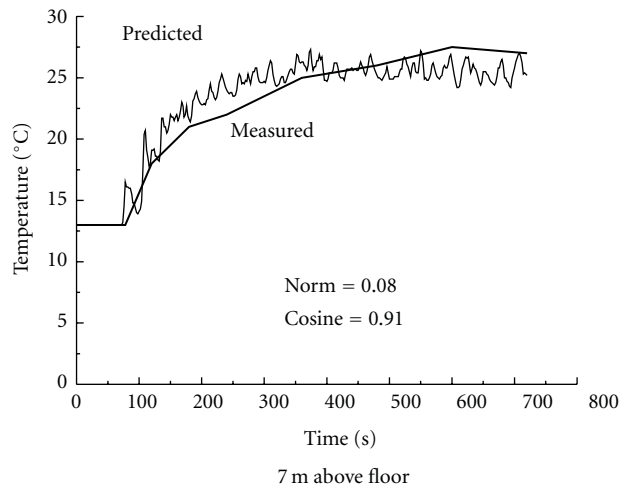
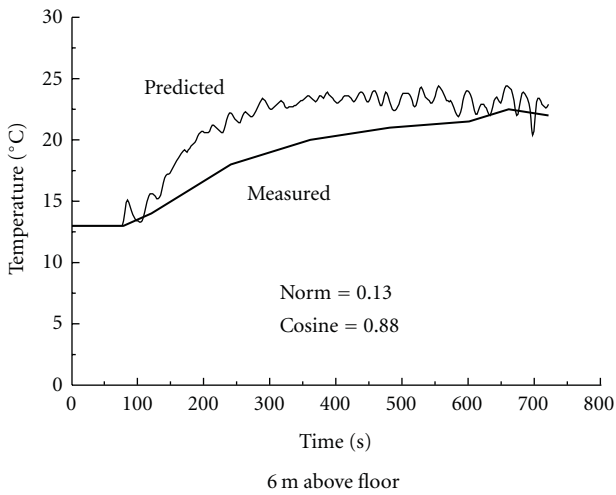
Predicted temperatures of Case 2 are shown in Figures 5(a) and 5(b). As the heat release rate of Case 2 was smaller than that of Case 1, two positions at 6 m and 7 m above floor on each thermocouple tree were compared. The predicted air temperature curve agreed well with experiment. The CFD tool FDS appears to be good for simulating the fire scenario with wind effect.

Predicted smoke layer heights at M1 to M3 are shown in Figure 4(b). The smoke layer of Case 2 fluctuated more vigorously than that of Case 1. A possible explanation is due to wind outside. Smoke layer height at M1 fluctuated, particularly near to the left inlet.

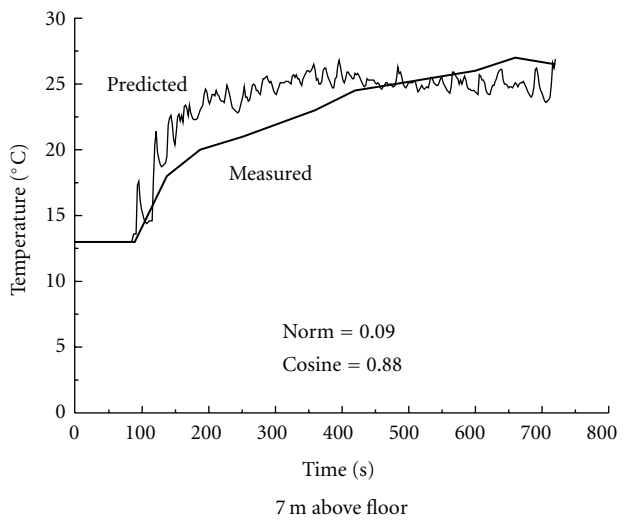
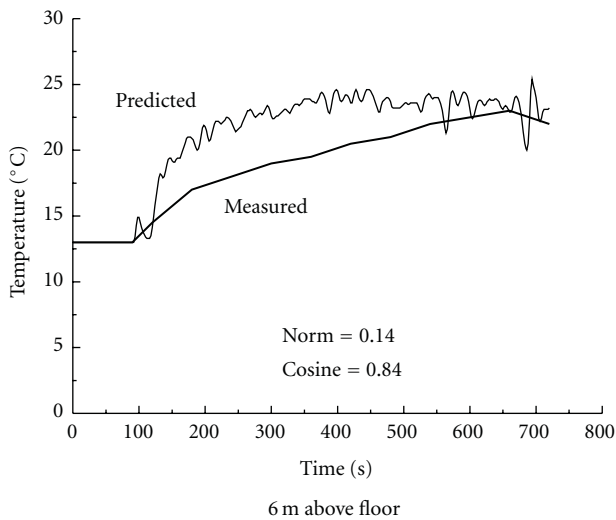
Observed descending of the smoke layer in the experiment was reported [58] to be about 1 m. Smoke fell down to the top of the vertical inlet vent at height 1 m. There were three vents near to the ceiling. Hot smoke exhausted through two vents at the ceiling, and air was sucked into the room through the third one close to the fire as shown in Figure 6. Predicted velocity vector profile across vents is also shown in Figure 6. As shown in Figure 6(b), the air flow velocity vector at the two vents on the right was towards the inside of the room, while at the left vent it was opposite. This was the same as what reported in the tests [58]. Predicted air temperature and smoke layer interface height were compared with the test results by applying functional analysis. Air temperature predictions in Figures 3 and 5 were



(a) T1

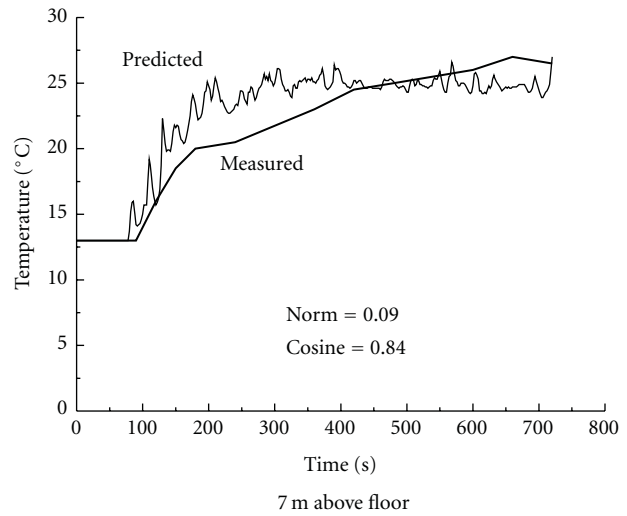
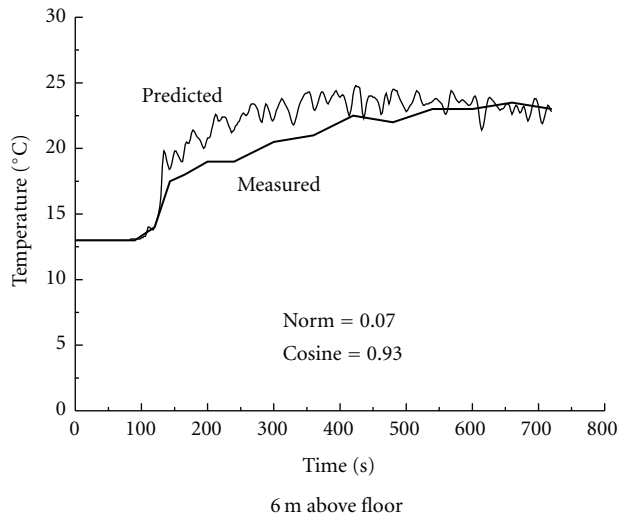


(b) T2



(c) T3

FIGURE 5: Continued.



(d) T4

FIGURE 5: Air temperature of Case 2.

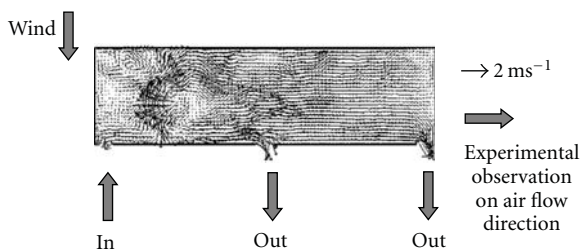


FIGURE 6: Predicted velocity vector across a plane with vents for Case 2.

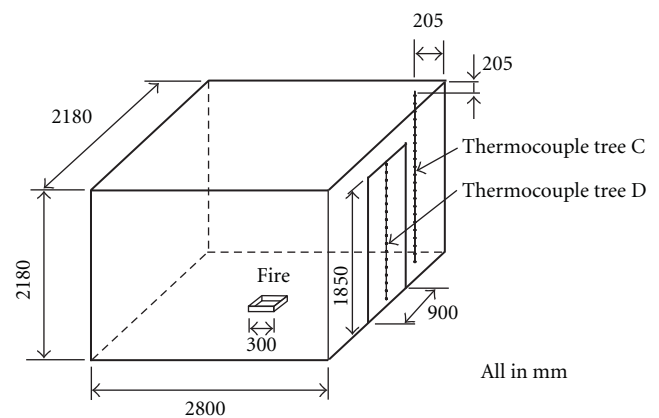


FIGURE 7: Test room by Steckler et al. [34].

justified by taking  $n$  to be 8 and  $s$  as 2. Results on norm and cosine are shown also in the figures. For Case 1, FDS predictions gave norms from 0.08 to 0.37, and cosines from 0.71 to 0.99. In Case 2, the norms were from 0.07 to 0.14, and cosines from 0.82 to 0.93. CFD results predicted at some positions were satisfactory and very close to those measured values. For example, norm of T4 at 4 m above floor is 0.01, approaching to 0. Cosine is 0.95 with value close to 1. However, the predicted results were fairly acceptable at some positions with large deviations. For predictions at T1 with 6 m above the floor, norm is 0.37 and cosine is 0.71. Further, predicted air temperatures increased faster than the observed rate in the test. More vigorous justification of fire models is necessary before using them. Therefore, CFD fire models should be improved for application on fire protection design and evaluation [60].

A scaling system can be set up based on the values of norm and cosine on key flow variables to denote how good the CFD predicted results agree with experiment. However, this cannot be only set up by research workers. Authorities with responsibility to accept fire safety provisions for PBD [22, 23] should play the key role in deciding whether to use a 3-point scale (bad, neutral, and good) or a 5-point scale (very bad, bad, fairly good, good and very good).

## 10. Free Boundary Conditions

In applying CFD to building fire hazard assessment, there are always windows and doors open to outside. Bi-directional flow would be observed experimentally, with hot gas flowing out and cool air coming into the room. There are many debates on specifying free boundary conditions for such openings. Flow parameters, particularly the pressure, have to be specified carefully. There are empirical correlations relating the pressure profiles across the vertical openings such as windows or doors, under different room geometries, heat release rates of the fires, and opening sizes. However, such boundary conditions might not give proper specification. A better approach is to extend the computing domains outside, as pointed out years ago by Schaelin et al. [60] in 1992 for simulating plume flow, and Mawhinney et al. [29] on fire studies in 1994. This part should be watched carefully as pointed out again before [21].

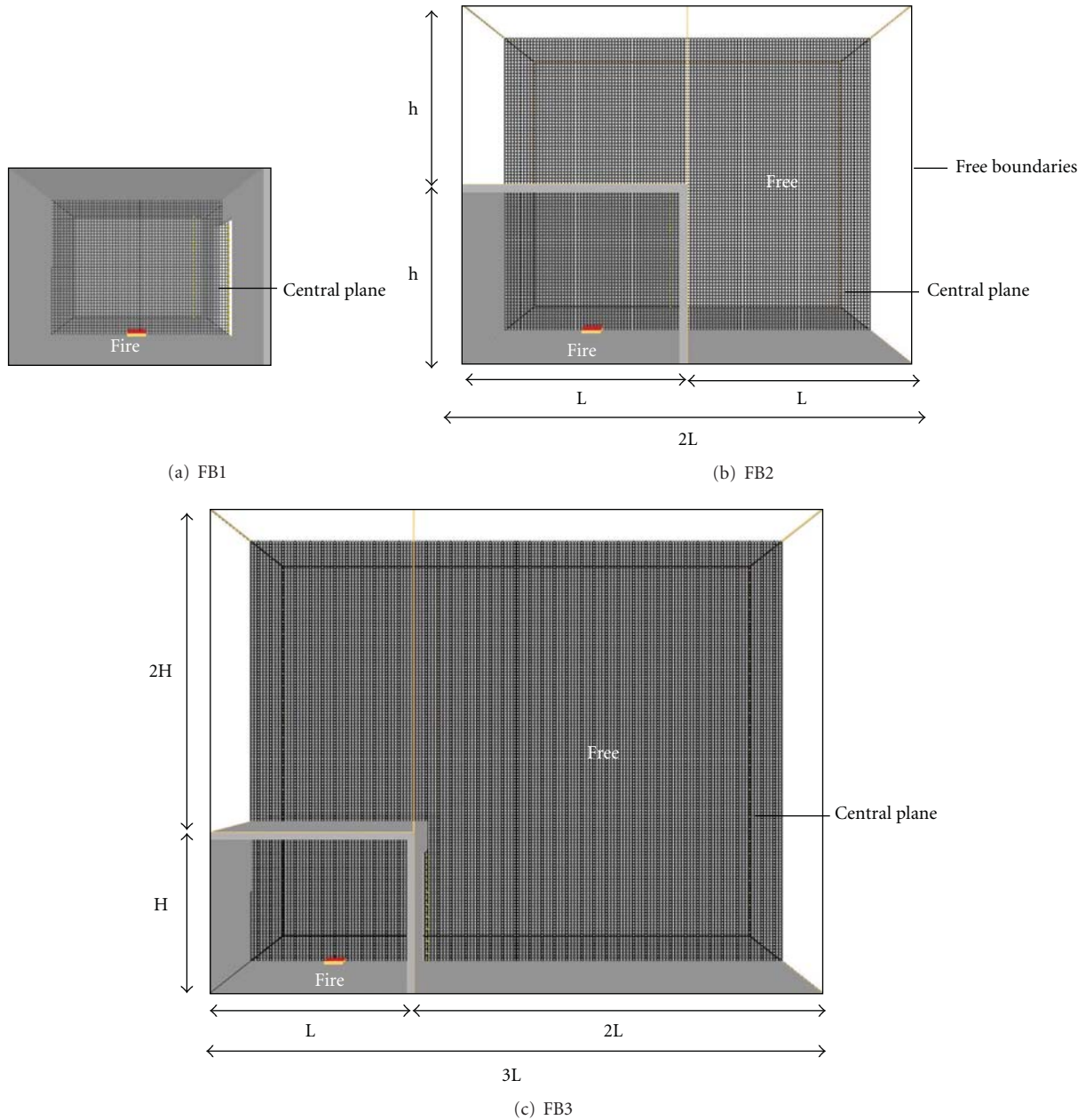


FIGURE 8: Three free boundary conditions.

The fire tests reported by Steckler et al. [34], Li and Chow [61] in a room of area 2.8 m by 2.8 m and height 2.18 m as shown in Figure 7 were taken as an example. A 0.3 m square methane burner of heat release rate 62.9 kW was placed at the centre of the test room. A door of width 0.9 m and length 1.85 m was located at the centre of the side wall. Two thermocouple trees, C and D, each with 22 probes, were placed at the corner and the doorway, respectively. Vertical air temperature profiles from floor to ceiling were measured at these two thermocouple trees.

Taking into account the accuracy and the computing time, cubic grids of size 0.05 m by 0.05 m by 0.05 m were used in CFD simulations with FDS. The room was divided into a grid system of 246,400 cells with 100 by 56 by 44 parts along

the  $x$ -,  $y$ -, and  $z$ -directions, respectively, in the FDS input file. Three free boundary conditions labeled as FB1, FB2, and FB3 were tested in FDS simulations.

For free boundary condition FB1, FDS menu for free openings was used without extending the computing domain to outside. Air flow parameters at the open boundary depend on whether the flow is outgoing or incoming [34]. Taking air pressure  $P$  as an example,  $P$  is related to horizontal velocity  $u$  by

$$P = \begin{cases} \frac{|u|^2}{2}, & \text{outgoing,} \\ 0, & \text{incoming.} \end{cases} \quad (5)$$

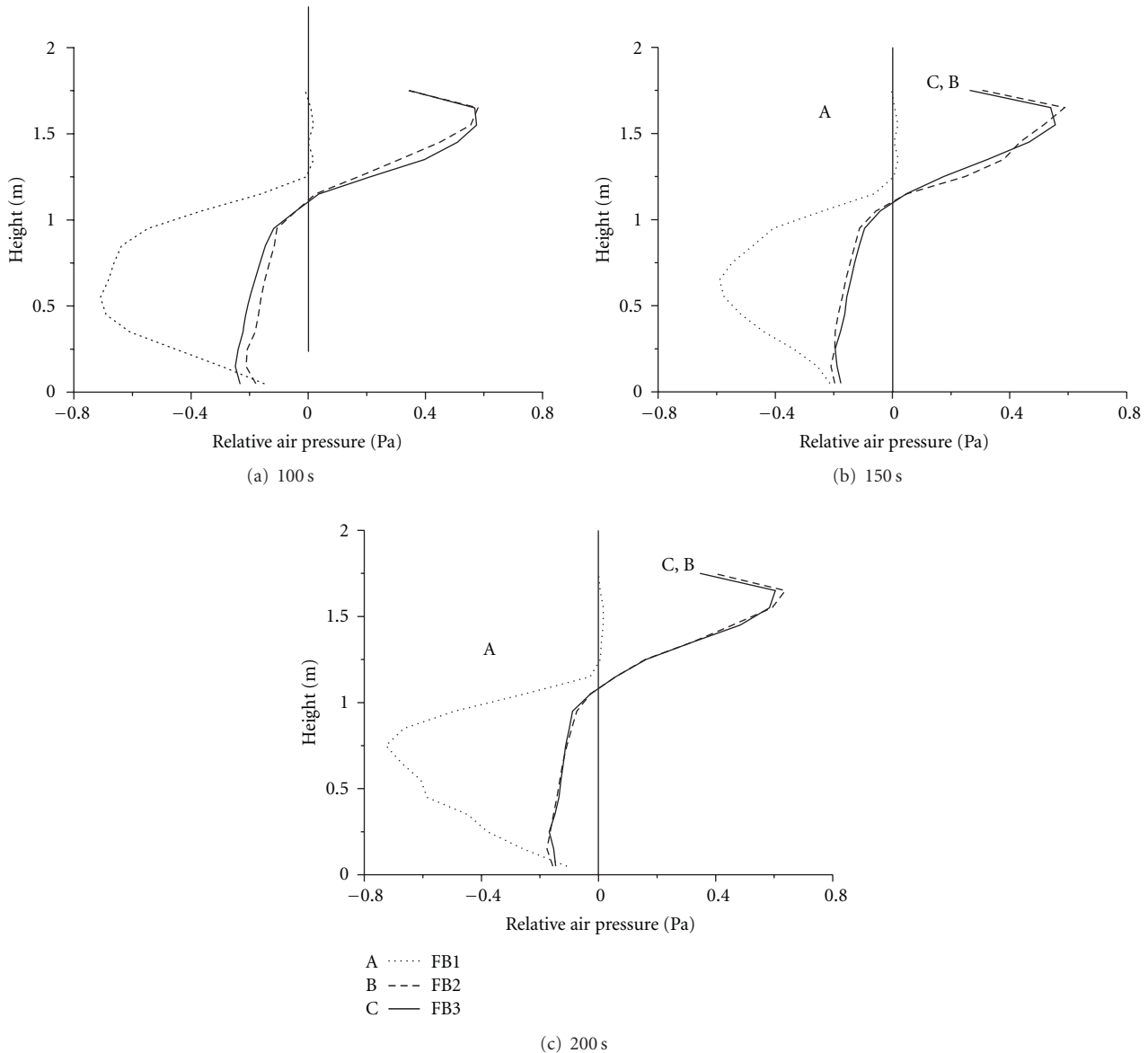


FIGURE 9: Relative air pressures at doorway.

The outgoing boundary condition assumes that the pressure perturbation is zero at an outgoing boundary and that  $P$  is constant along streamlines. The incoming boundary condition assumes that  $P$  is zero infinitely far away. At the boundary between two meshes, the pressure boundary condition is similar to that at an external open boundary. But  $P$  is taken from the adjacent mesh where the flow is incoming.

The lengths and heights of the extended space were once or twice of the room length and height, respectively, for FB2 and FB3. The input geometries of FDS simulations for these three boundary conditions are shown in Figure 8.

Relative air pressures with respect to ambient values at the doorway and horizontal components of velocity at 100 s, 150 s, and 200 s are shown in Figures 9 and 10. Air temperatures at different height at the corner in the room

are shown in Figure 11. In applying functional analysis to compare with measured air temperature, values of norm for simulations FB1, FB2, and FB3 are 0.015, 0.013, and 0.013 respectively, and values of cosine are 0.59, 0.58, and 0.57 respectively. Predicted air temperatures are very close to experiments using the three boundary conditions. All have low values of cosine. However, the pressure profiles across the door were entirely different in view of Figure 9. It is difficult to accept the predicted pressure profiles of FB1, though experimental pressure data were not available on that set of tests. Predicted values are not so satisfactory as in the first example of simulating smoke filling in a bigger hall. A possible explanation is because combustion plays a key role in simulating fire in a small room. Further investigation would be worked on simulating the combustion process in CFD fire models.

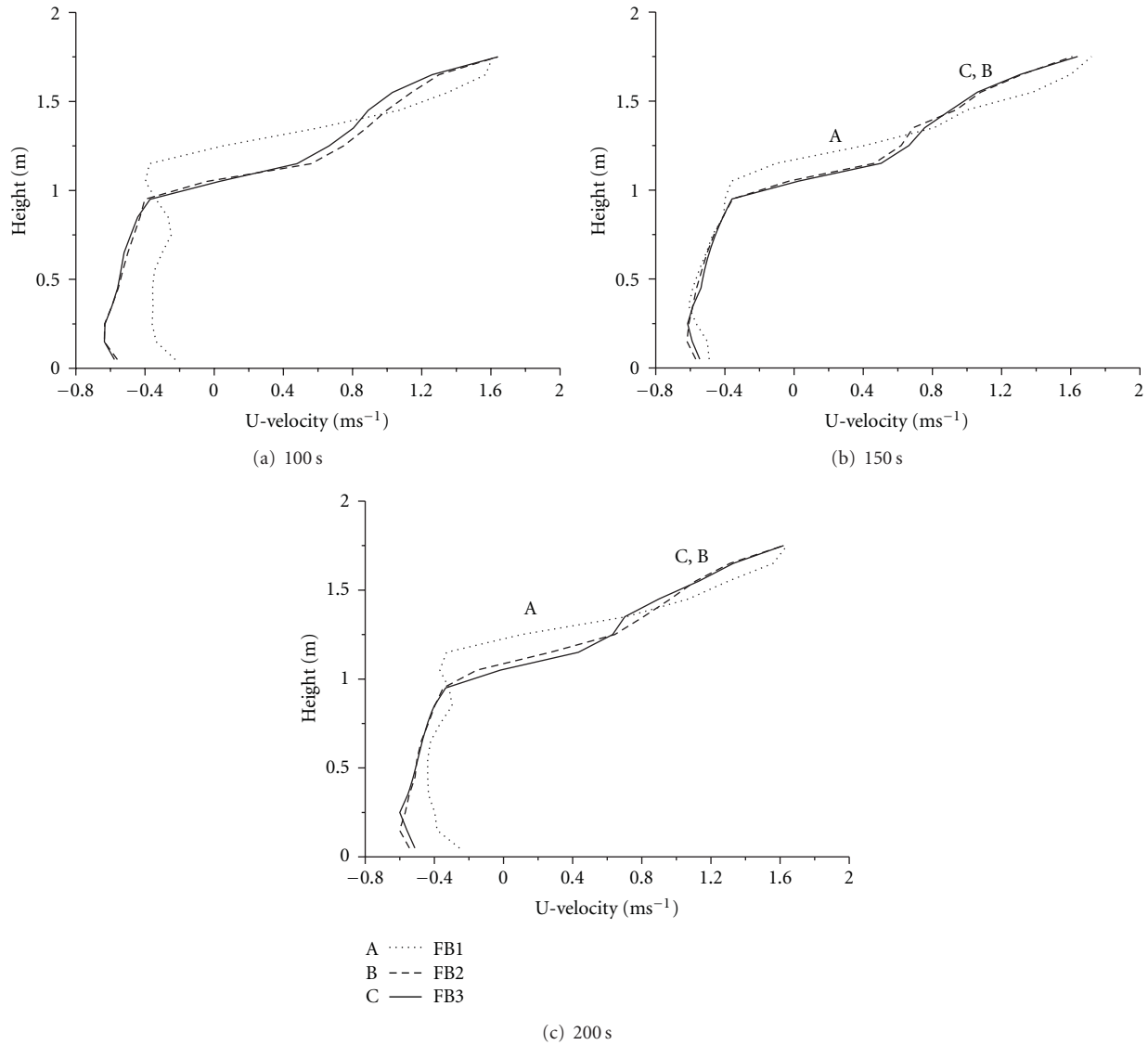


FIGURE 10: Horizontal velocity components at doorway.

**11. Conclusions**

Although CFD has been used in designing smoke exhaust systems in those atria [37–41] for over 30 years, not many studies were devoted to simulate turbulent mixing, intermediate combustion chemistry, and thermal radiation realistically without using empirical formula. Further, there were very few verification and validation works on the predicted results with limited full-scale burning tests, especially designed for CFD fire models. Fire engineers are then required to justify the CFD results while testing and commissioning the smoke exhaust systems [62]. Hot smoke tests in the atrium site [37–41] are therefore required to evaluate the performance of atrium smoke exhaust systems in many places including Hong Kong.

Fire models had been used in many projects but led to many arguments and debates on some submodels of those available tools. If the results are not demonstrated clearly,

say by full-scale burning test, the process would appear as a “curve-fitting exercise.” “Verification” exercises might be necessary, in addition to “engineering judgment.” Although the associated costs for carrying out the burning tests might be high, it is necessary for some projects to demonstrate that adequate fire safety is provided.

Engineering tools with CFD models are applied in fire safety engineering. There are many reasons why the CFD field model is so attractive. The predicted “microscopic” picture of the thermal environment described by the velocity vector diagram, the temperature, pressure and smoke concentration (taken as mass of chemical specie) contours are useful for deriving the relevant macroscopic parameters for engineering purposes. The calculated vertical distribution of air temperature is useful in providing the appropriate thermal sensitivity for sprinkler heads. Also, the air entrainment rates for a fire plume were calculated from the predicted horizontal velocity components.

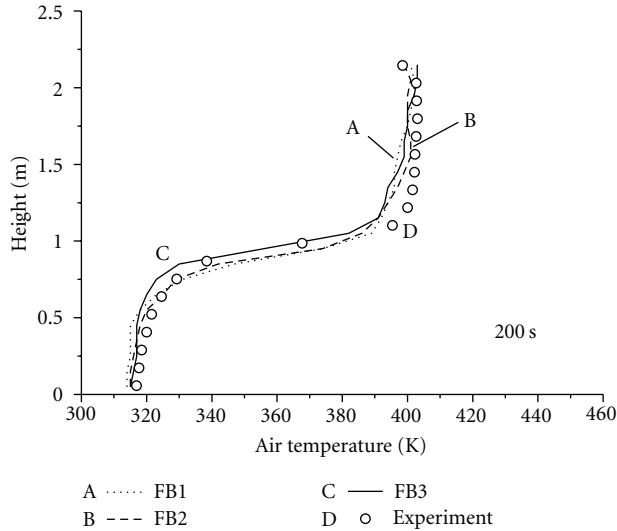


FIGURE 11: Air temperatures at 200 s by thermocouple tree C.

There is still room for improving the accuracy of those engineering tools. Verification and validation of those models is particularly important. As pointed out in Hong Kong [62], both building designers and relevant government officials should be properly trained in using fire models. Note that the development of fire model itself is very rapid. For example, three-dimensional simulations with CFD models can be handled readily with a personal computer now. But 20 years ago, only two-dimensional simulations could be carried out in a mainframe computer.

Relevant education and training must be provided [63, 64]. Offering degree programmes up to MSc level is necessary for upgrading the quality of fire engineering personnel. At least, continued professional development programmes are recommended to be offered regularly.

FDS [48, 49] is very suitable in fire safety engineering. However, there is still much development to do and careless application of the technique would lead to wrong results. Verification and validation studies such as those works started by the US Nuclear Regulatory Commission [36] are important. Full-scale burning tests [61, 62] for validating CFD fire field models are necessary.

## Nomenclature

$C_s$ :	Smagorinsky coefficient in LES model
$C_1, C_2, C_3, C_\mu, C_D$ :	Empirical parameters in RANS model
$G(\vec{x} - \vec{x}', \Delta)$ :	Filtering function
$h$ :	Enthalpy
$k$ :	Turbulence parameter
$\vec{m}$ :	A vector representing measured data
$m_i$ :	Measured data points
$n$ :	Index in functional analysis

$P$ :	Air pressure
$P_{rt}$ :	Subgrid-scale turbulent Prandtl number
$p_i$ :	Predicted data point
$\vec{p}$ :	A vector representing predicted data
$t$ :	Time
$u, v, w$ :	Velocity vector components
$\vec{x}$ :	Position vector
$\varepsilon$ :	Turbulence parameter
$\Delta$ :	Filter width
$\phi$ :	Time averaged value of flow variables
$\phi_t$ or $\phi(\vec{x}, t)$ :	Transient flow variables
$\phi'$ or $\phi'(\vec{x}, t)$ :	Fluctuation of flow variables
$\Omega$ :	Domain of interest.

## References

- [1] G. Cox, *Combustion Fundamentals of Fires*, Academic Press, London, UK, 1995.
- [2] M. L. Janssens, *An Introduction to Mathematical Fire Modeling*, Technomic Publishing, Lancaster, Pa, USA, 2nd edition, 2000.
- [3] W. K. Chow, "Thermal engineering tools in performance-based design for fire safety," *Heat Transfer Engineering*, vol. 29, no. 9, pp. 757–762, 2008.
- [4] G. Cox, "Turbulent closure and the modeling of fire by using computational fluid dynamics," *Philosophical Transactions of the Royal Society A*, vol. 356, pp. 2835–2854, 1998.
- [5] V. Novozhilov, "Computational fluid dynamics modeling of compartment fires," *Progress in Energy and Combustion Science*, vol. 27, no. 6, pp. 611–666, 2001.
- [6] D. B. Spalding, "Mathematical modelling of fluid mechanics, heat transfer and chemical reaction processes," Computational Fluid Dynamics Unit Report HTS/80/1, Imperial College of Science & Technology, London, UK, 1980.
- [7] S. V. Patankar, *Numerical Heat Transfer and Fluid Flow*, McGraw Hill, New York, NY, USA, 1980.
- [8] G. Cox and S. Kumar, "Computer modeling of fire," BRE Information Paper 2/83, Building Research Development, London, UK, 1983.
- [9] K. B. McGrattan, H. R. Baum, and R. G. Rehm, "Large eddy simulations of smoke movement," *Fire Safety Journal*, vol. 30, no. 2, pp. 161–178, 1998.
- [10] H. R. Baum, "Large eddy simulations of fires—from concepts to computations," *Fire Protection Engineering*, no. 6, pp. 36–42, 2000.
- [11] Y. Hasemi, "Numerical calculation of the natural convection in fire compartment," Research Paper 69, Building Research Institute (Japan), 1977.
- [12] A. C. Ku, M. I. Doria, and J. R. Lloyd, "Numerical modelling of unsteady buoyant flows generated by fire in a corridor," in *Proceedings of the 16th International Symposium on Combustion*, p. 1373, The Combustion Institute, Pittsburgh, Pa, USA, 1977.
- [13] H. R. Baum, R. G. Rehm, and G. W. Mulholland, "Computation of fire induced flow and smoke coagulation," in *Proceedings of the 19th International Symposium on Combustion*, vol. 19, pp. 921–931, The Combustion Institute, Pittsburgh, Pa, USA, 1982.
- [14] N. C. Markatos, M. R. Malin, and G. Cox, "Mathematical modelling of buoyancy-induced smoke flow in enclosures," *International Journal of Heat and Mass Transfer*, vol. 25, no. 1, pp. 63–75, 1982.

- [15] W. K. Chow, "Use of computational fluid dynamics for simulating enclosure fires," *Journal of Fire Sciences*, vol. 13, no. 4, pp. 300–334, 1995.
- [16] W. K. Chow, "Combustion effect on a building fire field model," in *Transport Phenomena on Heat and Mass Transfer*, J. A. Reziés, Ed., vol. 2, pp. 1203–1212, Elsevier, Amsterdam, The Netherlands, 1992.
- [17] S. R. Tieszen, "On the fluid mechanics of fires," *Annual Review of Fluid Mechanics*, vol. 33, pp. 67–92, 2001.
- [18] H. Tuovinen, "Modelling of laminar diffusion flames in vitiated environment," in *Proceedings of the 4th International Symposium of Fire Safety Science*, Ottawa, Canada, 1994.
- [19] W. R. Zeng, S. F. Li, and W. K. Chow, "Review on chemical reactions of burning poly(methyl methacrylate) PMMA," *Journal of Fire Sciences*, vol. 20, no. 5, pp. 401–433, 2002.
- [20] K. McGrattan, "Fire modeling—where are we now, and where are we going?" in *Proceedings of the 8th International Symposium on Fire Safety Science*, Tsinghua University, International Association for Fire Safety Science, Beijing, China, September 2005.
- [21] C. L. Chow and W. K. Chow, "A brief review on applying computational fluid dynamics in building fire hazard assessment," in *A Chapter in Fire Safety*, I. Søgaard and H. Krogh, Eds., Nova Science Publishers, 2009.
- [22] "BS 7974 Application of Fire Safety Engineering Principles to the Design of Buildings—Code of Practice," British Standards Institute, London, UK, 2001.
- [23] CIBSE Guide E, "Fire Engineering," The Chartered Institution of Building Services Engineers, London, UK, 2010.
- [24] J. H. Klote and J. Milke, "Design of smoke management systems," ASHRAE Publications 90022, 1992.
- [25] "ASTM E-1546 Standard Guide for Development of Fire-Hazard-Assessment Standards," American Society for Testing and Materials, Philadelphia, Pa, USA, 2000.
- [26] B. Hume, "Development of standards for fire field models," Fire Research Report 85, Fire Research Division, Office of the Deputy Prime Minister, London, UK, November, 2003.
- [27] W. K. Chow, "Review on fire models and their application to design based on 'fire engineering approach,'" in *Proceedings of the International Conference on Building Fire Safety*, pp. 12–24, Gardens Point Campus, Queensland University of Technology, Brisbane, Queensland, Australia, November 2003.
- [28] W. K. Mok and W. K. Chow, "'Verification and validation' in modeling fire by computational fluid dynamics," *International Journal on Architectural Science*, vol. 5, no. 3, pp. 58–67, 2004.
- [29] R. N. Mawhinney, E. R. Galea, N. Hoffmann, and M. K. Patel, "A critical comparison of a phoenics based fire field model with experimental compartment fire data," *Journal of Fire Protection Engineering*, vol. 6, no. 4, pp. 137–152, 1994.
- [30] Z. Wang, F. Jia, E. R. Galea, M. K. Patel, and J. Ewer, "Simulating one of the CIB W14 round robin test cases using the SMARTFIRE fire field model," *Fire Safety Journal*, vol. 36, no. 7, pp. 661–677, 2001.
- [31] W. L. Oberkampf and T. G. Trucano, "Verification and validation in computational fluid dynamics," SAND2002-0529, Sandia National Laboratories, Albuquerque, NM, USA, 2002.
- [32] R. D. Peacock, W. W. Jones, and R. W. Bukowski, "Verification of a model of fire and smoke transport," *Fire Safety Journal*, vol. 21, no. 2, pp. 89–129, 1993.
- [33] H. Ingasson and S. Olsson, "Interaction between sprinklers and fire vents," SP Report 1992.11, Swedish National Testing and Research Institute, Borås, Sweden, 1992.
- [34] D. Steckler, J. G. Quintiere, and W. J. Rinkinen, "Flow induced by fire in a compartment," NBSIR 82-2520, U.S. National Bureau of Standards, 1982.
- [35] J. Hietniemi, S. Hostikka, and J. Vaari, "FDS simulation of fire spread—comparison of model results with experimental data," ESPOO2004, VVT Working Papers 4, VVT Building and Transport, Espoo, Finland, 2004.
- [36] "Verification and Validation of Selected Fire Models for Nuclear Power Plant Applications (NUREG-1824, Vols. 1-7)," Draft Report for Comment, US Nuclear Regulatory Commission plans, <http://www.nrc.gov/reading-rm/doc-collections/nuregs/staff/sr1824/>.
- [37] W. K. Chow, "Necessity of carrying out hot smoke tests and a case study," in *Proceedings of the Workshop on the Trends of Fire Safety and Smoke Control in Building*, pp. 1–19, National Taipei University of Science and Technology organized by Architectural and Building Research Institute, Ministry of Interior, Taipei, Taiwan, December 2005.
- [38] W. K. Chow, "Atrium smoke exhaust and technical issues on hot smoke tests," in *ASME Summer Heat Transfer Conference*, pp. 1–4, San Francisco, Calif, USA, July 2005, Paper HT2005-72412.
- [39] W. K. Chow, "Technical issues on atrium hot smoke tests," in *Proceedings of the Fire Science and Engineering—the 2nd Conference on the Development of Performance-Based Fire Code*, pp. 267–272, November 2005.
- [40] W. K. Chow, "Atrium hot smoke tests in evaluating performance of smoke exhaust systems," in *Proceedings of the International Congress "Smoke Control in Buildings and Tunnels"*, School of Industrial and Telecommunication Engineers, Santander, Spain, October 2008.
- [41] W. K. Chow, S. S. Li, and C. L. Chow, "Justification of fire field models by atrium hot smoke tests," in *ASME Summer Heat Transfer Conference (HT '09)*, pp. 21–25, San Francisco, Calif, USA, July 2009.
- [42] E. E. Khalil, "Private communications at 10th AIAA/ASME Joint Thermophysics and Heat Transfer Conference," Chicago, Ill, USA, June-July 2010.
- [43] G. W. Zou, H. P. Tan, W. K. Chow, and Y. Gao, "Effects of varying Smagorinsky constant on simulating post-flashover fires," *International Journal of Computational Fluid Dynamics*, vol. 21, no. 2, pp. 107–119, 2007.
- [44] W. J. Minkowycz, E. M. Sparrow, G. E. Schneider, and R. H. Pletcher, *Handbook of Numerical Heat Transfer*, John Wiley & Sons, New York, NY, USA, 1988.
- [45] W. K. Chow and Y. L. Cheung, "Selection of differencing schemes on simulating the sprinkler hot-air layer problem," *Numerical Heat Transfer Part A*, vol. 35, no. 3, pp. 311–330, 1999.
- [46] W. Q. Tao, Y. L. He, Z. Y. Li, and Z. G. Qu, "Some recent advances in finite volume approach and their applications in the study of heat transfer enhancement," *International Journal of Thermal Sciences*, vol. 44, no. 7, pp. 623–643, 2005.
- [47] R. I. Issa, "Solution of the implicitly discretised fluid flow equations by operator-splitting," *Journal of Computational Physics*, vol. 62, no. 1, pp. 40–65, 1986.
- [48] K. B. McGrattan, H. R. Baum, R. G. Rehm et al., "Fire dynamics simulator (version 4)—technical reference guide," NIST Special Publication 1018, US Department of Commerce, National Institute of Standards and Technology, July 2004.
- [49] K. B. McGrattan, G. P. Forney, J. E. Floyd, S. Hostikka, and K. Prasad, "Fire dynamics simulator (version 4)—user's guide," NIST Special Publication 1019, US Department of Commerce, National Institute of Standards and Technology, July 2004.

- [50] S. J. Emmerich and K. B. McGrattan, "Application of a large eddy simulation model to study room airflow," in *Proceedings of the ASHRAE Winter Meeting*, pp. 1128–1140, San Francisco, Calif, USA, January 1998.
- [51] W. Zhang, A. Hamer, M. Klassen, D. Carpenter, and R. Roby, "Turbulence statistics in a fire room model by large eddy simulation," *Fire Safety Journal*, vol. 37, no. 8, pp. 721–752, 2002.
- [52] American Institute of Aeronautics and Astronautics, "Guide for the verification and validation of computational fluid dynamics simulations," in *American Institute of Aeronautics and Astronautics*, Reston, Va, USA, 1998, AIAA G-077-1998.
- [53] P. J. Roache, *Verification and Validation in Computational Science and Engineering*, Hermosa, Albuquerque, NM, USA, 1998.
- [54] G. W. Zou and W. K. Chow, "Evaluation of the field model, fire dynamics simulator, for a specific experimental scenario," *Journal of Fire Protection Engineering*, vol. 15, no. 2, pp. 77–92, 2005.
- [55] R. D. Peacock, P. A. Reneke, W. D. Davis W., and W. W. Jones, "Quantifying fire model evaluation using functional analysis," *Fire Safety Journal*, vol. 33, no. 3, pp. 167–184, 1999.
- [56] G. P. Forney and W. F. Moss, "Analyzing and exploiting numerical characteristics of zone fire models," *Fire Science and Technology*, vol. 14, no. 1, pp. 49–60, 1994.
- [57] W. K. Chow and G. W. Zou, "Numerical simulation of pressure changes in closed chamber fires," *Building and Environment*, vol. 44, no. 6, pp. 1261–1275, 2009.
- [58] B. Hägglund, K. Nireus, and P. Werling, *Effects of Inlets on Natural Fire Vents: An Experimental Study*, National Defence Research Establishment Department of Weapons and Protection, Stockholm, Sweden, 1996.
- [59] S. S. Li and W. K. Chow, "Application of computational fluid dynamics in simulating fire-induced air flow in large halls," in *Proceedings of the 8th Asia-Oceania Symposium on Fire Science and Technology*, Melbourne, Australia, December 2010.
- [60] A. Schaelin, J. van der Maas, and A. Moser, "Simulation of airflow through large openings in buildings," in *Proceedings of the ASHRAE Winter Meeting*, pp. 319–328, Anaheim, Calif, USA, January 1992.
- [61] S. S. Li and W. K. Chow, "Validation of fire models predictions with a room fire test," in *Proceedings of the Annual Meeting—SFPE Professional Development Conference and Exposition*, Scottsdale, Ariz, USA, October 2009.
- [62] W. K. Chow, "A brief on performance-based design for building fire safety," in *Proceedings of the International Conference on Safety & Security Management and Engineering Technology (ICSSMET '09)*, Chiayi, Taiwan, December 2009.
- [63] S. M. Lo and R. K. K. Yuen, "Views of building professionals in the implementation aspects of fire safety engineering approach in building design: a preliminary study," *International Journal on Engineering Performance-Based Fire Codes*, vol. 1, no. 3, pp. 129–133, 1999.
- [64] J. A. Milke, "Education issues," in *Proceedings of the 2nd Conference on Fire Safety Design in the 21st Century*, pp. 179–184, Worcester Polytechnic Institute, Worcester, Mass, USA, June 1999.

## Research Article

# Numerical Simulations for a Typical Train Fire in China

W. K. Chow,<sup>1</sup> K. C. Lam,<sup>1</sup> N. K. Fong,<sup>1</sup> S. S. Li,<sup>2</sup> and Y. Gao<sup>2</sup>

<sup>1</sup> *Research Centre for Fire Engineering, Department of Building Services Engineering, Area of Strength: Fire Safety Engineering, The Hong Kong Polytechnic University, Hong Kong*

<sup>2</sup> *Department of Building Engineering, Harbin Engineering University, Harbin, 150001 Heilongjiang, China*

Correspondence should be addressed to W. K. Chow, beelize@polyu.edu.hk

Received 12 November 2010; Accepted 2 February 2011

Academic Editor: Guan Yeoh

Copyright © 2011 W. K. Chow et al. This is an open access article distributed under the Creative Commons Attribution License, which permits unrestricted use, distribution, and reproduction in any medium, provided the original work is properly cited.

Railway is the key transport means in China including the Mainland, Taiwan, and Hong Kong. Consequent to so many big arson and accidental fires in the public transport systems including trains and buses, fire safety in passenger trains is a concern. Numerical simulations with Computational Fluid Dynamics on identified fire scenarios with typical train compartments in China will be reported in this paper. The heat release rate of the first ignited item was taken as the input parameter. The mass lost rate of fuel vapor of other combustibles was estimated to predict the resultant heat release rates by the combustion models in the software. Results on air flow, velocity vectors, temperature distribution, smoke layer height, and smoke spread patterns inside the train compartment were analyzed. The results are useful for working out appropriate fire safety measures for train vehicles and determining the design fire for subway stations and railway tunnels.

## 1. Introduction

Key functions of railway lines are for supporting mass transport for dense urban areas in the Far East [1], particularly important in China [2]. Traffic loadings for those railway lines in big cities are very heavy. Large number of passengers would stay inside the train vehicles for an hour. The enclosed train vehicles used to be crowded with passengers. The combustible contents can be high, depending on the train design and the luggage passengers carried. Consequent to so many accidents in public transport vehicles in the Far East, including bus fires burning up the whole vehicle within 15 minutes (e.g., [3]) and the arson underground train fires [4, 5], fire safety in the public transport systems is now a concern.

If a fire occurs, smoke and even flame would spread rapidly inside the compartment, threatening the life safety of passengers and lead to great property losses. A long list of fire safety requirements was specified for the railway systems. Whether such requirements are reasonable has to be watched. It is important to study the fire and smoke spreading inside passenger trains to ensure safe evacuation of passengers and reduce property losses.

As reviewed [6], the problems on railway system fires can be divided into train vehicles, subway stations, and railway tunnels. Train fires were studied quite extensively in the past decade. Examples are the train fire projects [7–9] in USA; those works on passenger train vehicles [10, 11] in Australia; the Daegu fire [12, 13] in Korea and the European works [14–16]. Works proposed in USA [7–9] were on fire safety design of train compartments, materials selection, design of fire detection and suppression systems, and emergency evacuation. Full-scale tests were conducted in Australia [10, 11] on fire and smoke spreading inside a passenger train. A collaboration project EUREKA [15] was set up by nine European countries from 1990 to 1992. Full-scale burning tests on a train were carried out including those tunnels [14] to study the fire size and safety, and a summary was presented [16]. Risks and possible consequences of fires in a train compartment were studied by Chow [17, 18]. Recommendations were made on the fire safety design of trains [18].

Railway transport in China (Mainland, Hong Kong and Taiwan) is developing rapidly. High-speed trains (those with travel speed over 250 km per hour) will be the key transport medium. Appropriate fire safety design has to be provided [6].

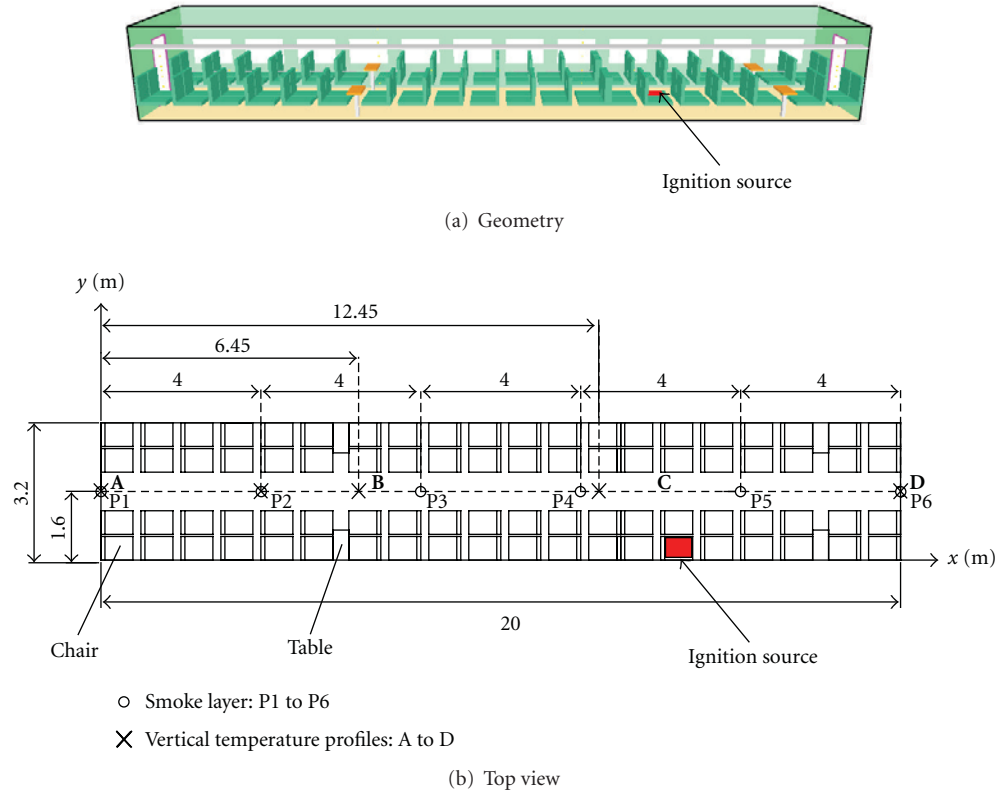


FIGURE 1: The typical train compartment.

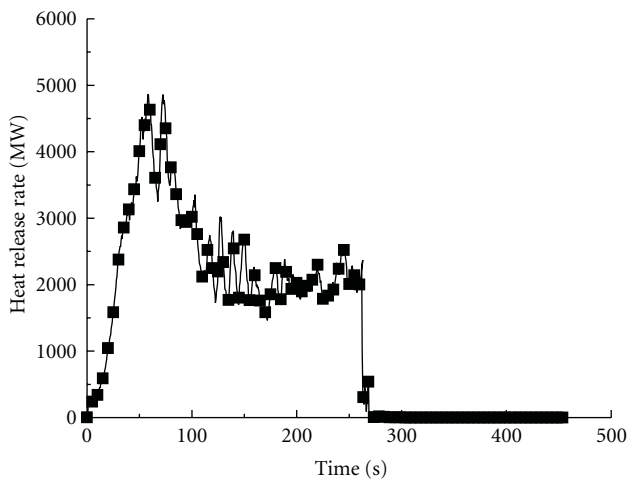


FIGURE 2: Predicted heat release rate in the train vehicle.

In this paper, fire environment in a train vehicle will be studied by Computational Fluid Dynamics (CFD) [19]. The model Fire Dynamics Simulator FDS 4.0.6 [20, 21] developed at the Building and Fire Research Laboratory, National Institute of Standards and Technology in USA was used. A typical train vehicle in China with two doors opened at the ends was considered. The heat release rate of the first ignited item was taken as the input parameter. Air velocity vectors,

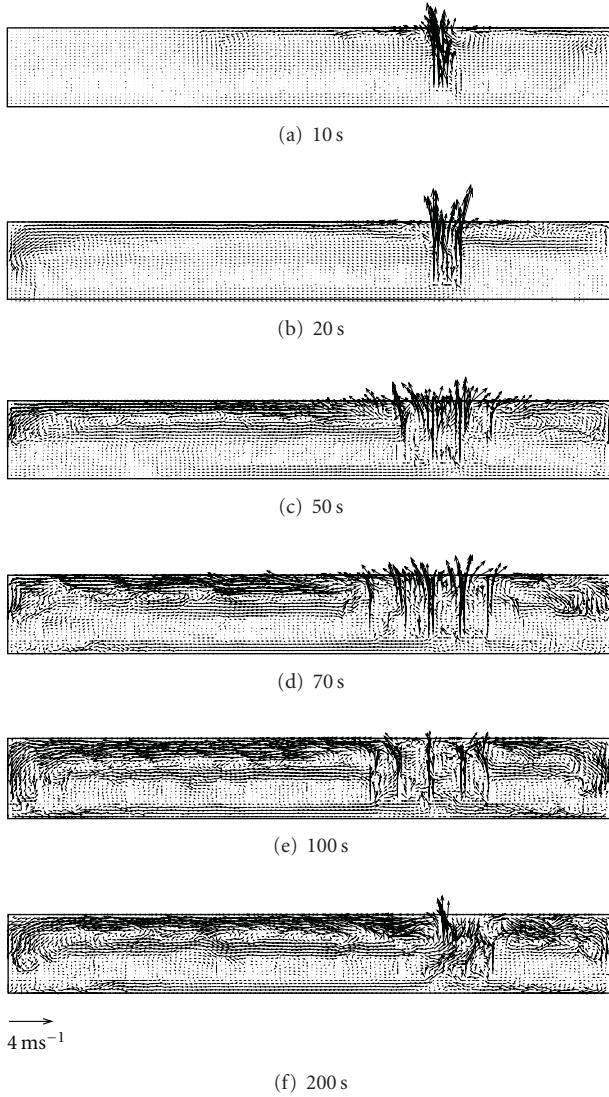
temperature distribution, smoke layer interface height, flame and smoke spread over the fire duration were predicted.

## 2. The CFD Model

The CFD software FDS [20, 21] was selected in this paper for simulating fires in a typical train vehicle. Smoke (including entrained air, combustion products and unburnt fuel vapor) produced from a fire is regarded as weakly combustible ideal gas flow of low Mach number. The set of Navier-Stokes equations was modified to derive the flow with filtering [22]. The turbulent part can be treated by direct numerical simulation (DNS) or large eddy simulation (LES) [19–22]. LES was adopted in this paper.

Combustion and radiation models are under development in FDS. Two combustion models can be selected, depending on the resolution of the underlying grids. Diffusion of fuel and oxygen is modeled directly for DNS with global one-step, finite-rate chemical reaction. The mixture fraction combustion model [20–23] based on the assumption of fast reaction and laminar diffusive flame is used for LES. This will resolve the diffusion of fuel and oxygen when the grids are not fine enough. In addition, the radiation absorption of gases inside the smoke layer is also considered.

In this paper, the mixture fraction model is used to describe the burning process of a fire. The model is based on the assumption that the combustion is mixing controlled.

FIGURE 3: Velocity vectors on the plane  $y = 6.7$  m across the fire.

All species of interest are described by a mixture fraction  $f(\vec{x}, t)$ . This a conserved quantity representing the fraction of species at a given point originated from the fuel. The mixture fracture  $f(\vec{x}, t)$  would satisfy the conservation law:

$$\frac{\partial \rho f}{\partial t} + \nabla \cdot (\rho \vec{u} f) = \nabla \cdot (\rho D \nabla f). \quad (1)$$

The relation between the mass fraction of each species and the mixture fraction is known as the “state relation.” The state relation for the oxygen mass fraction would provide the necessary information for calculating the local oxygen mass consumption rate.

The local heat release rate  $\dot{q}^m$  is computed from the local oxygen consumption rate by assuming that  $\dot{q}^m$  is directly proportional to the oxygen consumption rate and independent of the fuel involved. By solving the transport equations of oxygen concentration  $Y_O$ , the mass loss rate of oxygen  $\dot{m}_O^m$  can be deduced. Once the oxygen consumption rate is determined, multiplying it by the heat released per

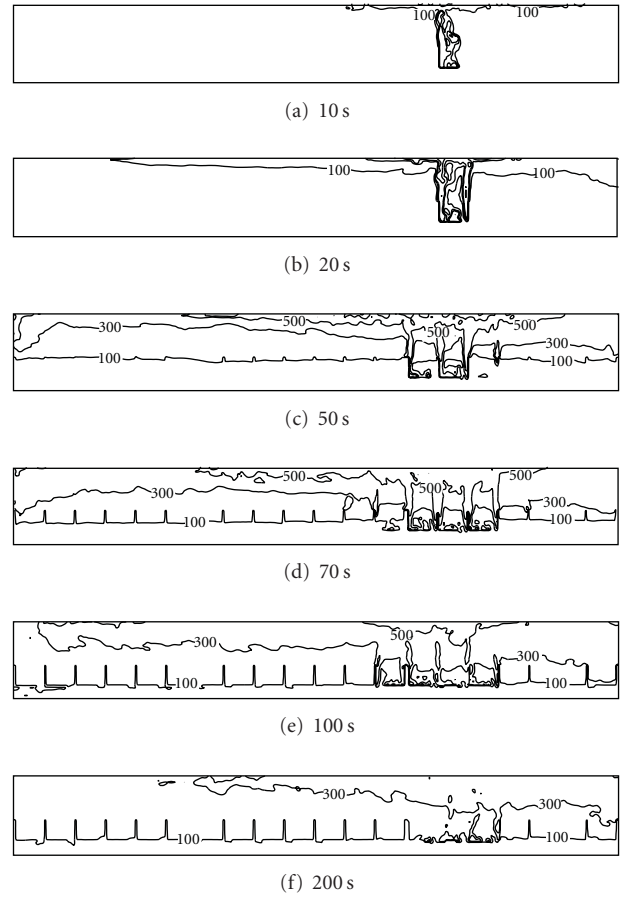
FIGURE 4: Temperature distributions on the plane  $y = 6.7$  m across the fire.

TABLE 1: Combustibles inside the train compartment.

Items	Material	Number	Size
Chairs	Upholstery	20	0.8 m × 0.55 m × 0.1 m
Chair backs	Upholstery	20	0.7 m × 0.55 m × 0.1 m
Tables	Spruce	4	0.7 m × 0.4 m × 0.05 m
Table stands	Plastic	4	0.1 m × 0.1 m × 0.75 m
Luggage shelves	Plastic	2	20.0 m × 0.4 m × 0.05 m
Flooring materials	Carpet	1	20.0 m × 3.2 m

unit mass of oxygen consumed  $\Delta H_O$  would give the local heat release rate  $\dot{q}^m$

$$\dot{q}^m = \Delta H_O \dot{m}_O^m. \quad (2)$$

Note that deviation of the mixture fraction equation (1) is not necessarily limited to fast chemistries.

Selection of the Smagorinsky constant  $C_s$  is important in applying LES. This point had been analyzed in simulating flashover fires [24]. The value was taken to be 0.2. Both the Schmidt number  $Sc_T$  and turbulent Prandtl number  $Pr_T$  were taken as 0.5.

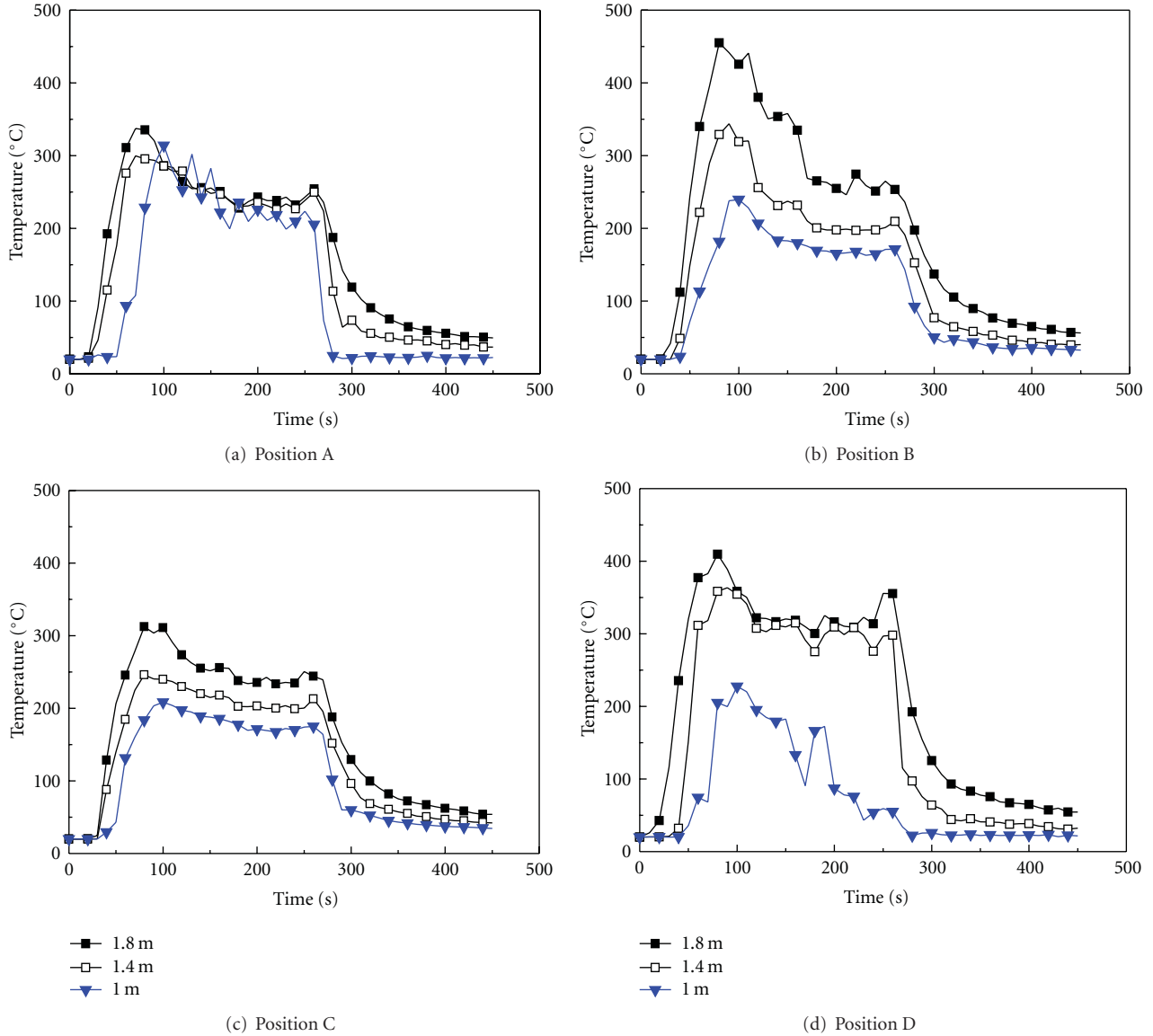


FIGURE 5: Temperatures at positions A, B, C, and D.

### 3. Numerical Experiments

A typical train compartment in the Far East with layout and geometry shown in Figure 1 was selected. The dimensions of the train compartment are of length 20.0 m, width 3.2 m and height 2.6 m. Fire environment induced by a train fire was simulated. Location of the fire is shown in Figure 1(a). Combustibles inside the train compartment are listed in Table 1.

The smoke layer height was studied at points P1 to P6. Vertical temperature profiles at positions A, B, C, and D as shown in Figure 1(b) were studied. Positions A and D were along the centreline of the door above the two ends, each with six points vertically. There were five vertical points at positions B and C.

Open flame with a heat release rate of 250 kW was taken as the heat release rate of the first ignited item. The heat

release rate increased linearly to a maximum value of 250 kW in 1 s, kept at this value up to 200 s and then decreased linearly to zero at 250 s.

Two opening doors were set at the two sides of the train compartment, and the open external boundaries were set. At open external boundaries, a term  $H$  expressing pressure, depending on whether the flow is outgoing or incoming is prescribed as:

$$H \begin{cases} \frac{|u|^2}{2}, & \text{outgoing,} \\ 0, & \text{incoming.} \end{cases} \quad (3)$$

The outgoing boundary condition assumes that the pressure perturbation  $\tilde{p}$  is zero at an outgoing boundary and that  $H$  is constant along streamlines. The incoming boundary condition assumes that  $H$  is zero infinitely far away. At

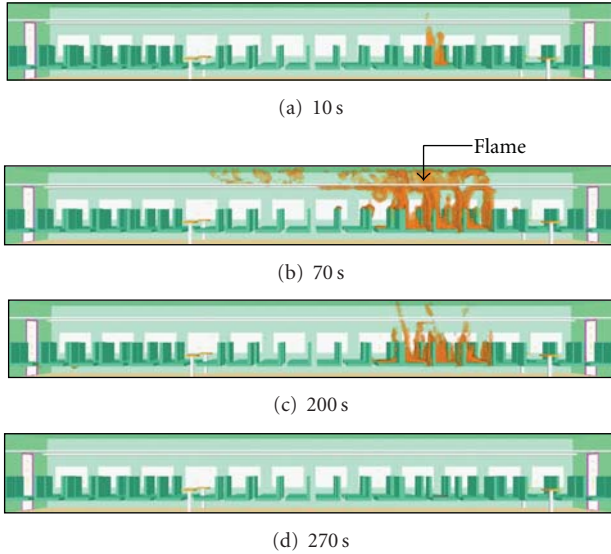


FIGURE 6: Flame spread inside the train compartment.

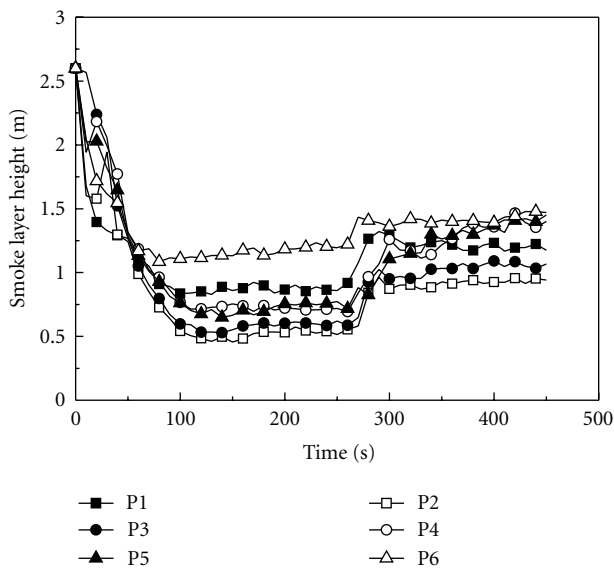


FIGURE 7: Smoke layer heights.

the boundary between two meshes, the pressure boundary condition is similar to that at an external open boundary, except that where the flow is incoming,  $H$  is taken from the adjacent mesh [20].

Other combustibles inside the train compartment would be ignited to generate heat, and then ignite more objects subsequently. The heat release rate curves inside the train compartment are shown in Figure 2. There were no other openings except the train doors at the two ends. As the combustion zone was far away from the doors, outside fresh air could not be supplied quickly. The heat release rate reached a maximum value of about 4.8 MW at 70 s. The value started to decrease to about 2 MW up to 270 s and then fell down to zero at about 270 s. Results are useful for

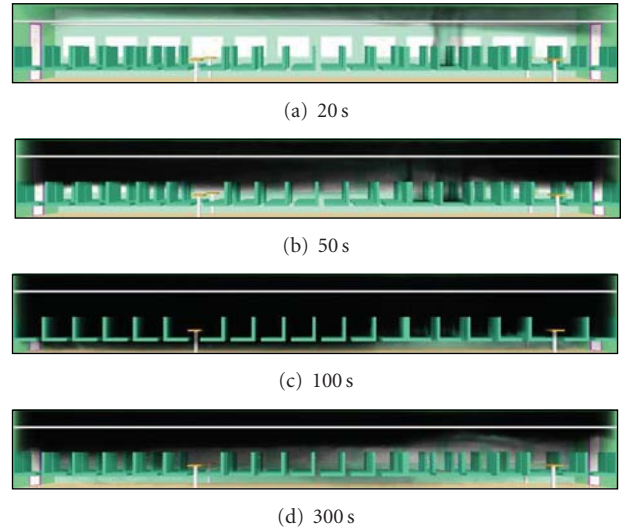


FIGURE 8: Smoke spread inside the train compartment.

determining the design fire [14, 16, 17] for subway stations and railway tunnels.

#### 4. Fire-Induced Flow

Air velocity vectors at the central plane ( $y = 0.9$  m) of the fire source are shown in Figures 3(a) to 3(f). The fire burnt only with a small area initially. As the fire grew up, bigger air circulation was observed until the flow reached the walls at the two ends of the train.

Temperature distribution at the central plane ( $y = 0.9$  m) are shown in Figures 4(a) to 4(f). Transient temperature curves at 1.8 m, 1.4 m and 1.1 m at positions A, B, C, and D are shown in Figures 5(a) to 5(d).

It is observed from the figures that the maximum temperature at those three heights could be over 200°C. The maximum value was up to 450°C at position C near to the fire. Such high temperatures would pose risks to life. Proper safety measures should be implemented to reduce the indoor temperature.

#### 5. Flame Spread

Both flame and smoke presented by FDS can be displayed by the postprocessor Smokeview [20, 21]. As discussed in the manual, fire by default is colored a dark shade of orange wherever the computed heat release rate per unit volume exceeds a user-defined cut-off value. This cut-off value refers to the heat release rate required at a node before calling it “fire” rather than “smoke”. Transparency or optical thickness of the fire was specified by the 50% flame depth for visualization. Taking a smaller value would give an opaque fire, and a high value would give a transparent fire.

Predicted flame spread inside the train compartment at 10 s, 70 s, 200 s and 270 s after starting to burn the first object are shown in Figures 6(a) to 6(d).

## 6. Smoke Spread

As observed in fire accidents, smoke spread is even more threatening than flame spread. Smoke layer height at points P1 to P6 are shown in Figure 7. Points P4 and P5 are roughly symmetric with respect to the first ignited item as in Figure 1(b). It is observed that the smoke layer height curves at points P4 and P5 basically overlapped. In view of this, data for point P4 was taken for comparison with others as in Figure 7.

As points P1 and P6 were near to the door, the smoke layer height was higher than the other three points. The smoke layer height increased with the distance away from the fire source. The smoke layer height decreased to below 1 m at all the points except for point P6. This situation would affect evacuation.

The approach to displaying smoke taken by Smokeview [19, 20] is to display a series of parallel planes, which will be colored black for smoke. The transparency value was estimated by using the time dependent soot densities computed by FDS corresponding to the grid spacings of the simulation. The transparencies are adjusted at a certain time interval to account for different path lengths through the smoke in different view directions. All the planes are combined together by the graphics hardware to form one image. The smoke “planes” might be visible under some view angles. Changing the viewing angle slightly will make the smoke appear more uniform.

The smoke spread process inside the train compartment is shown in Figures 8(a) to 8(d). As the flame spread out, the smoke layer height kept descending. When the fire was extinguished for the combustible material burnt out at 270 s, the smoke layer height started to move upwards gradually as in Figure 8(d).

## 7. Conclusion

In this paper, fire in a typical train compartment in the Far East was simulated using FDS 4.0.6 [20, 21]. Results indicated that serious consequences would be resulted in a train compartment fire due to the small enclosed space. Appropriate fire suppression and smoke exhaust systems should be provided to reduce the indoor temperature and keep the smoke layer high.

As flame spread depends on the materials inside the train compartment, the simulated results of temperature and smoke layer height would be different for different combustibles. Results on the heat release rate as shown in Figure 2 are also useful in determining the design fire [14–18] for subway stations and railway tunnels. Including movable fire load can give a much bigger fire than those specified in common guides [25, 26] as pointed out [16, 18].

## Acknowledgment

The work described in this paper was partially supported by a PolyU Grant for the Project “Aspects of Big Fires in Long Vehicular Tunnels” with account no. G-U842.

## References

- [1] P. C. Miclea, W. K. Chow, S. W. Chien, J. Li, A. H. Kashef, and K. Kai, “International tunnel fire-safety design practices,” *ASHRAE Journal*, vol. 49, no. 8, pp. 50–60, 2007.
- [2] L. Guilin, “Shanghai: status and trends in the urban public transport,” *Public Transport International – Special Edition*, pp. 10–11, 2002.
- [3] W. K. Chow, “Smoke control design for double-deck bus fires with a zone model,” in *Proceedings of the 13th International Heat Transfer Conference*, pp. 13–18, Sydney, Australia, August 2006.
- [4] South China Morning Post, “14 injured in peak-hour MTR arson attack,” South China Morning Post, Hong Kong, Editorial, A1, January 2004.
- [5] South China Morning Post, “Tageu’s subway line has been beset by disaster,” South China Morning Post, Hong Kong, Main Section, 10, January 2004.
- [6] W. K. Chow and J. Zhu, “Preliminary view on fire safety for rapid passenger rail system in China,” in *Proceedings of the Annual Fire Conference, Building and Fire Research Laboratory*, National Institute of Standards and Technology, Gaithersburg, Md, USA, April 2007.
- [7] R. D. Peacock, R. W. Bukowski, W. W. Jones, P. A. Reneke, V. Babrauskas, and J. E. Brown, “Fire safety of passenger trains: a review of current approaches and of new concepts,” Tech. Rep. 1406, National Institute of Standards and Technology, Gaithersburg, Md, USA, 1994.
- [8] R. D. Peacock, P. A. Reneke, W. W. Jones, R. W. Bukowski, and V. Babrauskas, “Concepts for fire protection of passenger rail transportation vehicles: past, present, and future,” *Fire and Materials*, vol. 19, no. 2, pp. 71–87, 1995.
- [9] R. D. Peacock, P. A. Reneke, J. D. Averill, R. W. Bukowski, and J. H. Klote, “Fire safety of passenger trains: phase 2. Application of fire hazard analysis techniques,” Tech. Rep. NISTIR 6525, National Institute of Standards and Technology, Gaithersburg, Md, USA, 2002.
- [10] V. P. Dowling and N. White, “Fire sizes in railway passenger saloons,” in *Proceedings of the 6th Asia-Oceania Symposium on Fire Science and Technology*, pp. 602–611, Daegu, Korea, March 2004.
- [11] V. P. Dowling, N. White, A. K. Webb, and J. R. Barnett, “When a passenger train burns, how big is the fire? Invited Lecture,” in *Proceedings of the 7th Asia-Oceania Symposium on Fire Science and Technology*, pp. 19–28, Hong Kong, September 2007.
- [12] D. H. Lee, W. S. Jung, C. K. Lee, S. K. Roh, W. H. Kim, and J. H. Kim, “Fire safety characteristics of interior materials of Korean railway vehicles,” in *Proceedings of the 6th Asia-Oceania Symposium on Fire Science and Technology*, pp. 735–741, Daegu, Korea, March 2004.
- [13] S. K. Roh, “A study on the emergency response manual for urban transit fires. Invited Lecture,” in *Proceedings of the 7th Asia-Oceania Symposium on Fire Science and Technology*, pp. 29–38, Hong Kong, September 2007.
- [14] G. B. Grant and D. Drysdale, “Estimating heat release rates from large-scale tunnel fires,” in *Proceedings of the 5th International Symposium on Fire Safety Science*, pp. 1213–1224, Melbourne, Australia, 1995.
- [15] A. Haack, “Fire protection in traffic tunnels: general aspects and results of the EUREKA project,” *Tunnelling and Underground Space Technology*, vol. 13, no. 4, pp. 377–381, 1998.
- [16] H. Ingason and A. Lönnemark, “Heat release rates from heavy goods vehicle trailer fires in tunnels,” *Fire Safety Journal*, vol. 40, no. 7, pp. 646–668, 2005.

- [17] W. K. Chow, "Fire safety in train vehicle: design based on accidental fire or arson fire?" The Green Cross, March/April, 2004, pp 7.
- [18] W. K. Chow, "Updated issues on performance-based design in Hong Kong," in *Proceedings of the 1st Global COE International Symposium*, vol. 26, Seoul, Korea, March 2009.
- [19] W. K. Chow, "Use of computational fluid dynamics for simulating enclosure fires," *Journal of Fire Sciences*, vol. 13, no. 4, pp. 300–334, 1995.
- [20] K. B. McGrattan, "Fire dynamics simulator (Version 4)," Tech. Rep. 1018, Fire Research Division, Building and Fire Research Laboratory, National Institute of Standards and Technology, Gaithersburg, Md, USA, 2006.
- [21] K. B. McGrattan and G. P. Forney, "Fire Dynamics Simulator (Version 4.0.6)," Tech. Rep. 1019, Fire Research Division, Building and Fire Research Laboratory, National Institute of Standards and Technology, Gaithersburg, Md, USA, 2006.
- [22] H. R. Baum, "Large eddy simulations of fires—from concepts to computations," *Fire Protection Engineering*, vol. 6, pp. 36–42, 2000.
- [23] K. B. McGrattan, H. R. Baum, and R. G. Rehm, "Large Eddy Simulations of Smoke Movement," *Fire Safety Journal*, vol. 30, no. 2, pp. 161–178, 1998.
- [24] G. W. Zou, H. P. Tan, W. K. Chow, and Y. Gao, "Effects of varying Smagorinsky constant on simulating post-flashover fires," *International Journal of Computational Fluid Dynamics*, vol. 21, no. 2, pp. 107–119, 2007.
- [25] NFPA, "NFPA 502, Standard for road tunnels, bridges, and other limited access highways," National Fire Protection Association, 2004.
- [26] PIARC, "Fire and smoke control in road tunnels," PIARC, 05.05B-1999.

## Research Article

# Simulation of Pharyngeal Airway Interaction with Air Flow Using Low-Re Turbulence Model

**M. R. Rasani, K. Inthavong, and J. Y. Tu**

*School of Aerospace, Mechanical and Manufacturing Engineering, RMIT University, Bundoora, VIC 3083, Australia*

Correspondence should be addressed to J. Y. Tu, [jiyuan.tu@rmit.edu.au](mailto:jiyuan.tu@rmit.edu.au)

Received 15 October 2010; Accepted 14 February 2011

Academic Editor: Guan Yeoh

Copyright © 2011 M. R. Rasani et al. This is an open access article distributed under the Creative Commons Attribution License, which permits unrestricted use, distribution, and reproduction in any medium, provided the original work is properly cited.

This paper aims to simulate the interaction between a simplified tongue replica with expiratory air flow considering the flow in the pharyngeal airway to be turbulent. A three-dimensional model with a low-Re SST turbulence model is adopted. An Arbitrary Eulerian-Lagrangian description for the fluid governing equation is coupled with the Lagrangian structural solver via a partitioned approach, allowing deformation of the fluid domain to be captured. Both the three-dimensional flow features and collapsibility of the tongue are presented. In addition, examining initial constriction height ranging from 0.8 mm to 11.0 mm and tongue replica modulus from 1.25 MPa to 2.25 MPa, the influence of both of these parameters on the flow rate and collapsibility of the tongue is also investigated and discussed. Numerical simulations confirm expected predisposition of apneic patients with narrower airway opening to flow obstruction and suggest much severe tongue collapsibility if the pharyngeal flow regime is turbulent compared to laminar.

## 1. Introduction

Collapse of the human pharyngeal airways during sleep has serious health complications with an estimated 10% of snorers being at risk to obstructive sleep apnoea [1, 2]. These episodes of partial or full cessation of breathing per hour, influence the quality of sleep, reduce brain oxygen saturation and have been linked to hypertension and heart failures [1]. The physiological mechanisms of such conditions are very closely related to flow in compliant tubes or channels. Extensive experiments of flow in Starling resistors have revealed rich variety of dynamics involved in such compressed collapsible tube systems [3, 4].

Not surprisingly, many numerical models have been developed to simulate the system and theorise the mechanisms involved in the collapse and self-excited oscillations of these compliant walls seen in the experiments. Earlier models include lumped parameter models [5] which integrated the flow variables along the whole vessel and various one-dimensional models (e.g., [6–8]) taking into account variation of flow variables in the longitudinal direction along the vessel but assume those variables do not vary within each

cross-section. More complicated two-dimensional models have also been developed, such as those by Luo and Pedley [6, 7, 9, 10], revealing certain conditions (function of Reynolds Number and membrane tension), where steady solution are stable and below which self-excited oscillation and vorticity waves are generated in the flow. More recent three-dimensional modelling of collapsible tubes captured strong buckling of the tube [11] and also revealed both possible mechanism for flow-wall energy extraction and critical Reynolds Number for onset of self-excited oscillations [12].

Applying these developments of flow in collapsible tubes to actual physiological phenomena presents a real challenge [1]. On the subject of obstructive sleep apnoea, Chouly et al. [2, 13] and Van Hirtum et al. [14] developed an asymptotic Navier-Stokes equation coupled with linear elastic shell elements to model flow-induced deformation of a simplified tongue subjected to expiratory flow. The collapse of the tongue onto the pharyngeal wall was also simulated via in-vitro experiments to validate their model assumptions and numerical results. In general, narrowing of the airway promotes increased transmural pressure via a venturi effect, resulting in partial collapse of the airway and a nonlinear

flow rate retardation as the intraluminal pressure difference is increased—a typical observation in collapsed channel called flow rate limitation.

The coupling between a two-dimensional, quasisteady, laminar, incompressible fluid flow with a shell model developed by Chouly et al. [2] was successful in obtaining efficient real-time results and was validated using pressurised latex in their experiments. Indeed, based on Reynolds Number, the flow is expected to be within the laminar ( $Re < 2000$ ) or transitional ( $2000 < Re < 10000$ ) regime. However, the complex morphology of the pharyngeal airway, could give rise to three-dimensional flow features which triggers transition or turbulence regimes at lower  $Re$  [15]. In fact, observation by Hahn [16] suggests turbulence kinetic energy at approximately 5% of the inlet velocity is not unexpected in the nasal cavity.

Both neurological and physiological factors have been implicated with apneic syndrome. Previous studies (e.g., [17]) have shown that apneic patients have in general, a narrower opening in the oropharynx region (perhaps, due to obesity or tissue buildup). Pharyngeal compliance among apneic and nonapneic subjects have also been shown to vary significantly, especially during expiratory flow [17].

Hence, the present study intends to instead consider a three-dimensional model of the expiratory fluid flow using a low- $Re$  turbulent model coupled to similar replication of the tongue. The effect of initial airway opening and the tongue stiffness on the collapsibility and flow inside the pharyngeal airway is investigated parametrically. Three-dimensional flow features and turbulence influence are also discussed.

## 2. Mathematical Model

**2.1. Governing Equation for Fluid.** Following the approach of Chouly and coworkers [2], a simplified three-dimensional flow configuration representing the pharyngeal airway is illustrated in Figure 1.

The converging flow through the narrowest opening in the oropharynx (at the base of the tongue) is expected to produce a jet stream and flow separation downstream of the constriction which is characterised by shear instability-induced turbulence [18]. Avoiding the intensive computational efforts involved with a three-dimensional Large Eddy Simulation (LES) and Direct Numerical Simulation (DNS), a more practical approach is employed. Steady, incompressible, turbulent flow in the three-dimensional tube is described using the Reynolds-Averaged Navier-Stokes (RANS) equations coupled with a Shear Stress Transport (SST)  $k$ - $\omega$  turbulent model:

$$\frac{\partial u_i}{\partial x_i} = 0, \quad (1)$$

$$\frac{\partial (u_j u_i)}{\partial x_j} = -\frac{1}{\rho} \frac{\partial p}{\partial x_i} + \frac{\partial}{\partial x_j} \left[ \nu \left( \frac{\partial u_i}{\partial x_j} + \frac{\partial u_j}{\partial x_i} \right) \right] + \frac{\partial \tau_{ij}^R}{\partial x_j}, \quad (2)$$

where  $u_i$  and  $p$  are the mean- or time-averaged velocities and pressure ( $i = 1, 2, 3$  for three-dimensional analysis),  $\rho$  is the fluid density and  $\tau_{ij}^R$  is the turbulent Reynolds stress tensor

$$\tau_{ij}^R = -\overline{u_i' u_j'}, \quad (3)$$

where  $u_i'$  represents the turbulent fluctuating velocity. Using Boussinesq's assumption, this Reynolds stress tensor is related to the mean velocities by the turbulent eddy viscosity:

$$\tau_{ij}^R = -\overline{u_i' u_j'} = \nu^T \left( \frac{\partial u_i}{\partial x_j} + \frac{\partial u_j}{\partial x_i} - \frac{2}{3} \frac{\partial u_k}{\partial x_k} \delta_{ij} \right), \quad (4)$$

where  $\nu^T = k/\omega$  is the turbulent eddy viscosity.

Therefore, in order to close the RANS equations (1) and (2), only the turbulent viscosity is required, which is determined by using 2 unknowns, that is, turbulent kinetic energy  $k$  and turbulent rate of dissipation  $\omega$ . The principle behind SST  $k$ - $\omega$  model is to blend the original  $k$ - $\omega$  and  $k$ - $\epsilon$  together such that, near the wall, the accuracy and robustness of the  $k$ - $\omega$  model is captured, while away from the wall (i.e., free stream or free shear regions), the accuracy of the  $k$ - $\epsilon$  is captured. Thus, the additional two equations required to solve for scalar variables  $k$  and  $\omega$  are [19]

$$\frac{\partial (u_j k)}{\partial x_j} = \frac{\partial}{\partial x_j} \left[ \left( \nu + \frac{\nu^T}{\sigma_k} \right) \frac{\partial k}{\partial x_j} \right] + P_k - 0.09k\omega, \quad (5)$$

$$\begin{aligned} \frac{\partial (u_j \omega)}{\partial x_j} &= \frac{\partial}{\partial x_j} \left[ \left( \nu + \frac{\nu^T}{\sigma_\omega} \right) \frac{\partial \omega}{\partial x_j} \right] + 2(1 - F_1) \frac{1}{\sigma_{\omega 2} \omega} \frac{\partial k}{\partial x_i} \frac{\partial \omega}{\partial x_i} \\ &+ \alpha \frac{\omega}{k} P_k - \beta \omega^2, \end{aligned} \quad (6)$$

where  $\sigma_k$ ,  $\sigma_\omega$ ,  $\sigma_{\omega 2}$ ,  $\alpha$ , and  $\beta$  are model constants (blended from the original model  $k$ - $\omega$  and  $k$ - $\epsilon$  constants),  $F_1$  represents the blending function which is dependant on the wall distance,  $P_k$  is the production of turbulence due to viscous forces (function of the mean velocities), and, thus, the last two terms in both equations are effectively representing the production and destruction of each  $k$  and  $\omega$ .

In addition, the SST model is further refined by employing a blending of the turbulent eddy viscosity formulation, allowing more accurate prediction of the eddy viscosity near and away from the walls:

$$\nu^T = \frac{a_1 k}{\max(a_1 \omega, SF_2)}, \quad (7)$$

where  $a_1$  is a model constant,  $F_2$  is another blending function (similarly depending on the wall distance) and  $S$  represents an invariant measure of the strain rate [19].

Equations (1), (2), (5), (6), and (7) represent the complete fluid model which is solved by the fluid solver. A low- $Re$  simulation with appropriate near-wall behaviour are readily captured in the SST  $k$ - $\omega$  model.

Assuming the flow is symmetrical about its mid-vertical plane, a half-model of the problem is constructed as depicted in Figure 2. Following similar notations by Luo and

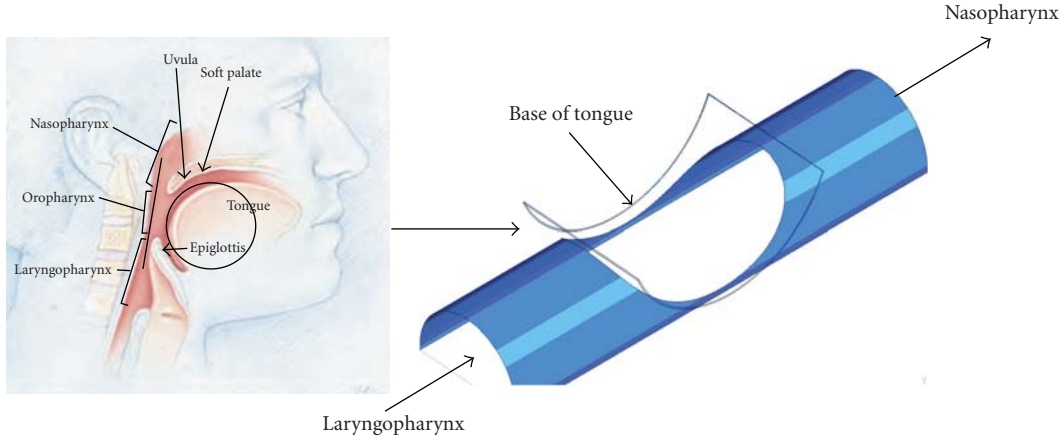


FIGURE 1: Pharyngeal airway model.

Pedley [6], the conditions imposed at each boundary are summarised as follows:

$$\text{Inlet: } p = p_{\text{in}}, x = -(L_u + L/2),$$

$$\text{Outlet: } p = p_{\text{out}}, x = (L/2 + L_d),$$

$$\text{Rigid Side Walls: } u_i = 0, y^2 + z^2 = d,$$

$$\text{Rigid Bottom Wall: } u_i = 0, y = -h,$$

$$\text{Elastic Wall: } u_i = U_i, \text{ on } \Gamma,$$

$$\text{Symmetrical Wall: } u_3 = 0, z = 0.$$

No slip boundary conditions at the walls implies that flow velocities  $u_i$  are zero at the rigid walls and at the elastic segment,  $u_i$  must match the elastic wall velocities  $U_i$ . At the inlet, a uniform upstream pressure  $p_{\text{in}}$  is specified, which implies a parabolic velocity profile definition at the inlet. While at the outlet, downstream pressure  $p_{\text{out}}$  has been fixed to zero implying a typical stress-free condition.

**2.2. Governing Equation for Structure.** For a continuum undergoing steady deformation, Cauchy's equation [20] is effectively a static equilibrium equation:

$$\nabla \cdot \sigma_{ij} + \mathbf{f} = 0, \quad (8)$$

where  $\sigma_{ij}$  is the stress tensor and  $\mathbf{f}$  is the external forcing term ( $i, j = 1, 2, 3$  for three-dimensional structures) which in this case, includes external pressure  $p_e$  plus the fluid pressure and fluid shear at the interface  $\Gamma$ . Mechanical properties of the tongue is not homogenous and anisotropic, more so with varying degrees of muscle activation. For simplicity, a homogenous isotropic material is assumed for the tongue, thus,  $\sigma = \mathbf{D}\epsilon$  where  $\epsilon$  is the strain vector and  $\mathbf{D}$  is the constitutive elastic stiffness matrix (which is a function of Young's modulus,  $E$ , and Poisson ratio,  $\nu$  of the structural material).

Considering small deformation theory, second-order terms in the Green-Lagrange strain tensor [20] could be

neglected. Thus, the strain-displacement relationship could be described as:

$$\epsilon_{ij} = \frac{1}{2} \left( \frac{\partial d_i}{\partial x_j} + \frac{\partial d_j}{\partial x_i} \right), \quad (9)$$

where  $d_i$  is the displacement tensor. Effectively, (8) and (9) represent the solid model, capturing the elastic wall deformation under external loads.

The tongue anatomy mainly consists of water (with reported density of  $1040 \text{ kg/m}^3$  [21]) and hence, is generally accepted as incompressible [22]. Accounting for that incompressibility, a Poisson ratio  $\nu$  of 0.499 has been used [2, 22] and is also adopted here. Tissues along pharyngeal airway have been reported with a range of moduli: 10–30 kPa for the vocal folds [23], 12–25 kPa for the soft palate [24] and 6 kPa [25] to 15 kPa [22] have been estimated for the tongue. In order to replicate the response of a real tongue, a hydrostatically pressurized latex shell tube was utilized by Chouly et al. [2, 13]. Similarly, a simulated shell modulus  $E$  in combination with an external pressure  $p_e$  that mimics this response is followed in this paper.

The elastic wall is assumed fixed everywhere except at the common face interfacing with the elastic segment of the fluid domain where an external pressure  $p_e$  is imposed simultaneously with the pressure  $p$  applied from the fluid domain.

### 3. Computational Method

A commercial finite volume solver (CFX) is used to solve the RANS equations in (1), (2), (5), (6), and (7). The fluid domain is subdivided into 8-noded three-dimensional hexahedral elements leading to an assembly of discretised algebraic equations in terms of the nodal unknowns  $u_i$ ,  $p$ ,  $k$ , and  $\omega$ . In general, finer meshes are located closer to the walls (elastic, rigid side and bottom) where higher velocity gradients are expected and flow separation or reattachment normally occur. In addition, denser meshes are also located in the vicinity of the constriction where sharp changes in pressure are expected.

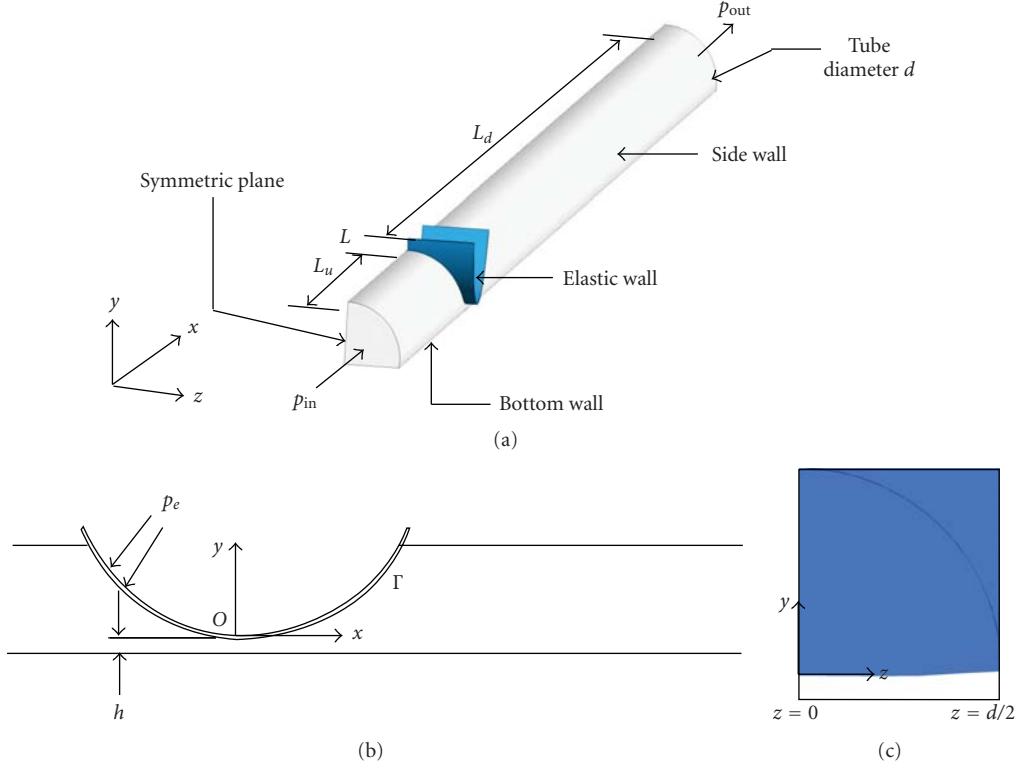


FIGURE 2: Model definition (a) isometric view, (b) side view looking at symmetrical plane, (c) frontal view looking from the inlet.

The governing fluid equations are based on a fixed Eulerian frame of reference in space. In order to account for boundary deformation and thus, deformation of the fluid mesh, an Arbitrary Lagrangian-Eulerian (ALE) description is employed in CFX. Effectively, in an ALE framework, the mesh velocity  $\tilde{u}_j$  is subtracted from the material velocity  $u_j$  in the differential operator [20, 26] on the left-hand side of transport (2), (5), and (6). Thus, an additional nodal unknown (i.e., mesh velocity  $\tilde{u}_j$ ) needs to be solved. CFX employs a diffusion model, which smoothes the internal domain nodal displacement according to a Laplace differential equation [19]:

$$\nabla \cdot (\Gamma_{\text{disp}} \nabla \delta) = 0, \quad (10)$$

where  $\delta$  is the nodal displacement relative to previous mesh positions,  $\Gamma_{\text{disp}}$  is some mesh stiffening parameter and (10) is solved subjected to specified nodal movement at the boundaries.

The commercial finite element solver (ANSYS) is used to solve the partial differential equations (8) and (9). Similarly, the structural domain is discretized into 8-noded SOLID185 elements and (9) is approximated using interpolation functions in terms of the unknown nodal deformations. Minimization of the variational total potential energy or weighted Galerkin residuals lead to an assembly of algebraic equation which could be solved as a function of imposed boundary conditions.

The fluid-structure interaction is achieved by satisfying either a velocity or displacement continuity (i.e., (11) or (12), resp.) and force equilibrium (13), at the common interface between both fluid and solid domain:

$$u_i = U_i \quad \text{on } \Gamma, \quad (11)$$

$$s_i = d_i \quad \text{on } \Gamma, \quad (12)$$

$$-p + \tau_{ij} = \sigma_{ij} \quad \text{on } \Gamma, \quad (13)$$

where  $u_i$  and  $s_i$  are, respectively, the flow velocity and boundary displacement on the interface,  $U_i$  and  $d_i$  are the structure velocity and displacement, respectively, on the interface. The terms on the left-hand side of (13) represent the fluid state of stress and the right-hand side is the stress on the structure.

In order to match these conditions simultaneously in both fluid and solid solvers, a successive iteration is employed in an ANSYS Workbench platform. The fluid variables are solved based on the initial geometrical configuration. The fluid pressure and shear forces at the elastic segment are interpolated to the nodes on the elastic wall. Applying them together with the external pressure and imposed boundary conditions, the solid solver solves for the deformation of the elastic wall. These nodal deflections are then interpolated back to nodes on the elastic boundary of the fluid, which is used to effect the mesh deformation on the fluid domain. The fluid solver then solves the unknown fluid variables using the current geometrical configuration and the process

is repeated until the nodal deflection and forces in (12) and (13) from current and previous coupling iterations are within a specified tolerance. The overall process can be summarised as in Figure 3.

Note that for steady conditions (where inertial effects are neglected and structural deformation reaches static equilibrium), elastic wall velocities  $U_i$  approaches zero.

Several runs with different downstream length  $L_d$  suggest that numerical results are not sensitive to the outlet proximity. In addition, finer mesh discretization also indicates similar overall wall shear distribution and more importantly, similar separation location off the elastic wall, suggesting adequate discretization.

## 4. Results and Discussion

In order to validate the structural model, a Poisson ratio of 0.499 and a Young's modulus  $E = 1.75$  MPa for the isotropic elastic wall was used, giving similar load-deflection response of the tongue replica to external pressure  $p_e$ , as expected in [2] (Figure 4).

*4.1. Parametric Investigation.* For the purpose of studying the influence of the following physiological variations on the collapsibility and flow pattern in the pharyngeal airway, the following range of parameters were simulated:

- (i) initial constriction height ( $h$ ) 0.8–11.0 mm,
- (ii) elastic wall modulus ( $E$ ) 1.25–2.25 MPa.

The initial constriction height is varied to simulate the effect of different degrees of opening behind the tongue within the oropharynx in apneic or nonapneic subjects. The opening gap behind the tongue is typically 11 mm [27] but is perhaps lower when subjects are in sleeping position. Preliminary study by Chouly et al. [18] reported an opening of between 1 to 2 mm during sleep supine position. In line with this, variations between 0.8 to 11.0 mm have been investigated in this paper.

The influence of the modulus of the tongue is also of interest. Variation of mechanical properties in the human population is not unexpected. The degree of variation in pharyngeal compliance measured by Brown et al. [17] among apneic patients could offer some insight into the variation of stiffness in the retroglossal region. Variations in the tongue stiffness is also indicative of the degree of muscle activation [21] and have been used to capture the directional activation of muscle tissues. In this paper, considering the replication of the tongue by an elastic shell, a  $\pm 0.5$  MPa variation is considered.

In order to investigate the first parameter, the elastic modulus  $E$  and external pressure  $p_e$  was fixed to 1.75 MPa and 200 Pa, respectively, while the initial constriction height  $h_o$  was varied. The nonlinear variation of the flow rate with intraluminal pressure difference  $\Delta p = p_{in} - p_{out}$  is shown in Figure 5(a) for various  $h_o$ , revealing typical flow rate limitation phenomena with increased expiratory efforts. In particular, the increased flow rate and reduced degree of flow plateauing, suggest much reduced flow obstruction or

collapse with increasing  $h_o$ . In addition, the lower degree of flow plateauing for the  $h_o = 11$  mm case would suggest a near-rigid flow rate is achieved and demonstrates the relatively low obstruction in nonapneic patients.

The second parameter investigated is the effect of tongue modulus on the expiratory flow interaction with the tongue. In order to investigate this parameter, a configuration with initial constriction height of 1.2 mm and  $p_e = 200$  Pa was used. The effect of softening and stiffening of the tongue modulus is summarized in Figure 5(b). Reduction in modulus translates to increased compliance of the airway cross-section to the applied pressures (as suggested by reduced constriction height  $h$  in Figure 5(b)). Thus, exacerbating its susceptibility to collapse and increases resistance to flow rate. The approximately linear trend of collapse with increasing  $\Delta p$  is consistent with the venturi effect, where the reduction in flow area underneath the elastic wall increases the flow velocity, thus, generating much lower mean pressure (suction) that further collapses the wall.

Comparing the relative influence of both parameters,  $h_o$  and  $E$ , to the wall collapse and flow rate, suggest that both parameters are important. For instance, a 40% stiffening of the tongue modulus ( $E = 1.25$  to 1.75 MPa) leads to approximately 11% reduction in wall collapse, as opposed to 10% reduction in collapse for a 50% increase in initial airway opening ( $h_o = 0.8$  to 1.2 mm).

Based on the hydraulic diameter,  $D = 4A/P$  where  $A$  is taken as the cross-sectional area at the inlet and  $P$  is the inlet perimeter, the Reynolds number,  $Re$  simulated in this investigation ranges from 274–9520. Considering a transitional flow regime in the pharyngeal airway replica (by using a low- $Re$  turbulent model), similar to those observed in previous laminar investigations, narrower opening along the airway predisposes patients to larger wall collapse and hence, more severe flow rate limitation.

*4.2. Elastic Wall Deflection.* The cross-section along the narrowest opening (for a  $h_o = 1.2$  mm case) is shown in Figure 6 for several intraluminal pressure differences  $\Delta P$ . As expected, in addition to increased deflection as  $\Delta P$  is increased, the profile also reveals a larger area close to the side walls where the tongue replica is supported and tends to narrow nonlinearly towards the symmetric plane  $z = 0$ . This profile perhaps influences the flow patterns and will be discussed in the next section. The difference in  $y$ -position at the side wall ( $z = 0.0125$ ) is due to the different downstream location of narrowest opening. This is associated to the downstream deflection of the elastic wall as pressure is applied in the axial direction to the upstream portion of the wall.

In comparison to laminar flow, the low- $Re$  turbulent flow predicts a more severe elastic wall collapse, as illustrated in Figure 7. This would suggest a much severe pressure drop is experienced by the elastic wall in transitional or turbulent flow as oppose to laminar flow. Indeed, examining the pressure contour in Figure 8, minimum suction pressure of  $-81$  Pa underneath the constriction is predicted in the low- $Re$  turbulent flow compared to approximately  $-30$  Pa in the laminar flow. This seems to be consistent with numerical

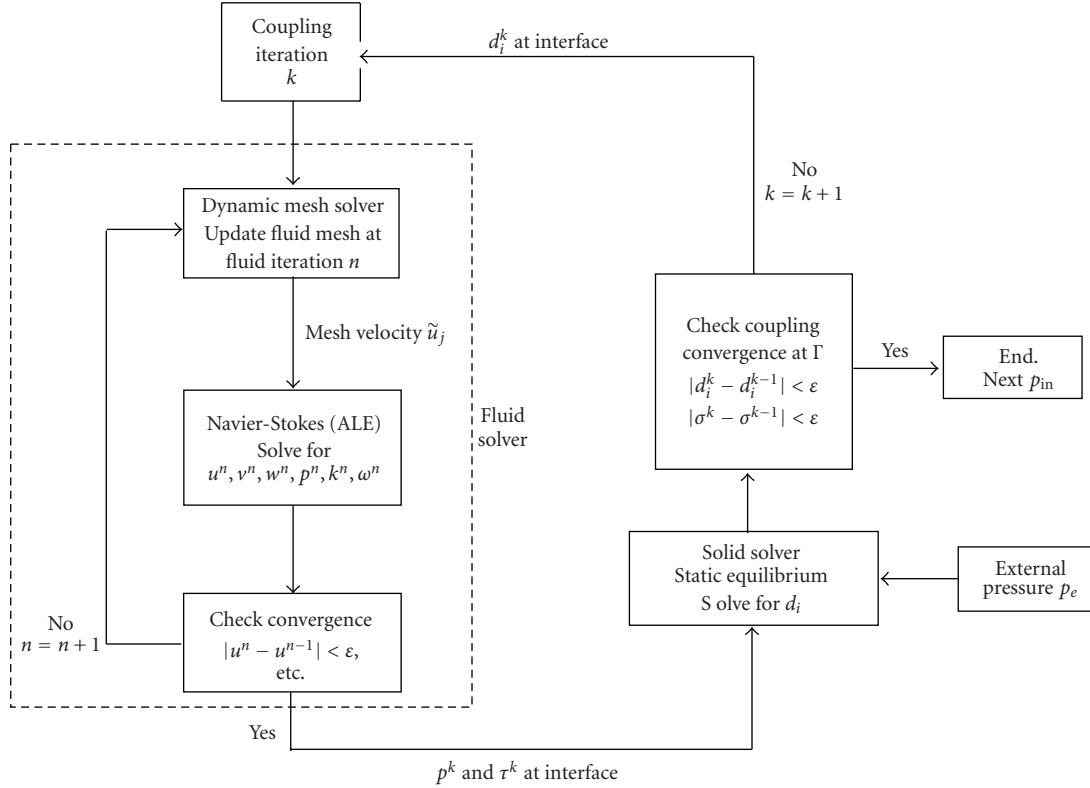
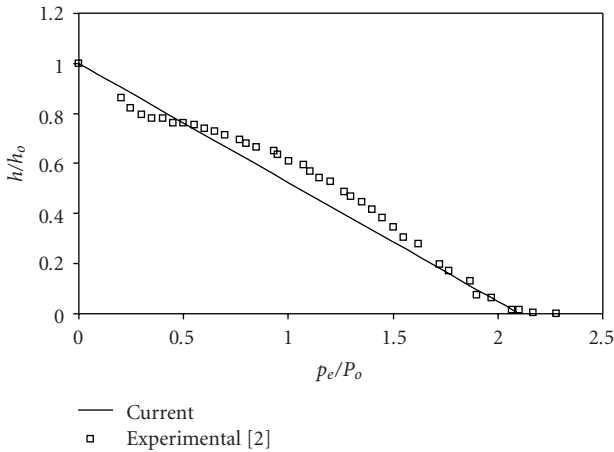


FIGURE 3: Fluid-structure coupling flowchart.

FIGURE 4: Pressure versus deflection curve for elastic wall. (Deflection is measured as lowest point on the symmetric plane. Normalization constants  $P_o = 1000$  Pa and  $h_o = 1.6$  mm.)

findings on a rigid pharynx by Shome et al. [15] where at similar flow rates, a 40% increase in pressure drop is predicted in turbulent flow compared to if the flow is laminar and this is expected to be more severe if the flow boundaries are collapsing, as indicated here. Thus, flow regime in the pharyngeal airway has significant effect on the degree of apneic obstruction and is important to be considered in pre-operative treatments.

**4.3. Three-Dimension Flow Features.** Typical flow patterns in the idealised airway are captured in Figure 9. In general, flow separates from the elastic wall, the bottom wall and the side walls. Three-dimensional recirculation is observed immediately downstream of the elastic wall above the jet streams in all  $\Delta P$ . Not surprisingly, swirling about the  $x$ -axis is also formed as the jet separates off the rigid bottom wall and is forced to follow the circular cross-section of the idealised airway.

Streamlines from upper and bottom half of the inlet reveals the tendency for the stream to migrate towards the side walls, where the cross-sectional area is more open. This side stream (as is also visibly shown by the velocity contours peaking towards the side) is more pronounced at higher  $\Delta P$  where the elastic wall deflection is further skewed downstream. Thus, the swirling strength of the inner recirculation core is increased as the outer streams follow the curvature of the walls.

Consequently, the pressure profile is also influenced by the lateral distribution of the cross-sectional opening and velocity. This is evident from the pressure profile plots along axial planes located at several lateral locations shown in Figure 10 where the critical suction pressure in the vicinity of the constriction is somewhat reduced closer to the side walls where a larger opening is anticipated.

The influence of the side wall onto the lateral pressure and velocity profile is also expected to influence the location of flow separation off both the tongue replica (elastic wall) and oropharynx base (rigid bottom wall). Figure 11 presents

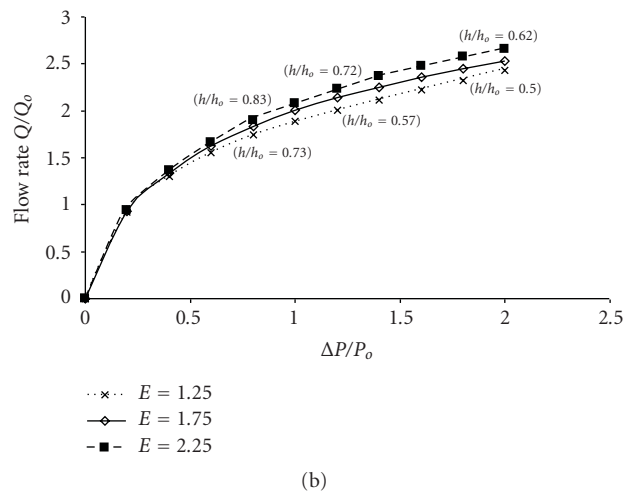
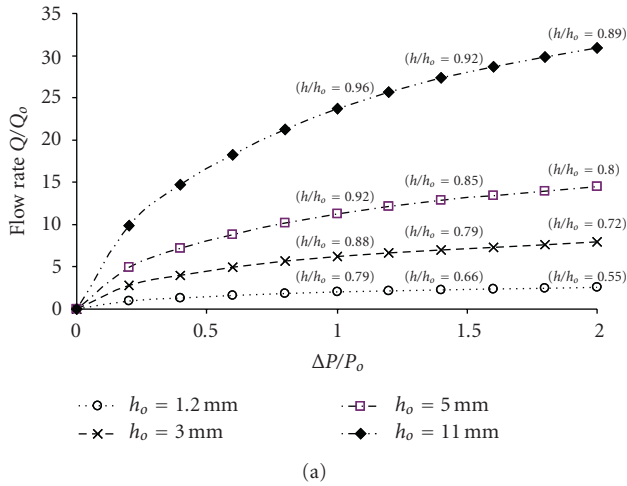


FIGURE 5: Parametric investigation (a) effect of initial airway opening  $h_o$  on flow rate  $Q$  and constriction height  $h$  for a fixed tongue replica modulus  $E = 1.75$  MPa, (b) effect of tongue modulus  $E$  on flow rate  $Q$  and constriction height  $h$  for a fixed initial opening  $h_o = 1.2$  mm ( $Q_o = 10$  L/min,  $P_o = 100$  Pa, and  $h_o =$  initial constriction height).

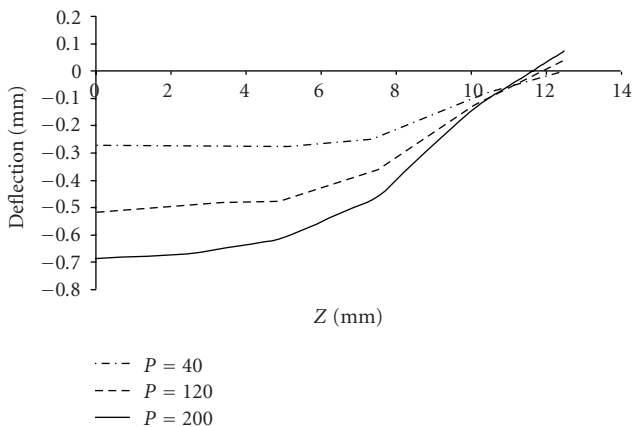


FIGURE 6: Deflection profile in the lateral direction across narrowest opening (see Figure 2(c)).

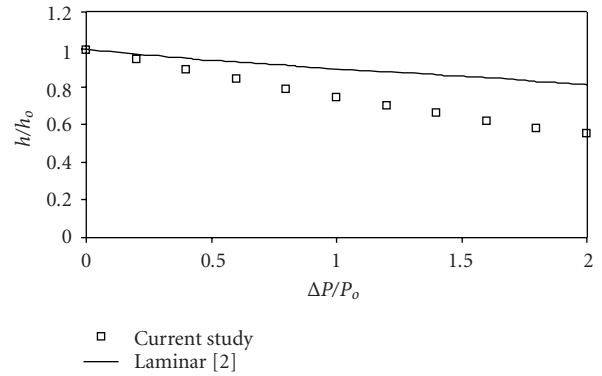


FIGURE 7: Elastic wall deflection with increasing  $\Delta P$  for a  $h_o = 1.2$  mm case. (Normalization constants:  $P_o = 100$  Pa and  $h_o =$  initial constriction height.)

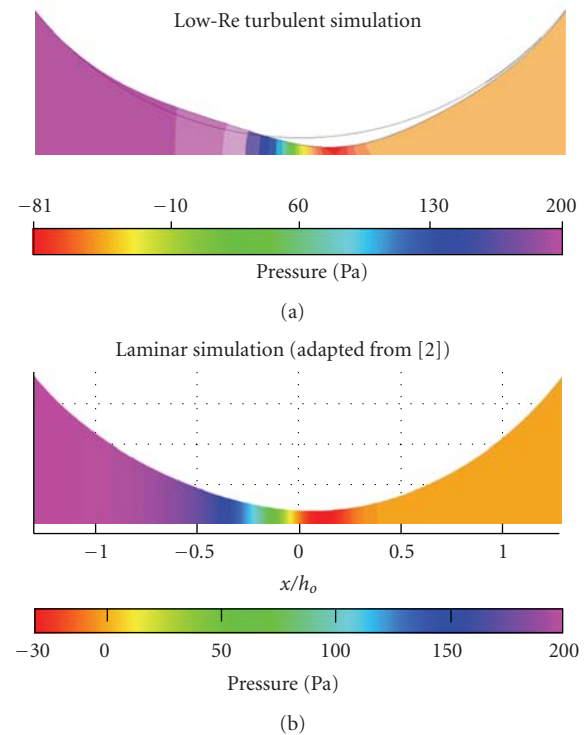


FIGURE 8: Pressure distribution in the vicinity of the constriction at  $\Delta P = 200$  Pa for case with initial constriction height = 1.2 mm and  $p_e = 200$  Pa ( $P_o = 100$  Pa,  $v_o = 10$  m/s and  $h_o = 15$  mm [2]).

the axial shear profile along the bottom walls at several lateral locations  $z = 0$ ,  $z = 0.005$  and  $z = 0.0$ , revealing a shift in the position of zero wall shear as the flow approaches the side walls. Thus, suggesting a delay in flow separation as the side wall is approached.

### 5. Conclusion

A three-dimensional low-Re turbulent rendering of the airway-tongue replica investigation by Chouly and coworkers [2, 13] and Van Hirtum et al. [14] have been conducted.

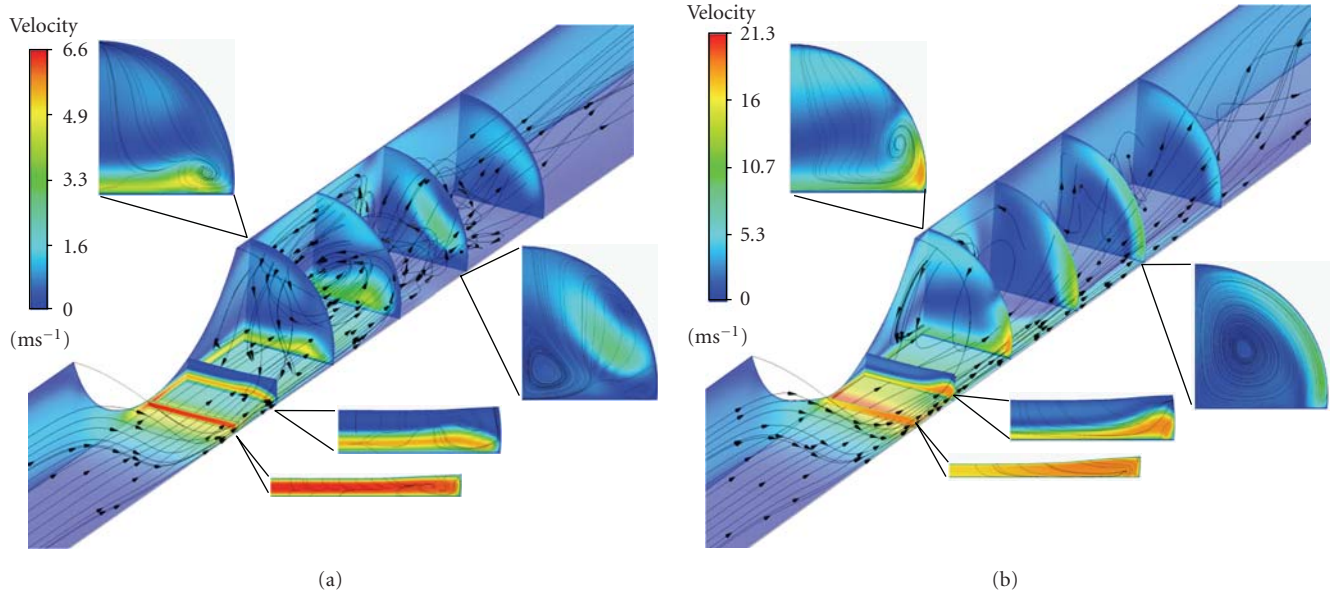


FIGURE 9: Streamline plot and contours of velocity along vertical symmetry plane, bottom wall and several axial cross-sections for (a)  $\Delta P = 20$  Pa and (b)  $\Delta P = 200$  Pa ( $h_o = 1.2$  mm case).

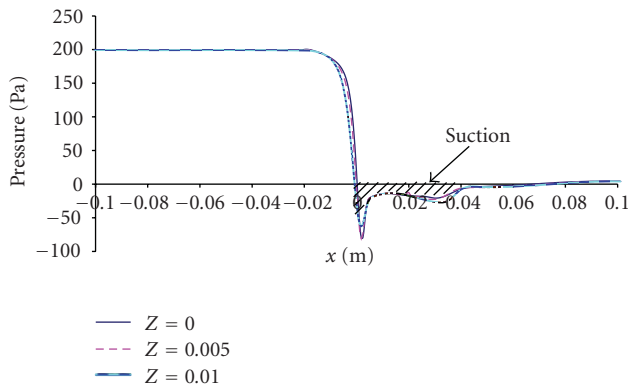


FIGURE 10: Pressure profile along several axial planes at top wall.

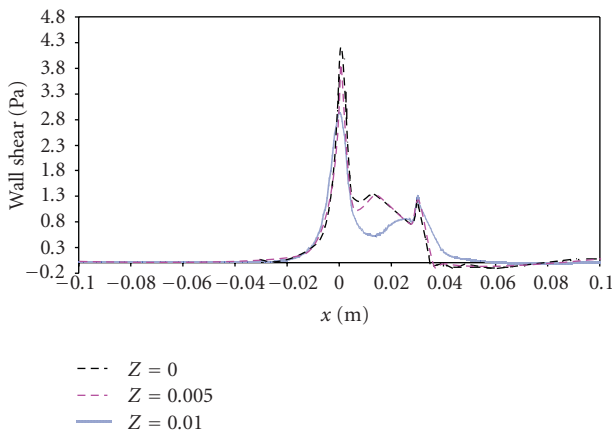


FIGURE 11: Wall shear profile along several axial planes at the bottom wall (note that elastic wall is located within  $-0.02136$  m <  $x$  <  $0.02136$  m).

The low-Re turbulent fluid-structure interaction simulation predicts a more severe pressure drop in the constriction compared to a laminar fluid-structure interaction, reflecting a similar trend as the turbulent rigid pharynx simulation by Shome et al. [15]. Similar flow rate limitation is observed with laminar flow, although more pronounced narrowing of the area behind the tongue is generated.

Parametric study representing some geometrical and mechanical factors that affects apnea in the airway was investigated. The investigation suggest that both a narrower opening and an increased compliance of the airway increases the susceptibility of apneic episodes. In addition, three-dimensional flow features relevant to the airway-tongue replica is also presented.

Brown et al. [17] had successfully measured changes in cross-sectional area along the pharyngeal airway during expiratory and inspiratory breathing pressures, on both apneic and nonapneic patient using an acoustic reflection technique, allowing pharyngeal compliance to be estimated as a function of the distance from the mouth. For future work, this varying stiffness along the pharyngeal airway could be incorporated in order to capture the interaction between multiple segments of differing compliance within the pharyngeal airway and how it influence collapse and reopening of the lumen. Ultimately, a real pharyngeal airway model could be used for the fluid-structure investigation.

## Acknowledgments

The authors acknowledge financial support from the Government of Malaysia via the sponsorship by the Ministry of Higher Education under the IPTA Academic Training Scheme awarded to the first author. The financial support provided by the Australian Research Council (project ID LP0989452) and by RMIT University through an Emerging

Researcher grant is also gratefully acknowledged. In addition, many thanks to Dr. Franz Chouly for many fruitful communications.

## References

- [1] C. D. Bertram, "Flow-induced oscillation of collapsed tubes and airway structures," *Respiratory Physiology and Neurobiology*, vol. 163, no. 17#8211;3, pp. 256–265, 2008.
- [2] F. Chouly, A. Van Hirtum, P. Y. Lagrée, X. Pelorson, and Y. Payan, "Numerical and experimental study of expiratory flow in the case of major upper airway obstructions with fluid-structure interaction," *Journal of Fluids and Structures*, vol. 24, no. 2, pp. 250–269, 2008.
- [3] C. D. Bertram, C. J. Raymond, and T. J. Pedley, "Mapping of instabilities for flow through collapsed tubes of differing length," *Journal of Fluids and Structures*, vol. 4, no. 2, pp. 125–153, 1990.
- [4] C. D. Bertram, C. J. Raymond, and T. J. Pedley, "Application of nonlinear dynamics concepts to the analysis of self-excited oscillations of a collapsible tube conveying a fluid," *Journal of Fluids and Structures*, vol. 5, no. 4, pp. 391–426, 1991.
- [5] A. I. Katz, Y. Chen, and A. H. Moreno, "Flow through a collapsible tube. Experimental analysis and mathematical model," *Biophysical Journal*, vol. 9, no. 10, pp. 1261–1279, 1969.
- [6] X. Y. Luo and T. J. Pedley, "A numerical simulation of steady flow in a 2-D collapsible channel," *Journal of Fluids and Structures*, vol. 9, no. 2, pp. 149–174, 1995.
- [7] T. J. Pedley, "Longitudinal tension variation in collapsible channels: a new mechanism for the breakdown of steady flow," *Journal of Biomechanical Engineering*, vol. 114, no. 1, pp. 60–67, 1992.
- [8] A. H. Shapiro, "Steady flow in collapsible tubes," *ASME Journal of Biomechanical Engineering*, vol. 99, no. 3, pp. 126–147, 1977.
- [9] X. Y. Luo and T. J. Pedley, "A numerical simulation of unsteady flow in a two-dimensional collapsible channel," *Journal of Fluid Mechanics*, vol. 314, pp. 191–225, 1996.
- [10] X. Y. Luo and T. J. Pedley, "The effects of wall inertia on flow in a two-dimensional collapsible channel," *Journal of Fluid Mechanics*, vol. 363, pp. 253–280, 1998.
- [11] A. L. Hazel and M. Heil, "Steady finite-Reynolds-number flows in three-dimensional collapsible tubes," *Journal of Fluid Mechanics*, no. 486, pp. 79–103, 2003.
- [12] M. Heil and S. L. Waters, "How rapidly oscillating collapsible tubes extract energy from a viscous mean flow," *Journal of Fluid Mechanics*, vol. 601, pp. 199–227, 2008.
- [13] F. Chouly, A. Van Hirtum, P. Y. Lagrée, X. Pelorson, and Y. Payan, "Modelling the human pharyngeal airway: validation of numerical simulations using in vitro experiments," *Medical and Biological Engineering and Computing*, vol. 47, no. 1, pp. 49–58, 2009.
- [14] A. Van Hirtum, X. Pelorson, and P. Y. Lagrée, "In vitro validation of some flow assumptions for the prediction of the pressure distribution during obstructive sleep apnoea," *Medical and Biological Engineering and Computing*, vol. 43, no. 1, pp. 162–171, 2005.
- [15] B. Shome, L. P. Wang, M. H. Santare, A. K. Prasad, A. Z. Szeri, and D. Roberts, "Modeling of airflow in the pharynx with application to sleep Apnea," *Journal of Biomechanical Engineering*, vol. 120, no. 3, pp. 416–422, 1998.
- [16] I. Hahn, *Modelling Nasal Airflow and Olfactory Mass Transport*, University of Pennsylvania, Philadelphia, Pa, USA, 1992.
- [17] I. G. Brown, T. D. Bradley, and E. A. Phillipson, "Pharyngeal compliance in snoring subjects with and without obstructive sleep Apnea," *American Review of Respiratory Disease*, vol. 132, no. 2, pp. 211–215, 1985.
- [18] F. Chouly, A. van Hirtum, P.-Y. Lagrée et al., "Simulation of the retroglossal fluid-structure interaction during obstructive sleep Apnea," in *Lecture Notes in Computer Science*, M. Harders and G. Szekely, Eds., pp. 48–57, Springer, Berlin, Germany, 2006.
- [19] ANSYS, ANSYS CFX Solver Theory Guide—Release 12.
- [20] G. Xia and C. L. Lin, "An unstructured finite volume approach for structural dynamics in response to fluid motions," *Computers and Structures*, vol. 86, no. 7-8, pp. 684–701, 2008.
- [21] F. A. Duck, *Physical Properties of Tissue: A Comprehensive Reference Book*, Academic Press, London, UK, 1990.
- [22] Y. Payan, G. Bettega, and B. Raphael, "A biomechanical model of the human tongue and its clinical implications," in *Lecture Notes in Computer Science*, W. M. Wells, A. Colchester, and S. Delp, Eds., pp. 688–695, Springer, Berlin, Germany, 1998.
- [23] Y. Min, I. Titze, and F. Alipour, "Stress-strain response of the human vocal ligament," in *NCVS Status and Progress Report*, pp. 131–137, 1994.
- [24] Y. Huang, D. P. White, and A. Malhotra, "The impact of anatomic manipulations on pharyngeal collapse: results from a computational model of the normal human upper airway," *Chest*, vol. 128, no. 3, pp. 1324–1330, 2005.
- [25] Y. Huang, A. Malhotra, and D. P. White, "Computational simulation of human upper airway collapse using a pressure/state-dependent model of genioglossal muscle contraction under laminar flow conditions," *Journal of Applied Physiology*, vol. 99, no. 3, pp. 1138–1148, 2005.
- [26] J. Donea, A. Huerta, J.-P. Ponthot, and A. Rodríguez-Ferran, "Arbitrary lagrangian-eulerian methods in encyclopedia of computational mechanics," in *Fundamentals*, E. Stein, R. de Borst, and T. J. R. Hughes, Eds., vol. 1, John Wiley & Sons, 2004.
- [27] E. Sforza, W. Bacon, T. Weiss, A. Thibault, C. Petiau, and J. Krieger, "Upper airway collapsibility and cephalometric variables in patients with obstructive sleep Apnea," *American Journal of Respiratory and Critical Care Medicine*, vol. 161, no. 2, part I, pp. 347–352, 2000.

## Research Article

# CFD-Guided Development of Test Rigs for Studying Erosion and Large-Particle Damage of Thermal Barrier Coatings

**Maria A. Kuczmariski, Robert A. Miller, and Dongming Zhu**

*NASA Glenn Research Center, Cleveland, OH 44131, USA*

Correspondence should be addressed to Maria A. Kuczmariski, maria.a.kuczmariski@nasa.gov

Received 25 November 2010; Revised 4 February 2011; Accepted 18 February 2011

Academic Editor: Guan Yeoh

Copyright © 2011 Maria A. Kuczmariski et al. This is an open access article distributed under the Creative Commons Attribution License, which permits unrestricted use, distribution, and reproduction in any medium, provided the original work is properly cited.

Burner rigs are routinely used to qualify materials for gas turbine applications. The most useful rig tests are those that can replicate, often in an accelerated manner, the degradation that materials experience in the engine. Computational fluid dynamics (CFD) can be used to accelerate the successful development and continuous improvement of combustion burner rigs for meaningful materials testing. Rig development is typically an iterative process of making incremental modifications to improve the rig performance for testing requirements. Application of CFD allows many of these iterations to be done computationally before hardware is built or modified, reducing overall testing costs and time, and it can provide an improved understanding of how these rigs operate. This paper describes the use of CFD to develop burner test rigs for studying erosion and large-particle damage of thermal barrier coatings (TBCs) used to protect turbine blades from high heat fluxes in combustion engines. The steps used in this study—determining the questions that need to be answered regarding the test rig performance, developing and validating the model, and using it to predict rig performance—can be applied to the efficient development of other test rigs.

## 1. Introduction

A thermal barrier coating (TBC) is a layer of thermally insulating ceramic applied over an oxidation-resistant bond coat on a metallic component. TBCs protect a component from high, prolonged cyclic heat loads and extend part life by reducing thermal fatigue and reducing oxidation through reducing the component temperature. When used in turbine engines, these coatings may reduce the cooling airflow needed through and over components and allow significantly higher gas operating temperatures, leading to improved engine performance, greater fuel efficiency, and reduced carbon dioxide emissions [1–4].

Thermal barrier coatings are used to coat components such as combustor liners and turbine blades. The first row of turbine blades in the high-pressure turbine region encounters especially high-temperature, high-pressure, and high-velocity gases. These “first blade” TBCs are particularly prone to damage by erosion and large-particle impact [5, 6]. When TBCs erode, the loss of insulation can lead to turbine blade damage from high heat exposure and may require

additional cooling air to be directed to the leading edge of the blades to compensate, leading to lower operating efficiency for the engine.

TBCs have been used in the turbine engines of fixed-wing aircraft for some time, but are just beginning to be used in rotary-wing aircraft turbine engines. Fixed-wing commercial aircraft most often operate in relatively clean environments, such as high altitudes and on dedicated take-off and landing sites—runways maintained to keep them relatively free of dust and debris. Rotary-wing aircraft operates in much dirtier environments: lower altitudes and take-off and landing in a wide variety of locations, including environments with high dust concentrations. Rotary-wing aircraft turbine engines often use particle separators to decrease the number of particles that reach the engine. Although these separators are more effective for larger particles, some debris can still reach the turbine blades, particularly under heavy loading conditions [7]. Therefore, erosion and impact damage of TBCs on the first blade of rotary turbine engines is of particular concern [6].

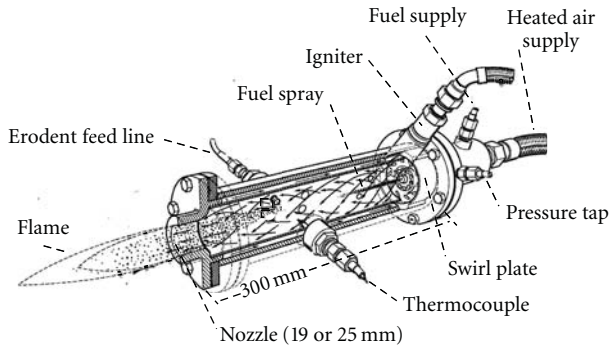


FIGURE 1: Schematic of an unducted burner-erosion rig.

Besides impact damage from large particles that enter from the outside environment, turbine blades may be struck by debris from within the engine, including pieces of TBCs that spall off the combustor walls [6]. In addition, old injectors that become damaged or clogged with dirt can spray fuel onto the combustor walls and deposit carbon. These deposits can break off in large “carbon balls” that can strike the turbine blades [8, 9]. Fine particles such as dust are a particular problem for rotary-wing aircraft because of their operating environments. In addition to erosion, small particles may, under certain conditions, melt and lead to corrosive attack of the TBC. A discussion of this failure mechanism is beyond the scope of this paper.

Burner rigs are torches that burn jet fuel and preheated air. They are generally used to evaluate, rank, and understand the behavior of high-temperature materials for gas turbine applications. With burner rigs, gas and preheated air are mixed within the burner, and the combustion products exit through a nozzle to accelerate the gases to Mach 0.3 or higher subsonic velocities. This is illustrated in the schematic in Figure 1. Development of new rigs to study erosion and large-particle impact damage was undertaken at the NASA Glenn Research Center with the goal of developing more erosion-resistant turbine engine thermal barrier coatings. This work was built on and guided by two previous burner erosion rigs: a rig that existed at NASA in the 1980s as described by Handschuh [10] and a rig at GE described by Bruce [11].

The burner rig described by Handschuh consisted of a jet fuel combustor modified to inject erosive aluminum oxide particles with an average diameter of 130 microns into the centerline of the combustor. Burning fuel in the combustor provided gas at high temperature and high velocity. The test rig had a converging nozzle and, because he wished to maintain a narrow stream of erodent particles, sonic velocity was used to provide the greatest particle acceleration possible while minimizing the dispersion of aluminum oxide as it traveled downstream toward the test specimen. Evidence of particle diffusion was seen at the test specimen surface, which increased with the test specimen distance from the nozzle exit. The center of this diffusive pattern was not along the centerline of the combustor, even though particles were introduced at that location. An alternative design was

mentioned that used a long vertical acceleration duct to allow the gas and particle velocities to become essentially the same. However, this design, while believed to be useful for studying the effect of particle velocity on the erosion process, was not implemented because it was thought that it would result in too much heat loss to the duct to produce high-temperature test conditions.

The burner rig described by Bruce consists of a combustor fed with jet fuel and compressed air that was modified to radially inject crushed alumina particles 50 and 560 micron in average diameter into the combustor in two horizontally opposite positions. Other erodent materials were considered, but alumina was selected because it produced damage patterns consistent with that observed in engines. The test specimens were cylindrical pins mounted on a carousel that rotated at 500 rpm, 50 mm from the burner rig exhaust. It was concluded that particle velocity is affected by the particle size and distance from the combustor opening, but negligibly affected by air pressure, air temperature, and fuel flow rate. CFD was used with a trajectory code to determine an inviscid 2D flow field in which the trajectory of spherical particles was calculated. The results of this model produced good agreement with available experimental measurements of particle velocities at 50 and 100 mm from the combustor exhaust, and it was used to predict velocities for other distances from the exhaust and other particle materials. Bruce indicates that excessively high flow rates could lead to particles bouncing off the test specimen surface interfering with incoming particles, leading to reduced wear rate.

The most useful test results come from rigs that can replicate turbine engine failure modes. To understand if the modifications to the current NASA burner rigs would make them suitable for erosion and large-particle impact damage studies, three questions needed to be answered: (1) would the particles come to the gas temperature in the burner-erosion rig? (2) would the particles move fast enough to accurately cause damage to the TBC surface? (3) how could the eroded region be broadened for cases where that would be advantageous, such as for more representative testing of small turbine blades? Rather than making best guesses as to whether the test rigs would meet these requirements, a CFD model was used to answer these questions.

This paper describes the CFD modeling used to guide modifications to previously existing NASA Glenn burner rigs through addition of an unattached duct to make them suitable for evaluating erosion and large-particle impact damage of TBCs for turbine engine applications and describes validation of the model to confirm that its predictions are accurate.

## 2. Experimental Design

Two separate burner rigs were to be modified: one for erosion studies and one for large-particle impact damage studies. Figure 2 shows a photograph of one of the burner-erosion rigs without a duct. The rigs are fired on a mixture of jet fuel and preheated air. Eroderent particles are transported to the burner using a powder feeder of the type used for plasma

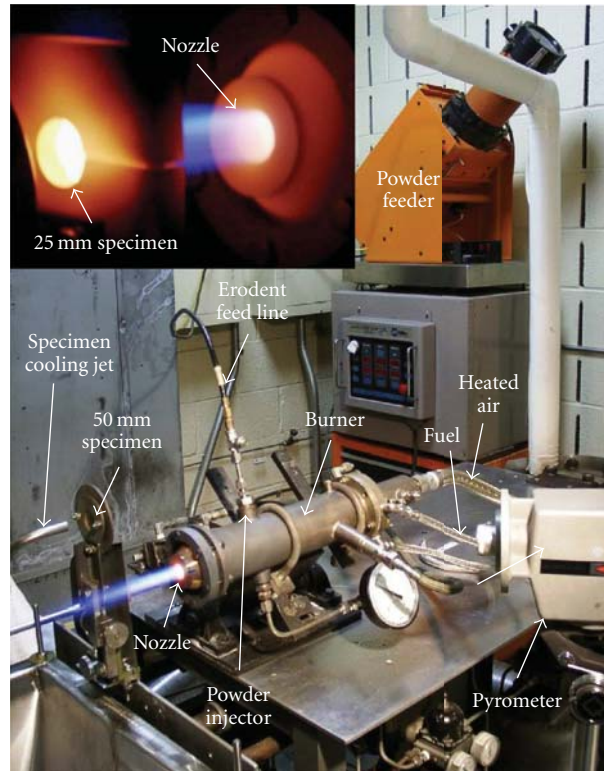


FIGURE 2: Photograph of an unducted burner-erosion rig during operation.

spraying introduced into the burner through a probe. The figures show that the particles come from the feeder, pass through the erodent feeding line, and are fed into the rig. The specimen and holder are shown in an idle position (not aimed at the specimen) in Figure 2; the burner pivots to move the flame into the path of the specimen for testing. Temperatures are generally measured using optical pyrometers, although thermocouples are an option. A unique feature of the NASA Glenn burner rigs is that they are routinely used for both ranking and fundamental studies of erosion of TBCs on turbine blades to guide development of erosion-resistant coatings.

Operating conditions were chosen to allow comparison to previous studies and to replicate TBC erosion in turbine engines. The particles used in this study had the physical properties of alumina. Initial CFD studies concentrated on single-particle sizes. For erosion studies, 26 micron and 50 micron diameter particle studies were conducted, since small particles were expected to be of particular concern in typical rotorcraft operating environments [12]. Nominal 26 micron diameter alumina particles are commercially available and can be reliably fed using plasma spray-type feeders of the type used for these experiments. 50 micron diameter particles were chosen to match the size used by General Electric in its studies of TBC erosion [11]. For large-particle impact damage studies, 560 micron diameter particles were chosen to match General Electric studies [11] and correspond to particle sizes that may originate from the combustor and are likely to cause impact damage [11]. Since real-world environments

would contain a range of particle sizes, later studies used a particle size distribution centered about either 26 microns for erosion studies or 550 microns for large-particle impact damage studies. Mach numbers of 0.3–1.0 with gas temperatures up to 1640 K were chosen to represent conditions likely to be encountered by the gases interacting with the turbine blades.

### 3. Model Description

The computational fluid dynamics code ANSYS FLUENT (ANSYS FLUENT software from ANSYS, Inc., Canonsburg, Pa.) was used to model the experimental apparatus. The code uses a finite volume method to discretize the continuity, momentum, and energy equations. A steady state, compressible flow, axisymmetric model was used; various regions, dimensions, and boundary conditions are shown on Figure 3(a) for the unducted model and Figure 3(b) for the model with an unattached duct. This duct is at a distance of 0.127 m from the nozzle exit. This figure shows a duct that is 0.305 m long with a diameter of 0.019 m (drawn as 0.095 m radius). The diameter and length of the duct shown in this figure were varied during the study. The figures show a portion of the burner liner, the nozzle, and a box showing pressure boundaries (in blue). Because this is an axisymmetric model, this figure may be rotated about the axis of rotational symmetry to form the axisymmetric figure. Note that the entire length of the burner,

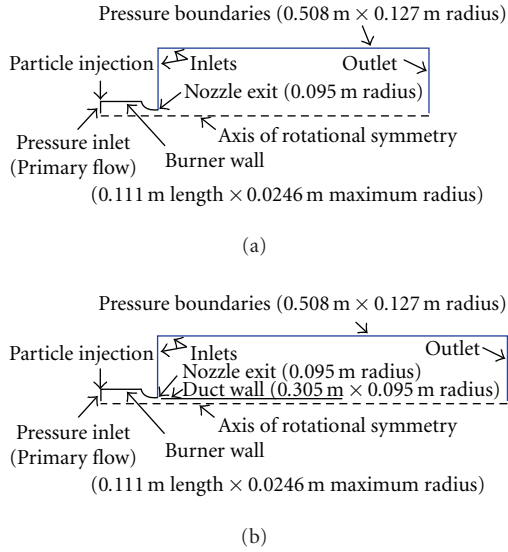


FIGURE 3: Diagram with dimensions and boundary conditions for (a) unducted burner-erosion rig; (b) a ducted burner-erosion rig.

before the injection region, was not modeled. Rather the region just before particle injection was treated as a pressure inlet.

A standard  $k$ - $\epsilon$  turbulence model was used with the C1-epsilon constant altered from the standard value of 1.44 to 1.56 because of the successful use of this turbulence model by Senesh and Babu to describe the potential core and other characteristics of similar jets [13]. Strictly speaking, the  $k$ - $\epsilon$  model is only applicable for fully developed turbulent flow [14]. For turbulent flow in pipes, the entrance length for fully developed flow is given by [15]:

$$\frac{l_e}{D} = 4.4Re_D^{1/6}, \quad (1)$$

where  $l_e$  is the entrance length (m),  $D$  is the pipe diameter (m), and  $Re_D$  is the Reynolds number based on pipe diameter (dimensionless).

The range of flows used in this study yielded Mach numbers at the nozzle exit from 0.3 to 1.0, with Reynolds numbers of about 17,000 and 51,000, respectively. Entrance lengths were found to be between about 0.42 to 0.51 m for the 0.01905 m diameter duct and between 0.58 and 0.74 m for the 0.0254 m diameter duct. Since the location of the specimen was at 0.3683 m, fully developed turbulent flow would not yet have been established by the time the flow reached the test specimen surface. Nonetheless, because the model with the modified C1 constant predicted a potential core having a length matching that observed experimentally—both in our case and with the work of Senesh and Babu [13]—it was felt that the  $k$ - $\epsilon$  model would be fully adequate for the needs of this paper. Standard wall functions and viscous heating were both used in the model.

The discrete phase model was activated to allow solid particles to be injected into the gas flow and their paths tracked. These particles were allowed to interact with the gas phase.

A spherical particle drag law from Morsi and Alexander was used [16]

$$C_d = a_1 + \frac{a_2}{Re} + \frac{a_3}{(Re)^2}, \quad (2)$$

where the values of the empirical constants  $a_1$ ,  $a_2$ , and  $a_3$  are described in Morsi and Alexander, and  $Re$  is the Reynolds number. This drag law was further modified for relative Mach numbers greater than 0.4 using a high Mach number drag law. ANSYS FLUENT computes the spherical particle drag coefficient in this range by using a look-up table that is a function of Reynolds number; this table is derived from published literature [17].

Injections were defined as inert particles released across the surface of the particle inlet. As mentioned previously, single-particle sizes of 26 and 50 micron diameter were used for erosion studies, and 560 micron diameter particles were used for large-particle impact damage studies. In the real world, a wide variety of particle sizes would impact the turbine blades in an engine. However, for the purposes of initial study, a simplified particle distribution containing three different sizes was used: 20, 26, and 32 microns for the erosion studies, and 500, 550, and 600 microns for the large-particle impact damage studies.

A second-order upwind scheme was used for both the momentum and energy equations, with an under-relaxation factor set to 0.3 for the momentum equation and 1 for the energy equation. The convergence criteria for the solutions were defined as scaled residuals below  $1 \times 10^{-5}$  for the momentum equation,  $1 \times 10^{-6}$  for the energy equation, and  $1 \times 10^{-3}$  for both the turbulent kinetic energy and dissipation rate. Decreasing these values, two orders of magnitude did not result in a change in the model predictions.

The sensitivity of the results to the grid density was studied using three different grid densities based on the number of cells used across the nozzle. A nonuniform grid was used over parts of the model to minimize the total number of computational cells. The maximum aspect ratio for the cells was 5 : 1. Using 10 cells across the nozzle yielded 15,393 total cells in the computational domain, 15 cells across the nozzle yielded 34,251 total cells, and 20 cells across the nozzle yielded 61,257 total cells. Comparisons were made among the grids for both temperature and velocity magnitude at a number of points spanning the nozzle radius at a distance of 0.1016 meter from the nozzle exit. Comparisons of temperature among the grids at identical points yielded differences of generally less than 1%, with the maximum difference being 3%. Similar comparisons of velocity magnitude yielded differences generally less than 2%, with the maximum difference being 6%. This shows that grid with 15,393 total cells, which was used for the rest of this study, is sufficient to achieve grid-independent results. The average  $y^+$  values ranged from about 30 for the Mach 0.3 cases to about 96 for the Mach 1.0 cases, within recommended values for these types of studies [14].

Simple restitution coefficients were assumed for these studies. The velocity restitution coefficient, which is the ratio of the velocity of a particle after a wall strike to its

velocity before a wall strike, was set to 0.5 for all collision angles. This is essentially consistent with values reported in the literature for small particles at room temperature [18, 19]. Note that a lack of angular dependence may imply a balanced combination of the effects of friction (whose effect is strongest at lower angles) and plastic deformation (whose effect is strongest at higher angles). Friction is related to surface roughness and particle size. Plasticity may be related to the hardness of the particle and the surface with which it collides.

For the case of large particles striking hard surfaces at room temperature, the restitution coefficient was measured to be near one (near elastic) for low-angle collisions falling to about 0.25 for high-angle collisions [18]. However, the duct is assumed to be mullite for the cases described in this paper, and mullite is soft at high temperature. The influence of hard versus soft substrates may be envisioned as a golf ball skipping on concrete versus skipping on partially dried mud. The near-elastic restitution coefficient measured for hard substrates at room temperature may not apply for mullite ducts. Therefore, even for the case of large particles, the directional restitution coefficient was set to 0.5 for the purposes of this study. Studies using a piecewise polynomial in terms of angle to match the data from reference 18 are described elsewhere [20]. The directional restitution coefficient for all cases was simply set to 1.0, making the angle of reflection equal to the angle of incidence.

The trajectory of a discrete phase particle in ANSYS FLUENT is predicted by integrating the force balance on the particle in a Lagrangian reference frame. The force balance equates the particle inertia with forces acting on the particle. For initial design-concept studies, following the most probable path of the injected particles allowed better visualization of particle trajectories within the rigs. Steady state trajectory simulations were performed. The integration time step is determined from [14]

$$\Delta t = \frac{\Delta t^*}{\lambda}, \quad (3)$$

where  $\Delta t$  is the integration time step (s),  $\Delta t^*$  is the estimated transit time for particle across computational cell (s), and  $\lambda$  is the step length factor (dimensionless).

The maximum number of time steps was set to 5000, resulting in completion of the trajectory calculations through the entire model domain. A step length factor of 5 was used. It can be seen from this equation that in high-velocity areas, the particle will move more quickly through a computational cell, and the integration time step will be larger. In relatively low-velocity areas, the integration time step will be correspondingly slower. Maximum particle time steps for these studies ranged from about  $6.75 \times 10^{-5}$  second for the 26 micron particles to  $4.5 \times 10^{-4}$  second for the 550 micron particles. ANSYS FLUENT uses a mean fluid phase velocity in the trajectory calculations when the flow is turbulent, unless a stochastic tracking approach is used; in this case, the instantaneous fluid phase velocity replaces the mean fluid phase velocity. A random walk model was used when stochastic tracking was performed to predict

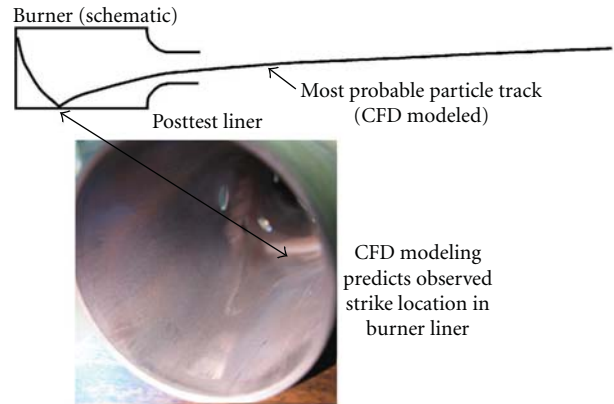


FIGURE 4: Model predictions of most probable location of particle strikes on wall correspond with eroded region seen in actual rig. Location of particle strikes/eroded region is about 0.05 m from the end of the liner/beginning of the nozzle.

the dispersion of particles due to turbulence [14]. Twenty stochastic tries with a time-scale constant of 0.15 were used. This last factor is related to the time spent in turbulent motion along the particle path [14].

#### 4. Model Validation

An important part of any modeling work is determining if the model predictions can be trusted. This is done by comparing the model predictions to experimental observations, experimental measurements, and/or analytical expressions, if available. An experimental observation provided the first evidence that the model was accurately predicting what was happening in the test rigs. The model predicted the most probable particle trajectories through the burner-erosion rig, showing where they would strike and bounce off an interior wall. Figure 4 is a simplified diagram showing the most probable path of one particle, along with a picture of a slightly eroded spot on the interior wall of the burner-erosion rig that corresponds to the predicted location of particle strikes—about 0.05 m (2 inches) from the nozzle exit. A large number of particles would actually be striking this location and locations around it due to effects such as the particle size distribution and turbulent dispersion. While the most probable trajectory is fully sufficient for our present requirements, future models employing statistical approaches and 3D models geometries are planned.

Model predictions agreed well with experimental temperature measurements. Figure 5 shows a plot of thermocouple measurements of the flame temperature at various positions along the centerline and CFD model prediction where an inlet temperature to the model domain of 1640 K was assumed. Inserts show an optical photograph and an infrared image of the hot central region of the burner-erosion rig flame. This figure illustrates that the gases exiting the nozzle display a hotter region known as the potential

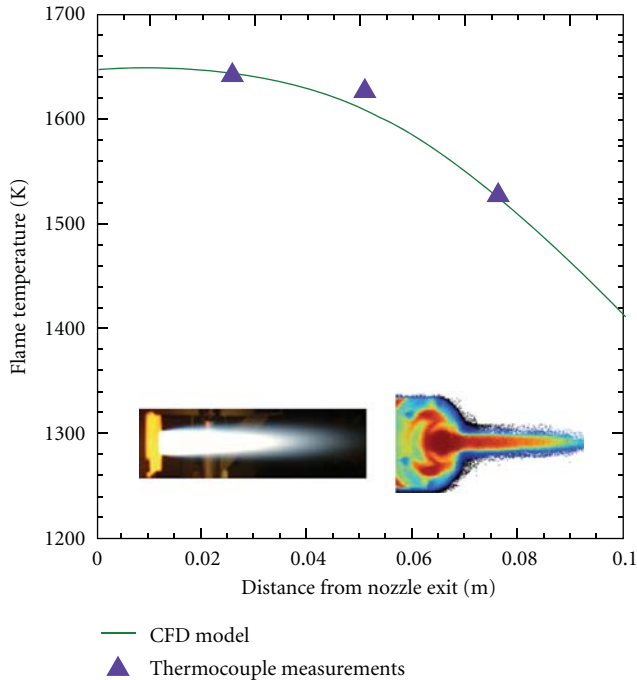


FIGURE 5: Measured and predicted temperatures versus distance from nozzle exit. Inserts show an optical photograph and an infrared image of the hot central region of the burner-erosion rig flame.

core, and that the CFD model correctly predicts the temperature distribution within the potential core. Good agreement between the two is another indication that the model is accurately predicting the burner-erosion rig performance.

Figure 6(a) shows a comparison at the same locations and for the same inlet Mach number between model predictions and experimental measurements taken using a Canon 50D digital camera. The camera is capable of sufficiently high resolution (15 megapixel), fast shutter speed (1/8000s), and high speed (12,800 ISO) that it can, with the right combination of lenses, be used as a streak camera to determine the velocities of the hot, glowing particles. At an inlet Mach number of 0.5, the model predicts a particle velocity of 160 m/s at 0.025 m (1 inch) from the nozzle outlet along the centerline; experimental streak photography measurements using the camera employing a telephoto-lens-plus-close-up lens combination observed particle velocities of about 165 m/s, as shown in Figure 6(b). This excellent agreement is another indication that the model successfully predicts the burner-erosion rig performance.

The model successfully explained the experimentally observed location of the eroded pattern on the test specimen, which was mostly below the centerline. Figure 7(a), a diagram of the most probable particle trajectories from the model for the case of a 0.305 m duct, shows that the smallest diameter particle modeled was predicted to have a trajectory that carried it to the lower half of the test specimen. The largest diameter particle reflected off the walls in such a way as to cause it to also strike the lower half of the test specimen. The particle moving closest to the centerline

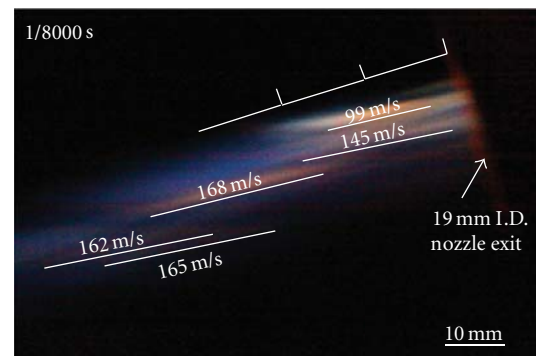
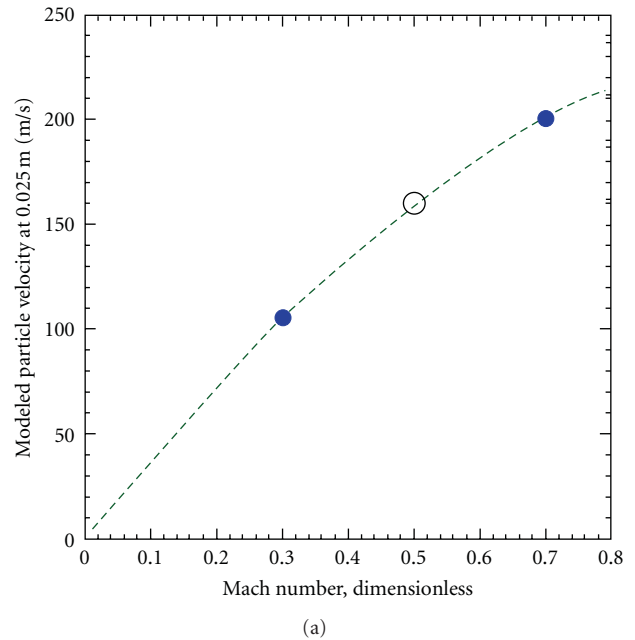


FIGURE 6: (a) Predicted particle velocities; (b) experimental measurements of particle velocity using a high-speed camera. Lines are drawn over particle traces for clarity.

strikes near the center of the test specimen. Figure 7(b) shows that the eroded region of the test specimen is mainly at and below the centerline, corresponding to the particle paths in Figure 7(a). Such agreement between model predictions and experimental observations provides further confidence in the model.

Two effects that would broaden the predicted particle track locations at the specimen would be inclusion of a large number of particles each having different diameters and inclusion of turbulent dispersion. In order to make an initial assessment of how dispersion may affect particle trajectories, and to examine this independent of particle size, one of the tracks from Figure 7(a) was re-examined, but with stochastic tracking applied. The 20 micron particle injected at 20 m/s was selected because the most probable path for this particle is predicted to remain above the centerline before exiting the burner and below the centerline after exiting the duct. This makes it easier to interpret the axisymmetric results in

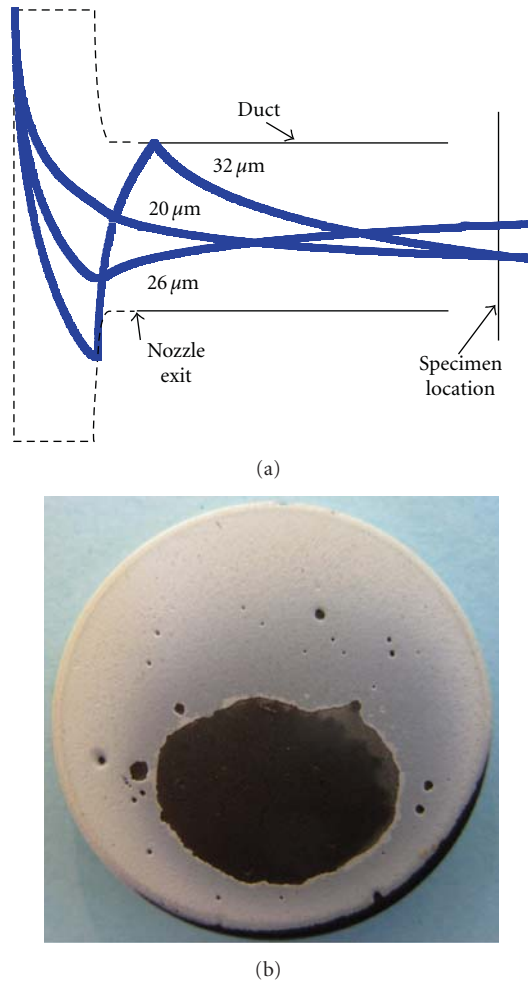


FIGURE 7: (a) Diagram of trajectories of three particles with different diameters in a Mach 0.5 ducted burner rig (0.305 m long duct); (b) experimental observation of eroded pattern on test sample. Model predictions correspond to experimental observations that most particle strikes occur below the centerline.

terms of which radial half the particle is actually travelling in. Figure 8 represents the results of this calculation. It shows the region of the burner and the region after the duct exit. In this figure, the particles are colored by velocity, with blue representing velocities as low as 20 m/s and red representing velocities as high as 294 m/s. The figure shows that within the burner, the particles do not deviate far from the most probable path. However, after the particles travel through the 0.305 m duct, the effect is to broaden the distribution of particle tracks considerably, filling up much the lower half of the duct. Significantly, those tracks traveling near the center of the duct are traveling at higher velocities. Since damage to the coated specimen is expected to be proportional to particle velocity raised to a power that initial studies suggest may be 3 [21], the amount of damage would be expected to be biased towards the higher velocity center of the duct exit. Furthermore, it may be useful to try to experimentally determine the injection velocity that causes the majority of the particles to exit near the center of the

duct. Future investigation of the effect of dispersion will benefit from future 3D models where particle tracks may be unambiguously visualized.

Figure 9 shows model predictions for particle velocity for the 0.305 m duct case as a function of distance from the nozzle for three different particle diameters compared to particle velocities obtained from an analytical expression that assumes a uniform gas stream. It is based on an existing expression [22] that was rederived for the case of nonzero initial velocity and combined with a drag law that covered the range of Reynolds numbers used in this study [23]. This equation is given by

$$x_f - x_i = \frac{4}{3} D \frac{\rho_p}{\rho} \int_{V_i}^V \frac{V_p dV_p}{0.2924 \left[ 1 + (9.06 / (\text{Re})^{0.5}) \right]^2 (V - V_p) |V - V_p|} \quad (4)$$

The plots of the CFD modeled and analytically modeled velocities agree very well with each other. The exception is the case where the largest diameter particle strikes the duct wall. The CFD model predicts that the velocity drops by a factor of two after the wall strike based on the assumed restitution coefficient of 0.5. The analytical model cannot account for the wall strike. However, it is interesting that the analytical modeling shows that much of the velocity lost after the wall strike is recovered after the particle travels further down the duct. The analytical curves in the figure were obtained using numerical integration due to the complexity of accurate drag law equations. The excellent agreement between the model predictions and the results of the analytical expression further validates the model.

## 5. Results

Initial computational runs focused on the nonducted burner-erosion rig. The particle temperature influences its hardness and, therefore, the damage it causes upon striking the specimen. Figure 10(a) shows the modeled heating of a 26 micron and a 550 micron particle in a ducted burner rig operated at Mach 0.5, as well as both the static and stagnation gas temperatures. The duct was 0.305 m long, with a diameter of 0.01905 m. The  $x$ -axis represents the radial distance from the nozzle exit of the burner rig. The 26 micron particle reaches the static temperature of the gas within the duct and then drops in temperature in line with the drop in the gas static temperature. The 550 micron particle, which has nearly 10,000 times the mass of the 26 micron particle, reaches a maximum temperature of about 600 K. The fact that the small particles come to high temperature is consistent with the streak-camera velocity measurements shown in Figure 6(a), where the particles are observed to glow. The large particles would not be glowing except possibly by reflection. Camera-based velocity measurements for the large particles may require the use of an external light source, such as a strobe. The lower temperature large particles may be harder (especially for certain erodents with strongly temperature-dependent properties) and, therefore, more

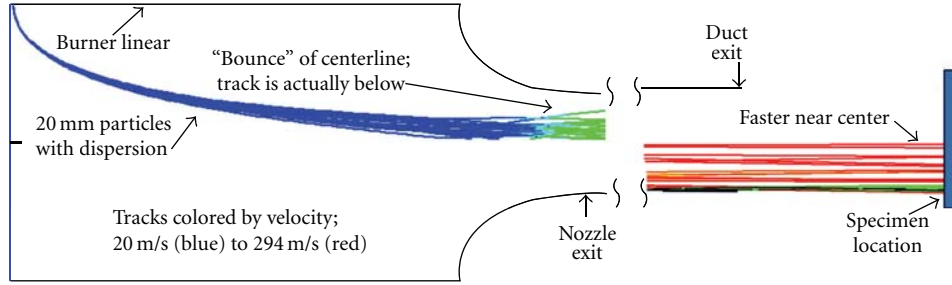


FIGURE 8: Diagram of trajectories of 20 micron particles in a Mach 0.5 ducted burner rig with turbulent dispersion.

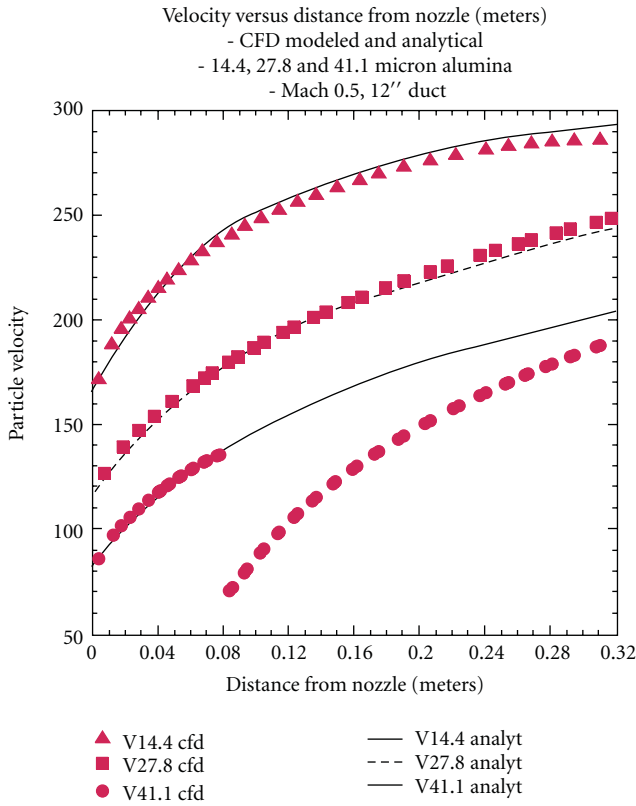


FIGURE 9: Comparison of particle velocity for particles with three different diameters obtained from model predictions with that obtained from an analytical expression of particle velocity with nonzero initial velocity in a Mach 0.5 burner rig (0.305 m long duct).

aggressive in degrading the TBC than the high-temperature small particles.

In order to validate these results, an examination of the particle temperatures under these conditions was undertaken using both a lumped capacitance model and a sphere in cross-flow model. Figure 10(b) examines the early stages of heating within the burner where gas temperature and pressure are essentially constant. Since heating was arbitrarily selected to occur over a narrow temperature range (293 to 360 K), the heat capacity and particle velocity do not vary greatly. Therefore, a lumped capacitance model can be

used to determine heat transfer coefficient,  $h$ , from the gas to the spherical particle [24]. This model means that the particle heats up uniformly—there is no gradient between surface and interiors temperatures. The lumped capacitance model is valid for spheres when the Biot numbers are less than 0.1. The Biot number for spheres may be expressed as

$$Bi = \frac{h(D/6)}{k}, \quad (5)$$

where  $h$  is the heat transfer coefficient ( $W/m^2 \cdot K$ ),  $D$  is the particle diameter (m), and  $k$  is the thermal conductivity ( $W/m \cdot K$ ).

Biot numbers for the 26 and 550 micron particles were found to be 0.0018 and 0.0038, respectively, well below the value of 0.1 necessary for the lumped capacitance model to apply.

According to the lumped capacitance model for heat transfer from a fluid to a sphere,

$$\frac{\theta}{\theta_i} = \frac{(T - T_\infty)}{(T_i - T_\infty)} = \exp\left[\left(\frac{-6h}{\rho DC_p}\right) \times t\right], \quad (6)$$

where  $T_i$  is the initial gas temperature (K),  $T_\infty$  is the free stream temperature (K),  $T$  is the sphere temperature (K),  $\rho$  is the sphere density ( $kg/m^3$ ),  $D$  is the sphere diameter (m),  $C_p$  is the sphere heat capacity ( $J/k \cdot K$ ), and  $h$  is the heat transfer coefficient ( $W/m^2 \cdot K$ ).

Rearranging this equation yields

$$\ln\left(\frac{\theta_i}{\theta}\right) = \left[\frac{6h}{\rho DC_p}\right] t. \quad (7)$$

This is a linear equation in which the slope is equal to  $6h/\rho DC_p$ .

Using data obtained from the ANSYS FLUENT model for the initial particle temperature rise, a plot of  $\ln(\theta_i/\theta)$  versus the particle residence time is produced for both 26 and 550 micron particles, and the slope of these curves was used to determine convective heat transfer coefficients of  $12,500 W/m^2 \cdot K$  for the 26 micron diameter particles and  $1260 W/m^2 \cdot K$  for the 550 micron diameter particles.

In order to validate these results, the heat transfer coefficient was calculated for a sphere in crossflow [24] and compared to those obtained from the lumped capacitance

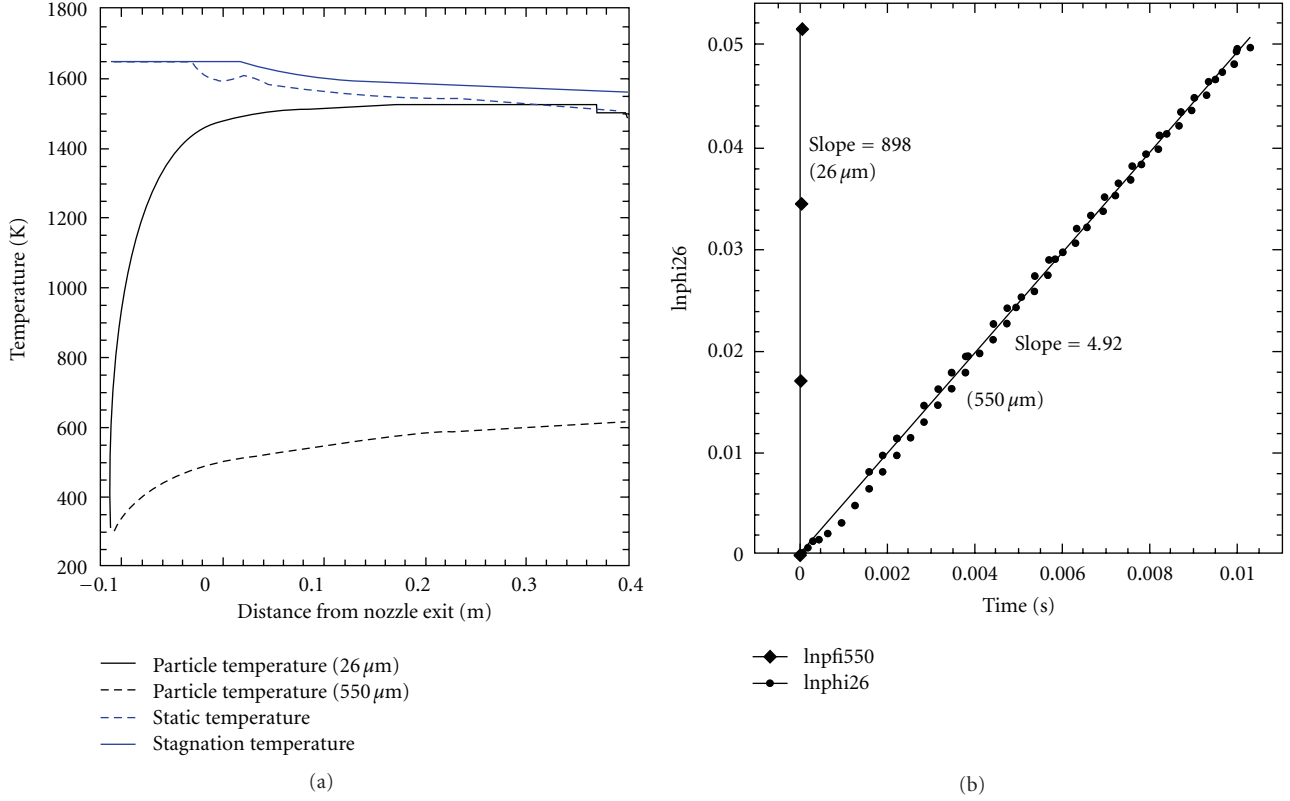


FIGURE 10: (a) Plot of particle temperatures for 26 and 550 micron diameter particles and gas static and stagnation temperature as a function of distance from the nozzle. (b) Plot of the logarithm of temperature ratio versus time for the early stages of particle heating for 26 and 550 micron particles.

model. A heat transfer correlation proposed by Whitaker gives a heat transfer correlation as [25]

$$\overline{Nu}_D = 2 + \left(0.4Re_D^{1/2} + 0.06Re_D^{2/3}\right)Pr^{0.4}\left(\frac{\mu}{\mu_s}\right)^{1/4}, \quad (8)$$

where  $Nu$  is the Nusselt number (dimensionless),  $Re$  is the Reynolds number (dimensionless), and  $Pr$  is the Prandtl number (dimensionless).

These dimensionless numbers are given by

$$Nu = \frac{hD}{k}, \quad Re = \frac{\rho\bar{u}D}{\mu}, \quad Pr = \frac{\nu}{\alpha}, \quad (9)$$

$$\nu = \frac{\mu}{\rho}, \quad \alpha = \frac{k}{\rho C_p},$$

where:  $h$  is the heat transfer coefficient ( $\text{W}/\text{m}^2\cdot\text{K}$ ),  $D$  is the spherical particle diameter (m),  $k$  is the thermal conductivity ( $\text{W}/\text{m}\cdot\text{K}$ ),  $\rho$  is the density ( $\text{kg}/\text{m}^3$ ),  $\bar{u}$  is the mean fluid velocity (m/s),  $\mu$  is the dynamic viscosity ( $\text{kg}/\text{m}\cdot\text{s}$ ),  $\mu_s$  is the dynamic viscosity evaluated at the spherical particle temperature ( $\text{kg}/\text{m}\cdot\text{s}$ ),  $\nu$  is the kinematic viscosity ( $\text{m}^2/\text{s}$ ), and  $\alpha$  is the thermal diffusivity ( $\text{m}^2/\text{s}$ ).

Equation (7) is valid for:

$$\begin{aligned} 0.71 < Pr < 380, \\ 3.5 < Re_D < 7.6 \times 10^4, \\ 1.0 < \left(\frac{\mu}{\mu_s}\right) < 3.2. \end{aligned} \quad (10)$$

$Re_D$  represents the Reynolds number based on the particle diameter. The conditions for this study yielded a Prandtl number of 0.71 (a typical value for air whether at 1640 K or at room temperature). Reynolds numbers based on the particle diameter varied from 5.6 for the 26 micron particles to 116 for the 550 micron particles, and a ratio of dynamic viscosities of 2.94, making (8) valid for use in validating the CFD results in this study.

Properties were evaluated at the free stream gas temperature,  $T_\infty$ , except for  $\mu_s$ , which was evaluated at the temperature of the sphere. The calculations used a gas velocity of 48 m/s plus a small correction for the particle injection velocities (10 m/s for the 26 micron particle, 3 m/s for the 550 micron particle); since injections start out at right angles to the flow, the relative velocities between 48 m/s and 3 m/s or 10 m/s were used. The Reynolds numbers were 5.6 for the 26 micron particles and 116 for the 550 micron particles. The pressure was 118550.25 Pa (1.17 atm). Gas thermal conductivity and viscosities were obtained from data

in Holman [26]. These calculations yielded heat transfer coefficients of  $8660 \text{ W/m}^2 \cdot \text{K}$  for the 26 micron particles and  $1060 \text{ W/m}^2 \cdot \text{K}$  for the 550 micron particles. Compared to the results from the lumped capacitance model, the calculated heat transfer coefficient is about 16% smaller for the 26 micron diameter particle and about 30% smaller for the 550 micron particle. The sphere in crossflow estimates agrees in magnitude with the lumped capacitance values obtained using CFD-predicted values for particle temperatures, thereby further validating the model predictions.

Although there are no standards applying to burner-erosion rigs, it is worth examining the ASTM G76-07 standard that applies to pressurized gas jet erosion testing, which recommends a minimum particle velocity of  $30 \pm 2 \text{ m/s}$  for erosion studies [27]. In an actual turbine engine, particles would be moving much faster, the turbine blade would be moving at a high tip speed, and the temperatures would be high. For the purposes of this study, faster moving particles are generally preferred, unless erosion begins to occur too rapidly. This would be more likely for the large-particle impact damage studies. Figure 11 shows the particle velocity as a function of distance from the injector for both 50 and 560 micron diameter particles at both Mach 0.4 and Mach 0.9 in the unducted rig. Except for the largest particles at the lowest Mach number, the model predicts that all the particles would come to at least the ASTM-recommended velocity by the time they reached the test specimen, with the lighter particles coming to a substantially higher velocity. Figure 12 shows the particle tracks for 27 micron diameter particles injected at three different injection velocities under Mach 0.5 conditions in the unducted rig. The highest particle velocity at the surface of a specimen located 0.076 m (3 inches) from the nozzle exit, and, therefore, the highest erosion rate occurs for particles that move roughly along the centerline of the test rig. Adjusting the particle injection velocity to move as many particles as possible along the centerline would maximize the erosion rate and place this maximum at the center of the test specimen.

The ASTM G76-07 standard calls for erosion regions that are relatively small in diameter; however, it may be desirable in certain cases to broaden the damaged region. For example, a wider erosion pattern may be more representative of exposure of small turbine blades in the engine. Tests using the experimental rig modeled for this paper found that moving the test specimen from 0.05 m to 0.15 m from the nozzle outlet broadened the eroded region. However, this also moves the test specimen to a cooler region of the flame and reduces the similarity to turbine engine temperature conditions. One way to maintain the temperature at the test specimen surface at  $2000^\circ \text{F}$  or above is to direct the hot gases and particles exiting from the nozzle into a duct. Modeling showed that when the duct diameter was equal to the nozzle diameter, the typical result was higher particle velocities with little loss of gas temperature. As mentioned earlier, cycling is accomplished in the NASA Glenn burner rigs by pivoting the rig, which can be an issue for the duct approach. Pivoting the rig would result in a misalignment or separation of the attached duct. A possible solution would be

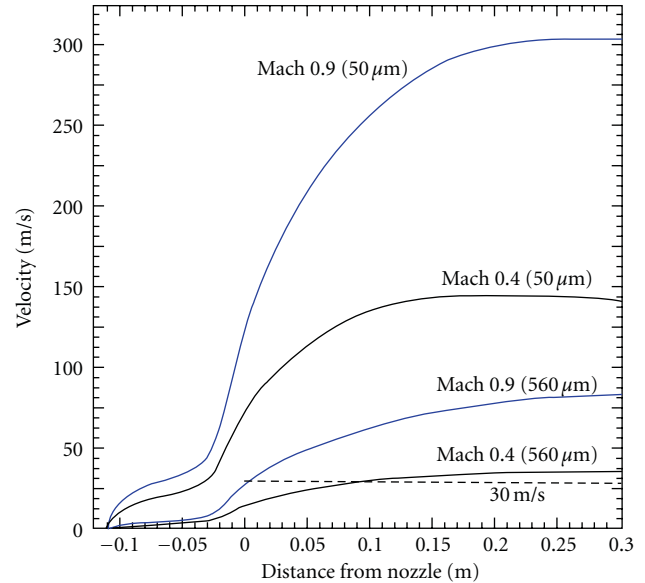


FIGURE 11: Particle velocity as a function of distance from the nozzle for Mach numbers of 0.4 and 0.9, and particle diameters of 50 and 560 microns in an unducted burner rig. The minimum recommended particle velocity of 30 m/s for erosion studies is shown by the dashed line.

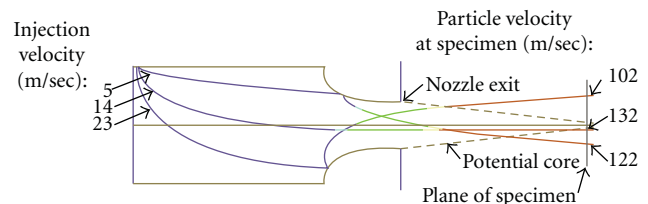


FIGURE 12: Most probable particle trajectories for various injection velocities in an unducted burner rig operated at a Mach number of 0.3 and a single-particle diameter of 26 microns. Note that interior bouncing can result in particles injected at higher velocities tracking toward the upper half of the test specimen, and particles injected at lower velocities can track toward the lower half of the test specimen.

to use an unattached duct, leaving a small distance between the nozzle exit and the duct. The model was used to examine the effects of ducts of different diameters and lengths on the gas temperature and velocity to determine if the rig performance would be adversely affected by an unattached duct.

Figure 13 shows the gas temperature and gas velocity as functions of distance from the nozzle exit for an unattached duct placed 0.0127 m from the nozzle outlet. As the duct diameter decreases, the gas temperature is maintained for a much longer distance. The gas velocity increases through the duct, which results in an increased particle velocity that is maintained farther down the duct as the particle diameter decreases. The smallest duct diameter in Figure 13 matches the diameter of the nozzle. The figure shows that high-gas temperature is maintained out to about 0.4 m for the duct having smallest diameter and the 0.305 m length. Therefore,

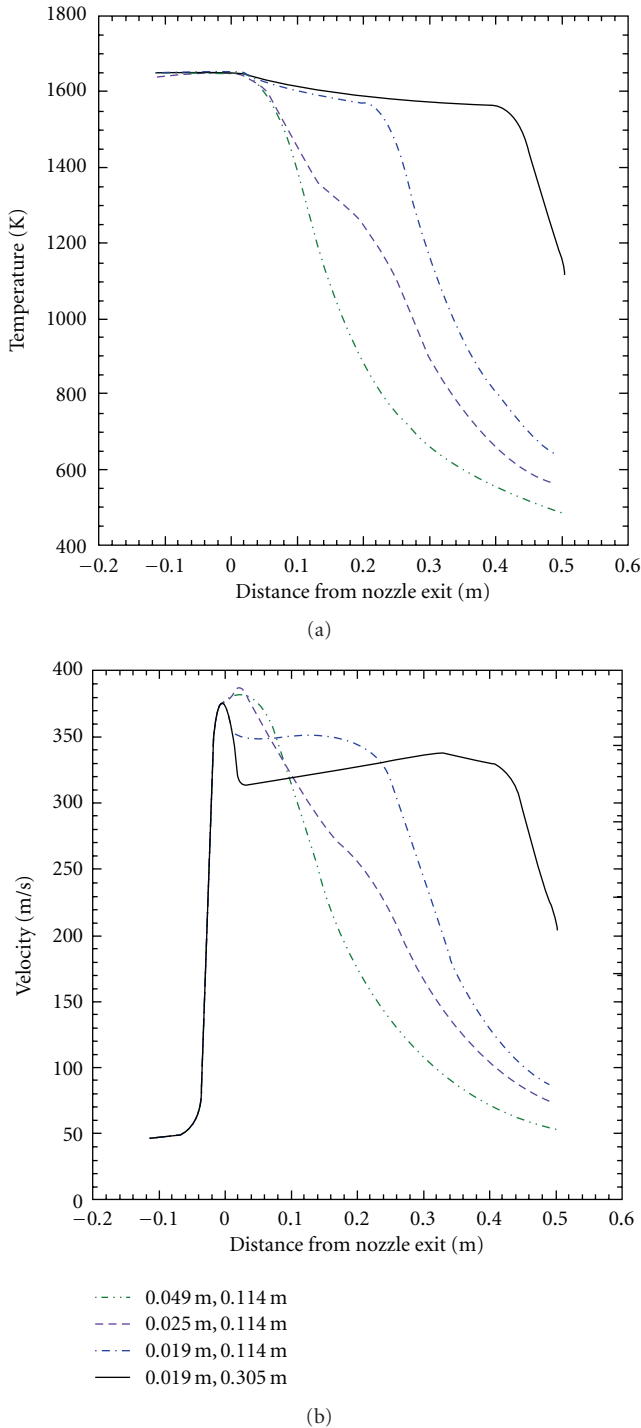


FIGURE 13: Plots as a function of distance from the nozzle exit of (a) gas temperature and (b) gas velocity for four different duct diameters (Mach 0.5 nozzle exit conditions).

the model predicts that an unattached ducted rig with the duct and nozzle of the same diameter of 0.01905 m gives the highest particle velocity, while still maintaining a high temperature at the test specimen surface.

Damage to the interior walls of the erosion and large-particle impact damage test rigs was identified as a potential

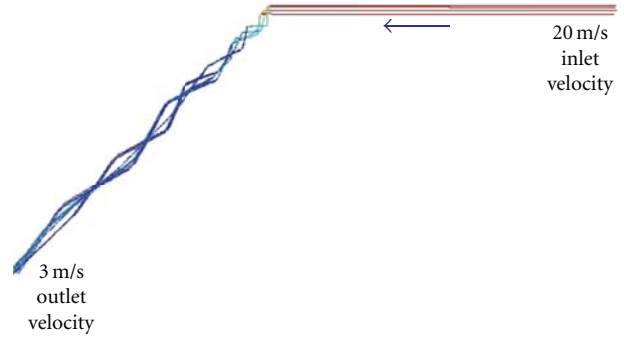


FIGURE 14: Particle tracks, with entrance and exit velocities, in 45 degree elbow. Outline of elbow is not shown in order to better show particle trajectories.

problem. This damage could be mitigated by reducing the particle velocities, but could result in failure to feed properly. Ideally, the particle velocities should be high enough to ensure that they are conveyed down the feed line, but low enough to avoid damage to the interior walls of the test rigs. A three-dimensional computational model of a 45 degree elbow was constructed to investigate whether particles leaving the feeder at a high velocity could be slowed before being injected into the test rigs. Since damage to the test rig walls would be most severe at the highest Mach numbers for the largest particle diameters, runs were conducted at Mach 0.7 for particles with a mean diameter of 550 microns. Model settings were the same as previously described for the test rigs. Figure 14 shows that the model predicts that particles injected at 20 m/s, a high enough velocity for conveying particles through a feed line, are slowed to about 3 m/s at the injection point into the test rig. This velocity would greatly decrease damage to the interior test rig walls. As shown previously, use of the unattached duct will cause particles to accelerate to a sufficient velocity by the time they reach the test specimen.

## 6. Conclusions

This paper described the process used to guide the design of test rigs for both erosion and large-particle impact damage studies of TBCs for turbine engine blades. The model demonstrated that the three major conditions necessary for successful testing with these rigs would be met for the 26 micron diameter particles. The erodent particles come to nearly the gas temperature for the unducted rig and to the gas temperature for the ducted rig, replicating the temperature experienced by particles in a turbine engine. The erodent particles would move at a sufficiently high velocity to replicate damage to blade coatings observed in turbine engines. In the unducted rig, small particles reach well above the ASTM minimum recommended velocity for erosion testing. The particle velocity can be increased through the use of an unattached duct, with the highest sustained velocity occurring for the 0.035 m duct with a duct diameter equal to the nozzle diameter. The eroded region can be broadened by moving the test specimen farther

from the nozzle and using an unattached duct to maintain particle temperature and increase particle velocity at the test specimen surface as long as the duct had the same diameter as the exit nozzle.

It was shown that the 550 micron particles could attain the ASTM minimum recommended velocity, and that the damage region on the test specimen could be broadened through the use of an unattached ducted rig with a diameter equal to the nozzle diameter. However, these larger particles did not come to the gas temperature. Fortunately, for the case of alumina erodent, this may not be a serious concern because the hardness of alumina does not change greatly with temperature. If other erodents were to be used, the effect of temperature on hardness may have to be considered. For the unattached duct case, the gas temperature and particle velocity are, as with the small particles, mostly maintained when the duct and the nozzle are of equal diameter. The fastest velocities and the highest erosion rates occur when the erodent particles exit as close to the centerline of the test rig as possible. The model demonstrated that potential damage to the interior walls of the test rigs caused by high inlet particle velocities could be mitigated through the use of a 45 degree elbow to slow the inlet particle velocities. These velocities would increase to test-velocity conditions as they are accelerated through the unattached duct.

Examples of excellent agreement of model predictions with experimental observations, experimental measurements, and an analytical expression of particle velocities demonstrate that this model can be used to predict the performance of the burner-erosion test rigs. This greatly decreased the development time for the rigs over trial-and-error approaches and allows predictions of future rig performance if operating conditions are changed. This computational approach can be applied to the development of a variety of rigs for materials testing.

## Acknowledgment

The authors gratefully acknowledge the support of this work by the NASA Fundamental Aeronautics program, Subsonic Rotary Wing project.

## References

- [1] D. Zhu and R. A. Miller, "Thermal-barrier coatings for advanced gas-turbine engines," *MRS Bulletin*, vol. 25, no. 7, pp. 43–47, 2000.
- [2] F. O. Soechting, "Design perspective on thermal barrier coatings," *Journal of Thermal Spray Technology*, vol. 8, no. 4, pp. 505–511, 1999.
- [3] N. P. Padture, M. Gell, and E. H. Jordan, "Thermal barrier coatings for gas-turbine engine applications," *Science*, vol. 296, no. 5566, pp. 280–284, 2002.
- [4] R. A. Miller, "Ceramic thermal barrier coatings," *Surface and Coatings Technology*, vol. 30, no. 1, pp. 1–11, 1987.
- [5] T. Strangman, D. Raybould, A. Jameel, and W. Baker, "Damage mechanisms, life prediction, and development of EB-PVD thermal barrier coatings for turbine airfoils," *Surface and Coatings Technology*, vol. 202, no. 4–7, pp. 658–664, 2007.
- [6] A. Maricocchi, A. Bartz, and D. Wortman, "PVD TBC experience on GE aircraft engines," *Journal of Thermal Spray Technology*, vol. 6, no. 2, pp. 193–198, 1997.
- [7] W. J. Tingle, W. R. Oliver, and K. Kirtley, *Particle Separator Using Boundary Layer Control*, General Electric Company, 2010.
- [8] T. E. Strangman, D. Narasimhan, J. P. Armstrong, and K. R. Karasek, *Carbon Deposit Inhibiting Thermal Barrier Coating for Combustors*, Honeywell International, Inc., New York, NY, USA, 2001.
- [9] T. E. Kuhn, W. G. Freeman, F. S. Maszk, D. P. Freiberg, K. A. Struzek, and L. A. Kobold, *Apparatus and Method for Controlling Combustor Liner Carbon Formation*, Honeywell International, Inc., New York, NY, USA, 2004.
- [10] R. F. Handschuh, "High temperature erosion of plasma-sprayed Yttria-stabilized zirconia in a simulated turbine environment," Tech. Rep., American Institute of Aeronautics and Astronautics, Nashville, Tenn, USA, 1985.
- [11] R. W. Bruce, "Development of 1232°C (2250°F) erosion and impact tests for thermal barrier coatings," *Tribology Transactions*, vol. 41, no. 4, pp. 399–410, 1998.
- [12] G. D. Roberts, R. T. Bhatt, P.J. Bonacuse et al., "A status of NASA rotorcraft research," type NASA/TP-2009-215369, NASA, 2009.
- [13] K. Senesh and V. Babu, "Numerical simulation of subsonic and supersonic jets," in *Proceedings of the 11th AIAA/CEAS Aeroacoustics Conference (26th AIAA Aeroacoustics Conference)*, pp. 3699–3711, AIAA, Monterey, Calif, USA, March 2005, AIAA 2005-3095.
- [14] ANSYS FLUENT 6.3 User's Guide, 2006.
- [15] D. C. Wilcox, *Turbulence Modeling for CFD*, DCW Industries, 2nd edition, 2000.
- [16] S. A. Morsi and A. J. Alexander, "An investigation of particle trajectories in two-phase flow systems," *The Journal of Fluid Mechanics*, vol. 55, pp. 193–208, 1972.
- [17] R. Clift, J. Grace, and M. E. Weber, *Bubbles, Drops, and Particles*, Dover, New York, NY, USA, 1978.
- [18] R. Swar, "Particle erosion of gas turbine thermal barrier coatings," in *Aerospace Engineering and Engineering Mechanics*, University of Cincinnati, Cincinnati, Ohio, USA, 2009.
- [19] A. Hamed, Y. D. Jun, and J. J. Yeuan, "Particle dynamics simulations in inlet separator with an experimentally based bounce model," *Journal of Propulsion and Power*, vol. 11, no. 2, pp. 230–235, 1995.
- [20] R. A. Miller, M. A. Kuczmariski, and D. Zhu, *Burner Rig with an Unattached Duct for Evaluating the Erosion Resistance of Thermal Barrier Coatings*, NASA/TM-2011-217008, 2011.
- [21] D. Zhu, R. A. Miller, and M. A. Kuczmariski, "Development and life prediction of erosion resistant turbine low conductivity thermal barrier coatings," in *Proceedings of the AHS International 65th Annual Forum*, pp. 1088–1094, NASA, May 2009.
- [22] R. C. Dykhuizen and M. F. Smith, "Gas dynamic principles of cold spray," *Journal of Thermal Spray Technology*, vol. 7, no. 2, pp. 205–212, 1998.
- [23] F. F. Abraham, "Functional dependence of drag coefficient of a sphere on reynolds number," *Physics of Fluids*, vol. 13, no. 8, pp. 2194–2195, 1970.
- [24] F. P. Incropera and D. P. DeWitt, *Introduction to Heat Transfer*, John Wiley and Sons, New York, NY, USA, 3rd edition, 1996.
- [25] S. Whitaker, "Forced convection heat transfer correlations for flow in pipes, past flat plates, single cylinders, single spheres, and for flow in packed beds and tube bundles," *AIChE Journal*, vol. 18, no. 2, pp. 361–371, 1972.

- [26] J. P. Holman, *Heat Transfer*, McGraw-Hill, New York, NY, USA, 8th edition, 1997.
- [27] ASTM G76 - 07, *Standard Test Method for Conducting Erosion Tests by Solid Particle Impingement Using Gas Jet*, 2007.

## Research Article

# Investigation of Swirling Flows in Mixing Chambers

Jyh Jian Chen and Chun Huei Chen

*Department of Biomechanics Engineering, National Ping Tung University of Science and Technology, Pingtung 912, Taiwan*

Correspondence should be addressed to Jyh Jian Chen, [chaucer@mail.npust.edu.tw](mailto:chaucer@mail.npust.edu.tw)

Received 9 November 2010; Revised 25 February 2011; Accepted 1 March 2011

Academic Editor: Guan Yeoh

Copyright © 2011 J. J. Chen and C. H. Chen. This is an open access article distributed under the Creative Commons Attribution License, which permits unrestricted use, distribution, and reproduction in any medium, provided the original work is properly cited.

This investigation analyzed the three-dimensional momentum and mass transfer characteristics arising from multiple inlets and a single outlet in micromixing chamber. The chamber consists of a right square prism, an octagonal prism, or a cylinder. Numerical results which were presented in terms of velocity vector plots and concentration distributions indicated that the swirling flows inside the chamber dominate the mixing index. Particle trajectories were utilized to demonstrate the rotational and extensional local flows which produce steady stirring, and the configuration of colored particles at the outlet section expressed at different  $Re$  represented the mixing performance qualitatively. The combination of the Taylor dispersion and the vorticity was first introduced and made the mixing successful. The effects of various geometric parameters and Reynolds numbers on the mixing characteristics were investigated. An optimal design of the cylindrical chamber with 4 inlets can be found. At larger Reynolds number,  $Re > 15$ , more inertia caused the powerful swirling flows in the chamber, and more damping effect on diffusion was diminished, which then increased the mixing performance.

## 1. Introduction

In the last decades, microfluidic devices have been widely utilized in microelectromechanical systems and employed as powerful instruments to perform biological experiments. Some products have been mass-produced, such as micropump, micromixer, microvalve, and even microreactor. Microfluidic devices have been developed for a broad range of applications. These applications cover genomic analysis [1, 2], chemical engineering [3], as well as lab-on-a-chip [4]. Effective mixing of various fluids is required in many miniaturized multicomponent flow systems. Fast mixing can reduce the time required for analysis and improve reaction efficiency in industrial applications. Micromixer can be integrated in a microfluidic system or used as a single device. Furthermore, the investigation of micromixers is the basis for understanding the transport phenomena in micro-scale systems. Traditionally, both the stirring and the creation of turbulent flow are exploited to improve the mixing characteristics in the macroscopic world. However, it is very difficult to create the conventional mixing mechanisms inside the miniaturized systems because the Reynolds number is rarely larger than 100.

In general, since the Reynolds number is very low in a microscopic system (Reynolds number,  $Re$ , indicates the ratio of inertia to viscous forces and is expressed as  $Re = UD_H/\nu$ , with  $U$  being the inlet flow velocity,  $D_H$  the hydraulic diameter of the microchannel, and  $\nu$  the kinematic viscosity), liquid flows inside microchannels are generally observed as laminar flows. Viscous forces dominate the flow fields, and vortices cannot exist in such flow. As a result of the small geometric sizes and the laminar flow regimes in microfluidic analytical devices, fast mixing cannot be achieved by the conventional methods. In a typical microfluidic device, the mixing of two or more miscible fluid streams is dominated by molecular diffusion, which is driven by a concentration difference and is a rather slow process. According to Fick's first law of diffusion, the flux of the diffusing species is proportional to the diffusivity and a divergence of the concentration [5]. In addition, the mixing time increases in proportion to the square value of the diffusing distance and furthermore depends on the diffusivity of the diffusing compound [6]. In order to speed up mixing, the essentials of a diffusion-based micromixer are, therefore, the maximization of the contact area of different fluids and the minimization of the diffusing distance. Among these

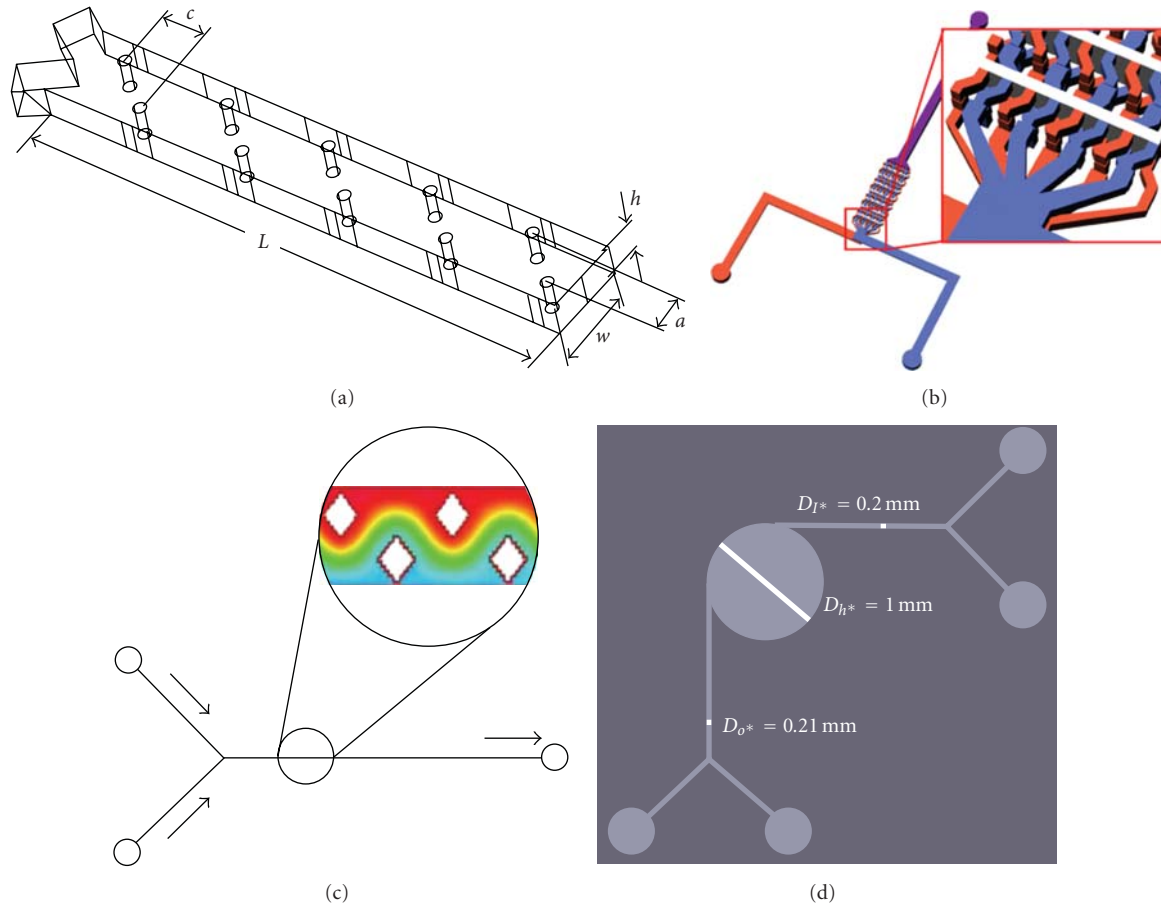


FIGURE 1: A few representative designs of the parallel laminated micromixers recently developed by other research. (a) Maeng et al. [14], (b) Cha et al. [17], (c) Bhagat et al. [18], and (d) Long et al. [26].

technologies a number of micromixers have been developed. These can be classified into two groups: active and passive micromixers. Though the time and channel length required for active mixing are less than those for passive mixing, the active micromixers are difficult to fabricate, clean, and integrate into microfluidic systems. The pronounced advantage of passive micromixers is that they utilize no external power except the mechanism used to drive the fluids into the microfluidic systems.

During the past ten years, studies on passive mixing in micromixers have been conducted. Nguyen and Wu [7] presented an elaborate review for the micromixers and reported on the progress of recent development of micromixers. Since generating a turbulent liquid flow inside the microdevice is complicated, the passive micromixers primarily have two types of mixing mechanisms, namely, chaotic advection and molecular diffusion. A chaotic advection micromixer refers to unit operation that stretches and folds fluid volumes over a channel cross-section [8, 9]. The challenges of chaotic micromixers are the microfabrication of complex structures. By considering the characteristics of molecular diffusion, some have dealt with the injection mixing, where one liquid fluid is injected into the other with microplumes [10]. Some studies proposed micromixers based on the increase

of the boundary surface, with the concept of lamination [11]. These designs split incoming streams into several narrower confluent streams and rejoined these narrower streams together. Then the contact surface of two fluids is implemented, and it increases the diffusion speed. The thickness of each fluid layer is greatly reduced in comparison with the characteristic diffusion length, which reduces the mixing time.

Parallel laminated mixers with simple two-dimensional structures were fabricated without difficulty, and mixing in such laminar flows can be very easily enhanced. In all of the aforementioned studies, two representative micromixers were discussed in detail. One design is a device with multiple intersecting channels. A micromixer based on the principle of distributive mixing was presented by Bessoth et al. [12], and the feasibility of the chip being used for mixing in the millisecond regime was demonstrated. Hinsmann et al. [13] also introduced a micromixing device. The fluid entering through the inlet was split and forced to flow under the separating layer. Then the fluid streams entered the main channel and were mixed. To improve the mixing by placing obstacles in the channel shown in Figure 1(a), Maeng et al. [14] created the disruption to the flow field, which reduced the diffusion path. An in-plane micromixer using the Coanda

effect was designed by Hong et al. [15], and a Poiseuille flow was produced in the perpendicular direction of the flow to achieve a great mixing performance. A passive micromixer using a recycle flow was devised by Jeon et al. [16], and a recycle flow was introduced from side channels to the inlet flow. Cha et al. [17] proposed a mixer designed for chessboard mixing shown in Figure 1(b), and the mixer achieved a high mixing performance in a very short channel length by enlarging the contact areas between two liquid fluids. Bhagat et al. [18] reported a planar passive mixer shown in Figure 1(c), and this design incorporated diamond-shaped obstructions within the channel to breakup and recombine the flows.

The other design split the main streams into several narrower streams and rejoined them together. A laminated micromixer was first reported by Koch et al. [19] who conducted two silicon-based mixers to achieve good mixing performances. The mixer geometries, which share an interdigital arrangement of inlet streams, were proposed by some researchers [20, 21]. Results suggested that geometric focusing of a large number of liquid streams is a powerful micromixing principle. In order to increase the mixing by reducing the diffusion distance, the main stream is needed to be split into several substreams. In the case of the mixer utilizing distributive mixing, the pressure loss is higher because of the narrower intersecting channels. A circular vortex micromixer with sixteen tangential inlets was presented by Bohm et al. [22]. The liquids were injected into the micromixer to induce a swirling flow field, and the mixing could be performed in a shorter time-scale. Lin et al. [23] developed a three-layer glass vortex mixer for low  $Re$ . Two inlet channels divide into 8 individual channels tangent to a circular chamber. The  $Re$  is higher than a value of 2.32, and a self-rotation effect is induced in the chamber. A swirl micromixer with two branch channels, a central chamber, and an exit tube was carried out by Jin et al. [24]. The dependence of the mixture viscosity and density on the mass fraction of solution was taken into consideration. The cost-effective mixing at  $Re > 500$  was obtained because of the generation of the swirling flow. Yang et al. [25] presented a vortex-type micromixer with four tangential inlets which utilized pneumatically driven membranes to generate a swirling flow. A mixing efficiency of 0.95 could be achieved in time period of 0.6 s for the two-membrane layout. A three-dimensional polystyrene vortex micromixer was demonstrated by Long et al. [26] and shown in Figure 1(d). The device employs one inlet, one vertical cylinder, and one outlet. Results were compared with the mixing performance of a two-dimensional square-wave channel.

For the vortex micromixer, many substreams are needed to improve the mixing since the mixing of two or more fluid streams occurs by virtue of molecular diffusion. To reduce the pressure and increase the contact area of two fluids, the mixing chamber inside the micromixer is imposed. In previous work [22, 23], eight or sixteen inlets were used to inject two different kinds of fluids into the mixing chamber. The more inlets utilized, the more significantly swirling effects could be seen. However, the experimental apparatus

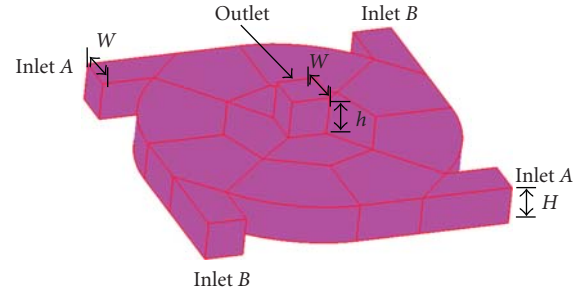


FIGURE 2: One of the basic configurations for the analysis. The diameter of the cylindrical chamber is equal to  $800 \mu\text{m}$ . The width,  $W$ , and height,  $H$ , of the inlets are set at the value of  $100 \mu\text{m}$ . The width, length, and height of the outlet are set at the value of  $100 \mu\text{m}$ .

would be more complicated in order to supply all these inlet flows. The effects of the numbers of the inlet channels have not been studied in detail. In all of the aforementioned studies, the effects of mixer geometries on flow characteristics inside the vortex micromixers were not investigated. The geometric effects of the mixer affect the liquid flows, so the success of the mixing depends strongly on this effect. In fluid dynamics, vorticity is considered as the circulation per unit area at a point in a fluid flow field. Besides, whereas two fluids are flowing in a flat channel, both convective and molecular diffusions contribute to mixing performance due to the Taylor dispersion effect. The combination of the radial dispersion and the vortex flow makes the mixing successful, and no previous studies examined the flow and mixing performances inside the vortex micromixer by utilizing the concepts of the vorticity and the Taylor dispersion. Characterization of the mixing performance of mixing devices using CFD simulations has been described in many publications. The particle trajectories are used to numerically study the mixing and fluidic behaviors by chaotic advection inside the microchannel. Therefore, understanding the fluid flows in vortex micromixer by utilizing the particle trajectories is of marked importance in the related fields of microfluidics.

The objective of the present study is to demonstrate a designed lamination micromixer with a right square prism, an octagonal prism, or a cylinder, plus several pairs of inlets and one outlet. A three-dimensional fluid field is used to describe the flow characteristics in the microfluidic system. The effects of swirling flows on mixing performances are expressed in terms of particle trajectories, vorticity profiles, concentration distributions, and mixing indexes. The effects of various geometric parameters and  $Re$  on the mixing characteristics were also investigated.

## 2. Mathematical Model

Figure 2 schematically depicts one of the basic configurations for the analysis. The physical problem is that the liquids to be mixed enter the mixing chamber at a specified speed from several tangential inlets and then flow out from the outlet channel at the central location of the chamber. The physical domain is a three-dimensional volume consisting of a right

square prism, an octagonal prism, or a cylinder.  $W$  is the width of the inlet channel, and  $H$  is the height of the inlet channel. In addition,  $h$  is the height of the outlet channel having the length and the width of  $L$ . The boundary surfaces of the domain are solid, rigid, and impermeable walls. It is assumed that the steady state is reached in the chamber and the channels; the variations of the concentration do not modify the viscosity and the density of the fluid; the channel walls are assumed to be smooth. The effects of surface tension on the interaction between two miscible liquids on Earth are masked by the effects of gravity and density. On Earth, miscible liquids effectively combine into one relatively homogenous (or equally distributed) solution [27]. There is no real interface when liquids are perfectly miscible. Surface tension forces in this study are neglected.

The equations to be solved are the continuity equation, the Navier-Stokes equations, and the conservation of species equations, along with the appropriate boundary conditions. The following assumptions have been adopted to obtain a proper mathematical formulation of this problem.

- (1) Fluid flow is Newtonian and laminar. As reasonably assumed herein, the fluid is incompressible since the velocities encountered in this type of flow are expected to be markedly lower than the sonic velocity in the fluid.
- (2) All thermophysical properties of the liquid are to be evaluated at the fixed reference temperature of 300 K.
- (3) Gravity is negligible.
- (4) The nonslip and nonpenetration conditions are usually encountered at solid surfaces.

The conservation of mass and momentum equations are solved to determine the flow field of the liquids. In symbolic notation, the continuity equation can be expressed as follows:

$$\nabla \cdot \vec{U} = 0, \quad (1)$$

where  $\vec{U}$  is the fluid velocity vector.

The momentum equation for a continuum is the analogue of Newton's second law for a point mass. In symbolic notation the momentum equation is expressed as

$$\rho \vec{U} \cdot \nabla \vec{U} = -\nabla P + \mu \nabla^2 \vec{U}, \quad (2)$$

where  $\rho$  is the fluid density,  $P$  is the pressure, and  $\mu$  is the fluid viscosity.

Species transport by pressure-driven flows occurs as a result of convection and diffusion and can be described by the combined species convection-diffusion equation. In symbolic notation the diffusion-convection equation is

$$\rho \vec{U} \cdot \nabla \phi = D \nabla^2 \phi, \quad (3)$$

where  $D$  is the diffusivity and  $\phi$  is the mass concentration. This equation must be solved together with (1) and (2) in order to achieve computational coupling between the velocity field solution and the concentration distribution.

The liquids enter into the mixing chamber from several tangential inlets and then flow out from the outlet channel at the central location of the chamber. The rotation of a fluid about a vertical axis can be observed in the chamber. Reynolds number in the physical domain,  $Re$ , indicates the ratio of inertial forces due to rotation of a fluid about a vertical axis to viscous forces. The effects of inertia on the elastic instabilities in Dean and Taylor-Couette flows were investigated through a linear stability analysis [28]. It was shown that, when rotation of the inner cylinder drives Taylor-Couette flow, the Reynolds stresses produce energy, and thus are destabilizing, while for the flow driven by the rotation of the outer cylinder alone, the Reynolds stresses dissipate energy, thus stabilizing the flow. The stability of axially symmetric flow at nonzero Reynolds number was also analyzed [29]. The effect of inertia on axisymmetric disturbances was investigated and showed that inertia tended to destabilize the flow. The physical system in our micromixer is that the liquids enter the mixing chamber with a fixed wall from several tangential inlets and then flow out from the outlet channel at the central location of the chamber. So inertia force tends to destabilize a system, and then the mixing performance can be enhanced. On the other hand, viscous force tends to stabilize a system and damp out perturbations, such as the diffusion.

### 3. Numerical Analysis

For a better understanding of the fluid flow and the mixing characteristics in the mixer, a computational fluid dynamics package, CFD-ACE+, using a finite volume approach is utilized to simulate three-dimensional flow fields as well as two-fluid mixing. A nonlinear steady-state algorithm is used for hydrodynamic calculations, and a linear steady-state one is applied to solve the diffusion-convection equation. The inlet boundary condition is set to have the same constant velocity for two fluids, and the outlet is assumed to be a constant pressure condition. The user scalar module enables us to compute the transport of species. In this study, the transport mechanism in fluid volumes is assumed, and species do not affect the velocity, or any other computed field. For the scalars, the boundary conditions are generalized as:

$$\alpha \left( D \frac{\partial \phi}{\partial n} \right)_B + b \phi_B = c. \quad (4)$$

For the Dirichlet boundary conditions at the inlet,  $a$  is set to 0,  $b$  is set to 1, and  $c$  is set to 1 (for species A) or 0 (for species B).

This study considered three different configurations of the flow system. The general configuration consists of a right square prism, an octagonal prism, and a cylinder (c.f. Figure 3). Three dimensional structured grids are employed. The grid systems of the computation domain are chosen to assure the orthogonality, smoothness, and low aspect ratios to prevent the numerical divergence. Poor grid systems can enhance the numerical diffusion effects. Numerical errors due to discretization of the convective terms in the transport equation of the concentration fields introduce an

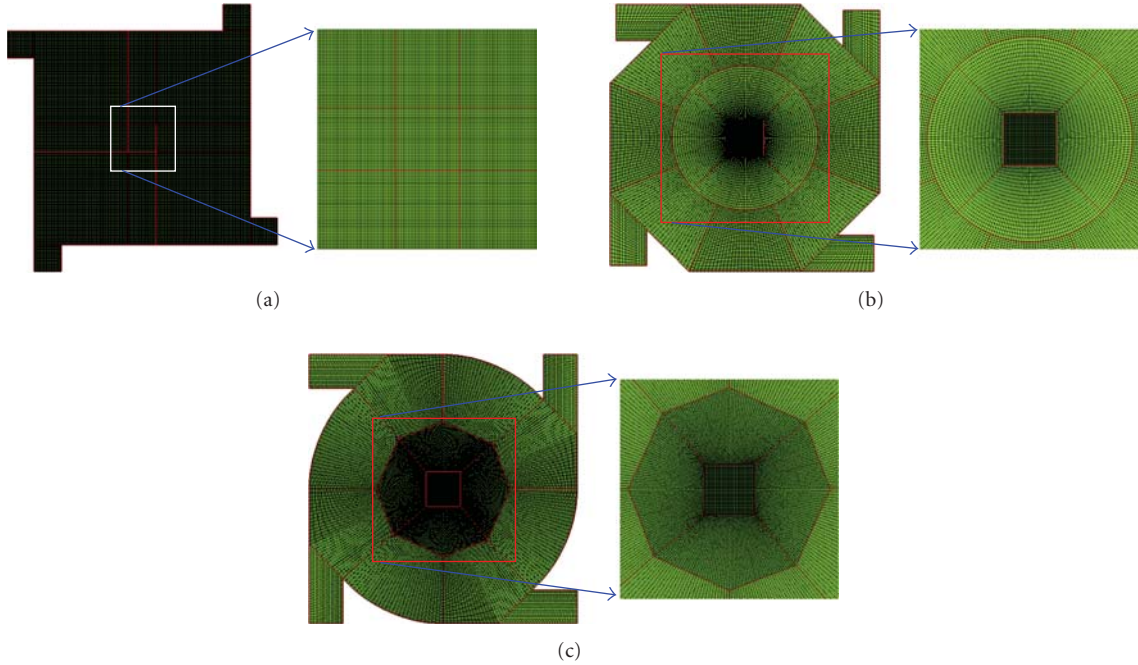


FIGURE 3: Grid systems of three configurations: (a) right square prism, (b) octagonal prism, and (c) cylinder.

additional, unphysical diffusion mechanism [20]. This so-called numerical diffusion is likely to dominate diffusive mass transfer on computational grids. Higher-order discretization schemes reduce the numerical errors. Numerical diffusion strongly depends on the relative orientation of flow velocity and grid cells, and it can be minimized by choosing grid cells with edges parallel to the local flow velocity. Regarding to our grid systems shown in Figure 2, the numerical diffusion can be reduced comprehensively in the computational results. To minimize the effects of the meshing on mixing, the mesh density is increased until the mixing index variation is less than 5%.

The SIMPLEC method is adopted for pressure-velocity coupling, and then all spatial discretizations are performed using the second-order upwind scheme. The algebraic multigrid (AMG) solver is utilized for pressure correction, whereas the conjugates gradient squared method (CGS) and preconditioning (Pre) solver are employed for velocity and species corrections. The solution is considered to be converged when the relative errors of all independent variables are less than  $10^{-4}$  between the sweeps  $n$  and  $n + 1$ .

The cross-sectional images of outlets obtained from the CFD software are converted to text formats. The uniformity of mixing at sampled sections is assessed by determining the mixing index  $\varphi$  of the solute concentration, which is defined as

$$\varphi = 1 - \frac{\int_A |I - I_{ave}| dA}{\int_{A_0} |I_0 - I_{ave}| dA}, \quad (5)$$

where  $I$  is the concentration value (between 0 and 1) on the sampled section  $A$ ,  $I_0$  is the concentration value at the inlet plane  $A_0$ , and  $I_{ave}$  is the averaged value of the concentration

over the sampled section. The mixing index  $\varphi$  range is from 0 for no mixing to 1 for complete mixing.

#### 4. Conceptual Design

In this section, the design concept of a three-dimensional swirling micromixer is introduced. From the preliminary studies on the vortex micromixers, a strongly rotational motion of the fluids is generated. A designed lamination micromixer with a chamber, plus several pairs of inlets and one outlet, is demonstrated. The diameter of the cylindrical chamber is equal to  $800 \mu\text{m}$ . The inlets are tangential to the chamber, and the outlet is located in the central region of the chamber. The width,  $W$ , and height,  $H$ , of the inlets are set at the value of  $100 \mu\text{m}$ . The width, length, and height of the outlet are set at the value of  $100 \mu\text{m}$ , too. All the inlets are symmetric with the central axis of the mixing chamber. The fluid properties are set to the physical and thermodynamic properties of water, which are diffusivity,  $D$ , of  $1 \times 10^{-9} \text{ m}^2/\text{s}$ , kinematic viscosity,  $\nu$ , of  $1 \times 10^{-6} \text{ m}^2/\text{s}$ , density,  $\rho$ , of  $1 \times 10^3 \text{ kg}/\text{m}^3$ . The fluid with red color stands for species A, and the fluid with blue color for species B. The concentration of species is normalized as one and zero for the inlet of species A and species B, respectively. The parameters of the above values are used, unless noted otherwise.

A streak line is defined as a line formed by the particles which pass through a given location in the flow field [30]. In a steady flow, the streak lines coincide with the stream lines and the particle trajectories. These streak lines can be seen as the trajectories of the particles released from the specific locations of the inlets to the outlet and used to describe the nature of the flow field inside the micromixer. Figure 4 depicts the streak lines as the fluids flow through

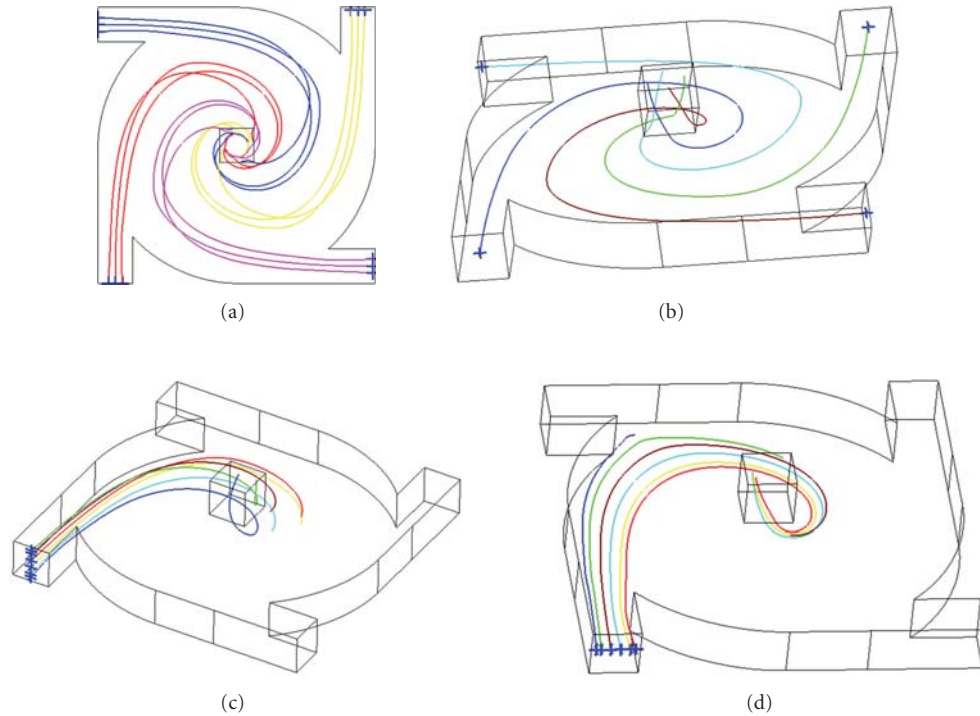


FIGURE 4: The trajectories of the microfluidic flow in the mixer. (a) Top view of the streak lines in the micromixer. (b) Four streak lines starting from the central locations of the four inlets. (c) Six streak lines starting from the six specific locations along vertical central line of one inlet. (d) Six streak lines starting from the six specific locations along horizontal central line of one inlet.

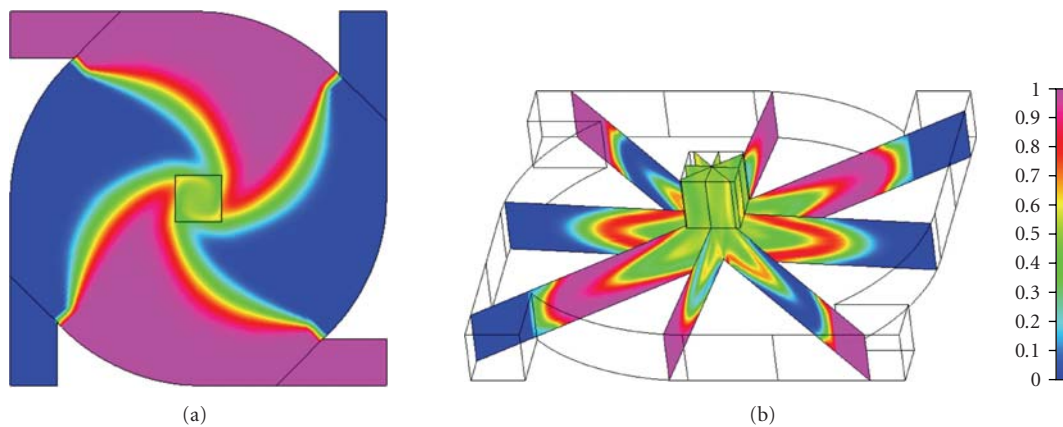


FIGURE 5: Numerical mixing results of mixer with cylinder (a) from the top view and (b) at 8 cross-sectional areas.

the cylindrical chamber at the inlet velocity of 0.75 m/s and the chamber height of  $100\ \mu\text{m}$ . The corresponding  $Re$  is 75. The initial positions of particles are shown as markers “+” illustrated in the figures. Fluids enter the chamber in the tangential directions, and the flow is almost unidirectional. As the fluid approaches the entrance of the other fluid, the fluid is deflected and forms a clockwise vortex (Figure 4(a)). These streak lines are symmetric with the center of the chamber. The rotational flow field is observed and extends towards the outlet of the mixer (Figure 4(b)). As shown in Figures 4(c) and 4(d), the trajectories are quite regular.

Thus the stretching of the interface can be presented, and the rotational and extensional local flow can produce steady stirring in the chamber.

In order to perform a comprehensive analysis of the mass transfer mechanism in vortex micromixer, the cross-sectional concentration distributions are utilized to demonstrate the mixing characteristics. The concentration distributions for mixing in the cylindrical chamber are shown in Figure 5. The predicted concentration distribution of two fluids regarded from the top and eight cross-sectional areas are presented in Figures 5(a) and 5(b), respectively. In order

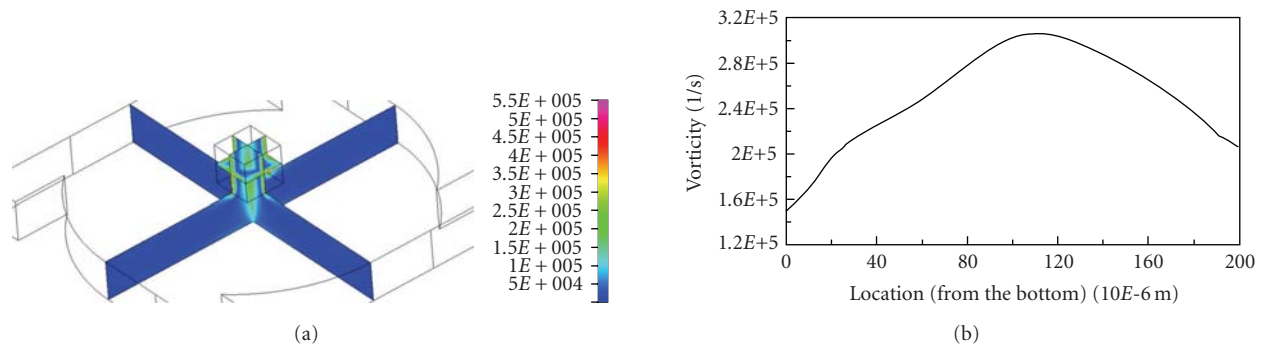


FIGURE 6: (a) The vorticity distributions at three cross-sectional areas of the chamber with cylinder and (b) numerical results of vorticity profiles along the central line of the mixer.

to improve the mixing, two different fluids enter into the four inlets alternately. The inlet channel is tangential to the mixing chamber, and a rotation flow field is induced owing to the high inertia force, as shown in Figure 5(a). The fluid, A, meets the other fluid, B, near the inlet B and the interface of two fluids becomes curved. The contact area of two fluids is increased. Then two fluids enter into the outlet channel. Because the area of the outlet is much smaller than that of the chamber, the diffusion distance of two fluids in the outlet channel becomes smaller and the mixing can be enhanced. Two fluids flow tangentially into the chamber and flow clockwise inside the chamber. Since the outlet is located at the central region of the chamber, fluids tend to flow out of the outlet channel and the vortex flow is formed. Flows in the angular and radial directions are both significant. Whereas two fluids are flowing in a capillary tube, both convective and molecular diffusions contribute to mixing performance due to the axial dispersion effect. This is the so-called Taylor dispersion. In this micromixer, the height of the chamber is small, and the shear force establishes the radial concentration gradient enhancing the mass transport rate in the radial direction. The radial dispersion effect can be observed in Figure 5(b). This system shows the mixing characteristics similar to Taylor dispersion, with contributions from both diffusion and convection. The combination of the radial dispersion and the vortex flow makes the mixing successful. In fluid dynamics, vorticity is the curl of the fluid velocity. It can also be considered as the circulation per unit area at a point in a fluid flow field. It is a vector quantity whose direction is along the axis of the fluid's rotation. So the value of the vorticity inside the chamber volume can be seen as the indicator of the vortex flow. Figure 6(a) shows the vorticity distributions at three cross-sectional areas of the chamber with cylinder, the same as the case illustrated in Figure 4. It is presented that the vorticity is much larger near the central region of the chamber and the outlet channel than in other regions. So the rotation rate of the fluid is greatest at the center and decreases progressively with distance from the center. The vorticity greatly depends on the velocity gradient in the mixer. The fluids enter into the outlet channel, and the gradient of the velocity near the wall of the channel becomes larger; then the vorticity increases more. As shown

in Figure 6(b), the vorticity along the central axis from the bottom of the chamber increases, reaches the maximum value near the entrance of the outlet channel, and then decreases to the location of the outlet. The vortex flow is intensified more near the entrance of the outlet channel; the contact areas of fluids can be further enlarged.

In an effort to understand the two-fluid mixing inside the mixer, the velocity vector planes are utilized to demonstrate the rotation of the fluid flows. Figure 7 illustrates the mixing and flow characteristics at eight cross-sectional areas from the bottom of the chamber for the case presented in Figure 4. The location of the cross-sectional area in Figure 7(a) is  $25\ \mu\text{m}$  from the bottom of the chamber. The distance between the following, from Figures 7(b) to 7(h), are  $25\ \mu\text{m}$  apart. The concentration distributions and the vector planes are shown. With respect to the mass transport mechanism in mixing, two fluids flow tangentially into the chamber and the radial component of velocity grows because fluids tend to flow through the outlet channel. These two components result in an overall rotating flow field inside the chamber. The fluids flow clockwise, and the contact area between them increases as shown in Figure 7(a). In the central region of the chamber, and the mixing performance is great. The rotation effect grows as the fluids move away from the bottom of the chamber. The mixing region spreads from the central region, and the mixing becomes much better, as presented in Figure 7(b). Whereas the fluids approach the top of the chamber, the mixing region shrinks owing to the no-slip conditions at the wall of the chamber. However, the rotation effect increases, as shown in Figure 7(c), the mixing is enhanced even more. At the location of the upper wall of the chamber, the pattern of the mixing characteristics, as shown in Figure 7(d), is similar to the pattern in Figure 7(a). The circulation of the fluid flow in the chamber is clearly observed. The maximum velocity is also shown near the central region of the chamber. Then the fluids enter into the channel of the outlet. The distance of molecular diffusion is reduced much more as the fluids flow from the chamber into the channel. Thus the rotating flow achieves superior mixing. The increased interface area of two fluids can promote a mass transfer based on diffusion. The configurations of interfacial areas between two different fluids play an important role

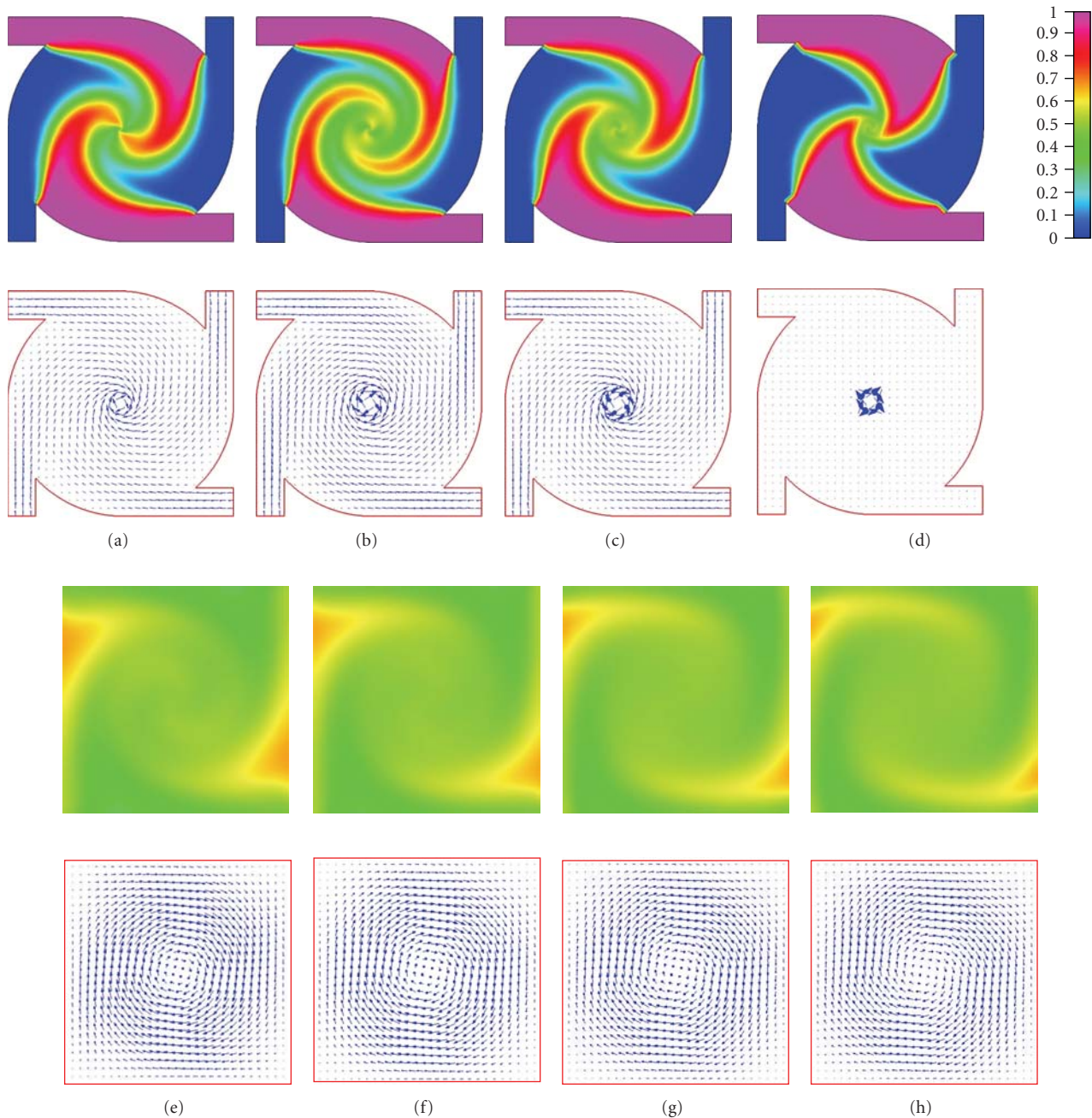


FIGURE 7: The concentration distributions and the vector planes at eight cross-sectional areas from the bottom of the chamber. (a)  $25 \mu\text{m}$ , (b)  $50 \mu\text{m}$ , (c)  $75 \mu\text{m}$ , (d)  $100 \mu\text{m}$ , (e)  $125 \mu\text{m}$ , (f)  $150 \mu\text{m}$ , (g)  $175 \mu\text{m}$ , and (h)  $200 \mu\text{m}$  from the bottom of the chamber.

in the micromixers. As shown in Figure 8, the interfacial regions of two fluids are demonstrated. The interfacial regions represent the area in which the concentration over the sampled section is equal to the value of the concentration equal to 0.5. Due to the cylindrical chamber of the mixer, as the case shown in Figure 4, the interfacial area between two fluids was stretched. Four inlets and one outlet in the mixer are studied to show the influences of self-rotation effects; it is found that interfacial layers are stretched spirally from the intersections of the inlet channels and the chamber to

the central region of the chamber. The interfacial regions between two fluids are enlarged, and steady stirring flow is created, which are exploited to enhance the mixing performances.

## 5. Results and Discussion

This study solved the concentration distributions of liquid fluids in the micromixers, and the effects of various geometric parameters on momentum and mass transports in

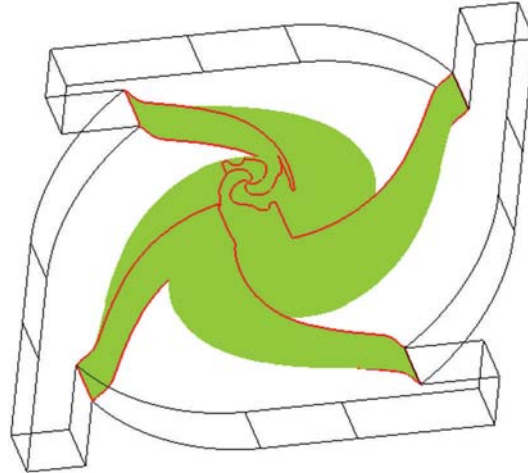


FIGURE 8: Interfacial regions of the concentration equal to 0.5.

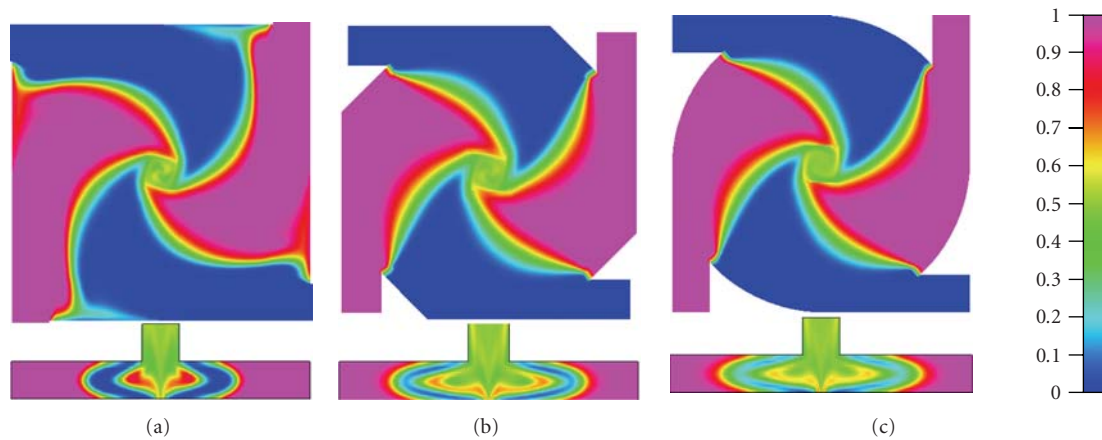


FIGURE 9: The results of mixing with various configurations: (a) right square prism, (b) octagonal prism, and (c) cylinder.

solution were examined. It also investigated the influences of various Reynolds numbers on the momentum and mass transfer characteristics in the fluids in terms of the mixing index and concentration distributions. In the following micromixers with different geometric chambers which are right square prism, octagonal prism, and cylinder with four inlets and one outlet are studied to show the influences of self-rotation effects on mixing.

The following is a comparison of the transfer of momentum and mass in mixing chambers with different configurations and examining the influences of the various geometrical parameters on mixing results. The length of the right square prism is equal to  $800\ \mu\text{m}$ . The length of each side of the octagonal prism is about  $200.63\ \mu\text{m}$ , and the distance between two opposite sides of the octagonal prism is equal to  $800\ \mu\text{m}$ . The diameter of the cylinder is equal to  $800\ \mu\text{m}$ . Figure 9 summarizes the results of mixing with various configurations. The velocity of all inlets is equal to  $0.75\ \text{m/s}$ , and the height of the mixing chamber,  $h$ , is  $100\ \mu\text{m}$ , as well as the height of the inlet channel. The predicted

concentration profiles of two fluids regarded from the top and the cross-section are presented. Corresponding results are listed from left to right for chambers which are right square prism, octagonal prism, and cylinder, respectively. The corresponding mixing index of the outlet is  $0.881$ ,  $0.877$ , and  $0.893$ . The radial dispersion in the chamber is affected by the configurations of the mixing chamber. In Figure 9(a), the interface of two fluids can be clearly observed. The effect of the radial dispersion is the smallest for the case of right square prism. From the results shown in Figure 9(c), the mixed fluids are well dispersed near the central region of the chamber, and the effect of the radial dispersion is the largest for the cylinder. The vortex flow is intensified more for the cylindrical chamber where the contact areas of fluids can be further enlarged. Results show that the self-rotation effect is enhanced in micromixers with cylindrical chamber, which makes this mixer an effective vortex mixer.

To perform the higher mixing index, various numbers of inlets are used to investigate the mixing characteristics of micromixers with the chambers of octagonal prism, as

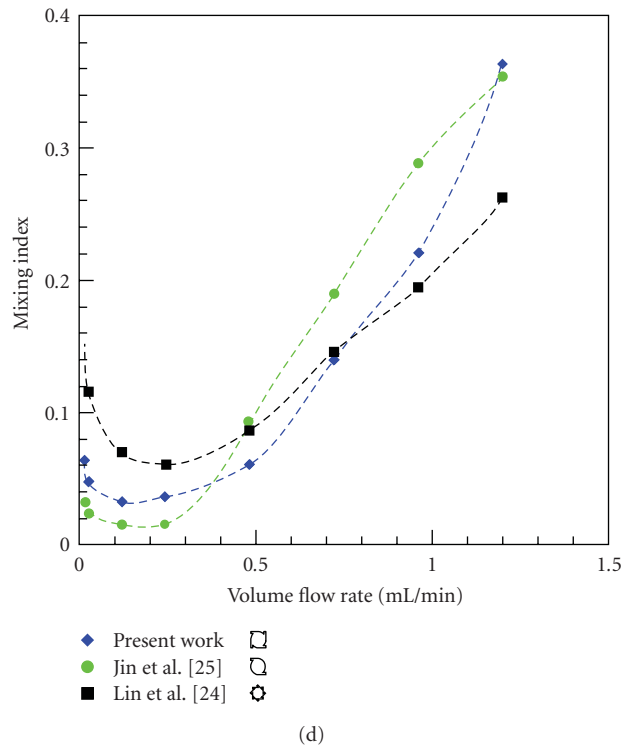
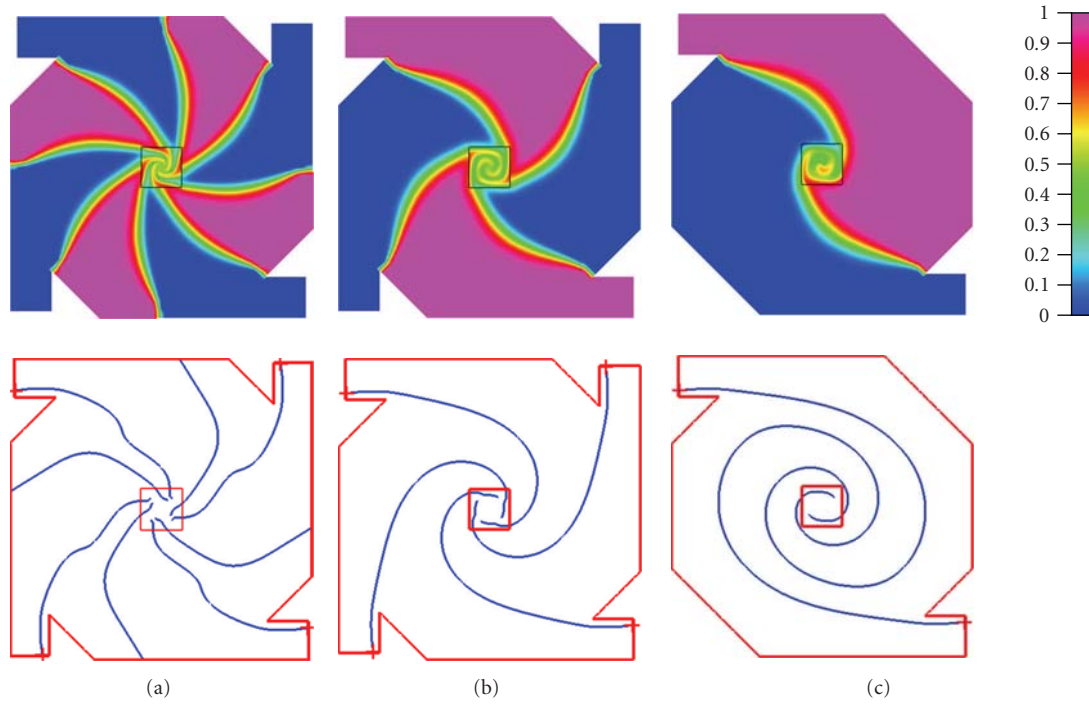


FIGURE 10: The results of concentration distributions and streak lines with various numbers of inlet channels: (a) 8, (b) 4, and (c) 2. (d) Comparison results with the previous study [23, 24].

shown in Figure 10. Results of 8, 4, and 2 inlets with the inlet velocity, equal to 0.25 m/s, 0.5 m/s, and 1 m/s, respectively, are presented in Figures 10(a), 10(b), and 10(c), respectively. For the number of inlets equal to 8, the contact areas of two

fluids increase dramatically. The shape of the cross-sectional area of the outlet is square, and 8 inlets are used in the mixer. It is found that the pattern of the mixing characteristics is not symmetric with respect to the center of the chamber.

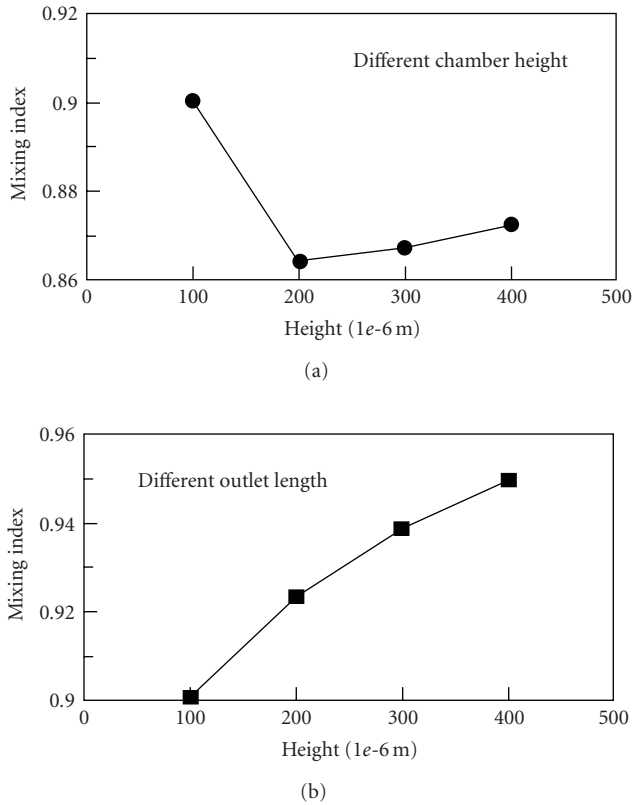


FIGURE 11: The effects of chamber heights and the length of the outlet channel on mixing.

As the red fluid (species A) approaches the entrance of the blue fluid (species B), it is deflected and forms a clockwise vortex. Then it flows into the entrance of the outlet channel. The fluid of species B meets the fluid of species A around the joint of the inlet and the chamber, where it is deflected and also forms a clockwise vortex. However, the inlet velocity is small (0.25 m/s), and it enters the outlet channel directly. The swirling effects are shown in Figure 10(a). Figure 10 also depicts the streak lines as the fluids flow through the chamber with octagonal prism. It is shown in Figure 10(a) that the trajectories of species B are quite similar to the cases shown in Figures 10(b) and 10(c). However, the trajectories of species A are different from the trajectories of species B. For the case of 4 inlets, the contact areas of two fluids decrease in the chamber. Due to the large inlet velocity (0.5 m/s), it swirls around the central region at a longer path and it is the result of the large mixing region that is created. For the case of 2 inlets, the contact areas of two fluids decrease significantly, and the interfacial layer only exists from the joint of the inlet of species A and the chamber to the other joint along the diagonal line. The corresponding mixing index for the chambers with 8, 4, and 2 inlets is 0.676, 0.785, and 0.681, respectively. The mixing chamber with 4 inlets shows the greatest mixing index among these micromixers. So an optimal design of the chamber with 4 inlets can be found. This study analyzes three different configurations of a microfluidic system via numerical simulations. The results

are compared with the previous works [23, 24]: lamination micromixers with a cylinder, plus one or four pairs of inlets and one outlet. Results of various total inlet flow rates on the mixing performance are presented in Figure 10(d). Because the inertial force of the fluids was so small that it is negligible at flow rates less than 0.5 mL/min, mixing is dominated by pure molecular diffusion. The interface between streams is large for the circular vortex micromixer with 8 tangential inlets. One can see that mixing in this micromixer is the highest. When the flow rate is greater than 0.5, the increased inertial force enlarges the rotational flow. The mixing in the vortex micromixer with 2 tangential inlets is improved. Our designed mixer with 4 inlets can perform well for the range of flow rate from 0 to 1.2 mL/min.

The effects of the chamber heights,  $H$ , and the outlet channel lengths,  $h$ , on mixing in the cylindrical chamber are presented in Figure 11. The predicted mixing index at various chamber heights (upper portion) and at various channel lengths (bottom portion) is shown. Corresponding results are listed from (1) to (4) for chamber height equal to 100  $\mu\text{m}$ , 200  $\mu\text{m}$ , 300  $\mu\text{m}$ , and 400  $\mu\text{m}$ , respectively, with the length of outlet channel being 100  $\mu\text{m}$ . And corresponding results are listed from (5) to (8) for channel length equal to 100  $\mu\text{m}$ , 200  $\mu\text{m}$ , 300  $\mu\text{m}$ , and 400  $\mu\text{m}$ , respectively, with the height of chamber being 100  $\mu\text{m}$ . The mixing index of the chamber decreases at the start and then increases slowly because the vortex flow is weak for the cases with larger chamber length. Nevertheless, the contact areas in the chamber with larger volume are augmented. The mixing can be improved, and the mixing index starts to increase for the cases (3) and (4). Whereas two fluids enter into the outlet channel, the axial flow of fluids is dominant and the rotation of the fluids is almost constant along the channel. The contact areas are enlarged with the increasing channel length; then the mixing index improves as well.

Figure 12 plots the effects of various inlet velocities on the mixing for the height of the mixing chamber being 100  $\mu\text{m}$ . They show not only the mixing within the microchamber, but also the vortex index of the mixer. The inertial force is very important when the inlet velocity is 1 m/s and the corresponding  $Re$  is 100. Because the wall of the inlet channel is tangential to the wall of the chamber and the inertial force drives the liquid flow forward, the fluid meets the other fluid with strong inertia. The large inertia force causes the fluid to proceed fast and for a large clockwise vortex to form. Inertia force tends to destabilize a system, whereas viscous force tends to stabilize a system and damp out perturbations, such as the diffusion. From the definition of  $Re$ , strong inertia causes the powerful vortex flow in the chamber, and the damping effect on diffusion is diminished. The mixing performance can be enhanced.  $Re$  decreases with the decreasing inlet velocity, and the viscous force becomes dominant. The inertial effect is not very obvious, and the area of mixing region on the top wall is decreased. The inertial force is very trivial when the inlet velocity is 0.1 m/s. The competition between inertia and viscous force permits the shape of the interface to be clearly observed. It is extremely apparent that the mixing index is the lowest. Because the mixing at a position depends on the upstream

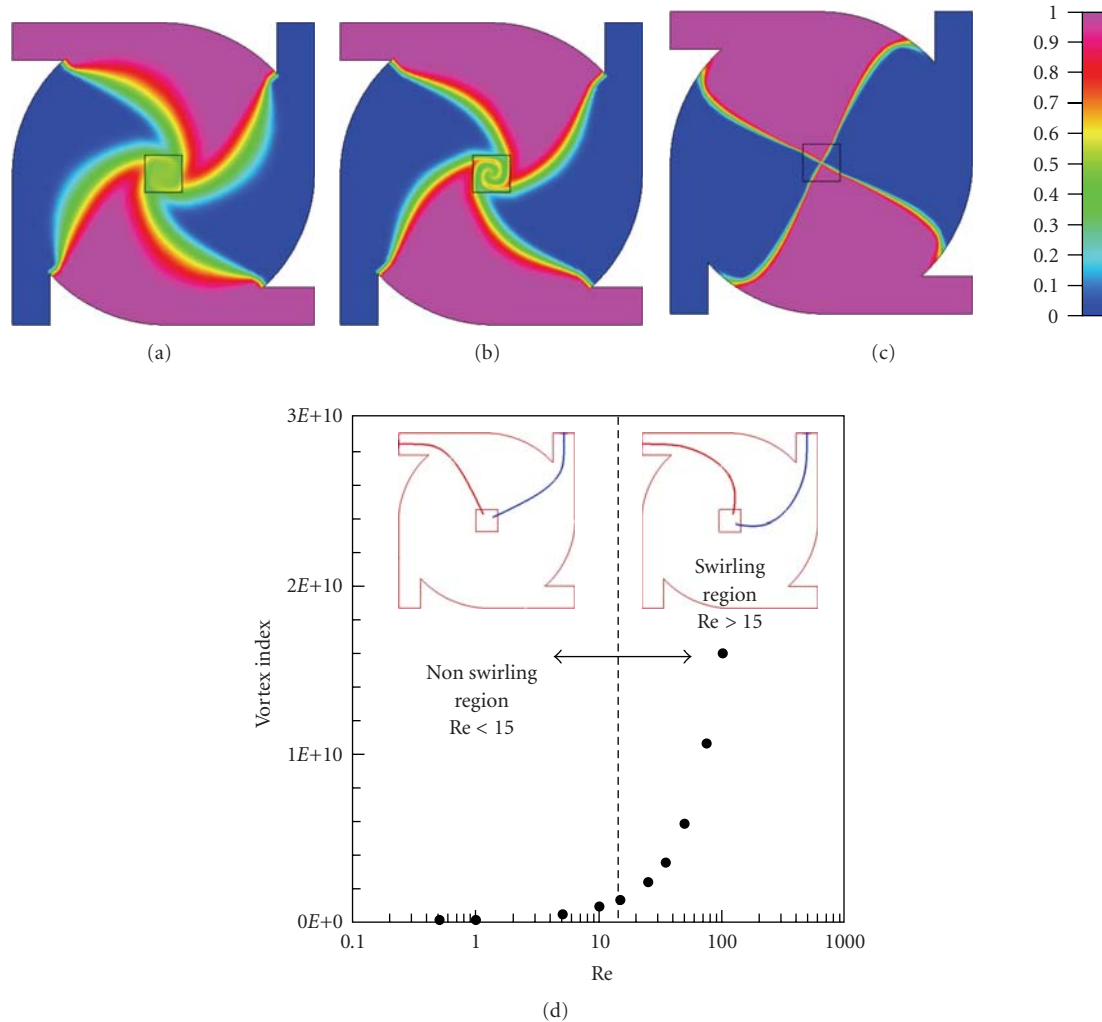


FIGURE 12: The results of mixing with various inlet velocities: (a) 1 m/s, (b) 0.5 m/s, and (c) 0.1 m/s. (d) The profile of the vortex index inside the chamber.

history of the flow, the vorticity history determines the mixing performance at a cross-section of the channel. A vortex index represents the vorticity history of a flow [14] and is introduced into our study. The influences of inlet velocity on vortex index are plotted in Figure 12(d). A large inlet velocity represents a large Re. At low Re,  $0.5 < Re < 15$ , viscous forces in the fluid are larger than inertial forces; thus, inertia can be neglected. The streak lines from the center of the two inlets shown in the upper of Figure 12(d) almost direct towards the outlet. No swirling flow can be observed. This is the so-called no swirling region. When the Re are 15–100, both viscous and inertial forces are important. The streak lines shown in the upper right side of Figure 12(d) are deflected. The rotational and extensional flow can be created in the chamber, and the interface between the two fluids increases. Therefore the mixing performance is also improved.

The particle trajectories for the micromixer at various inlet velocities are investigated. The particle trajectories are the traces where the particles are released from the specific

locations of the inlets to the outlet. In Figure 13(a), particles are released from the four inlet sections viewed from the inlet. Three lines which are located at the central line of the cross section, at the offsets of central line of 25 and 35  $\mu\text{m}$ , are selected. Twenty-four particles per line are chosen. The configuration of colored particles at the outlet section can represent the mixing performance qualitatively and expressed at Re of 100, 50, and 10 in Figures 13(b), 13(c), and 13(d), respectively. Particles are labeled with a specific color. The particle with red color stands for species A and the particle with blue color for species B. From the particle distributions, it is easily understood that the self-rotational effect is very advanced at an Re of 100 and the pattern of the particle distribution is very irregular. Particles with different colors are spread over the entire cross section. Then the mixing can be enhanced. Whereas the inlet velocity decreases to the value of 0.5 m/s, corresponding to an Re of 50, four spiral-like patterns are created at the outlet cross section. Obviously, the stretched flows of the micromixer in the angular direction can be seen, and the interface of the two

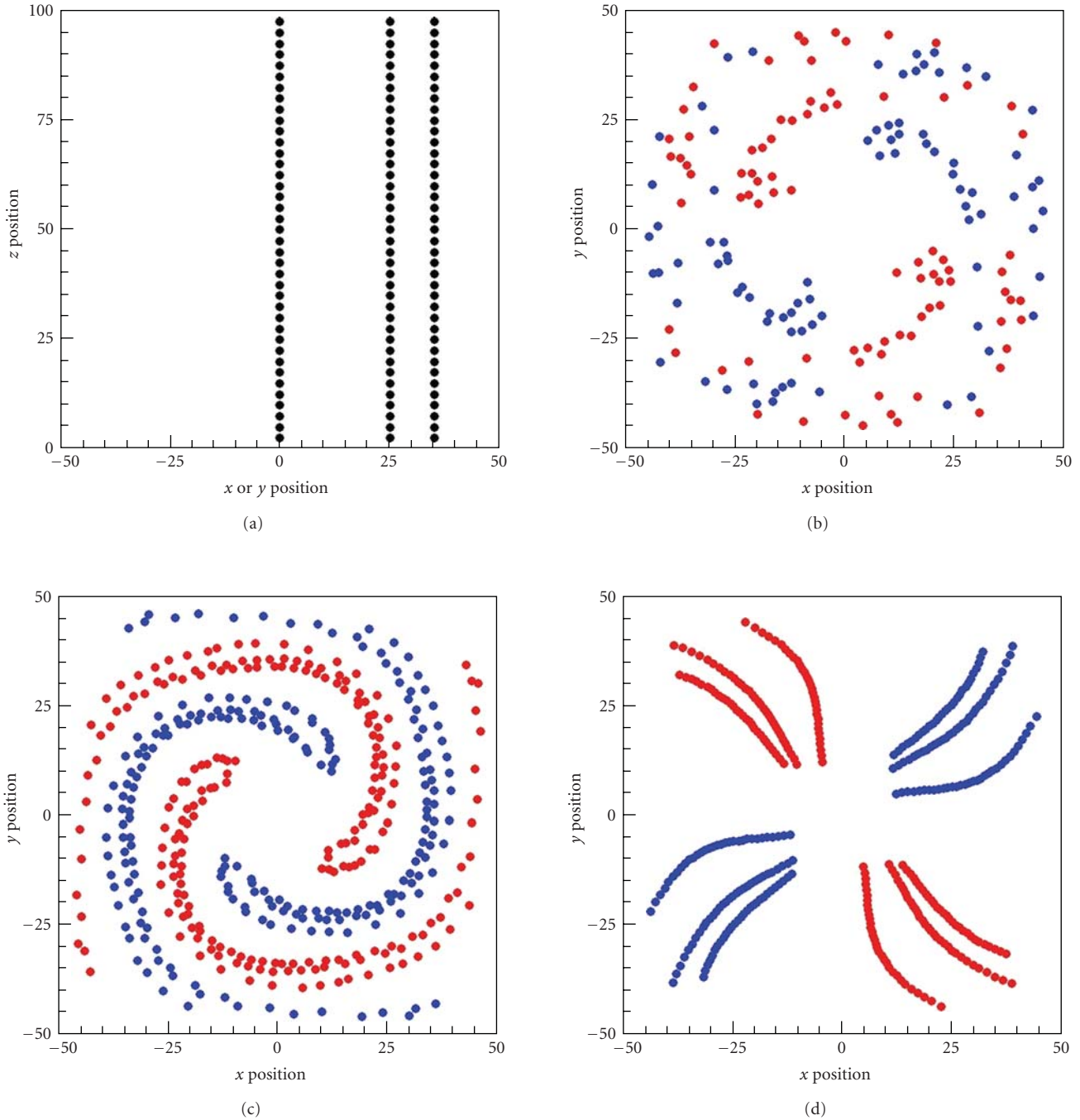


FIGURE 13: (a) Particles are released from the four inlet sections viewed from the inlet. Three lines which are located at the central line of the cross section, at the offset of lines of 25 and 35  $\mu\text{m}$ , are selected. Twenty-four particles per line are chosen. The configuration of colored particles at the outlet section at Re of (b) 100, (c) 50, and (d) 10.

fluids is enhanced. These clockwise patterns are more orderly than these of an Re of 100. And a similar pattern can be seen at the outlet section in Figure 12(b). No rotational effect is observed at a Re of 10 (shown in Figure 13(d)). The patterns of the particle distributions are very simple and like straight lines. The exchange of two fluids is negligible, and the mixing is very poor.

## 6. Conclusions

This study investigated the steady behavior of three-dimensional momentum and mass transfer in micro chamber which consists of a right square prism, an octagonal prism, or a cylinder. The research was studied by a computational fluid dynamics software using a finite element

approach. Results which were presented in terms of particle trajectories, vorticity profiles, and concentration distributions indicated that the swirling flows inside the chamber dominate the mixing index. Particle trajectories were utilized to demonstrate the rotational and extensional local flows which produce steady stirring, and the combination of the radial dispersion and the vortex flow makes the mixing successful. The effects of various geometric parameters and inlet velocities on momentum and mass transfer mechanisms were discussed in detail. In addition, numbers of inlets significantly affect mixing characteristics. The mixing index decreases by using fewer inlets. With larger numbers of inlets, the significant swirling effects could be seen, and thus, the mixing index is higher. It is also shown that the force driven by the inertia has a crucial impact on the mixing. At higher Reynolds number,  $Re > 15$ , inertia causes more vortex flow in the chamber and diminishes the damping effect on diffusion, thereby leading to a higher mixing performance. Finally the configurations of colored particles at the outlet section were applied to qualitatively predict the performance of micromixers. Particular emphasis was placed on a qualitative analysis of the physical phenomena, which will benefit the study of microfluidic components in industrial applications.

## Acknowledgments

The authors would like to thank the National Science Council of the Republic of China for financially supporting this research under Contract no. NSC 96-2221-E-020-021. We are also grateful to the National Center for High-performance Computing for computer time and facilities.

## References

- [1] M. K. McQuain, K. Seale, J. Peek et al., "Chaotic mixer improves microarray hybridization," *Analytical Biochemistry*, vol. 325, no. 2, pp. 215–226, 2004.
- [2] S. R. Nugen, P. J. Asiello, J. T. Connelly, and A. J. Baeumner, "PMMA biosensor for nucleic acids with integrated mixer and electrochemical detection," *Biosensors and Bioelectronics*, vol. 24, no. 8, pp. 2428–2433, 2009.
- [3] C. Rosenfeld, C. Serra, C. Brochon, V. Hessel, and G. Hadziioannou, "Use of micromixers to control the molecular weight distribution in continuous two-stage nitroxide-mediated copolymerizations," *Chemical Engineering Journal*, vol. 135, no. 1, pp. S242–S246, 2008.
- [4] N. Gadish and J. Voldman, "High-throughput positive-dielectrophoretic bioparticle microconcentrator," *Analytical Chemistry*, vol. 78, no. 22, pp. 7870–7876, 2006.
- [5] P. I. Frank, P. D. David, L. B. Theodore, and S. L. Adrienne, *Fundamentals of Heat and Mass Transfer*, John Wiley & Sons, New York, NY, USA, 2006.
- [6] E. L. Cussler, *Diffusion Mass Transfer in Fluid Systems*, Cambridge University Press, New York, NY, USA, 2009.
- [7] N. T. Nguyen and Z. Wu, "Micromixers—a review," *Journal of Micromechanics and Microengineering*, vol. 15, no. 2, pp. R1–R16, 2005.
- [8] J. M. Ottino and S. Wiggins, "Introduction: mixing in microfluidics," *Philosophical Transactions of the Royal Society A: Mathematical, Physical and Engineering Sciences*, vol. 362, no. 1818, pp. 923–935, 2004.
- [9] C. S. Lu, J. J. Chen, J. H. Liau, and T. Y. Hsieh, "Flow and concentration analysis inside a microchannel with lightning grooves at two floors," *Journal of Biomechanics Engineering*, vol. 2, pp. 13–32, 2009.
- [10] R. Miyake, T. S. J. Lammerink, M. Elwenspoek, and J. H. J. Fluitman, "Micro mixer with fast diffusion," in *Proceedings of the 6th IEEE International Workshop Micro Electromechanical System (MEMS '93)*, pp. 248–253, IEEE Computer Society Press, San Diego, Calif, USA, February 1993.
- [11] H. Mobius, W. Ehrfeld, V. Hessel, and T. Richter, "Sensor controlled processes in chemical microreactors," in *Proceedings of the 8th International Conference on Solid-State Sensors and Actuators (Transducers '95)*, pp. 775–778, Stockholm, Sweden, June 1995.
- [12] F. G. Bessoth, A. J. DeMello, and A. Manz, "Microstructure for efficient continuous flow mixing," *Analytical Communications*, vol. 36, no. 6, pp. 213–215, 1999.
- [13] P. Hinsmann, J. Frank, P. Svasek, M. Harasek, and B. Lendl, "Design, simulation and application of a new micromixing device for time resolved infrared spectroscopy of chemical reactions in solution," *Lab Chip*, vol. 1, no. 1, pp. 16–21, 2001.
- [14] J. S. Maeng, K. Yoo, S. Song, and S. Heu, "Modeling for fluid mixing in passive micromixers using the vortex index," *Journal of the Korean Physical Society*, vol. 48, no. 5, pp. 902–907, 2006.
- [15] C. C. Hong, J. W. Choi, and C. H. Ahn, "A novel in-plane passive microfluidic mixer with modified tesla structures," *Lab Chip*, vol. 4, no. 2, pp. 109–113, 2004.
- [16] M. K. Jeon, J. H. Kim, J. Noh, S. H. Kim, H. G. Park, and S. I. Woo, "Design and characterization of a passive recycle micromixer," *Journal of Micromechanics and Microengineering*, vol. 15, no. 2, pp. 346–350, 2005.
- [17] J. Cha, J. Kim, S. K. Ryu et al., "A highly efficient 3D micromixer using soft PDMS bonding," *Journal of Micromechanics and Microengineering*, vol. 16, no. 9, pp. 1778–1782, 2006.
- [18] A. A. S. Bhagat, E. T. K. Peterson, and I. Papautsky, "A passive planar micromixer with obstructions for mixing at low Reynolds numbers," *Journal of Micromechanics and Microengineering*, vol. 17, no. 5, pp. 1017–1024, 2007.
- [19] M. Koch, D. Chatelain, A. G. R. Evans, and A. Brunnschweiler, "Two simple micromixers based on silicon," *Journal of Micromechanics and Microengineering*, vol. 8, no. 2, pp. 123–126, 1998.
- [20] S. Hardt and F. Schonfeld, "Laminar mixing in different interdigital micromixers: II. numerical simulations," *AIChE Journal*, vol. 49, no. 3, pp. 578–584, 2003.
- [21] P. Lob, H. Pennemann, V. Hessel, and Y. Men, "Impact of fluid path geometry and operating parameters on I/I-dispersion in interdigital micromixers," *Chemical Engineering Science*, vol. 61, no. 9, pp. 2959–2967, 2006.
- [22] S. Bohm, K. Greiner, S. Schlautmann, S. de Vries, and A. van den Berg, "A rapid vortex micromixer for studying high-speed chemical reactions," in *Proceedings of the 5th International Conference on Micro Total Analysis Systems (micro-TAS '01)*, Monterey, Calif, USA, October 2001.
- [23] C. H. Lin, C. H. Tsai, and L. M. Fu, "A rapid three-dimensional vortex micromixer utilizing self-rotation effects under low Reynolds number conditions," *Journal of Micromechanics and Microengineering*, vol. 15, no. 5, pp. 935–943, 2005.
- [24] S. Y. Jin, Y. Z. Liu, W. Z. Wang, Z. M. Cao, and H. Koyama, "Numerical evaluation of two-fluid mixing in a swirl micromixer," *Journal of Hydrodynamics*, vol. 18, no. 5, pp. 542–546, 2006.

- [25] S. Y. Yang, J. L. Lin, and G. B. Lee, “A vortex-type micromixer utilizing pneumatically driven membranes,” *Journal of Micromechanics and Microengineering*, vol. 19, no. 3, Article ID 035022, 2009.
- [26] M. Long, M. A. Sprague, A. A. Grimes, B. D. Rich, and M. Khine, “A simple three-dimensional vortex micromixer,” *Applied Physics Letters*, vol. 94, no. 13, Article ID 133501, 2009.
- [27] J. A. Pojman, N. Bessonov, V. Volpert, and M. S. Paley, “Miscible fluids in microgravity (MFMG): a zero-upmass investigation on the international space station,” *Microgravity Science and Technology*, vol. 19, no. 1, pp. 33–41, 2007.
- [28] Y. L. Joo and E. S. G. Shaqfeh, “The effects of inertia on the viscoelastic Dean and Taylor-Couette flow instabilities with application to coating flows,” *Physics of Fluids A*, vol. 4, no. 11, pp. 2415–2431, 1992.
- [29] D. O. Olagunju, “Inertial effect on the stability of viscoelastic cone-and-plate flow,” *Journal of Fluid Mechanics*, vol. 343, pp. 317–330, 1997.
- [30] H. Wang, P. Iovenitti, E. Harvey, and S. Masood, “Numerical investigation of mixing in microchannels with patterned grooves,” *Journal of Micromechanics and Microengineering*, vol. 13, no. 6, pp. 801–808, 2003.

## Research Article

# Numerical Computation and Investigation of the Characteristics of Microscale Synthetic Jets

Ann Lee,<sup>1</sup> Guan H. Yeoh,<sup>1,2</sup> Victoria Timchenko,<sup>1</sup> and John Reizes<sup>1</sup>

<sup>1</sup> School of Mechanical & Manufacturing Engineering, University of New South Wales, Sydney, NSW 2052, Australia

<sup>2</sup> Australian Nuclear Science and Technology Organisation (ANSTO), PMB 1, Menai, NSW 2234, Australia

Correspondence should be addressed to Guan H. Yeoh, guan.yeoh@ansto.gov.au

Received 12 December 2010; Accepted 2 February 2011

Academic Editor: Chaoqun Liu

Copyright © 2011 Ann Lee et al. This is an open access article distributed under the Creative Commons Attribution License, which permits unrestricted use, distribution, and reproduction in any medium, provided the original work is properly cited.

A synthetic jet results from periodic oscillations of a membrane in a cavity. Jet is formed when fluid is alternately sucked into and ejected from a small cavity by the motion of membrane bounding the cavity. A novel moving mesh algorithm to simulate the formation of jet is presented. The governing equations are transformed into the curvilinear coordinate system in which the grid velocities evaluated are then fed into the computation of the flow in the cavity domain thus allowing the conservation equations of mass and momentum to be solved within the stationary computational domain. Numerical solution generated using this moving mesh approach is compared with an experimental result measuring the instantaneous velocity fields obtained by  $\mu$ PIV measurements in the vicinity of synthetic jet orifice  $241\ \mu\text{m}$  in diameter issuing into confined geometry. Comparisons between experimental and numerical results on the streamwise component of velocity profiles at the orifice exit and along the centerline of the pulsating jet in microchannel as well as the location of vortex core indicate that there is good agreement, thereby demonstrating that the moving mesh algorithm developed is valid.

## 1. Introduction

A synthetic jet, similar to a pulsed jet, is formed from the ingestion and expulsion of fluid through an orifice into a fluid-filled space [1]. One unique feature is that the jet is produced entirely by the working fluid of the flow system. It can thus transfer linear momentum to the flow system without net mass injection across the flow boundary. The mechanism of such a jet is sometimes known as a “zero-net-mass-flux” jet [2]. In a synthetic jet, the actuating flow is generated by an oscillating diaphragm located opposite the orifice in a cavity. As the diaphragm oscillates, the flow exhibits a periodic behavior. Under certain operating conditions, the fluid separates, leading to the formation of discrete vortical structures. This so-called vortex shedding phenomenon is important for thermal management applications because the cooling performance is highly dependent on the interaction of these trains of discrete vortical structures and the wall to be cooled.

A number of useful studies have been carried out on synthetic jets in the context of pulsating jet actuators

impinging on submerged surfaces in quiescent fluid media in order to better understand the thermal characteristics for localized cooling. Campbell et al. [3] illustrated the use of synthetic air micro jets for effective cooling of laptop processors while Mahalingam et al. [4, 5] established the feasible application of synthetic jets for high-power electronic cooling through an integrated active heat sink. Smith and Swift [6] as well as Pavlova and Amitay [7] indicated that heat transfer enhancement increased dramatically through the use of synthetic jets over continuous jets thereby offering better cooling performance. Gillespie et al. [8] investigated the effectiveness of a rectangular synthetic jet impinging on an unconfined heated plate exposed to the ambient, while Trávníček and Tesař [9, 10] proposed the alternative use of annular synthetic jet which has shown to provide more attractive features over a simple round nozzle impinging jet [11, 12], in particular the increased wall transport phenomena by the applied pulsation.

To account for the transient movement of the actuator wall, an explicit tracking of the membrane accompanied by a moving mesh is implemented via solving the governing

equations in a form represented by a three-dimensional body-fitted curvilinear coordinate system in a fixed computational domain. A methodology for moving the mesh points, which respects the boundary movement(s), eliminates the need for remeshing, and satisfies the geometric conservation law (GCL), is adopted. The published literature reports very few numerical analyses on the interactive combination of the highly favorable synthetic jet characteristics and proven effectiveness of microchannel flows. At the same time, very limited experimental data is available for comparison. The objective of this paper is to assess the validity and performance of the grid movement methodology against micro-scale synthetic jet experiment carried out at the University of New South Wales.

## 2. Mathematical Model

In this section, the governing equations and the numerical methodology used for the simulation of moving boundary flows are presented. A collocated, structured, and body-fitted grid is employed. The physical coordinates ( $x$ ,  $y$ ,  $z$ , and  $t$ ) are related to the computational coordinates ( $\varepsilon$ ,  $\gamma$ ,  $\omega$ , and  $\tau$ ) through the generic transformations:

$$\begin{aligned} x &= x(\varepsilon, \gamma, \omega, t), \\ y &= y(\varepsilon, \gamma, \omega, t), \\ z &= z(\varepsilon, \gamma, \omega, t), \\ t &= \tau. \end{aligned} \quad (1)$$

Initially at rest ( $t = 0$ ), the grid within the physical domain can be constructed via the method of transfinite interpolation according to Gordon and Thiel [13] which consists of generating the interior mesh from the boundary grid data using appropriate interpolation functions or ‘‘blending’’ functions. In three dimensions, the interpolation operation is

$$\bar{r}_{i,j,k} = P^i + P^j + P^k - P^i P^j - P^i P^k - P^j P^k + P^i P^j P^k, \quad (2)$$

where  $\bar{r} \equiv r^i \equiv (x, y, z)$ ,

$$\begin{aligned} P^i &= f_i \bar{r}_{1,j,k} + (1 - f_i) \bar{r}_{I,j,k}, \\ P^j &= g_j \bar{r}_{j,1,k} + (1 - g_j) \bar{r}_{i,j,k}, \\ P^k &= h_k \bar{r}_{i,j,1} + (1 - h_k) \bar{r}_{i,j,k}, \end{aligned} \quad (3)$$

$$\begin{aligned} P^i P^j &= f_i g_j \bar{r}_{I,j,k} + f_i (1 - g_j) \bar{r}_{I,1,k} + (1 - f_i) g_j \bar{r}_{1,j,k} \\ &\quad + (1 - f_i) (1 - g_j) \bar{r}_{1,1,k}, \\ P^i P^k &= f_i h_k \bar{r}_{I,j,K} + f_i (1 - h_k) \bar{r}_{I,j,1} + (1 - f_i) h_k \bar{r}_{1,j,K} \\ &\quad + (1 - f_i) (1 - h_k) \bar{r}_{1,j,1}, \\ P^j P^k &= g_j h_k \bar{r}_{i,j,K} + g_j (1 - h_k) \bar{r}_{i,j,1} + (1 - g_j) h_k \bar{r}_{i,1,K} \\ &\quad + (1 - g_j) (1 - h_k) \bar{r}_{i,1,1}, \end{aligned} \quad (4)$$

$$\begin{aligned} P^i P^j P^k &= f_i g_j h_k \bar{r}_{I,j,K} + f_i g_j (1 - h_k) \bar{r}_{I,j,1} \\ &\quad + f_i (1 - g_j) h_k \bar{r}_{I,1,K} + f_i (1 - g_j) (1 - h_k) \bar{r}_{I,1,1} \\ &\quad + (1 - f_i) g_j h_k \bar{r}_{1,j,K} + (1 - f_i) g_j (1 - h_k) \bar{r}_{1,j,1} \\ &\quad + (1 - f_i) (1 - g_j) h_k \bar{r}_{1,1,K} \\ &\quad + (1 - f_i) (1 - g_j) (1 - h_k) \bar{r}_{1,1,1}. \end{aligned} \quad (5)$$

In the above equation,  $f_i$  varies monotonically from  $f_1 = 0$  to  $f_I = 1$  for  $i = 1, 2, \dots, I$ . Analogous expressions involving functions  $g_j$  and  $h_k$  apply for interpolation in the  $j$  and  $k$  directions for  $j = 1, 2, \dots, J$  and  $k = 1, 2, \dots, K$ , respectively. For simplicity, the blending functions  $f_i$ ,  $g_j$ , and  $h_k$  may be taken to be linear. They may also be formulated with added complexity to concentrate more grid points near the physical boundaries or to include the specification of derivative boundary conditions to force the grid lines to intersect the physical boundaries orthogonally.

**2.1. Governing Equations.** The general form of the governing equations (continuity, momentum, enthalpy, and solid temperature) transformed into the body-fitted curvilinear coordinate system ( $\xi^l \equiv (\varepsilon, \gamma, \omega)$ ) is given accordingly as follows.

Continuity:

$$\frac{\partial \rho_l}{\partial \tau} + \frac{1}{\sqrt{g}} \left[ \frac{\partial}{\partial \xi^l} (\rho_l (U^{\xi^l} - U_g^{\xi^l})) \right] = 0. \quad (6)$$

Momentum:

$$\begin{aligned} \frac{\partial (\rho_l U_i)}{\partial \tau} + \frac{1}{\sqrt{g}} \left[ \frac{\partial}{\partial \xi^l} (\rho_l (U^{\xi^l} - U_g^{\xi^l}) U_i) \right] \\ = - \frac{1}{\sqrt{g}} \frac{\partial}{\partial \xi^l} (\beta_{il} p) + \frac{1}{\sqrt{g}} \frac{\partial}{\partial \xi^l} \left( \mu_l \sqrt{g} g^{lm} \frac{\partial U_i}{\partial \xi^m} \right) \\ + \frac{1}{\sqrt{g}} \frac{\partial}{\partial \xi^l} \left( \mu_l \frac{\beta_{kl}}{\sqrt{g}} \frac{\partial}{\partial \xi^m} (\beta_{lm} U_k) \right), \end{aligned} \quad (7)$$

where  $\rho_l$  and  $\mu_l$  are the density and dynamic viscosity, respectively.

The various coefficients in (6) and (7) are

$$\beta_{il} = \frac{\partial r^j}{\partial \xi^m} \frac{\partial r^k}{\partial \xi^n} - \frac{\partial r^k}{\partial \xi^n} \frac{\partial r^j}{\partial \xi^m} \quad (8)$$

with  $i, j, k$  and  $l, m, n$  being cyclic:

$$\sqrt{g} g^{lm} = \sum_{k=1}^3 \frac{\beta_{kl} \beta_{km}}{\sqrt{g}} \quad \sqrt{g} = \det \begin{vmatrix} \frac{\partial x}{\partial \varepsilon} & \frac{\partial y}{\partial \varepsilon} & \frac{\partial z}{\partial \varepsilon} \\ \frac{\partial x}{\partial \gamma} & \frac{\partial y}{\partial \gamma} & \frac{\partial z}{\partial \gamma} \\ \frac{\partial x}{\partial \omega} & \frac{\partial y}{\partial \omega} & \frac{\partial z}{\partial \omega} \end{vmatrix}. \quad (9)$$

The fluid velocity components in the  $\varepsilon$ ,  $\gamma$ , and  $\omega$  directions are given as

$$U^{kl} = \sum_{k=1}^3 \beta_{kl} U_k \quad (10)$$

while the grid velocity components in the  $\varepsilon$ ,  $\gamma$ , and  $\omega$  directions are, respectively, are given as

$$U_g^{kl} = \sum_{k=1}^3 \beta_{kl} U_g^l. \quad (11)$$

In (13),  $U_g^l$  are the instantaneous grid velocities in  $x$ ,  $y$ , and  $z$  directions at a fixed point ( $\varepsilon$ ,  $\gamma$ , and  $\omega$ ) in the computational domain. These are given as

$$U_g^1 = \left( \frac{\partial x}{\partial t} \right)_{\varepsilon, \gamma, \omega}, \quad U_g^2 = \left( \frac{\partial y}{\partial t} \right)_{\varepsilon, \gamma, \omega}, \quad U_g^3 = \left( \frac{\partial z}{\partial t} \right)_{\varepsilon, \gamma, \omega}. \quad (12)$$

The grid movement methodology that is employed in this present study to determine the instantaneous grid velocities in (14) is described in the next section.

**2.2. Grid Movement Methodology.** The use of body-fitted coordinate system along with the time-dependent transformation approach eliminates the need to explicitly track the membrane in the physical domain. Furthermore, the discretisation accuracy near the moving membrane is far better resolved as the grid lines conform to the body shape. One key feature of the grid movement methodology in this paper is the avoidance of the time-consuming remeshing step of the grid within the physical domain. The body-fitted moving mesh algorithm based on the approach proposed by Anwer et al. [14] is applied herein. It is a cheaper and accurate alternative for moderately complex geometries, and, more importantly, it automatically satisfies the GCL in which failure to enforce the GCL leads to inaccuracies in the computations.

Figure 1 shows a typical domain of the synthetic jet generator whereby the moving membrane is normally located at the bottom of the cavity. The surface mesh points at the top of the cavity can be taken to be fixed while the surface mesh points surrounding the moving membrane are allowed to move according to the imposed instantaneous displacement function.

At the bottom surface, the instantaneous grid velocities can be analytically obtained through differentiating the instantaneous displacement function with time. In order to determine the internal instantaneous grid velocities, the velocities over the mesh points within the region can be gradually relaxed from their corresponding rigid values at the top surface through a weighting function  $f(d)$ , where  $d$  is the distance of the mesh point under consideration from the origin of the frame attached to the surface of the moving

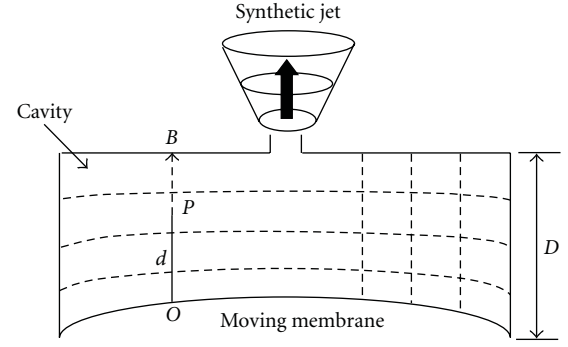


FIGURE 1: A typical geometric representation of the synthetic jet generator.

membrane. Consider a mesh point  $P$  as shown in Figure 1. Denoting the distance of  $B$  from the dynamic origin  $O$  as  $R$ , the mesh velocity at point  $P$  is given as

$$U_g^l(P) = U_{g, \text{membrane}}^l(P)(1 - f(d)), \quad (13)$$

where  $f(d) = 0$  for  $d = d_{\min}$  and  $f(d) = 1$  for  $d = D$ . The weighting function  $f(d)$  may take any suitable form. For simplicity, a linear weighting function is adopted:  $(d - d_{\min}) / (D - d_{\min})$ . As aforementioned, the membrane velocity  $U_{g, \text{membrane}}^l(P)$  in (15) can be determined from an analytical function, to be described later. Once the mesh velocities are obtained via (15), the mesh point locations at the new time are found by

$$\begin{aligned} x^{n+1} &= x^n + U_g^1(P)\Delta t, \\ y^{n+1} &= y^n + U_g^2(P)\Delta t, \\ z^{n+1} &= z^n + U_g^3(P)\Delta t. \end{aligned} \quad (14)$$

**2.3. Numerical Scheme.** The governing equations are discretised by the finite volume technique (FVM) on a structured collocated grid arrangement. In the interior of the flow domain, the hybrid differencing scheme which switches between the first-order upwind differencing and second-order central differencing based on the local Péclet number is adopted for the advection terms. The pressure gradients and diffusion terms are discretised using the second-order central differencing scheme. Pressure correction algorithm such as SIMPLE is applied to link the collocated velocity and pressure fields. The determination of the velocities at the control volume faces is achieved through the application of the Rhie and Chow [15] interpolation procedure. A full-implicit iterative procedure is employed to capture the unsteady physics of the flow. The algebraic forms of the governing equations are solved by employing the strongly implicit procedure (SIP) by Stone [16]. Within each time step, convergence is ascertained when the mass residual falls below  $10^{-5}$ .

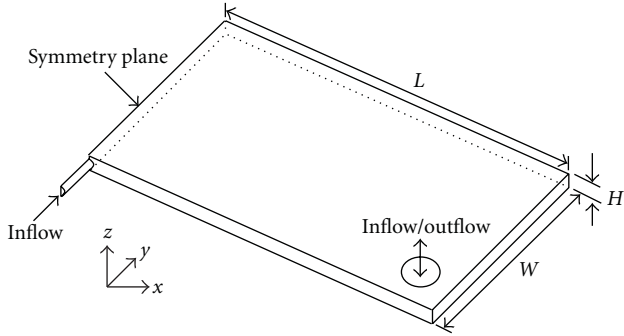


FIGURE 2: Schematic diagram of three-dimensional micro synthetic jet.

### 3. Problem Definition

A schematic diagram of the three-dimensional geometry is shown in Figure 2. The width and depth of the rectangular test section have been designed to be of  $5000\ \mu\text{m}$  and  $500\ \mu\text{m}$ , respectively. To enhance the numerical calculations, the length of rectangular test section was halved, 15 mm long, using the assumption of symmetry relative to the centerline of the jet. To model the syringe which acted as the piston/cylinder device for the synthetic jet actuator and was connected at the mid-depth of the test section, an additional pipe with a diameter of  $700\ \mu\text{m}$  was attached to the computational domain to be able to generate the pulsating flow through the orifice. In order to simulate the piston effect as the plunger moved in and out of the barrel of the syringe, the length of this pipe was varied through time.

For the geometry described in Figure 2, a mesh of  $95 \times 36 \times 41$  was generated which resulted in a total of 140,220 control volumes. Denser mesh was concentrated around the orifice to resolve the fluid flow characteristics of the synthetic jet. Sensitivity analysis was performed by comparing the numerical results against a finer mesh (twice the number of grid points); the variation of the fluid flow fields was found to be negligible. A time-step of  $1/200$  of the period of oscillation of the membrane was employed. For the inlet/outlet boundary located some distance away from the orifice, a static pressure was imposed to allow the possibility of the fluid entering or leaving the domain.

The motion of the synthetic jet actuator was fully simulated in the calculation. Structural simulations indicated that the plunger could be simulated by varying in a sinusoidal fashion in time, so that, rather than solving the complex fluid-solid interaction problem, the instantaneous displacement of the membrane  $Y_m$  was assumed to be

$$Y_m = A \sin(2\pi ft), \quad (15)$$

where  $A$  is the displacement amplitude and  $f$  is the frequency of oscillation. The membrane oscillation frequency and amplitude are activated based on the frequency  $f = 240\ \text{Hz}$  and amplitude  $A = 265\ \mu\text{m}$ .

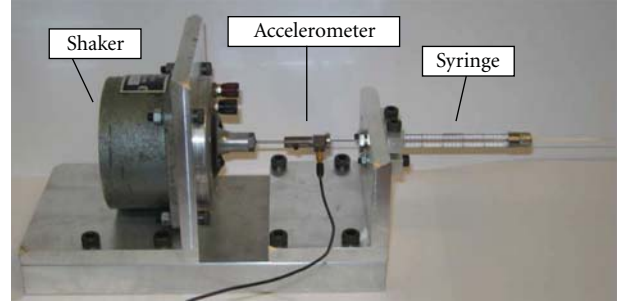


FIGURE 3: Experimental apparatus.

### 4. Experimental Setup

The validity and performance of the grid movement methodology is assessed against experiments of micro synthetic jets in quiescent fluid media conducted by Sinclair et al. [17] at the University of New South Wales. In their experiment, a  $25\ \mu\text{L}$  syringe acting as a piston/cylinder device for the synthetic jet actuator that consists of a  $700\ \mu\text{m}$  diameter plunger in a  $730\ \mu\text{m}$  diameter barrel is used. The barrel of the syringe is connected to a 50 mm long, 25-gauge stainless steel needle (ID/OD =  $241/500\ \mu\text{m}$ ) which is connected to the test section and acts as the orifice for the synthetic jet. The plunger is connected to a 1.1 kg force voice coil shaker by a steel connecting rod and grub screw connection piece. An ICP accelerometer is fixed with adhesion between the connection piece and the plunger. As can be seen in Figure 3, the shaker and syringe configuration were held in line together by a rig made from aluminum.

A sinusoidal waveform produced by function generator and amplified by a 25 W amplifier was supplied to the shaker, to oscillate the plunger. The shaker motion was captured by the accelerometer whose factory-calibrated sensitivity was given as  $10.87\ \text{mV/m/s}^2$ . The sensitivity was confirmed for the current experimental setup by calibrating it against an accelerometer calibrator. The accelerometer was supplied with a constant current signal from a charge amplifier with ICP mode which outputs the signal from the accelerometer to a data acquisition system.

The syringe needle connects to a rectangular test section 5 mm wide, 30 mm long, and  $500\ \mu\text{m}$  deep shown in Figure 4. The needle lies perpendicular to the channel with the orifice in line with one of the test section walls. The working fluid entered the channel through inlet/outlets located behind each end of the rectangular channel. The test section geometry was fabricated in polydimethylsiloxane (PDMS) from a mould consisting of a 25-gauge needle and a  $500\ \mu\text{m}$  thick aluminum spacer. The PDMS section was bonded to a glass slide with the use of a corona [18]. A 25-gauge needle was inserted into the test section and aligned under a microscope with one of the channel walls. An epoxy was used to secure the needle in position, and silicone sealant was used around the outside edge of the test section and around the inlet/outlet connections for extra durability.

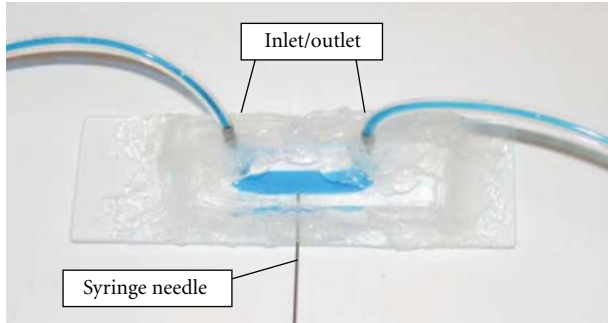


FIGURE 4: The PDMS test section with blue dye added to the water for clarity.

Instantaneous velocity fields were obtained using the  $\mu$ PIV technique with a high-speed  $\mu$ PIV system in a plane bisecting the jet. Image pairs were acquired by a high-speed CMOS camera connected to an inverted microscope. The field of view was volume illuminated by a dual Nd:YLF laser system with a wavelength of 527 nm and a maximum repetition rate of 10,000 Hz per laser head. The timing of the laser system and camera was controlled by a PIV synchronizer through the PIVsync software. The flow of purified water was seeded with red fluorescing  $2\ \mu\text{m}$  diameter. A filter cube allowed the excitation light from the laser to pass through the objective and onto the test section while only allowing the light emitted from the particles to be imaged by the camera. The time delay between pulses for image pairs was  $25\ \mu\text{s}$  in order to capture the fast moving particles along the centreline.

The spatial resolution of the system is determined by the interrogation process. The final interrogation windows size was  $32 \times 32$  pixels ( $28 \times 28\ \mu\text{m}$ ), and the depth of correlation was  $16\ \mu\text{m}$  which defined the interrogation volume. To achieve this resolution a high seeding concentration of 0.09% was used to ensure 2-3 particles per interrogation volume. With adjacent interrogation windows being overlapped by 50% the final spatial resolution of the system is  $14\ \mu\text{m}$ . The synchronizing for the high-speed PIV system was based on timing from the high-speed camera. At full camera resolution the maximum rate that image pairs can be acquired at is 500 Hz, which would allow pairs to be taken from 25 different times within the oscillation cycle (for an operating frequency,  $f = 240\ \text{Hz}$ ).

A multipass interrogation scheme was used with  $64 \times 64$  pixels in the first pass and  $32 \times 32$  pixels in the second pass with 50% overlap used in both passes. The 64 pairs of velocity fields generated at each phase were extracted from a total of 768 cycles and used to produce the 25 phase average velocity fields. All signals generated were captured using a 4-channel 16-bit data acquisition card, which was used to acquire the signal from the accelerometer at a sampling rate of 20 kHz. After sampling, the acceleration data was filtered with a series of high-pass filters to remove the DC offset present in the signal without significantly changing the waveform. The data was integrated numerically to determine the velocity profile and integrated again for the displacement

profile. More details on the experiment can be referred to in Sinclair et al. [17].

## 5. Results and Discussions

Integration of the accelerometer data yielded a plunger displacement with a profile that appeared qualitatively sinusoidal. A clearance volume between the plunger and syringe wall exists, which could also permit fluid flow. Therefore the exact volume of fluid ejected through the orifice over a cycle could not be calculated from the measured plunger displacement.

The use of a high-speed  $\mu$ PIV system, while capable of measuring up to 10,000 image pairs per second, did not allow phase locked measurements to be made, which meant that special care was needed to be taken to ensure accurate measurement. The devised dividing of the actuation cycle into phases required that all signals were to be at the desired frequency and remain constant throughout the measurement period. The data taken from the accelerometer was used to check the actuation frequency over the measurement period of 3.2 seconds or 768 cycles. The actual measured frequency of the actuation cycle in the experiment was 240.01 Hz which would mean a shift of 0.032 of a cycle by the end of the measurement period. To keep the drift of each phase location below 0.01 of a cycle, only the first 16 image pairs at each phase were used to generate the phase averaged fields. Averaging from only 16 pairs compared to the intended 64 significantly decreased the accuracy of the results.

Without synchronization of the image acquisition to the actuation cycle the locations of each of the 25 measurement points within the cycle are unknown. Thus, the locations of the measurement phases were determined by comparison with the numerical results at a single phase, and all other phases shifted according to their separation. The peak velocity measured from the  $\mu$ PIV data was used as the reference velocity and phase. This maximum velocity was used to determine the maximum velocity that would occur in the simulation, and the phase location of this point in the simulation results was then assigned to the  $\mu$ PIV case.

Nondimensional time  $t$  was calculated from the ratio between the physical time and the period of oscillation  $t = t^*/T$ , whilst the distances from the centre line of the jet and also from the orifice are nondimensionalised with respect to diameter of the orifice. Setting  $t = 0$  at bottom dead center of the plunger stroke, the maximum velocity just outside the orifice in the simulations occurred at  $t = 0.26$ . Therefore the maximum  $\mu$ PIV case was set to  $t = 0.26$ , and all image pairs located were shifted accordingly.

Velocity vector plots for experimental and numerical results for different phases during the first half of the expulsion stage are plotted side by side in Figure 5. In Figure 5(a), the early stage of vortices formation adjacent to the exit of orifice can be seen. At  $t = 0.18$ , the vortices become more visible and shift along with the flow coming out from the orifice in streamwise direction. At the end of

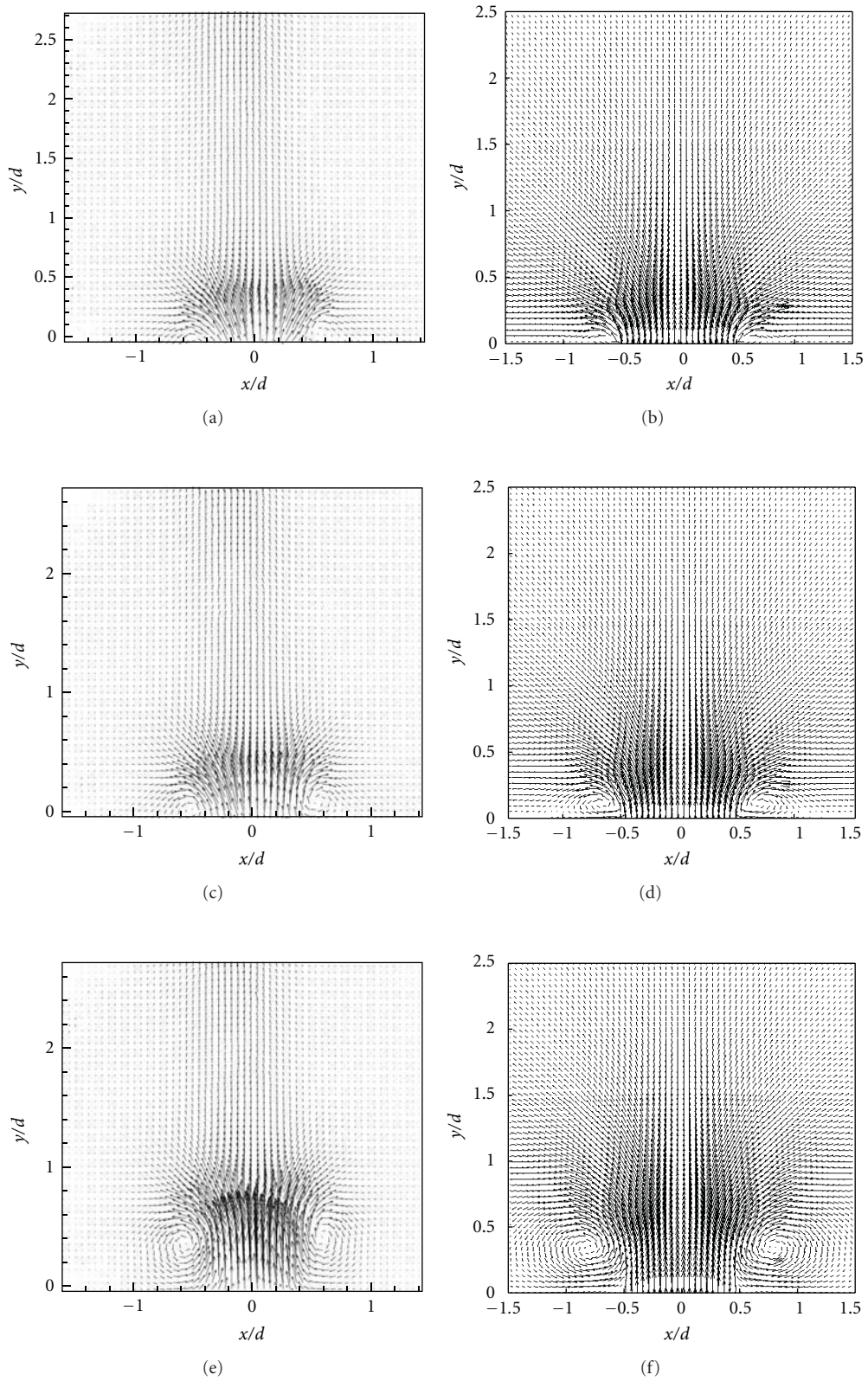


FIGURE 5: Comparison of experimental and numerical velocity vector plots during four phases of expulsion phase:  $t = 0.14$  ((a), (b)),  $t = 0.18$  ((c), (d)), and  $t = 0.26$  ((e), (f)).

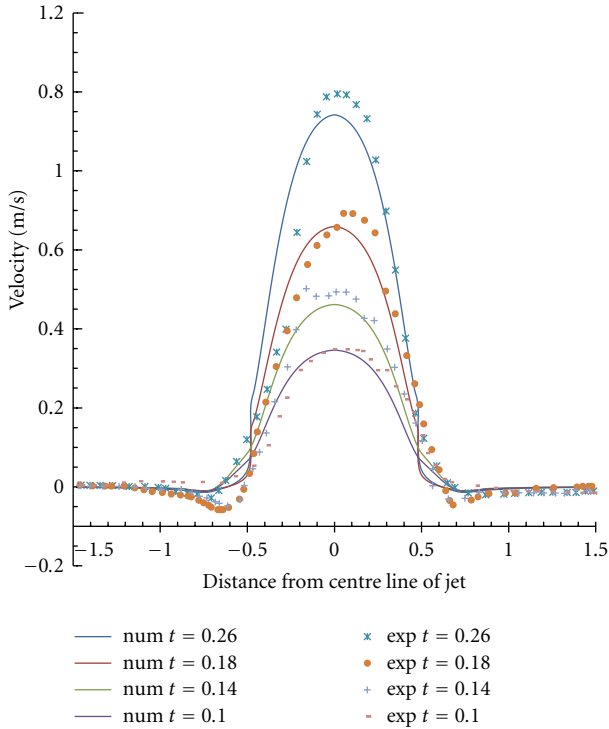


FIGURE 6: Comparison of experimental and numerical streamwise component of velocity profiles at orifice exit during the four phases of the expulsion phase.

the first half of the expulsions stage, that is, at  $t = 0.26$ , two apparent vortices are seen at about half orifice diameter away from the orifice exit. The vector plots presented show good agreement in terms of vortex core location and general flow field for numerical and experimental results. A slight asymmetry in the experimental results can be seen in all three vector plots. The vortex core on the right side of the plots appears further downstream than the vortex core on the left side at each phase. Possible reason could be attributed to slight imperfections at the test section orifice or a misalignment between the desired test section plane and the plane of focus of the microscope lens.

As for quantitative data comparison, the row of velocity vectors located closest to the plane of the orifice, 0.1 d in front, has been used to extract the orifice exit profiles of streamwise velocity components. In Figure 6, profiles from the first half of the expulsion part of the cycle are presented. The velocity distribution early in the expulsion phase,  $t = 0.1$ , showed a developing profile which becomes parabolic by the time it reaches its maximum,  $t = 0.26$ . At this time, numerical solution recorded a maximum velocity of 0.979 m/s in the near vicinity of the orifice, whereas experimental data recorded a value of 0.985 m/s. Overall, both numerical and experimental results showed good agreement for all of the time instants. Again, experimental results show the asymmetry velocity profile as the peak velocity did not reside on the centreline.

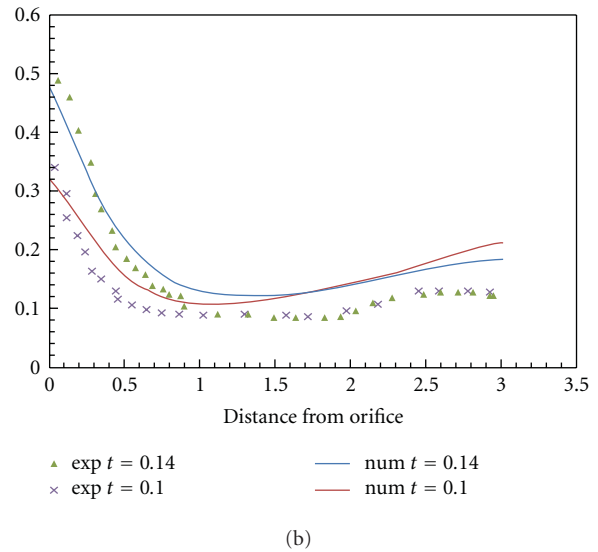
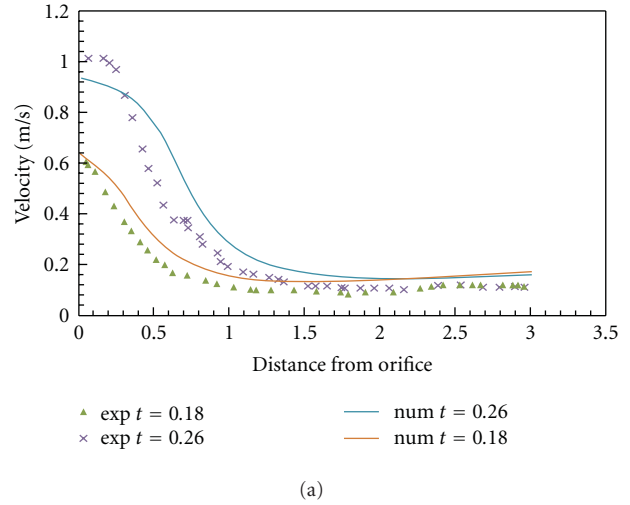


FIGURE 7: Comparison of experimental and numerical streamwise component of velocity profiles along the jet centreline during the four phases of the expulsion phase.

In Figure 7 the streamwise component of velocity along the centreline was compared for the same part of the expulsion phase. The small discrepancies of velocity magnitude could be due to the misalignment of the test device as spotted in the asymmetry velocity profile in Figure 6 which then resulted in slightly higher centreline velocity right above orifice. Overall, Figure 7 shows good agreement of numerical results in predicting the general trend of velocity profiles at orifice exit and along the centreline of the pulsating jet for all times. This leads us to the conclusion that the phase locations determined for the experimental results from the numerical data based on peak velocity were reasonable.

## 6. Conclusions

The moving mesh algorithm as proposed was found to be efficient and accurate as it eradicated the need for

either re-meshing or solving a new evolution equation for the Jacobian. This method also enforced GCL as grid points were moved by using mesh velocities and not the other way round. The comparison presented demonstrates good agreement, thereby confirming that the moving mesh algorithm developed is valid and is able to resolve the flow fields of microsynthetic jets. The validity of the moving mesh algorithm was assessed against the measured streamwise component of velocity profiles at the orifice exit and along the centerline of the pulsating jet in a micro-channel as well as the location of vortex core at different time instants of the expulsion stage. Good agreement was achieved between the measurements and numerical predictions. The comparison presented thereby confirms that the moving mesh algorithm is developed to be valid and able to resolve the flow fields of micro synthetic jets.

## Nomenclature

$d$ :	Orifice diameter
$f$ :	Actuator frequency
$f(d)$ :	Weighting function
$h_f$ :	Fluid enthalpy
$H$ :	Depth
$\sqrt{g}$ :	Jacobian of body-fitted coordinate system
$L$ :	Length
$n$ :	Outward drawn normal
$p$ :	Fluid pressure
$P^i, P^j P^k$ :	Interpolation or “blending” functions
$t$ :	Time in the physical coordinates
$t^*$ :	Time, $s$
$T$ :	Period of actuation cycle
$U$ :	Fluid velocity
$U_g$ :	Grid velocity
$W$ :	Width
$w$ :	Width of the micro-channel
$Y_m$ :	Displacement of membrane
$x, y, z$ :	Physical coordinates in the Cartesian frame.

## Greek Symbols

$\beta_{il}, \beta_{lm}$ :	Grid transformation coefficients
$\rho_f$ :	Fluid density
$\mu_f$ :	Fluid viscosity
$\tau$ :	Time in the computational coordinates
$\tau'$ :	Period of oscillation
$\varepsilon, \gamma, \omega$ :	Body-fitted coordinate system.

## References

- [1] A. Glezer and M. Amitay, “Synthetic jets,” *Annual Review of Fluid Mechanics*, vol. 34, pp. 503–529, 2002.
- [2] M. Gordon and J. Soria, “Scalar mixing of zero-net-mass-flux jets in crossflow,” in *Proceedings of the 14th Australasian Fluid Mechanics Conference*, pp. 729–732, 2001.
- [3] J. S. Campbell, W. Z. Black, A. Glezer, and J. G. Hartley, “Thermal management of a laptop computer with synthetic air microjets,” in *Proceedings of the 6th Intersociety Conference on Thermal and Thermomechanical Phenomena in Electronic Systems (ITHERM '98)*, pp. 43–50, May 1998.
- [4] R. Mahalingam and A. Glezer, “Air cooled heat sinks integrated with synthetic jets,” in *Proceedings of the 8th Intersociety Conference on Thermal and Thermomechanical Phenomena in Electronic Systems*, pp. 285–291, June 2002.
- [5] R. Mahalingam, N. Rumigny, and A. Glezer, “Thermal management using synthetic jet ejectors,” *IEEE Transactions on Components and Packaging Technologies*, vol. 27, no. 3, pp. 439–444, 2004.
- [6] B. L. Smith and G. W. Swift, “A comparison between synthetic jets and continuous jets,” *Experiments in Fluids*, vol. 34, no. 4, pp. 467–472, 2003.
- [7] A. Pavlova and M. Amitay, “Electronic cooling using synthetic jet impingement,” *Journal of Heat Transfer*, vol. 128, no. 9, pp. 897–907, 2006.
- [8] M. B. Gillespie, W. Z. Black, C. Rinehart, and A. Glezer, “Local convective heat transfer from a constant heat flux flat plate cooled by synthetic air jets,” *Journal of Heat Transfer*, vol. 128, no. 10, pp. 990–1000, 2006.
- [9] Z. Trávníček and V. Tesař, “Annular synthetic jet used for impinging flow mass-transfer,” *International Journal of Heat and Mass Transfer*, vol. 46, no. 17, pp. 3291–3297, 2003.
- [10] Z. Trávníček and V. Tesař, “Annular impinging jet with recirculation zone expanded by acoustic excitation,” *International Journal of Heat and Mass Transfer*, vol. 47, no. 10–11, pp. 2329–2341, 2004.
- [11] J. Lepičovský, K. K. Ahuja, and R. H. Burrin, “Tone excited jets, part III: flow measurements,” *Journal of Sound and Vibration*, vol. 102, no. 1, pp. 71–91, 1985.
- [12] J. Lepičovský, K. K. Ahuja, and M. Salikuddin, “An experimental study of tone-excited heated jets,” *Journal of Propulsion and Power*, vol. 2, no. 2, pp. 149–154, 1986.
- [13] W. J. Gordon and L. C. Thiel, “Transfinite mappings and their application to grid generation,” in *Numerical Grid Generation*, J. F. Thompson, Ed., pp. 171–192, Elsevier, New York, NY, USA, 1982.
- [14] S. F. Anwer, N. Hasan, S. Sanghi, and S. Mukherjee, “Computation of unsteady flows with moving boundaries using body fitted curvilinear moving grids,” *Computers and Structures*, vol. 87, no. 11–12, pp. 691–700, 2009.
- [15] C. M. Rhie and W. L. Chow, “An numerical study of the turbulent flow past an airfoil with trailing edge separation,” *AIAA Journal*, vol. 21, no. 11, pp. 1525–1532, 1983.
- [16] H. L. Stone, “Iterative solution of implicit approximations of multidimensional partial differential equations,” *SIAM Journal on Numerical Analysis*, vol. 5, pp. 530–558, 1968.
- [17] A. Sinclair, V. Timchenko, J. A. Reizes, G. Rosengarten, and E. Leonard, “An experimental and numerical study of a micro-synthetic jet in a shallow cavity,” in *Proceedings of the 6th ASME Conference on Nanochannels, Microchannels and Minichannels*, Darmstadt, Germany, 2008.
- [18] K. Haubert, T. Drier, and D. Beebe, “PDMS bonding by means of a portable, low-cost corona system,” *Lab on a Chip*, vol. 6, no. 12, pp. 1548–1549, 2006.

## Research Article

# Recent Efforts for Credible CFD Simulations in China

**Li Li, Bai Wen, and Liang Yihua**

*Aeronautics Computing Technique Research Institute (ACTRI), P.O. Box 90, Xi'an 710068, China*

Correspondence should be addressed to Li Li, westlili@163.com

Received 6 October 2010; Accepted 12 January 2011

Academic Editor: Guan Yeoh

Copyright © 2011 Li Li et al. This is an open access article distributed under the Creative Commons Attribution License, which permits unrestricted use, distribution, and reproduction in any medium, provided the original work is properly cited.

In this paper some recent efforts for credible computational fluid dynamics (CFD) simulations in China are reviewed. The most important effort is that, following similar activities in the West such as ECARP and AIAA Drag Prediction Workshops, a series of workshops on credible CFD simulations had been initiated. These workshops were with ambitions to assess the status of CFD in China. Another major effort is an ongoing project to establish a software platform for studying the credibility of CFD solvers and performing credible CFD simulations. The platform, named WiseCFD, was designed to implement a seamless CFD process and to circumvent tedious repeating manual operations. It had also been a powerful job manager for CFD with capabilities to support plug and play (PnP) solver integration as well as distributed or parallel computations. Some future work on WiseCFD was proposed, and also envisioned was how WiseCFD and the European QNET-CFD Knowledge Base can benefit mutually.

## 1. Introduction

In the last decades, computational fluid dynamics (CFD) has undergone a strong development and has become a powerful tool both for the analysis and understanding of fluid dynamics phenomena, and for the design and optimization of aerodynamic performance of aircrafts or aerospace vehicles. This progress has been made possible with the advent, in the meantime, of faster and faster supercomputers with increasing memory capabilities, and with the rapid progress of modern numerical computing technology. However, the limitations of CFD need to be addressed due to the lack of knowledge of physical phenomena and appropriate physical modeling as well as limited experimental information. In addition, CFD is strongly affected by the numerical methodology employed (e.g., geometrical modeling, spatial discretization scheme, time accuracy computing, etc.) and computer resources. Therefore, the question of the credibility of the numerical solution is naturally proposed. In other words, to make the numerical simulations practicable, a crux stage is to perform a credibility analysis for the simulation, whose primary target is to assess and eliminate uncertainty in computation as possible. In terms of the authoritative guidance given by AIAA in 1998, the basic activities are CFD verification and validation (V&V) [1].

In developed countries, the activities related to CFD credibility analysis started early, and were paid extensive attentions, especially that they had laid many special projects and workshops with the intent of developing large databases of numerical solutions and experimental data of basic reference test cases to be used for CFD V&V. The ECARP (European Computational Aerodynamics Research Project) involved 39 European partners for validation of CFD codes and assessment of turbulence models in Europe during the period 1993 to 1995 with a special research edition for close in 1997 [2]. At the end of 1998, in order to provide the scientific and industrial communities with a validation and experimental methodologies ranging from subsonic, transonic to supersonic, and hypersonic regimes, the European Community Commission began to support the setup of the Thematic Network FLOWNET (Flow Library on the Web network). The ultimate goal of this thematic network is to stimulate collaboration between industrial and research partners in order to evaluate continuously the quality of the simulations and the performance of CFD software, the scope being to improve complex design in aeronautical and aerospace industry [3]. In 2000, 44 participating organizations across Europe were brought together for a four-year project QNET-CFD, EU Network on Quality and Trust in the Industrial Application of Computational Fluid

Dynamics [4]. Its main objective was to improve the level of trust that can be placed in industrial CFD calculations by assembling, structuring, and collating existing knowledge encapsulating the performance of models underlying the current generation of CFD codes. During the course of the project, QNET-CFD sponsored series of workshops in 2001, 2002, and 2003. Following the end of the EU Network in July 2004, its Knowledge Base passed to the control of a committee of the European Research Community of Flow, Turbulence, and Combustion (ERCOTAC) with the remit of enhancing and expanding the Knowledge Base and bringing it online for the benefit of applied fluid dynamicists and CFD users worldwide.

AIAA Applied Aerodynamics Technical Committee (APATC) had sponsored a series of Drag Prediction Workshops since 2001. The objectives of these workshops were (1) to assess the state-of-the-art computational methods as practical aerodynamics tools for aircraft forces and moment prediction, (2) to impartially evaluate the effectiveness of existing computer codes and modeling techniques, and (3) to identify areas needing additional research and development. The first Drag Prediction Workshop (AIAA-DPW-I) was held in June of 2001. Its challenge was to compute the lift, drag, and pitching moment for the DLR-F4 subsonic wing-body transport configuration [5]. The second Drag Prediction Workshop (AIAA-DPW-II) was held in June of 2003. At this time the emphasis was on the determination of installed pylon-nacelle drag increments and on grid refinement studies with the hope of seeing reduced code-to-code scatter. The geometries used were DLR-F6 wing-body (WB) and wing-body-pylon-nacelle (WBPN) combinations [6]. The third Drag Prediction Workshop (AIAA-DPW-III) is planned to be held in June 2006. The focus of the workshop will be on “blind” drag prediction accuracy; a priori experimental data will not be available for comparison. In addition to the DLR-F6 wing-body with or without FX2B faring transport models, two wing-alone models, DPW-W1 and DPW-W2, are also included to encourage academic participation and allow more exhaustive grid convergence studies [7].

In March 2004, in order to more broadly assess the current capabilities of different computational methodologies, the CFD Validation of Synthetic Jet and Turbulence Separation Control (CFDVAL2004) workshop was held in Williamsburg, Virginia [8]. Three different test cases, all of which were carried out experimentally by NASA Langley Research Center, exercised various aspects related to the flow physics of separation control. The workshop was structured to the series of Refined Turbulence Modeling workshops sponsored by the ERCOTAC, 10th of which was held in France in October 2002.

Comparatively, similar activities are rare in the past in China. In recent years the status is gradually changing. The theory and application studies for CFD credibility are paid much more attentions. Since 2000, CFD credibility analysis and experimental verification for aerodynamic numerical software had been determined a national key project among aerodynamic advanced research projects. From then on, many efforts for credible CFD simulations were made. In

this paper our goal is to outline some outstanding efforts among them. The first important effort is The National CFD Uniform Test Cases Computation Workshop, following similar activities in the West such as ECARP and AIAA Drag Prediction Workshops. Such series of workshops were jointly sponsored by CARDC and ACTRI with intent to assess the state-of-the-art computational fluid dynamics (CFD) of China and to identify research areas in the near future. Another is WiseCFD software platform for aerodynamic credibility analysis, which is one of prominent outputs of an ongoing project at ACTRI [9]. It is designed to implement a seamless CFD process and to circumvent tedious repeating manual operations. Besides, efforts related to international collaborations for CFD credibility analysis are also reported; especially how WiseCFD and other validation databases, for example QNET-CFD, can benefit mutually is envisioned.

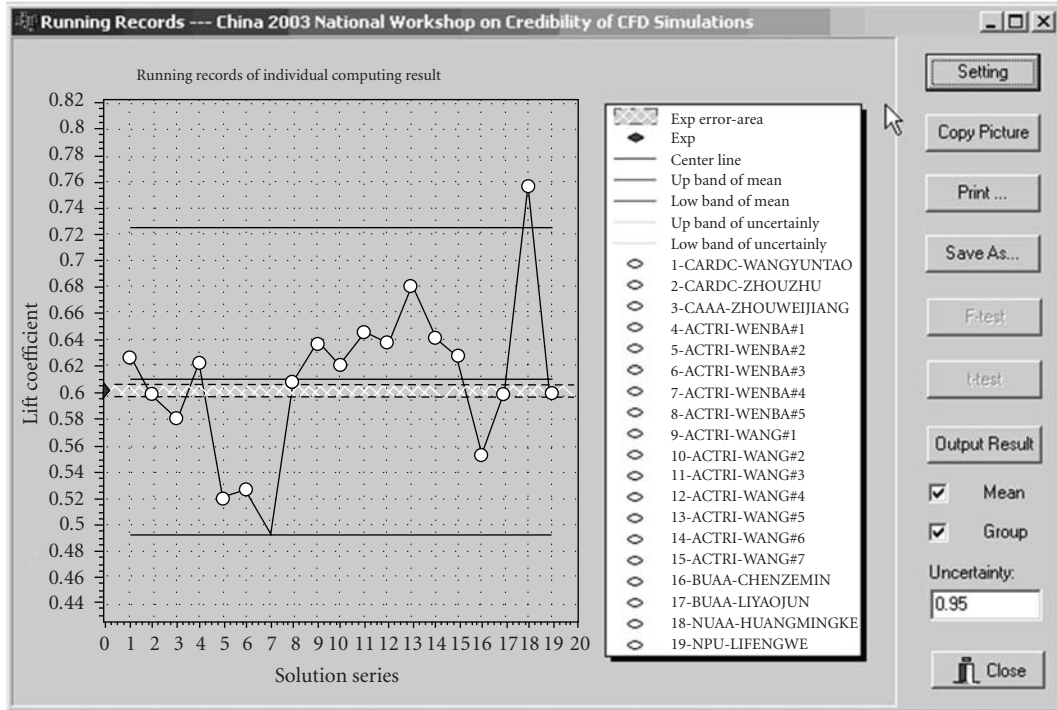
## 2. China National CFD V&V Workshops

The mainstream collective CFD V&V activities in China are two successive workshops organized by CARDC and ACTRI in 2003 and 2005, respectively. Besides, some following actions are also taken later on [10]. Both of these workshops are to assess the state of the art of CFD in China, and to identify areas needing additional research and development to promote prediction accuracy.

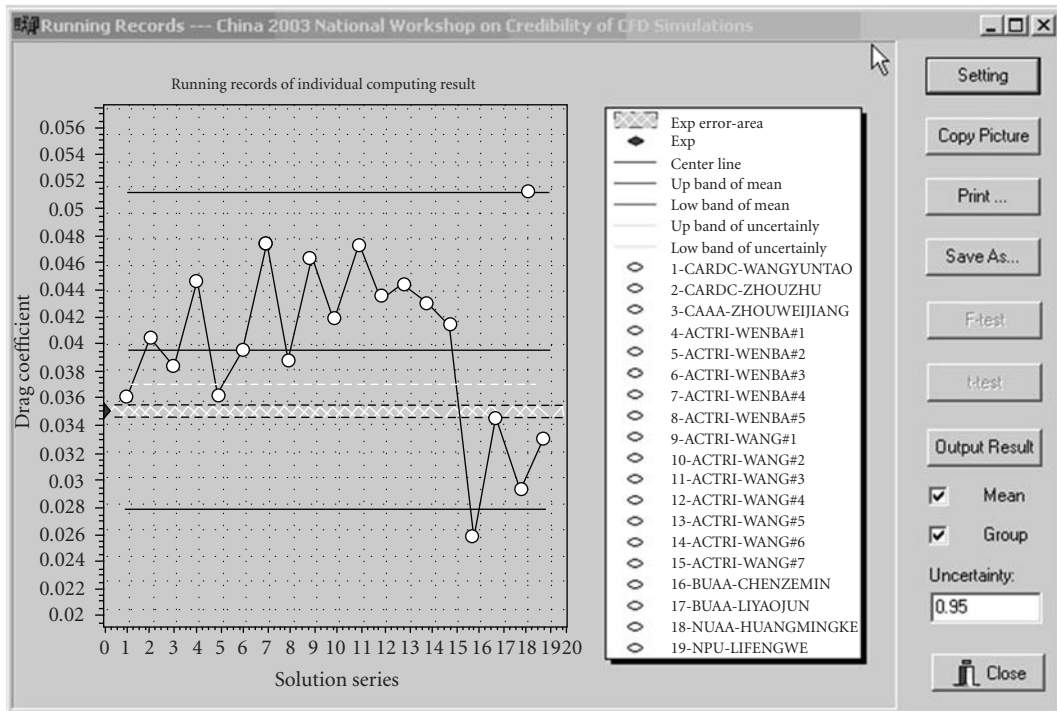
The first effort to hold a workshop in 2003 was abandoned for some reasons, but resulted in a great promotion of relative researches and a special edition of papers [11]. The special edition was composed of 17 papers from 9 organizations. The selected test cases include the DLR-F4 wing-body combination, NLR-7301 two elements airfoil at high lift, and blunt cone at hypersonic speed. The emphasis is the prediction accuracy for drag and heat flux. The participants are required to perform their computations using the geometry and grid files provided by head organizers and are also encouraged to generate their own grid for simulation. The geometry of DLR-F4 configuration is the same as that of AIAA DPW-I [5]. Its challenge for this workshop is to compute the lift, drag, and pressure distribution at typical wing section 0.185, 0.238, 0.331, 0.409, 0.512, 0.636, and 0.844 along the wing for a specific condition ( $Re = 3 \times 10^6$ ):

$$M_\infty = 0.75, \quad \alpha = 0.93^\circ (C_L = 0.6). \quad (1)$$

The dominant computational grid is provided by CARDC. Some of participants also generate their own grid. There are 9 papers reporting 19 computational results. Only 2 results are obtained using Euler computation. The rest employ Reynolds-Averaged Navier-Stokes (RANS) technique with proper turbulent models. The typical turbulent models include Spalart-Allmaras (SA) and Baldwin-Lomax (BL). A statistical analysis for these results is shown in Figure 1. It is observed that results from the workshop are quite scattered. Most of the results have over-predicted the lift and drag. For the case of NLR-7301 high-lift airfoil, two geometries are considered depending upon the gap size between the wing and the single-slotted trailing edge flag, respectively, 1.3%



(a) Lift coefficient



(b) Drag coefficient

FIGURE 1: Statistical analysis of computational results for DLR-F4 wing-body configuration from the 1st National CFD Uniform Test Cases Computation Workshop.

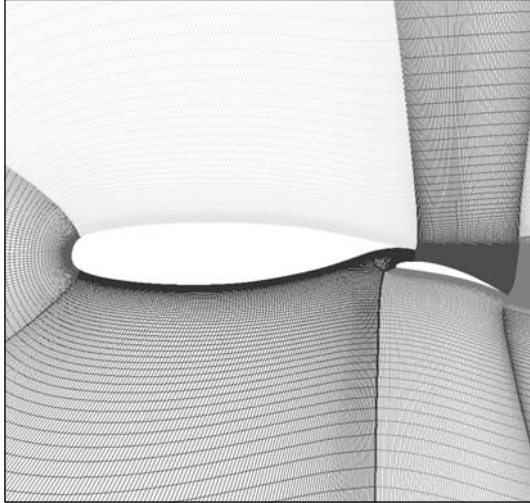


FIGURE 2: NLR-7301 two elements high lift airfoil and its typical grid topology from ECARP and FLOWNET (2.6% flap-gap).

and 2.6%, being as a percentage value of the main wing chord. The computational conditions are

(1) 1.3% flap-gap

$$M_\infty = 0.185, \quad \alpha = 6^\circ, \quad Re = 2.51 \times 10^6 \quad \text{and} \quad (2)$$

(2) 2.6% flap-gap

$$M_\infty = 0.185, \quad \alpha = 13.1^\circ, \quad Re = 2.51 \times 10^6. \quad (3)$$

The dominant grids used in this workshop for such configurations are multi-block structured patched ones, which can be also found from ECARP and FLOWNET libraries. Their topology and cells number are completely identical with 9 blocks and 144832 cells. In Figure 2, a typical grid topology is shown. Results required to be submitted include

- (1) lift coefficient, drag coefficient, and their convergent histories,
- (2) pressure coefficient distributions of the main wing and the flap,
- (3) skin friction coefficient distributions of the main wing and the flap, and
- (4) velocity profiles of the boundary layer at typical locations.

There are 5 contributors for the test case. Among them, besides results of RANS plus turbulent models, some results of Large Eddy Simulation (LES) are also reported. Figure 3 shows a typical pressure coefficient distribution computational result by ACTRI employing RANS with SA turbulent model. For this challenge, in order to promote the prediction accuracy for large flow separation near the wall, a wider and more elaborate variety of turbulent models (SA, BL,  $k - \omega$ , Jones-Launder, JB, and SGS, etc.) have been considered in these contributions. Some scatters are found for this test case.

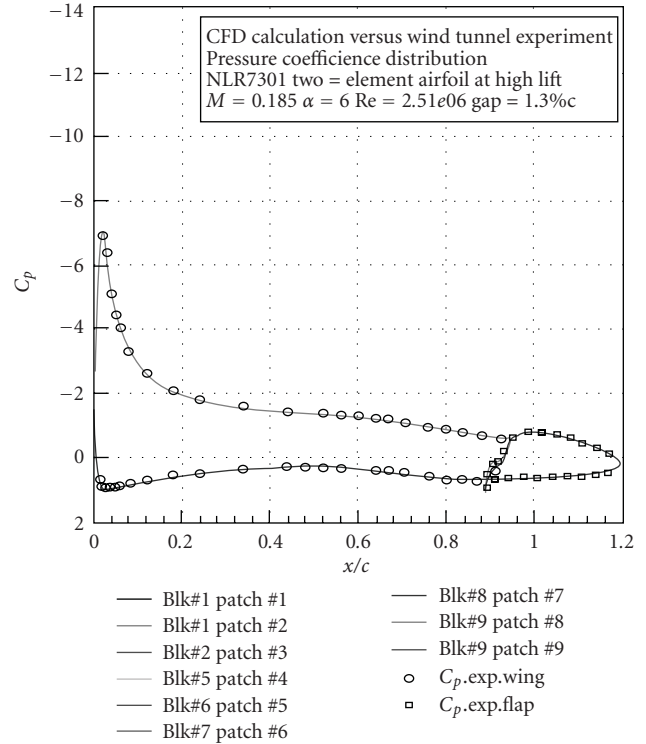


FIGURE 3: Pressure coefficient distribution by ACTRI for NLR-7301 two elements airfoil (1.3% flap-gap).

The geometry and its dominant computational grid of the third test case, hypersonic blunt cone, are both provided by CARDC. Its challenge is to accurately predict heat flux for the following conditions:

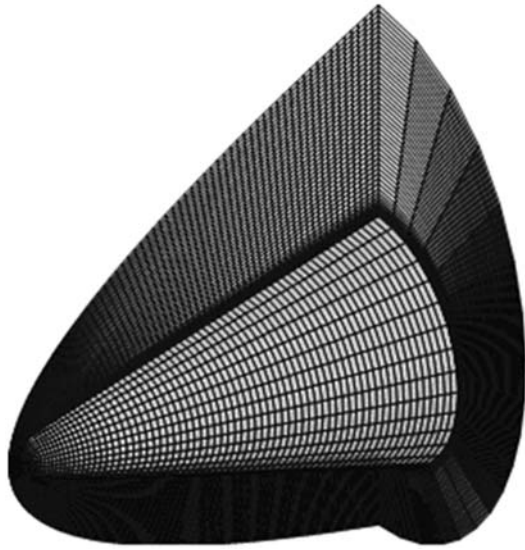
$$M_\infty = 10.6, \quad T_\infty = 47.3 \text{ K}, \quad T_{\text{wall}} = 294.44 \text{ K}, \quad (4)$$

$$\alpha = 0^\circ, 20^\circ, \quad Re = 3.937 \times 10^6.$$

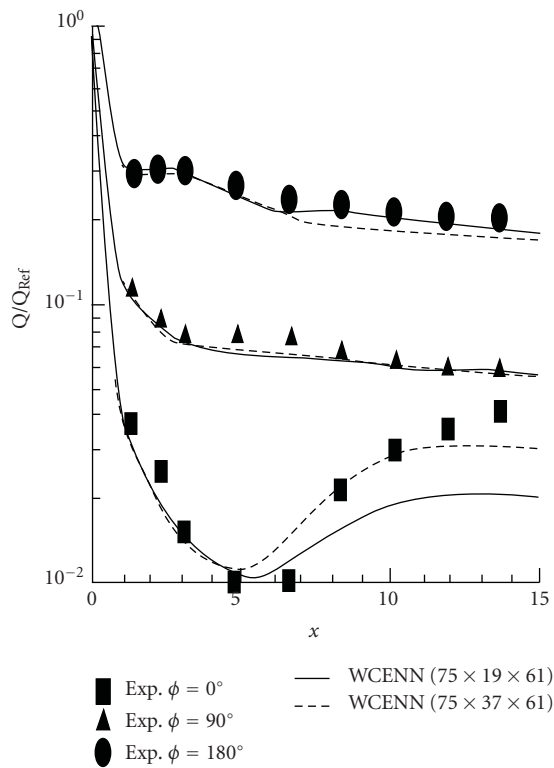
There are 6 contributors having reported their results on the workshop. Figure 4 shows a typical result for this test case by CARDC. From these contributions, one important observation is that a higher order scheme is obviously superior for heat flux prediction based on the same computational grid.

The second national effort for credible CFD simulations started from September 2004. The formal workshop was held in Inner Mongolia, June 2005. The emphasis of this workshop is the simulation of high attack angle problem, where the CT-1 standard model provided by CARDC [12] is computed for six main force coefficients (i.e., axial force coefficient, normal force coefficient, side force coefficient, X force coefficient, Y force coefficient, and Z force coefficient), lift coefficient, and drag coefficient. The computations were performed at the following flow conditions:  $M_\infty = 0.5$ ,  $Re = 1.4 \times 10^6$ , angles of attack between  $-5^\circ$ , and  $105^\circ$ , and sideslip angles  $\beta = 0^\circ, 5^\circ, 15^\circ$ .

There are 34 attendees from 12 workgroups of 9 organizations. Most results are obtained by RANS technique plus proper turbulent models. The turbulent models involved include SA, BL,  $k - \omega$ , and SST. Part results are from



(a) Computational grid and topology



(b) Heat flux

FIGURE 4: Typical computational results for hypersonic blunt cone configuration from the 1st National CFD V&V Workshop.

Euler computation. Besides, few results from Detached Eddy Simulation (DES, hybrids of LES and RANS) and Lattice Boltzmann Method (LBM) are reported. Figure 5 shows a typical result from the workshop, where the lift coefficients from different contributors are given. Results of

this workshop exhibit the state of the art of CFD researches in China.

It is shown that for a high attack angle problem, great progresses have been made in the recent years. Briefly speaking, for CT-1 model, we had concluded that (1) the computational aerodynamic characteristic (e.g., lift, drag, and pitching moment) under medium attack angle is of good agreement with experimental data, (2) the computational angle to occur unsymmetrical side force agrees with experimental data well, while the amplitude of the side force is closed to from experiments, and (3) when the sideslip angle does not equal to zero, the computational angle making the yawing moment in reverse agrees with experimental data by and large. Nevertheless, some limits are also observed. They are (1) the attack angle corresponding to the maximal lift coefficient from computations is offset to that from experiments, (2) there exist obvious gaps between computations and experiments for results at attack angles between 40° and 60°, and (3) prediction accuracy of moment characteristic at high attack angle is not enough.

### 3. Integrated Software Platform for Credible CFD Simulations: WiseCFD

Since 2000, ACTRI had begun to develop an integrated software platform for aid to assess the credibility of CFD solvers and to perform a credible CFD simulation with less human errors. Its main objective is to develop an intuitive user environment that allows the user to prepare, submit, monitor, and manage large numbers of CFD simulation jobs for parametric studies during the course to perform CFD credibility analysis, and also to implement an integrated management for data and software.

The system architecture of the WiseCFD platform is shown in Figure 6, which comprises a V&V Case Library and five major functional modules as its main parts. The Case Library can be alternatively regarded as a special database for CFD verification and validation. Large amount of reliable data had been collated in the past several years and integrated in the database. The five functional modules are used to implement different functions in the system, for example, solver management, case data management, parameter sensitivity management, the batched job management, and data analysis and comparison. In this way, an automatic seamless CFD process is built up, which thus greatly enhances computing efficiency and electively reduces uncertainty in simulation.

Currently, the WiseCFD platform has the published version 2.0, whose main graphic user interface (GUI) is shown in Figure 7. There are four different view areas on the GUI that include (1) the toolbar area at the top, (2) the case catalog tree area at the left, (3) the operating panel area in the middle, and (4) the information hint area at the bottom. The toolbar is used to provide a shortcut access to different functions related to software management, computing job management, data backup, or system help. The view area for case catalog tree is used to display hierarchy-arranged case data in a way similar to Windows catalog tree. The top level

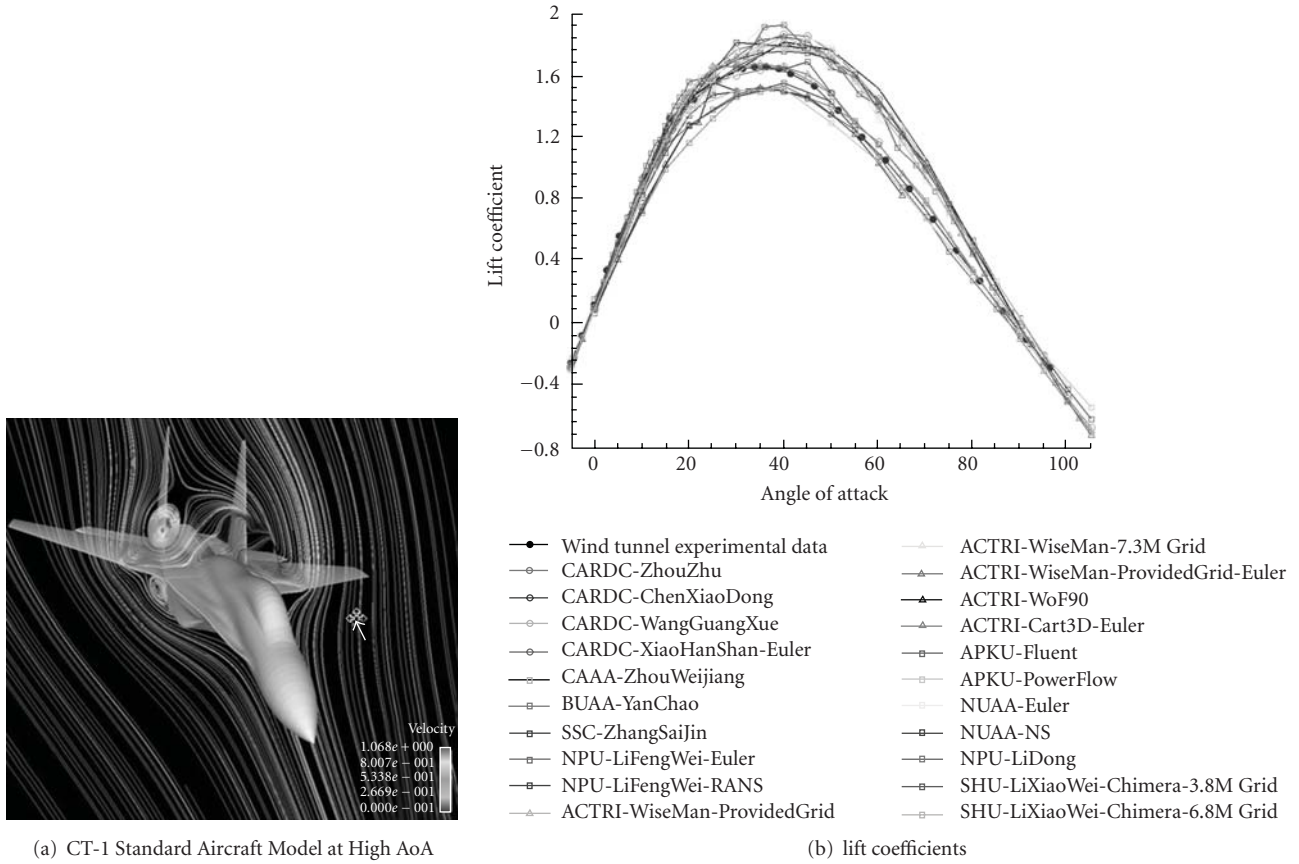


FIGURE 5: A typical computational result for high AoA model from the 2nd National CFD Uniform Test Cases Computation Workshop.

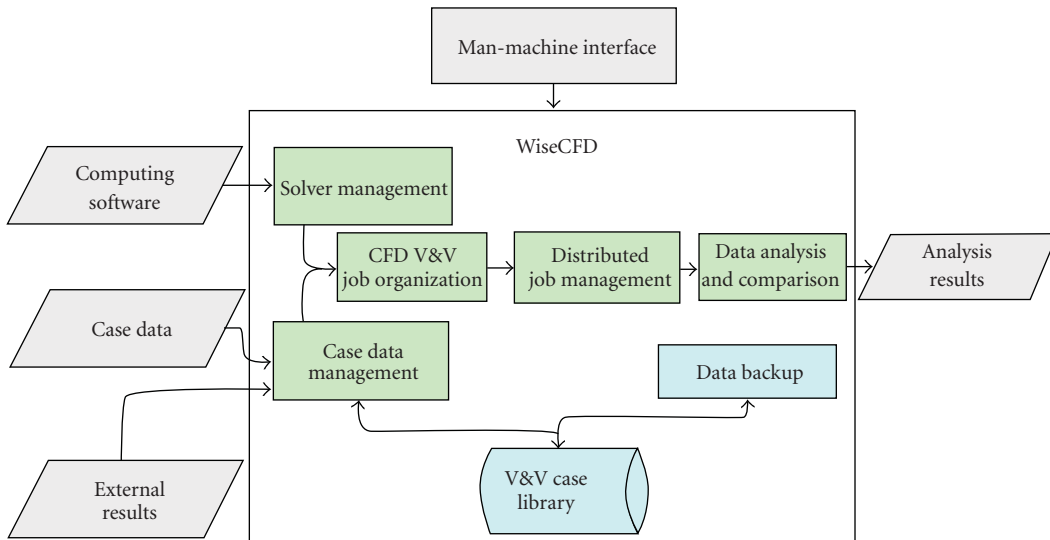


FIGURE 6: System architecture of the WiseCFD platform.

is the case type, which can be designated as three different classes: verification case, validation case, and application challenge case. The second level is the practical test case. The third level is the computational solver to be used for the test case, and the fourth is the so-called study case that

is used to record practical analysis activity. At each level, different operation panels will be shown in the panel view area. Through these panels, the functions related to case data management, computing software management, study case management, computational results management, and data

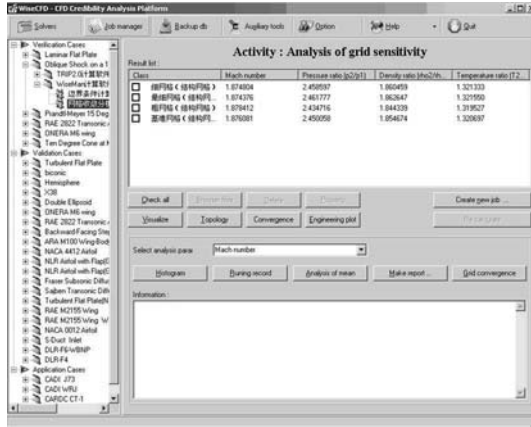


FIGURE 7: Graphic user interface (GUI) of the WiseCFD Platform.

analysis and comparison can be accessed. The main features of WiseCFD v2.0 are briefly summarized here:

- (1) it provides a convenient and user-friendly graphical user interface;
- (2) it provides an extensible database for CFD verification and validation, in which 6 verification cases, 20 validation cases and 3 application challenge cases are available in current version;
- (3) with an extensible open framework for software integration, and with the use of data-exchange standards (e.g., plot3d and CGNS), it supports the plug and play (PnP) software integration, from which different in-house and commercial CFD codes have been integrated in this simple way;
- (4) with the function for parameter sensitivity analysis and management, it allows the user to prepare large amount of different input files for CFD credibility analysis in similar simple way;
- (5) with the capability for distributed job management, it allows the user easily to submit and monitor the large batched CFD jobs, and to effectively utilize available computing resources under the Windows and the Linux cluster environments as well;
- (6) with abundant auxiliary tools for data analysis and comparisons, it not only provides a simple way for aerodynamic data extraction (i.e., WiseADC), engineering curve plot (i.e., WiseECG), data statistical analysis (i.e., WiseSAT), and grid convergence analysis (i.e., WiseGCI), but also customizes manifold interfaces in script with general commercial pre- and postprocessors such as ICEM-CFD, Gridgen, Gambi, Tecplot, Ensignt, and VisIt;
- (7) it has a perfect help system, in which not only the help documents related to system operations are available, but also a collection of literatures related to CFD credibility analysis is provided; the collection has collected and collated many important literatures that almost cover each process in CFD verification, validation, prediction, and calibration.

## 4. Future Work and Conclusions

In the present paper, we have outlined some recent efforts for CFD credible simulations in China, whose basic activities are verification and validation in terms of international authority. The aspects of verification and validation must always be addressed with an emphasis on the quantification of the uncertainties due to the model assumptions (either physical or geometrical) and to the numerical and experimental approximations. There are various roadmaps for CFD V&V, but the most regular one is through different workshops. Following similar activities in the West such as ECARP and Drag Prediction Workshops, two successive national workshops for V&V of CFD simulations had been organized by CARD and ACTRI in the past years with intent to assess the state of the art of computational fluid dynamics of China and to identify areas needing additional research and development. And most recently, some following actions have been initiated.

Development of a software platform for performing credibility analysis is a creative idea. The attempt has been tried in ACTRI to develop the WiseCFD platform. The main components of the platform include the Case Library, the graphical user interface for jobs management, the tool for credibility and parameter analysis, and the auxiliary tools for data extraction, analysis, and comparisons, where the Case Library for CFD verification and validation is the kernel for the system. Large amount of experimental data and CFD results have been integrated, which results in a useful validation database similar to that of FLOWNET and QNET-CFD in Europe. Nowadays the WiseCFD platform has integrated several in-house and commercial RANS CFD codes using its PnP integrated strategy. In the near future, it is hoped to involve some more CFD codes with advanced numerical methods such as DES or even LES/DNS for better prediction of flow structures around, for example an aircraft, and also provide the capabilities to perform credibility analysis for such type of solvers.

However, CFD V&V requires much involvement. It's still a long way for China. China should be more involved in international activities. Through these collaborations, it is expected that the West and China can benefit mutually. For example, in connection with the QNET-CFD thematic network, WiseCFD can contribute and enjoy available resources.

## Acknowledgments

This work is supported by the State Key Development Program of Basic Research of China (973) under Grant no. 2009CB723804. The authors would also like to express their acknowledgment for anonymous reviewers for their good comments to enrich this work.

## References

- [1] AIAA-G-077-1998, *Guide for the Verification and Validation of Computational Fluid Dynamics Simulations*, American Institute of Aeronautics and Astronautics, 1998.
- [2] W. Haase, E. Chaput, E. Elsholz, M. A. Leschziner, and U. R. Muller, "ECARP-European computational aerodynamics

- research project: validation of CFD codes and assessment of turbulent models,” *Notes on Numerical Fluid Mechanics*, vol. 58, 1997.
- [3] M. Marini, R. Paoli, F. Grasso, J. Periaux, and J. A. Desideri, “Verification and validation in computational fluid dynamics: the FLOWnet database experience,” *JSME International Journal, Series B*, vol. 45, no. 1, pp. 15–21, 2002.
  - [4] C. Hirsch, “The QNET-CFD project,” *The QNET-CFD Network Newsletter*, vol. 2, no. 4, pp. 4–5, 2004.
  - [5] D. W. Levy, T. Zickuhr, J. Vassberg et al., “Summary of Data from the first AIAA CFD drag prediction workshop,” *AIAA paper 2002-0841*, 2002.
  - [6] M. J. Hemsch and J. H. Morrison, “Statistical analysis of CFD solutions from 2nd Drag prediction workshop,” *AIAA paper 2004-0556*, 2004.
  - [7] <http://aaac.larc.nasa.gov/tsab/cfdlarc/aiaa-dpw/>.
  - [8] C. L. Rumsey, T. B. Gatski, W. L. Sellers 3rd, V. N. Vatsa, and S. A. Viken, “Summary of the 2004 CFD validation workshop on synthetic jets and turbulent separation control,” *AIAA Paper 2004-2217*, 2004.
  - [9] Y. H. Liang, Y. Yang, Z. Zhu et al., “CFD credibility analysis platform WiseCFD,” in *Proceeding of 12th National Computational Fluid Dynamics Conference*, pp. 775–780, Chinese Aeronautics Computation Technique Research Institute, Xian, China, 2004.
  - [10] W. Bai, “Remark on CFD application techniques for aerodynamic design of large civil aircraft,” in *The Application and Development of CFD in Large Civil Aircraft*, G. H. Wu and Y. C. Chen, Eds., 2009.
  - [11] Z. B. Chen and W. Bai, “Special edition for credible Aerodynamic computations,” *Aeronautical Computer Technique*, vol. 32, 2004 (Chinese).
  - [12] J. Q. Wu, Z. L. Fan, Z. He, and Y. J. Wang, “Research on the tests technology at high angles of attack in 2. 4m transonic wind tunnel,” *Experiments and Measurements in Fluid Mechanics*, vol. 18, no. 4, pp. 43–48, 2004 (Chinese).